Australian Acoustical Society

A.C.N. 000 712 658

Acoustics 2000

putting the science and technology to work

Conference Proceedings

Joondalup Resort
Western Australia
15 - 17 November 2000

The Australian Acoutiscal Society (Western Australian Division) is grateful for the generous support of the following companies:

Acoustic & System Sales

Acoustic Research Laboratories Pty Ltd

Adamsson Engineering & Construction Pty Ltd

Alcoa World Alumina Australia

Barclay Engineering

I.N.C. Corporation Pty Ltd

Insulation Solutions

Insulwest

MB & KJ Davidson Pty Ltd

National Commercial Insulation

Nois Air Pty Ltd

Noise and Vibration Measurement Systems Pty Ltd

Pyrotek Pty Ltd

Cover design by ERM Australia

ISBN 1 74052 033 5

Proceedings

AUSTRALIAN ACOUSTICAL SOCIETY

ABN: 53 713 798 177, ACN: 000 712 658

ANNUAL CONFERENCE 2000

Acoustics 2000 Putting the Science and Technology to Work

Joondalup Resort, Western Australia, 15-17 November 2000

Edited by

Terrance Mc Minn and Graeme Yates

ADAMSSON ENGINEERING PTYLTD

Adamsson Engineering is proud to be involved with the Australian Acoustical Society and sponsors of the 2000 annual conference.

GENERAL RANGE OF PRODUCTS & SERVICES.

Architectural Noise Control
Noise and Vibration Control for Industry.

WALL ATTENUATORS.
Acoustic Louvres.
Cross Talk Silencers.

DUCT ATTENUATORS
Cylindrical Attenuators
Type RAS Rectangular Attenuators
Type TS Rectangular Attenuators

DOORS & ENCLOSURES
Range of Acoustic and airtight doors
Timber doors
Steel doors
Frameless Acoustic Enclosures

NOISE &VIBRATION ISOLATION
Range of vibration isolators
Kinetic floating floors and wall isolation

NOISE ABSORPTION
Wall baffle and ceiling panels
Duct lagging & acoustic quilting

SPECIAL PURPOSE EQUIPMENT
Engine silencers. Blow off silencers
Industrial attenuators. Reactive attenuators

Adamsson Engineering Pty Ltd.
7 Hector Street West
Osborne Park WA 6017

P.O. Box 1294
Osborne Park Business Centre
WA 6916

Ph: (08) 9242 7677
Fax: (08) 9242 7678

email: beauadamsson@adamssoneng.com.au
www.adamssoneng.com.au

Dedication

These Proceedings are dedicated to Graeme Yates in recognition of the work he put into the organization of this conference and particularly the organization and formatting of the conference papers. Graeme passed away in October 2000 after a prolonged illness. The Society extends its condolences to his family, colleagues and friends.

Through his role as NHMRC Senior Research Fellow at The Auditory Laboratory, Department of Physiology at The University of Western Australia, Graeme became a world-renowned researcher. He published extensively and achieved a high local, national and international profile. He also achieved high recognition as an educator with influence in post graduate and undergraduate teachings at The University of Western Australia.

Graeme had a deep involvement in acoustics within Australia over many years. He was a founding member of the Western Australian Division of the Australian Acoustical Society in 1971 and maintained close and executive involvement throughout this period. He was a Chairman of the WA Division in 1996 to 97 and Federal President from 1997 to 1999.

To his West Australian colleagues in acoustics he had elder statesman status. Graeme had the unique ability to grasp the science of an acoustic issue and, in a helpful way, discuss and clarify the scientific principles. He will be missed and remembered for many personal attributes but also in his love of acoustics and the way he used his scientific skill to challenge and extend people around him in all fields of acoustics.

ACOUSTICS 2000 Putting the Science and Technology to Work

Contents

Session UW-3 Sonar And Communication Systems

Session AC-4 Acoustics And The Built Environment 1

Session UW-4 Propagation And Geo-Acoustic Inversion 1

Session AC-5 Acoustics And The Built Environment 2

Session UW-5 Sources and Scattering

Session AC-6 Workshop – Active Noise Control

Session UW-6 Marine Bio-Acoustics And Fisheries Acoustics

Session AC-7 Noise Control

Session UW-7 Propagation And Geo-Acoustic Inversion 2

ACOUSTICS - putting the science and technology to work

Conference of the Australian Acoustical Society
Joondalup Resort, Western Australia, 15-17 November 2000

KEYNOTE PAPER

Time-Reversal Acoustics

W.A. Kuperman[1] , W.S. Hodgkiss[1], T. Akal[2], S. Kim[1], G. Edelmann[1] and H.C. Song[1]

[1]Marine Physical Laboratory/SIO and [2]SACLANTCEN Undersea Center

Abstract

Phase conjugation (PC) has been demonstrated in nonlinear optics, laboratory ultrasonics and most recently, in ocean acoustics. PC can be implemented in the time domain by a "time reversal mirror." A brief review of the physics of a TRM is presented. This is followed by a presentation of the results of a set of ocean acoustic experiments in which a TRM was implemented. Applications of the TRM process are discussed.

Introduction

Phase conjugation (PC) is a process that has been first demonstrated in nonlinear optics [1] and then in ultrasonic laboratory acoustic experiments [2], and most recently in ocean acoustics [3]. PC takes advantage of reciprocity, a property of wave propagation in a static medium and a consequence of the invariance of the linear wave equation to time reversal. Therefore, PC in the frequency domain can be implemented in the time domain by a time reversal mirror (TRM) or phase conjugate mirror.

In this paper, we briefly review the physics of a TRM and then present the results from a series of ocean acoustic experiments in which a TRM was implemented. Possible applications are discussed.

Review of TRM

Excellent overview articles on TRM can be found in Refs. 2 and 4. We briefly review the TRM in the context of ocean acoustics.

Figure 1 illustrates the components of a TRM experiment in the ocean. A probe source (PS) indicated by one of the rectangles on the vertical receive array (VRA), sends out a pulse that is received at the source-receive array (SRA). The dispersed signal with all its multipath structure is time reversed and retransmitted by the SRA. The resulting signal multipath structure collapses to a spatial and temporal focus (original PS pulse length) at the original PS position that is co-located in range with the VRA.

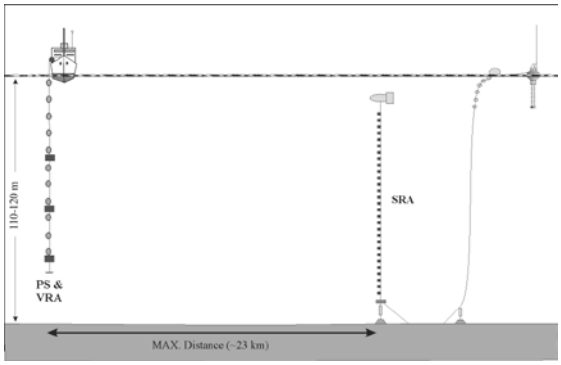

Figure 1. Experimental setup of generic time reversal mirror experiment in the ocean.

The size of the focal region depends on the wavelength and the effective aperture of the SRA which increases due to the waveguide nature of acoustic propagation in the ocean over the free space. Analysis using image methods, including attenuation effects of the ocean bottom, indicates that the diffraction limit on the size of the focal region was reached experimentally [5].

PC or TRM is relevant to the recent trends in acoustic signal processing which have emphasized utilizing knowledge of the environment, e.g., matched field processing (MFP) [6]. However, MFP requires accurate knowledge of the environment along the propagation path. Phase conjugation is an environmentally self-adaptive process that can be applicable to localization and communication in complicated ocean environment. The fact that a TRM both spatially and temporally refocuses energy with the aid of a probe suggests that ocean self-equalization with respect to communication processing is possible [5]. In fact, this self-equalization process was demonstrated experimentally as described below.

TRM experiments in the ocean

We have conducted a series of four ocean acoustic experiments off the west coast of Italy (see Fig. 2). The first two in 1996 and 1997 used a 450 Hz SRA which was hardwired to Formiche Island. These experiments were the first to implement and demonstrate the TRM process in the ocean [3,7,8]. At 450 Hz, focal distances out to 30 km were demonstrated, the multi-day stability of focal region was demonstrated and a new process to

shift the focal range was derived and experimentally confirmed.

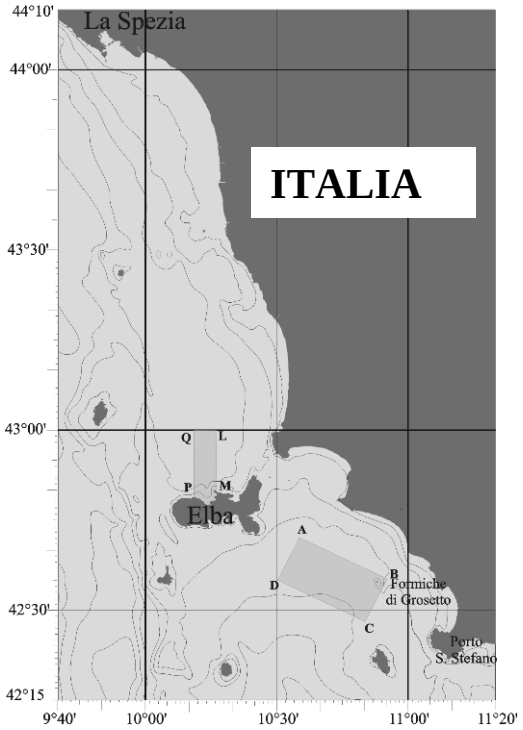

Figure 2. Location of ocean acoustic time reversal mirror experiements off the west cost of Italy.

The third experiment conducted in 1999 used a 3500 Hz array [5]. The SRA was moored and tethered to a remote, self-contained buoy system with all electronics/computers so that it functioned as a node on the local area network (LAN). However, the probe source was not fixed to the VRA so that field measurements were often not obtained at the precise focal position. Focal ranges out to about 15 km were demonstrated (the maximum LAN range at that time). Data in the Formiche and Elba areas with different bottom types were taken and markedly different dispersion characteristics were observed. The totality of the data indicates that both for the 450 Hz and 3500 Hz experiments the diffraction limit on the focal size was achieved. A short communication sequence indicated communication utility, though in this first communication exploration, the quantity of data was insufficient to perform statistical bit error analysis [5]. Finally, an upslope experiment with the SRA in 100 m, PS in 30 m of water at a range of 10 km demonstrated a remarkable focusing ability with 3 dB extent of only 1 m.

The fourth experiment was carried out recently north of Elba in between May 19 and June 13, 2000 using a 3500 Hz SRA. Some of the goals include: 1. To obtain sufficient data to characterize the error rate of the self-equalization undersea process as applicable to undersea acoustic communication. 2. To perform TRM measurements to provide data to begin to explore applications of focused acoustic fields to active sonar concepts. In particular, echo to reverberation enhancement are studied. 3. To measure stability and fluctuation properties of the focused field out to significant ranges in both flat and sloping regions.

Ocean Acoustic Environment

The ocean environment was quite variable throughout the experiment. An example of the spatio-temporal variability is shown in Fig. 3 for 9 CTD sites north of Elba on three consecutive days. There is a very distinct spatial dependence on the profiles. Additional data from oceanographic moorings will provide valuable environmental data set. In addition, hydrosweep bathymetry, seismic profiling, expendable bottom penetrometer (XBP) measurements and cores were taken during the experiment along with acoustic transmission loss (TL) runs.

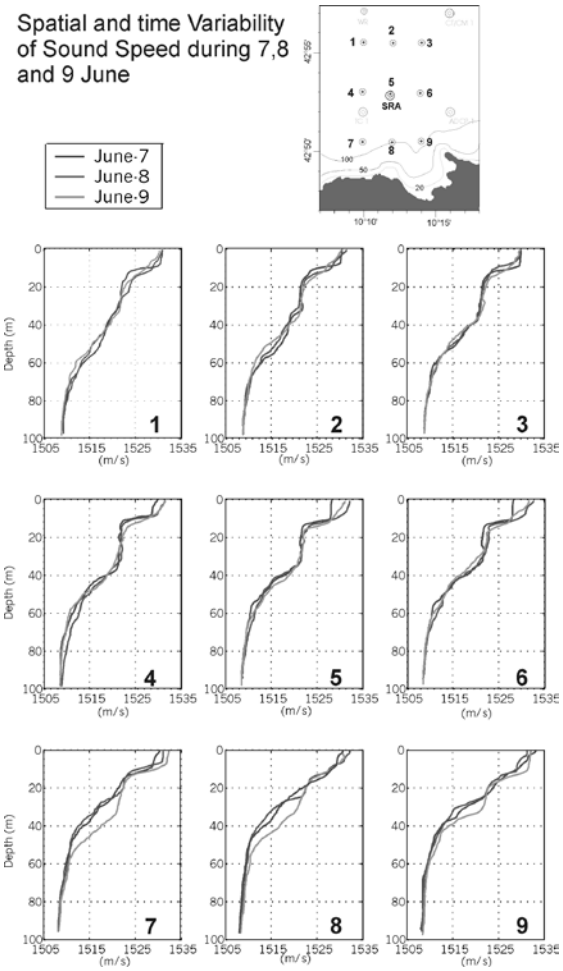

Figure 3. Sound speed profiles on three consecutive days at nine different positions north of Elba derived from CTDs.

Size of the focal region in up-slope environment

The size of the focal region in a range-independent waveguide is analyzed using an image approach in Ref. [5]. Here we extend the analysis to a range-dependent upslope waveguide where extremely sharp focal regions are obtained as shown in Fig. 4.

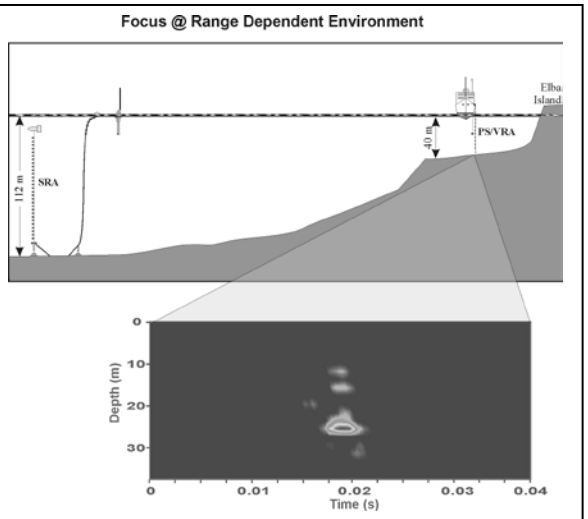

Figure 4. Geometry and data example for the range dependent TRM experiment.

Figure 5 shows measured focal sizes at 3500 Hz for three different environments: the Formiche, flat Elba and sloping Elba areas. Superimposed are the theoretical predictions based on the image approach, which are in good agreements with the measured ones.

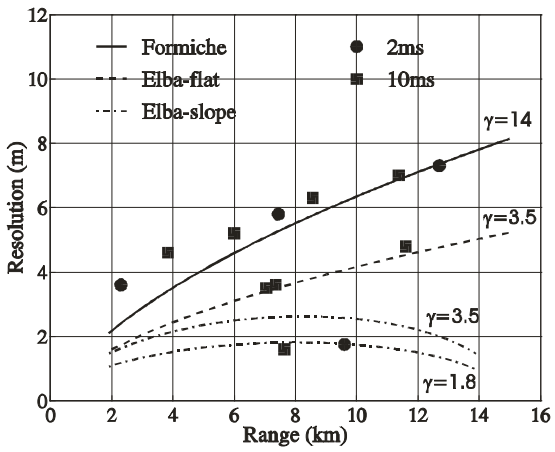

Figure 5. Comparison between the measured vertical focal sizes and the calculated resolution based on the image aperture method with appropriate bottom attenuation for 3500 Hz in three different environments.

The resolution is determined by the effective aperture of the array L_e, i.e., effective angle θ_e which depends on the water depth D, range R, and bottom attenuation. In flat bottom as shown in Fig. 6(a), $\theta_e \approx \sqrt{D/2\gamma R}$ where the factor 2 accounts for two-way propagation and γ is a parameter determined from the bottom characteristics [5]. For a wedge shaped ocean, the effective angle θ_w can be defined as

$$\theta_w \approx \sqrt{DR_0 / 2\gamma R(R - R_0)},$$

where R_0 is the range to the apex and the slope of the bottom is defined as $\alpha \approx D/R_0$ (see Fig. 6(b)). In a wedge ocean, each bounce of sound propagating from a PS to a time reversal array reduces the reflection angle by 2α, decreasing the overall attenuation in the two-way propagation which results in $\theta_w > \theta_e$.

(a)

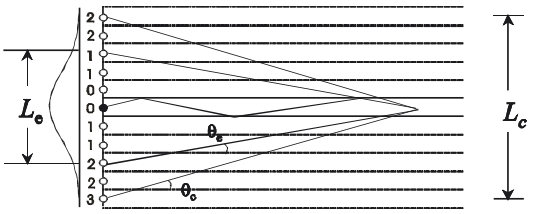

(b)

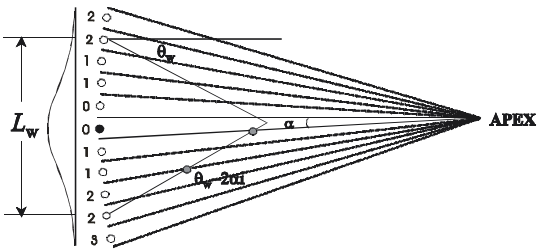

Figure 6: Schematic of image arrays: (a) for Pekeris waveguide and (b) for a sloping environment. The image aperture L_c is determined by the critical angle θ_c of the bottom. The effective aperture L_e is smaller due to attenuation in the ocean bottom that causes the shading of the image sources. In a sloping environment, the grazing angles changes by 2α for each bounce with the bottom which results in a difference in the effective aperture L_w. The labels at the image sources indicate the number of interaction with the bottom.

Self-equalization underwater communications

The communication experiments were performed in the fixed-fixed configuration with both the SRA and VRA operated remotely. A 2-ms CW probe source signal was received at the SRA, time reversed thereby creating the basic symbol for the communication sequence. This TR bit is then copied onto a random sequence (plus and minus ones) to produce a 10 second, 5000 bit coded communication sequence for acosutic transmission to the VRA at a range of 8 km. The communication terminology for this coding is Binary Phase Shift Keying (BPSK). One way broadside and single source control communications experiments were also performed. A subset of the BPSK focused results as received at the VRA is shown in Figure 7 along with broadside and single source control examples. Decoding was done by the synchronized correlator receiver or matched filter as shown in Figure 8. The dot plots on the right are an indication of the robustness of the communication process. With no noise or ocean variability, one would expect only two dots on the real axis at plus and minus one. Preliminary analysis suggests successful decoding with the best results from the time-reversed process. Data were also taken for other types of coding: BPSK, QPSK, 8-PSK and 8-QAM in order to explore the potential for higher bit rate communications.

The communications experiments were also conducted in the upslope range-dependent environment in Fig. 4 where the SRA was operated remotely and the

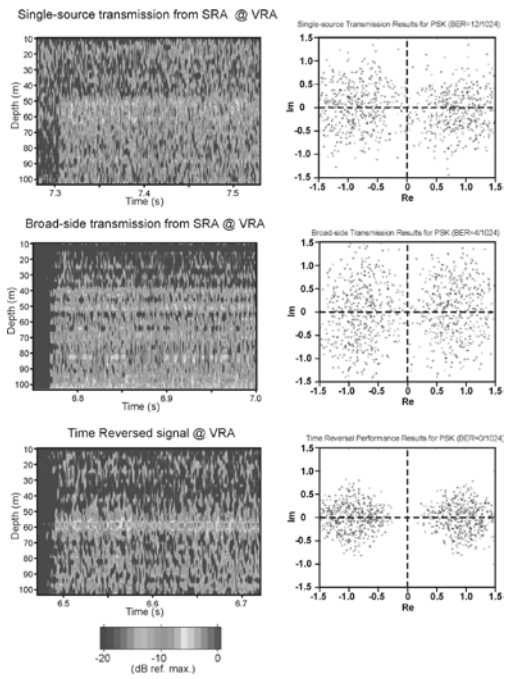

Figure 7. Range-independent: An example of time reversal communication result compared to one-way transmission control examples: single source and broadside. Bit error is denoted by BER.

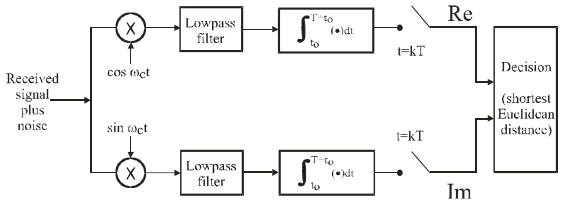

Figure 8. Block diagram of a BPSK decoding system. The received signal and noise is separated into its quadrature components. They are both filtered and passed through a synchronized integrate-and-dump receiver. The output of the receiver, every T=2 ms, is the position of a single bit in the complex plane. The logical decision is the closest Euclidian distance to either ± 1. The original bit was coded with a phase of $\pm 90^\circ$ representing either 1 or 0.

PS/VRA was 9.8 km away in 40-m water. Figure 9 shows again the performance of two-way time reversal communication is better than one-way single source and broadside communications.

Echo to Reverberation enhancement

The main goal was to demonstrate that (bottom) reverberation is minimized from the range where there is a time reversed (TR) produced focus in the water column. For example, Figure 10 shows this effect. The R/V Alliance deployed the probe source at 60-m depth

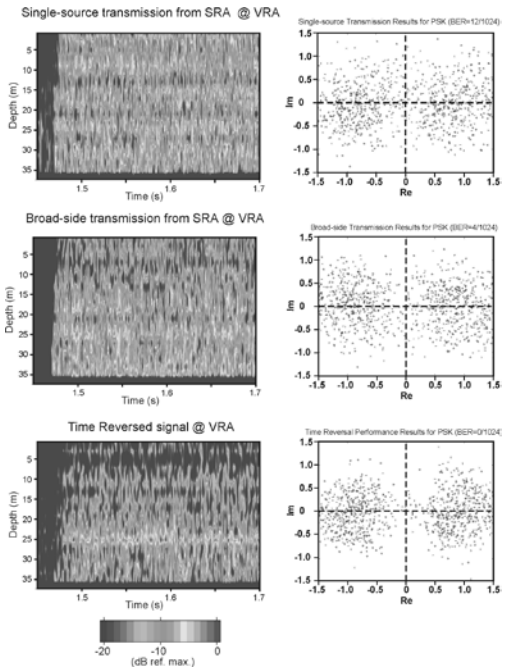

Figure 9. Same as Fig. 7 except in upslope range dependent environment as shown in Fig. 4. The two-way time-reversal communication shows a better performance than one-way single source and broadside communications.

and foci were produced at various ranges, while, at the same time, reverberation from the outgoing time-reversed SRA signal was recorded by the SRA. We see a decrease in the TR reverberation (notch) at that time which corresponds to the TR focus at 1.7 km and 4.7 km range in the example. Single source, monostatic reverberation measurements for cw tones and LFM chirps were also taken. Finally a set of towed probe source runs were made in conjunction with the SRA to determine if we can trace out a path of minimum bottom reverberation return related to the moving focal range.

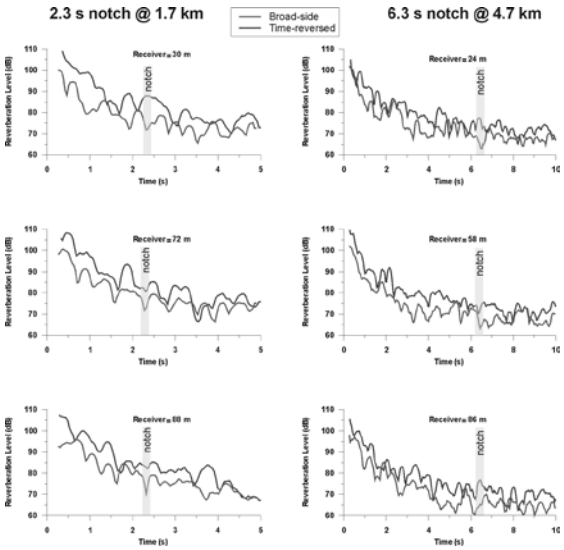

Figure 10. Examples of echo -to-reverberation enhancement compared to reverberation from a broadside transmission. The position of notch indicated the range at which the SRA was focusing.

TR Experiments including a target

An artificial target was deployed from the Manning together with a probe source. It consisted of a 30-m air-filled hose folded 7 times. Figure 11 shows the geometry of one of the experiments and Figure 12 shows bistatic results in which the Manning provided the probe source signal which was time reversed at the SRA, echoed off the target at the Manning with the echo shown being the VRA reception at the Alliance. The broadside control results do not show a target detection.

Conclusions

We have implemented acoustic Time Reversal Mirrors in the ocean which perform as well as they would in an ideal laboratory setting. In particular, the measured focus size was shown to be at the diffraction limit, even for the complex ocean environments in which the experiments were performed. Furthermore, we have demonstrated the potential utility of the time reversal

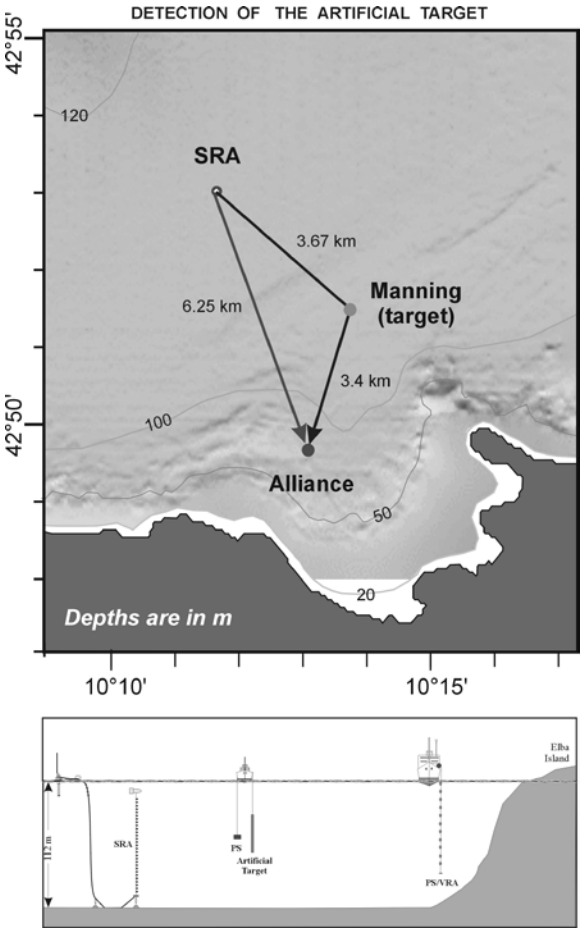

Figure 11. Bistatic scattering, time reversal geometry. Manning had an artificial "fire hose" target and a probe source.

physics when applied to sonar and acoustic communications.

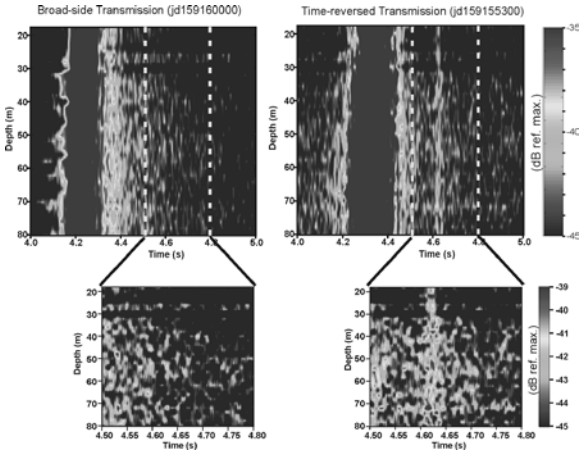

Figure 12. Example of data obtained using the bistatic configuration as shown in Figure 11.

Acknowledgements

This research was supported by the Office of Naval Research, USA.

References

1. B.Y. Zel'dovich, N.F. Pilipetsky, and V.V. Shkunov, *Principles of Phase Conjugation* (Springer-Verlag, Berlin, 1985).

2. M. Fink, Time-reversed Acoustics, *Physics Today*, 34-40 (1997).

3. W.A. Kuperman, W.S. Hodgkiss, H.C. Song, T. Akal, C. Ferla, and D.R. Jackson, Phase conjugation in the ocean: Experimental demonstration of a time reversal mirror, *J. Acoust. Soc. Am.*, 103, 25-40 (1998).

4. M. Fink, Time-reversed Acoustics, *Scientific American*, 91-97 (1999).

5. T. Akal, G. Edelmann, Seongil Kim, W.S. Hodgkiss, W.A. Kuperman, and H.C. Song, Low frequency and high frequency ocean acoustic phase conjugation experiments, 5th ECUA, Lyon, France (2000).

6. A.B. Baggeroer, W.A. Kuperman, and P.N. Mikhalevsky, An overview of matched field methods in ocean acoustics, *IEEE J. Oceanic Eng*., 18, 401-424 (1993).

7. W.S. Hodgkiss, H.C. Song, W.A. Kuperman, T. Akal, C. Ferla, and D.R. Jackson, A long range and variable focus phase conjugation experiment in shallow water, *J. Acoust. Soc. Am*., 105, 1597-1604 (1999).

8. W.A. Kuperman, W.S. Hodgkiss, H.C. Song, P. Gerstoft, P. Roux, T. Akal, C. Ferla, and D.R. Jackson, Ocean acoustic time-reversal mirror, 4th ECUA, Rome, Italy (1998).

ACOUSTICS - putting the science and technology to work

Conference of the Australian Acoustical Society
Joondalup Resort, Western Australia, 15-17 November 2000

Session AC-1 Environmental Noise 1

Continuing The Evaluation Of The American Fhwa Traffic Noise Model In Australia – The Queensland Study

Mark Batstone[1], Stephen Samuels[2]

[1]Environmental Officer, Queensland Department of Main Roads, [2]Director, TEF Consulting and Visiting Research Fellow, UNSW

Abstract

During the last three years two independent, substantial evaluation studies of the American FHWA Traffic Noise Model (TNM) have been undertaken in Victoria and Queensland. The present paper describes the evaluation study undertake in Queensland. This compliments the results presented at the 1999 AAS Conference for the Victorian study. The focus of the Queensland study was on the traffic noise emission source component of the model. Thus it differed somewhat from the Victorian study which concentrated on predictions at building facades. Using scientifically valid procedures, traffic noise measurements and TNM predictions were conducted at 35 sites in and around the South East Queensland area. Overall, the study indicated that TNM is a reasonably good predictive model for the types of Queensland conditions covered in the study. It also identified opportunities to reduce the extent of data collection from the five TNM vehicle categories to two (light and heavy). Further research into the effects of pavement type, especially over the range of chip seal and concrete pavement textures, on the performance of TNM was found to be warranted.

Introduction

Prediction of road traffic noise has traditionally been predicted throughout Australia utilising the L_{10} index, with the well-known UK Method, commonly known as CoRTN, Calculatoin of Road Traffic Noise (UK DoT 1988). This model has already been extensively evaluated and calibrated for Australian conditions (Saunders, Samuels, Leach & Hall 1983). More recently, several alternative indices such as the L_{eq} have been recommended as the basis of performance criteria. The American FHWA Traffic Noise Model (TNM) (Menge et al 1998) is one of the newer methods that has been specifically designed to predict L_{eq} levels. In future, it is expected that TNM will be applied or evaluated by Australian State road authorities for routine traffic noise assessments.

An evaluation study of TNM undertaken recently in Queensland is summarised and discussed in the present paper. This study was undertaken by and on behalf of the Queensland Department of Main Roads (QDMR) (QDMR 2000). The aims and objectives of the study were somewhat comparable to a similar study conducted previously in Victoria for VicRoads (Huybregts and Samuels 1999). However the focus of each of these studies did reflect the nature of the road conditions and noise indices of particular interest to the two State road and traffic authorities involved. While the Victorian study concentrated on predictions at building facades, the primary interest in Queensland was on the traffic noise emission source component of the model.

While the Victorian study had dealt with the L_{eq}(16 hr) for daytime noise assessment and the L_{eq}(8hr) for night time, in Queensland the indices adopted were the L_{eq}(24 hr) and the worst L_{eq}(1hr) between 10PM and 6AM . These particular indices were selected in relation to their likely future use in Queensland, especially in conjunction with evolving traffic noise policies. That different noise indices were involved has little or no significance to the outcomes and conclusions presented herein, since it has been well established that there are strong correlations between these various indices (Brown 1989, Huybregts and Samuels 1998).

The Evaluation Study

Introduction

The Queensland TNM evaluation study was conducted within the framework of an established, empirically based scientific procedure (Saunders et al 1983). It involved the collection of noise, traffic, site and other relevant data at a range of representative sites. From there then predictions of the traffic noise indices were conducted with TNM and compared to the measured values. The difference between each Predicted Noise Index (PNI) and its corresponding Measured Noise Index (MNI) is referred to as the Prediction Difference (PD), which is given by the simple relationship of Equation 1.

$$PD = PNI - MNI \quad (1)$$

To conduct the TNM evaluation study, PD values were determined for the two Traffic Noise Indices involved. Suibsequently and this led to the establishment of PD sub-populations that were utilized for the statistical analyses.

Data Collection and Verification

All together, noise, traffic and related site and other data have been collected at a total of 35 sites in Queensland. Throughout the study all data were collected in accord with the relevant provisions of Standards Australia (1984). In this way data of the highest scientific, technical and quality standards were obtained. Further details of the data collection processes are given in QDMR (2000) and a summary of the range of data obtained appears in Table I.

Table I. Data Summary

Parameter	Core Sites*	Sensitivity Sites*
Number of Sites	21	14
Road types	Freeways Highways Arterials	Freeways Highways Arterials
Pavement types**	DGAC 21 OGAC 0 CS 0 PCC 0	DGAC 4 OGAC 2 CS 6 PCC 2
Traffic speeds(km/h)	70 to 100	70 to 110
Traffic volumes (Veh/day)	6000 to 70000	6000 to 70000
Road/receiver distances(m)	15	15 to 40
Microphone situations	All free field	All free field
Barrier/screening	0 Sites with barriers 21 Sites without barriers	4 Sites with barriers 10Sites without barriers

**Core Sites were those where full 24 hour data were collected, while at Sensitivity Sites only the worst one hour samples were collected between 10PM and 6AM. Given that the data collected for the Core sites also include the worst 1 hour levels, there was some duplication of sites between Core and Sensitivity sites.*

***DGAC = Dense Graded Asphaltic Concrete CS = Chip Seal, or Bituminous Seal*

OGAC = Open Graded Asphaltic Concrete PCC = Portland Cement Concrete

Data analysis

Similar to the Victorian study, a preliminary data analysis was conducted to determine the nature of the overall data population and sub- populations of PDs. This involved examination of any trends apparent in the data and application of goodness of fit tests to find the forms of the data distributions. The overall outcomes of the various goodness-of-fit tests indicated that the data sets could be analysed using methods that assume the data are normally distributed. The results of these preliminary analyses suggested that the Queensland data were of similar quality and type as those of previous studies . These data could, therefore, be analysed subsequently using the well-established techniques of those earlier studies (Huybregts and Samuels, 1999).

Analyses were then carried out on both the Core and Sensitivity Site data collected in Queensland. The ranges of P.Ds were – 3 to + 7 dB(A) and –5to+ 7 dB(A) in the case of the Core and Sensitivity Sites, respectively. All P.Ds determined in the Queensland study are illustrated in Figure 1. It should be noted here that TNM does not include a factor for the chip seal pavement type. Thus, as an interim measure, the

TNM factor for PCC pavement types was adopted as a surrogate for chip seals, on the basis of previous Australian studies on the effects of pavement type on traffic noise (Samuels and Dash 1996). The outcomes of the present study have indicated that this approach resulted in prediction differences similar to those on the other pavements included in the study. This is demonstrated in Figure 1. However it is important to note that this observation only applies to the types and textures of chip seal and PCC pavement surfaces tested. Also it is not yet clear if this outcome is artifact of the modelling processes incorporated in TNM or of some acoustic similarity between these two types of pavements included in the present study. Resolving this uncertainty is an issue worthy of future investigation.

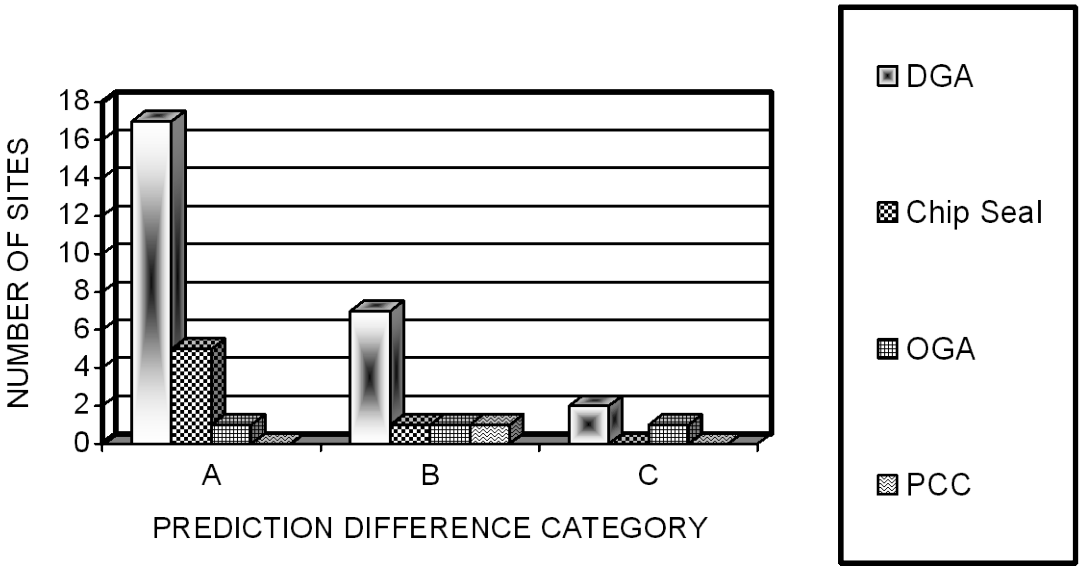

Prediction Difference Categories A, B and C correspond to Prediction Differences of ±- 0-2, 2-5, 5-7 dB(A) respectively.

Figure 1. Prediction Differences determined in the Queensland study

Due to space limitations, two other aspects of the statistical analyses are not covered in detail herein. These concern the nature of the traffic noise source lines for two-lane, two-way roads and the vehicle traffic classifications assigned within TNM (QDMR 2000). Under the site and traffic conditions covered in the Queensland study, it was found to be acceptable to apply the UK DoT(1988) approach for a two-lane, two-way roadway of considering it as a single line noise source. Similarly, the UK DoT(1988) approach of classifying traffic into just two categories of light/passenger and heavy/commercial vehicles was also found satisfactory for TNM modelling. Future application of these two outcomes could significantly reduce the costs incurred by Road and Traffic Authorities in collecting the data required for traffic noise modelling work. There was felt to be a need for further research into these issues, particularly as far as undertaking traffic noise predictions with TNM on Australian pavements is concerned. For this reason the possible relationship between PD and pavement type was not explored further in the present study.

Results

The distributions of the Prediction Differences were quantified in terms of their means and standard deviations. These are presented in Table II, along with the corresponding results from the Victorian study (Huybregts and Samuels 1999). It is apparent that similar results were obtained in both studies of TNM. Including it in future predictions as part of a so-called correction factor for each relevant State (Saunders et al 1983) can compensate for the mean Prediction Difference. Thus it is not a measure of the accuracy of a prediction method. On the other hand, the standard deviation does provide useful measure of accuracy. Results shown in Table II may be interpreted as indicating that TNM performed well in predicting L_{eq} traffic noise levels at those sites and under the conditions of the present studies.

In considering the applications of what appears in Table II, it is important to note one key difference between the two studies. In Victoria all measurements and predictions were conducted at the facades of buildings, the majority of which were residences. However in Queensland free field conditions were adopted throughout. Since TNM, unlike the UK Method, does not include a façade reflection parameter, the Victorian results for the TNM mean P.Ds might be deemed to incorporate this factor. Such is not the case for the Queensland results.

Table II. Prediction Differences (dB(A))

	Victorian Results		Queensland Results	
	L_{eq}(16hr)	L_{eq}(8hr)	L_{eq}(24hr)	L_{eq}(1hr)
Mean	0.6	-1.4	1.0	- 0.4
Std Dev	1.9	2.5	2.3	2.6

Conclusions And Recommendations

The performance of TNM was evaluated in Queensland using a well-established, rigorous, empirically and statistically based methodology. On the basis of this study, as summarised in the present paper, the following conclusions have been drawn.

- TNM performed well in predicting traffic noise levels at the types of sites and under the conditions covered by the study. The results are summarized in Table II above.

- Comparisons of the results of the present study with those from a similar study conducted previously in Victoria indicated that the performance of TNM in Queensland was comparable to that determined in Victoria.

- At sites with chip seal pavements where the TNM factor for PCC pavements was adopted as a surrogate, prediction differences similar to those on the other pavements included in the study ensued. The reasons for this outcome are not yet clear.

- Under the various conditions of the present study, the following adaptations to TNM appeared to be generally satisfactory.

    1) Combination of the five TNM vehicle classification groupings to two (being light and heavy vehicles).

    2) Modelling of a two-lane, two-way road as a single line noise source.

Furthermore, the following recommendation has been made.

- The effects of pavement type, especially chip seals, on the performance of TNM be investigated further.

References

BROWN, A.L.(1989). Some simple transformations for road traffic noise scales. Australian Road Research, Vol.8, No.4, pp 309-312.

HUYBREGTS,C.P. and SAMUELS,S.E.(1998). New relationships between L_{10} and L_{eq} for road traffic noise. Proc. Internoise 98, Auckland, New Zealand.

(1999). Evaluating the American Traffic Noise Model in Melbourne.

Proc. An. Conf. Aust. Acoustical Soc., pp07-104. AAS, Victoria.

MENGE,C.W., ROSSANO,C.F., ANDERSON,G.S. and BAJDEK,C,J.(1998). FHWA traffic noise model – Version 1.0 technical manual. Report FHWA-PD-96-010. FHWA, Washington, DC, USA.

NEILSEN,H.L.(1996). Road traffic noise – Nordic prediction method. TemaNord 1996:525. Nordic Council of Ministers, Copenhagen, Denmark.

QUEENSLAND DEPARTMENT OF MAIN ROADS (2000). Evaluation of TNM in Queensland. Report G99ED1, QDMR, Brisbane.

SAMUELS, S.E. and DASH, D. (1996). Development of low noise pavement surfaces in Australia. Proc PIARC 3rd International Symposium on surface characteristics, Christchurch, New Zealand.

SAUNDERS,R.E., SAMUELS,S.E., LEACH,R. and HALL,A. (1983). An evaluation of the UK DoE traffic noise prediction method. Australian Road Research Board Research Report 122. ARRB, Vermont South, Victoria.

STANDARDS AUSTRALIA (1984). Acoustics – Methods for the measurement of road traffic noise: AS 2072. Australian Standards Association, Homebush, NSW.

UK DEPARTMENT of TRANSPORT (1988). The calculation of road traffic noise. HMSO, London, UK.

Factors Affecting Community Response to Noise

Graeme E Harding F.A.A.S., M.A.S.A., M.I.I.A.V.

Abstract

Planners, governments and regulatory bodies, with advice from environmental bodies, strive to determine and apply noise limits to aircraft noise, road traffic noise, train noise, noise from industry, noise from places of entertainment, car race tracks, shooting ranges, etcetera, etcetera; based on studies of acceptability of the noise intrusion of populations long exposed to the noise source being considered. Despite the best efforts of these bodies, substantial groups or whole communities will sometimes react vigorously to noise from new developments apparantly no different to that long accepted by other people or communities. From over forty years of study and consideration by the author, qualitative moderating factors that need to be considered to better judge likely community reaction to new developments are suggested and discussed in this paper.

Differences in Noise Sensitivity Exist to be Studied and Used in Planning

Contrary to what might be expected, there are real differences in the sensitivity to noise of different communities. The different sensitivity of the communities means that one community exposed to a noise is hardly disturbed or worried about the noise, whilst another community reacts to the same noise with vigour, anger, publicity, law suites etc.

Acknowledging and studying the factors indicating differences or causing differences in noise sensitivity can allow an anticipation of the likely reaction of a community to the potential introduction of a noise. In turn, the likely reaction to a potential noise can be incorporated into and be part of planning that could avoid widespread adverse reaction or even condemnation.

Communities; can mean as little as a few houses across the river; or can mean several suburbs of a city.

In the eastern states of Australia there have been several examples of great surprise by governments and authorities as a result of vigorous and vociferous community reaction to the noise introduced by new transport routes, or new industry zoning. The most notable examples might be the change in runways and flight routes associated with Sydney Airport, and the extension of the Eastern Freeway in Melbourne.

The cause of these planning errors is the assumption that all people are equal, and that as a consequence all communities are equally sensitive to noise. The reality is that people are diverse, even in respect to response to various noises. Just as some people will choose to go to an orchestral concert, whilst others will choose to go to a rock concert; so too are some people highly affected by say train noise whilst others are not, and consciously or unconsciously this results in selection of place of residence.

The result of this natural selection of residential area, and acclimatisation, is that one community can be much more sensitive to a particular form of potentially intruding noise than another community.

The result of this evolution of residential areas was clearly shown twenty years ago by the studies of Andy Hede and Bob Bullen in their survey of community reaction to aircraft noise. Melbourne had recently established a new airport and there had not been enough time for the communities to fully evolve, with the paradoxical result that the regression line for community response to the aircraft noise showed that those Melbourne communities receiving high levels of aircraft noise were less disturbed by the noise than those receiving lower noise levels.

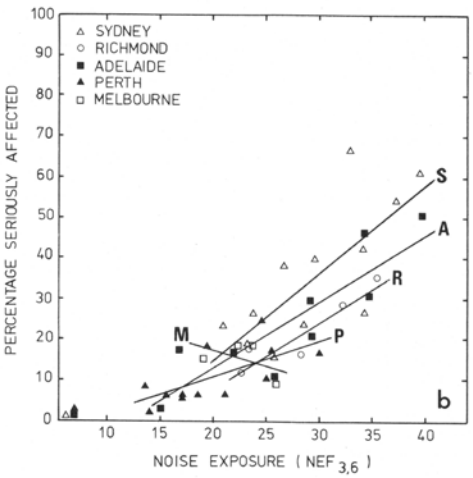

FIGURE 9.1 Dose/response functions for standard NEF (a) and revised NEF (b) with separate regression lines for each airport.

AS the new airport was fairly close to the old airport, a high proportion of residents exposed to higher noise levels were, through acclimatisation or residential selection, less sensitive to noise from the new airport than residents in semi-rural areas newly exposed to quite low levels of aircraft noise. The reverse gradient for percentage seriously affected as a function of noise exposure is clearly shown in figure 9.1 in reference 1. Figure 9.1b is reproduced above.

Factors Considered

Not considered in this paper are individual or personal factors, including age, gender, education level, occupational status and the like. The following are considered:

- Acclimatisation, or Sensitisation of individuals to the potentially intrusive noise
- Changing Values
- Perceived Necessity and Community Benefit versus Private Gain
- Dependency on the industry that is the Noise Source
- Fear Associated with the Noise Source
- Pride in, and Protection of the Home and Family
- Perceived Ease of Control
- Priority of Establishment
- Time of day
- Character of the intruding noise - signal to noise ratio

Acclimatisation, or Sensitisation of individuals to the potentially intrusive noise

If the noise intrusion is moderate so that, whilst ever present, life is only marginally disturbed, many people will become acclimatised and inured to the noise; whilst others exposed to the same noise climate will become sensitised to the noise and unable to tolerate it. Examples of sensitisation can be seen in the domestic life of a household when young son plays raucous "music" which is suffered for a while by a parent (trying to concentrate and prepare a tax return); then can be stood not one second more.

Acoustical consultants are accustomed to telephone calls from a couple who have just moved from a quiet suburban house to a new inner city apartment. The people phone saying they have been in their nice new apartment for one, two, four or whatever weeks and cannot sleep at night. They seek to retain the services of an acoustical consultant to reduce the traffic noise ingress. If they have only been in their new apartment for a week or so, it is suggested that rather than paying consulting fees they wait a month, as they may become acclimatised to the noise. Occasionally the couple will phone back within a week saying they have had enough, and could they be advised of the potential for effective noise control. Conversely the people may be phoned a month or so after their first contact, to find that they now advise that the traffic noise is not as disturbing as before. These latter people have become acclimatised to the noise.

Discussions with people living alongside railway lines is enlightening; the residents will tell you that the train noise does not worry them; some positively like the train noise! Many note that visitors ask "How on earth do you put up with that noise?". When I visit my daughter's place I hear the nearby level crossing bells which she does not hear. Similarly in houses with chiming clocks, visitors will have disturbed nights because of the clock's striking and chiming, yet the residents are undisturbed.

Many other examples will be known to readers of this divergent response of people to potentially intrusive noise.

Changing Values

In the late 1960's the Post Master General's department aimed to provide stand-by generator sets for telephone exchanges throughout Australia, and I was involved in designing a range of standardised installations of different sizes ranging from 15kVA for rural exchanges to 175kVA for towns and suburbs. I designed the noise

control mechanisms on the basis of achieving typical environmental background noise levels in relevant 1/1 octave bands, being particularly conscious of the fact that in the typical country town the post office was between the bush nursing hospital and the police station which would not want their operations disturbed by noise.

I was right and wrong. As the generator sets were installed and started to operate I was accused of "over-design", as the local residents could not properly hear the generator sets start up over the noise of the storm that caused a power failure! Within ten years the reliability of the generator sets was established, and when residents were questioned they thought the generator sets were "not too noisy".

Perceived Necessity and Community Benefit versus Private Gain

People clearly distinguished between noise arising from a person or organisation's private gain; and that arising from an unavoidable noise source for community good.

People do not suffer lightly the noise which benefits one person or a select group at the expense of others, but will tolerate surprisingly high noise levels for the community good.

There are many disturbing noise sources that are accepted by the community as necessary, unavoidable, and for the community benefit; such as neighbours mowing their lawns, the council mowing the football oval, the collection of rubbish, etc. etc.

This is best illustrated by what I learnt early in my life; namely, that noise which was perfectly acceptable when from a generator set at a hospital, could be absolutely unacceptable to the community when from a generator set at the factory of an international cigarette manufacturer.

Another example comes from the Myer Music Bowl in Melbourne which is used for concerts for the young people. The bands have regularly complained of the restrictions on the frequency of concerts, and in particular of complaints of excessive disturbance made by the Prince Henry's Hospital; when the hospital never complained about the annual Christmas "Carols by Candlelight"! Carols by Candlelight aims to appeal to young people as well as old and so is not as different in character as may be surmised; the difference in the reaction of the hospital staff and patients is thus related to the connotation of community good of an event broadcast round the world.

Dependency on the industry that is the Noise Source

Many a small town depends for its livelihood upon its own local industry, and the noise from some of these industries is horrendous. On one occasion I had to measure the boundary noise of a country industry, and was proposing to measure the noise after hours so as to be free of the noise of the delivery semi-trailers. The manager could not understand; and at one point in our conversation said "Why can't you measure the factory noise on the footpath with the trucks going past?". He was quite right, the trucks made no significant contribution to the noise on the street boundary which was dominated by the industry noise. The school teacher approached me, and for our joint information I measured the industry noise at his house, one or two kilometre from the industry at the other end of the town. Again; the industry noise could easily be measured notwithstanding other background noises. Before I left the town I checked with the shire engineer in the somewhat noisy shire offices, and learnt that they had no trouble with the industry!

The above scene is repeated in every small sawmill town and large towns with manufacturing industry throughout Australia.

Fear Associated with the Noise Source

The effect of fear of aircraft crashes by residents living near airports on their judgement of aircraft noise intrusion is well established, see for example references 2 and 5. What I have found in work associated with highway up-grades and freeways, is that residents living near bends and similar physical features of the highway are much more likely to volunteer both their fear of a truck coming through the front room and the disturbing noise of the trucks. More than one such person has volunteered words such as "with trucks it is not like trains that have to stay on the rails".

Obviously in the case of significant road works it is possible to alter cross-falls on bends, provide protective rail guards and similarly, to alleviate residents anxiety and reduce their concentration on traffic noise and consequently expressed annoyance.

Pride in, and Protection of the Home and Family

Streets in a suburb, and suburbs in a city differ in the pride the home owners' have of their area. The greater the pride, the greater the efforts that residents, individually and collectively, will go to protecting their environment. The difference between areas of high pride in house and home; and areas where presumedly there is greater pride in football teams can best be dis-

cerned by walking along the streets and observing the standard of house and garden maintenance. The nature strips, gardens and homes that show most loving care will be the ones for whom the people will fight to protect against intrusions of all sorts, including noise.

Protection of one's home and family also includes not only the protection of the environment in which the family live, but also importantly the future through depreciation of the value of the home.

That the value of homes really does change significantly was brought home to me when courteously asking the real estate agent who buys his milk and paper at the milk bar at the same time as I do; how business was. He replied that since the freeway had extended to our area, sales and prices had risen magnificently.

Perceived Ease of Control

Some noise sources, such as steam blow-offs every day, are correctly perceived by the community as localised noise sources that are easily controlled; and hence are unacceptable. By contrast people rationalise that the noise intrusion of the neighbour's lawn mowing is not preventable, and hence is accepted; however if silent laser lawn mowers cost only $200.00 we could expect motor mower use to be initially restricted, and ultimately forbidden to be used.

The moral of this aspect is that the community has a collective intelligence which recognises what can reasonably be expected in the way of noise control.

Neither the community nor industry are infallible, and sometimes they get it wrong and think that in this scientific age it would be easy for a wealthy oil company to control the noise of their refinery so as to reduce the noise intrusion into the community. One oil refinery that I worked with for tens of months was spending about 1M$/dB for the first few decibel and were aiming for 15dB noise reduction if possible.

I know of many industries that have incorporated all practical noise control to the point where they would do no more. When the community actually appreciates that all had been done that could be done, then in every instance the community accepted the situation.

Priority of Establishment

The general assumption by both the residential community, and commerce and industry, is that the first-comer to the area has first rights. Thus if an industry builds near an established residential area, it is regarded by residents as unfair, and certainly considered that the industry should not be permitted to detract from the amenity of the residential area in any way. Conversely, if the industry is established first, then the general resident acknowledges that the industry has "first right".

None of the above, so far as I know is recognised at law in Australia. Certainly in Victoria, the legal situation is that it takes only one house to require an industry to abate its noise; and in many instances the effect can be to close the industry down. The situation is aggravated by an almost total lack of planning for noise isolation.

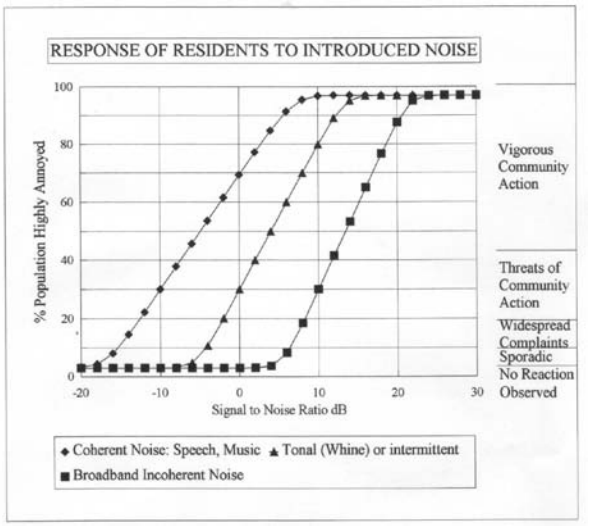

Time of day

Many industries know when it is safe to operate; they start after the proverbial; "man of the house" has departed for work; with cessation being before he arrives back home. The result is that ninety percent of the residences have no residents when the industry operates. The remnant few residents exposed to the intrusive noise during the day find they cannot get support for concerted action.

This technique has allowed more than one industry with really intrusive noise to continue to operate against murmuring complaints for years. The operations of these industries only become known to consultants or authorities when they depart from their regular and restricted routine. One example was a manufacturer of plastic agricultural pipe that was practically forced to increase production during a long, severe drought. Once supported complaints had been made to the EPA they found they had extensive and expensive noise control work to be done; more than they could afford.

Character of the Intruding Noise - Signal to Noise Ratio

That the degree of intrusion into community life of noise from transport, industry, sport and entertainment

is dependant on the character and magnitude of the potentially intruding noise is well known.

Some sounds are specifically designed or selected to attract the attention of people; such as telephone bells, reversing beepers, burgular alarms, level crossing bells etcetera. When heard by other than their intended audience these noise sources are highly intrusive, much more disturbing or intrusive than a bland characterless noise. The defining feature in this regard is that the noises are both tonal and intermittent.

Various attempts have been made to set a relationship between noise level and community response. Without taking into account both the character and the background noise level any attempt will fail to model the sought after relationship. Implicit in all such models is the assumption that the potentially annoying noise is unwanted; without such an assumption the model may predict that Beethoven's Pastoral Symphony should be in-audible.

The figure below shows the author's attempt to incorporate both the character of the noise and the level of the potentially intruding noise relative to the background noise.

This figure was prepared seven years ago, and it has proven to be valuable to illustrate the concepts.

Planners and politicians can readily see that there is a remnant proportion of all populations that always respond as highly annoyed, and another remnant proportion of all populations that never respond as highly annoyed; in the figure both remnants are set as 3%.

Planners and politicians also readily see that just 10% of the citizens of a suburb makes thousands of objectors or voters.

As the graph also shows, the annoyance potential of the an intruding noise is very dependant on the character of the noise. Whilst the graph gives an idea of this dependance, there are certain spectral and dynamic assumptions built into the graph; for example it allows for the normal dynamic range and spectral distribution of speech and music with the result that even with a signal to noise ratio of -10dB there is speech intelligibility and the music tune can be followed. The graph also allows one to show that when road traffic is near a receiver and has the high variability of discrete vehicles, then it should be treated as “Intermittent”, whilst distant traffic with its steady atonal character is treated as "Broadband incoherent noise".

Summary

There is a body of information that planners and authorities can use to better understand acoustical planning and hence better plan buffer zones, noise controls and separation of residential areas from highways, freeways, aerodromes, flight paths, and industry.

The two important factors may be summarised as:

> Firstly; that through evolution of the residential communities there are real differences in the perception of potentially intruding noise from community to community so that what is unnoticed by one community is intolerable by another community.
>
> Secondly; that community reaction to intruding noise depends upon quality factors discussed in this paper that may be qualitatively assessed.

References and Bibliography

1. Andrew HEDE and Robert BULLEN (**1982**) "Aircraft Noise in Australia: A Survey of Community Reaction" N.A.L. Report No. 88

2. Henk M. E. MIEDEMA and Henk VOS (**1999**) "Demographic and Attitudinal Factors that Modify Annoyance from Transport Noise" J. Acoust. Soc. Am. **105** (6) 3336 - 3344

3. Annon "Assessment of Noise with respect to Community Response" ISO/R 1996-1971

4. Leo L. BERANEK (**1954**) "Acoustics" "Criteria for Residential Areas" pages 421 to 423 McGraw-Hill Book Company

5. J. S. BRADLEY (**1993**) "Disturbances Caused by Residential Air Conditioner Noise" J. Acoust. Soc. Am. **93** (4) Pt 1 1978 - 1986

6. James M FIELDS (**1993**) "Effect of Personal and Situational Variables on Noise Annoyance" J. Acoust. Soc. Am. **93** (5) 2753 – 2763

7. James M FIELDS (**1998**) "Reactions to Environmental Noise in an Ambient Noise Context in Residential Areas" J. Acoust. Soc. Am. **104** (4) 2245 - 2260

8. Henk M. E. MIEDEMA, Henk VOS and Ronald G de JONG (**2000**) "Community Reaction to Aircraft Noise: Time-of-Day Penalty and Tradeoff between Levels of Overflights" J. Acoust. Soc. Am. **107** (6) 3245 - 3253

9. Karl Theodor KALVERAM, Joachim WIERMERS and Joachim VOGT (**1999**) "Relationship between Physical Noise Level, Experienced Annoyance, and Physiological Reaction"

Sixth International Congress on Sound and Vibration 1441 - 1446

10. J. HATFIELD, R.F.S. JOB, P. PEPLOE, N.L. CARTER, R. TAYLOR and S MORRELL "Demographic Variables may have a Greater Modifying Effect on Reaction to Noise When Exposure Changes" Noise Effects 98 527 – 530

11. R.F.S. JOB, J. HATFIELD, P. PEPLOE, N. L. CARTER, R. TAYLOR and S MORRELL "Negative Attitudes to Noise Exposure have a Pure Modifying Effect on Noise Reaction" Noise Effects 98 632 - 634

A New Countermeasure Method for Wind-induced Noise with use of Wide-sense Digital Filter in the Hierarchical Form and Its Field Experiments

Kazutatsu Hatakeyama[1] and Mitsuo Ohta[2]

[1]Kinki University, [2]Honorary Professor of Hiroshima University

Abstract

A wind-induced noise influenced the acoustic measurements in the outdoor environment especially in the measurement of low frequency acoustic signals. In this paper, a new trial of dynamical countermeasure method for the wind-induced noise will be proposed from two different viewpoints. The first method is proposed by considering the effective usage of the successive information of wind velocities. By expanding the multivariate moment generating functions in the statistically orthogonalized series form, the generalized multi-variate regression model of the wind-induced noise on the wind velocisies and the dynamical computer-aided algorithm for estimating the unknown acoustic signals will be newly derived. The second method is proposed by considering the arbitrary probability distribution forms of wind-induced noise and acoustic signals. That is, by introducing the inverse Gaussian distribution function and hierarchically expanding the joint probability function on wind-induced noise and wind velocity, the generalized regression model for predicting statistically the wind-induced noise based on wind velocity will be proposed, and then the dynamical algorithm for detecting the acoustic signals will be proposed from Bayesian viewpoint. Finally, the effectiveness of both methods will be experimentally confirmed.

1. Introduction

When measuring the acoustic signals in the outdoor environment, it is difficult to evaluate correctly the acoustic environment because the observed data are usually contaminated by the random background noise. One of these background noises is the wind-induced noise. The wind-induced noise fluctuates randomly owing to the temporal changes of wind velocity at the observation point and shows arbitrary probability distribution forms of non-Gaussian type. It is necessary to establish some systematic countermeasure methods for the wind-induced noise especially when measuring the low frequency acoustic signals, because the wind-induced noise includes many components in a low frequency range and most of their effects can not be reduced with use of the usual methods (such as the usage of wind screen and others). The physical mechanism of wind-induced noise is not known and the stationary property of wind-induced noise can not be assumed. Thus it is difficult to derive the countermeasure method for the wind-induced noise.

Here, we will pay our attention to the fact that the wind-induced noise is generated from the temporal change of wind velocity, which can be measured separately when observing the acoustic data. The wind velocity changes relatively slower than the changes of the wind-induced noise and, in addition to the amplitude of wind velocities, the wind direction is also important. Then, for predicting the whole probability form of wind-induced noise, we should solve the problems that how to consider the time (or directional) characteristics of them and how to consider the non-Gaussian property of them. From the first viewpoint, we should observe the velocities in different times and/or positions, and consider the multiple correlations between the wind-induced noise and these velocities. Then we should construct the systematic prediction algorithm with use of these data. From the second viewpoint, the general framework was indroduced newly in analizing the level fluctuations.

In this paper, from the above viewpoint, a new trial of dynamical countermeasure method for the wind-induced noise will be proposed from two different viewpoints. That is, the countermeasure methods based on the information on the time fluctuation of wind-induced noise and on the level fluctuation of the noise will be proposed.

The first method will be proposed by considering how to use effectively the successive information of wind velocities. In order to detect various correlation of the wind-induced noise with the wind velocities, we first consider the set of wind velocities (the data of wind velocities at the present time and at the past time, and/or in many directions and positions). Then, we will expand the multivariate moment generation function hierarchically and derive the multi-variate form of generalized regression model of the wind-induced noise on the set of wind velocities. Next, by predicting

various statistics of the wind-induced noise with use of the set of wind velocities recursively, we can evaluate the true acoustic signals dynamically which are embedded under the wind-induced noise. The predicted statistics of wind-induced noise can be reflected hierarchically into each expansion coefficient of signal detection algorithm.

The second method will be proposed by considering the arbitrariness of level fluctuation of wind-induced noise. When studying the stochastic systems, Wiener process and its related statistical properties are fundamentally important from the theoretical viewpoint. The probability distribution of the first-passage-time of this process is expressed by the inverse Gaussian distribution function, which has the flexibility of expressing widely various type probability distribution forms of symmetrical and non-symmetrical types[1]. Based on this fact, many researches had been carried out especially in the fields of biology, the diffusion process, queuing systems and others [2]. Then, after deriving newly the orthogonal polynomials associated with inverse Gaussian distribution function, the generalized regression model for predicting the wind-induced noise based on wind velocity will be proposed by expanding orthogonally the joint probability function. Each expansion coefficient reflects hierarchically the lower and higher order statistics of phenomena. Then, by expanding Bayes' theorem hierarchically with use of the inverse Gaussian distribution function and its associated orthogonal polynomials, a computer-aided algorithm for estimating the unknown state of energy stochastic systems under random measurement and wind-induce noises will be newly established. The predicted statistics of wind-induced noise can be reflected hierarchically into each expansion coefficient of signal detection algorithm.

Finally, the experimental confirmation of the proposed methods has been confirmed by applying it to the actual data of field measurement.

2. Theoretical Considerations

2-1 Generalized Multi-variate Regression Model of Wind- induced Noise on Wind Velocities

In order to utilise the previous results, we will firstly consider the averaged relationship between a wind noise v_k and a wind velocity u_k^2 (power) :

$$v_k = \tau \cdot u_k^2, \tag{1}$$

where n: a priori known integer, and τ : known proportional constant. But the temporal changes of a wind noise can not be explained only with use of the averaged relationship in Eq.(1). Then, we will consider the deviations from the averaged relationship :

$$\varepsilon_k = v_k - \tau \cdot u_k^2. \tag{2}$$

Then, we will detect and utilise the correlation information embedded under ε_k as much as possible, by using the information on the wind velocities powers. Here, we consider the m observations of wind velocities $u_{1k}^2, u_{2k}^2, \cdots, u_{mk}^2$ (u_{1k}^2 is the present velocity $u_{1k}^2 = u_k^2$) at the different time stages or positions. In the case when using the time sequence of wind velocities, $u_{1k}^2 = u_k^2, u_{2k}^2 = u_{k-1}^2, \cdots, u_{m-1k}^2 = u_{k-m+2}^2$ and $u_{mk}^2 = u_{k-m+1}^2$. From the viewpoint of grasping the whole probability form of the deviations of a wind-induced noise without minimum information losses, the joint probability function $P(\varepsilon_k, u_{1k}^2, u_{2k}^2, \cdots, u_{mk}^2)$ should be considered.

By introducing the joint characteristic function $M(\theta, \theta_1, \theta_2, \cdots, \theta_m)$ associated with the joint probability function on wind-induced noise and wind velocities, the hierarchically expanded joint characteristic function can be obtained as :

$$\begin{aligned}
&M(\theta, \theta_1, \theta_2, \cdots, \theta_m) \\
&\equiv < \exp\{\varepsilon_k \theta + u_{1k}^2 \theta_1 + \cdots + u_{mk}^2 \theta_m\} > \\
&= \exp\{\sum_{i+i_1+\cdots+i_m=1}^{\infty} \kappa_{i,i_1,\cdots,i_m} \theta^i \theta_1^{i_1} \cdots \theta_m^{i_m}\} \\
&= \exp\{\kappa_{0,1,\cdots,0} \theta_1 + \kappa_{0,2,\cdots,0} \theta_1^2 / 2\} \cdots \\
&\quad \bullet \exp\{\kappa_{0,0,\cdots,0,1} \theta_m + \kappa_{0,0,\cdots,0,2} \theta_m^2 / 2\} \\
&\quad \bullet \sum_{i_1+\cdots+i_m=0}^{\infty} g_{i_1,\cdots,i_m}(\theta) \theta_1^{i_1} \cdots \theta_m^{i_m} \\
&\quad \bullet /(i_1! \cdots i_m!),
\end{aligned} \tag{3}$$

where $\kappa_{i,i_1,\cdots,i_m}$ denotes the $(i, i_1, \cdots, i_m)$-th joint cummulant of the wind noise and the wind velocities :

$$\kappa_{0,\cdots,0,1,0,\cdots,0} = < u_{ik}^2 >, \tag{4}$$

$$\kappa_{0,\cdots,0,2,0,\cdots,0} = < (u_{ik}^2 - < u_{ik}^2 >)^2 >, \tag{5}$$

$$\begin{aligned}
&g_{i_1,\cdots,i_m}(\theta) \\
&= \frac{\partial^{i_1+i_2+\cdots+i_m}}{\partial \theta_1^{i_1} \partial \theta_2^{i_2} \cdots \partial \theta_m^{i_m}} \sum_{\substack{i+i_1+i_2+\cdots+i_m=1 \\ i_1,i_2,\cdots,i_m>2}}^{\infty} \\
&\quad \exp\{\kappa_{i,i_1,i_2,\cdots,i_m} \theta_1^{i_1} \theta_2^{i_2} \cdots \theta_m^{i_m}\} |_{\theta_j=0}.
\end{aligned} \tag{6}$$

The correlation information among the wind noise and the wind velocities can be reflected in each expansion coefficient hierarchically.

The characteristic function on a deviation ε_k conditioned by the set of wind velocities $u_{1k}^2, u_{2k}^2, \cdots, u_{mk}^2$ is defined as follows :

$$M(\theta) = < \exp\{\varepsilon_k \theta\} \mid u_{1k}^2, u_{2k}^2, \cdots, u_{mk}^2 > = \int \exp\{\varepsilon_k \theta\} p(\varepsilon_k \mid u_{1k}^2, u_{2k}^2, \cdots, u_{mk}^2) d\varepsilon_k, \quad (7)$$

which can be calculated with use of the joint moment generating function $M(\theta, \theta_1, \cdots, \theta_m)$. First, the joint probability distribution of wind velocities $u_{1k}^2, u_{2k}^2, \cdots, u_{mk}^2$ can be given by using the inverse Laplace transform of $M(0, \theta_1, \cdots, \theta_m)$ as follows :

$$P(u_{1k}^2, u_{2k}^2, \cdots, u_{mk}^2) = \sum_{i+i_1+\cdots+i_m=1}^{\infty} g_{i_1,\cdots,i_m}(0) \prod_{j=1}^{m} \frac{1}{\sqrt{\kappa_{0,\cdots,0,2,0,\cdots,0}}} H_{i_j}\left(\frac{u_j^2 - \kappa_{0,\cdots,0,1,0,\cdots,0}}{\sqrt{\kappa_{0,\cdots,0,2,0,\cdots,0}}}\right) \exp\{-(u_j^2 - \kappa_{0,\cdots,0,1,0,\cdots,0})^2 / \sqrt{2\pi\kappa_{0,\cdots,0,2,0,\cdots,0}}\}. \quad (8)$$

Then, by using Eq.(8) and taking the inverse Laplace transformation of the moment generating function $M(\theta, \theta_1, \cdots, \theta_m)$, $M(\theta)$ can be derived as follows :

$$M(\theta) = \sum_{i+i_1+\cdots+i_m=1}^{\infty} g_{i_1,\cdots,i_m}(\theta) \cdot \prod_{j=1}^{m} \{\frac{1}{\sqrt{\kappa_{0,\cdots,0,2,0,\cdots,0}}} H_{i_j}\left(\frac{u_j^2 - \kappa_{0,\cdots,0,1,0,\cdots,0}}{\sqrt{\kappa_{0,\cdots,0,2,0,\cdots,0}}}\right)\} / \{1 + \sum_{i_1+\cdots+i_m=1}^{\infty} g_{i_1,\cdots,i_m}(0) \cdot \prod_{j=1}^{m} \frac{1}{\sqrt{\kappa_{0,\cdots,0,2,0,\cdots,0}}} H_{i_j}\left(\frac{u_j^2 - \kappa_{0,\cdots,0,1,0,\cdots,0}}{\sqrt{\kappa_{0,\cdots,0,2,0,\cdots,0}}}\right)\}. \quad (9)$$

Finally, by differentiating Eq.(9) N times, the statistical prediction of arbitrary moments of a deviation term ε_k can be derived in the form of function on the observation of wind velocities :

$$< \varepsilon_k^N \mid u_{1k}^2, u_{2k}^2, \cdots, u_{mk}^2 > = \sum_{i_1+\cdots+i_m=0}^{\infty} g_{i_1,\cdots,i_m}^{(N)}(0) \prod_{j=1}^{m} \frac{1}{\sqrt{\kappa_{0,\cdots,0,2,0,\cdots,0}}} \cdot H_{i_j}\left(\frac{u_j^2 - \kappa_{0,\cdots,0,1,0,\cdots,0}}{\sqrt{\kappa_{0,\cdots,0,2,0,\cdots,0}}}\right) / \{1 + \sum_{i_1+\cdots+i_m=1}^{\infty} g_{i_1,\cdots,i_m}(0) \prod_{j=1}^{m} \frac{1}{\sqrt{\kappa_{0,\cdots,0,2,0,\cdots,0}}} \cdot H_{i_j}\left(\frac{u_j^2 - \kappa_{0,\cdots,0,1,0,\cdots,0}}{\sqrt{\kappa_{0,\cdots,0,2,0,\cdots,0}}}\right)\}, \quad (10)$$

where $g_{i_1,\cdots,i_m}^{(N)}(0) = (\partial/\partial\theta)^N g_{i_1,\cdots,i_m}(\theta)|_{\theta \to 0}$.

That is, the generalized multi-variate regression model can be realised for predicting the arbitrary moments of the wind noise with use of the wind velocities.

2-2 A Wide-Sense Digital Filter for Detecting Acoustic Signals Embedded under Wind-induced noise

In the same analytical viewpoints as in section 2.1, a dynamical signal detection method under the background and the wind noises can be derived.

Now, we will pay our special attention to the engineering problem of estimating the unknown state of stochastic systems contaminated by a random measurement noise. By analysing the physical mechanism based on the additive property of energy quantities, the system and observation equations could be generally formulated as :

$$x_{k+1} = F_k(x_k, u_k), \quad y_k = H_k(x_k, v_k), \quad (11,12)$$

where x_k and y_k denote the unknown state of stochastic system at a certain time stage k and its observation contaminated by a random measurement noise v_k (which includes a wind-induced noise) of arbitrary distribution type. The input u_k, whose statistics are given a priori, and the background and wind-induced noise v_k are assumed to be independent each other and themselves. The statistics of a wind-induced noise can be grasped with use of the proposed general regression model based on the information on a wind velocity u_k. Then, the statistics of v_k can be given at each time stage.

Then, the discrete estimation problem under consideration is how to detect x_k based on the set of contaminated observations $Y_k(=\{y_1, y_2, \cdots, y_k\})$. For detecting the acoustic signal x_k with use of the noisy observation recursively, the conditioned joint moment generating function should be considered :

$$M^*(\theta, \theta_1) =< \exp\{x_k\theta + y_k\theta_1\} \mid Y_k >$$
$$= \int \exp\{\theta \cdot x_k + y_k\theta_1\} p(x_k, y_k \mid Y_{k-1}) dx_k. \quad (13)$$

Here Y_k is the set of past-contaminated observations $Y_k = \{y_1, y_2, \cdots, y_k\}$. Then, by considering Bayes theorem, the moment generating function $M^*(\theta)$ on the unknown acoustic signals x_k can be calculated with use of Eq.(13) in the same way as in section 2.1.

$$M^*(\theta) =< \exp\{\theta \cdot x_k\} \mid Y_k >$$
$$= \int \exp\{\theta \cdot x_k\} p(x_k, y_k \mid Y_{k-1}) dx_k \,/\, p(y_k \mid Y_{k-1}). \quad (14)$$

As the results, the unified algorithm of estimating the unknown acoustic signals under these random noises can be obtained :

$$< x_k^N \mid Y_k >$$
$$= \sum_{j=0}^{\infty} g_j^{*(N)}(0) \frac{1}{\sqrt{\kappa_{0,2}^*}} H_j\left(\frac{y_k - \kappa_{0,1}^*}{\sqrt{\kappa_{0,2}^*}}\right)$$
$$\Big/ \left\{ 1 + \sum_{j=1}^{\infty} g_j^*(0) \frac{1}{\sqrt{\kappa_{0,2}^*}} H_j\left(\frac{y_k - \kappa_{0,1}^*}{\sqrt{\kappa_{0,2}^*}}\right) \right\}, \quad (15)$$

where $\kappa_{i,j}^*$ denotes the (i,j)-th predicted joint cummulant of x_k and y_k.

$$\kappa_{1,0}^* =< x_k \mid Y_{k-1} >, \quad \kappa_{0,1}^* =< y_k \mid Y_{k-1} >, \quad (16,17)$$
$$\kappa_{2,0}^* =< (x_k - \kappa_{1,0}^*)^2 \mid Y_{k-1} >, \quad (18)$$
$$\kappa_{0,2}^* =< (y_k - \kappa_{0,1}^*)^2 \mid Y_{k-1} >. \quad (19)$$

Each expansion coefficient can be calculated as follows :

$$g_j^{*(N)}(0) = (\partial / \partial\theta)^N g_j^*(\theta) \mid_{\theta \to 0}, \quad (20)$$

$$g_j^*(\theta) = \left(\frac{\partial}{\partial\theta_1}\right)^j \exp\{ \sum_{m=3}^{\infty} \kappa_{0m}^* \theta_1^m / m!$$
$$+ \sum_{i=1}^{\infty} \sum_{m=0}^{\infty} \kappa_{im}^* \theta^i \theta_1^m / i!m! \} \mid_{\theta_1 \to 0}. \quad (21)$$

The predicted statistics on the unknown state and the background noise (including the wind-induced noise) are reflected hierarchically in each expansion coefficient in Eq.(15) . In the algorithm, the successive observation y_k has been processed linearly and nonlinearly through the Hermite polynomial functions.

Finally, by combining Eq.(21) with the unified prediction algorithm :

$$< x_{k+1}^N \mid Y_k >= \int x_{k+1}^N p(x_{k+1} \mid Y_k) dx_{k+1}$$
$$=< F_k^N(x_k, u_k) \mid Y_k >, \quad (22)$$

which can be derived from Eq.(12), the dynamical state estimation algorithm in a recursive form can be realized.

2.3 Generalized Regression Model Of Wind-Induced Noise On Wind Velocitiy Based On Inverse Gaussian Distribution

For predicting the wind-induced noise v_k based on the information on wind velocity u_k^2 (energy), we will directly pay our special attention to the joint probability function on wind-induced noise and wind velocity $P(v_k, u_k^2)$, which includes any kinds of statistical information between wind-induced noise and wind velocity. For grasping the whole probability form of a wind noise without minimum information losses, we will expand $P(v_k, u_k^2)$ with use of inverse Gaus-sian distribution function and its associated orthogonal polynomials in the hierarchical orthogonal series form :

$$P(v_k, u_k^2) = IG(v_k; m_k, s_k) \cdot IG(u_k^2; M_k, S_k)$$
$$\bullet \sum_{m=0}^{\infty} \sum_{n=0}^{\infty} A_{mn} \cdot \phi_m^{(1)}(u_k) \cdot \phi_n^{(2)}(u_k^2), \quad (23)$$

where $IG(v_k; m_k, s_k)$ and $IG(u_k^2; M_k, S_k)$ denote the inverse Gaussian distribution functions on v_k and u_k^2, whose associated orthogonal functions are expressed as $\phi_m^{(1)}(v_k)$ and $\phi_n^{(2)}(u_k^2)$.

$$IG(x; m, s) = m \cdot (s / 2\pi x^3)^{1/2}$$
$$\bullet \exp(-(x - m \cdot s)^2 / 2 \cdot s \cdot x), \quad (24)$$

where $m =< x >^2 / < (x - < x >)^2 >$, $s =< x > /m$. For realizing $\phi_m^{(1)}(v_k)$ and $\phi_n^{(2)}(u_k^2)$ in the concrete forms, the Schmit's orthogonalization technique should be used because the orthogonal polynomials associated with the inverse Gaussian distribution function are not known. That is, $\phi_m^{(1)}(v_k)$ and $\phi_n^{(2)}(u_k^2)$ will be constructed by adopting the set of independent functions The statistical parameters of these inverse Gaussian distribution functions are a priori decided as follows (the detailed expressions are omitted here):

$$\left.\begin{aligned} m_k &= <v_k>^2 / <(v_k - <v_k>)^2>, \\ s_k &= <v_k> / m_k, \\ M_k &= <u_k^2>^2 / <(u_k^2 - <u_k^2>)^2>, \\ S_k &= <u_k^2> / M_k. \end{aligned}\right\} \quad (25)$$

The expansion coefficients can be determined as:

$$A_{mn} = <\phi_m^{(1)}(v_k) \cdot \phi_n^{(2)}(u_k^2)> . \quad (26).$$

Thus, the probability distribution function on wind-induced noise v_k conditioned by wind velocity u_k^2 can be derived :

$$P(v_k \mid u_k^2) = IG(v_k; m_k, s_k) \sum_{m=0}^{\infty} \sum_{n=0}^{\infty} A_{mn} \cdot \bullet \phi_m^{(1)}(v_k) \cdot \phi_n^{(2)}(u_k^2) / \sum_{n=0}^{\infty} A_{0n} \cdot \phi_n^{(2)}(u_k^2). \quad (27)$$

This means that the probability form of a wind-induced noise can be predicted successively with use of the observation of a wind velocity at each time, based on the flexibility of inverse Gaussian distribution.

As a wind-induced noise v_k shows the typical non-Gaussian distribution forms, so we should predict not only its mean and variance but also the other higher order statistics at the same time. Any kinds of statistical information on a wind-induced noise can be expressed by the polynomial function $f(v_k)$ of arbitrary order N, based on the Wierstrass's interpolation theorem. Then, based on Eq.(27), the generalized regression model for predicting the statistics $< f(v_k) \mid u_k^2 >$ of polynomial functional form can be given as follows:

$$< f(v_k) \mid u_k^2 > = \sum_{m=0}^{\infty} \sum_{n=0}^{\infty} A_{mn} \cdot C_{Nm} \cdot \bullet \phi_n^{(2)}(u_k^2) / \sum_{m=0}^{\infty} A_{0n} \cdot \phi_n^{(2)}(u_k^2), \quad (28)$$

where C_{Nm} denotes the coefficient that satisfies the relation : $f(v_k) = \sum_{m=0}^{N} C_{Nm} \cdot \phi_m^{(1)}(v_k)$.

Finally, any kinds of statistics of a wind-induced noise v_k can be universally predicted based on Eq.(28), which can be calculated recursively with use of successive information on a wind velocity.

2.4 Dynamical Estimation Algorithm Based On The Otrhogonally Expanded Bayes' Theorem By Using Inverse Gaussian Distribution Function And Its Associated Orthogonal Polynomials

Now, we will pay our special attention to the engineering problem of estimating the unknown state of stochastic systems contaminated by a random measurement noise (Eqs.(11) and (12)) from the same viewpoint in section 2.3. For deriving the estimation algorithm, the Bayesian viewpoint is firstly employed:

$$P(x_k \mid Y_k) = P(x_k, y_k \mid Y_{k-1}) / P(y_k \mid Y_{k-1}) \quad (29)$$

Then, for obtaining the reasonable estimate of x_k for arbitrarily fluctuating stochastic system, not only the linear but also the nonlinear correlation informations between the unknown state x_k and the observation y_k should be utilized. It is a good plan to introduce the hierarchically expanded expression for the joint probability functions on x_k and y_k. By expanding the joint probability function $P(x_k, y_k \mid Y_{k-1})$ on x_k and y_k conditioned by Y_{k-1}, the following expression can be obtained :

$$P(x_k, y_k \mid Y_{k-1}) = IG(x_k; m_{k|k-1}, s_{k|k-1}) \cdot IG(y_k; M_{k|k-1}, S_{k|k-1}) \sum_{m=0}^{\infty} \sum_{n=0}^{\infty} A_{mn} \cdot \phi_m^{(1)}(x_k) \cdot \phi_n^{(2)}(y_k), \quad (30)$$

where $IG(x_k; m_{k|k-1}, s_{k|k-1})$ and $IG(y_k; M_{k|k-1}, S_{k|k-1})$ denote the Inverse Gaussian distribution functions on x_k and y_k. The parameters $m_{k|k-1}$, $s_{k|k-1}$, $M_{k|k-1}$ amd $S_{k|k-1}$ are calculated by the predicted values of mean and variance on x_k and y_k respectively as follows :

$$\left.\begin{aligned} m_{k|k-1} &= x^{*2}_{k|k-1} / \Gamma_{k|k-1}, \\ s_{k|k-1} &= x^{*}_{k|k-1} / m_{k|k-1}, \\ M_{k|k-1} &= y^{*2}_{k|k-1} / \Omega_{k|k-1}, \\ S_{k|k-1} &= y^{*}_{k|k-1} / M_{k|k-1}, \\ x^{*}_{k|k-1} &= <x_k \mid Y_{k-1}>, \\ \Gamma_{k|k-1} &= <(x_k - x^{*}_{k|k-1})^2 \mid Y_{k-1}>, \\ y^{*}_{k|k-1} &= <y_k \mid Y_{k-1}> \\ &= <H_k(x_k, v_k) \mid Y_{k-1}>, \\ \Omega_{k|k-1} &= <(y_k - y^{*}_{k|k-1})^2 \mid Y_{k-1}> . \end{aligned}\right\} \quad (31)$$

$\phi_m^{(1)}(x_k)$ and $\phi_n^{(2)}(y_k)$ are the orthogonal polynomials of orders m and n respectively associated with $IG(x_k; m_{k|k-1}, s_{k|k-1})$ and $IG(y_k; M_{k|k-1},$

$S_{k|k-1}$. Then, the expansion coefficient A_{mn} in Eq.(30) can be determined by using the predicted statistics on x_k and a priori given statistics on v_k :

$$A_{mn} = < \phi_m^{(1)}(x_k) \cdot \phi_n^{(2)}(y_k) \mid Y_{k-1} > = < \phi_m^{(1)}(x_k) \cdot \phi_n^{(2)}(H_k(x_k, v_k)) \mid Y_{k-1} > . \quad (32)$$

From Eq.(11), the orthogonally expanded Bayes' theorem in the form of statistical series expression can been derived and the arbitrary statistics on x_k, expressed by a polynomial function $f(x_k)$ of order N based on the Wierstrass's interpolation theorem, can be estimated as follows :

$$< f(x_k) \mid Y_k > = \sum_{m=0}^{N} \sum_{n=0}^{\infty} A_{mn} \cdot C_{Nm} \cdot \phi_n^{(2)}(y_k) \Big/ \sum_{n=0}^{\infty} A_{0n} \cdot \phi_n^{(2)}(y_k), \quad (33)$$

where the orthogonal property of $\phi_n^{(1)}(x_k)$ was used (The detailed derivation process was omitted because of the page limitation). The coefficient C_{Nm} in Eq.(33) is the coefficient that satisfies the following relation for the function $f(x_k)$ of order N : $f(x_k) = \sum_{m=0}^{N} C_{Nm} \cdot \phi_m^{(1)}(x_k)$.

Based on the system equation (see Eq.(11)), the following algorithms of predicting the arbitrary statistics given by an arbitrary polynomial $< x_{k+1}{}^N \mid Y_k >$ can be derived as Eq(22), which includes the prediction algorithms of mean and variance values of the unknown signal x_{k+1}.

By combining Eq.(33) with Eq.(22), the computer-aided algorithm of state estimation is derived in the recurrence calculation form matched to the successive processing of the observed data for the actual stochastic systems under random measurement noise.

3. Experimental Confirmations

The effectiveness of proposed estimation theory has been experimentally confirmed by applying it to the actual acoustic data in the outdoor field contaminated by the random background and wind-induced noises. The estimated results by the proposed method in 2.1 and 2.2 are shown in Fig.1, and the results by the method in 2.3 and 2.4 are shown in Fig.2. Other experimental results are omitted owing to the page limit.

4. Conclusions

In this paper, for the acoustic system in an outdoor environment, a new derivation of the systematic countermeasure method for the wind noise was proposed with use of the wind velocities. We will thank to Mr.M.Kubo, Mr.K.Furukawa and Mr.H.Kondo for their helpful assistance.

References

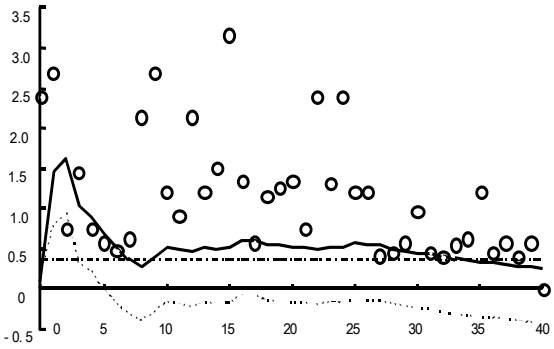

Fig.1 A estimated results of unknown acousitc signals contaminted by wind-induced noise. The observed values y_k are marked as (○) and the ture acoustic signals x_k are lined as (.....). The estimated values of x_k are lined as (_____) by the proposed method and as (_ _ _ _) by the propoese mehtod using the past data of wind velocities.

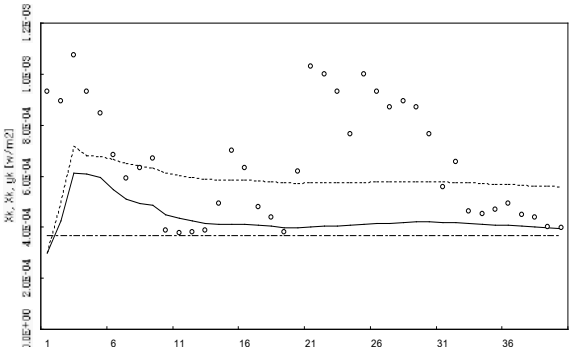

Fig.2 An estimated results of unknown acoustic signals under wind-induced noise. The observed values are marked as (o) and the true acoustic signals are lined as (– ·– ·–). The estimates are lined as (--------: by proposed method based on inverse Gaussian distribution) and (———: by proposed method with using the statistics of wind-induced noise in the learning period). The sampling interval is 0.5 s.

1) B.Jorgenson : Statistical properties of the generalized inverse Gaussian distribution (Springer, New York, 1982). 2) J.Inoue and S.Sato : The first-passage-time problem for one-dimensional diffusive process under the relation with IGD, Proc. 5th symposium on random fluctuation phenomena and stochastic process, 1990. 3) M.Ohta et al.: A restoration method of medical x-ray images based on an extended regression analysis method, Trans.IEICE, J74-D, 3, 1991, pp.444. 4) K.Hatakeyama & M.Ohta, Research Report on Random Phenomena and Stochastic Process (1995.11) . 5) T.Katayama:Kalman Filter and Applications (Asakura, 1983). 6) Anderson,B.D.O. & Moore,J.B.:Optimal Filtering (Prentice-Hall,1979).

A Preliminary Evaluation Of The FHWA TNM Model In Sydney

Derek Langgons[1] and David Eager[2]

[1]Dick Benbow & Associates and [2]University of Technology, Sydney.

Abstract

This paper presents the results of a preliminary evaluation of the accuracy of the United States FHWA's TNM road traffic noise model compared to the widely used CORTN traffic noise model. The method of assessment closely followed the methods established by Huybregts and Samuels (1999). Simultaneous monitoring of road traffic noise levels, traffic volumes and weather conditions was undertaken for approximately 7 days at six sites within the Sydney metropolitan area. A basic statistical analysis was carried out to provide an indication of the accuracy of the TNM model predictions compared to the CORTN predictions and the actual measured values. Whilst only a limited amount of data was collected, this preliminary evaluation supports the findings of Huybregts and Samuels and demonstrates that the TNM model is at least as accurate as the accepted model.

Introduction

In 1998, the United States Federal Highway Administration (FHWA) released its Total Noise Model (TNM) road traffic noise model (Menge *et al.*, 1998).

This paper presents the results of a preliminary evaluation of the TNM model in Sydney. The purpose of the study was to provide further support to the findings of Huybregts and Samuels (1999) whilst evaluating the accuracy of the TNM model for predicting noise descriptors used for traffic noise assessment in New South Wales.

The TNM model incorporates recent vehicle noise emission measurements in one-third octave band spectra; facilitates modelling of four different pavement types; allows for calculation of noise emissions vehicles accelerating away from control points and includes allowances for the effects of intervening rows of buildings, ground surfaces and heavy vegetation.

The model calculates sound level contours and can generate a series of different views to help visualise input data.

Therefore the model presents an excellent opportunity for the assessment of road traffic noise impacts. However, it is important to validate the accuracy of the model for use in Australia.

Huybregts and Samuels (1999) conducted an extensive evaluation of the TNM model in Melbourne. The evaluation was carried out following the scientific procedures developed by Saunders *et al.* (1983) in their evaluation of the UK Department of Transport's Calculation of Road Traffic Noise (CORTN) method (UK DoT, 1988).

The study was commissioned by VicRoads and therefore primarily assessed the prediction of L_{eq}(16hr) and L_{eq}(8hr) noise descriptors.

The study found that the TNM model provides a greater degree of accuracy than the CORTN model when used to calculate L_{eq}(16hr). The study also recommended several calibration factors that could be applied to the calculated values using TNM.

Assessment of road traffic noise levels in New South Wales involves the use of the L_{eq}(15hr), L_{eq}(9hr) and L_{eq}(1hr) descriptors. Therefore, these descriptors were used in this study.

Measured road traffic noise levels were compared to predicted noise levels using both the TNM and modified CORTN models. A basic statistical analysis was carried out to compare the accuracy of the TNM model in relation to the modified CORTN model.

Methodology

The methodology used in this study broadly followed the procedures established in Samuels and Saunders (1982) and followed in Huybregts and Samuels (1999). The methodology can be summarised as follows:

Selection of appropriate assessment sites

Six sites were selected for assessment in this study. The number of sites was limited due to resource and timing constraints. The selection of sites aimed to keep the majority of variables that could affect the modelling constant throughout the sites.

All sites were located next to straight sections of roadway with uninterrupted flow. At all sites the roadway was flat, ie zero gradient. The road pavement surfaces at each location were all dense graded asphaltic concrete in reasonable to good condition.

At all six sites, road traffic noise from the roadway under assessment was the predominant noise source. The objective was to ensure that there were no other sources of industrial or community related noise that may have significantly effected the noise measurement results. Discussions with the residents at each location helped to determine the sources of noise in the area.

At five of the locations, the roadway was undivided single carriageways. However at one of the locations (Site 5), the roadway was dual carriageway with a 0.5m dividing median.

Roadways with a significant percentage of heavy vehicle flow were selected for five of the locations. One location (Site 1) was selected in a residential area with heavy vehicle restrictions.

Speed limits at five of the sites were either 60 km/h or 80 km/h. One site (Site 1) was located within a 50 km/h zone.

As most road traffic noise impacts, and subsequently most road traffic noise assessments, occur at residential premises, it was considered appropriate to ensure assessment points were located at residential dwellings. This also helped to ensure the security of monitoring devices.

The use of residential premises for the noise monitoring points restricted the available separation distance to the roadway. Therefore, at five of the locations, the separation distance to the nearest carriageway was approximately 25 metres. At one of the noise monitoring points (Site 6) there was an area of undeveloped land between the roadway and the residence and therefore the monitoring point was 110 metres to the nearest carriageway.

Each assessment site was selected so that the noise monitoring point was exposed to road traffic noise without shielding. There were no road traffic noise barriers installed at any of the sites. The topography of the ground between the roadway and the noise measurement point was flat.

Determination of necessary modelling parameters at each site

All necessary modelling parameters for each model were determined at the sites. This involved the measurement or estimation of variables such as roadway geometry and gradient, pavement material, distance from road to receiver, ground cover type and the presence of any barrier, structure or topographical shielding.

Simultaneous measurement of road traffic noise levels, traffic conditions and meteorological conditions at each site

The measurement of road traffic noise was carried out in accordance with Australian Standard (AS) 2702 – 1984 (Standards Association of Australia 1984). Noise levels were measured using environmental noise loggers that comply with AS 1259 – 1990 (Standards Australia 1990) for Type 2 sound level meters.

Traffic measurement and analysis was undertaken by Corner Counters Pty Ltd. The measurements were carried out using Archer 400 Series Vehicle Classifiers. Class breakdowns were analysed in accordance with the Golden River Vehicle Classification Scheme GRCS-10. This is equivalent to the AUSTROADS 1194 Class Scheme.

Continuous monitoring was carried out at each site for approximately 7 days. This resulted in a total of 666 hours of valid data from the six sites.

Analysis of data

The measured hourly L_{eq} noise levels for each site were extracted from the noise monitoring data. The periods of monitoring that may have been effected by inclement weather were removed from the data set.

The L_{eq}(15hr) and L_{eq}(9hr) descriptors were then calculated for each day at each site.

Traffic condition analysis was undertaken by Corner Counters Pty Ltd. The output files from the tube counters were analysed to determine the following:

a) Total volume of vehicles for each hour of each day.

b) 85^{th} percentile speeds for combined flows for each hour of each day.

c) Class volumes and percentages of daily combined flow for each site.

Prediction of noise levels at each site using both the modified CORTN model and the TNM model

The site specific variables were entered into each model. The hourly traffic volumes, heavy vehicle percentage and 85^{th} percentile speeds were also entered.

The models were run and the predicted hourly L_{eq} noise levels from each model were compiled.

Comparison of the predicted noise levels to the actual measured noise levels for each of the key descriptors.

Following the prediction of the hourly L_{eq} noise levels for each hour of valid data during the monitoring periods, the predicted L_{eq}(15hr) and L_{eq}(9hr) noise levels were calculated for each day of data and for each of the two models.

It was then possible to group the measured and predicted values into three data sets for each site. One data set contained the measured hourly L_{eq} noise levels, the predicted hourly L_{eq} using the modified CORTN model and the predicted hourly L_{eq} using the TNM model. The second and third data sets were for the measured and predicted values for L_{eq}(15hr) and L_{eq}(9hr) noise levels.

Huybregts and Samuels (1999) established a value know as the prediction difference (PD) for evaluating the noise models. The prediction difference is:

PD = Predicted noise level – Measured noise level (1)

The prediction difference was calculated for the hourly L_{eq}, L_{eq}(15hr) and L_{eq}(9hr) data sets for each day and for each site. For the purposes of this evaluation, the prediction differences for each site were then combined and treated as three separate populations.

Whilst there was no detailed statistical analysis carried out to support the assumption that the prediction differences for each site could be combined and treated as individual populations, the following points can be noted:

a) As stated earlier, the selection of assessment sites was carried out to minimise the differences in each site that could effect the model results.

b) A rigorous analysis carried out by Huybregts and Samuels (1999) determined that it was valid to group the prediction differences as one sample population.

Therefore we were now left with three data sets; a set of prediction differences for the L_{eq}(1hr) descriptor for all six sites, a set of prediction differences for the L_{eq}(15hr) descriptor for all six sites and a set of prediction differences for the L_{eq}(9hr) descriptor for all six sites.

The prediction difference was plotted against the measured value for each of the three sets. This provided an indication of the accuracy of the noise models in relation to the measured value.

Normal distribution tests were then carried out for each data set. Following the tests, the mean and standard deviations for each set were calculated to evaluate the accuracy of the models.

Results

A basic review of the prediction differences for each hour at each site was undertaken. The following points became apparent:

a) The CORTN predictions were well above the measured noise levels during the early morning periods. This is due to the limitations of the CORTN model in modelling low traffic flows.

b) The TNM Model tended to under predict noise levels during low flow periods.

c) The prediction differences for both models at Site 1, where there was no heavy vehicle flows and low vehicle speeds, were approximately equivalent to the prediction differences at other sites where heavy vehicle percentages and vehicle speeds were high.

d) The accuracy of the models was also consistent for the site where there was a large separation distance to the receiver point.

Detailed statistical analysis to prove or disprove these observations was not carried out as part of this preliminary evaluation.

The prediction differences for the L_{eq}(1hr), L_{eq}(15hr) and L_{eq}(9hr) descriptors for both models were plotted against the measured values. The graphs are presented as Figures 1, 2 and 3.

The plots show that there is no significant relationship between the prediction difference and the measured L_{eq}. Similar plots carried out by Huybregts and Samuels (1999) also found that there was no significant relationship between these parameters. Their observations were supported by regression analysis.

Tests for normality were undertaken for each data set. Two basic tests were undertaken. In the first test, frequency histograms were plotted for each of the CORTN and TNM prediction difference for each set.

Observation of the frequency histograms found that data for the L_{eq}(1hr) prediction differences approximately fit a normal distribution curve. However, there was no clear distribution curve for the remaining descriptors. A second test was undertaken to provide more detail.

The second test involved calculating the interquartile range and standard deviation for each set. If the data sets are approximately normal, than the interquartile

range divided by the standard deviation should be approximately 1.3 (Mendenhall and Sincich, 1995).

The results of the second test found that the IQR/s values for the L_{eq}(1hr) prediction differences for both models were close to 1.3. The L_{eq}(15hr) prediction difference distribution for the CORTN model could also be considered a normal distribution.

It is unlikely that the prediction difference data sets for both L_{eq}(15hr) and L_{eq}(9hr) would not be normal if the source of the data, the L_{eq}(1hr) data set approximates a normal distribution. It is likely that if more data was captured, normal distributions would be prevalent.

In the study undertaken by Huybregts and Samuels (1999) a Chi-squared goodness of fit test was carried out. The result of the test indicated that the data was normally distributed.

Therefore, it was considered reasonable to calculate the mean and standard deviations of the data sets assuming normal distributions for this preliminary evaluation. The results of the calculations are presented in Table 1.

Table 1: Calculated mean and standard deviation for each set

Descriptor	Modified CORTN model		TNM model	
	Mean	SD	Mean	SD
L_{eq}(1hr)	2.2	2.8	0.3	2.8
L_{eq}(15hr)	2.3	2.5	0.7	2.7
L_{eq}(9hr)	1.4	1.9	-1.0	2.3

The results presented in Table 1 demonstrate that the mean values for prediction difference using TNM are closer to the goal of zero than the mean values for the modified CORTN method. It should be noted that an overall adjustment factor of –0.7 dB was applied to the CORTN model in accordance with the recommendations made in Samuels and Saunders (1982).

The standard deviations for both models are similar for each descriptor.

However, as stated in Huybregts and Samuels (1999), a calibration factor can be applied to each model to account for the mean offset. Therefore, in evaluating the accuracy of a model, the standard deviation is more appropriate.

The results presented in Table 1 therefore indicate that the TNM model is as accurate as the modified CORTN model. However there are two key points that should be noted:

a) The evaluation was carried out for six sites and over several days only at each site. This resulted in relatively small data sets compared to those compiled for detailed studies.

b) The evaluation was carried out for straight roadways with zero gradient and uninterrupted flows. There are many other types of roadways that should be evaluated before commenting upon the overall accuracy of the model.

The mean and standard deviations of the prediction difference in the detailed evaluation carried out by Huybregts and Samuels (1999) are presented in Table 2.

Table 2: Mean and standard deviation of the prediction differences (Huybregts and Samuels 1999)

	TNM L_{eq}(16hr)	CORTN L_{10}(18hr)	TNM L_{10}(18hr)	TNM L_{eq}(8hr)
Mean	0.6	4.4	-1.4	-1.4
SD	1.9	2.7	2.2	2.5

The means and standard deviations calculated by Huybregts and Samuels differ slightly to those calculated in this study. This may be due to the difference in noise descriptors selected, assessment sites or perhaps most likely, the size of the sample sets.

Figure 1: Prediction difference plotted against measured Leq (1hr)

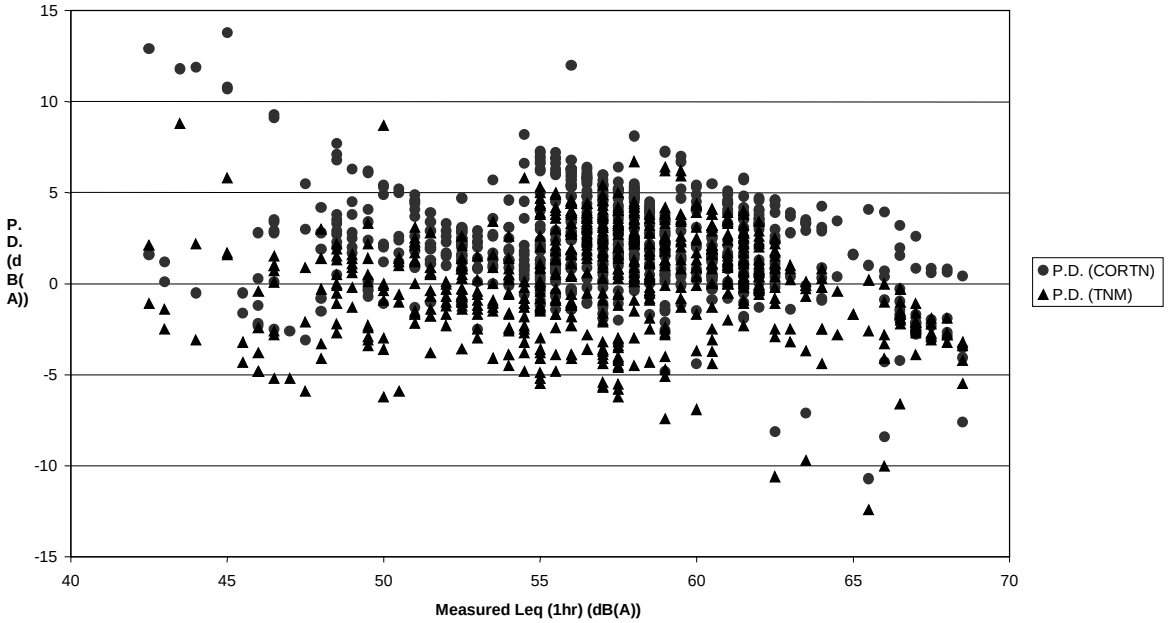

Figure 2: Prediction difference plotted against measured Leq (15hr)

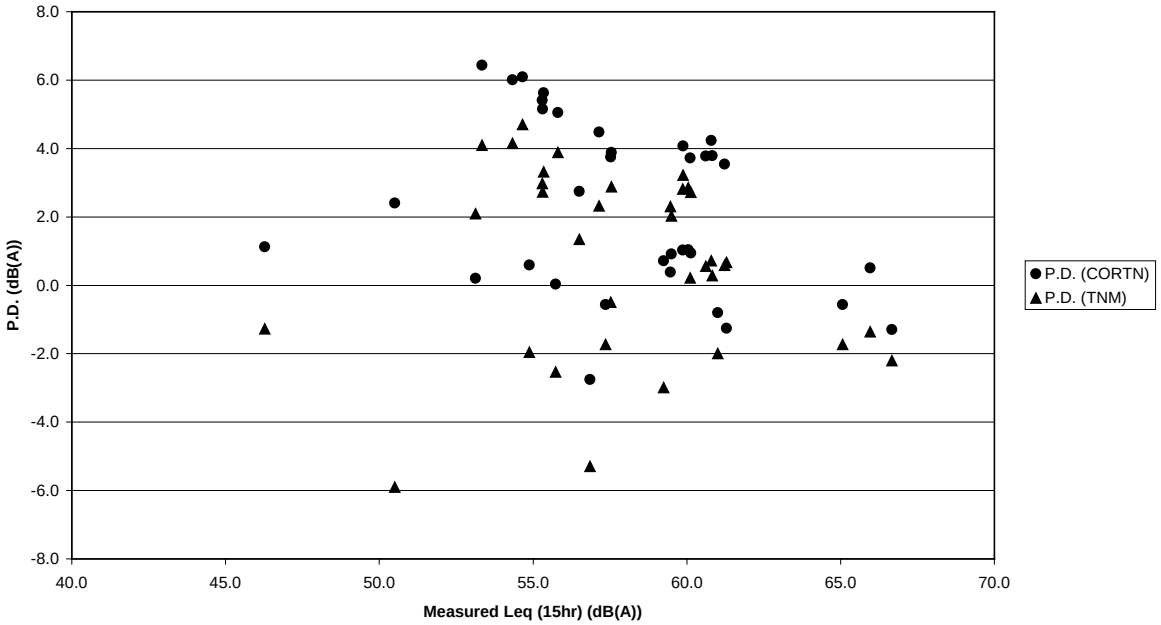

Figure 3: Prediction difference plotted against measured Leq (9hr)

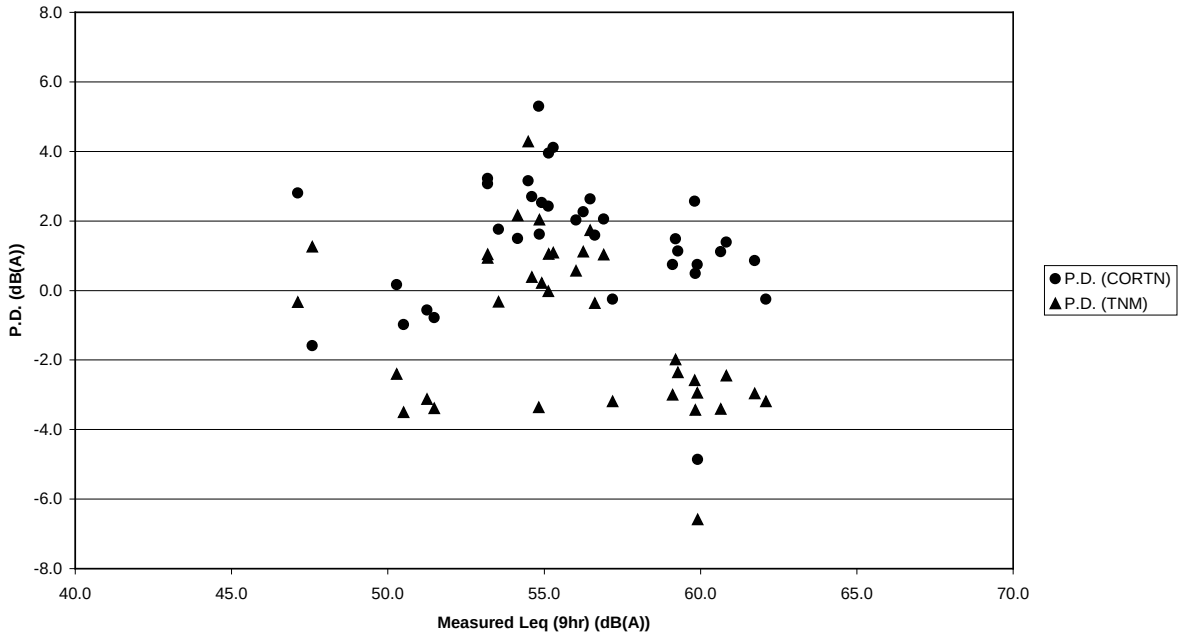

Conclusions

The aims of this study were to provide a preliminary evaluation of the accuracy of the US FHWA TNM traffic noise model in Sydney. A total of 666 hours of valid data was obtained across 6 sites. Noise predictions for all 666 hours were undertaken using the modified CORTN model and the TNM model.

It was determined that the TNM model generally predicted noise levels closer to the measured noise levels than the modified CORTN model. The calculated standard deviations also indicated that the TNM model was as accurate as the CORTN model.

There are several factors that need to be addressed in future studies in order to provide a definitive evaluation of the TNM model. The accuracy of the model to predict traffic noise in interrupted flow situations is one example. However, this study indicates that the TNM model could be used by engineers and planners with the same degree of reliability as the CORTN model.

References

Huybregts, N. and Samuels, S., *Evaluating the American FHWA Traffic Noise Model in Melbourne*, AAS Annual Conference, Melbourne, Nov 1999.

Menge, C.W., Rossano, C.F., Anderson, G.S., and Bajdek, C.J., *FHWA Traffic Noise Model, Version 1.0, Technical Manual*, U.S. Department of Transport, Federal Highway Administration, Washington DC, USA, 1998.

Mendenhall, W. and Sinsich, T., *Statistics for Engineering and the Sciences*, Prentice-Hall Inc. New Jersey, USA, 1995.

Saunders, R.E., Samuels, S.E., Leach, R. and Hall, A., *An evaluation of the UK DoT traffic noise prediction method*, Australian Road Research Board Research Report 122. ARRB, Vermont South, Victoria, 1983.

Samuels, S.E. and Saunders, B.E., *The Australian Performance of the UK DoE Traffic Noise Prediction Method*, 11th Australian Road Research Board Proceedings, 1982.

UK Department of Transport, *Calculation of Road Traffic Noise*, HMSO, London, UK, 1988.

ACOUSTICS - putting the science and technology to work

Conference of the Australian Acoustical Society
Joondalup Resort, Western Australia, 15-17 November 2000

Session UW-1 Target Detection, Classification And Calibration

Adaptive Non-Gaussian Processing for Enhanced Sonar Detection in Biological Noise Interference

Derek C. Bertilone and Damien S. Killeen

Defence Science Technology Organisation, HMAS Stirling, Rockingham WA 6958, Australia.

Abstract

We describe research underway at DSTO Stirling to develop adaptive non-Gaussian sonar processors to enhance the detection of narrowband signals in the presence of impulsive biological noise interference. We briefly discuss the statistical nature of snapping shrimp underwater noise, and describe the design of non-Gaussian processors that estimate the probability distribution for the background noise as each block of data is read-in, and then tune the receiver to optimise detection of weak signals buried in that noise. Some experimental results are presented.

Introduction

Conventional sonar detectors are optimised to detect signals buried in a background of Gaussian noise. The Gaussian assumption is effective for many underwater environments, particularly when the dominant source of the noise is due to distant shipping or surface effects associated with wind or rain. But in the presence of intense, sustained impulsive interference, the noise is highly non-Gaussian and conventional sonars perform poorly. These harsh conditions apply when the ambient noise is dominated by certain types of biological noise, such as that due to populations of snapping shrimp, sperm whales or dolphins.

Here we describe some research underway at DSTO Stirling, to develop adaptive non-Gaussian processors for passive sonar detection. We briefly discuss the statistics of snapping shrimp noise, and describe the development of a narrowband processor that estimates the statistical properties of background noise as each block of time-series data is read in, and then tunes the receiver to detect weak signals buried in that noise. In this way, the receiver automatically adapts to changing noise conditions.

Biological noise statistics

Snapping shrimp noise often dominates the ambient noise environment of warm, shallow waters. Individual shrimp make very sharp, impulsive clicks by snapping closed their large claw and ejecting a fine jet of water [1]. The superposition of clicks from large populations of shrimp leads to a sustained background crackle that sounds remarkably like fat frying in a pan. Most of the shrimp noise energy lies above 2 kHz, but in several data sets in which the contribution from surface noise is at a particularly low level, we find the shrimp noise dominating down to the low frequencies that are used for passive narrowband detection.

An example of a shrimp noise time-series is shown in Fig.1. This shows the in-phase component of the data from a complex demodulated 50-450 Hz passband, that was recorded from an omnidirectional sonobuoy in the Timor sea in water of depth 70 m. The data was pre-whitened at the sensor by 4.5 dB/octave.

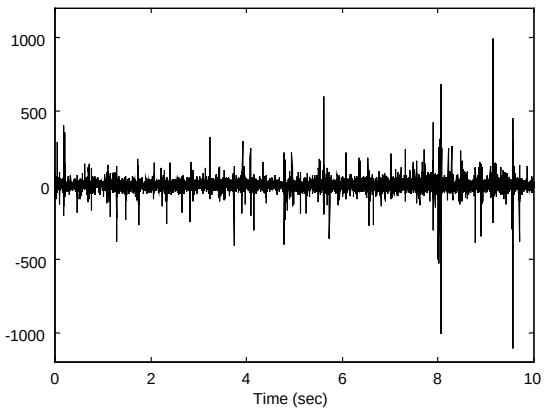

Figure 1. In-phase time-series for shrimp noise; 50-450 Hz complex demodulated passband.

The spikiness of the time-series gives rise to a much higher probability of obtaining extreme sample values compared with Gaussian noise. For example, Fig.2 shows the exceedance probability for the envelopes in a 5 minute segment of data that passed the Kolmogorov-Smirnov two-sample test of stationarity at the 5% significance level. The triangles show the experimental data, and the dash-dot curve shows the prediction of the Gaussian model. The envelope distribution is clearly extremely 'heavy-tailed,' and this gives rise to a severe false-alarm-rate problem when conventional detectors are used.

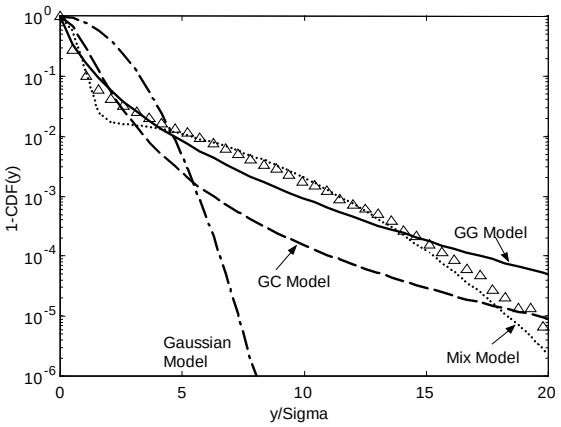

Figure 2. Envelope exceedance probability; 50-450 Hz complex demodulated passband.

The other curves in Fig.2 show the predictions of three probability models commonly used to represent the bivariate distribution for the in-phase and quadrature components of heavy-tailed noises. Shown are the generalised Cauchy (GC), generalised Gaussian (GG), and Gaussian-Gaussian mixture (Mix) models [2-3]. These and other simple analytic models that we have investigated fail to give a good fit to the data. However, just including heavy-tailed distributions into the design of the receiver, is often sufficient to ensure significant gains when the noise is highly non-Gaussian.

Non-Gaussian narrowband detection

The theory of incoherent detection of random sinusoids buried in non-Gaussian noise is discussed in [4]. For detection in a passband, we first complex demodulate the received data,

$$\hat{x}_i = x_{I,i} + j\, x_{Q,i} \tag{1}$$

Here the real and imaginary parts are the in-phase and quadrature samples. Noise-only samples are modeled as independent and identically distributed samples from a bivariate probability density with circular symmetry,

$$P_N\left(x_I, x_Q\right) = h\left(\sqrt{x_I^2 + x_Q^2}\right) \tag{2}$$

The locally optimum detector (LOD) is the optimum detector (eg. in the Neyman-Pearson sense) as signal strength approaches zero. If the passband is centred on the signal frequency, and a total of *N* data samples are received, then the LOD is given by ([2], [4]),

$$\left|\sum_{i=0}^{N-1} g_{lo}\left(y_i\right)\hat{x}_i\right|^2 + \sum_{i=0}^{N-1} l_{lo}\left(y_i\right) > \gamma \tag{3}$$

where γ is a threshold, y_i is the envelope time-series,

$$y_i = \sqrt{x_{I,i}^2 + x_{Q,i}^2} \tag{4}$$

and g_{lo}, l_{lo} are memoryless nonlinear filters,

$$g_{lo}(y) = \frac{-h'(y)}{y\,h(y)} \tag{5}$$

$$l_{lo}(y) = \frac{h''(y)}{h(y)} + \frac{h'(y)}{y\,h(y)} - \left(\frac{h'(y)}{h(y)}\right)^2 \tag{6}$$

The second term on the LHS of Eq.(3) is negligible when the number of samples is sufficiently large ([4]).

If the passband is centred on a frequency f_0, and the signal has arbitrary frequency f within that passband, then the large sample LOD becomes,

$$\left|\sum_{i=0}^{N-1} g_{lo}\left(y_i\right)\hat{x}_i\, e^{-j2\pi i(f-f_0)\Delta t}\right|^2 > \gamma \tag{7}$$

where Δt is the time-interval between samples of the complex-valued time-series.

For detection in impulsive noise, the locally optimum nonlinearity is a decreasing function of envelope. For example, if the noise is described by the generalised Cauchy model,

$$P_N\left(x_I, x_Q\right) = \frac{\nu}{\pi\beta^2}\left\{1 + \frac{x_I^2 + x_Q^2}{\beta^2}\right\}^{-(\nu+1)} \tag{8}$$

then the optimum nonlinear filter is given by,

$$g_{lo}(y) = \frac{2(\nu+1)}{\beta^2}\left(1 + \frac{y^2}{\beta^2}\right)^{-1} \tag{9}$$

Here $\nu > 1$ and β are model parameters.

The LOD effectively scales each complex-valued data sample by the output of the nonlinear filter applied to the envelope of that sample. A data sample with large envelope is highly likely to be contaminated by a noise spike, and the output of the nonlinear filter will scale down the amplitude of that sample. This reduces the impact of that sample on the detection statistic, and the result is to cut down the broadband noise contributed to the spectrum by noise spikes.

Nonparametric detection is an alternative, sub-optimal approach to signal detection that doesn't depend on any particular noise model. The 'hard-limiter narrowband

correlator' (HNC) detector is widely used in impulsive noise environments [4-5]. In this case we replace the locally optimum filter in (7) by,

$$g_{hnc}(y) = \frac{1}{y} \tag{10}$$

The HNC detector has the useful property that it gives constant false-alarm-rate (CFAR) performance over the entire class of noise with circularly symmetric bivariate densities.

Adaptive non-Gaussian processor

Our adaptive non-Gaussian processor uses a modified version of (7) to carry out lofargram (time-frequency) processing. The modifications are (i) each segment of data is tapered with a window, w_i, to reduce spectral leakage, (ii) we average the detection statistics from a number of data segments to reduce variance, and (iii) we use FFTs to compute detection statistics for a range of frequencies. The detection statistic at each frequency bin, k, is given by,

$$T(k) = \sum_{m=1}^{M} \left| \sum_{i=0}^{N-1} w_i \, g(y_{m,i}) \hat{x}_{m,i} \, e^{-j2\pi ik/N} \right|^2 \tag{11}$$

$$k = 0,\ldots, N-1$$

where M denotes the number of segments, N denotes the number of complex-valued samples per segment, and the subscripts refer to the i^{th} sample of the m^{th} segment. Equation (11) specifies pixel intensity over each line of the time-frequency display. We have two versions of the processor; one based on parametric locally optimum detection, and the other on the HNC nonparametric detector.

Adaptive parametric non-Gaussian processor

We choose a parametric model for the bivariate noise distribution and derive the nonlinear filter using (5). A schematic diagram illustrating the structure of the processor is shown in Fig.3. We begin by reading-in a block of raw data corresponding to a single line of the display, and then complex demodulate the passband of interest, and decimate appropriately. This gives a block of complex-valued time-series data. We estimate the parameters of the background noise from this block of data, and feed these parameters into the nonlinear filter to tune the receiver to the prevailing noise conditions. We then run the same complex time-series data through two paths of the receiver. In one path we compute the envelope of each sample, and then pass it through the nonlinear filter. We then mix the output of the filter with the complex time-series data in the other path. The resulting time-series is passed on to a conventional lofargram processor for segmentation, windowing etc. The parameters of the filter change as each new block of raw data is read-in, so the processor adapts to slow changes in the noise statistics.

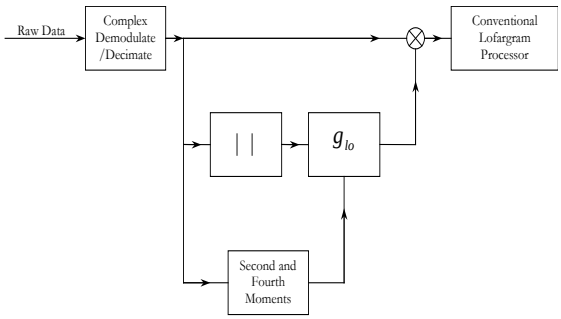

Figure 3. Adaptive non-Gaussian processor based on parametric locally optimum detector.

We have experimented with a number of noise models, including the generalised Cauchy (GC), the generalised Gaussian (GG) and two-component Gaussian-Gaussian mixture (Mix) model, and consistently obtained best results using the GC model. The nonlinear filter is then given by (9), and there are two parameters to estimate from the received data.

Our technique for estimating the noise parameters is based on the assumption that the tonals are sufficiently weak that their presence in the received data does not significantly affect the statistics of the passband being analysed. More specifically, we assume that the second and fourth moments of the complex demodulated time-series are not significantly affected by the presence of the signal. This assumption will be reasonable provided the width of the passband is large compared with the bandwidth of a tonal, and provided that the tonals are not too intense. On the other hand, the passband should not be so wide that the white noise assumption is invalid. We typically use passbands several hundred hertz wide, and have obtained good results using pre-whitened sonobuoy data.

We estimate the model parameters by applying method of moments to the marginal distribution. We read-in a block of complex-valued data, pool together the in-phase and quadrature samples, and compute the second and fourth moments, m_2 and m_4. An advantage of the GC model is that the model parameters are very simply related to these moments,

$$\nu = \frac{2m_4 - 3(m_2)^2}{m_4 - 3(m_2)^2} \tag{12}$$

$$\beta^2 = \frac{2m_2 m_4}{m_4 - 3(m_2)^2} \tag{13}$$

Because no iterative computations are used to estimate the model parameters, the processing can be carried out

rapidly. Thus the computational cost of the adaptive non-Gaussian processor is only a little more than for a conventional lofargram processor.

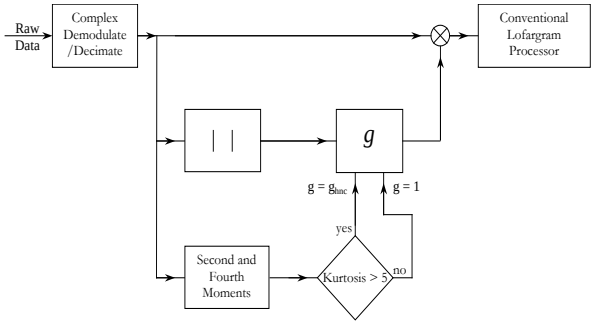

Figure 4. Adaptive non-Gaussian processor based on the HNC nonparametric detector.

Adaptive nonparametric non-Gaussian processor

We have also implemented a version of the processor based on the nonparametric HNC detector. Here we replace the locally optimum filter with the HNC filter, (10). Theoretical studies have shown that the HNC detector performs poorly in Gaussian noise. Because of this, we design the processor so that it estimates the statistics of the noise in each block of data, and only applies the HNC filter when the noise is sufficiently impulsive to give a performance gain. A schematic diagram illustrating the structure of the processor is shown in Figure 4. After the data has been complex demodulated and decimated, the second and fourth moments of the combined in-phase and quadrature data are computed, and from this the kurtosis of the marginal distribution is computed. The more impulsive the noise is, the higher the kurtosis. If the kurtosis is larger than a pre-selected threshold, then the nonlinear filter is set to the HNC filter. If not, then the filter is set equal to unity, which is equivalent to carrying out conventional processing on that block of data. The time-series data is then run through the two paths of the processor, as before. Based on theoretical performance curves, we have selected a kurtosis threshold of 5 for our processor and have obtained good results.

Display processing

The display processing used for adaptive non-Gaussian processing is the same as for conventional lofargram processing. We typically use two techniques, spectral equalisation and/or histogram mapping.

For spectral equalisation we use the order-truncate-average (OTA) algorithm ([6]) applied to each line of the time-frequency display independently of the others. To apply OTA, we first compute the median of the detection statistics for all bins within a window centred on the bin of interest. We estimate the sample mean within that window, but including only those bins that have a value less than some constant times the median. The constant is chosen to have a value that will ensure that those bins containing a strong signal are excluded from the estimate. The detection statistic at the bin of interest is then divided by this sample mean.

Histogram mapping is also applied to each line of the time-frequency display, independently of the others. We compute the dB value of the detection statistic in each bin, and map each value to one of 32 levels. The mapping is obtained from the histogram of bin values, as follows. The 50% lowest bin values are all mapped to level 1, and the 5% highest bin values are all mapped to level 32. For the remaining bin values, the mapping assigns the 30 levels in such a way that each level is populated by an equal number of bins. Thus the central portion of the histogram is equalised.

Experimental results

Figures 5-7 present a side-by-side comparison of the outputs of a conventional lofargram processor, adaptive parametric processor, and adaptive nonparametric HNC processor. The time-series data was recorded from an omnidirectional sonobuoy in the Timor sea, at a time when several surface vessels were in the vicinity. The background noise was dominated by snapping shrimp. The 50-450 Hz passband was analysed, where many tonals from the surface vessels can be found, but only a section of the full passband is shown. All of the time-frequency displays shown here have identical display processing (histogram mapping only).

The squiggly curve that can be seen just off centre in each display, is the Doppler-distorted signature from the aircraft that recorded the sonobuoy data. A number of tonals from the surface vessels can also be observed. Several have been labelled; S_1 to S_7. The parametric and nonparametric processors perform almost equally well, and both perform considerably better than the conventional lofargram. Many tonals that are clearly evident in the non-Gaussian outputs, are completely buried in the noise in the conventional output.

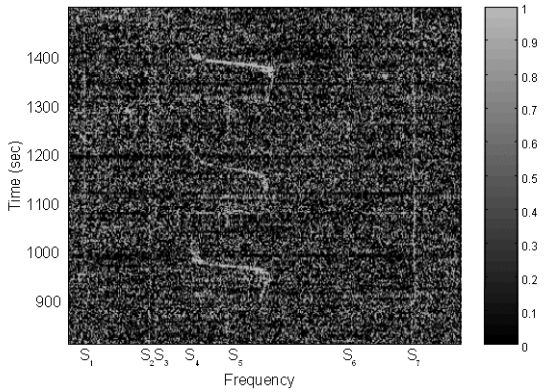

Figure 5. Conventional processor.

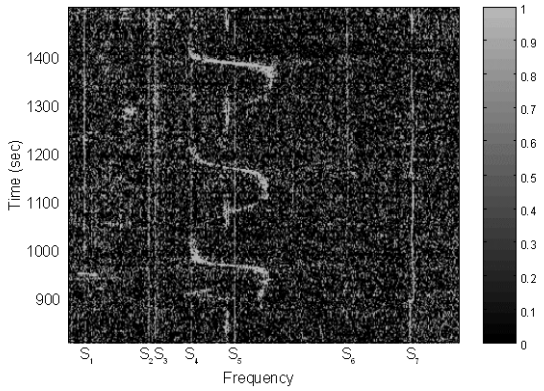

Figure 6. Parametric non-Gaussian processor.

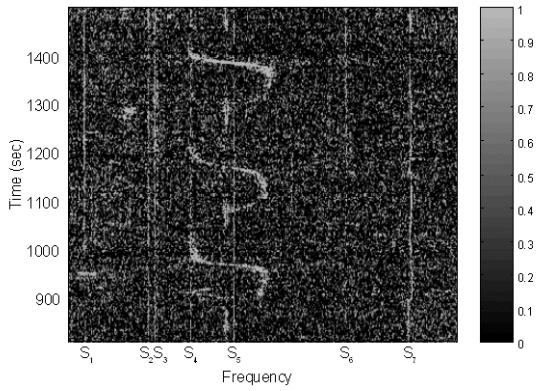

Figure 7. Nonparametric non-Gaussian processor.

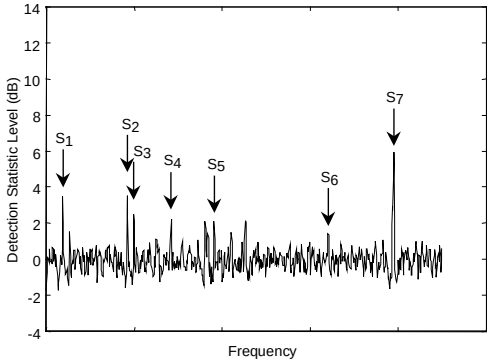

Figure 8. Conventional processor.

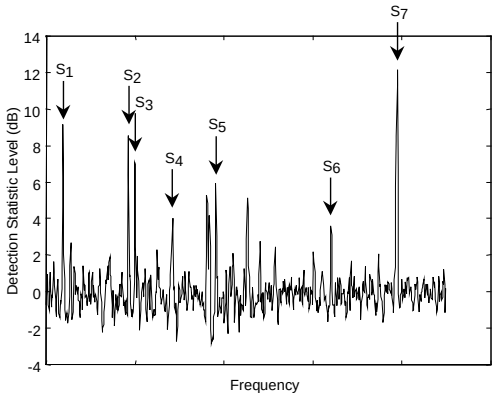

Figure 9. Parametric non-Gaussian processor.

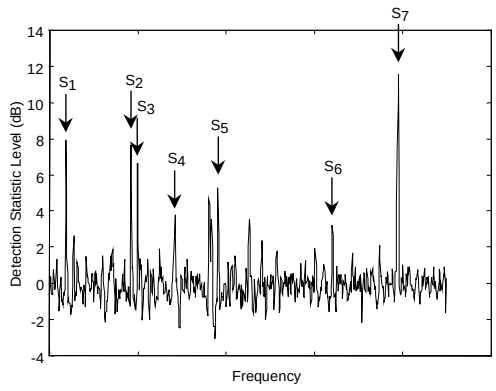

Figure 10. Nonparametric non-Gaussian processor.

Figures 8-10 show corresponding spectra computed for a 5 minute segment of data. Here OTA was applied to equalise each spectrum. We quantify the non-Gaussian processing gains by computing deflections,

$$d = \frac{E\{T(k)\,|\,H_1\} - E\{T(k)\,|\,H_0\}}{\sqrt{\mathrm{var}\{T(k)\,|\,H_0\}}} \qquad (14)$$

Here $E\{T|H_1\}$ is the detection statistic in the signal-plus-noise bin, and $E\{T|H_0\}$, $\mathrm{var}\{T|H_0\}$ are estimated by computing the sample mean and sample variance of the detection statistics in a window of 100 noise-only bins. The measured deflections are presented in Table 1 below.

	Conventional	Parametric	Nonparam.
S_1	10 dB	15 dB	14 dB
S_2	10 dB	14 dB	13 dB
S_3	8 dB	12 dB	12 dB
S_4	7 dB	8 dB	8 dB
S_5	7 dB	11 dB	10 dB
S_6	5 dB	10 dB	10 dB
S_7	14 dB	21 dB	21 dB

Table 1. Deflections of selected tonals.

Non-Gaussian processing increases the deflections by up to 7 dB over conventional spectral processing. Also note that the parametric version of the processor gives marginally better performance than the nonparametric version.

Conclusion

Biological noise is sometimes highly impulsive, and significant non-Gaussian effects may persist down to the low frequencies used for passive narrowband detection. Significant sonar performance gains can be obtained by including non-Gaussian statistics into the design of the receiver. We have not discussed potential problems that can arise with this type of processing. Performance losses can occur at large SNRs as a result of the nonlinear filtering, and this problem is currently under investigation.

References

1. D.H.Cato and M.J.Bell, "Snapping shrimp noise in Australian shallow waters at frequencies up to 200 Hz," Materials Research Laboratory, Maribyrnong, Vic., Tech.Rep., MRL-TR-91-23 (1992).

2. N.H.Lu and B.A.Eisenstein, "Detection of weak signals in non-Gaussian noise," IEEE Trans. Information Theory, **IT-27**, 755 (1981).

3. D.C.Bertilone and D.S.Killeen, "Statistics of biological noise and the performance of generalised energy detectors for passive detection," to appear in IEEE J.Oceanic Eng.

4. S.A.Kassam. *Signal Detection in Non-Gaussian Noise*, Springer-Verlag (1988).

5. S.A.Kassam, "Nonparametric hard limiting and sign detection of narrow-band deterministic and random signals," IEEE J. Oceanic Engineering, **OE-12**, 66 (1987).

6. R.O.Nielsen, *Sonar Signal Processing*, Artech House (1991).

Classification Of Underwater Transients Using Wavelet Techniques

Dragana Carevic and J.A. Ward

Maritime Operations Division, DSTO Stirling and Murdoch University, W.A.

Abstract

Classification of underwater transients presents a challenging problem as the signals may be noisy and highly non-stationary, and the classes poorly defined. Parameters, such as aspect, range, target depth and sea depth, and general variability of ocean conditions may affect the classifier performance. So a classifier should take into account as many of the above parameters as possible and be robust with respect to noise.

Wavelet packet decompositions (WPD) have shown promise for detection and classification of transients. They provide flexible representations of signals by selectively matching their time and frequency characteristics, but are sensitive to signal time shifts. As the presence of the background noise makes it difficult to align transients, which may introduce temporal dispersion, the performance of the WPD-based classifier can be seriously affected.

In this paper we show that using a shift invariant version of the WPD addresses the temporal dispersion problem, and improves classification performance. Several approaches to noise suppression are also considered

Introduction

This paper reports on work in progress. It concerns the use of wavelet packets for feature selection in transient signal classification. We do not give a lot of technical detail, but hope to give the reader insight into the strengths and weaknesses of this approach. A more technical discussion of our work will be given in a subsequent paper.

Wavelet transforms have become prominent over the past 15 years because they provide localised time-scale-frequency information. Wavelet packets, which generalise wavelet transforms, are a library of bases from which a best basis is often chosen according to some cost criteria. The use of wavelet transforms for transient detection and classification has been the focus of many recent papers, including [1],[2],[4],[9] and [11]. Much of this work is empirical, showing that the wavelet based methods give better results than standard Fourier methods when applied to certain data sets. Our work has been motivated by [11] which uses 'energy maps' derived from a wavelet packet decomposition to produce features for classification, and in the next section we give a brief description of this approach.

For the purposes of classification, the transients need not be distinguished on the basis of their location in time. So, ideally, the selected features for classification should be time invariant in the sense that they are the same for each transient, independent of its position in time. However, features derived from wavelet-type decompositions will not normally have this invariance because small time-shifts of a signal may lead to significant changes to its wavelet coefficients. One way to overcome this problem would be to align the transients in time, before decomposing, but the presence of noise makes this difficult. As we will see, the use of energy maps goes a long way to alleviating the problem, but we will propose a method for calculating energy maps that produces features that are actually invariant to (unchanged by) time shifts.

The transient signals of interest are underwater signals obtained via passive sonar. They may vary in duration, depending on transient class, and the measured signals usually have a low signal to noise ratio. The characteristics of the signals tend to be ill-defined as many of the transients are actually incoherent and highly non-stationary. So Fourier and matched filter methods do not work well. The redundancy of the wavelet packet decomposition allows for a non-parametric feature extraction algorithm that adapts reasonably well to different classes of transients.

Basic algorithm of Learned and Willsky

The algorithm proposed in [11] extracts features for classification from the energy map associated with a wavelet packet decomposition of the signal. This decomposition provides information about the signal's

time-frequency content in each of a number of *bins*. Since many transients lack coherence, in [11], bin energies are used rather than individual coefficients. This results in the loss of any time resolution provided by each bin, but increases robustness relative to noise. The algorithm consists of six steps, which we list and then comment on briefly. It is assumed that a *training data set*, selected from across all classes, has been identified. The steps are:

1. Calculate a wavelet packet decomposition for each signal in the training data set.

2. Calculate the energy map of each signal from its decomposition.

3. Compensate for the presence of noise.

4. Derive an energy map profile for each class.

5. Reduce the dimension of the set of training feature vectors by focusing on the energy content of certain dominant bins.

6. Classify each new signal using the reduced set of training feature vectors and a rule such as nearest neighbour, or a neural network.

We now give more information on those aspects of the algorithm that are of most interest to us.

The wavelet-packet decomposition

In most descriptions of the wavelet transform or wavelet packet decomposition, authors start with a function φ defined on **R**, the *scaling function*, and derive the *wavelet function* ψ which provides the fundamental building blocks for an orthogonal representation of various classes of functions on **R**. They derive sequences *h* and *g* that are used to efficiently determine the coefficients in the orthogonal expansion. However, in practice, only sampled function values are available, and the analysis is made on (finite) sequences. This analysis can be done without explicit knowledge of either φ or ψ, just using *h* and *g*, and that is a natural place to start here.

The wavelet and wavelet packet decompositions of a square-summable (finite energy) signal $x=(x_n)$ in $l^2=l^2(\mathbf{Z})$ are obtained using low-pass and high-pass filtering, and down-sampling operations (keeping evenly indexed terms), iteratively. This process can be described as follows. Assume that a summable (often finite) real sequence $h=(h_n)$ is given, and that $g=(g_n)$ is defined by $g_n=(-1)^n h_{-n+1}$ for each n. The fundamental operators H and G are defined on l^2 by $y=Hx$ and $z=Gx$, where for each integer n

$$y_n = (\tilde{h} * x)_{2n} \text{ and } z_n = (\tilde{g} * x)_{2n},$$

* is discrete convolution and the ~ -operation is defined by $\tilde{u}_k = \overline{u}_{-k}$ for each sequence u. In spite of the down-sampling, x can be recovered (*perfectly reconstructed*) from Hx and Gx provided that

$$HG^* + GH^* = 0 \text{ and } HH^* + G^*G = I, \quad (1)$$

where the superscript * is used to denote an adjoint operator. When (1) holds, the pair *(h,g)* is called a *quadrature mirror filter*. Obviously it imposes some restrictions on the sequence *h*, as do other design criteria of the underlying wavelet such as regularity and symmetry. Typically it is assumed that:

1. $\sum_k h_{2k} = 2^{-1/2} = \sum_k h_{2k+1}$;

2. $\sum_k h_{2k} h_{k+2l} = 0$ for all non-zero integers l;

3. $\sum_k |k|^M |h_k| < \infty$ for some integer $M>0$;

to ensure perfect reconstruction, orthogonality and some regularity. If *h* has these properties, then it corresponds to a low-pass filter $m_0(\xi) = \sum_k h_k e^{ik\xi}$, and *g* to a high-pass filter $m_1(\xi) = \sum_k g_k e^{ik\xi}$. The sequence Hx is an averaged or low-frequency component of x, while Gx is a detail or high frequency component. These components are orthogonal, and it can be shown that Hl^2 and Gl^2 are orthogonal subspaces of l^2, and $l^2 = Hl^2 \oplus Gl^2$ (see [3]).

At each stage of the *wavelet transform* algorithm, the high frequency component is retained and the low frequency component is itself decomposed into low and high frequency components. This can be repeated, although in practice when x has finite length, say of dyadic length 2^L, at most L times. After J iterations, it produces components Gx, GHx, GH^2x, ..., GH^Jx and $H^{(J+1)}x$. These correspond to decreasing frequency bands, with GH^jx giving the *wavelet coefficients* of x at level $j+1$, for $j=0,1,\ldots,J$, and $H^{(j+1)}x$ *the scaling coefficients* at level $J+1$. An iterative process may be used to recover x from these coefficients, and the basic step is $H^jx = H^*H^{(j+1)}x + G^*GH^jx$ for each j.

At each stage of the *wavelet packet decomposition* algorithm, both low and high frequency components are decomposed. This gives rise to a dyadic tree. For example, after three iterations the table has the following structure:

x							
Hx				***Gx***			
HHx		***GHx***		*HGx*		*GGx*	
HHHx	***GHHx***	*HGHx*	*GGHx*	*HHGx*	*GHGx*	*HGGx*	*GGGx*

The table is organised into a number of *levels* (four in the diagram above), with the *0-level* containing the signal itself, and giving its finest time-resolution. Time resolution decreases as level increases. There are 2^j *bins* of coefficients on the *j* level. The bins correspond to frequency bands, and can be arranged in increasing frequency order across the level. Each bin at level *j* (a parent) produces two new bins at level *j+1* (its children).

The wavelet packet tree for a signal is highly redundant. It 'contains' many bases, including the associated wavelet basis, which to level 3, corresponds to the boldface bins in the above diagram. In many applications the goal is to select a basis from the dictionary that is optimal in some sense, and this leads to a discussion of a best basis. However in this paper we do not use best basis as our goal is to exploit the redundancy of the wavelet packet decomposition to best focus the energy of the signals.

To see the effect of time shifts on wavelet type decompositions, let *x'* denote the shift of *x* by *1*, such that $x'_n=x_{(n-1)}$ for each *n*. Then the low and high frequency components of *x'* are *y'=Hx'* and *z'=Gx'* respectively, where for each integer *n*

$$y'_n = (\tilde{h} * x')_{2n} = (\tilde{h} * x)_{2n-1} \text{ and}$$

$$z'_n = (\tilde{g} * x')_{2n} = (\tilde{g} * x)_{2n-1}.$$

So, at the first level y' and *z'* may be obtained by filtering *x* (instead of *x'*) and retaining the odd index terms (rather than the even index terms that give the components for *x* itself). The first level decomposition of the *1*-shift of *x* may be very different to that of *x*. However, those of the other shifts of *x* are easy to describe. The components of an *even (2k)*-shift are k-shifts of the components of *x*, and of an *odd (2k+1)*-shift of *x* are k-shifts of the components of *x*. Furthermore, if we decompose to *j* levels, then we may group the integer shifts of *x* into 2^j groups in such a way that the low (and high frequency) components of all shifts in one group are shifts of each other. These observations will be important later.

We note that in practice each signal *x* is a 'finite' sequence. For computational reasons, it is often assumed (as we do) that *x* is periodic, so that both *Hx* and *Gx* will be periodic with exactly half the period of *x*. We suspect this assumption was also made in [11] although this is not stated explicitly. (The reader should refer to [15] for a discussion of the practical issues associated with this assumption).

Energy maps and class profiles

The average energy *e* of a vector $w=(w_1,w_2,\ldots w_N)$ is defined to be $e=(w.w^T)/N$. *The energy map* $e^{(x)}$ for a signal *x* measures the average energy in each bin of its wavelet packet decomposition; that is, it gives the distribution of average energy across all bins. If *x* has been decomposed to *J* levels, then $e^{(x)}$ is a vector with $K=2^{(J+1)}-1$ components, and its k^{th} component $e^{(x)}_k$ is the average energy of the coefficient sequence of *x* in bin *k* for $k=1,2,\ldots,K$. Since the average energy is the same for all (cyclic) shifts of a vector, our previous discussion on the effect of time shifts on wavelet type decompositions, explains why the coordinates of the energy map have a certain robustness to time shifts of *x* that make them more useful for classification than the coefficients themselves. However they are not invariant to all time shifts, and we address this issue later.

Noise compensation

Because *x* is noisy, the average energy of a bin *k* has a transient energy component $e^{(s)}_k$ and a noise energy component $e^{(n)}_k$. If the noise is uncorrelated with the transient, then the average energy in each bin is just the sum of these. The noise energy may mask features of the energy map that would be useful for classification, and so it is important to compensate for the noise. This is done in [11] by first determining the mean of the 'average energies' (variance) due to noise in each bin *k*, and then normalising $e^{(x)}_k$ by this average. Other noise compensation methods are possible, and we have investigated some of these. More details are given in a later section.

Class profiles

The normalised energy maps of the test signals in a given class provide an energy profile of that class. They are hopefully indicative of the energy maps of all signals in that class. Energy maps are highly redundant, and feature selection is needed to determine a smaller set of features useful for classification. The feature selection method in [11] uses a singular value decomposition of the energy matrix (containing the energy maps) for each class, and restricts attention to certain bins with large average energy. The feature set is also reduced by discarding those coordinates that are descendents, where there is parent-child redundancy in the corresponding bins. This leaves a small number of features that seem to be good descriptors for the class data under investigation. However these classes appear to be clustered linearly, and it is not obvious that the method will always give good class separability.

Performance

The authors say that 'the wavelet-packet based features obtained by their method for biologically generated underwater acoustic signals yield *86%* to *100%* correct classification when used as input for a neural network and a nearest neighbour rule'. These results were obtained for classification amongst three classes, using the Daubechies *14*-point filter for all experiments. It is

possible (likely?) that other filters would give better results, and this should be investigated. The authors also say that their results 'provide convincing evidence that the wavelet packet transform can be effectively used as the basis for robust, systematic feature extraction and automatic identification of transient signals that cannot be well-characterized by parametric signal models'. We agree with this comment and this has motivated our work.

Our Project

We have noted that time shifts may move energy across bins, and so alter the energy map. We can avoid this problem by using a 'shift-invariant' version of the WPD that uses the flexibility that exists in the downsampling step of the WPD. We have also investigated alternative methods of noise compensation and feature reduction.

Shift-invariant wavelet packet decomposition

Several methods for compensating for the sensitivity of the WPD to the signal's position in time have been proposed recently [4],[12],[13],[14]. We have used the one proposed by [4]. At each stage of a WPD we really have a choice - to downsample keeping the evenly indexed terms of the filtered sequences, or to keep the odd indexed terms. With either we would retain perfect reconstruction.

Previously we introduced operators H and G to correspond to the even downsampling of the WPD. Let H' and G' be the operators that correspond to odd downsampling. The shift-invariant wavelet packet decomposition is obtained by choosing between the options of applying the pair H and G or H' and G', at each step of the decomposition (node) on the basis of minimising a cost function which measures the entropy of the resulting components. In its simplest form, the choice is made by comparing the combined costs of Hx and Gx, and of $H'x$ and $G'x$.

The decomposition is shift-invariant in the sense that best-basis searches produce bases for the original signal and its integer translates that have the same structure and total cost. This bases may not be optimal, relative to the given cost function, because a choice between (H,G) and (H',G') that is optimal for a given node, may exclude more cost-efficient options that arise when the decomposition is extended to more levels. So more cost-efficient bases can be obtained by 'looking ahead'; that is decomposing to deeper levels, before deciding which pair to apply [10]. However, the computational complexity of the decomposition may increase significantly.

To understand the impact of using such a shift-invariant WPD to calculate energy maps, we must consider the effect of time shifts. Again suppose that x' is the *1*-shift of x. Then it is easy to check that $Hx'=H'x$, $H'x'=\tau^{-1}Hx$, $Gx'=G'x$, and $G'x'=\tau^{-1}Hx$, where τ is a *1*-shift to the right. So for x we are choosing between components Hx and Gx and $H'x$ and $G'x$, while for x' the choice is really between $H'x$ and $G'x$, and $\tau^{-1}H$ and $\tau^{-1}Gx$. So, provided that the cost function does not depend on shifts, the average energy of each of the low (and of the high pass) components will be the same for both x and x' (whether we 'look ahead' or not). So the energy map is now the same for all time shifts of x, even if the decomposition is to more levels.

Noise compensation

If the noise is uncorrelated with the signal, then the average energy in each bin is just the sum of the average energy due to the transient and that due to the noise; that is $e^{(x)}_k = e^{(s)}_k + e^{(n)}_k$. In [11] $e^{(x)}_k$ is normalised by the variance due to noise in bin k. We investigated two other noise compensation methods. The first is *hard thresholding* of the coefficients obtained in the wavelet or wavelet packet decomposition [5],[6]. The second method *noise subtraction* assumes that the signal and noise are uncorrelated, and simply subtracts an estimate of the average noise energy in bin k from $e^{(x)}_k$.

Experimental results

At this stage our experimentation is not complete. However, the results that we present should give the reader some idea of the effectiveness of our methods.

We used a database of underwater acoustic transients that contained six different transient classes. Of the six classes, five are submarine generated transients and the sixth is biologically generated. The transients are not stationary and the time duration of the signals varies from *0.08* to *6* seconds. All transients are noisy, with signal-to-noise ratios (SNRs) that vary from approximately *0* dB to *10* dB.

We used three types of wavelet packet decomposition: the standard WPD (denoted by StWPD) and two versions of the shift invariant WPD, one (SIWPD-0) with no 'look ahead' and the other (SIWPD-1) looking ahead one level at each stage. Shannon's entropy cost function was used for the shift invariant decompositions. We investigated the effect of decomposing to different levels, namely *4*,*5*, and 6, which produces energy maps of length *31*, *63* and *127* respectively. Our basic wavelet was *Symlet8*. We tried all three noise reduction methods described in earlier sections, and we denote these by Nnorm. for the noise normalisation approach of [11], Nsubtr. for noise subtraction, and Nthresh. for hard thresholding. We used an empirically determined threshold. The effectiveness of the features computed in this way for classification was tested using classifiers based on the nearest-neighbour decision rule

[7], and both the *leave-one-out* (LOO) [7], and simple *multiple tests* (MT) methods. We did not include feature reduction when using LOO, but for MT used a feature reduction method that emphasised between-class separation. The results obtained using LOO method are shown in Table 1. It can be seen that, in general, better classification results were obtained by using a shift-invariant WPD, along with the thresholding method for noise suppression. For MT, the error rates averaged from 12-15% when using a shift-invariant decomposition.

Feature Type	Maximum WPD level 4	5	6
StWPD, Nnorm.	12.40	9.60	9.60
StWPD, Nsubtr.	14.80	11.20	9.60
StWPD, Nthresh.	12.00	9.60	10.00
SIWPD-0, Nnorm	8.80	8.00	8.80
SIWPD-0, Nsubtr.	6.40	8.40	7.20
SIWPD-0, Nthresh.	9.60	7.20	5.20
SIWPD-1, Nnorm.	12.00	8.00	10.00
SIWPD-1, Nsubtr.	10.00	8.40	8.80
SIWPD-1, Nthresh.	9.20	6.00	6.40

Table 1: Error rates (%) for LOO method when using WPD energy maps (with no feature reduction), and a nearest neighbour classifier.

Conclusion

We believe that improved classification of underwater transients can be achieved by using features that have been extracted from an energy map derived from a shift-invariant wavelet packet decomposition. There is no obvious benefit to looking ahead, although better results may be obtained by decomposing to deeper levels. Noise thresholding as a noise reduction method seems to give the best results in general. It seems likely that even better results could be obtained by using a more sophisticated feature extraction process, or by using one of the new adaptive (and shift invariant) wavelet packet decompositions [8]. We are encouraged by our preliminary results, and hope to extend them in the future.

Acknowledgement: The authors wish to thank Mr Marc Masoni from Thompson-Marconi for many stimulating and useful discussions.

Bibliography

[1] Bailey, T.C., T. Sapatinas, K.J. Powell and W.J. Krzanowski, Signal detection in underwater sound using wavelets, *J. Amer. Stat. Soc.*, (1997).

[2] Carmona, R.A., Wavelet identification of transients in noisy time series, in *Proc. SPIE Math. Imag.*, vol. 2825, 342-351 (1996).

[3] Daubechies, I., *Ten lectures on wavelets*, CBMS-NSF Regional Conference Series in Applied Mathematics, vol. 61, SIAM, 1992.

[4] Del Marco, S. and J. Weiss, Improved transient signal detection using a wavepacket-based detector with an extended translation invariant wavelet transform, *IEEE Trans. Sig. Proc.*, 45(4), 841--850 (1997).

[5] Donoho, D.L., De-noising by soft-thresholding, *IEEE Trans. Info. Theory*, 41(5), 613-627 (1995).

[6] Donoho, D.L. and I.M. Johnstone, Ideal spatial adaption by wavelet shrinkage, *Biometrika*, 81, 425-455 (1994).

[7] Fukunaga, K., *Introduction to statistical pattern recognition*, Academic Press, 1990.

[8] Guo, H., *Theory and applications of the shift-invariant, time-varying and undecimated wavelet transforms*, Masters Thesis, Rice University, 1995.

[9] Guanghui, Z., H.Zailu and H. Zhengquiang, Wavelet packets algorithm and its application in signal detection, in *Proc. SPIE Mathematical Imaging*, vol. 2034, 426-431 (1993).

[10] Lang, M., H. Guo, J.E. Odegard, C.S. Burrus and R.O. Wells Jnr., Nonlinear processing of a shift-invariant DWT for noise reduction, in *Proc. IEEE Conf. on Time-Frequency and Time-Scale Analysis*, 1-4 (1994).

[11] Learned, R.E., and A.S. Willsky, A wavelet packet approach to transient signal classification, *App. Comp. Harm. Anal.*, 2, 265-278 (1995).

[12] Liang, J. and T.W. Parks, A translation invariant wavelet representation algorithm with applications, *IEEE Trans. Signal Proc.*, 44, 225-232, 1996.

[13] Pesquet, J.-C., H. Krim, and H Carfantan, Time-invariant orthonormal wavelet representations, *IEEE Trans. Signal Proc.*, 44(8), 1964-1970, 1996.

[14] Simoncelli, E.P., W.T. Freeman, E.H. Adelson and D.J. Heeger, Shiftable multiscale transforms, *IEEE Trans. Inform. Theory*, 38, 587-607, 1992.

[15] Strang, G. and T. Nguyen, *Wavelets and filter banks*, Wellesley-Cambridge Press, 1996.

Stochastic Resonance Applications in Underwater Acoustic Signal Detection

Ross L. Dawe and Edwin R. Galbreath

Maritime Operations Division, Aeronautical and Maritime Research Laboratory,
Defence Science and Technology Organisation
P.O. Box 1500 Salisbury
South Australia 5108, Australia.

Email: ross.dawe@dsto.defence.gov.au, edwin.galbreath@dsto.defence.gov.au

Abstract

This paper describes current research on the use of stochastic resonance for sonar applications. The aim is to develop a robust sonar detector designed specifically to look for very weak or "stealthy" targets, such as those with a typical probability of detection (PD) of a few percent or less. A working prototype is called ISHTAR, which stands for "Improved Sonar Harnessing Temporal Acoustic Resonances" and is an extension of a conventional sonar processing, detection and information display chain. A brief description of some of the theory will be given for Gaussian, exponential, Rayleigh and chi-squared noise statistics. This will be followed by an example of ISHTAR successfully applied to the passive detection of test signals in sea trial data.

Introduction

This paper describes some recent work in applying the principles of stochastic resonance to the detection of very weak fluctuating acoustic signals in a background of ocean ambient noise. One application is to the passive detection of signals by antisubmarine warfare sonars, where the received signal to noise ratio is typically extremely weak and variable due to environmental effects. A second application is to modulation processing, also known as DEMON (DEModulation Of Noise) processing: this is also often used to passively detect targets including torpedoes. An experimental sonar detector has been constructed based on stochastic resonance: it is called "ISHTAR", which stands for Improved Sonar Harnessing Temporal Acoustic Resonances.

The inspiration for ISHTAR comes from Urick [1, p.387]: "*At a fixed value of the probability of false alarm the effect of signal fluctuations is to increase the probability of detection when the signal is weak and to decrease the probability of detection when the signal is strong. … This effect, better detection during signal surges at low signal to noise ratios and poorer detection during signal fades at high signal to noise ratios – is observed regularly during detection trials at sea as a slower falloff of the probability of detection with range than would be predicted using the conventional receiver operating characteristic curves.*"

For practical military applications, it is the weak signals that are of more interest. With natural fluctuations making these weak signals more detectable, the idea is to use stochastic resonance to produce random artificial fluctuations that, on average, enhance the detectability of the weak signals. The penalty is that the artificial signals partially suppress the strong signals that are of lesser importance.

The phenomenon of stochastic resonance is described by Bulsara and Gammaitoni [2] and in an extensive review by Gammaitoni et al. [3]. The method is based on deliberately adding noise into a nonlinear system containing a signal to be detected against a background of ambient noise. Some current applications of stochastic resonance in other fields include 'dithering' in electronic analogue to digital converters, as well as superconducting quantum interference devices (SQUIDS). For a sonar application the necessary nonlinearity is in the statistics of the acoustic signal plus noise probability density function.

The version of stochastic resonance used here works by taking the incoming sonar data and deliberately injecting into the system a series of known artificial signal fluctuations drawn from a distribution of zero mean Gaussian random numbers. The net effect is to increase the effective output signal to noise ratio, but only under the right conditions. An important caveat for this particular sonar application is that the observer must know and control the statistical properties of the added fluctuations, otherwise the fluctuations simply increase the noise interference.

To show how these added artificial signals can improve the observer's probability of detecting the natural signals, four separate statistical distributions will be considered: Gaussian, exponential, Rayleigh and Chi-

squared. In each case an example of receiver operating characteristic (ROC) curves will be given, so as to demonstrate the effect on the probability of detecting the signal for a given probability of false alarm and noise statistics. Finally, some results produced by the ISHTAR detector when applied to sea trial data will be shown.

Gaussian statistics

To see how the fluctuations can enhance the probability of detecting a weak signal, consider the following example based on Gaussian statistics for each of the distributions of noise, fluctuating signals and added artificial fluctuations. Here μ is the mean and σ is the standard deviation. In what follows the subscripts '*s*', '*n*' and '*a*' on quantities refer to the signal, noise and added artificial signal fluctuations respectively.

The Gaussian probability density function (pdf) is described for $-\infty < x < \infty$ by

$$f(x) = \left(\frac{1}{\sqrt{2\pi\sigma^2}}\right)\exp\left(\frac{-(x-\mu)^2}{2\sigma^2}\right). \quad (1)$$

This pdf has its mean and variance replaced by (μ_n, σ_n^2) if just noise is present, $(\mu_n+\mu_s,\ \sigma_n^2+\sigma_s^2)$ if a signal with Gaussian fluctuations plus noise is present, or $(\mu_n+\mu_s+\mu_a,\ \sigma_n^2+\sigma_s^2+\sigma_a^2)$ if artificial Gaussian fluctuations are added in. For a constant signal $\mu_s \neq 0$ but $\sigma_s = 0$.

It is necessary to determine the detection index *d*. This is defined by Urick [1] as being

$$d = (M_1 - M_2)^2 / \sigma^2 \quad (2)$$

where M_1 is the mean of the signal, noise and artificial signal fluctuations together, M_2 is the mean of the noise and artificial signal fluctuations together and σ^2 is the variance of the noise. Here $d \to 0$ describes the worst case scenario when the signal is vanishingly small. The definition (2) shows that increasing *d* corresponds to an increase in signal strength relative to the spread of the distribution. For a constant signal in Gaussian noise statistics the detection index is given by $d_n = \mu_s^2/\sigma_n^2$, but when the signal undergoes Gaussian fluctuations the detection index becomes $d_{sn} = \mu_s^2/(\sigma_n^2+\sigma_s^2)$. When Gaussian artificial signal fluctuations are added to the system then $d_{sna} = \mu_s^2/(\sigma_n^2+\sigma_s^2+\sigma_a^2)$.

Now define a fluctuation index *k* for Gaussian statistics in the same manner as Urick [1], where the subscripts on each *k* indicate the origin of the fluctuations:

$$k_{sn}^2 = (\sigma_s^2+\sigma_n^2)/\sigma_n^2 \ , \quad (3a)$$

$$k_{sna}^2 = (\sigma_s^2+\sigma_n^2+\sigma_a^2)/\sigma_n^2 \ . \quad (3b)$$

The next step is to construct receiver operating characteristic (ROC) curves, which are plots of the probability of detection (PD) as a function of the probability of false alarm (PFA) for various values of the detection index. The PFA is found by integrating (1) for $f_n(x)$ from an arbitrary threshold *T* to ∞ to obtain

$$PFA = \frac{1}{2}erfc\left(\frac{1}{\sqrt{2}}\left[\frac{T}{\sigma_n} - \frac{\mu_n}{\sigma_n}\right]\right). \quad (4a)$$

Here *erfc(x)* is the complementary error function [4]. This expression applies for those cases where the artificial signal fluctuations added in each frequency bin at each time step are known, so that the decision threshold can be adjusted accordingly. This can be accomplished for each frequency bin by summing the artificial signals added over several time steps and dynamically adjusting the threshold accordingly.

If the fluctuating artificial signals are completely unknown, then integrating (1) for $f_{na}(x)$ gives

$$PFA_{na} = \frac{1}{2}erfc\left(\frac{T-\mu_n-\mu_a}{\sqrt{2}\sqrt{\sigma_n^2+\sigma_a^2}}\right). \quad (4b)$$

In this case the added artificial signal fluctuations are effectively just additional noise against which the natural signal must be detected and so will degrade the average detection performance.

The expressions for PD are obtained by integrating (1) from *T* to ∞ for $f_{sn}(x)$ and $f_{sna}(x)$ and using the expressions for *d* and *k* for Gaussian statistics to give

$$PD_{sn} = \frac{1}{2}erfc\left(\frac{1}{\sqrt{2}k_{sn}}\left[\frac{T}{\sigma_n} - \sqrt{d_n} - \frac{\mu_n}{\sigma_n}\right]\right), \quad (5a)$$

$$PD_{sna} = \frac{1}{2}erfc\left(\frac{1}{\sqrt{2}k_{sna}}\left[\frac{T}{\sigma_n} - \sqrt{d_n} - \frac{\mu_n}{\sigma_n} - \frac{\mu_a}{\sigma_n}\right]\right). \quad (5b)$$

Here PD_{sn} applies for natural fluctuating Gaussian signals: if instead the incoming signal is constant then $k_{sn} = 1$ in (5a). The expression for PD_{sna} applies when there are added artificial signal fluctuations as well as a fluctuating natural signal. Equations (4a) and (5a), originally derived by Urick and Gaunaurd [5], can be used to generate the ROC curves by varying *T*. Simply by setting $\mu_a = 0$ and replacing k_{sn} with k_{sna} means that

these same ROC curves also apply when added artificial signal fluctuations are present.

Figure 1 shows a set of ROC curves for a detector based on Gaussian noise statistics for d_n = 0, 1, 4, 9, 14 and 25 when μ_n = 0. The solid lines apply when there are no signal fluctuations such that k_{sn} = 1, while the dashed lines apply for the case where there are signal fluctuations such that k_{sn} = 2. Note that the dashed lines could just as easily be for k_{sna} = 2 and μ_a = 0. The case k_{sn} = 1, for which σ_s = 0, produces the familiar set of ROC curves for a constant signal in a background of white Gaussian noise as given by Urick [1] and the Sonar Modelling Handbook [6].

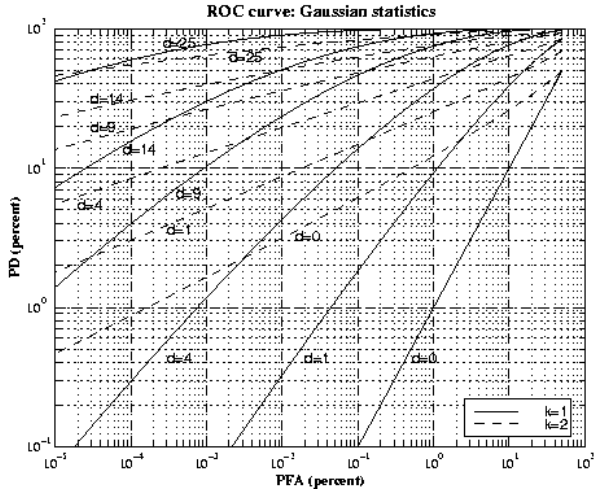

Figure 1. Gaussian ROC curves, which are plots of PD versus PFA for various values of the detection index d_n for the cases of no fluctuations (k = 1) or some fluctuations (k = 2).

Inspection of Figure 1 shows that for a fixed value of PFA the effect of the signal fluctuations is to increase PD when the signal is relatively weak. For example, at PFA = 10^{-2}% and d_n = 4 it can be seen that PD increases from 4.2% when k = 1 to 19% when k = 2. For PFA = 10^{-4}% and d_n = 4 it can be seen that PD increases from 0.3% for k = 1 to 8.5% for k = 2. Of particular note in Figure 1 is that the biggest relative increase in PD for a given value of PFA occurs for very small values of d_n, which corresponds to the weakest signals. Hence the appearance of fluctuations, regardless of whether they are natural or artificial, significantly boosts the sonar observer's chances of detecting especially weak signals.

The drawback of this detector is that the technique actively suppresses strong signals. For example, for a PFA = 10^{-2}% and d_n = 25, Figure 1 shows that PD = 90% for k = 1 and PD = 73% for k = 2. This drawback is corrected simply by running a conventional detector in parallel with a stochastic resonance detector, although extra display space then needs to be used to show the results to the observer.

Exponential statistics

Exponential statistics are often applicable as a good approximation to the input statistical distributions typically observed with power detectors (equivalent to energy detectors) [6, 7]. Examples of these types of detectors include passive systems such as sonobuoys and hull mounted arrays. In practice chi-squared statistics (see below) are the generalised case, but exponential statistics are mathematically more tractable and amenable to analysis. The exponential probability density function (pdf) is described by

$$f(x) = \left(\frac{1}{\mu}\right)\exp\left(\frac{-x}{\mu}\right) \qquad \text{for } x \geq 0, \tag{6}$$

while $f(x)$ = 0 otherwise. For exponential statistics the mean μ is also the standard deviation. Hence this pdf has its mean replaced by μ_n if just noise is present, $\mu_n+\mu_s$ if a signal is also present, or $\mu_n+\mu_s+\mu_a$ if artificial signals are added in. It is assumed that the artificial signals are drawn from an exponential distribution. As the standard deviation is the same as the mean, it is now necessary to add standard deviations rather than variances when calculating the detection index from (2). This gives $d_n = \mu_s^2 / \mu_n^2$ and when artificial signals are inserted $d_{na} = \mu_s^2 / (\mu_n + \mu_a)^2$.

The fluctuation index k is defined in a different manner for exponential statistics compared to the version used for Gaussian statistics, so that

$$k_{sn} = \frac{\mu_s + \mu_n}{\mu_n} = \sqrt{d_n} + 1 \ , \tag{7a}$$

$$k_{sna} = \frac{\mu_s + \mu_n + \mu_a}{\mu_n} = \sqrt{d_n} + 1 + \frac{\mu_a}{\mu_n} \ . \tag{7b}$$

Here k_{sna} applies when artificial signals have been added to the system, and reduces to k_{sn} when $\mu_a \to 0$. Integrating the exponential pdf (6) in the form of $f_n(x)$, $f_{sn}(x)$ and $f_{sna}(x)$ from an arbitrary threshold T to ∞, for the case where the added artificial signals are known exactly, gives PFA and PD as

$$PFA_n = \exp\left(\frac{-T}{\mu_n}\right) \ , \tag{8}$$

$$PD_{sna} = \exp\left(\frac{-T}{\mu_n k_{sna}}\right), \tag{9}$$

where use has been made of (7). To obtain the expression for PD_{sn}, replace k_{sna} in (9) with k_{sn}.

Figure 2 is a set of ROC curves generated from the expressions for PFA and PD for the cases where the exponential fluctuation index k = 1.0 or 1.5. Here k can be either k_{sna} or k_{sn}, with k = 1.5 representing relatively weak fluctuations. Consider an example where PFA = 10^{-2}% and d_n = 1, corresponding to a relatively very weak signal. This gives PD = 1% when k = 1 and PD = 2.4% for k = 1.5. Calculations based on increasing k still further gives PD = 4.5% for k = 2, while for k = 3 then PD rises to 10%. In practice such an increase would lead to a significant improvement in the cumulative probability of detection over a lengthy search period.

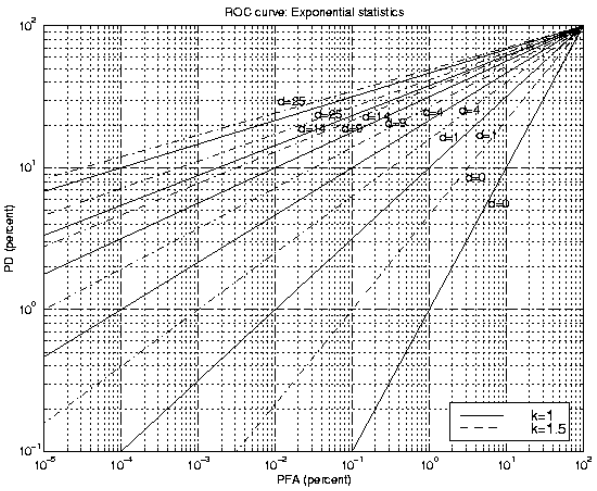

Figure 2. Exponential ROC curves for the cases of no fluctuations (k = 1) or some relatively weak added artificial signals (k = 1.5).

Rayleigh statistics

Rayleigh noise statistics are a good approximation to the input statistical distributions typically observed with amplitude detectors [6, 7, 8]. The Rayleigh pdf is the square root of the exponential distribution discussed above and is described by:

$$f(x) = (2x/\mu)\exp\left(-x^2/\mu\right) \qquad \text{for } x \geq 0, \qquad (10)$$

while $f(x)$ = 0 otherwise. Here the mean is given by $(\pi\mu)^{1/2}/2$ and the standard deviation is $\{(1-\pi/4)\mu\}^{1/2}$, so that the pdf again depends on just one variable. Hence (10) has μ replaced by μ_n if just noise is present, $\mu_n+\mu_s$ if a signal is also present, or $\mu_n+\mu_s+\mu_a$ if artificial signals are added in. It is assumed that the random artificial signals come from a Rayleigh distribution.

The mean and standard deviation for a Rayleigh pdf both depend on the same parameter, which means the standard deviations and not the variances must be added together when calculating the detection index from (2). After some algebra this gives

$$d_n = \frac{\pi}{4-\pi}\left(\sqrt{\frac{\mu_s}{\mu_n}+1}-1\right)^2 , \qquad (11a)$$

$$d_{na} = \frac{\pi}{4-\pi}\left(\sqrt{\frac{\mu_s}{\mu_n+\mu_a}+1}-1\right)^2 . \qquad (11b)$$

Rearranging (11) to obtain expressions in terms of μ_s/μ_n and $\mu_s/(\mu_n+\mu_a)$ gives

$$\frac{\mu_s}{\mu_n} = \left(\frac{4}{\pi}-1\right)d_n + \sqrt{4d_n\left(\frac{4}{\pi}-1\right)} , \qquad (12a)$$

$$\frac{\mu_s}{\mu_n+\mu_a} = \left(\frac{4}{\pi}-1\right)d_{na} + \sqrt{4d_{na}\left(\frac{4}{\pi}-1\right)} . \qquad (12b)$$

The fluctuation index k is defined in a different manner for Rayleigh statistics compared to the versions used for Gaussian or exponential statistics above. Define

$$M_{sn} = \frac{\mu_s+\mu_n}{\mu_n} = 1+\left(\frac{4}{\pi}-1\right)d_n + \sqrt{4d_n\left(\frac{4}{\pi}-1\right)} , \qquad (13a)$$

$$M_{sna} = \frac{\mu_s+\mu_n+\mu_a}{\mu_n} = M_{sn} + \frac{\mu_a}{\mu_n} = M_{sn} + k_{na} . \qquad (13b)$$

Here the quantity M_{sn} applies when the natural signal is present, while the quantity M_{sna} applies when both the natural signal and Rayleigh distributed artificial signals are present Here $k_{na} = \mu_a/\mu_n \geq 0$ is the fluctuation index for the artificial signals based on Rayleigh statistics.

The PFA and PD are again calculated by integrating the pdf from the arbitrary threshold T to ∞. For the case where the added artificial signals are known exactly, these expressions are

$$PFA_{na} = \exp\left(\frac{-T^2}{\mu_n+\mu_a}\right) , \qquad (14)$$

$$PD_{sn} = \exp\left(\frac{-T^2}{\mu_n M_{sn}}\right) , \qquad (15a)$$

$$PD_{sna} = \exp\left(\frac{-T^2}{\mu_n(M_{sn}+k_{na})}\right) , \qquad (15b)$$

where use has been made of (12) and (13). Just as was the case for the previous distributions, the difference in PD when the artificial signals are added is accounted for by the fluctuation index inside the denominator.

Figure 3 is a plot of ROC curves generated from the expressions for PFA and PD for various values of the fluctuation index k_{na} = 0 and 0.5. Consider an example of detecting a relatively very weak signal where PFA = 10^{-2}% and d_n = 1. When there are no artificial signal fluctuations k_{na} = 0 and PD = 1.9%. Increasing the strength of the fluctuations increases the value of PD: relatively small fluctuations where k_{na} = 0.5 gives PD = 3.8%. Calculations show that increasing k_{na} still further to 1.0 gives PD = 6.2%, while k_{na} = 2 gives PD = 12%. A similar trend in PD occurs for other combinations of d_n and PFA for relatively weak signals.

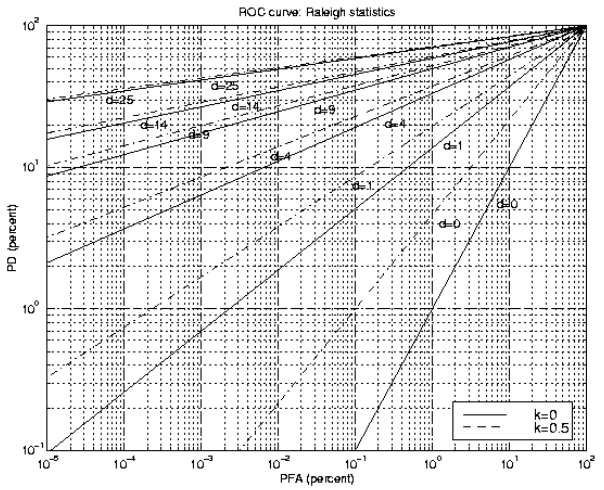

Figure 3. Rayleigh ROC curves for the cases of no fluctuations (k_{na} = 0) or some relatively weak added artificial signals (k_{na} = 0.5).

Chi-squared statistics

The chi-squared probability density function represents typical measured power values at the hydrophone input. It is the generalised case of Gaussian or exponential statistics described above and the derivation of the ROC curves follows similar steps. The chi-squared pdf is described by [4]:

$$f(x) = \frac{x^{\nu/2-1}}{2^{\nu/2}\Gamma(\nu/2)} \exp\left(-\frac{x}{2}\right) \quad \text{for } 0 \le x < \infty, \qquad (16)$$

while $f(x) = 0$ otherwise. Here ν is an integer and represents the number of degrees of freedom of the system. For a chi-squared distribution the mean is ν and the variance is 2ν. The pdf for the case when only natural noise is present is given by (16) but with $\nu = \mu_n$. The pdf for those cases when a natural signal or artificial signals are present is similar but with an appropriate subscript on $f(x)$ and an appropriate expression for ν. For example, a natural signal mixed with just noise has $\nu = \mu_n + \mu_s$, while the case of a natural signal mixed with both natural noise and added artificial signals has $\nu = \mu_n + \mu_s + \mu_a$. The detection index for chi-squared noise statistics is $d_n = \mu_s^2 / 2\mu_n$. When artificial signals are added to the system the detection index becomes $d_{na} = \mu_s^2 / 2(\mu_n + \mu_a)$. The fluctuation index for chi-squared statistics is defined as

$$k = (\mu_n + \mu_a)/\mu_n \ . \qquad (17)$$

Following the same steps to calculate PFA and PD as for the earlier distributions and requiring the added artificial signals to be known leads to

$$PFA_n = \Gamma\left(\frac{\mu_n}{2}, \frac{T}{2}\right) \Big/ \Gamma\left(\frac{\mu_n}{2}\right) , \qquad (18)$$

$$PD_{sna} = \frac{\Gamma\left(\frac{1}{2}\left[\sqrt{2d_n\mu}_n + \mu_n k_{na}\right], \frac{T}{2}\right)}{\Gamma\left(\frac{1}{2}\left[\sqrt{2d_n\mu}_n + \mu_n k_{na}\right]\right)} \ . \qquad (19)$$

Here $\Gamma(\alpha)$ is the Gamma function and $\Gamma(\alpha, \beta)$ is the Incomplete Gamma function [4, 9]. PD_{sn} is obtained by setting k_{na} = 1 in (19). For the special case of ν = 2 these expressions reduce to the exponential distribution case, whereas for large ν these expressions approach the case for Gaussian statistics described above.

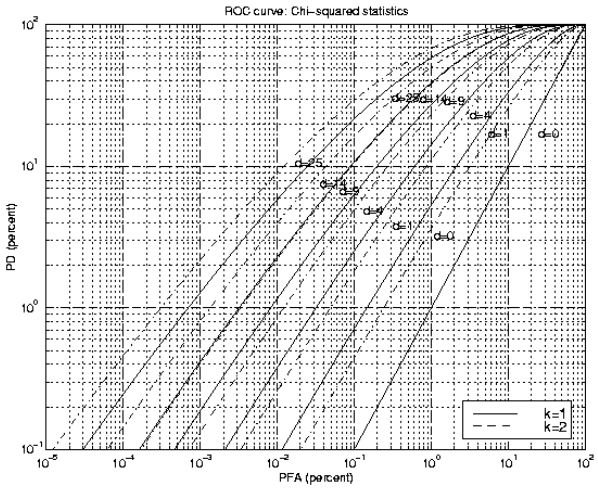

Figure 4. Chi-squared ROC curves for μ_n = 1 for the cases of no fluctuations (k = 1) or some relatively weak added artificial signals (k = 2).

Figure 4 is a plot of ROC curves for chi-squared statistics, generated from (18) and (19) for various values of the fluctuation index k_{na} and μ_n = 1. Once again it can

be seen that there is an improvement in PD as k_{na} is increased for fixed combinations of d_n and PFA.

Results

A detector based on using stochastic resonance with known artificial signals, called ISHTAR, has been constructed and uses zero-mean Gaussian artificial signals. Figure 5 shows the results when ISHTAR was applied to a set of sea trial data recorded using a DIFAR sonobuoy. The test signal in this case was a train of active CW sonar pulses emitted by a sonar research projector: the pulses were Doppler shifted to 745 Hz at the sonobuoy. Each pulse was emitted for 0.1 seconds and they were spaced 1.0 seconds apart, which represents a severely fluctuating signal.

The individual plots in Figure 5 are vertically aligned to allow comparison at each frequency. The large plot at the bottom is a lofargram of time (seconds) versus frequency (Hz) for the conventional passive detector. The vertical lines on this display are interfering signals from various sources around the trial site in the Gulf of St. Vincent. The plot second from bottom is an automatic line integration (ALI) histogram, which has summed the received power over the length of the data set for the conventional detector. The test pulses are not visible in either the conventional lofargram or the ALI.

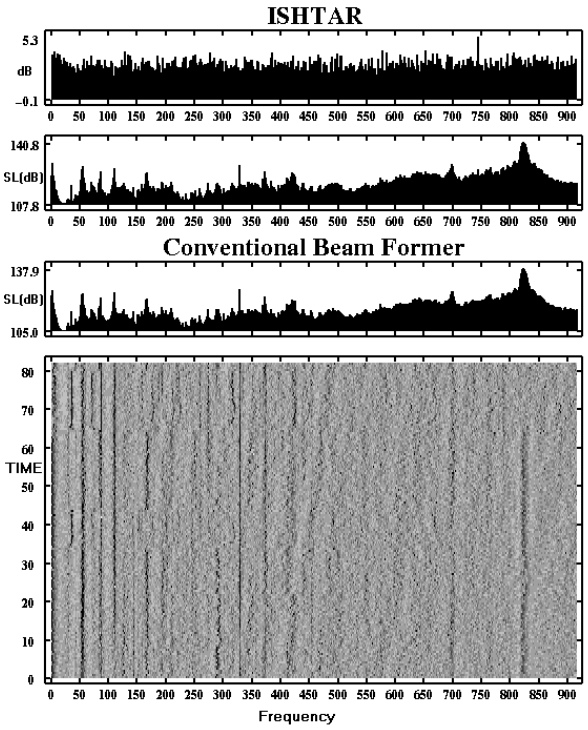

Figure 5. ISHTAR working in tandem with a conventional detector for a DIFAR sonobuoy. The test signal was a train of active CW pulses received at 745 Hz. The sequence of plots is a conventional lofargram (bottom), a conventional ALI (second from bottom), an ISHTAR ALI (second from top) and a DALI plot (top).

The second plot from the top in Figure 5 is another ALI display, but this time it uses the sum of values which have been individually adjusted using the stochastic resonance technique built into ISHTAR. The cumulative effect of the CW test pulses appears as a small peak appearing at 745 Hz which would normally be indistinguishable from the background noise.

The top plot in Figure 5 has been specially designed for use with ISHTAR. This is a plot in decibels of the difference between the conventional ALI (second from bottom) and the ISHTAR ALI (second from top) and is referred to as a 'difference ALI' or 'DALI' display. In the DALI plot at the top the cumulative effect of the test CW pulses appears as a clearly detectable peak at 745 Hz. The background in the DALI display has some additional scatter due to random temporary reinforcement with the ambient noise and the background interference, but there are no significant additional spikes which would create a false alarm. One of the development aims of ISHTAR is that the enhanced detection of weak fluctuating signals does not come at the price of creating too many false alarms.

A similar analysis for two other DIFAR sonobuoys further away in the same search field also showed a clear detection of the CW pulses. The strength of the target signal spike in the equivalent DALI displays for those other buoys showed an expected decrease with increasing range.

Acknowledgments

This work is supported through the award of the third RAN Science Scholarship. The authors would like to thank the trials staff of Maritime Operations Division (Salisbury) and Crew 3 of RAAF 10 Squadron for collecting the trial data.

References

[1] R. J. Urick (1983). *'Principles of Underwater Sound'*, 3rd edition, McGraw-Hill: New York, NY, USA.

[2] A. D. Bulsara and L. Gammaitoni (1996). *'Tuning In To Noise'*, Physics Today, March 1996, p.39-45.

[3] L. Gammaitoni, P. Hänggi, P. Jung and F. Marchesoni (1998). *'Reviews of Modern Physics'*, **70**(1), p.223-287.

[4] M. Abramowitz and I. A. Stegun (1970). *Handbook of Mathematical Functions, with Formulas, Graphs, and Mathematical Tables*, 7th printing, Dover Publications: New York, NY, USA.

[5] Urick R. J. and Gaunaurd G. C. (1972). "Detection of Fluctuating Sonar Targets", United States Naval Ordnance Laboratory Technical Report 72-47.

[6] '*Sonar Modelling Handbook, Volume 1. Modelling Procedures and Environments'*, DRA/Mar TM (USSF) 91172, UK Defence Research Agency, ARE Southwell, Portland, Dorset DT5 2JS. (Contents classified up to UK Confidential).

[7] J. Paterson (1992). '*An Analysis and Comparison of the Detection Threshold for Narrowband Amplitude and Power Detectors (U)*', DRA TM(USSF) 92148, UK Defence Research Agency, Southwell, Portland, Dorset DT5 2JS. (UK Restricted and Commercial in Confidence).

[8] R. O. Nielsen (1991). '*Sonar Signal Processing*', Artech House: Boston, MA, USA.

[9] I. S. Gradshteyn and I. M. Ryzhik (1994). *'Table of Integrals, Series, and Products'*, 5th edition Ed. A. Jeffrey, Academic Press: San Diego, CA, USA.

Some Dry Facts about Underwater Acoustics Measurements

Suszanne Thwaites

National Measurement Laboratory, Sydney.

Abstract

The National Measurement Act prescribes a set of Australian Legal Units of Measurement and describes in detail their definition, their use and their status in law. This serves to minimise errors, lack of definition and disputes in the use of measurements in law and in any other transactions. However, it also means that incorrect use of the units can lead to situations where measurement results may be difficult to defend. This paper outlines the current situation with respect to underwater acoustics and suggests some remedies that involve minimum cost and inconvenience.

1. Introduction

In order that measurements of physical quantities can be used by people to enact any dealing or contract or transaction between them there has to be mutual recognition of the skills and instruments used to make those measurements. This obvious fact, so intimately connected to the flow of money or goods, means that the setting up of a system of weights and measures has been one of the first activities associated with the beginnings of civilisations about as far back into history as you would care to go. When transactions are very local or communities small in number individual recognition of competence (and honesty) can work but it doesn't take long for the idea of a central reference held by a disinterested party of general approval, to take hold.

In 1875 the metric system and the SI units were formalised under the Convention of the Metre (the "Metric Treaty") to which Australia is now a signatory. Australia's measurement system acquired its current form in 1960 with the passing of the National Measurement Act.[1]

2. The National Measurement Act (1960)

To people reading this act it can appear that they may be better off without it. The choice is either complete deregulation or as foolproof and global a system as is possible. The Act has some problems as we shall see but once an act like this is in place not only does it regulate and protect it can also be contravened. When such an Act establishes a measurement system, it must also seek to make its use, so far as is reasonable, mandatory.

The National Measurement Act establishes the concept of Australian Legal Units for the measurement of physical quantities. It lists these quantities and their units in the regulations to the act. Use of an Australian Legal Unit has a very well defined meaning, described in Part II Section 10 of the Act.

"When, for any legal purpose, it is necessary to ascertain whether a measurement of a physical quantity for which there are Australian legal units of measurement has been made in terms of those units, that fact shall be ascertained by means of, by reference to or by derivation from… an appropriate Australian primary standard of measurement."

The central concept in this process is traceability. Traceability means that every measurement can be demonstrated to refer back, via the use of calibrated instruments and competent personnel, to an appropriate standard. If this principle is not adhered to it can be very difficult to defend the measurements. This is outlined in Section 12 of the Act which goes on to say,

"…every contract, dealing or other transaction made or entered into for any work, goods or other thing that is to be done, sold, carried or agreed for by measurement of a physical quantity shall be made or entered into by reference to Australian legal units of measurement of the physical quantity, and if not so made or entered into is void."

The essential point here is that if a quantity and its unit are listed in the regulations to the Act it is mandatory that this unit be used if this quantity is being measured. The Act directs the CSIRO to establish and maintain or cause to be maintained primary or appropriate standards for the units and the traceability chain must generally end at these standards. This is the function of the National Measurement Laboratory

3. Australian Legal Units

The list of units in the Act is very long and divided into two Schedules.

Schedule 1.

- SI Base Units of Measurement
- SI Derived Units of Measurement With Special Names
- Non-SI Units of Measurement used with SI Units of Measurement
- Additional Derived Units of Measurement

Schedule 2

- Additional Legal Units of Measurement

The base units are kilogram (kg), mole, metre (m), second (s), candela (cd), Kelvin (k) and ampere (A). Amongst the long list of derived units with special names are Hz, Pa, V, W, N, rad and C (coulomb). Under "Non-SI units used with SI Units" is dB in the context of sound measurements and quantities like velocity and density appear as Additional Derived Units. All the units in Schedule 1 are Australian legal units.

Schedule 2 contains a number of non-SI units such as foot and horsepower. Use of any one of these units is restricted to specific purposes or organisations that are listed in the Act. For instance horsepower may be used for defence equipment and foot may be used for submarine depth. Use for any other purpose or by any other organisation not specified in the list has no legal basis but it does not invalidate contracts.

4. Traceability and the Use of Australian Legal Units

Traceability is demonstrated by an unbroken chain of reference from the final result back to an appropriate standard. It is important that the traceability chain is not broken. For instance, if a certificate is issued for the open circuit voltage sensitivity of a hydrophone it is not sufficient once the hydrophone is terminated, say by a preamplifier.

One way that the laboratories can demonstrate this conformance is by being admitted to membership of the National Association of Testing Authorities (NATA) and taking part in their continuing programs of proficiency testing. Scope of membership is very specific with accreditation only being conferred for well-defined tests. Although NATA is not a government organisation it is the single nationally and internationally recognised provider of accredition for test houses within Australia. It also has a mutual recognition arrangement via APLAC (Asia Pacific Laboratory Accreditation Cooperation) by which certificates issued by NATA accredited laboratories under the regulations to the Act are accepted by the other participants.

However, NATA accreditation does not guarantee traceability to NML. Laboratories can obtain NATA accreditation where there is no physical standard and no legal unit. In this case membership confers credibility via the judgement of peer review of techniques, equipment and competence yielding results which can be defended using expert witnesses.

Certificates issued under the regulations to the Act generally refer to a calibration report provided by the NATA test house. The National Measurement Act prescribes in the regulations what information a certificate should contain. In particular, as well as the calibration result, the certificate must show or refer to an uncertainty estimate for the measurement, within a given confidence interval, and also a period of time for which the certificate is valid

It is in the interests of any organisation to establish their continuous traceability to NML for any physical measurements which may be used in dealings with any other party. Laboratories may choose some other option but will have difficulty defending the credibility of their measurements. If a physical standard for a quantity exists but the quantity does not have an Australian Legal Unit (ie it is not listed in the Act) then it is still a very good idea to be traceable to the standard. The measurements are certainly much easier to defend than if there were no standard. If the unit is in the Act but there is no physical standard it is still mandatory to use that unit. Defence of the measurement results is tricky.

On the other hand it is the prerogative of any organisation which deals extensively with overseas entities to use some other agreed upon standard since these transactions are not covered by the Act. It is definitely not in the interests of any organisation to leave the traceability undefined. There are numerous examples in the field of air acoustics to demonstrate this fact. Unfortunately there are no organisations in Australia that are NATA accredited for underwater acoustic measurements.

5. International Traceability and the Metric Treaty

The Metric Treaty is administered by the International Committee of Weights and Measures (CIPM). The individual signatories to the Metric Treaty are represented by their National Measurement Institutes (NMI). The CIPM interacts with national measurement systems and authorities via their respective National

Measurement Institutes. Although the treaty coordinates many aspects of international measurement it does not confer automatic recognition of standards between the member nations. Various agreements between individual nations for specific standards have been negotiated but it is the norm that this is not the case. The two quotations from the National Measurement Act given above do not apply to contracts etc relating to exportation or importation of goods.

Recently the CIPM began a process of comparisons of standards between NMIs, designed to lead to a global Measurement Recognition Arrangement. Australia (NML) as a highly developed nation in this respect is a participant in most of these comparisons.

Of immediate interest in this meeting are the comparisons in air acoustics, vibration, high frequency ultrasound for medical use and ultrasound power for therapeutic use. Test artefacts are being circulated to the chosen nations at this time and NML has already completed its calibrations of the acoustics standards and vibration standards with the two ultrasonics ones to arrive in December this year. The acoustics and vibration results are known, unofficially, to be excellent. Eventually these results will be entered into a global database and form the basis of the recognition by other treaty nations of our primary standards and, conversely, our recognition of theirs. Clearly we need to be very convinced before we agree to such recognition.

6. International Comparisons in Underwater Acoustics

A key comparison in underwater acoustics is also underway but its start has been greatly delayed as a consequence of the unique standards arrangements in this area. Possibly due to historical accident, most NMIs do not maintain underwater acoustics standards. Although a significant number of naval organisations do, as we have seen, the CIPM cannot recognise these as national standards. However, it is common practice in many countries to give NMIs the legislative right to designate and qualify some other internal organisation to hold the national standard for them. The National Measurement Act confers this right on NML.

Unfortunately this is rarely simple in practice. In fact the only nations in a position, at last, to participate are UK, Germany, Russia, China, and USA. Of these Germany, China and USA have had some fairly time consuming dealings in establishing recognition by their respective NMIs of their respective standards. In Germany the Physikalisch-Technische Bundesanstalt (PTB) is represented by Wehrtechnische Dienststelle fur Schiffe und Marinewaffen (WTD71), in China NIM will do the calibrations rather than Hangzhou Applied Acoustics Research Unit (HAARI) which is the more well known underwater acoustics establishment. In the USA the Underwater Sound Reference Division (USRD) will participate on behalf of the National Institute for Science and Technology (NIST) which doesn't hold underwater acoustics standards. A number of other nations have indicated interest but have yet to settle internal complications. The coordinating laboratory is the National Physical Laboratory (NPL) of UK, one of the few NMIs to hold a standard.

There has been a number of other international and internal comparisons of underwater acoustics measurements involving, variously, Europe, UK, Russia and China which have produced a significant body of knowledge on standard methods and artefacts. These have usually been based on the IEC documentary standards, IEC 60565[2] and 60565(A)[3] on the calibration of hydrophones. Two interesting recent reports of some comparisons are Robinson et al[4] and Enyakov et al[5].

7. Underwater Acoustics in Australia

As with the other nations mentioned above, most underwater acoustics activity in Australia is associated with naval applications. The majority of underwater acoustics transducers are used for ranging and imaging and othe oceanographic applications.

NML does not have a physical standard for underwater acoustics transducer sensitivity. Nor does it have a de facto standard held by some other organisation and consistently used in a traceable manner although a number of organisations run in-house calibration systems. Therefore underwater acoustics measurements in Australia are generally not demonstrably traceable to anything.

The quantity, 'sensitivity', referring to acoustic transducers is not listed in the Act. This means that there is no specific unit which must be used with this quantity. Whilst on the one hand this appears to absolve people from being traceable to a national standard, it also means that there is no straight forward means for establishing the credibility of hydrophone sensitivity measurements. The quantities pressure (Pa), sound pressure level, sound intensity level and sound power level (dB) have Australian legal Units, implicitly in the context of air acoustics. Where this leaves underwater acoustics is unclear.

Many hydrophones are supplied with calibration certificates traceable to overseas measurement standards. For instance NIST is popular in defence circles in Australia. However, careful checks should be made on the existence and reliability of offshore standards, and the traceability and the legal status in the foreign nation. Calibration information supplied with transducers and calibrators often gives very sweeping statements of reference and frequently shows typical or batch test results rather than a test of the specific item delivered.

It is also rare to see any information about the period of validity of the test and it should be kept in mind that if the measurements are to be used within Australia they may be costly and difficult to defend.

8. Calibrating Hydrophones

The frequency range covered by the generic term 'underwater acoustics' ranges from < 1 Hz through to ~500 kHz. There is no single calibration technique that covers this range and many of them are technically difficult and certainly not available as off the shelf products. Most of the methods for calibrating hydrophones are listed below in Table 1. Those classed as absolute do require other measurements, such as voltage or frequency, to be traceable to primary standards. The ones marked with an asterix are described in IEC 60565 or 60565(A). Most of the methods can be classed, according to the principle used, into three types. The last two methods are generally only seen in medical applications.

1. Reciprocity. This requires at least one reciprocal transducer and is an absolute technique.

2. Physical calibration. In these methods the sound pressure at the hydrophone is calculated from measurement of other parameters of the system. This method can be absolute or relative.

3. Comparison with a calibrated transducer. This cannot be an absolute method.

Method	Range	
Water pistonphone*	1 – 50 Hz	Absolute
Vibrating column*	10 Hz-3 kHz	Absolute
Free field reciprocity*	1 – 500 kHz	Absolute
Coupler reciprocity	1 Hz – 2 kHz	Absolute
Compensation*	0.1 – 1000 Hz	Absolute
Air pistonphone	250 Hz	Relative
Comparison in water*		Relative
Comparison in air		Relative
Interferometry	0.5 – 20 MHz	Absolute
Radiation balance	~10mW- ~15 W	Absolute

Table 1
Methods for calibrating hydrophones.

In IEC 60565 the free field reciprocity method includes pulsed and continuous wave excitation and the compensation description includes both piezoelectric and electromagnetic methods. The description of the vibrating column method only describes movement of the water bath and not the method where the transducer is moved. Coupler reciprocity is not included but both NPL and USRD have advanced research programs, using this method, to form a low frequency reference. The USRD method is described in Zalesak[7]. The interferometric method measures displacement and is usually restricted to frequencies above 500 kHz and hydrophones of the membrane type. It is included here because the facility already exists at NML. The radiation force balance method measures total power output and it also exists at NML.

Apart from frequency, static pressure is also an important variable and it requires sophisticated high pressure vessels. Some of the methods can be run in a pressure vessel.

9. An "appropriate" Underwater Acoustics Standard

The USRD gives the following reasons for maintaining their standards.

"USRD transducer standards are used to verify specifications, to show conformance with contractual obligations, to show conformance with environmental laws, and to provide a reference base for advancing science and technology within the underwater acoustics community."[7]

This is a useful summary of what could be needed of a standard in Australia. It implies that the measurement result firstly, is correct, secondly, is demonstrably traceable (ie. has some legal status) and thirdly, has an uncertainty estimate to a stated confidence level.

Typical scenarios where it might be needed are in the delivery of goods or services to a contract, (eg checking tolerances, performance testing), demonstrating compliance, (eg noise and safety regulations) and comparing scientific results. With the growing use of quality systems it is becoming increasingly routine for organisations to require demonstration of a quality system before they will do business. Accreditation to ISO 17025[8] requires traceability to physical standards.

On the other hand hydrophone sensitivity is not a quantity having an Australian Legal Unit with the consequences discussed in Section 4 above. However, it has been shown that although this absolves users from the onus of demonstrating traceability to a standard it also places their measurements in a position where credibility is very difficult to establish.

While the USRD may be able to set up standards, using some of the methods in Table 1, to cover the entire frequency range used and also to cover other variables, like static pressure, this is clearly out of the question in Australia. As it says in the National Measurement Act, a standard needs to be "appropriate" and we might include in this phrase reasonable compromises with regard to cost and convenience. Such compromises would be achieved at the cost of a reduced frequency range and accuracy and would not include high static pressure measurements.

A good starting point is to work with whatever facilities already exist that could serve as a standard. From this point of view the most important feature is that it is absolute. Then to qualify, and be designated, as the national standard by NML requires establishing the right machinery around it. In particular,

- The other measurements involved (eg volts, frequency) need to be formally traceable to NML.
- The uncertainties need to be estimated according to the ISO/IEC Guide to the Expression of Uncertainty in Measurement.[9]
- The necessary competencies in the personnel need to be established.
- A comparison of results with a recognised institution should be undertaken to validate the system.
- NATA accreditation to ISO 17025.
- The facility needs to be run as a fee earning service available to the public.

Once a standard is established according to these dot points individual traceability to the standard becomes the problem of the user. Most of the requirements above are activities which NML carries out routinely. However, it is very unlikely that an underwater acoustics standard would be constructed at NML unless there was a strong concerted push from a customer base of a reasonable size.

The only facilities in Australia which run an absolute calibration program are the DSTO facility at Woronora Dam and Thompson Marconi Sonar at their Rydalmere (Sydney) facility. At the Woronora Dam installation reciprocal hydrophones, ITC 1042, are calibrated by free field reciprocity fairly closely in line with the methods described in IEC 60565. The frequency range is currently restricted to ~50<f<~300 kHz. At TMS Bruel and Kjaer 8103 and also in-house designed hydrophones are calibrated by reciprocity in a tank. Frequencies are generally below 20 kHz.

10. Conclusion

The real answer to the question of whether Australia requires an underwater acoustics standard can only come from the potential users. The need for a standard from a legal point of view is undeniable from the facts given in this paper. Whether individual users have systems which conform to these requirements can now be judged for themselves. A simple intercomparison of hydrophone calibration, over a restricted frequency range and without regard for method would soon establish whether users were getting the right answer. This would not be too difficult to organise.

Alternatively it might be argued that Australia has survived so far without a standard so why make trouble? In answer to this, people from the air acoustics area can testify to the growing awareness in the community and the legal profession of the implications of the National Measurement Act. At the NML the number of calibrations performed specifically for use in litigation continues to increase.

References

1. National Measurement Act (1960)
2. IEC Standard 60565, “Calibration of Hydrophones”, Geneva, International Electrotechnical Commission, 1977.
3. IEC Standard 60565A, First supplement to Publication 565, “Calibration of Hydrophones”, Geneva, International Electrotechnical Commission 1977.
4. S.P Robinson, G.J Green R.C.Preston, L.Pierlinckx, L Kofoed, C.Skodborg, A.Roy, Y.Mori, A.Brenner, D.Kruger, S.Buoogo, G.Cannelli, L.Troiano, C.Runborg and G.Gooch,, “International comparison of free field hydrophone calibrations in the frequency range 10 kHz to 315 kHz.” Metrologia, Vol 36 4, 1999.
5. A.M. Enyakov, S.M. Likhatchev, V.A. Platonov, W.J. Yuan, Y.B. Wang and J.Q. Li, “A Russian-Chinese international comparison of hydrophone calibration methods.” Metrologia, Vol 36 4, 1999.
6. J.F.Zalesak, “Transfer coupler reciprocity: A new low frequency coupler reciprocity technique for the absolute calibration of field hydrophones under full environmental conditions.”, J.Acoust.Soc.Am. Vol 105 4, 1999.
7. USRD web page, http://www.nuwc.navy.mil/npt/USRD.
8. AS ISO/IEC 17025-1999 “General requirements for the competence of testing and calibration laboratories.”
9. ISO/IEC “Guide to the Expression of Uncertainty in Measurement”

Modelling passive detection in a complex noise environment

Mark G. Hazen

Defence Research Establishment Atlantic, Dartmouth NS, Canada
(On exchange to Maritime Operations Division, DSTO Salisbury, Australia)

Abstract

In sonar modelling detection is usually assumed to take place against a background of noise that is well behaved in the frequency band or time interval around the target signal. This background is often characterized by a mean level, with some variability that can be described statistically. Often the background noise is assumed to be gaussian due to its generation from a large number of 'distant' sources. In many scenarios this is a reasonable assumption; however, in littoral waters this characterization is often inadequate since local shipping and biologics clutter the background environment with discrete narrowband and transient signals. To model detectability (or observability) of target emissions, the masking effect of these other signals must be included. It is suggested that this masking can be modelled by an extension of the usual sonar equation detection algorithm to include a statistical characterization of the number and type of expected signals in an environment.

Introduction

The detection of passive acoustic signals has traditionally been modelled as the detection of a narrowband coherent signal within a background of broadband incoherent noise [1]. In deep ocean environments with no nearby shipping this model has worked well. Thus, noise is typically described in sonar performance models as a set of spectral levels and fluctuations for a number of frequency bands. In each of these bands the statistical qualities of the noise are assumed to be stable. Indeed, the study of ambient noise [2, 3, 4] has concentrated on understanding the mechanisms that govern the broad band noise. Even Dyer [2] who explored the statistical properties of ocean acoustics, was mostly interested in how many signals combined to form the broadband background.

Shifting sonar operations into littoral waters or a shipping lane is problematic for the sonar modeller since the assumptions of the traditional detection model are unlikely to apply. The noise background will generally consist of both background noise and distinct, perhaps identifiable, interfering signals. The probability that the target signal may be masked by a coherent noise source (clutter) can increase significantly.

In this paper it is argued that the simple broadband description of the noise field is inadequate for modelling passive sonar operations in complex environments. In general, it leads to optimistic predictions of sonar performance because it ignores the non-broadband portion of the ambient noise. It is suggested instead that the ambient noise be decomposed into a broadband background level and distinct non-target signals, which are categorized as clutter. To set up the problem this paper will first discuss the nature of clutter. Following this, an extension to the classic detection model that accounts for simple clutter will be derived. This model will then be examined to see how probability of detection varies with the parameters introduced. Finally, some recommendations will be made about the types of data required to drive such a model.

Clutter

Acoustic clutter is defined as any acoustic signal that is distinct from the background level in the detection space and cannot be associated with the target of interest.

The source mechanisms for clutter lines are typically local to the area of the sensor and may be coherent in nature. An example is the propulsion and machinery lines emitted by fishing fleets. These sources, when distant, blend to give an incoherent increase to the overal noise field, but when closer to a sensor resolve into individual coherent clutter elements. Dyer [2] developed a model that relates numbers of distant shipping signals to increases in broadband noise levels and shows how broadband shipping levels may be estimated using area shipping statistics. Bannister et al. [3] validated Dyer's model with data from the Pacific and Atlantic. However, the issue of local and/or distinct signals is not addressed.

Similarily, biological sources like whales are known to emit a variety of signals. The finback whale in particular is known to emit a family of signals of long duration in a small band centred on 20 Hz. Cato [4] has

reported the effects of choruses of biological noise in Australian waters that cause a change in the overall noise level at certain times of the day. While the overall effect on broadband noise has been included in models as an increased ambient noise level, individual sources that are close enough to a sensor not to have blended into the background have not.

For both the biological and mechanical noise cases the result is that narrow to medium band clutter signals show up in displays and interfere with the detectability of signals. While this effect may be minimal in a deep ocean scenario, the amount of clutter in littoral environments is substantially higher, and therefore the effect on predicted sonar performance is greater as well.

Passive airborne sonar models at the Defence Research Establishment Atlantic model detection as a combination of the probability of simultaneously detecting several narrowband signals [5]. Masking and other operator-effects are modelled by defining an evidential quality parameter for each of the various signals. Signals in heavily cluttered parts of the frequency domain are given lower evidential quality to offset the optimism inherent in the detection calculations versus broadband noise. This method, while moderately effective, clearly does not model the true detection process.

However, if the ambient noise is decomposed into a broadband background noise and sets of clutter lines, then models can be developed that explicitly account for masking effects.

Simple Clutter Model

In this section a simple model is developed to account for masking of narrowband signal lines by clutter. In the interest of simplicity it will be assumed that:

1) There are M types of clutter signals $\{C_1,,C_M\}$ for which statistics on numbers occuring in a particular frequency band, expected width, and intensity are known. These statistics are invariant in the frequency band of interest (B_w).

2) The signal of interest is narrowband with known statistics and is present in B_w.

3) The time extent of the clutter is of the same order as the signal to be detected.

4) The broadband background can be modelled as C_0 with a single clutter element that covers B_w.

Masking is defined as the opposite of detection. That is, if the signal, l_0, cannot be detected, then it has been masked by clutter from one of the sets C_i. Thus,

$$P_D = 1 - P(l_0 \text{ masked by clutter}). \qquad (1)$$

Although the model is general enough to be used in other situations, the development here will assume that detection takes place by a human operator using a frequency-time-intensity (FTI) display format.

The probability that l_0 is masked is the probability that l_0 lies close enough to one or more of the clutter elements. Although, we state the case in terms of a known l_0, the case can easily be generalized to an unknown l_0 by applying a probability measure to the likelihood that l_0 has a particular frequency f_0 and then integrating over the band of interest. This is shown in Equation 2,

$$P(l_0 \text{ masked}) = \int_{B_w} P(l_0, f) \mathrm{P_M}(l_0, c \in \{C\}) df \ , \qquad (2)$$

where $P_M(l,c)$ is the probability of signal l being masked by clutter element c. The probability of l_0 being centred at frequency f_0 will depend upon the characteristics of the signal of interest. In the case of a well-defined, stable source the probability that the signal is centred at f_0 may reduce to an indicator (or delta) function centred at f_0. Alternatively, if little is known besides a limiting frequency band, then signal probability is modelled by a uniform distribution over the band. In this paper it is assumed that the signal is known, and therefore Equation 2 reduces to:

$$P(l_0 \text{ masked}) = \mathrm{P_M}(l_0 = f_0, c \in \{C\}). \qquad (3)$$

Since it only takes a single clutter element to mask a line, the probability that l_0 is masked can be calculated as the probability that at least one clutter element masks l_0. The probability of at least one of the clutter lines masking l_0 is related to the probabilities of each sets of clutter $\{C_j\}$ masking l_0 by:

$$P(l_0 \text{ masked by at least one element})$$

$$= 1 - \prod_{j=1}^{M} \left(1 - P_M\left(l_0, \{C_j\}\right)\right). \qquad (4)$$

Thus, the problem of determining the probability of detecting l_0 in the presence of clutter becomes on substitution of Equation 4 into Equation 1:

$$P_D = \prod_{j=1}^{M} \left(1 - P_M\left(l_0, \{C_j\}\right)\right). \quad (5)$$

In order for $c \in C_j$ to mask l_0 it must be close enough (in frequency) and intense enough. By keeping B_w small the clutter intensity can be assumed to be independent of frequency and therefore the probabilities of these two conditions are independent.

$$P_M\left(l_0, c_i \in C_j\right) = P(c_i \text{ overlaps } l_0) \times P(c_i \text{ loud enough to mask } l_0). \quad (6)$$

In addition it has been assumed that for each type of clutter, C_j, that the clutter elements c are identically distributed. The number of elements of a particular clutter type C_j that must be considered is modelled by the distribution of expected number of elements, P(siz(C_j) = n). Since it is the probability that at least one of the elements of C_j masks l_0 that is required Equation 7 is obtained.

$$P_M\left(l_0, \{C_j\}\right) = \sum_{n=1}^{\infty} P(\text{siz}(C_j) = n)\left(\prod_{i=1}^{n}\left(1 - P_M(l_0, c_i)\right)\right) \quad (7)$$

It now remains to examine the elements of the RHS of Equation 6.

Probability that c_i is close to l_0 - $P(c_i \text{ overlaps } l_0)$

The probability that a particular clutter element, c_i, is close enough to mask l_0, is the probability that the centre frequency of c_i, f_c, is close enough to the centre frequency of l_0, f_0, that they overlap. This probability will be formulated in terms of frequency, however, it is a simple process to transform the result to numbers of display pixels if desired. Similar expressions can also be derived to handle transient signals by examining signal and clutter extent with respect to time.

How close is close enough to mask? Harris [6] states that two lines are indistinguishable if there is less than a 6 dB difference between the lower peak, and the valley between the two. Thus, if signal width is defined by the shift from centre frequency at which intensity has dropped by 6 dB then the maximum frequency separation at which a clutter element could mask/merge with the signal line is:

$$D_{\max} = \frac{R_l + R_c}{2}, \quad (8)$$

where R_l and R_c are the –6 dB bandwidths of l_0 and c_i respectively.

Applying Equation 8 as the measure closeness gives:

$$P(c_i \text{ overlaps } l_0) = P\left(|f_c - f_0| \le D_{\max}\right). \quad (9)$$

Since f_0 is fixed by the choice of l_0, Equation 9 is a statement of the probability that f_c exists within a range about f_0. Thus, we obtain:

$$P(c_i \text{ overlaps } l_0) = \int_{f_0 - D_{\max}}^{f_0 + D_{\max}} P(f_n = f)df. \quad (10)$$

As an example of the use of Equation 10 we assume that $c_i \in C_j$ may occur equally likely anywhere within a band, B_j, of width b_j; i.e. $P(f_i=f)$ is uniformly distributed within B_j. Note that B_j is slightly larger than B_w, since B_j must account for the possibility of clutter lines occurring on both sides of l_0. Using the closeness criteria $D_{\max}$ we define B_j to be the frequency band:

$$\left[\min(B_w) - D_{\max}, \max(B_w) + D_{\max}\right]. \quad (11)$$

Using the assumed uniform distribution for $P(f_i=f)$ and the bandwidth B_j:

$$P(f_i = f) = \frac{1}{b_j}, \quad (12)$$

and

$$\int_{f_0 - D_{\max}}^{f_0 + D_{\max}} P(f_i = f)df = \frac{2D_{\max}}{b_j}. \quad (13)$$

Probability that c_i is more intense than l_0

The sonar equation detection model is based on the average signal-to-noise ratio (SNR) which is deter-

mined for each signal. This SNR is then modified by a term to account for the statistics of the noise and signal (called detection threshold – DT) or noise, signal and display system (called recognition differential – RD) to obtain a signal excess (SE) value. SE includes assumptions about the distribution of signal and noise intensity and is set to have pre-specified probabilities of detection and false-alarm when SE=0.

In general the sonar equation describes the process of being able to detect the difference in intensity between a single display element containing signal and noise, and the surrounding elements that are assumed to contain noise. In terms of an FTI display this can be described as detecting the difference in brightness between a single pixel and the surrounding pixels.

The process for determining the detectability of a single pixel from ambient noise has been extended to apply to a line of pixels, such as those that result from a narrow band tonal signal in a FTI display. The key concept is that the process of detecting a line can be described asa power detector, where the operator integrates the intensity of all the pixels in the line and the average intensity of the surrounding ambient noise to form a perceived SNR. The entire process would be deterministic if there were no variability in the signal or background. However, in the real world there can be a great deal of variability in both. One of the challenges of sonar performance prediction is in estimating the distributions of signals and noise properly. The usual assumption for single line detection is that the background is Gaussian distributed and stationary over time so that integration over time does not increase the noise estimate. The signal, however, is assumed to be coherent over time and thus integration does increase the signal level. This increase in signal is usually reflected in the DT/RD values used in calculating SE.

In our model the statistics of each of the M clutter types will be different, and, in fact, some clutter types will be coherent, not incoherent. For coherent clutter integration over more cells will not improve SNR, in this regard detection in these cases may be more similar to active sonar detection in the presence of reverberation then traditional passive sonar detection.

In general, then, the probability that c_i is "loud enough" to mask l_0 will be a function of the intensity of each and their underlying distributions. For the case of C_0, the broadband noise case, calculations are completed as in traditional sonar model. For other types of clutter the modeller will need to know if the clutter is coherent or incoherent, and will need to make assumptions about how the clutter fluctuates. In all cases it is important that the DT/RD values are based on consistent values of mean probability of detection and false alarm. Thus, the probability can be written as:

$$P(\text{loud enough}) = P(SE(C_j, l_0) \geq 0), \qquad (14)$$

where we use the set notation C_j instead of an individual clutter element c_i since the calculation is based on the general statistics of C_j.

Model Summary

Putting the pieces back together, the results of Equations 14 and 13 are combined using Equation 6 and substituted into Equation 7 to give the probability of at least one clutter element masking l_0. Since both Equations 13 and 14 depend only on C_j, the product in Equation 7 can be expressed as the product of (13) and (14) raised to the n^{th} power.

$$P_M\left(l_0, \{C_j\}\right) = \sum_{n=1}^{\infty}\left[P(\text{siz}(C_j) = n) \times \left(1 - \frac{2D_{\max}}{b_j} P(SE(C_j, l_0) \geq 0)\right)^n\right] \qquad (15)$$

Now taking Equation 15 and substituting into Equation 5 the complete model for probability of detection in the presence of clutter is:

$$P_D(l_0) = \prod_{j=1}^{M}\left(1 - \sum_{n=1}^{\infty}\left[P(\text{siz}(C_j) = n) \times \left(1 - \frac{2D_{\max}}{b_j} P(SE(C_j, l_0) \geq 0)\right)^n\right]\right) \qquad (16)$$

Example

Figures1-3 show the probability of detection as the amount and type of clutter are varied for a synthetic detection case. In all cases the signal characteristics are held constant. Detection threshold (DT) is set to give a PD = 50% and PFA of 10^{-4}. Source level, transmission loss and broadband noise levels are assumed so that in the base case of broadband noise only, the SE = 10 dB. Signal width is 0.1% the frequency bandwidth. Using a fairly common assumption of log-normal transition curve to convert SE to P_D, with σ = 10 dB this gives the baseline probability of detection of 84%.

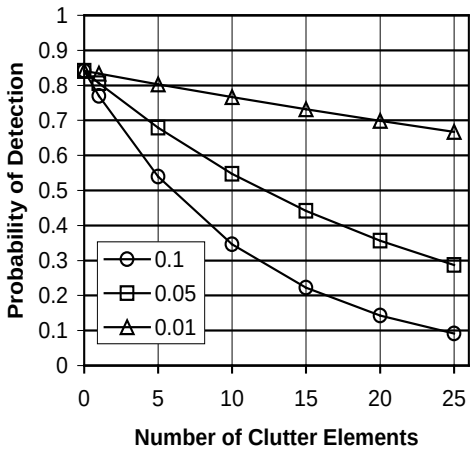

Figure 1: Probability of detection as a function of number of clutter elements present for three values of clutter element width: 10%, 5% and 1% of band width.

In Figure 1 the variation in probability of detection with numbers of clutter lines is displayed, i.e., the probability of exactly *n* clutter elements is 1.0. For the calculations clutter-element widths of 10%, 5%, and 1% of the frequency bandwidth are used. Clutter intensity levels are set to be 20 dB higher than the background noise and use a lognormal transition curve with $\sigma = 10$ dB.

As the number of clutter elements increases, the band is increasingly covered by the clutter. Thus, the probability of detection drops from that of the background noise to that of a background that has the same mean level as the clutter. It is clear that a few wide clutter elements or a large number of thinner ones can substantially impact detection performance.

Figure 2 shows the variation of the probability of detection using the model, as a function of the mean clutter intensity, while Figure 3 shows the variation as a function of clutter fluctuation. In both cases the clutter element width is held fixed at 5% of the bandwidth.

In Figure 2 probability of detection decreases both when the mean intensity of the clutter increases and when the number of clutter elements in the band increase. However, in Figure 3 the probability of detection depends non-linearly on the fluctuation of the clutter. Since the signal level is held constant at 10 dB above the background noise. When the mean clutter intensity is also 10 dB, then the SE is 0, which is the mean of the assumed lognormal fluctuation distribution. Probability of detection is not 50% at this point because the detection against the background noise is still 84% which shifts the overall probability up. For SE > 0, increasing fluctuation decreases the probability of detection since it becomes more likely that the actual clutter intensity will be high enough to mask the signal. For SE < 0, increasing fluctuation increases the probability of detection since it becomes more likely that the clutter intensity will not be high enough to mask the signal.

From this simple example it can be seen that there is a transition similar to that described by Dyer as the amount of clutter in a band increases. The detection scenario changes from detection governed by background noise characteristics to detection governed by clutter characteristics. Fortunately, Dyer also noted that as large amounts of clutter begin to govern the detection process, the overall statistics also begin to look more like the random background noise but with higher mean levels. It is in the transition zone, where assuming the background level gives optimistic results and assuming the clutter levels gives pessimistic results, that the model proposed in this paper has a role.

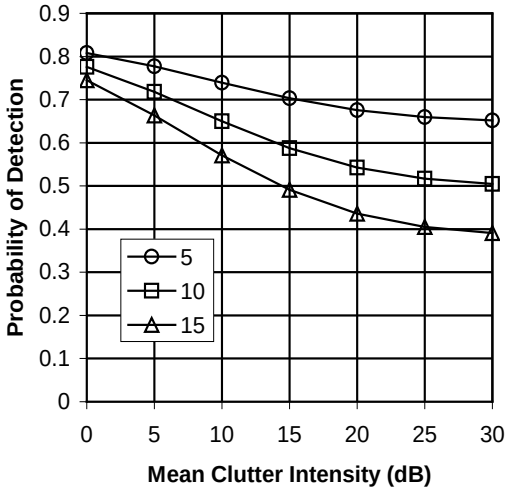

Figure 2: Probability of detection as a function of mean clutter intensity for three amounts of clutter present (5, 10 and 15 elements) in the band, and a clutter width of 5% of the bandwidth.

Input Data Requirements

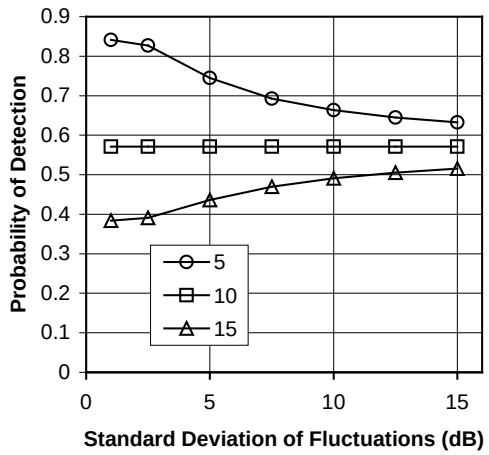

Figure 3: Probability of detection as a function of clutter intensity fluctuation for three values of mean clutter intensity (5, 10, and 15 dB).

As in any modelling exercise, as more detail is added to a model, the amount of input data required to drive the model also increases. In the model described by Equation 16 a number of new types of input data are required, based around the decomposition of ambient noise into a set of M clutter types. For each clutter type C_j the model requires:

1) A distribution giving the expected number of clutter elements occuring within a frequency band;

2) An expected clutter element width in frequency (-6 dB from peak); and,

3) A distribution giving the expected intensity of a clutter element, and a fluctuation model for use in determining the DT/RD value and transition curve.

Programs have been developed at the Defence Research Establishment Atlantic to begin collecting data of this type. However, to this point they remain labour intensive.

Summary

A simple extension of traditional sonar performance modelling has been proposed that allows the incorporation of non-broadband noise characteristics. It has been suggested that ignoring the noise clutter in passive sonar modelling can produce overly optimistic predictions of sonar performance.

By imposing some simplistic assumptions on the clutter and signal statistics, the implications of this model for passive sonar performance prediction have been explored.

However, in order to use such a model for actual predictions a more robust and detailed accounting of the ambient noise environment is required. Some examples of the types of clutter information that are required for this particular model have been suggested.

Acknowledgements

A portion of this work was completed by Chantal Gilbert as part of a Summer Research Assistantship at DREA. Funding for this work comes from Defence R&D Canada, Thrust 1CA12.

References

1. Urick, R.J. Principles of Underwater Sound. 3rd Ed., McGraw-Hill Book Company, New York, 1980.

2. Dyer, I. Statistics of Distant Shipping Noise. J. Acoust. Soc. Am. 53, 1972, 564-570.

3. Bannister R.W., Denham R.N., Guthrie K.M., Browning D.G. and Perrone A.J. Variability of low-frequency ambient sea noise. J. Acoust. Soc. Am. 65, 1979, 1156-1163.

4. Cato, D. The Biological Contribution to the Ambient Noise in Waters Near Australia. Acoustics Australia, Vol 20, No. 3, 1993, 76-80.

5. Hazen, M.G. and Graham, R. Probabilistic Assessment of Realistic Acoustic Detection Effectiveness (PARADE) Model: Theoretical Development. DREA Technical Memorandum 94/202, January 1994.

6. Harris, F.J. On the use of windows for harmonic analysis with the discrete Fourier transform. Proceedings of the IEEE, Vol 66, No. 1, January 1978, 51-84.

ACOUSTICS - putting the science and technology to work

Conference of the Australian Acoustical Society
Joondalup Resort, Western Australia, 15-17 November 2000

Session AC-2 Workshop – Environmental Noise Monitoring

ACOUSTICS - putting the science and technology to work

Conference of the Australian Acoustical Society
Joondalup Resort, Western Australia, 15-17 November 2000

Session UW-2 Arrays And Imaging Systems

Matched-Field Processing Classification

Ahmad T. Abawi and Phil Schey

SPAWAR Systems Center
San Diego, CA 92152-5001
W. A. Hodgkiss
Marine Physical Laboratory, Scripps Institution of Oceanography
San Diego, CA 92152-6400

Abstract

Data from the SWellEx-99 experiment is used to examine the detection and classification performance of adaptive matched field processing on large horizontal line arrays.

INTRODUCTION

Matched field processing (MFP) has traditionally been performed using vertical line arrays. During the Shallow Water Cell Experiment SWellEx-96, which was conducted off the coast of San Diego in spring of 1996, it was shown that MFP could also be performed using horizontal line arrays (HLA). The MFP correlation using the 250-meter long HLA used in this experiment was large enough for detection, but because of the high side-lobes, classification by depth was not possible. However, simulations predicted that MFP on an approximately 500-meter long HLA would provide classification by depth. To verify this prediction, the SWellEx-99 experiment was conducted in spring of 1999. During this experiment, which was conducted in approximately 200 meters of water over complex bottom bathymetry, a number of horizontal line arrays were deployed. A J15-3 source, which transmitted multi-tone signals at various levels, was towed along various tracks. The signal from this source was recorded on 500-meter long horizontal line arrays, which had between 37 and 52 elements. The map of the experiment, the source track as well as the locations of the arrays are shown in Fig. (1).

To introduce the reader to the terminology and the types of processing used in this paper, a brief introduction to matched field processing is presented in Section 2. In Section 3 we present matched field processing results using data recorded on two large horizontal arrays, followed by conclusions in Section 4.

MATCHED FIELD PROCESSING

Matched field processing (MFP) is a generalization of plane wave beamforming where the measured field at the receiving array is matched with the solution of the wave equation for a given source position [1], [2]. Since the acoustic field has unique spatial structure for each source position, matching the measured field with the computed field allows localization. Whereas plane wave beamforming provides an estimate of source bearing, matched field processing provides estimates of the source range and depth with a vertical line array and estimates of the source range, depth and bearing with tilted and horizontal line arrays. The source position generally corresponds to the point with the maximum correlation in the so-called matched field ambiguity volume. For a source in motion, matched field ambiguity volumes can be formed as a function of time and a target track, containing estimates of source range, depth and bearing, is obtained by picking the points with the maximum MFP correlation. For a moving source the data covariance matrix is computed as a function of time. For each time, the MFP correlation is computed according to

$$C(r,z,\vartheta,f;t)=\frac{W^{*}(r,z,\vartheta,f)R(f;t)W(r,z,\vartheta,f)}{Tr(R)}$$

In the above equation $R(f;t)=p^{*}(f;t)p(f;t)$ is the data covariance matrix, where $p(f;t)$ is the vector of complex pressures at the array and *t* is the time along the track. For a linear or conventional processor the weight vector, *W,* is replaced by the replica vector, *S.* The replica vector is a vector of complex pressure fields at the array due to a source located at (r,z,ϑ) and can be obtained from a propagation model.

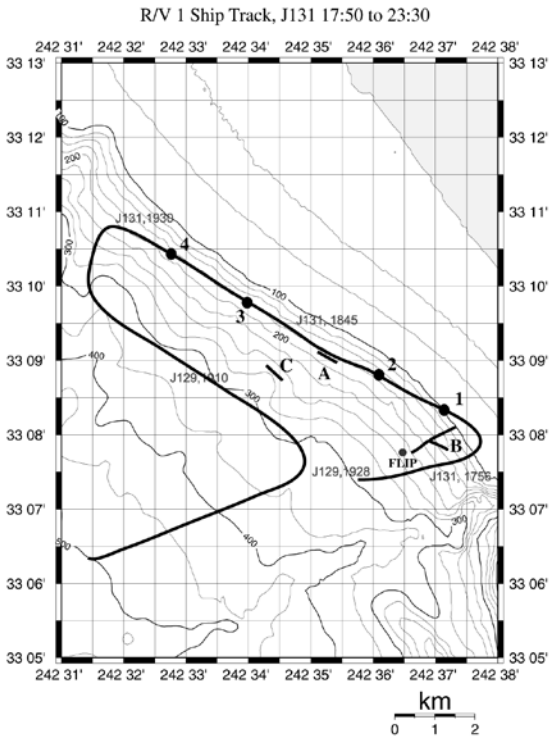

Figure 1: *This map shows the site of the experiment. The source is towed along the track shown. The data are recorded on arrays A, B and C. Only data on arrays A and B are processed for this paper. The processing time for array A is 60 minutes. During this time the source is towed between point 1 and point 4. The processing time for array B is 30 minutes. During this time the source is towed between point 2 and point 3.*

The adaptive processor used in this paper is the minimum variance distortionless response processor (MVDR) with the white noise gain constraint. The weight vector for this processor is given by

$$W = \frac{(R+\varepsilon)^{-1} S}{S^{*}(R+\varepsilon)^{-1} S}.$$

The amount of white noise, ε, added to the diagonal of the covariance matrix is adjusted to keep the white noise gain, $G_w = (W^{*}W)^{-1}$, at a given level. The white noise gain used in this paper was –3 dB.

The normalization used in the expression for the MFP correlation guarantees that the output of the processor, for normalized replica vectors, is unity for perfect data-model match. The MFP correlation is computed for each range, depth and bearing by searching over these parameters. A matched field ambiguity surface is obtained by plotting the MFP correlation as a function of two of the three spatial parameters. Of course, in doing so the third variable is set equal to the value that is obtained after an exhaustive search over all three variables in the parameter search space. To increase detection, the average correlation is computed by incoherently summing individual correlations over frequency:

$$\overline{C}(r,z,\vartheta;t) = \frac{1}{N}\sum_{i=1}^{N} C(r,z,\vartheta,f_i;t)$$

RESULTS

In this section we present matched field processing classification results using data recorded on Array A and Array B. Array A was deployed at 173 meters of water. It was 500 meter long and had 36 elements. Array B consisted of two arrays deployed in the shape of a Y. The long leg of the array, which was 1000 meters, was deployed perpendicular to the isobathymetric contour lines over a 10% slope, which resulted in a vertical aperture of 100 meters. The shorter leg of the array was 500 meters and it was deployed parallel to the isobathymetric contour lines over essentially flat bottom. The data that are presented here are those recorded on the short leg of array B. Data were processed by using 16 phones over an array aperture of 430 meters.

The arrays recorded data as the source was towed along the upper track shown in Fig. (1). The source transmitted multi-tone signals at different source levels. The first set of 13 tones at a source level of 155 dB was transmitted at 58, 76, 91, 106, 125, 142, 160, 176, 213, 247, 295, 350 and 400 Hz. The next set of 13 tones at a source level of 132 dB was transmitted at 56, 74, 89,..,398 Hz.

Figure (2) shows MFP results using data recorded on Array A. The processing time was 60 minutes during which the source was towed between point 1 and 4. These results were obtained by using the linear processor discussed in the previous section. Each panel in Fig. (2) is a range time record. These range time records were obtained by first searching in range, depth and bearing to obtain a three dimensional track of the source. The source's range, bearing and depth were estimated by selecting those values in the search space, which resulted in the maximum MFP correlation. After the source's location was estimated, the range time records were obtained by focusing the beamformer at the source's depth and bearing and displaying the MFP correlation as a function of range and time.

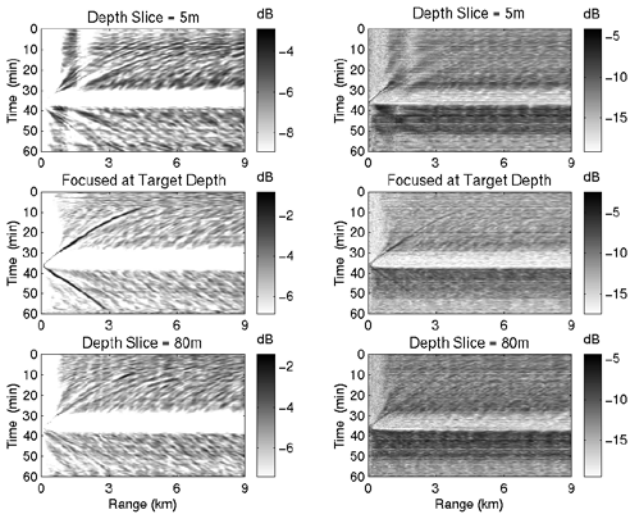

Figure 2: *This figure shows MFP range time record for data recorded on array A. The column of images on the left are for the 155 dB source level and those on the right are for the 132 dB source level. The MFP range time records were obtained using the linear processor. Each row of images in the above figure shows the range time record when the beamformer is focused at a different depth. Note that when the beamformer is focused at the correct source depth, a dark target track is obtained. This demonstrates the classification-by-depth capability of MFP.*

To examine the depth classification capability of matched field processing, in each of the three panels in the two columns of Fig. (2) the beamformer is focused at a different depth. In the top two panels it is focused at 5 meters, in the middle two panels it is focused at the true source depth (55 m) and in the bottom two panels it is focused at 80 meters depth. The images in the left column are for the 155 dB source level and those in the right column are for the 132 dB source level. It can be clearly seen that when the beamformer is focused at the true depth of the source, the MFP correlation is high, resulting in a dark source track. This is true everywhere except at broadside where MFP does not have any depth resolution. This robust feature of matched field processing can be used to classify targets as surfaced or submerged.

Figure (3) shows the same type of results for data recorded on Array B. The three panels in the left column show range time record for the beamformer focused at three different depths for the 155 dB signal level. The three panels in the right column show the same results for the 132 dB signal level. The processing time for Array B was 30 minutes. During this time the source was towed between point 2 and 3. The results shown in Fig. (3) also verify the depth classification capability of matched field processing. Note that the target track can only be detected when the beamformer is focused at the true target depth. This is true even for the 132 dB signal, showing that MFP classification by depth is robust even for weak signals.

CONCLUSIONS

In this paper data from the SwellEx-99 experiment were used to examine the depth classification of matched field processing with the use of long horizontal line arrays. Data were used from two horizontal arrays with different apertures, deployment depth and arrays design. Using data on both arrays, it was demonstrated that MFP using data on horizontal arrays can be used as a target classification tool. It was also shown that this method is robust at weak signal levels.

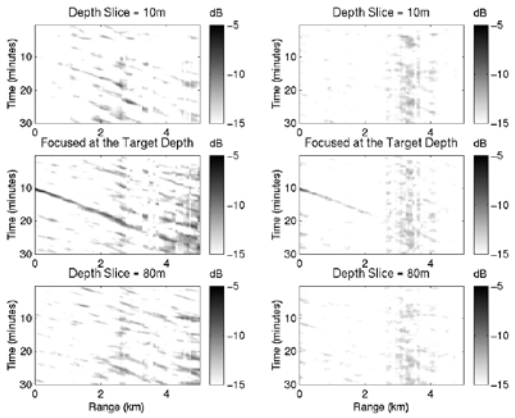

Figure 3: *This figure shows MFP range time record for data recorded on array B. The column of images on the left are for the 155 dB source level and those on the right are for the 132 dB source level. The MFP range time records were obtained using the MVDR processor. Each row of images in the above figure shows the range time record when the beamformer is focused at a different depth. Note that when the beamformer is focused at the correct source depth a target track is visible. In the case of the 132 dB source level no target track can be detected at other depths.*

RERERENCES

1. **H. P. Bucker**, Use of calculated fields and matched field detection to locate sound sources, *J. Acoust. Soc. Am.*, 59 , pp. 368-373, 1976.

2. **Newell O. Booth *et al.***, Source localization with broad-band matched field processing in shallow water, *IEEE Journal of Oceanic Engineering*, 21(4), pp. 402-412, 1996.

Solid Slim Diameter Towed Array To Revolutionise Off-Shore Seismic Exploration

Andrew Gallagher

Thomson Marconi Sonar Pty Ltd
274 Victoria Road, Rydalmere, NSW 2116 Australia

Abstract

The Offshore exploration for Petro Chemical resources is a world-wide industry using Seismic Reflective techniques. This paper will report on the successful Australian development, production and exportation of a revolutionary solid streamer towed array for this industry. The paper will consider traditional seismic exploration using large diameter oil filled non-robust arrays and the limitations on operations and mission efficiency this imposed. The paper will then consider the inherent efficiencies of more robust solid arrays in increasing the operational window for seismic exploration by decreased sensitivity to sea-state conditions and other operational issues. The paper will then report on the successful development of a robust solid array in Australia leveraged off indigenous Naval towed array development including the acoustical and flow noise reduction issues and the subsequent award of the 1997 Australian Design Award. The paper will also report on the significant export success of the product and recent development of the next generation array.

Introduction

Thomson Marconi Sonar Pty Limited in Australia (TMS Pty) is the World's largest producer of towed arrays with the export of both Naval and Commercial Seismic towed arrays providing the bulk of this production output. A key factor to TMS Pty's success in this field is attributed to Australian innovation in Towed Arrays with TMS Pty leveraging off innovative Naval towed array formats to develop new and more robust Seismic Towed Arrays.

Off-shore Seismic Industry and Methodologies

The off-shore Petro- chemical/Geo physical research and survey industry is a robust, high yield and high risk industry. The industry currently surveys to a capacity of about 400,000 km^2 per annum and utilises a annual operating budget for streamer surveys of approximately $1billion USD. The cost of survey ships and systems s for this industry are significant and dictates a high utilisation cost for operations at approximately $2500USD per km^2. The scale of operations can be understood by consideration of one vessels operations:

- A large seismic vessel sails 20,000 to 25,000 on-line kilometres per year;
- Using 8 streamers, this equates to >7000 km^2/pa;
- Average daily production in good weather is about 40 km^2 ;
- 175 to 200 days per year on survey and on-line seems typical today -ie 55%;
- True cost of operation on a 8 streamer vessel = $30million/pa;
- Hence break-even price of data = $4000/$km^2$ (8 streamers); and
- Every extra day production has a value of $160,000

Figure 1 – Seismic Operations

The survey methodology employed is a generic technique with differences only in terms of the receiver type, deployment type, logistics and aperture geometries. The receiver is an array of sensors embedded in the ocean (either streamed near its surface or fixed near

the sea-bed). The source is a large low frequency acoustic source (mass-drop) applied at the ocean surface typically by air guns. There is no direct sensing or excitation of elastic waves in the earth (even in 4C OBC!). The ocean is the real source and receiver, and the boundary conditions determine data fidelity.

The towed streamer methodology dominates over the fixed sensor format due to its overwhelming productivity advantage and the repeatability of data. About $1billion worth of streamer has been acquired by the industry. Streamer sections typically last between 2 and 4 years in regular service. The price of streamer sections has fallen steadily as quality has risen. Today complete fluid filled digital streamer sells for under $300k per km (ie it's a commodity). 99% of new streamers use 24bit A/D digital telemetry

Limitations of Traditional Streamers

Traditionally oil filled streamers were employed due to the need for oil based isolation of seismic streamer noise and vibration. Total Noise runs between 1 uBars and 50 uBars (6Hz to 200Hz) are typical in seismic operations depending on conditions with surveys being shut down at 5 to 10 uBars average. Inherent noise sources include:

- Vessel Radiated Noise;
- Turbulent Boundary Layer (flow noise);
- Vibration-generated Noise;
- Sea State Acoustic Noise; and
- Other Vessels (propulsion and air guns).

Turbulent noise is generally below 3 uBars at 5kts and is a (rising) function of tow speed, The Spectrum is broad, and is incoherent between channels and hence not of great concern. Vibration noise is, however, of real concern and is a function of sea state and tow system mechanical movement and is generally coherent between channels. Vibration noise can range from below 2uBars to over 20 uBars (6Hz to 200Hz band) depending on conditions.

Conventional oil(fluid) filled streamer structures are limited in intrinsic hydrophone vibration sensitivity through several coupling mechanisms. The dominant mechanism is the bulge wave - gives rise to high levels of vibration sensitivity at low frequencies. Another mechanism is asymmetric fluid mass loading caused by hydrophones not being perfectly centred in the hose, section giving lateral sensitivity. For a typical fluid filled streamer group the total vibration sensitivity is over 140dB re 1uPa/m/s^2 in the lowest octave. This equals 1000 uBar per g

TMS Pty Innovation

Due to these limitations of traditional streamers, TMS Pty recognised a strategic market opportunity for their solid array technology. To create a new and more robust seismic streamer, TMS Pty adapted the proven KARIWARRA solid towed array technology developed in Australia by DSTO and TMS Pty for the Royal Australian Navy. This array had already been proven to enjoy significant performance and logistical advantages over traditional oil filled naval towed arrays. The development methodology leveraged directly off TMS Pty's comprehensive Military solid streamer development capability. Engineering resources were transferred from military to the seismic domain including key resources in analysis, modeling, mechanical design, acoustic transducers, tow testing facilities and methods, vibration testing facilities. The starting point was development of a Functional Performance Specification (FPS) structured on a helical development model - design - build - test - evaluate - design - build - test etc. Final product qualification was driven by the FPS plus additional requirements learned during development. Initial design goals for TMS Pty were:

- Produce a robust streamer section using solid buoyancy and compatible with legacy systems;
- Self noise performance at least as good as 80mm diameter fluid filled cable (WG24);
- Special attention to reducing vibration sensitivity;
- Low risk transition to full scale manufacture; and
- Cost "comparable" with 80mm fluid filled cable.

The development proved very successful with TMS Pty able to realise signigficant market success over a relatively short period moving from a non player in the industry to one of the key streamer manufacturers and the World's largest towed array manufacturer with comprehensive towed array facilities at their 22,500 sq metre facility in Sydney NSW, at the 2.500 sq metre facility in Adelaide S.A. and also at their new Australian owned facility in Houston Texas.

Figure 2 – TMS Pty's Towed Array Facility in Sydney

The time-line of market penetration is:

- 1991 Initial market research starting with Australian military solid streamer "KARIWARRA";
- 1992 Detailed discussions with contractors;
- 1992 Conceptual design #1 (Project Fast track);
- 1993 Conceptual design #2 (Project Slimline);
- 1994 Final discussions with Contractors - agreement reached with the first customer Western Geophysical INC of the United States;
- 1994-1996 Development and industrialisation;
- 1996-1997 several design refinements introduced during initial production;
- Sentry made available to open market; and
- 400km produced to date.

Conclusion

Technical innovation, adaptive engineering and dynamic industrial methodologies has allowed TMS Pty to realise significant export success. This is no better illustrated than in the success of TMS Pty in the export of towed array sonars especially Seismic streamer arrays. Production capability for these arrays is measured in the tonnes and creates a approximately $45 MAUD export industry for TMS Pty.

Tracking of Airborne Acoustic Sources using an Undersea Hydrophone Array

I. S. D. Solomon and A. J. Knight

Defence Science and Technology Organisation, P.O.Box 1500, Salisbury 5108, Australia.

Abstract

Underwater hydrophone sensors are known to receive acoustic energy emitted by airborne sources, such as turbo-prop aircraft. Using an array of hydrophone sensors, together with some standard signal processing, the estimation of both Doppler shifted tonal frequency and conical bearing (of the airborne signal) is possible. In this paper this information is used to estimate the trajectory of the airborne source over time. An Extended Kalman Filter is developed to estimate the position and velocity of the aircraft, as well as the rest frequency of the tonal emitted. The tracker is evaluated using simulation scenarios, which include manoeuvres, generated from recordings of aircraft trajectories. The results indicate that the tracker is able to "close-in" on the true trajectory when the aircraft reaches its "closest point of approach"; the subsequent position, velocity and rest frequency estimates are seen to be good.

Introduction

Sonar tracking studies have mainly considered the "bearings-only" problem, where the position and velocity of acoustic sources (or contacts) are estimated from only bearing measurements. In the recent literature algorithms have been proposed which use one or more Doppler frequency measurements (from tonals), in addition to bearing measurements, to track contacts. Almost all the literature considers the contacts to be in the same plane as the array, and so only two-dimensional tracking is performed. However for aircraft tracking from undersea hydrophone arrays the problem is more complicated; the problem is not only three-dimensional, since the aircraft is at a higher altitude than the array, but also the aircraft is in the air and the acoustic energy it radiates propagates through an air-water interface prior to being received by the array [1] ie two acoustic "layers" are present. This tracking problem has not been considered in the literature, and turns out to be of greater complexity than the standard two-dimensional (single layer) problem; a preliminary investigation into this problem was noted in [2,3].

The Maximum Likelihood Estimator (MLE) is known to be the optimal estimator, but it is rarely used for tracking due to its computational cost. The most common tracking algorithm is the Kalman filter (KF) [4,5], which is attractive because of its low complexity and high computation speed. Other tracking algorithms include Pseudo-Linear Estimators (PLE), Hidden Markov Models (HMM), Probabilistic Multiple-Hypothesis Trackers (PMHT) and Particle Filters. In this paper the KF approach is considered.

The parameters estimated by the tracker are the position of the aircraft (x,y,z), the velocity of the aircraft (v_x,v_y) and the (fixed) rest frequency (f_o) of the tonal emitted by the aircraft; the vertical velocity component v_z of the aircraft is assumed to be zero. These parameters are to be estimated from the aircraft Doppler frequency and bearing measurements, which are extracted by low level signal processing [6]; the measurements are assumed to be available at each time interval ie no missing measurements. Since the parameters to be estimated (x,y,z,v_x,v_y,f_o) are non-linearly related to the measurements it is necessary to use a modified version of the KF algorithm, called the Extended Kalman Filter (EKF) [4,5]. Cartesian coordinates were chosen here to reduce the inherent complexity.

The propagation path of the aircraft signal is of significant importance. In this paper it is assumed that the sound waves penetrating the air-water interface obey Snell's law; experiments are currently being conducted to investigate this assumption. It is also assumed that the propagation of the aircraft signal is via a direct path; this will however not be true all the time. Hence modifications made are presented in [7], for using multiple tracker models so that tracking of aircraft may be possible even when bottom-bounce or surface-bounce paths are the only paths providing sufficiently strong signals.

Generation of Simulated Data

The method of generating simulated data, which consists of bearing and Doppler frequency measurements, is now outlined. Figure 1 depicts how the acoustic energy from the aircraft reaches the array after passing through an air-water interface. As can be seen the acoustic signal from the aircraft refracts as it enters the water, since the speed of sound in water is different to that in air. In this paper it is assumed that the speed of

sound in water c_w = 1500 m/s and the speed of sound in air c_a = 340 m/s; both media are also assumed to be homogeneous. The elevation angle of the signal in air (angle of incidence) is denoted as ϕ_a, while the elevation angle of the signal in water (angle of refraction) is denoted as ϕ_w. Note that there exists a critical angle of incidence, at which there is no refraction but total internal reflection, and this angle is approximately 13°.

The coordinate system used in this paper is illustrated in Figure 2. The array is arbitrarily chosen to be at (0,0,0) and is aligned along the *y*-axis. The depth of the array can vary over time and at time index *k* is *d(k)*. The position of the aircraft is $(x_a(k),y_a(k),z_a(k))$; the aircraft's altitude is allowed to vary over time and note $z_a(k)$ is the altitude relative to the array (since the array is at the origin). The bearings, measured by the array, are measured anti-clockwise from the positive *x*-axis. (Note the time index *k* is often dropped for clarity).

The location of the aircraft varies as follows (for zero acceleration)

$$x_a(k) = x_a(k-1) + v_x(k)\Delta_T$$
$$y_a(k) = y_a(k-1) + v_y(k)\Delta_T$$

where Δ_T is the inter-sample time in seconds, and the instantaneous aircraft velocity components are $v_x(k)$ and $v_y(k)$.

Independent Gaussian noise is added to the *x*, *y* and *z* components of the aircraft's position and also to the depth of the array; these are to model random perturbations in the aircraft's flight, and errors in the measurements of array depth. The standard deviation of the noise introduced are σ_x = 25 m, σ_y = 25 m, σ_z = 25 m and σ_d = 2 m.

Given the location of the aircraft, at a given time, the location at which the radiated sound from the aircraft enters the air-water interface may be calculated. The horizontal range of the aircraft from the array, at a particular time, is $R = \sqrt{x_a^2 + y_a^2}$, and if we denote the refractive index as $\rho = c_a / c_w$, then from Figure 1 it is clear that the range

$$\begin{aligned} R &= d\tan\phi_w + (z_a - d)\tan\phi_a \\ &= d\tan\phi_w + (z_a - d)\sin\phi_a / \sqrt{1-\sin^2\phi_a} \\ &= d\tan\phi_w + (z_a - d)\rho\sin\phi_w / \sqrt{1-\rho^2\sin^2\phi_w} \end{aligned}$$

where in the second equation we have expressed $\tan\phi_a$ as $\sin\phi_a/\cos\phi_a$ (and $\cos\phi_a = \sqrt{1-\sin^2\phi_a}$), and in the third equation we have used Snell's law ($\sin\phi_a = \rho\sin\phi_w$). The third equation, which is non-linear in the unknown ϕ_w, is solved by iterating over all values of ϕ_w (from 0 to 90 degrees in 0.1 degree increments) and finding the value that gives the smallest error (this search is very fast). Once the value of ϕ_w is determined, the intermediate point at which the radiated sound enters the air-water interface (x_i,y_i) may be calculated as follows

$$x_i = \mathrm{sgn}(x_a)\, d\tan\phi_w \Big/ \sqrt{1 + (y_a^2 / x_a^2)}$$
$$y_i = x_i y_a / x_a$$

where sgn(x_a) is negative one if x_a is negative and is positive one otherwise. Note the first equation correctly ensures that x_i has the same sign as x_a, and the second equation will provide the correct sign for y_i as long as x_i has the correct sign.

Once the intermediate point has been determined, at a given time instant, one can generate the bearing and Doppler frequency measurement data for that same time instant. The conical bearings as measured by the array (with respect to broadside) are calculated as follows for the general case ($-180^o \le \theta \le +180^o$)

$$\theta = \arctan\left\{ y_i \Big/ \left(\mathrm{sgn}(x_i)\sqrt{x_i^2 + d^2} \right) \right\}$$

and for the case of a linear array (with left/right ambiguity) as

$$\theta = \arctan\left\{ y_i \Big/ \sqrt{x_i^2 + d^2} \right\}$$

where in this case $-90^o \le \theta \le +90^o$. The actual azimuth of the intermediate point (and the aircraft location) is $\theta_s = \arctan\{y_i/x_i\} = \arctan\{y_a/x_a\}$. The Doppler of the received sound may then be calculated as

$$f = \frac{f_o}{1 + (v_y \sin\theta_s \sin\phi_a + v_x \cos\theta_s \sin\phi_a)/c_a}$$

where f_o is the rest frequency of the aircraft signal. Note ϕ_a is readily calculated once ϕ_w is known (using Snell's law). Measurement noise is then added to the bearing and Doppler time series (σ_θ = 3° and σ_f = 1 Hz). Given $\theta(k)$ and $f(k)$, the tracker has to estimate the aircraft trajectory, its velocity components and the rest frequency of the emitted signal.

Tracking Algorithm

Kalman filters [4,5] recursively estimate the parameters of interest, which are called the state variables. The sufficient statistics for the KF are the state variables, and their associated covariances. The KF estimates the state variables, at a given time, from the dynamics of the system (via the process equations) and from the so called innovations. The dynamics of the system are represented by the so called state transition matrix, while the innovations indicate the deviation of the tracker from the measurements; the KF uses time-varying gain (Kalman gain) to vary the contributions of the innovations in the estimation of the state variables. The relationship between the measurements and the state variables are represented by the so called measurement matrix.

Extended Kalman Filters are obtained using a Taylor expansion of the non-linear equations in the process or measurement system, around the current state estimate [4,5]. First order EKF use only the first order terms; higher order terms are accounted for by the process or measurement noise. In this paper Cartesian coordinates are used for the state variables, and so the measurement equations turn out to be non-linear while the process equations are linear. Filter initialisation is very important, in particular since Cartesian coordinates are used for the state variables. In the algorithm to be outlined, the user can specify if the aircraft height is to be estimated, if acceleration is to be modelled, if the rest frequency of the tonal emitted by the aircraft is to be estimated, and, finally, if in fact the array is a linear array (ambiguous bearing). The equations given here are for the general case; for specific cases subsets of the matrices and vectors are used.

The state variables may be written in vector form as $\hat{\mathbf{x}}(k) = \left[\hat{x}(k), \hat{y}(k), \hat{z}(k), \hat{v}_x(k), \hat{v}_y(k), \hat{a}_x(k), \hat{a}_y(k), \hat{f}_o(k)\right]^T$ where $\hat{a}_x(k)$ and $\hat{a}_y(k)$ are the estimates (at time *k*) of the instantaneous aircraft acceleration. Since all the state variables relate to the aircraft, the subscript "a" has been dropped. The EKF developed is now detailed; the complex part of the algorithm is the measurement matrix, since the state variables are non-linearly related to the measurements $\theta(k)$ and $f(k)$.

Given the state variables at time *k*, the intermediate point $\left(\hat{x}_i(k), \hat{y}_i(k)\right)$ is calculated in a similar manner as for the simulations in the previous section. First the elevation angle in water $(\hat{\phi}_w)$, or angle of refraction, is estimated by solving

$$\sqrt{\hat{x}^2 + \hat{y}^2} = d\tan\hat{\phi}_w + (\hat{z} - d)\rho\sin\hat{\phi}_w \Big/ \sqrt{1 - \rho^2\sin^2\hat{\phi}_w}$$

and then the intermediate point is estimated as

$$\hat{x}_i = \mathrm{sgn}(\hat{x}) d\tan\hat{\phi}_w / \sqrt{1 + \left(\hat{y}^2 / \hat{x}^2\right)}$$
$$\hat{y}_i = \hat{x}_i \hat{y} / \hat{x}$$

Once the intermediate point is estimated, the bearing of the aircraft (as determined by the tracker) is estimated (for the general case) as

$$\hat{\theta} = \arctan\left\{\hat{y}_i \Big/ \left(\mathrm{sgn}(\hat{x}_i)\sqrt{\hat{x}_i^2 + d^2}\right)\right\}$$
$$= \arctan\left\{\mathrm{sgn}(\hat{x}_i) b\right\}$$

where $b = \hat{y}_i / \sqrt{\varsigma}$ and $\varsigma = \hat{x}_i^2 + d^2$ (for the linear array case $\mathrm{sgn}(\hat{x}_i)$ is dropped). The Doppler frequency of the aircraft signal (as determined by the tracker) is estimated as

$$\hat{f} = \frac{\hat{f}_o}{1 + \left(\hat{v}_y \sin\hat{\theta}_s \sin\hat{\phi}_a + \hat{v}_x \cos\hat{\theta}_s \sin\hat{\phi}_a\right)/c_a}$$

where $\hat{\phi}_a$ is readily calculated once $\hat{\phi}_w$ is known (using Snell's law), and the azimuth angle $\hat{\theta}_s = \arctan\left\{\hat{y}_i / \hat{x}_i\right\} = \arctan\left\{\hat{y} / \hat{x}\right\}$.

Now there are two measurements (bearing and Doppler frequency), at a given time, and there are eight state variables. Hence the measurement matrix **H**(*k*), which is used to estimate the Kalman gain, is a 2x8 matrix and is

$$\mathbf{H}(k) = \begin{bmatrix} h_{1,1} & h_{1,2} & h_{1,3} & 0 & 0 & 0 & 0 & 0 \\ h_{2,1} & h_{2,2} & h_{2,3} & h_{2,4} & h_{2,5} & 0 & 0 & h_{2,8} \end{bmatrix}$$

where for a first order EKF (and p = 1, 2, 3)

$$h_{1,p} = \frac{\partial \hat{\theta}}{\partial \tilde{x}_p} = \frac{\partial \hat{\theta}}{\partial \hat{x}_i}\frac{\partial \hat{x}_i}{\partial \tilde{x}_p} + \frac{\partial \hat{\theta}}{\partial \hat{y}_i}\frac{\partial \hat{y}_i}{\partial \tilde{x}_p}$$

$$h_{2,p} = \frac{\partial \hat{f}}{\partial \tilde{x}_p} = \frac{\partial \hat{f}}{\partial \hat{\theta}_s}\frac{\partial \hat{\theta}_s}{\partial \tilde{x}_p} + \frac{\partial \hat{f}}{\partial \hat{\phi}_a}\frac{\partial \hat{\phi}_a}{\partial \tilde{x}_p}$$

$$h_{2,4} = \frac{\partial \hat{f}}{\partial \hat{v}_x}$$

$$h_{2,5} = \frac{\partial \hat{f}}{\partial \hat{v}_y}$$

$$h_{2,8} = \frac{\partial \hat{f}}{\partial \hat{f}_o}$$

The partial derivatives relating to the bearing are (for the linear array case)

$$\frac{\partial \hat{\theta}}{\partial \hat{x}_i} = \frac{1}{1+b^2}\frac{-\hat{y}_i\hat{x}_i}{\left(\hat{x}_i^2 + d^2\right)^{3/2}}$$

$$\frac{\partial \hat{\theta}}{\partial \hat{y}_i} = \frac{1}{1+b^2}\frac{1}{\left(\hat{x}_i^2 + d^2\right)^{1/2}}$$

$$\frac{\partial \hat{x}_i}{\partial \hat{x}} = \frac{d\sec^2\hat{\phi}_w}{\sqrt{1+\left(\hat{y}^2/\hat{x}^2\right)}}\frac{\partial \hat{\phi}_w}{\partial \hat{x}} + \frac{d\tan\hat{\phi}_w\left(\hat{y}^2/\hat{x}^3\right)}{\left(1+\left(\hat{y}^2/\hat{x}^2\right)\right)^{3/2}}$$

$$\frac{\partial \hat{y}_i}{\partial \hat{x}} = \frac{\hat{y}}{\hat{x}}\frac{\partial \hat{x}_i}{\partial \hat{x}} - \frac{\hat{x}_i\hat{y}}{\hat{x}^2}$$

$$\frac{\partial \hat{x}_i}{\partial \hat{y}} = \frac{d\sec^2\hat{\phi}_w}{\sqrt{1+\left(\hat{y}^2/\hat{x}^2\right)}}\frac{\partial \hat{\phi}_w}{\partial \hat{y}} + \frac{d\tan\hat{\phi}_w\left(-\hat{y}/\hat{x}^2\right)}{\left(1+\left(\hat{y}^2/\hat{x}^2\right)\right)^{3/2}}$$

$$\frac{\partial \hat{y}_i}{\partial \hat{y}} = \frac{\hat{y}}{\hat{x}}\frac{\partial \hat{x}_i}{\partial \hat{y}} + \frac{\hat{x}_i}{\hat{x}}$$

$$\frac{\partial \hat{x}_i}{\partial \hat{z}} = \frac{d\sec^2\hat{\phi}_w}{\sqrt{1+\left(\hat{y}^2/\hat{x}^2\right)}}\frac{\partial \hat{\phi}_w}{\partial \hat{z}}$$

$$\frac{\partial \hat{y}_i}{\partial \hat{z}} = \frac{\hat{y}}{\hat{x}}\frac{\partial \hat{x}_i}{\partial \hat{z}}$$

$$\frac{\partial \hat{\phi}_w}{\partial \hat{x}} = \frac{\hat{x}/\left(\hat{x}^2+\hat{y}^2\right)^{1/2}}{d\sec^2\hat{\phi}_w + (\hat{z}-d)\rho\cos\hat{\phi}_w\left(1-\rho^2\sin^2\hat{\phi}_w\right)^{-3/2}}$$

$$\frac{\partial \hat{\phi}_w}{\partial \hat{y}} = \frac{\hat{y}/\left(\hat{x}^2+\hat{y}^2\right)^{1/2}}{d\sec^2\hat{\phi}_w + (\hat{z}-d)\rho\cos\hat{\phi}_w\left(1-\rho^2\sin^2\hat{\phi}_w\right)^{-3/2}}$$

$$\frac{\partial \hat{\phi}_w}{\partial \hat{z}} = \frac{-\rho\sin\hat{\phi}_w\left(1-\rho^2\sin^2\hat{\phi}_w\right)^{-1/2}}{d\sec^2\hat{\phi}_w + (\hat{z}-d)\rho\cos\hat{\phi}_w\left(1-\rho^2\sin^2\hat{\phi}_w\right)^{-3/2}}$$

For the case of unambiguous bearing measurements $h_{1,p} \rightarrow \mathrm{sgn}(\hat{x}_i)h_{1,p}$ (p = 1, 2, 3).

The partial derivatives relating to the Doppler are

$$\frac{\partial \hat{f}}{\partial \hat{\theta}_s} = \frac{-\hat{f}_o\left(\hat{v}_y\cos\hat{\theta}_s\sin\hat{\phi}_a - \hat{v}_x\sin\hat{\theta}_s\sin\hat{\phi}_a\right)/c_a}{\left(1+\left(\hat{v}_y\sin\hat{\theta}_s\sin\hat{\phi}_a + \hat{v}_x\cos\hat{\theta}_s\sin\hat{\phi}_a\right)/c_a\right)^2}$$

$$\frac{\partial \hat{f}}{\partial \hat{\phi}_a} = \frac{-\hat{f}_o\left(\hat{v}_y\sin\hat{\theta}_s\cos\hat{\phi}_a + \hat{v}_x\cos\hat{\theta}_s\cos\hat{\phi}_a\right)/c_a}{\left(1+\left(\hat{v}_y\sin\hat{\theta}_s\sin\hat{\phi}_a + \hat{v}_x\cos\hat{\theta}_s\sin\hat{\phi}_a\right)/c_a\right)^2}$$

$$\frac{\partial \hat{f}}{\partial \hat{v}_x} = \frac{-\hat{f}_o\cos\hat{\theta}_s\sin\hat{\phi}_a/c_a}{\left(1+\left(\hat{v}_y\sin\hat{\theta}_s\sin\hat{\phi}_a + \hat{v}_x\cos\hat{\theta}_s\sin\hat{\phi}_a\right)/c_a\right)^2}$$

$$\frac{\partial \hat{f}}{\partial \hat{v}_y} = \frac{-\hat{f}_o\sin\hat{\theta}_s\sin\hat{\phi}_a/c_a}{\left(1+\left(\hat{v}_y\sin\hat{\theta}_s\sin\hat{\phi}_a + \hat{v}_x\cos\hat{\theta}_s\sin\hat{\phi}_a\right)/c_a\right)^2}$$

$$\frac{\partial \hat{f}}{\partial \hat{f}_o} = \frac{1}{1+\left(\hat{v}_y\sin\hat{\theta}_s\sin\hat{\phi}_a + \hat{v}_x\cos\hat{\theta}_s\sin\hat{\phi}_a\right)/c_a}$$

$$\frac{\partial \hat{\theta}_s}{\partial \hat{x}} = \frac{-\hat{y}}{\hat{x}^2+\hat{y}^2}$$

$$\frac{\partial \hat{\theta}_s}{\partial \hat{y}} = \frac{+\hat{x}}{\hat{x}^2+\hat{y}^2}$$

$$\frac{\partial \hat{\theta}_s}{\partial \hat{z}} = 0$$

$$\frac{\partial \hat{\phi}_a}{\partial \tilde{x}_p} = \left(\frac{\rho\cos\hat{\phi}_w}{\cos\hat{\phi}_a}\right)\frac{\partial \hat{\phi}_w}{\partial \tilde{x}_p}$$

Now consider the state transition matrix **F**(k), which describes the dynamics of the system. Since there are eight state variables, the state transition matrix is an 8x8 matrix, and is

$$\mathbf{F}(k) = \begin{bmatrix} 1 & 0 & 0 & \Delta_T & 0 & \Delta_T^2/2 & 0 & 0 \\ 0 & 1 & 0 & 0 & \Delta_T & 0 & \Delta_T^2/2 & 0 \\ 0 & 0 & 1 & 0 & 0 & 0 & 0 & 0 \\ 0 & 0 & 0 & 1 & 0 & \Delta_T & 0 & 0 \\ 0 & 0 & 0 & 0 & 1 & 0 & \Delta_T & 0 \\ 0 & 0 & 0 & 0 & 0 & 1 & 0 & 0 \\ 0 & 0 & 0 & 0 & 0 & 0 & 1 & 0 \\ 0 & 0 & 0 & 0 & 0 & 0 & 0 & 1 \end{bmatrix}$$

The state covariance **P**, which along with the state variables are the sufficient statistics, are updated as

$$\mathbf{P}(k+1|k) = \mathbf{F}(k)\mathbf{P}(k|k)\mathbf{F}^T(k) + \Gamma\mathbf{Q}(k)\Gamma^T$$

where the matrix **Q**(*k*) is the process noise covariance (possibly time varying), and Γ is the noise matrix. Note the notation **P**(*k*+1|*k*) indicates that the sufficient statistics at time instant *k* are used to make estimates for time instant (*k*+1).

Now the innovation covariance **S**(*k*+1), the Kalman gain **W**(*k*+1) and state covariance **P**(*k*+1|*k*+1) may be calculated as follows

$$\mathbf{S}(k+1) = \mathbf{H}(k+1)\mathbf{P}(k+1|k)\mathbf{H}^T(k+1) + \mathbf{R}(k+1)$$
$$\mathbf{W}(k+1) = \mathbf{P}(k+1|k)\mathbf{H}^T(k+1)\mathbf{S}^{-1}(k+1)$$
$$\mathbf{P}(k+1|k+1) = (\mathbf{I} - \mathbf{W}(k+1)\mathbf{H}(k+1))\mathbf{P}(k+1|k)$$

where **R**(*k*+1) is the measurement error matrix, which was chosen to reflect the accuracy of the measurements (see [7]).

The innovations are the difference between the measurements and the tracker estimates $\left(\hat{\theta}, \hat{f}\right)$. The bearing innovation, at time index *k*, is

$$e_1(k+1) = \theta(k+1) - \arctan\left\{\frac{\hat{y}_i}{\mathrm{sgn}(\hat{x}_i)\sqrt{\hat{x}_i^2 + d^2}}\right\}$$

For the linear array case $\mathrm{sgn}(\hat{x}_i)$ is dropped. The innovation for the Doppler frequency is calculated as

$$e_2(k+1) = f(k+1) - \frac{\hat{f}_o}{1 + \left(\hat{v}_y \sin\hat{\theta}_s \sin\hat{\phi}_a + \hat{v}_x \cos\hat{\theta}_s \sin\hat{\phi}_a\right)/c_a}$$

Using the innovations and the Kalman gain, the new estimates of the state variables at time index (*k*+1) are calculated as

$$\tilde{\mathbf{x}}(k+1) = \mathbf{F}(k)\tilde{\mathbf{x}}(k) + \mathbf{W}(k+1)\mathbf{e}(k+1)$$

where $\mathbf{e}(k+1) = [e_1(k+1), e_2(k+1)]^T$. This equation is the output of the tracker.

Note this tracker can be modified to : (a) include multiple Doppler frequency lines (when present); (b) use the derivative of the bearing and Doppler frequency values; and (c) use Polar coordinates for the state variables (instead of the Cartesian coordinates used).

In this paper it has been assumed that the aircraft signal reaches the array via a direct path. This may not always be the case, and hence one needs to consider other possible propagation paths. In [7] extensions to this tracker are proposed so that multiple tracker models may be employed, in order to enable tracking when multiple (time-varying) propagation paths are present.

Performance Analysis

Consider the scenario shown in Figure 3. The array is arbitrarily chosen to be present at (0,0) and is aligned parallel to the *y*-axis. The fixed parameters are as follows : rest frequency is 68 Hz, altitude (z_a) is 200 m, array depth (d) is 100 m. In this example the aircraft flies along a straight-line path (--) parallel to the array for 200 s; since we consider an inter-sampling time (Δ_T) of 1s, this corresponds to 200 measurements. The first measurement from the aircraft, obtained by the array, was when the aircraft was at (+3.0,-16.5) km and the aircraft traveled at 165 m/s.

The tracker was run as follows : (a) rest frequency is to be estimated; (b) left/right ambiguity is not present; (c) acceleration state variables are not used; and (d) aircraft altitude is to be estimated. The tracker was initialised at the position (+10.0,-25.0) km, with an initial altitude of 1100 m. The rest frequency (f_o) was initialised at 120 Hz, the initial velocity was (+75,+75) m/s, and the covariances (**P**(0) and **Q**(k)) were given robust values (see [7]).

The solid line shows the tracked path in Figure 3; the starting point is depicted by the small circle (o). The tracked path was initially a large distance away from the actual path, but as the aircraft moved closer to the array the tracked path approached the true path. After the aircraft passed the array the distance between the true and tracked paths became quite small. While conducting simulations, it was clearly noted that although obtaining more measurements does decrease the error between the paths, the substantial reduction is obtained when the aircraft gets close to its "closest point of approach" (CPA). This is readily understood by noting that the bearing and Doppler frequency measurements vary most near CPA, and so the most information is provided to the tracker around CPA. This key feature was seen in many scenarios.

The final altitude estimated (not shown) was 1097 m, which differed significantly from the true value of 200 m and was very close to the initial altitude provided to the tracker of 1100 m. The poor estimation of aircraft altitude was seen in many scenarios, but this was found to not adversely effect the estimation of the other parameters. The estimated velocity, shown in figure 4, varies a lot until about 90 seconds (close to CPA), and then is seen to settle down; the final estimate being (-1.7,+163.4) m/s, which is close to the true

value of (0,+165) m/s. The errors in the tracked bearing and Doppler frequency values indicated essentially random fluctuations (due to noise in the measurements) although a positive bias in the bearing error was noticeable.

The bearing and Doppler frequency measurements, along with the tracker values, are shown in Figure 5. It is clearly seen that the measurements are closely tracked and there is less variation in the tracker curves as opposed to the noisy measurements. As mentioned earlier, both the bearing and Doppler frequency measurements are seen to vary most near CPA (100 s). Also shown is the estimated rest frequency (--) which started at 120 Hz; prior to CPA it is seen to deviate somewhat (from 68 Hz), but settles down after CPA to a final value of 67.7 Hz.

The tracker was tested with increased measurement noise ($\sigma_\theta = 10^o$ and $\sigma_f = 5$ Hz) and was still found to be robust (see [7]). The tracking accuracy was found to improve when the rest frequency was known, and hence not estimated. No significant improvement in performance was observed when the height was assumed to be known, and hence not estimated.

The above example was for a synthetically generated straight-line trajectory; now consider a real trajectory, obtained from Global Positioning System (GPS) recordings aboard an aircraft. The depth of the array was set to 100 m. For this real trajectory, since it contains manoeuvres, it was observed that good performance was only achieved when the rest frequency was known. Note to track manoeuvring targets a number of strategies are possible (see [7]).

The tracker was run such that left / right ambiguity was present, the altitude was being estimated, and acceleration state variables were used. Figure 6 shows the tracking of a manoeuvring aircraft; 800 measurements were obtained here during the 800 seconds ($\Delta_T = 1$ second). The aircraft started around (+3,-3) km, then it crossed over to the other side of the array and then travelled away parallel to the *y*-axis. Near (-3,+15) km the aircraft started to turn around (clockwise on the positive *x* half plane) and then travelled towards the array. When the aircraft got close to the array, it turned around again (clockwise on the negative *x* half plane), and travelled away parallel to the *y*-axis until about (-1,+12) km.

The trackers performance in Figure 6 is clearly good. The tracker quickly jumped to approximately (+30,-8) km, providing a good bearing estimate but not range, and by the time CPA was reached (at around (-3,0) km) the tracker was performing very well as it tracked the image (providing good bearing and range estimates). It continued to track the image as the first turn occurred, although some deviation is seen from the true trajectory here. After the turn the tracker followed the true path as the aircraft approached the array, and then tracked the second turn very well. Note when the aircraft flies almost along the *y*-axis, the tracker may jump from the image to the true path (or visa versa); this is due to the array being along the *y*-axis and hence the difficulty in knowing if a manoeuvre is occurring here or the noise is perturbing the measurements.

Conclusion

An Extended Kalman Filter has been developed for the problem of aircraft tracking using bearing and Doppler frequency measurements, obtained from an undersea array of hydrophones. At each time instant the tracker estimates the position of the aircraft, its velocity and the rest frequency of the acoustic signal it radiates. The tracker was tested using simulations and found to perform well, even for manoeuvring aircraft.

References

[1] B. G. Ferguson, K. W. Lo, "*Transiting Aircraft Parameter Estimation using Underwater Acoustic Sensor Data*", IEEE Journal of Oceanic Engineering, Vol. 24, No. 4, October 1999, pp. 424-435.

[2] T. Parkinson, "*Tracking with Bearing and the Narrowband Doppler effect*", private communication, 1998.

[3] S. M. Tonissen, "*Aircraft tracking from bearing/frequency data*", private communication, 1998.

[4] Y. Bar-Shalom, T. E. Fortmann, "*Tracking and Data Association*", Academic Press, 1988.

[5] Y. Bar-Shalom, X. R. Li, "*Estimation and Tracking*", Artech House, 1993.

[6] I. S. D. Solomon, A. J. Knight, D. F. Liebing, S. B. Faulkner, "*Sonar beamforming using Fourier Integral Method*", Underwater Defence Technology (UDT) Conference (Pacific 2000), Sydney, Australia, February 2000, pp. 182-186.

[7] I. S. D. Solomon, A. J. Knight, S. Foster, D. F. Liebing, "*Aircraft Tracking using an Undersea Array*", Defence Science and Technology Organisation (DSTO) Technical Report (in press).

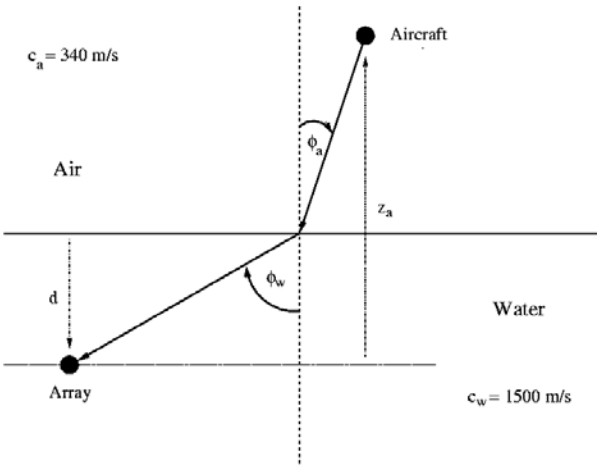

Figure 1 : *Acoustic energy from aircraft refracts at the air-water interface.*

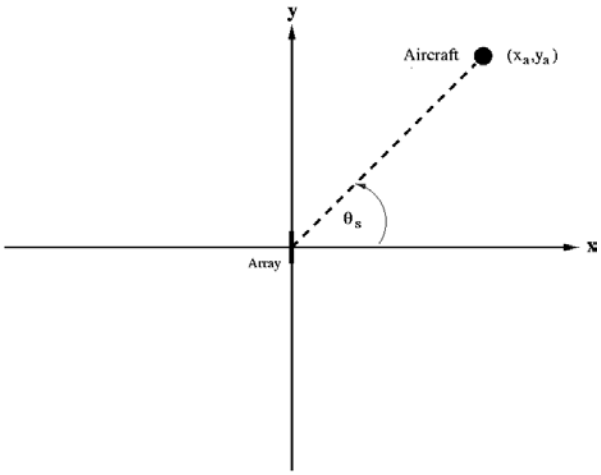

Figure 2 : *Coordinate system used : aircraft is at (x_a,y_a), the array is at (0,0) and is along the y-axis.*

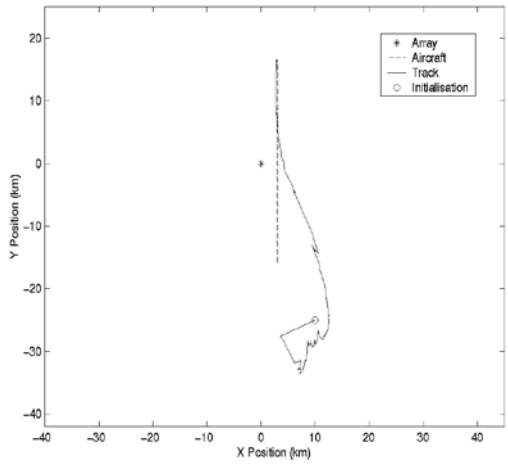

Figure 3 : Tracking of aircraft as it flies parallel to the y-axis.

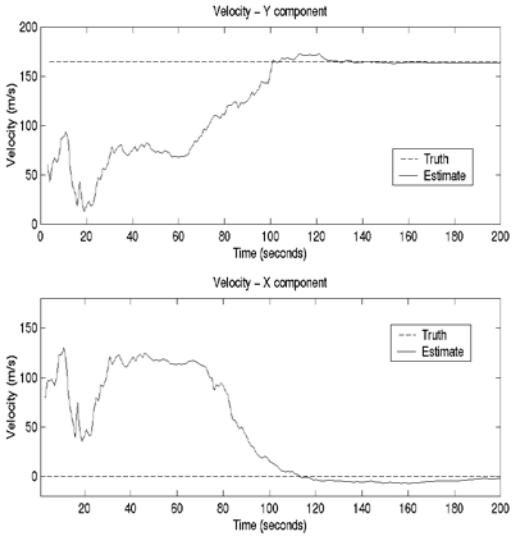

Figure 4 : *Estimated Velocity*.

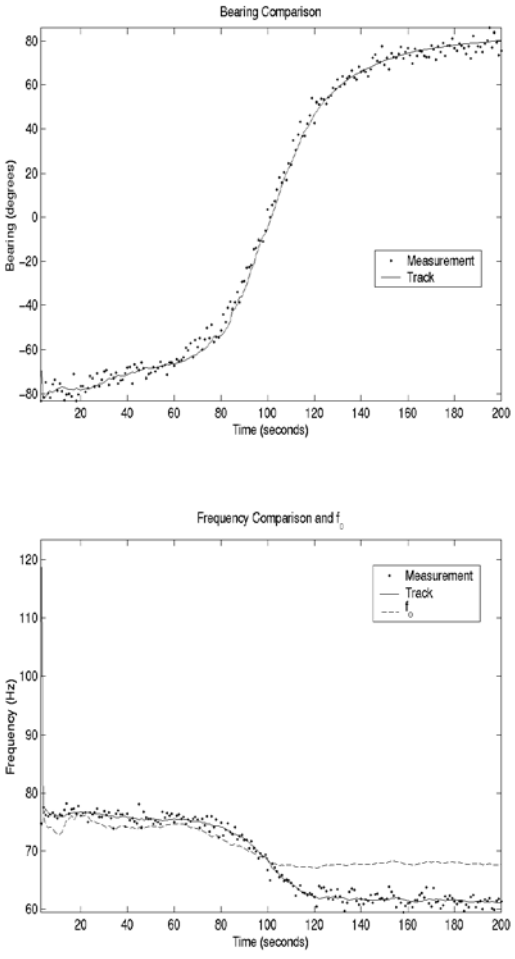

Figure 5 : *Tracking of measurements*.

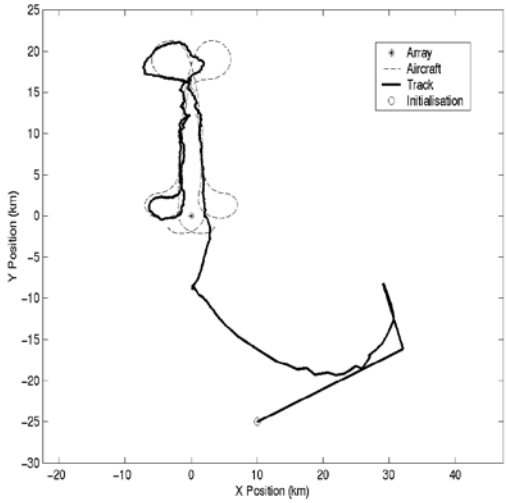

Figure 6 : *Tracking of manoeuvring aircraft.*

3D Acoustic Imaging of Objects in Water

Dr Alain Maguer, Robert Vesetas, Frederic Azemard

Thomson Marconi Sonar Pty, 274 Victoria Road, Rydalmere, NSW 2116, AUSTRALIA

Abstract

Thomson Marconi Sonar is developing a high frequency sonar (λ~0.5mm) for the RAN to assist in Mine Identification in turbid water. The sonar uses an Omni-directional transmitter and a 2D receive array using near-field focussed beamforming on receive only to produce a 3-dimensional image from a single transmission. The azimuth resolution required of the sonar requires an array aperture of order 500λ. However, practicable limitations on the number of receiver elements of ~3000 leads to a sparse array with significant grating lobes, a limited signal to clutter ratio of order 30dB, and hence a limited dynamic range of the sonar. Conversely for many targets their surface is relatively smooth compared to the acoustic wavelength, causing strong specular reflections which can mask weaker reflections from rougher surfaces which behave as diffuse scatters. This then leads to a high dynamic range of information reflected from the target compared between specular and diffuse reflectors.

This paper describes methods that have been investigated to improve imaging in these situations. (a) Different array geometries primarily the sparse random, and sparse spiral arrays have been investigated to determine their merits. The spiral array allows the level of clutter to be controlled in the azimuth direction. (b) Techniques to limit the amplitude of specular reflections and hence limit the dynamic range of the data prior to beamforming will also be described. (c) Additionally, maximizing the range resolution of the sonar, by using a high bandwidth for the transmitted signal, allows the clutter to be confined in the range direction..

The paper concludes with examples of acoustic images obtained in a test tank and in Harbour showing the improvements that have been achieved using these techniques.

INTRODUCTION

The Royal Australian Navy HUON Class Minehunter Coastal (MHC) requires that the Mine Disposal Vehicle (MDV) should be capable of prosecuting mines in water conditions of both clear and low visibility. The MDV used on the MHC, the Celsius Double-Eagle, uses a low light video camera to assist with mine prosecution. However, current optical technology does not permit positive identification or categorization of mines in the turbid water conditions that are prevalent around the north coast of Australia. Turbid water conditions require clearance divers to use touch for positive identification or categorization of sonar contacts. This time-consuming and dangerous process confirms if the contact is a mine and allows further categorization of mine type.

TMS Pty, in partnership with the Australian Department of Defence, Defence Science and Technology Organization (DSTO) and Commonwealth Scientific and Industrial Research Organization (CSIRO) have completed the early development of an Acoustic Mine Imaging (AMI) system. This system offers a solution to the operational requirement and will allow classification and categorization using a Mine Disposal Vehicle (MDV) in turbid water.

The AMI system uses an ultrasonic frequency, sonar to allow safe maneuvering of the Double-Eagle MDV near the mine and for classification of the sonar contact. It also generates higher resolution zoomed images of areas of interest on the mine to allow categorization of the mine type. Because the range of different parts of a target can be determined from the times-of-return of acoustic reflections in the acoustic image, three-dimensional images can be formed which can be rotated for easier recognition. Both the manoeuvre and zoomed images can be used to determine characteristics of the target mine such as lengths, widths, etc. of both the complete mine and also its detailed features.

The sonar uses an Omni-directional transmitter and a 2D receive array using near-field focussed beamforming on receive only to produce a 3-dimensional image from a single transmission. The azimuth resolution required of the sonar requires an array aperture of order 500λ. However, practicable limitations on the number of receiver elements of ~3000 leads to a sparse array with significant grating lobes, a limited signal to clutter ratio of order 30dB, and hence a limited dynamic range of the sonar. Conversely, for many targets, their surface

is relatively smooth compared to the acoustic wavelength, causing strong specular reflections which can mask weaker reflections from rougher surfaces which behave as diffuse scatters. This then leads to a high dynamic range of information reflected from the target compared between specular and diffuse reflectors.

The first part of this paper describes methods that have been investigated to determine the optimum sparse array geometries, which will provide the best clutter reduction. Secondly, techniques to limit the amplitude of specular reflections and hence limit the dynamic range of the data prior to beamforming will also be described. Additionally, the influence of the sonar bandwidth, maximizing the range resolution of the sonar, and allowing the clutter to be confined in the range direction will be presented.

Operation in Near-field

Considering the frequency as well as the array size, a range of the order of 75 meters is obtained for the far-field of the array. Hence, near-field beamforming is compulsory for the zoom mode. The acoustic return from a specular reflector to each receiver gives a time-of-flight that defines an ellipsoid. The ~3000 receivers in the array thus create 3000 ellipsoids which all pass through the position of the specular reflector, and then diverge at different angles depending upon the position of the transmitter, receivers and reflector. As the sonar operates in the near-field, with strong focussing, the ellipsoids rapidly separate, which assists in reducing the level of clutter at positions away from the point reflector. The ellipsoids are shown in Fig. 1.

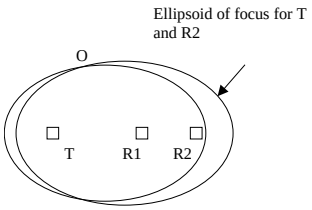

Figure 1: Ellipsoids of focus for transmitter and two receivers located at T, R1 and R2 respectively.

Array shape and sensors distributions

As mentioned before, practicable limitations on the number of receiver elements of the order of 3000 leads to a sparse array for the AMI project.

In order to reduce the low side radiation level achievable with a sparse array, many proposed designs for high-resolution two-dimensional arrays are based upon the random distribution of elements, as selected by TMS for its AMI prototype. However, for ultra-Wideband array the selection of random array is not the optimal choice.

In fact, based on [1], the random distribution of an array is not seen as the best solution. According to the authors, the most important issue in the array design is to get, for a 2D array, a projection of the sensors in x- and y-axes, which gave a periodic distribution. Thus, in the best case, the distance between two following and projected sensors had to be the same. This article also mentions the possibility of using a spiral array which could improve the image quality, without however explaining how to build it.

In order to validate the results mentioned in [1], TMS decided to perform some simulations for comparing the beampattern obtained with different sensor distribution.

Four main simulations have been done using a point transmitter as a source with four different arrays (random, square, square tilted and spiral). For each case, the 3D beampattern of the array was computed. In the simulations, the volume around the target is created. To be able to see the volume, three plane slices are done passing through the target (Oxy view, xOz view and yOz view)

Random array:

The random array will be considered as the reference to compare with the other shape arrays. Its receivers distribution is shown in Fig. 2.

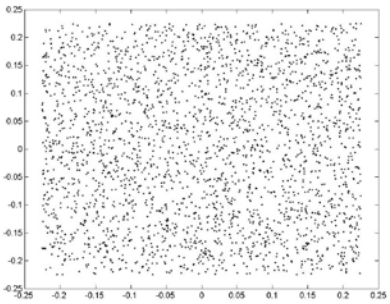

Figure 2: Position of receivers in random array

Fig. 3 represents the obtained beampattern.

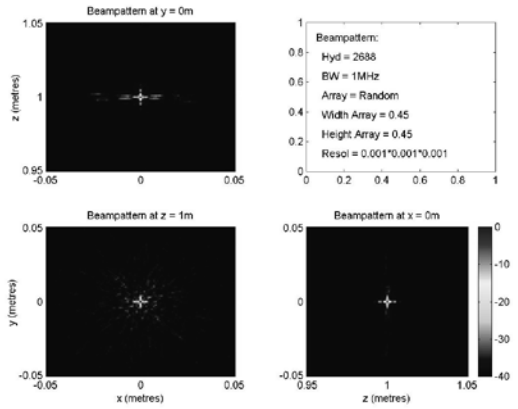

Figure 3: Beampattern of random array

Periodic array:

The shape shown in Fig. 4 corresponds to a Square Tilted Array. This array has been obtained from a square array for which periodicity has been taken away in the x and y direction as proposed in [1]. To get a linear projection in x and y, each line must be shifted from the other by 1/51 horizontal distance between two sensors. The same has to be done in the y-direction. The following figure is the illustration of this theoretical array.

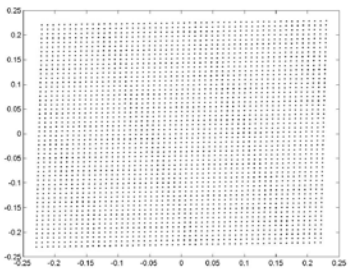

Figure 4: Position of receivers in Square Tilted array

Fig. 5 represents the obtained beampattern.

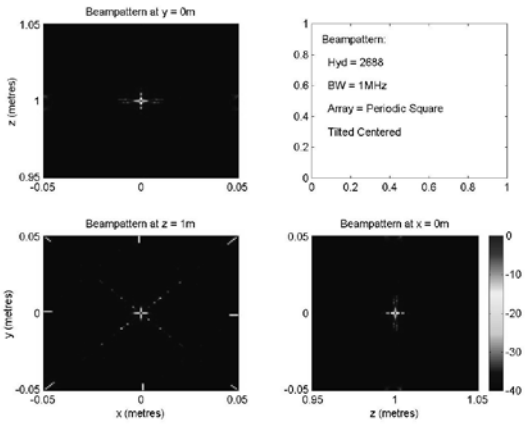

Figure 5: Beampattern of Square Tilted array

This solution is the best one achieved for periodic arrays studied till there. Some grating lobes are present in very defined directions. In comparison with the random case, the clutters (in x- and y-direction) here are in defined position and reach then relative high level of noise (-20 dB). In the random case, the clutters are more spread and reach only –30 dB. Based on that, this distribution is no further considered.

Spiral array:

The spiral array mentioned in [1] seems to give good results but the way to design the spiral is not explained. Moreover, clear results are not presented. The physical sense seems to opt for the most uniform distribution. In our case, the size of the array and the number of sensors are determined. As the equation of the spiral in polar is r=**a***θ, the parameter **a** needs to be set to obtain the desired distribution. In that perspective, **a** is obtained by solving an equation which expresses that the distance D1 between two following pegs on the spiral (curvilinear distance) is in relation with the distance D2 between two 'circles' of the spiral (=2*Pi*a). Fig. 6 illustrates the distribution.

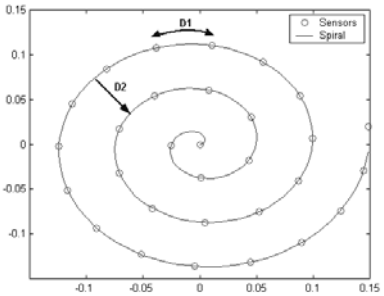

Figure 6: Position of receivers in spiral

Many simulations have been done, changing the ratio D1/D2. According to the physical sense, the most uni-

form distribution should be obtained for D1=D2. This is shown in Figures 7 and 8.

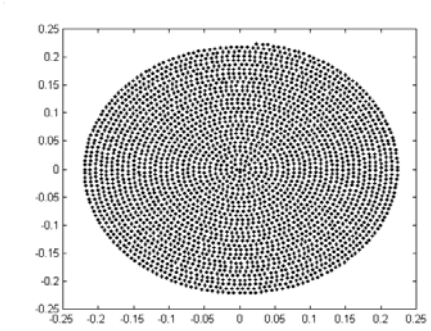

Figure 7: Position of receivers in Spiral array

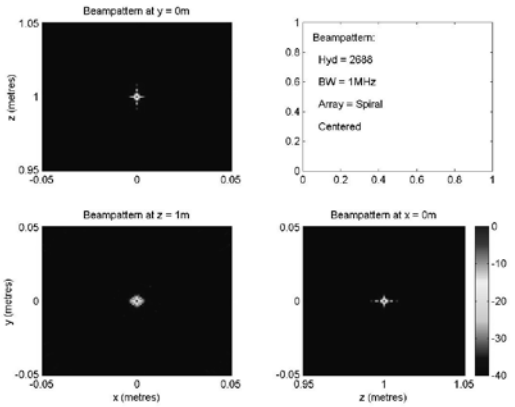

Figure 8: Beampattern of Spiral array (D1 = D2)

This array gives better results in terms of clutter level than in the random case. However, we can observe some noise (under –25 dB) near the target. In the random case, the noise just around the target seems not to be as important. Other simulations were performed by changing the ratio D2/D1, but the best results were found for D1=D2.

The differences obtained with the random and the spiral array is more obvious using an 80-dB scale. The beampatterns for the random and spiral arrays using an 80dB scale range is shown in Fig 9. In Fig9(lower) a disc (10-cm diameter) can be observed in which the maximum level of noise (-50 dB) is much lower than in the random case (-30 dB). Outside this disc, a circle (3-cm width) appears in which the noise is approximately the same as in the random case. Inside this, the noise is lower than in the random case.

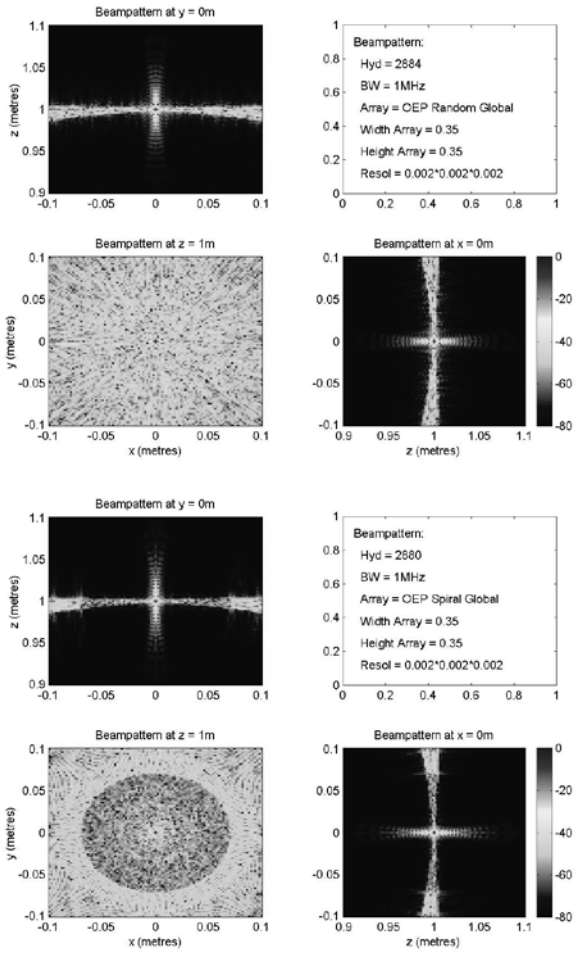

Figure 9: Beampattern of (upper) Random array; (lower) Spiral array (D1 = D2)

To try to explain the reason of the disc, let us do a slice of the previous figure. For y=0 and z=1m Fig. 10 shows the result.

On the top figure (random array), the noise is randomly spread. On the bottom figure (spiral array), the noise for -0.07<x<0.07 is lower than for the same x in the random case. However, two “grating lobes” appears with a level a little bit higher (but still of the order of –40 dB) than in the random case.

In the case of a 1D periodical array, the first grating lobe appears for $x=\lambda/d$, where λ is the wavelength and d, the distance between pegs. In the spiral case, d=0.0058 m and λ is varying due to the linear frequency variation. After calculation, it is found that $0.069<\lambda/d<0.096$m. The results got on the figure are then in full agreement with theory.

Based on that explanation, it is obvious that the low clutter level disc diameter is increasing with range. Therefore, the clutter rejection will be more effective (more spread) with the increase of target range.

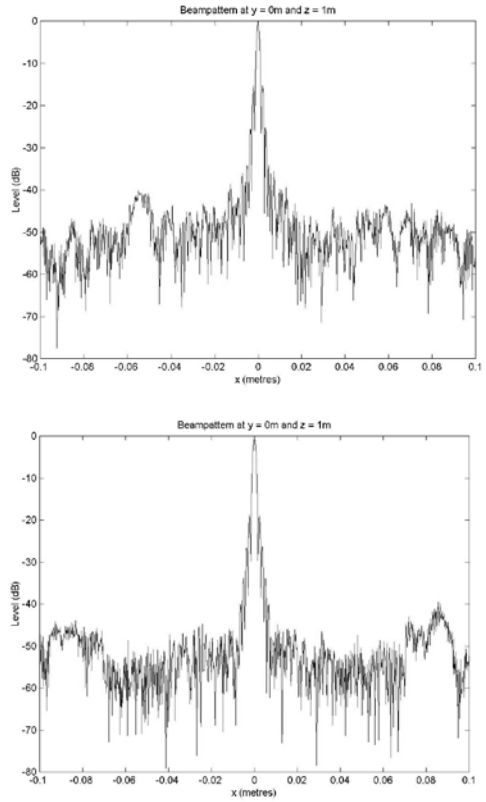

Figure 10: Beampattern slice in X direction for (a) upper - Random array; (b) lower - Spiral array (D1 = D2)

Results on real targets in a tank

Measurements were performed in collaboration with CSIRO, in their tank. The array used in this tank was a synthetic array, in the sense that one only single receiver, which can be moved in different places, was used to acquire the data. Fig. 11 shows the image of a point transmitter using the spiral array. The color scale does not have the same range as the previous plots, however the level of clutter in the disc is about –40dB which is similar to the simulation result in Fig. 9 (b). The non-symmetry is thought to be due to the point transmitter not being located exactly along the boresight of the array.

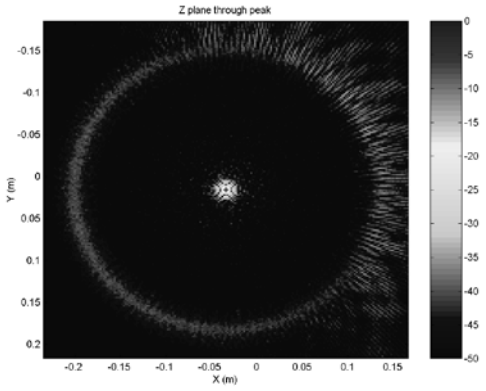

Figure 11: Experimental Image of a point Transmitter

Fig. 12 shows experimental images that show the improvement in image quality obtained with a 10 cm shackle imaged at 1 meter.

The following remarks can be made:

- The shackle shape is better well defined with the spiral array than with the random array
- The obtained signal-to-clutter ratio is higher (around 5 dB) with the spiral array than with the random array.
- A strong specular echo from the target blurs (through its sidelobes) part of the image in the random case. This phenomena is much less seen in the spiral case.

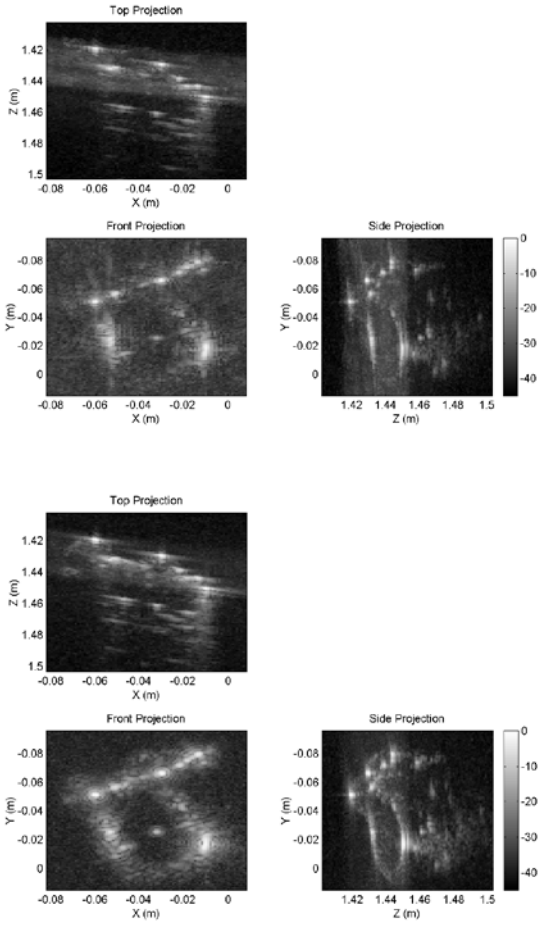

Figure 12: Acoustic image of a Shackle using (a) upper - Random array; (b) lower - Spiral array (D1 = D2); 3The three images show maximum intensity projections onto the YX, ZX and YZ axes of the 3D image volume

Control of Clutter

The wide dynamic range of the signals received by the sonar causes the clutter produced by a specular reflector to dominate the final image. To reduce the level of clutter the following options are available: (a) use a wide bandwidth (b) compress the dynamic range of the data prior to beamforming.

Use of wide bandwidth

Another method to reduce the effect of the clutter is to use a wide bandwidth for the sonar. The range resolution of the sonar is inversely proportional to the bandwidth and is given by $\Delta R = 0.88\frac{c}{2}\frac{1}{B}$; where ΔR = range resolution measured at –3dB level, B = bandwidth, c = speed of sound.

For AMI, which can operate at bandwidth of typically 200kHz to 1MHz the range resolution varies from approximately 5mm to 1mm respectively. The wider bandwidth reduces the thickness of each ellipsoidal "clutter bowl", which in turn decreases the contributions from the clutter bowls to the beamformer output at each voxel[1].

Fig. 13 shows the beampattern of the Spiral array using a bandwidth of 100kHz. The clutter level is now significantly increased compared to that in Fig. 9, where a bandwidth of 1MHz was used. The approximate change in clutter level is seen of the order of 10 dB which corresponds to 10log(1MHz/100kHz).

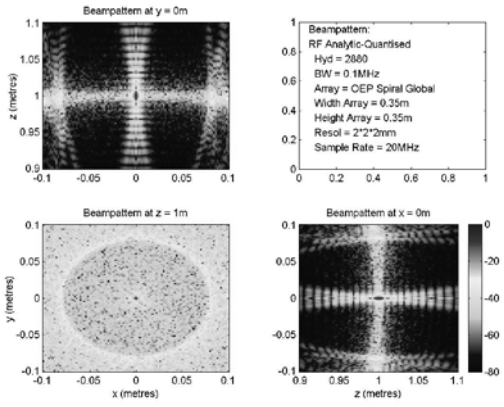

Figure 13: Beampattern of Spiral array (D1=D2) using Bandwidth of 100kHz results in higher clutter (c.f. Fig. 9)

Data Compression prior to beamforming

Sonar data from real objects shows a wide dynamic range between specular reflections and returns from diffuse reflectors. The clutter pattern from a specular reflection appears as a bowl, possibly tilted that passes through the position of the specular reflector.

An alternative method was also used to control the dynamic range of the data prior to beamforming so that the clutter bowl in the 3D image was suppressed before it was able to contaminate the 3D image. Several compression techniques were evaluated, $\log(A+1)$[2], A^p, and clipping; and found to give good results. However, the choice of the optimal parameter value was found to be very data dependent. Fig. 14 shows an acoustic image of a target with no data compression.

[1] Voxel = VOLume Element. Its size is selected to be the same or smaller than the azimuth and range resolutions.

[2] A = Amplitude of the data used for beamforming

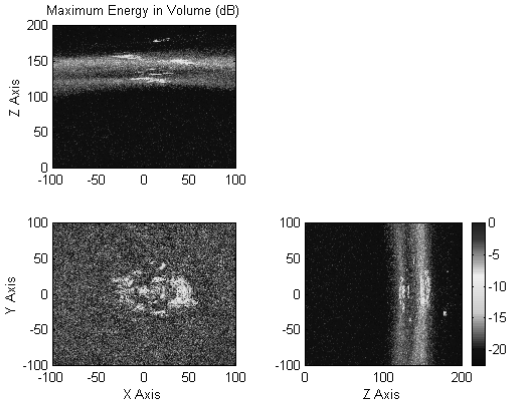

Figure 14: Acoustic image of target showing significant clutter from specular reflections

Fig. 15 shows the same data processed using data compression. It shows reduced clutter, also some surface detail in the zOx view of the "cigar" type shape of the target can now be seen. Compression can cause the range sidelobes due to specular reflectors to increase in level, however this effect can be reduced by choosing a wide bandwidth or by applying a frequency domain window to the sonar data.

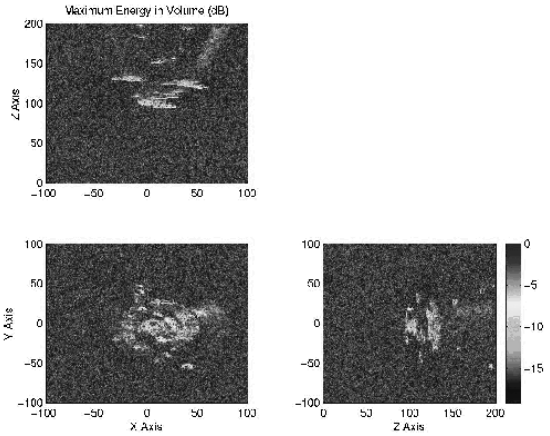

Figure 15: Image of target using sonar data that was compressed prior to beamforming

Conclusion

Use of a spiral array can theoretically reduce the level of clutter in a small region around bore-sight. This has been confirmed using experimental measurement of the beampattern of the spiral array and also by imaging a target.

The clutter can also be reduced by operating with as high a bandwidth as practical. Processing methods that control the dynamic range of the data prior to beamforming are also shown to be effective in reducing the impact of clutter in images.

References

[1] J.L.Schwartz B.D.Steinberg , "Ultrasparse, Ultrawideband Arrays", IEEE Transactions on Ultrasonic, Ferroelectrics, and Frequency Control, Vol 45, No. 2 March 1998

Acoustic Daylight – Using Ambient Noise To See Underwater

Mark L. Readhead

Maritime Operations Division, Defence Science and Technology Organisation

Abstract

Detection of targets in the ocean using sound is traditionally achieved with either passive or active sonar. Acoustic daylight is a new technique being developed, which relies on the ambient noise in the ocean to provide the acoustic illumination necessary to detect a target. The presence of a target scatters some of the incident sound which can be collected by a suitable acoustic lens to produce an image of the target.

An acoustic daylight imaging system developed at Scripps Institution of Oceanography is described, and images obtained of planar, cylindrical and spherical targets are presented. It was able to image all targets, with varying resolution and contrast between the target and background. In some cases it was able to distinguish between different target compositions through the reflected spectral content. A more sophisticated imaging system being developed by the DSTO will also be described.

Introduction

Traditionally the search for underwater targets by sound has been performed with passive or active sonar. In active techniques sound is projected into the water by the listening platform, and a target in the vicinity scatters some of this sound energy back towards the listener. Passive sonar relies upon the emission of sound by the target, which can be picked up by the listener.

Passive sonar is inherently a covert method. The listener does not emit any sound and so does not provide any acoustic signal by which the target can detect its presence. Since it relies upon sound being emitted by the target, it cannot be used for targets which are inherently silent. Active sonar by its nature flags the position of the searching platform to the target.

In both active and passive sonar the presence of background noise degrades the performance of the detection equipment and so lowers detection ranges.

Acoustic daylight

In optics there are three ways by which one commonly observes an object. In the first instance, it might emit light. This is how we see the stars. If it isn't a light emitter, but the observer is in dark surroundings, he can shine a torch and thereby see the target from the light it reflects. However, most commonly there is already sunlight present and objects are perceived when they scatter this light. The observer can distinguish between different objects because of the frequencies of light they scatter and/or the intensity of the light scattered by each. We call the first property colour and the second contrast.

In underwater acoustics, passive sonar is analogous to the first optical case. In this instance the object emits sound rather than light. Active sonar is like the second technique in which a torch is replaced by a sound projector. In the mid-1980's Buckingham suggested using the acoustic equivalent of scattered light in which ambient noise provides the source of ensonification. By analogy with optics the proposed method was called "acoustic daylight".

Ambient noise is generated in the ocean by several mechanisms, including distant shipping, breaking waves, and biological sources. In warm shallow waters around Australia's coastline, snapping shrimp are the dominant source, make a snapping sound extending from 500 Hz to more than 200 kHz.

First experiment

The first acoustic daylight experiment was conducted off Scripps Pier in southern California in 1991 (Berkhout, 1992; Buckingham *et al.*, 1992). In this experiment the noise was produced by snapping shrimp under the pier pilings and from the surf. Targets consisting of 25 mm-thick sheets of 0.9 x 0.77 m plywood board faced with neoprene rubber were placed on poles 6.1 and 12.2 m from a hydrophone at the focus of a parabolic reflecting dish. As the targets were swivelled on their poles they appeared broadside or end-on to the acoustic lens. Depending on the orientation of the acoustic lens and the targets, the latter reflected the ambient noise or blocked it. It was also noted that the

targets reflected some intensities more than others, providing evidence for acoustic colour.

The overall result of this first acoustic daylight experiment was to show that a target can alter the noise field, but being a parabolic reflector with a single hydrophone at its focus, it formed a single beam and so corresponded to just one pixel of an image. To build up an image a multi-beam acoustic lens is necessary. If the system was broadband, it would be able to make use of the acoustic colour characteristic.

ADONIS

The first operational acoustic daylight system was designed and built at Scripps Institution of Oceanography, in a research group including Mike Buckingham, Chad Epifanio and John Potter. The acoustic camera was called 'ADONIS', which stands for Acoustic Daylight Ocean Noise Imaging System. It was designed to collect broadband data between 8 and 80 kHz in ambient noise of 20-70 dB re 1 $\mu Pa^2/Hz$. Figure 1 shows its assembly; a detailed description appears in Readhead (1998).

It consisted of an approximately planar array at the focal plane of a 3 m reflecting dish. The dish was comprised of neoprene foam on a fibreglass base and provided approximately 18 dB gain. Beamwidths varied from 3.4° at the lowest frequencies, to 0.6° at the highest frequencies. The field of view was 10° in the horizontal and 8° in the vertical. The whole assembly could be rotated around a vertical mast, providing 360° coverage in the horizontal.

The array was made by EDO Corporation and consisted of 130 piezoelectric hydrophone elements arranged in an elliptical pattern as shown in the inset in Figure 1. Each element was 20 mm x 20 mm EC-76, a US Navy type-V lead zirconate titanate, with a sensitivity over most of its frequency range of –188.8 dB re 1 V/μPa.

Electronic gain of 100 dB was provided in multiple stages. Preamplifiers were incorporated into the array housing before transfer of the data to the underwater electronics canister. Here the signals were further amplified and pre-whitened. Rather than send the amplified sinusoidal data to the surface, 16 spectral estimates were sent instead. This cut down the data rate appreciably. Multiplexers were then used to serially transmit the data to an analogue to digital converter board in a computer on the surface where it was stored on hard disk. The computer also contained a digital signal processing board which processed the data for display on a video monitor. Moving images were displayed with an update rate of 25 Hz.

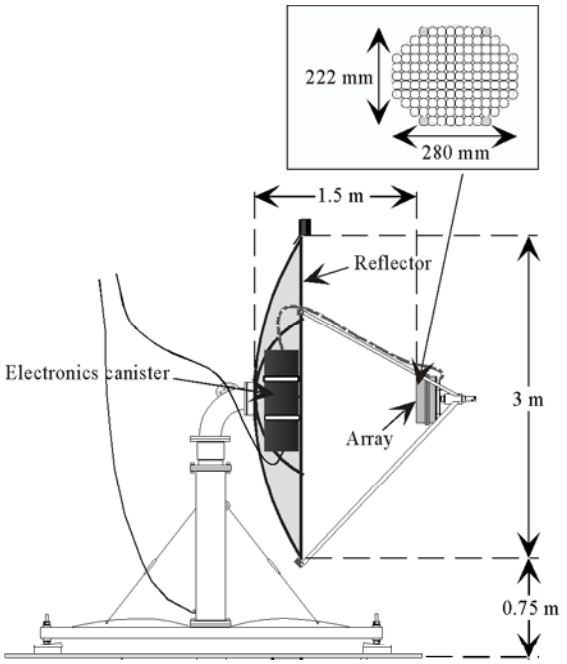

Figure 1. Side view of ADONIS. The array layout is shown in the inset.

Deployments

ADONIS was deployed under a moored barge in 7 m of water in San Diego Bay in August 1994 and October-November 1995. Planar, cylindrical and spherical targets were imaged. The panels were fixed to a 3 m x 3 m frame and were mostly 1 m x 1 m sheets of 3.2 mm thick aluminium faced with 6.4 mm thick closed-cell neoprene foam, with the foam side facing the acoustic lens. The panels were also reversed and compared with 6.4 mm thick aluminium, 3.2 mm thick corrugated galvanised iron, and 6.4 and 12.7 mm thick plywood coated with a thin layer of resin or 5 mm of fibreglass.

The cylindrical targets were 113 *l* polyethylene drums of 76 cm height, 50 cm diameter, and with a wall thickness of 5 mm. These drums were filled with wet sand, sea water or syntactic foam. They were deployed in the water column or dropped onto the sea floor. The spherical target was a hollow, air-filled titanium sphere of 70 cm diameter and a wall thickness of 15 mm. It was held in a metal cage in the water column and made negatively buoyant by the addition of lead weights.

Since San Diego Bay was shallow and calm, there were almost no breaking waves. The dominant sources of acoustic noise in the 8–80 kHz frequency range came from harbourside industrial activities, shipping traffic, sea mammals and snapping shrimp. The noise field was highly anisotropic, aiding in the illumination and detection process. It also had large temporal varia-

tions, as shown in Figure 2 by the 1 s time series of noise data collected by an ITC 6050C hydrophone. Figure 3 shows the effect of this non-stationarity in the noise field on 12 sequential images, representing 17 ms of data spread over 0.5 s, of the spherical target. Intensity variations of more than 20 dB are evident. By temporal averaging over 1 s and adjusting the colour axis for each image to account for the differing mean intensities, stable images were produced.

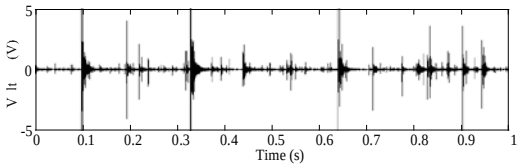

Figure 2. Time series of ambient noise collected by ITC6050C hydrophone.

Images

Figure 4 collects together a number of images formed during the deployments of ADONIS (Epifanio, 1997; Epifanio et al., 1999; Readhead, 1998). Each image consists of a boxcar average of a 10 s time series, corresponding to 250 frames. Often several frequencies have been averaged, and these are noted by specifying the range of frequencies. In most cases the resultant intensities are mapped into the jet colour map after bicubic spatial interpolation. This map grades from blue at low intensities to red at high intensities.

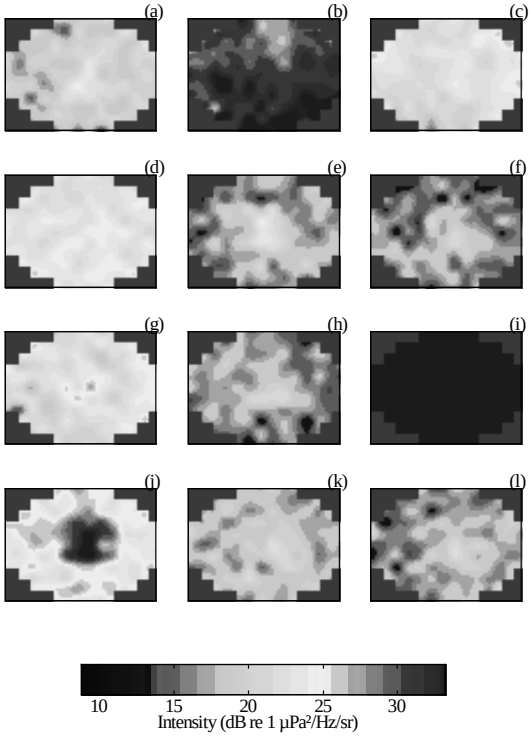

Figure 3. 12 sequential images of the suspended sphere at 75 kHz with boxcar averaging of 25 frames of logarithmic intensity data.

Bar target

Figure 4a shows the scene falling within the field of view of ADONIS, based on the known location, size and range of the target frame, and the field of view of ADONIS. The horizontal line in the background delineates the horizon, with the sea surface above and the sea bottom below. Three neoprene-coated aluminium

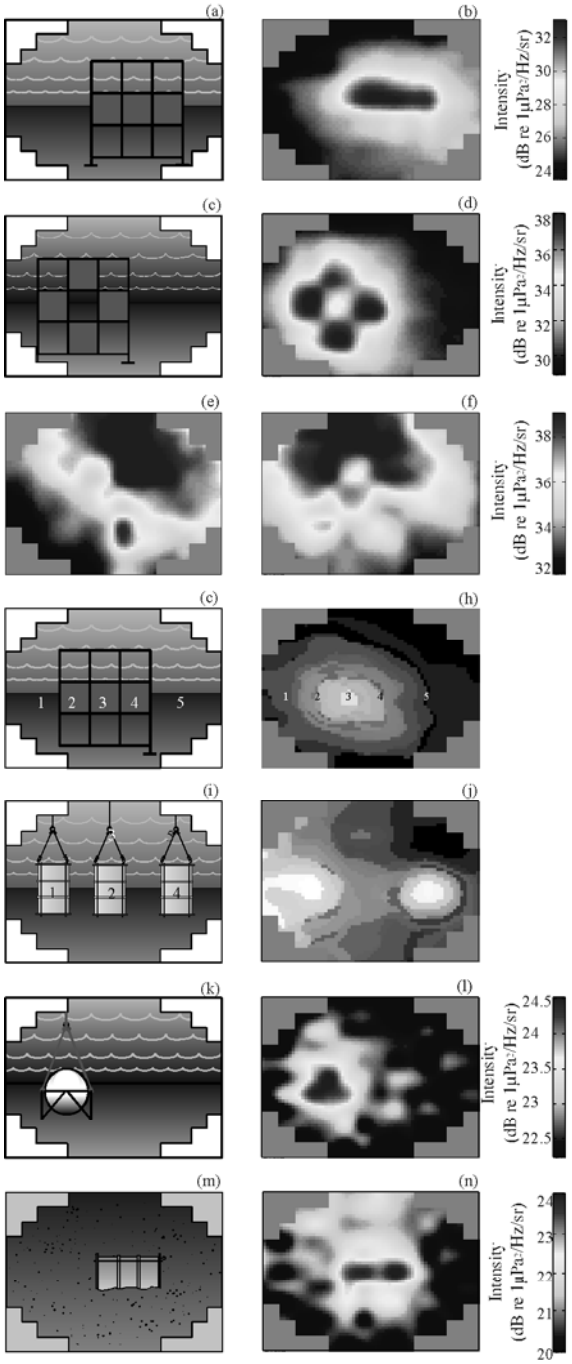

Figure 4. Sketch of field of view of ADONIS for a) bar target, c) fenestrated cross, g) multi-metal panels, i) suspended drums, k) suspended sphere and m) bottom drum. Acoustic daylight images for b) bar target, d), e) and f) fenestrated cross, h) multi-metal panels, j) suspended drums, l) suspended sphere and n) bottom drum.

panels form a bar on the target frame at a range of 38 m.

Figure 4b presents an image for the high frequencies of 57-75 kHz. The data corresponded in time to the use of an angle grinder for hull maintenance on a vessel moored along the pier. Acoustic noise was injected into the water for several seconds at a time, greatly increasing the ambient noise level, and raising the acoustic contrast from a more usual 3.5 dB to 9 dB at these higher frequencies.

Fenestrated cross

With the angle grinder still injecting noise into the water, the panels were rearranged to form a fenestrated cross (Figure 4c). Again all target panels are clearly defined and visible with an acoustic contrast of 9 dB for 57-75 kHz data (Figure 4d). Even the hole is visible in the image, with a contrast of 4 dB between it and the panels.

A different source of ensonification was provided by a boat passing behind the target. Figures 4e and 4f show two images formed from boxcar averaging 1 s (25 frames) of 57-75 kHz data. The two images are separated in time by 1.2 s. The boat is passing from right to left behind the cross, with Figure 4e showing the boat just to the right of the cross, and Figure 4f showing it almost directly behind the cross. The target panels block some of the boat noise, creating four holes in the noise field with an inverse contrast of more than 3 dB. Some of the boat noise passes through the hole in the cross. These images show that passing boats can be used as a source of opportunity to silhouette targets.

Multi-metal panels

To test the potential of acoustic daylight to discriminate between targets based on differences in both reflected intensities and frequencies, three metal targets were placed in the frame: 3.2 mm thick aluminium covered with 6.4 mm neoprene foam, with the metal side facing ADONIS, 6.4 mm thick aluminium, and 3.2 mm thick corrugated galvanised iron. Figure 4g shows the panels forming a bar in ADONIS' field of view, with the aluminium/neoprene panel labelled as 2, the thicker aluminium panel as 3, and the galvanised iron panel as 4.

In Figure 4h linear trapezoidal colour mapping has been employed in which red, green and blue correspond to low, medium and high frequencies, respectively. The aluminium/neoprene panel is seen with a reddish tint, indicating its propensity to reflect only lower frequencies well. The galvanised iron panel appears bluish, corresponding to its good reflectivity of only the higher frequencies. The thick aluminium panel reflects well at all frequencies and appears whitish. Note also that the luminosity of the three panels is well above the background.

Suspended drums

The panel targets presented a planar surface normal to the look direction of the acoustic lens. Cylindrical targets would only present a line normal to the look direction, and so would represent more of a challenge for imaging. Figure 4i shows the arrangement of the suspended drums as seen by the acoustic lens. The order of the drums from left to right was foam, water and sand-filled. Figure 4j shows the image with linear trapezoidal colour mapping depicting the different frequency components. The foam-filled drum reflected well at all frequencies as it had a much lower acoustic impedance than water. Thus it appears white. The sand-filled drum had a higher impedance than water, but allowed a greater penetration of low frequency sound as the sand was wet. Some of this energy could reflect off the rear wall of the drum back towards the acoustic lens. Absorption in the wet sand ruled out significant penetration to the rear wall and back by the high frequencies. As the sand-filled drum does not reflect high frequencies as well, it lacks a strong blue component and appears yellow. The water-filled drum has a slight blue tinge, indicating that it only reflects the higher frequencies to any significant degree. It was only weighed down by its 10 kg cage. When moving, the rusty metal parts of the drum cage and supporting shackle rubbed together, producing sound. This was most noticeable when large boat wakes passed over the targets. Hence the water-filled drum and shackle were probably not observed by scattered ambient noise, but by self-noise.

Suspended sphere

A sphere presented only a small patch normal to the look direction, and so was an even more difficult target to image. Figure 4k shows the field of view seen by ADONIS at the 20 range. The images formed from the upper three frequencies, 57–75 kHz are shown in Figure 4*l*. The acoustic contrast is more than 2 dB.

It is noticeable in Figure 4*l* that the equator and upper hemisphere of the sphere is visible, but that the lower hemisphere is not seen. The equator is illuminated by noise propagating in a horizontal direction from behind ADONIS, but the upper and lower hemispheres would not be visible by such noise, as it would be reflected up or down, away from ADONIS. The upper hemisphere may have instead been illuminated by noise scattering off the surface towards the sphere, and then back in the direction of ADONIS. There would be considerably less scattering of sound off the muddy bottom, and so the lower hemisphere would be much less illuminated. It is also notable that the image of the sphere is similar to the simulated image shown in Potter (1994).

Bottom drums

In all target deployments reported so far, the acoustic contrast has been between the noise scattered by the target and that scattered by or originating in the surrounding water. A more difficult test was to try and image the drums when on the sea floor. In this case the contrast would be between noise scattered by the drums and the mud.

ADONIS was tilted so as to point to the sea floor. Figure 4m shows the field of view of ADONIS with the foam-filled drum on the sea floor. The corresponding image is shown in Figure 4n for the upper frequencies (57–75 kHz). The drum is clearly visible, with an acoustic contrast of 4 dB. These values are comparable with or better than for the drum when in the water column, partly because there is less background noise around the drum. The possibility of the sea floor and drum forming a propitious corner reflector arrangement cannot be ruled out either.

Beyond ADONIS

ADONIS could only resolve objects within its fixed depth of field, which was set by the separation between reflector and array. Because of the way the signal processing was incorporated into the underwater electronics, most of the incoming acoustic data was not used. This limited the testing of post-processing algorithms.

The next step is to build a phased array. A prime advantage of one is that all the data can be used and targets at different ranges of most of the 2π half space can be imaged without the need for re-focusing. Increasing the resolution is obtained by sampling to higher frequencies or increasing the aperture of the array. To achieve a beamwidth of 1° requires a filled array of 10,000 elements, or a Mills Cross with 200 elements. The latter has large sidelobes in the orientation of the cross arms. A random sparse array of the same number of elements has the same total sidelobe energy, but it is more evenly spread in all directions (Steinberg, 1976). The computational load is high, since 64 Mbytes/s of data is acquired if 12-bit sampling is used for frequencies to 80 kHz. This can be compared to ADONIS' modest 3 kbytes/s.

DSTO's array

DSTO is currently building a random sparse phased array of 2 m x 2 m aperture, which has 256 hydrophone elements. It is modular, comprising four identical sub-arrays, each 1 m x 1 m and with 64 elements. Figure 5 shows the design. The sub-arrays are held in a 3 m x 3 m galvanised iron frame, each being rotated by 90º with respect to each other to maintain the maximum randomness. The hydrophones are ITC 8257 units, which are sensitive between 10 and 150 kHz. They have preamplifiers of 60 dB fixed gain, leading to a sensitivity of –132 dB re 1 V/μPa over most of the frequency range. They are glued into stainless steel holders, which in turn are screwed into the face plate of a stainless steel box. To eliminate sound from penetrating from the rear of the array, the boxes are air-filled. Divinycell foam and an anechoic material reduce reflections of sound coming in from the front and reflecting from the box back towards the hydrophone elements. The hydrophone cables run through the box to an electronics canister.

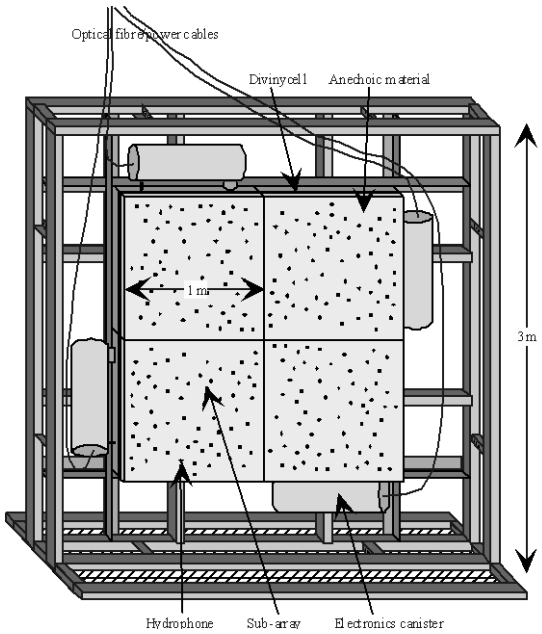

Figure 5. Design of DSTO's array.

Figure 6 is a block diagram of the electronics processing. The signal from each hydrophone is amplified and pre-whitened. Based on experience with ADONIS where passing boats could swamp out the electronics, the next amplification stage incorporates automatic gain control. Each signal passes through a sample and hold stage and a group of 32 hydrophone signals are multiplexed before being 12-bit digitised at 400 kHz each. The digital stream from all 64 hydrophones is repackaged and sent to the surface via an optical fibre cable at a rate of 1 Gbaud. At the surface the data streams from two arrays pass through FIFOs, are synchronised, pass through another FIFO and are sent via a HIPPI link controller to an SGI Origin200 Gigachannel computer. Data from all four arrays is logged at a continuous rate of 154 Mbytes/s on a RAID array of 20 hard disks.

Due to the very high data rate the data is post-processed. The first stage is beamforming. As the array is yet to be completed, in place of actual data the anticipated performance of the array is demonstrated

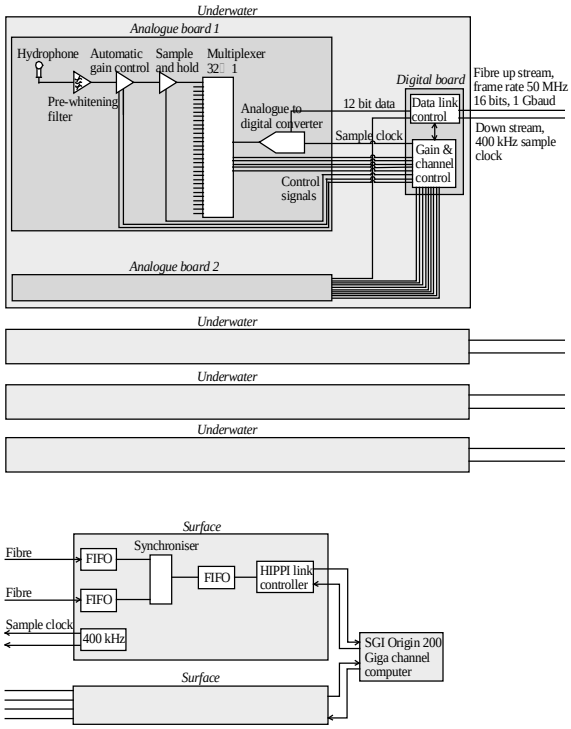

Figure 6. Block diagram of electronics for DSTO's array.

by an example of a point spread function in Figure 7. This shows the image which would be formed at 100-108 kHz of a point target located at a range of 50 m, 0º longitude and 0º colatitude when ensonified by a point noise source, such as a snapping shrimp, located 40 m from the target at 0º. The beamwidth to the 3 dB points is 0.35°, and the highest sidelobes contained within ±10º are down by 15 dB. In reality the image would be degraded by other extraneous background noise. At 140 kHz the beamwidth has improved to

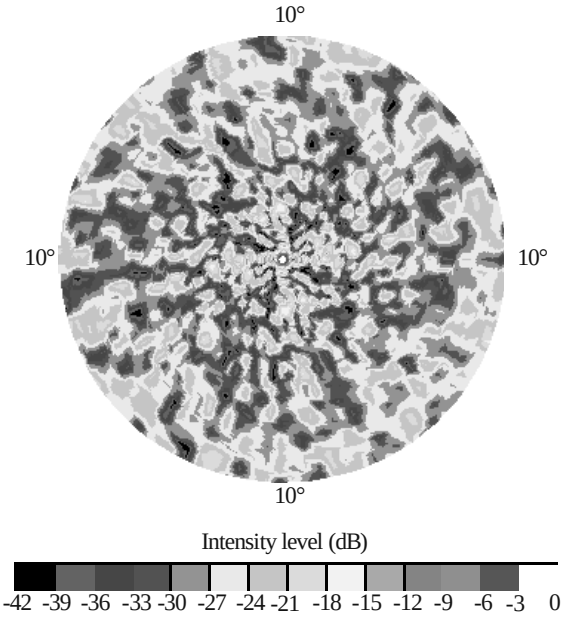

Figure 7. Point spread functions at 100-108 kHz.

0.16°.

Conclusions

Acoustic daylight potentially has a number of advantages over conventional active and passive sonar. Like a passive sonar, it can look for specific signals within one of its beams. It can also look for silent targets and does not have a degraded performance in regions of high ambient noise. In fact, since it uses the ambient noise, it should have an enhanced performance in such regions. Since it does not produce its own sound, it should have a lower power consumption than an active sonar, and so is suited to use on an underwater remotely operated vehicle. Its covert nature has important tactical advantages. Since it produces a pictorial image, with sufficient resolution it should be easier to interpret than current sonar system displays, which require trained operators. The introduction of false colour to the images should ease discrimination between different targets.

Acknowledgments

The author wishes to express his gratitude to Prof. Michael Buckingham and Mr (now Dr) Chad Epifanio for his visits to the Scripps Institution of Oceanography. These visits to Scripps were made possible through the awarding to the author of the inaugural Royal Australian Navy Science Scholarship.

The author also thanks Messrs Manuel DeSousa and Brain Rayment for assistance in the mechanical design and drawing of the DSTO array, and to Mr Christian Lees for the design of the electronics.

References

Berkhout, B.V. (1992). *Acoustic daylight: imaging the ocean with ambient noise*, unpublished MS thesis, University of California, San Diego, 86 pp.

Buckingham, M.J., Berkhout, B.V. and Glegg, A.L. (1992). "Acoustic daylight: imaging the ocean with ambient noise", *Nature* **356**, 327–329.

Epifanio, C.L. (1997). *Acoustic daylight: passive acoustic imaging using ambient noise*, unpublished PhD thesis, University of San Diego, 311 pp.

Epifanio, C.L., Potter, J.R., Deane, G.B., Readhead, M.L. and Buckingham, M.J. (1999). "Imaging in the ocean with ambient noise: the

ORB experiments", *Journal of the Acoustical Society of America* **106**, 3211–3225.

Potter, J.R. (1994). "Acoustic imaging using ambient noise: some theory and simulation results", *Journal of the Acoustical Society of America* **95**, 21–33.

Readhead, M.L. (1998). "Acoustic daylight at Scripps Institution of Oceanography", *DSTO Aeronautical and Maritime Research Laboratory Research Report DSTO-RR-0136*, Melbourne, 136 pp.

Steinberg, B.D. (1976). *Principles of aperture and array system design: including random and adaptive arrays*, Wiley, New York, 356 pp.

ACOUSTICS - putting the science and technology to work

Conference of the Australian Acoustical Society
Joondalup Resort, Western Australia, 15-17 November 2000

Session AC-3 Environmental Noise 2

A Comparison of Environmental Legislation Associated with Noise in Queensland and Western Australia

Namiko Ranasinghe

Department of Environmental Protection

Abstract

Whilst the general purpose of the environmental legislation associated with noise is essentially the same for Queensland and Western Australia, there are considerable differences in the actual legislation. The purpose shared by the two states originates from the principles of ecologically sustainable development. More specifically, the purpose is to ensure that environmental noise is managed at acceptable levels, without compromising the flexibility to allow for reasonable economic, cultural and social activity. (Jenkins, 1997) This paper will investigate the legislation in place to manage environmental noise in the two states and provide a comparison between the two states. The issues discussed in this paper may be used to develop or improve state government legislation to manage environmental noise.

1.1 Introduction

The purpose of this paper is to investigate environmental legislation in two Australian states, namely, Queensland (Qld) and Western Australia (WA) and the items of legislation reviewed are listed below:

- the *Environmental Protection (Noise) Policy 1997* (referred to as Qld's Noise Policy);
- Part 2A of the *Environmental Protection Regulation 1998* (referred to as Qld's Nuisance Regulations); and
- the *Environmental Protection (Noise) Regulation 1997* (referred to as WA's Noise Regulations).

The administering authority for the former two items of legislation is primarily, Qld's Environmental Protection Agency (EPA-Qld). Similarly, the last item of legislation in the above list is administered by WA's Department of Environmental Protection (DEP-WA). However, in both states, the local authorities have a very important role in the management of environmental noise.

1.2 Brief history

Qld's Noise Policy commenced in 1997 replacing the *Noise Abatement Act 1978-1989*. Later in 1999, Qld's Nuisance Regulations were introduced replacing some of the sections of Qld's Noise Policy. Qld's Nuisance Regulations were developed to provide a state-wide approach to resolving nuisance complaints with such tools as nuisance abatement and infringement notices. Prior to the commencement of Qld's Nuisance Regulations, nuisance was generally handled under local government laws. There appeared to be diverse nuisance laws from one local authority to another, ranging from small local authorities that generally adopted *ad hoc* procedures of handling nuisance, to large local authorities that had set procedures in place. The larger local authorities had such mechanisms as infringement notices in place as well providing a convenient enforcement tool to manage nuisance.

WA's Noise Regulations took effect in 1998, replacing the *Noise Abatement (Neighbourhood Annoyance) Regulations 1979*. WA's Noise Regulations were introduced to operate under the *Environmental Protection Act 1986*. Similarly, Qld's Noise Policy replaced the *Noise Abatement Act 1978-1989*, fulfilling the need to develop legislation under the newly introduced *Environmental Protection Act 1994*.

1.3 Definitions

The definition of some of the terms used in this document are listed here:

- **Assigned noise level** means a noise level which cannot be exceeded in a specified period of time.
- **Influencing Factor (IF)** means a number ranging from 0 to 20, which is calculated for each noise-sensitive premise receiving noise taking into account the amount of industrial and commercial land and the presence of major roads within a 450 metre radius around the noise receiver.
- $\mathbf{L_{Aeq}}$ means the A-weighted, equivalent, time averaged, sound pressure level in a specific period of time within the meaning of the Australian Stan-

dards *AS1055-1997 Acoustics - Description and Measurement of Environmental Noise.*

- **L_{Amax}** means the A-weighted, maximum, sound pressure level in a specified period of time. If L_{Amax} is an assigned noise level, this means an A-weighted, sound pressure level which is not to be exceeded at any time.

- **L_{A1}** means the A-weighted, sound pressure level that is equalled or exceeded for 1% of a specified period of time. If L_{A1} is an assigned noise level, this means an A-weighted, sound pressure level which is not to be exceeded for more than 1% of the time.

- **L_{A10}** means the A-weighted, sound pressure level that is equalled or exceeded for 10% of a specified period of time. If L_{A10} is an assigned noise level, this means an A-weighted, sound pressure level which is not to be exceeded for more than 10% of the time.

- **L_{A90}** means the A-weighted, sound pressure level that is equalled or exceeded for 90% of a specified period of time.

- **L_{Linpk}** means the Linear-weighted peak sound pressure level.

In General, WA tends to commonly use slow settings in contrast to Qld, where fast settings are commonly used.

1.4 Exclusions

WA's Noise Regulations do not deal with:

- noise within one premise, e.g. in a workplace;

- noise from traffic on roads, or trains, except model trains;

- noise from aircraft, except model planes; and

- noise from safety warning devices.

WA's Noise Regulations identify a list of special cases allowing reasonable amounts of activities that benefit the community as follows:

- agricultural noise, provided properly managed;

- activities approved by the minister to be unable to meet the standards of the regulation;

- bell ringing and calls to worship, provided certain conditions are met;

- blasting, provided certain standards are met;

- construction activities, provided certain standards are met;

- equipment used on residential premises, provided certain standards are met;

- outdoor concerts under certain conditions; and

- community activities, provided certain management procedures are met.

Qld's Nuisance Regulations exclude:

- non-domestic animal noise;

- audible traffic signal noise, if the signal complies with Australian Standards *AS1742.10-1990 Pedestrian Control and Protection*;

- blasting noise, if it meets prescriptive requirements;

- outdoor shooting range noise, if it meets prescriptive requirements; and

- outdoor shooting range noise, if it meets prescriptive requirements.

These exclusions allow the officers of the administering authority (e.g. EPA-Qld, DEP-WA or local authority) to dismiss complaints, which may be motivated by other reasons rather than environmental reasons.

2.1 Annoyance characteristics

Qld's Nuisance Regulations identifies annoyance characteristics of noise as steady-continuous, fluctuating, intermittent, tonal or impulsive nature. WA's Noise Regulations narrow annoyance characteristics down to tonality, modulation and impulsiveness. Qld's Nuisance Regulations also include vibration. For example, there are prescriptive vibration requirements for blasting activities in Qld unlike WA's Noise Regulations which have no such vibration requirements.

2.2 Adjustments

WA's Noise Regulations suggests that the adjustments in Table 2.21 should be included in the measured levels.

Table 2.2.1: Adjustments for annoyance

Adjustment where noise emission is not music – these adjustments are cumulative to a maximum of 15 dB		
Where tonality is present	Where modulation is present	Where impulsiveness is present
+ 5 dB	+ 5 dB	+ 10 dB
Adjustment where noise emission is music		
Where impulsiveness is not present	Where impulsiveness is present	
+ 10 dB	+ 15 dB	

Qld deals with adjustments as in the Australian Standards *AS1055-1997 Acoustics - Description and Measurement of Environmental Noise*. This is however, not stated in the actual noise legislation. The noise legislation refers to the Noise Measurement Manual which contains some discussions on how to make adjustments to measured levels giving consideration to annoyance characteristics.

2.3 Quality objective vs assigned noise levels

Qld's Noise Policy defines an acoustic quality objective which is a goal of achieving an ambient level of 55 dB(A) or less for most of Queensland's population living in residential areas. It is further explained that this ambient level in a residential area is to be measured over 24 hours as the long-term L_{Aeq} outside a dwelling in the area.

WA Noise Regulations provide a step by step method of determining assigned noise levels using an Influencing Factor (IF) which takes into account the amount of industrial and commercial land and the presence of major roads within a 450 metre radius around the receiver. The IF value can range from 0 to 20 in most cases.

The assigned noise levels have been categorised according to the type of premises receiving noise as below:

- noise sensitive premises at locations within 15 metres of a building directly associated with a noise sensitive use;
- noise sensitive premises at locations further than 15 metres from a building directly associated with a noise sensitive use;
- commercial premises; and
- industrial and utility premises.

Consider a 24-hour period starting at 7 am on a Monday. Consider also the type of premises receiving noise to be a noise sensitive premise, at a location within 15 metres of a building directly associated with a noise sensitive use. The assigned noise levels were calculated using IF = 0 and IF = 20 as in Table 2.3.1.

Table 2.3.1: Calculated assigned noise levels

Time of day	Assigned noise levels in decibels calculated for IF = 20		
	L_{A10}	L_{A1}	L_{Amax}
7 am to 5 pm	65	75	85
5 pm to 10 pm	60	70	75
10 pm to 7 am	55	65	75
Time of day	Assigned noise levels in decibels calculated for IF = 0		
	L_{A10}	L_{A1}	L_{Amax}
7 am to 5 pm	45	55	65
5 pm to 10 pm	40	50	65
10 pm to 7 am	35	45	55

The assigned noise levels in Table 2.3.1 above can be plotted into Graph 2.3.1. For the purposes of comparing the assigned noise levels to the acoustic quality objective, the assigned noise levels have been converted to L_{Aeq} values assuming that the sound pressure level outside the L_{A10} tends to sit at 1 dB(A) below the L_{A10} value. Furthermore, for the purpose of simplifying what usually is a quite complicated chart recording of instantaneous sound pressure levels, the L_{Amax}, L_{A1} and L_{A10} have been brought forward to the beginning of the period under consideration in Graph 2.3.1, hence the peaks at the beginning of each period block. The period blocks are defined in Table 2.3.1 above.

Graph 2.3.1: Quality objective vs assigned levels

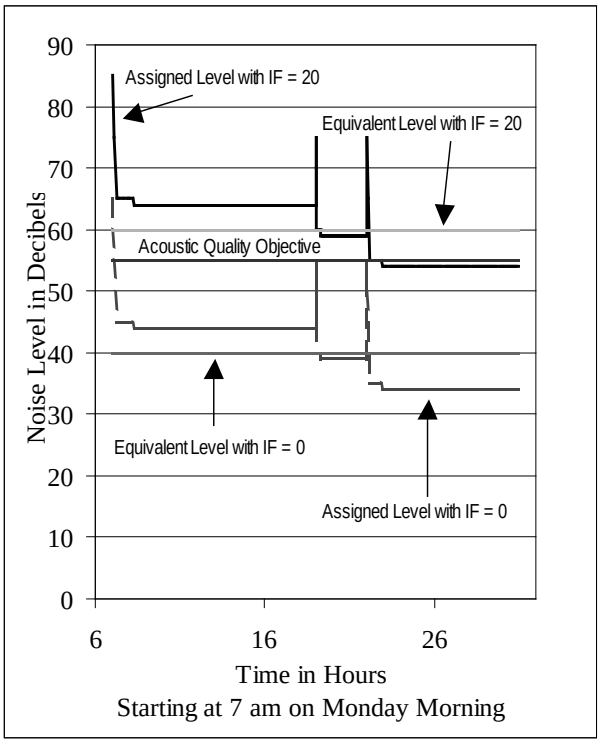

The assigned noise levels allow for a range of L_{Aeq} values of approximately 40 to 60 dB(A) where as acoustic quality objective is fixed at 55 dB(A). The acoustic quality objective value is obviously within the range of assigned noise levels but closer to the upper limit of 60 dB(A).

Therefore, based on the consideration here, the acoustic quality objective appears to be less conservative as compared to the assigned noise levels. However, this does not mean that it could be concluded that Qld's noise requirements are less conservative as compared to WA's requirements because of many source specific requirements Qld has as compared to WA which is discussed below. It should also be noted that the above calculations only apply to the scenario under consideration here.

The advantage of having an acoustic quality objective over assigned noise levels is it provides a simple number to compare measured levels to, however, such simplicity also introduces a lack of flexibility which is obviously available through the assigned noise level system. The prescriptive requirements attached to special cases (discussed below) tend to be more stringent in Qld as compared to WA e.g. requirements which apply to blasting.

2.4 Occupancy order vs non-conforming uses

Undoubtedly, the order of occupancy of land can give rise to the most complex noise complaints which penalise administering authorities with considerable time consumption in trying to resolve such complaints. A typical example of this is residences encroaching on industrial areas e.g. workshops or factories. In Qld, one of the matters for consideration in assessing a noise complaint is the order of occupancy of the source and receiver of noise. This provides the administering authority with a mechanism by which to dismiss unreasonable complaints.

A similar set up is exists in WA. Complications introduced by non-conforming uses (e.g. a workshop operating legally on residential zoned land) and changes to land zonings are to be treated as special cases. Generally, if there are two land uses associated with a particular site (e.g. an industry operating legally on residential zoned land) the tendency is to treat the site as an industrial site (with adequate justification of course) in calculating the IF value. This results in less conservative assigned noise levels which may provide a means by which to reduce or eliminate unfair assigned noise levels being allocated to particular activities.

2.5 Exceptional situations

Both Qld and WA have provisions by which to address exceptional situations. In Qld, noise level requirements are set case by case through environmental licensing. Obviously, there are cases where the standard licence condition levels as in Table 2.5.1 cannot be met by a certain activity. In such cases, a complaints driven approach is adopted. A complaints driven approach requires the responsible person to manage the noise in the event of a complaint. It usually involves the preparation of a noise management plan following any complaints to address the concerns of the each complainant.

In WA, where there are genuine cases when a person cannot reasonably or practicably meet the assigned noise levels, an application must be made to the Environment Minister which will go through a fair public process and approval is may be granted subject to conditions and restrictions.

Table 2.5.1: Qld's Standard Licence Limits

Noise limits at a noise sensitive place	
Period	Adjusted maximum Sound pressure level for a given period
Monday to Saturday 7 am - 6 pm	Background noise level plus 5 dB(A)
Monday to Saturday 6 pm - 10 pm	Background noise level plus 5 dB(A)
Monday to Saturday 10 pm - 7 am	Background noise level plus 3 dB(A)
All other times and Public holidays	Background noise level
Noise limits at a commercial place	
Period	Adjusted maximum Sound pressure level for a given period
Monday to Saturday 7 am - 6 pm	Background noise level plus 10 dB(A)
Monday to Saturday 6 pm - 10 pm	Background noise level plus 10 dB(A)
Monday to Saturday 10 pm - 7 am	Background noise level plus 8 dB(A)
All other times and Public holidays	Background noise level plus 5 dB(A)

2.6 Special cases

The special cases with prescriptive noise level requirements in Qld and WA are listed in Table 2.6.1 below.

Table 2.6.1: Special cases in QLD and WA

Description	Qld	WA
Blasting	□	□
Agricultural	□	□
Construction	□	□
Household equipment	□	□
Bellringing or calls for worship	□	□
Community activities	□	□
Entertainment and sporting venues	□	□
Traffic signal	□	□
Outdoor shooting range	□	□
Domestic animals	□	□
Spa blowers and pool pumps	□	□
Air-conditioning equipment	□	□
Refrigeration equipment	□	□
Indoor venues	□	□
Amplifying devices	□	□
Power boat	□	□
Airports	□	□
Public roads	□	□
Railways	□	□

The crosses in Table 2.6.1 do not necessarily mean there are no particular requirements for the listed type of noise. The acoustic quality objective and the assigned noise levels would apply to these cases. The ticks include where the requirement refers to another document which needs to be complied with as well. For example, meeting the Australian Standards *AS1742.10-1990 Pedestrian control and protection* is specifically quoted as a requirement in Qld's Nuisance Regulations.

Note that the exclusions discussed in Section 1 above correspond to the items in the Table 2.6.1 to a certain extent. As mentioned previously, the exclusions provide some guidance to the administering authority to dismiss complaints. If the prescriptive requirements for the special cases above are met, the administering authority can form the opinion that the source of noise under consideration is not a nuisance.

There are product labelling requirements in Qld. However, to date these requirements have not come into force. The targeted products in product labelling requirements are:

- chainsaws;
- domestic air-conditioners;
- domestic pool pumps;
- grass-cutting machines;
- mobile air-compressors;
- mobile garbage compacters; and
- pavement breakers.

2.7 Noise measurement

In Qld, L_{A10} values are used to describe source noise levels and L_{A90} values are used to describe background noise levels. This is particularly commonly used in assessing the impact from continuous sources such as air-conditioning units. L_{Aeq} values are also used to describe source noise. For impact noise, L_{Linpk} values are commonly used.

In contrast to WA, where slow settings are commonly used in the noise meters, Qld tends to use fast settings.

Generally, both in Qld and WA, A-weighted network is commonly used as the goal of the legislation is to protect the public from noise nuisance, thereby, improving the quality of life. This is appropriate as the A-weighted network takes the human hearing range into account. Linear-weighted settings are used, however, to assess some impact noise such as blasting.

2.8 Public consultation

As required by law, both Qld and WA have consulted the public in arriving at the final draft of the environmental legislation associated with noise. The invaluable advantage in carrying out elaborate consultation procedures is that issues are brought into the attention of the administering authority. However, such consultation procedures have proven to be cumbersome and at times, not all parties are satisfied with the final result. Such consultation can also result in the lowering of standards. Any persons drafting legislation will need to be aware of such problems and how to manage such problems. In general, it is good practice to incorporate stringent requirements in the initial drafts of legislation. This will allow for the standards to be lowered with later drafts without compromising the quality of the noise environment.

3.1 Recommendation

Drafting of environmental legislation can be very challenging, particularly, when you take into account stakeholder consultations. Various community and industry groups will have contrasting priorities and arriving at a common agreement can sometimes be extremely difficult. Both Qld and WA have attempted to strike a balance between managing environmental noise whilst allowing economic, cultural and social activities. In summary, Qld's environmental noise legislation has its strength in its simplicity which allows for easy practicability. WA's environmental noise legislation is a little more complex yet it allows for flexibility from one noise environment to another. It is recommended that in drafting such legislation, a conservative approach should be adopted initially. This allows for any negotiations during the stakeholder consultation process. Furthermore, it should be acknowledged that the individuals involved with the drafting of the legislation discussed here, undoubtedly would have had to overcome a number of challenges in arriving at the existing legislation. Whilst there may be some shortcomings in this legislation, it should be acknowledged that some guidance has been provided by this legislation to assist with decision making.

Bibliography

1. Australian Standards, *AS1055-1997 Acoustics - Description and Measurement of Environmental Noise*, Australia.
2. Australian Standards, *AS1742.10-1990 Pedestrian Control and Protection*, Australia.
3. Department of Environmental Protection, *Environmental Protection Act 1986*, Western Australia.
4. Department of Environmental Protection, *Environmental Protection (Noise) Regulation 1997*, Western Australia.
5. Department of Environmental Protection, *Environmental Protection (Noise) Regulations 1997, Summary of the Regulations*, Western Australia.
6. Department of Environmental Protection, *Noise Abatement (Neighbourhood Annoyance) Regulations 1979*, Western Australia.
7. Environmental Protection Agency, *Environmental Protection (Noise) Policy 1997*, Queensland.
8. Environmental Protection Agency, *Environmental Protection Act 1994*, Queensland.
9. Environmental Protection Agency, *Environmental Protection Regulation 1998*, Queensland.
10. Environmental Protection Agency, *Noise Abatement Act 1978-1989*, Queensland.
11. Environmental Protection Agency, *Noise Measurement Manual, Third Edition, 1 March 2000*, Queensland.
12. Jenkins, Dr B, *Preface of Environmental Protection (Noise) Regulations 1997, Summary of the Regulations*, Western Australia.

If you have any queries, you are welcome to use the contact details below:

- Telephone: (08) 9222 7141
- Facsimile: (08) 9322 1598
- E-mail: Namiko_Ranasinghe@environ.wa.gov.au

A Comparison of the Noise Criteria Which Apply To Fixed Industrial Noise Sources in the Different States Within Australia

J. R. M^{c}Loughlin

SVT Engineering Consultants

Abstract

Each of the States within Australia has different noise criteria. These criteria have been set independently and the extent of their application, the technical details and the enforcement approaches are different in each State. Thus it is quite feasible for an industrial source in one State to be assessed as compliant, whilst it may be assessed in another to be excessive. This paper presents a comparison of the noise criteria that apply to industrial sources in the various States within Australia.

Introduction

Annoyance from intrusive noise is not solely dependent on the level of noise but also on the type or quality of the noise, the number of noise events and the receiver's sensitivity to the noise. The type of sound refers to the features of a sound that make it identifiable to a listener such as tonality, impulsiveness, steadiness or irregularity and the balance between high and low frequencies.

The fundamental approach to assessing intrusive noise, therefore, involves determining the noise level, applying corrections for the type of noise and comparing this value with limits set by regulatory authorities. While this approach is common to most of the States within Australia, noise criteria vary from State to State in terms of absolute noise limits, noise descriptors, consideration of background noise, assessment of intrusive characteristics, applicable meteorological conditions and enforcement approaches.

This paper summarises the major differences in noise criteria between each of the States. (Tasmania has been excluded from this comparison, as there are currently no criteria that apply to industrial noise emissions in Tasmania.)

The relevant criteria are defined in the following documents:

- **Victoria**:- State Environmental Protection Policy (Control of Noise from Commerce, Industry and Trade) No. N-1
- **New South Wales**:- NSW Industrial Noise Policy
- **Northern Territory**:- Waste Management and Pollution Control (Environmental Noise) Regulations
- **Queensland**:- Environmental Protection (Noise) Policy
- **Australian Capital Territory**:- Environmental Protection Regulations
- **South Australia**:- Environmental Protection (Industrial Noise) Policy
- **Western Australia**:- Environmental Protection (Noise) Regulations

Regulation of intrusive noise is an ongoing process and it is acknowledged that many of the aforementioned documents are subject to periodic review and amendment.

Noise Descriptors

Environmental noise varies enormously in sound pressure level, frequency, duration, and other characteristics and it is not possible to fully describe any sound by a single figure. However, noise limits are generally set in terms of single figures. To set noise limits in any other way would be at best cumbersome and at worst unworkable. The most commonly used descriptors are:

- Equivalent Continuous Sound Pressure Level, (LAeq,T)
- Maximum Sound Pressure Level, (LAmax); and
- Statistical descriptors such as LA10 and LA90, which indicate the noise level exceeded for a given percentage of time.

The Equivalent Continuous Sound Pressure Level (LAeq,T) is often regarded as the average noise level over a given period. More correctly, it is the sound pressure level that, if maintained at a constant level, would contain the same sound energy as the varying signal over the same time period. However, LAeq,T often conceals the pattern of noise variation over time, which can be important in determining human response. It is becoming more common for regulatory authorities to adopt LA10 as the noise descriptor. The

LA10 is the noise level that is exceeded for 10% of the measurement period and is used to describe the average of the maximum levels over the measurement period. Because this descriptor places an emphasis on the higher noise levels it is thought to correlate more closely with human response to noise.

The LA90 noise level, (the noise level exceeded for 90% of the measurement time), is commonly used to describe background noise.

Table 1 compares the primary noise descriptors adopted by the various States.

***Table 1**. Summary of Primary Noise Descriptors*

State	Primary Noise Descriptor
WA	LA10*
VIC	LAeq
NSW	LAeq
NT	LA10*
QLD	LAeq,24h
ACT	LA10
SA	LAeq

* Both WA and NT also specify noise limits in terms of LA1 and LAmax so as to allow for brief louder noises.

Noise Limits

Table 2 summarises the noise limits that apply in each State for day, evening and night periods. The noise limits presented are the minimum noise limits with no adjustment to account for the proximity of industrial and commercial areas or major roads.

The definitions of day, evening and night periods differs slightly from State to State and in some States no evening period is defined.

Where noise limits are specified for more than one noise descriptor the limits that apply to the primary descriptor are presented.

***Table 2**. Summary of Noise Limits*

	Noise Limit – dB(A)		
State	**Day**	**Evening**	**Night**
WA	45	40	35
VIC	45	40	35
NSW	50	45	40
NT	45	40	35
QLD	*	*	*
ACT	45	-	35
SA	47	-	40

* Queensland has an "Acoustic Quality Objective" of 55 dB(A) or less averaged over 24 hours for most of the population living in residential areas.

Consideration of Background Noise

For noise from an industrial source to be considered intrusive it must be audible above background noise. For this reason it is appropriate to consider background noise levels when setting environmental noise criteria. The "background plus" approach is used in some jurisdictions where acceptable noise limits are set in terms of the measured background level plus a certain margin, typically 5 dB. However, there are arguments against adopting this approach, which are outlined below.

The background level of an area increases as the level of activity in the area increases, particularly in industrial areas. If each sound source was permitted individually to emit sound up to 5 to 10 dB above the background level, then the combined sound energy from all the sources could cause an increase in the background level. Subsequently the maximum allowable levels for new industrial sources would increase with the increasing background level. This effect is termed the "creeping background".

To include measured background noise levels in the derivation of noise criteria would require that the sources that constitute background noise would have to be clearly defined. This could lead to debate over issues such as, for example, whether existing industries in the same area as a proposed new development should be included or excluded in the assessment of background noise.

The need to exclude certain sources from the assessment of background noise makes accurate measurements very difficult. Furthermore, background noise levels are very rarely consistent from day to day and from season to season. Instead they are likely to fluctuate, being influenced by factors such as prevailing weather conditions, variations in traffic flow and so on. This further complicates the measurement of background noise and can lead to the situation where the noise criteria will vary according to how and when the background noise is measured.

Several States account for background noise by considering the land use in the vicinity of the receiving premises. In these States the base noise limit is increased by an "influencing factor" based on the land zoning and/or presence of major roads in the area of interest.

Table 3 summarises the methodologies adopted by the various States when considering background noise.

***Table 3**. Summary of Methods for Considering Background Noise*

State	Method for Consideration of Background Noise
WA	Influencing Factor
VIC	Influencing Factor
NSW	Background + 5 dB & Influencing Factor
NT	Influencing Factor
QLD	N/A
ACT	N/A
SA	Background + 5 dB

The methods used for calculating influencing factors and measuring background noise levels vary in each of the relevant States.

Adjustments to Noise Limits for Intrusive Noise Characteristics

The A-weighted sound level is the most common method for assessing the perceived magnitude of noise. However, it is important to be aware that A-weighting has been developed to describe the effects of noise in terms of a single figure value. As such, A-weighting is not always an accurate indicator of perceived loudness. In fact, the more annoying characteristics contained in a sound, (tonal components, impulsiveness etc), the less effective the A-weighted level is for predicting annoyance.

To account for this, environmental noise emissions are commonly adjusted for intrusive characteristics before comparison with noise limits. Intrusive characteristics include tonality, impulsiveness, modulation, intermittency and excessive low frequency content.

Tables 4 and 5 summarise the adjustments applied for intrusive noise characteristics in the various States.

***Table 4**. Summary of Adjustments for Tonality, Impulsiveness and Modulation*

	Adjustments in dB		
State	**Tonality**	**Impulse**	**Modulation**
WA	5	10	5
VIC	1 to 7	1 to 6	N/A
NSW	5	2 to 5	N/A
NT	5	10	5
QLD	2 or 5	2 or 5	N/A
ACT	5	5	5
SA	5	5	5

***Table 5**. Summary of Adjustments for Intermittency and Low Frequency, and Maximum Adjustments for all Characteristics*

	Adjustments in dB		
State	**Intermittency**	**Low Frequency**	**Max**
WA	-	-	15
VIC	3 to 5	-	-
NSW	5	5	10
NT	-	-	15
QLD	-	-	-
ACT	-	5	10
SA	-	-	-

As well as having different adjustments for intrusive noise characteristics, each of the States has different methods of assessing the nature of the noise. These range from subjective assessments to complex analysis of measured data.

Meteorological Conditions

Certain meteorological conditions may increase noise levels by focussing sound propagation paths at a receiving location. This refraction of sound occurs during temperature inversions and where there is a wind gradient.

Wind can increase ambient noise levels by rustling foliage and creating turbulence when passing over or around structures. At higher wind speeds, the noise produced by the wind will tend to drown out noise from industrial and transportation sources. Wind can also create extraneous noise on noise monitoring equipment. Where wind speeds increase with height the effects on sound propagation are similar to those when temperature inversions occur but the effects are restricted to locations downwind of the noise source.

Noise level predictions are an important aspect of environmental impact assessments for new proposals. Although this is not generally covered in the States' regulatory noise criteria, guidance is provided on the appropriate meteorological conditions for noise prediction by the Environmental Protection Agencies of some States.

In Western Australia the EPA has produced a draft guidance note[1] which specifies that noise predictions should demonstrate compliance with the noise regulatory noise limits for 98 per cent of the time for the month of the year in which worst case weather conditions prevail.

The New South Wales Industrial Noise Policy specifies that noise limits are expected to apply under weather conditions that would be expected to occur for a significant period of time. Weather conditions that occur for 30 per cent of the time are considered to be significant.

In Victoria the EPA has produced a guide to the measurement and analysis of noise[2] which recommends that predicted noise levels should be based on weather conditions favouring propagation that occur for 20 per cent of the time.

The effects of meteorological conditions on noise level predictions can be as high as 20dB. This clearly has a large impact on the extent of noise control treatments required for new proposals and the size of noise buffer zones.

Conclusion

In the late 1980s the Organisation for Economic Co-operation and Development (OECD) undertook an international study to analyse trends in noise exposure and assess the effectiveness of noise abatement policies. This study[3] recommended that countries should develop a coherent national strategy and that this should be coordinated between national, regional and local authorities. It is clear, however, that there is a lack of uniformity within the details of the policies and Regulations of the various States within Australia. Legislation in each state has been developed independently and this has led to a range of noise control approaches among the States.

The need for different noise limits for the various States can be justified on the basis of the characteristics of the area and the expectations of the populations. However, the differences between the policies and Regulations for each of the States are not restricted to the noise limits, but include the basic noise descriptors, assessment of intrusive noise, scope of application, enforceability, and so on. This makes direct comparisons between the States very difficult and increases the uncertainty for industry. Comprehensive guidance on the basic format, content and scope of application for noise policies and Regulations would best be provided at a federal level.

References

1. W.A. EPA – "Guidance for the Assessment of Environmental Factors (In accordance with the Environmental Protection Act 1986) – Environmental Noise" No.8 (Draft)

2. Victoria EPA – "A Guide to the Measurement and Analysis of Noise" – Publication No.280

3. OECD – "Fighting Noise in the 1990s" OECD, Paris, 1991

ACOUSTICS - putting the science and technology to work

Conference of the Australian Acoustical Society
Joondalup Resort, Western Australia, 15-17 November 2000

Session UW-3 Sonar And Communication Systems

2093 Variable Depth Sonar - Australian Modifications Tooptimize Performance In Littoral Conditions

Dr Ian Bedwell and Mr Ian Irving

Thomson Marconi Sonar Pty Limited in Australia Address: 274 Victoria Road, Rydalmere, NSW 2116 Australia

Abstract

The Thomson Marconi Sonar 2093 Variable Depth Mine-Hunting Sonar is a World Leading Sonar in service with a large number of Navies. The system is currently entering service with the Royal Australian Navy (RAN). This paper will report the design modifications undertaken by Thomson Marconi Sonar Pty Limited in Australia (TMS Pty) to optimise 2093 Sonar performance in the harsh operating environment, of Australia and South East Asia, which consists of warm water, shallow operating conditions and marine interference (eg snapping shrimp). The paper will also report on the success of this activity undertaken in partnership with the engineers at TMS Ltd United Kingdom shown by recent sea-trials onboard NUSHIP HUON, where in un-alerted detection trials 2093 was proven to find 29 out of 29 targets as laid by the Commonwealth. The paper will report on the modifications undertaken covering

- Classification arrays re-design;
- Re-design of the transducer material and size;
- Re-design of the raddii of curvature of the transducer matrix to improve beam patterns;
- Implementation of a classification image database enables comparison of current image with a library of images;
- Implementation of a route survey database enables greater ships speed of advance and clearance rates by the comparison of the current and history image; and
- Operator performance optimisation.

Mine Avoidance Sonar For Optimal Freedom Of Manouvre

Lieutenant-Commander Col ELLIS RANR

Thomson Marconi Sonar Pty Limited in Australia

Abstract

This paper reports on the Australian designed and developed PETREL Three Dimensional Forward Looking Sonar. This sonar is the first true real-time three dimensional sonar in the World and has revolutionised a number of naval missions by optimising warship freedom of manoeuvre. The paper will report on the collaborative development of this system in Australia by Thomson Marconi Sonar Pty limited and the Royal Australian Navy (RAN) to meet the RAN's demanding requirements. This will include discussion of the systems engineering required across the unique transducer array, real-time three dimensional signal processing and the need to optimise system format to work in Australia's acoustically harsh coastal region that culminated in the award of the 1998 Australian Design Award. The paper will then report on the operational success of the system and its ability to provide for the first time instantaneous spatial resolution of the sea-bed ahead of the vessel and the systematic detection of all sea-bed and water column dangers. The efficiency implications of this increased safety, optimised detection and ensured coverage will be projected. The paper will consider the inherent advantages of an intuitive real-time three dimensional display in optimising the reaction time and efficiency.

Introduction

The PETREL TSM 5424 is an Australian designed and developed sonar that provides real-time intuitive three dimensional representation of the sea-bed and water column ahead of the vessel for optimal navigational safety and mine avoidance. PETREL is the culmination of a five year collaborative development by Thomson Marconi Sonar Pty Limited in Australia (TMS Pty), the Royal Australian Navy (RAN), Defence Science and Technology Organisation (DSTO) and the Defence Acquisition Organisation (DAO). This collaboration commenced as a DAO NSW initiative under the former Defence Industrial Development (DID) programme. The PETREL project highlights the significant successes of the often un-heralded DID programme. Reviewing PETREL's development milestones identifies the project doctrine evident in the many successful DID projects and clearly missing from the few over-publicised failures. These features are;

- A defined capability requirement originating from ADF users;
- A innovative but logical solution;
- A long-term financial commitment by both DAO and industry in the DID outcome, within a phased development path, and
- A industry commitment to transition the project from DID to production.

Requirement

PETREL originated from a RAN vision, which originated in a series of studies undertaken by the RAN and DSTO on freedom of tactical manoeuvre. Freedom of manoeuvre is a key force multiplier as a warship that can safely pass through areas denied to the enemy due to mines or natural hazards, has a significant tactical advantage over the opposing force. This inherent fact of maritime warfare was re-emphasised by the Gulf war, where the hazard imposed by Iraqi sea-mines, including un-sophisticated moored contact mines, was sufficient to prevent the World's most powerful maritime nation from undertaking amphibious operations in support of Operation Desert Storm.

These operational studies recognised that traditional search-light sonar systems were of limited value for mine avoidance. These sensors propagate a one dimensional transmission of finite beam-width ahead of the vessel. The nature of the search-light means that only a small section of the water ahead of the vessel is ensonified at any one time, therefore a clear sonar screen may be indicative of a slow sweep and miss interpreted echo rather than safe water. This problem can be exacerbated by inexperienced operators miss-identifying targets or becoming engrossed in one detected danger. Potentially as dangerous, is the high false alarm rate inherent within Search-Light systems leading to operator fatigue and inattention to warnings. Studies also highlighted the limitations of traditional search-lights

in acoustically harsh conditions where the long detection ranges claimed in "ideal conditions" were found to vary significantly from area to area in Australian conditions destroying the operators trust of the system.

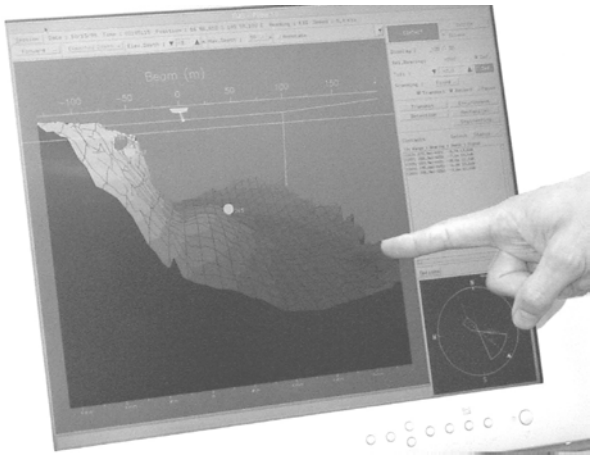

Figure 1 – PETREL intuitive display of Fitzroy Island Qld steep-to coast-line (HMAS MERMAID)

Another identified limitation of traditional systems was their flat plan formats such as the common PPI (Plan Position Indicator). These traditional displays demand significant training and are interpretive in format, that is they require a dedicated operator continually reviewing the data to monitor and report changes. Subsequently such displays have been located in the Sonar Control Room (SCR) or equivalent area away from the ship's Bridge, with reporting by a dedicated operator to the Officer Of the Watch (OOW) or Navigator (NO) for avoidance. This situation is not optimal, the Sonar operator is not normally a qualified Mariner and therefore does not have the requisite skills to make safe avoidance manoeuvre decisions, nor does the man conning the ship have the spatial data required to do so safely.

These studies culminated in a recognition that safe mine and obstacle required;

- Detection ranges prescribed by the target strength of the threat and the Tactical Diameter of the host vessel;
- Optimum reaction based on a clear, easily operated Bridge display;
- Manpower neutrality;
- High fidelity data for low false alarm;
- Systematic coverage of the area ahead of the vessel, and
- Robust performance in acoustically harsh and dynamic littoral waters.

Innovation

This operational requirement led to a submission by the then Thomson Sintra Pacific, now TMS Pty, for development of a unique three dimensional sonar to capable of providing systematic coverage, high fidelity, low false alarm and capable of being operated by the OOW/NO to reduce reaction time and achieve manpower neutrality. The proposed concept was Volumetric Acoustic Processing (VAP) technology. VAP employs an array orientated in the vertical plane to propagate a number of beams, narrow in the vertical and wide in the horizontal, stacked one on top of the other. The returns from these respective beams are then received on a frequency agile array orientated in the horizontal plane. Frequency domain provides vertical resolution, phase comparison in the horizontal plane discriminates azimuth and time series determines range. The VAP concept also ensured the proposed sonar had a rapidly increasing Signal to Noise Ratio as the target range decreases. This meant that a change in background level or target strength causes only a small change to the maximum detection range, allowing to be capable of maintaining a consistent detection range under a variety of environmental conditions.

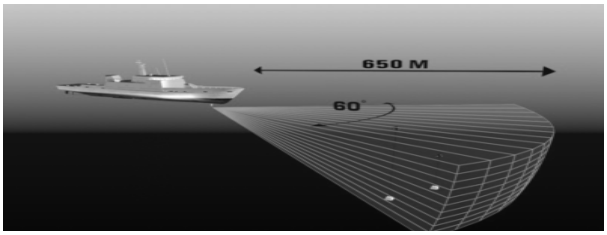

Figure 2 – 3D Sonar Propagation schematic

It was also recognised that the high fidelity three dimensional vector model of the water column and seabed, could be exploited to create a real-time, intuitive, three dimensional image. This provided rapid reaction to dangers as the officer conning the vessel can intuitively see real-time vector model of the navigational situation. By providing a real-time three dimensional ensonification PETREL was also capable of internal spatial awareness and subsequently display "intelligence". PETREL undertakes automatic monitoring of the spatial data providing audible and visual alarms when conditions pre-set by the operator, such as a safety least depth or minimum distance closure on a point target are exceeded. This further reduces the operational burden on the operator and optimises safety.

Investment And Phasing

Like many successful DID projects, the VAP DID was formed on the basis of equally shared funding between DAO NSW and TMS Pty. A risk management strategy was also implemented including use of a phased ap-

proach with the outcomes of each phase being used as the determinate for the next phase. This phased approach was collaboratively managed by TMS and DAO NSW. As importantly, both parties maintained a strong commitment to outcomes via regular Integrated Project Team (IPT) partnering meetings.

VAP Phase One – Algorithm Study: May 1994 to July 1994, involved a theoretical analysis of the VAP concept including detection and tracking algorithms. The study set the basic architecture of the sonar. The phase was marked by the close and constructive involvement of DAO and DSTO within TMS Pty's engineering analysis.

VAP Phase Two – Static Brass-board: from August 1994 to July 1995, developed and undertook successful demonstration of the VAP concept during static engineering trials at DSTO's Woronora Dam Test Facility. Trials employed a brass-board engineering system comprising TMS software and DSTO test equipment. It was during the processing and analysis of these trials that the capability to exploit the three dimensional data as real-time three dimensional displays was recognised.

VAP Phase Three – Dynamic Demonstrator: August 1995 to September 1996, involved the development and dynamic sea-trials of a prototype PETREL in Jervis Bay onboard the DSTO trials vessel MV *Kimbla*. This phase included sea-trials of the prototype three dimensional display developed as a TMS Pty self funded activity. Trials proved the VAP concept and identified issues and deficiencies. A key feature of this phase was the transparency of the activity with open dialogue on the deficiencies and their rectification. Deficiencies included non robust design for the mechanical stabilisation which prevented mechanical roll stabilisation and electrical supply deficiencies. The initial three dimensional display software was also found to be defective, ultimately dictating the implementation of entirely new software. Another major impediment to trials was a lack of robust position fixing and vessel heading data, with the systems chosen to provide this reference data to the PETREL lacking the precision required for successful operations.

Figure 3 – 3D Data visualisation of Bombora Rock transit merged to existing chart

VAP Phase Four – Three Dimensional HCI: This was the final DID phase February 1996 to October 1997, implemented the modifications identified during Phase Three sea-trials. This included identification of the Frequency Modulated (FM) propagation mode to increase detection range and successful redevelopment of the intuitive display. The latter required resolution of the bottom surface extraction methodology, fusion of past data with current, and the overlay of point target information on the sea-bed model. This was achieved by use of 3DXRT™ Commercial Of The Shelf (COTS) software, adapted by TMS Pty software specialists.

Phase 4 also determined the functional requirements for the PETREL display via consultation with a significant number of RAN specialist seaman officers, collectively representing some 150 years of mariner experience. As importantly, these specialists represented a key cross section of professional sub-specialisation's including, hydrographic surveying, mine warfare, amphibious warfare and sub surface warfare. A review of Geographic Information Systems (GIS) technologies and consultation with DSTO was undertaken to draw upon the considerable advances made in the three dimensional presentation of logged data. The IPT included review of the OOW functional role on the Bridge. This demonstrated that the display must be visible and readily exploitable from any number of places on the Bridge including, the primary conning position, the radar console, the Commanding Officer's chair and from the forward Bridge aspect. As importantly, the display needed to be as "hands free" ensuring the OOW maintained his/her primary purpose of monitoring and controlling navigation safety. Finally, the display needed to readily provide spatial awareness

and contact monitoring, including the need for high levels of system "intelligence" for displaying least depth and closest point of approach of contacts.

Phase 4 also included studies of PETREL's angular resolution and performance with a view to adapting the PETREL design for the role of hydrographic feature detection onboard the RAN's survey vessels. These studies confirmed that the fundamental wet-end capability of the FM production PETREL were in keeping with RAN Hydrographic Service requirements, but established that the display functions would need to be adapted and integrated into a Hydrographic System Suite for efficient operations. The latter analysis is continuing as a TMS Pty self funded activity with virtual reality displays being considered in the development of a dedicated survey watch-keeping display for hydrographic variants of PETREL.

Industry Commitment To Transition

Whilst the DID phases had achieved all identified aims, the PETREL was by no means fully developed at the end of the jointly funded DID activities. The next stage was typical of all successful DID's, in that TMS Pty continued self funded development and trials of the PETREL to transition the developmental system and prototype to a production capable system. This phase included finalisation and fine-tuning of the display design, ruggedisation of the prototype's architecture, implementation of a re-designed direct drive gear-box for robust mechanical roll stabilisation and a successful extended sea-trial of the system onboard MV *Kimbla* from March to May 1998. This sea-trial was highly successful and included demonstration of all required capabilities to RAN Officers.

These sea-trials also confirmed the robust performance of the PETREL by demonstration of reliable detection, tracking and display of mine-like point targets and complex sea-bed terrain ahead of the vessel. The trial also proved PETREL was intuitive and easy to learn with the operation of PETREL by an RAN Officer during close navigation scenarios after only 15 minutes of instruction.

After successful trials TMS Pty entered a self funded production consolidation phase to establish performance and production benchmarks and to identify and qualify spares, logistics, system configuration and documentation. TMS Pty were at this stage, actively marketing the PETREL to meet the RAN's mine and obstacle avoidance requirement within the FFG Upgrade Project SEA 1390 and the ANZAC Class Underwater Systems and Weapons Upgrade Project SEA 1348. PETREL was selected after a competitive tender. During this period PETREL also won the prestigious Australian Design Award, a source of great pride to TMS Pty's staff and to the many DSTO, RAN and DAO NSW staff that had collaborated in the project.

In parallel, another jointly funded DAO/TMS Pty activity was implemented in December 1998, for a long-term operational evaluation of the pre-production prototype onboard HMAS MERMAID. The prototype was successfully fitted and set to work in 5 months within a production standard ship installation. MERMAID successfully completed the first phase of trials in August 1999. MERMAID is currently undertaking a 5 month operational evaluation during programmed survey operations in acoustically harsh northern Australian and PNG waters. System performance has exceeded modelling and many new roles for the PETREL both in general RAN operations and Hydrographic operations have been identified by HMAS MERMAID's Commanding Officer. As importantly, this phase has identified a large number of minor software modifications that will be implemented into the production Display to optimise functionality.

Figure 4 –PETREL Trials HMAS MERMAID

Conclusion

History teaches that tactical freedom of manoeuvre remains a key force multiplier in coastal maritime operations. The Australian designed and developed PETREL is a unique Sonar which will optimise freedom of manoeuvre for the RAN's frigates and if required the RAN's new Patrol Vessels, providing intuitive, real-time, high resolution data systematically ahead of the vessel. This capability is the direct result of a DID project that grew out of the vision of RAN officers, the efforts of DAO NSW and the indigenous technical capability of TMS Pty and DSTO. PETREL is now a production system, at sea, selected for the RAN's frigates and also is now realising strong export sales potential. As such PETREL represents one of the many successes of DAO's former DID concept.

Digital Underwater Acoustic Communications

Michael B. Porter[1], Vincent K. McDonald[2], Paul Baxley[2] and Joseph Rice[2]

[1]Science Applications International Corp., La Jolla, USA
[2] SPAWAR Systems Center, San Diego, USA

Abstract

In recent years, there has been a resurgence of interest in wireless (i.e. acoustic) underwater links. Such links will form the backbone of undersea internets. These in turn will be used to link sensors such as hydrophone arrays or to connect ships and off board platforms, to mention just a few applications. A variety of digital modems have now been developed based on FSK (frequency-shift keying), DPSK (Differential phase-shift keying), and QPSK (quadrature phase-shift keying). The latter are typically implemented with sophisticated adaptive equalizers that attempt to remove the ocean multipath. A key research issue is to determine which methods perform best and when. The choice depends on power level, desired bit-rate, and on the environmental conditions. Obviously transmission loss and ambient noise play an important role; however, multipath and Doppler spread are also important. To better understand signaling performance, we are conducting an extensive sequence of sea tests (SignalEx) in a variety of conditions and with diverse modem schemes. We also transmit extensive channel probes to measure the propagation conditions and associate that with modem performance. This paper will summarize the lessons from the first set of experiments.

Multistatic Developments For Acoustic Surveillance

Anthony B. Richard

Thomson Marconi Sonar Pty Ltd

Abstract

Airborne ASW and Acoustic Surveillance has been prompted into significant evolution over the past decade, resulting in a shift of the emphasis from passive to active techniques. This paper will report the Bi-static and Multi-static developments being undertaken in Australia by a collaboration of Thomson Marconi Sonar Pty Limited (TMS Pty), the Royal Australian Navy (RAN) and the Defence Science and Technology Organisation (DSTO) including consideration of the operational issues, the system developments in deployable acoustic sources and receivers and the transducer developments that have been undertaken to facilitate these developments. The paper will also consider on the significant success of these developments including reporting the success of sea-trials to date.

Introduction

There are two major multistatic programs currently being undertaken in Australia today;

- Joint Project 1441 Bistatic Barra CTD follows on from the successful Low Frequency Active Sonobuoy progam;
- SEA 1100 which is a combined passive and active towed array sonar and sonobuoy processing system for the Royal Australian Navy's FFG-7 and ANZAC frigates.

Both projects have grown out of the operational vision of the ADF's Project Director for the Defence Material Organisation - Sonar Ranges Group. This vision has extended the use of sensors to maximise the command flexibility available to the Officer in Tactical Command (OTC) in both the deployment methodologies and acoustic options. A key feature has been the use of a single prime contractor, TMS Pty, providing optimal system commonality and function.

SEA 1100 – ASSTASS

TMS Pty won a competitive tender against US & German bids in 1998 to design and build a Low Frequency Active & Passive Sonar System (LFAPS) within Phase 3 of the Australian Surface Ship Towed Array Surveillance Sonar (ASSTASS) Project. This system allows the Commonwealth to perform capability evaluation. The outcome being to prepare a specification for the acquisition phase to install onto all FFG-7 and ANZAC frigates from 2001 to 2005.

Major requirements of ASSTAASS Phase 3 was for the use of low risk, established technologies leveraging off existing Commonwealth investments. LFAPS is designed to have minimum impact on the ship, and be flexible to evolving operational requirements. Being an evaluation program, the aim was to look at a range of sonar functions to see how they contribute to ships capability, by exploring traditional passive and more recent Bi-Static & Multi-Static operations. The LFAPS system includes:

- An combined Active and Passive Towed Array;
- A Streamer Handling System;
- Transmission and Receiving hardware and displays;
- Open architecture ATM communications networks for sensor and processed data transmission throughout the system;
- A Sonobuoy Receiver and Processor; and

- A Surface Ship Towed Array Passive Processing System (SSTAPPS).

The figure below depicts the basic LFAPS components as installed on HMAS ANZAC in January 1999. The two major components being the towed array sonar transmission and reception system which is winchable from the ship's quarterdeck, and can be deployed up to 1.5km behind the ship; and a sonobuoy receiving system mounted on the ship's mast. A major feature of the LFAPS system is the ATM protocol applied to the complex combat data system for the first time. This open architecture concept allows for a "plug & play" approach allowing the RAN, TMS and other sub-contractors to change, enhance and re-configure the LFAPS set-up rapidly for trial purposes.

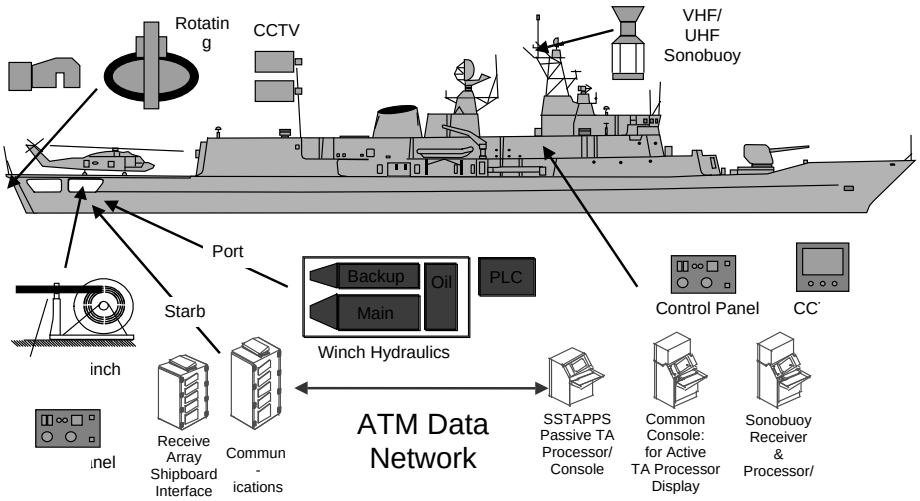

Figure 1 – SEA 1100 Phase 3 - System

A second LFAPS Shipset was to be installed on an RAN ADELAIDE Class FFG, HMAS NEWCASTLE, however, due to the trials successes on ANZAC, the system will now be re-configured as an en-capsulate system for use on trials vessels of opportunity.

The combination of passive and low frequency active towed array and stand off sonobuoys has been demonstrated as a significant sonar capability for surface ship combatants of the RAN. The combination of TA for long range detection and sonobuoys for mid-range detection is providing significant improvements to the ship's acoustic seascape. The use of sonobuoys is also providing assessment of ownship signature data for emission control and vulnerability LFAPS is providing a system which incorporates operator techniques for towed array and sonobuoys developed in Australia with RAN and RAAF over many years.

Jp 1441 Bi-Static Barra

The Bi-Static BARRA Project is a Capability Technology Demonstration (CTD) programme and is an outcome of the highly successful Low Frequency Active Sonobuoy system project conducted by TMS in the period from 1996 to 1998. The purpose of the CTD is to develop these systems to allow operational performance assessments to be carried out, and to develop concepts of operations for airborne multi-statics. Under the JP 1441, TMS Pty has been contracted to develop and supply air-certified source buoys which are optimised for use with the Australian Barra AN/SSQ801-B horizontal planar array sonobuoy, and DIFAR.

Additionaly an Australian SME, Acoustic Technologies Pty Limited, have been contracted to develop and supply a number of 8 channel multi-static and passive sonobuoy processors called RAPTOR capable of being installed and removed from RAAF AP-3C Orion aircraft.

JP 1441 program is addressing methods and tactics for multistatic operations, as well as the issues related to the use active transmissions on our marine environment. TMS Pty have developing and/or are manufacturing two of the principle deployable sensors being used within the ADF's multi-static acoustic surveillance projects. These are the BARRA AN/SSQ-801B passive receiver sonobuoy and the Rapid Area Search Sonar Projector Used Tactically In Narrowband (RASSPUTIN) deployable coherent source sonobuoy.

BARRA is an optimum buoy for multi-statics, as it is capable of receiving low frequency active transmissions across a wide acoustic aperture formed by its Horizontal Planar Array (HPA) and beam-forming across this array to determine the direction of the source. In any acoustic system, the longer the array within the plane of the received sound, the better the angular resolution in that plane. By having a wide HPA, BARRA can provide very accurate azimuthal discrimination (bearing). The more commonplace

DIFAR arrays do not employ wide acoustic base-line. For angular resolution they rely on pressure gradient resolution for direction. This does not provide the same angular accuracy's and also has the disadvantage of suffering 'bearing pull', that is two separate sound sources on different bearings will not be resolved as separate contacts but will be presented as a single source on a bearing that is the vector sum of the two separate bearings. BARRA can resolve and discriminate the multi return environments inherent with multi-statics and provide target discrimination and high resolution bearings. Additionally, unlike traditional pressure gradient receivers, BARRA is able to achieve this bearing accuracy by conventional beam-forming making it suitable for a wide range of processing technologies. Key BARRA parameters are:

- Fully Automatic operation
- Interactive Electronic Function select and Command Function select for optimal mission planning
- Multi-life settings from 0.5 to 4 hrs
- Multi depth settings shallow to deep
- Acoustic frequency range 10 – 2500 Hz
- 99 selectable communications frequencies
- Operation up to Sea-State 5

The RASSPUTIN source buoy provides a coherent sound source for multi-statics. The use of coherent source for multi-statics is superior to explosive sources for tactical, logistic and political reasons. Tactically RASSPUTIN is fully programmable for transmission, allowing co-ordination of different sources or to allow the surface unit to clear the RASSPUTIN datum prior to transmission. This increases the OTC's flexibility whilst complicating the enemies tactical picture. Logistically RASSPUTIN obviates the air safety issues involved in deployment of explosive sources and simplifies the storage implications onboard vessels and aircraft. RASSPUTIN also avoids energy being wasted in unusable frequencies. Politically the buoy can be used in peace-time or for low contingency sovereignty assertion without risking escalation. The use of explosive sources is becoming increasingly unsuitable for peace-time operations due to environmental pressure groups. The use of explosives in lower contingency confrontations may risk unwanted escalation of the situation. RASSPUTIN is seamlessly exploitable in both air and surface ship sonobuoy systems.

RASSPUTIN exploits a Vertical Linear Array (VLA) using high powered flextensional barrel stave DIABOLO projectors. These have been developed by TMS Pty are are compatible with the DIABOLO projectors used within the TMS Pty developed Horizontal Linear Active (HLA) towed array within another ADF project. This provides optimal commonality between towed and deployed acoustic sources. Trials to date have confirmed that the RASSPUTIN buoys are achieving planned beam pattern and target source levels. The buoys have been successfully trialed in both free floating trials and air launched trials. TMS Pty are currently producing the pre-production RASSPUTIN to support on-going ADF trials, additionally the capability has generated significant overseas interest and potential sales have been identified to a number of leading regional and World-wide Defence Forces.

Figure 2 – RASSPUTIN

Key RASSPUTIN Parameters are:

- Source Level 205 dB
- Frequency 1800 Hz Bandwidth 300 Hz
- Vertical beam pattern 20^{o}
- Interactive Electronic Functionality for optimal mission planning
- Multi-life settings
- Multi depth settings shallow to deep
- Automatic function Class D High Powered Switching amplifer with high energy battery system
- GPS integrated into surface unit

The RAPTOR Multistatic Sonobuoy Processor has been continually evolving since 1996 from the LFA Sonobuoy Systems study, and the LFAPS surface ship implementation. It has benefited from extensive ADF operator input in its operational user interface. Developed by Acoustic Technologies using COTS based technologies, the RAPTOR Sonobuoy Processor has been a test bed during extensive trials in both airborne and surface ship multistatic and passive operations.

Figure 3 Multistatic RAPTOR Sonobuoy Processor in RAAF P3-C Orion

The Sonobuoy Receivers are PC based, and was developed for Thomson Marconi Sonar by a local communications company, WinRadio. The 3 part rack system was designed by Australia's Defence Science & Technology Organisation (DSTO), who also performed EMI/EMC and air certification tests.

A specially prepared Piper Chieftain with a four tube CAD launcher fitted to the rear door has been developed by TMS for sonobuoy air deployment testing. This aircraft is also currently used for Barra Lot Acceptance testing at the Sonobuoy Test Range at Jervis Bay, south of Sydney and has been used throughout the RASSPUTIN source buoy development. A Bell Jet Ranger helicopter has also been used during the trials and qualification program. The specially designed sonobuoy gravity launch tube can be seen in the figure 4.

Figure 4 – Aircraft of Opportunity Launcher Systems

Trials have used the aircraft described above and also a dedicated Sonobuoy Trials vessel, which is operated and maintained by TMS. The Test Boat, *MV Kimbla*, is a twin diesel 350hp, 19metre, glass hulled vessel capable of operating 100nm out to sea. It has a full time crew, with part time divers and performs sonobuoy recovery and other related trials activities.

Trials have been undertaken at the ADF/DSTO Sonobuoy Test Range near Jervis Bay NSW on the Eastern Seaboard about two and half hours drive south of Sydney. The Range Facility is fully instrumented and operates from a ridge 160 m above sea level, and looks due east to the sonobuoy drop site about 25km off the coast. These facilities were originally developed for Sonobuoy Production Lot Acceptance testing and have been used extensively during the development and qualification of the RASSPUTIN buoy with JP1441.

Trials Results To Date

RASSPUTIN has been subject to successful Air Separation trials with both CAD & Gravity Launched buoys. These trials were completed in August ,1999. Fully Functional buoys were successfully air launched in November,1999, with Environmental Qualification Trials being successfully were completed in June with more than 35 operational buoys built and deployed. Critical Design Review & Production Readiness was completed in July. RASSPUTIN production Pilot Run & Acceptance Test will be conducted in August, with deliveries to the Australian Defence Forces and French Navy, for operational evaluation trials, in October.

The RAPTOR processing system and associated RF link has proved very successful in all trials in both airborne and surface ship configurations. The system has been operated by RAAF and RAN personnel during exercises and trials across the range of Australian operational areas from deep, cold waters to warm and shallow tropical waters. The system has proven itself to be in many cases superior in perofrmance to the larger and

more expensive sonobuoy processing capabilites fitted to the RAAF P3C aircraft.

The BARRA Buoy has been deployed extensively as a multi-static receiver buoy in both SEA 1100 and JP1441 trials. The buoys planar array configuration has proved vastly superior to traditional DIFAR format sonobuoys for multi-static and bi-static reception as shown in Figure 5 below. TMS Pty are continuing to develop the BARRA to incorporate performance enhancements including potentially GPS, in-buoy processing and advanced acoustics.

Conclusion

TMS Pty and the ADF, have been progressively and collaboratively realising the vision of the Sonar & Ranges Project Office, to provide the ADF a holisitc mutlti-static Acoustic Surveillance capability. This activity has been steadily expanding the Australian multistatic capability through the use of indigenous and responsive technologies. In Australia, the success of tese multi-static programmes is significant and due to the collaboration of TMS Pty with ADF and with Small to Medium Enterprises working together to provide specific solutions to meet the ADF operational requirements.

Figure 2 - Detection Performance in Shallow of Barra - Array gain of Barra provides bearing discrimination against reverberation in shallow water environments

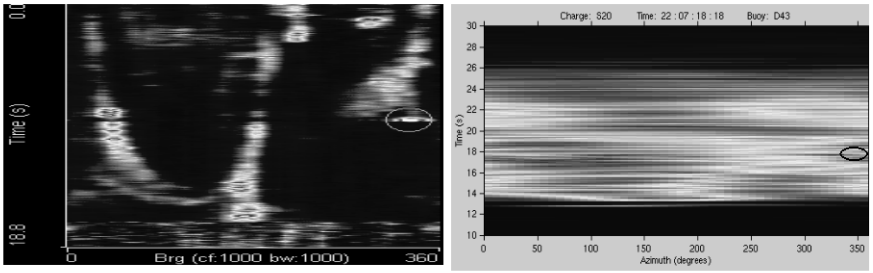

Figure 5 – Comparison of BARRA & DIFAR in multi-static trials

Modeling of the Target Strength of Air-filled Tubes as Passive Reflectors for Low-Frequency Active Sonar

Z Y Zhang[a)]

DOTSE, Auckland Naval Base, Devonport, Auckland, New Zealand

Long, air-filled tubes have been proposed as low-cost artificial targets for active sonar trials because of their strong resonance at low frequencies. Modeling them as long cylindrical air columns, this paper examines the following issues related to their target strength: (1) their backscattering and bistatic target strength and associated horizontal and vertical directivities; (2) the change of resonance frequencies with deployment depths; (3) the far field conditions that need to be satisfied in sonar trials. For typical configurations, our calculations show the following conclusions. (1) For frequencies up to 10 times of the resonance frequency, the bistatic target strength is essentially omnidirectional in the plane normal to the cylinder axis. (2) For a tube pressurized with a regulator to maintain its shape as it descends, its resonance frequency increases with deployment depth and this increase follows a simple analytic expression. (3) As distances to the cylinder axis increases, the scattered pressure field quickly transits from being cylindrical to spherical divergence. However, along directions of the far field pressure nulls, the field falls off much more quickly. The validity of these conclusions is restricted to cylinders whose length is much greater than its diameter so that scattering from its ends is negligible.

INTRODUCTION

Sound scattering from air-filled cylinders underwater has some remarkable features: the transition from Rayleigh to resonant scattering occurs at a frequency hundreds of times lower than that for a liquid, elastic, or rigid cylinder of the same radius. Furthermore, the scattering strengths in this region are thousands of times greater than those of a rigid cylinder of the same size[1].

These features make air-filled cylinders suitable as passive reflectors for low frequency active sonar. To achieve the same target strength at the low frequency concerned, the radius required is hundreds of times smaller than those of a rigid cylinder of same length. Air-filled cylinders are also favored over air-filled spheres because of their broader resonance peaks, smaller required radius, and better scattering directivities near broadside[2].

Recently a rubber tube reflector similar to that in Ref. 2 was constructed at our laboratory as a low-cost artificial target. This paper studies its backscattering and bistatic target strength. In addition, we also examine two issues related to scattering from air-filled cylindrical targets; (A) the change of resonance frequency with deployment depth; and (B) the transition from near to far field and under what conditions the target can be treated as in the far field. Both are of practical importance. The resonance frequency is the primary concern in the design of such a reflector and the far field condition determines how far away we should place the target from projectors and receivers in active sonar trials.

THEORY

Our study follows Stanton's[3] analysis. The geometry is shown in Figure 1. For a plane wave of angular frequency ω, unit amplitude incident on a fluid cylinder of radius a and length L (L>>a), the scattered pressure P_s at a receiver (r,θ,ϕ) can be approximated as an integral along the cylinder

$$P_s = \frac{-iH(\theta_i,\phi)}{\pi}\int_{-L/2}^{L/2}\frac{\exp[ik(r_s + z\cos\theta_i)]}{r_s}dz \quad (1)$$

Where the z-axis runs along the cylinder axis with its origin at the middle of the cylinder, k is the wave number outside the cylinder. The parameter r_s is the distance from a differential scattering element to the receiver, $r_s = (r^2 + z^2 - 2rz\cos\theta)^{1/2}$, r is the distance to the origin, θ is the elevation angle ($\theta = \pi/2$ is broadside), ϕ is the azimuthal angle, the direction of incidence is $(\theta = \theta_i, \phi = 0)$.

The function $H(\theta_i,\phi)$ is a summation involving θ_i, ϕ, and material properties,

[a)] Now at Maritime Operations Division, P.O.Box 1500, Salisbury, SA 5108, Australia.

$$H(\theta_i,\phi)=\sum_{m=0}^{\infty} b_m \cos(m\phi) \tag{2}$$

$$\begin{aligned} &b_0=-1/(1+iC_0), \quad b_{m>0}=-2/(1+iC_m)\\ &C_m=\frac{N_m(x)-\beta_m(x_1)N_m^{'}(x)}{J_m(x)-\beta_m(x_1)J_m^{'}(x)},\\ &\beta_m=gh\frac{J_m(x_1)}{J_m^{'}(x_1)}, \end{aligned} \tag{3}$$

$$\begin{aligned} &x=ka\sin\theta_i, \quad x_1=k_1 a\sin\theta_1=x/h,\\ &g=\rho_1/\rho, \quad h=c_1\sin\theta_i/(c\sin\theta_1),\\ &k=\omega/c, \quad k_1=\omega/c_1,\\ &\theta_1=\arccos(c_1\cos\theta_i/c) \end{aligned} \tag{4}$$

where ρ,ρ_1 are densities, c,c_1 are sound speeds, outside and inside the cylinder respectively, J_m,N_m are Bessel functions of the 1st and 2nd kind, and the primes indicate derivatives with respect to argument. (Our b_m is related to Stanton's B_m by $B_m=i^m b_m$).

Eq.(1) is obtained by combining Stanton's Eqs.(23-24), assuming that end effects are negligible and the internal field of the finite cylinder is the same as that of an infinite cylinder, i.e., a differential element of the cylinder scatters sound as if it were part of an infinite cylinder of the same radius. Eqs. (2-5) were obtained by adapting Stanton's results to oblique incidence, taking into account refractions into the cylinder.

In the far field (see discussions later for far field conditions), the integral in Eq.(1) can be evaluated simply. The resultant scattered pressure can be written as the product of a spherical (r^{-1}) divergence term and a directivity term

$$P_s=(e^{ikr}/r)\,f(\theta_i,\theta,\phi) \tag{5}$$

$$f(\theta_i,\theta,\phi)=(-iL/\pi)V(\theta_i)H(\theta_i,\phi) \tag{6}$$

and the target strength TS is defined as

$$\mathrm{TS}=20\log_{10}|\,f(\theta_i,\theta,\phi)\,| \tag{7}$$

where $H(\theta_i,\phi)$ represents the change with azimuthal angle ϕ (horizontal directivity) and is given by Eq.(2); $V(\theta_i,\theta)$ represents the change with elevation angle θ (vertical directivity) and is given by

$$\begin{aligned} &V(\theta_i,\theta)=(\sin\Delta)/\Delta\\ &\Delta=kL(\cos\theta_i-\cos\theta)/2 \end{aligned} \tag{8}$$

We make the following observations:

(1) The vertical directivity follows the well-known sinc pattern. It depends on cylinder length but is independent of cylinder material properties. Its major lobe is within the angles $\arccos(\cos\theta_i\pm\lambda/L)$ (9)

(2) The horizontal directivity depends on cylinder radius and cylinder material properties. It is independent of cylinder length and is the same as that of an infinitely long cylinder of same radius.

(3) The scattering amplitude is proportional to cylinder length L at all frequencies.

(4) For backscattering $(\theta=\pi-\theta_i,\phi=\pi)$, the scattering function becomes

$$f(\theta_i)=\frac{-iL}{\pi}\frac{\sin(kL\cos\theta_i)}{kL\cos\theta_i}\sum_{m=0}^{\infty}(-1)^m b_m \tag{10}$$

For later comparison, we also give a limiting form of the field near the cylinder. When the near field condition $\lambda<r<<L^2/(4\lambda)$ is satisfied, the scattered field approaches that from an infinite cylinder with cylindrical ($r^{-1/2}$) divergence,

$$\begin{aligned} P_s=(-i/\pi)H(\theta_i,\phi)[\lambda/(r\sin\theta_i)]^{1/2}\\ \exp(ikr\sin\theta_i+\pi/4) \end{aligned} \tag{11}$$

Equation (11) was obtained by adapting Stanton's Eq.(13) to oblique incidence.

TARGET STRENGTH

Similar to the design in ref.2, the rubber tube is pressurized with a regulator to maintain its shape. The air density within a constant volume cylinder at isothermal conditions depends on ambient pressure as follows[4]

$$\rho_1=\rho_0(1+9.7\times10^{-5}\rho\, d)\ \text{kg/m}^3 \tag{12}$$

where ρ_0 is the density of the air at zero depth, d is water depth in meters. Throughout this paper we use the following nominal values, ρ_0 = 1.24 kg/m^3, c_1 = 345 m/s, ρ = 1000 kg/m^3, c = 1500 m/s.

Figure 2 shows the frequency dependence of the backscattering TS at three deployment depths for the rubber

tube target. We note that increasing the deployment depth increases the resonant frequency and broadens the resonance peaks. However, the peak target strength, along with the target strength above 1 kHz (ka>0.07) remains unchanged.

Figure 3(a) shows the backscattering TS versus frequency at different incidence angles and a deployment depth of 50 m. Because the target is long in terms of wavelength (kL = 15 at 200 Hz), the scattering has very narrow beams in the vertical plane and is very sensitive to changes in incident angles, especially at higher frequencies. Therefore, current-induced target tilt must be minimized during sea trials. In practice, we may offset this sensitivity by ensuring there is a spread of arriving angles that enclose the direction of broadside and by using broadband sources that enclose the resonance frequency.

Decreasing the target length reduces the sensitivity to incident angles, but also lowers the target strength, as expected from Eq.(10). In Fig.3(b) the length of the target was halved, vertical sensitivity is decreased and the peak TS at resonance also decreases by 6 dB.

Figure 4 shows the difference between bistatic and backscattering TS versus azimuthal angle in the horizontal plane ($\theta = \pi/2$). The small radius of the tube means that ka <<1 for the frequency concerned ($ka \approx 0.14$ at 2 kHz) and the scattering can be considered omnidirectional in the horizontal plane up to 2 kHz

RESONANCE FREQUENCY

As we have seen above, the fundamental resonance frequency is an important factor in the shape of the low frequency response of the target. Here we derive the condition for resonance and show that the resonance frequency can be expressed as a simple function of radius a, and deployment depth d.

The fundamental resonance occurs when C_0 = 0 in Eq.(3) so that b_0 attains its maximum value one. Setting

C_0 = 0 and using the asymptotic form of the Bessel functions for small arguments [Eq.(9.1.12-9.1.13) of Ref.(5)], we obtain the condition for the resonance frequency

$$x = \{2g/[-\ln(\gamma x/2)]\}^{1/2} h \tag{13}$$

where the constant $\gamma = 1.781$, x, g, h are as defined in Eq.(4). For broadside incidence, Eq.(13) reduces to the resonance condition derived by Weston[6] using an independent method.

Eq.(13) is easily solved by recursion,

$$\begin{aligned} x_0 &= (2g)^{1/2} h \\ x_{n+1} &= \{2g/[-\ln(\gamma x_n/2)]\}^{1/2} h, n = 0,1,2,... \end{aligned} \tag{14}$$

Three or four iterations quickly converge to a solution x_r with a relative error less than 10^{-3}. Given cylinder radius and incidence angle, the resonant frequency f_r is obtained by

$$f_r = (cx_r)/(2\pi a \sin\theta_i) \tag{15}$$

Ignoring temperature changes with water depth, Eqs.(12-13) can be used to study the change of resonance frequency with deployment depth. Figure 5 shows the change of ka with deployment depth for broadside incidence. There are actually three curves. Curve 1 is obtained from Eq.(14) with 3 iterations. Curve 2 is obtained by finding the zeros of C_0 numerically, without using approximations of the Bessel functions. Curve 2 completely overlaps curve 1, indicating that approximating the Bessel functions in this case introduces negligible error. Curve 3 (dashed curve) is an empirical fit to curve 2, given by

$$ka = 4.9\times10^{-3}(1+0.097d)^{0.563} \tag{16}$$

Figure 5 shows that this simple expression yields an excellent fit to the exact solutions. Eq.(16) can be written in terms of the resonant frequency f_r

$$f_r = (1.17/a)(1+0.097d)^{0.563} \text{ Hz} \tag{17}$$

where a and d are in meters. The resonant frequency given by Eq.(17) also matches those shown in Fig.2. It is interesting to note that Eq.(17) is in a similar form to the resonance frequency for spherical bubbles[7].

Using a finite element model Malme[2] calculated the target strength of a gum rubber tube of inner radius 1.55 cm, wall thickness 1.3 cm, and operating depth 90 m. His results (Figs.7 and 11 in ref.2) show a resonance frequency of 320 Hz. For an air column of the same inner radius, Eq.(17) gives a resonant frequency of 272 Hz. The difference is likely due to the effect of the rubber wall. We found that increasing the water depth to 125 m reproduces well Malme's results, indicating that the effect of the wall is similar to increasing the deployment depth. We also note that Malme's experimental measurements appear to indicate a lower resonant frequency.

TRANSITION FROM NEAR TO FAR FIELD

To arrive at Eq.(5) from the integral in Eq.(1), the receiver needs to be in the acoustic far field

$r >> \max[L, \lambda, L^2/(4\lambda)]$ (λ is the wavelength outside the cylinder) so that wavefront curvature effects from the scattering elements are negligible. For the frequencies concerned in this paper, $r >> L^2/(4\lambda)$ is the most restrictive. To answer the question of how far is "far enough", we investigate the transition of the scattered pressure from the near, cylindrical spreading to the far, spherical spreading field. The results of this section give us guidance as to how far the target should be placed from the source and receivers in designing trials.

In this section, we compare the scattered fields produced by Eq.(1) with its two limiting solutions Eqs.(5) and (11). The integral in Eq.(1) was evaluated numerically and we refer to them as exact results. For simplicity, we consider only broadside incidence $\theta_i = \pi/2$ and the common factor $(-iH/\pi)$ in Eqs.(1,5,11) was ignored.

Figure 6 shows the beam pattern of the scattered pressure at different fraction or multiples of $r_c = L^2/\lambda$. The thin solid line (marked by $r = \infty$) is the far field solution given by Eq.(6), other results at different ranges were obtained by numerical integration of Eq.(1). We see that the pressure nulls are as given by Eq.(9) and as range increases, the beam pattern approaches that of the far field. At $r = r_c$, the exact beam pattern is close enough to the far field pattern except near the pressure nulls of the sinc functions.

Figure 7 compares the exact pressure amplitude with the near and far field solutions as range increases. It illustrates the transition from the near, cylindrical spreading to the far, spherical spreading field. The solid curves are the exact results, the dotted curves are from Eq.(11), and the dashed curves are from Eq.(5). In addition, the dash-dotted curve for the case of θ = 65° is from the following equation

$$p = \pi L/(r^2 \cos\theta) \qquad (17)$$

Figure 7 shows that for $r < 0.1 r_c$ the scattered field approaches that of an infinite cylinder and falls off as $1/r^{1/2}$; for $r > r_c$ the far field Eq.(6) applies and the field falls off as 1/r, except for θ = 65°, which is near a null of $V(\pi/2,\theta)$ in Eq.(8), as also shown in Fig.6. In this case we found the exact field decays as $1/r^2$ and Eq. (17) gives a good fit as shown.

The results of this section show that the target should be placed at least $r_c = L^2/\lambda$ away from the source and receiver to get accurate, far-field results.

SUMMARY

We draw the following conclusions about the far field target strength of air-filled, pressure-regulated (i.e., constant volume) cylinders:

(1) The vertical directivity obeys a sinc pattern, with its shape dependent on λ/L and incident angles.

(2) The horizontal directivity is essentially omnidirectional up to 10 times of the resonant frequency.

(3) The frequency and breadth of the resonance increases with deployment depth. The resonant frequency can be written as a simple function of cylinder radius and deployment depth.

(4) The peak target strength at resonant frequency is $20\log_{10}(L/\pi)$, independent of deployment depth.

(5) The scattered near fields have cylindrical divergence. The scattered far fields have spherical divergences, except along certain directions indicated by the nulls of the vertical directivity pattern, where the field diverges as $1/r^2$.

The analysis in this paper is based on the following assumptions:

(1) Each scattering element of a finite cylinder scatters sound as if it was part of an infinite cylinder, i.e., the scattered pressure field on the surface of the cylinder is the same as that of an infinite long cylinder.

(2) The effect of the tube wall is ignored.

The first assumption restricts our analysis to long ($L >> a$) cylinders with negligible scattering from its ends. The second assumption restricts the wall material to be compliant, less absorptive, and with acoustic impedance close to that of water.

REFERENCES

1. T.K. Stanton, "Simple approximate formulas for backscattering of sound by spherical and elongated objects," J. Acoust. Soc. Am. 86, 1499-1510 (1989).

2. C. I. Malme, "Development of a high target strength passive acoustic reflector for low-frequency sonar applications", IEEE J. Oceanic Eng., 19, 438-448 (1994).

3. T.K. Stanton, "Sound scattering by cylinders of finite length. I: Fluid cylinders," J. Acoust. Soc. Am. 83, 55-63 (1988).

4. C.S. Clay,"Low-resolution acoustic scattering models. Fluid-filled cylinders and fish with swim bladders," J. Acoust. Soc. Am. 89, 2168-2179(1991).

5. M. Abramowitz and I.A. Stegun (eds.), Handbook of Mathematical Functions (Dover, New York, 1964)

6. D.E. Weston, "Acoustic interaction effects in arrays of small spheres," J. Acoust. Soc. Am. 39, 316-322 (1966).

7. C.S. Clay and H. Medwin, Acoustical Oceanography: Principles and Applications (Wiley, New York, 1977).

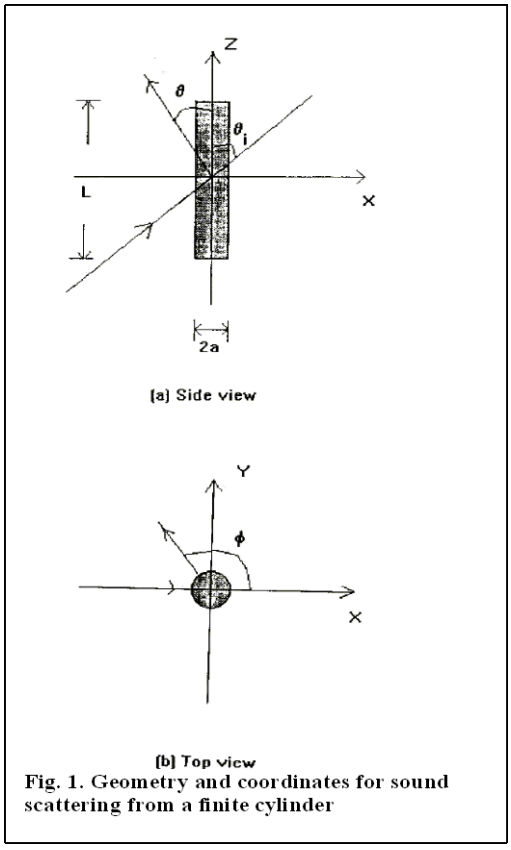

Fig. 1. Geometry and coordinates for sound scattering from a finite cylinder

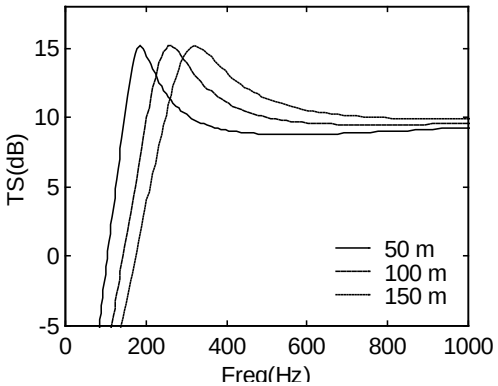

Fig.2. Backscattering TS versus frequency at three deployment depths for a gum rubber tube of outer diameter 55 mm, inner diameter 34 mm, length 18 m. Broadside incidence, the effect of tube wall is ignored.

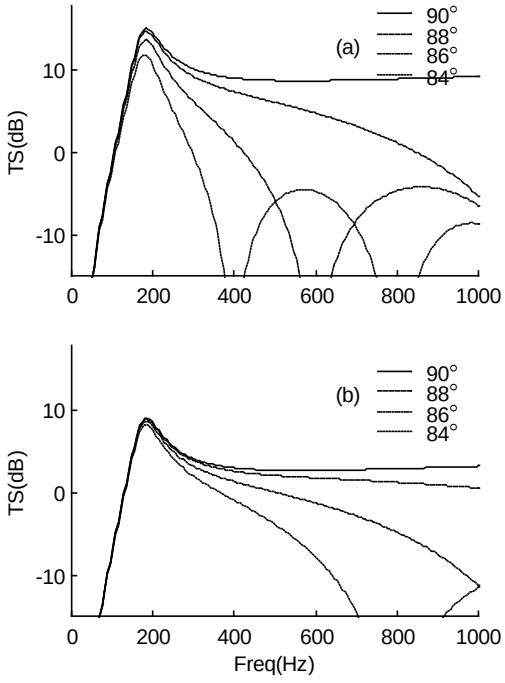

Fig.3. Backscattering TS versus frequency at different incidence angles (broadside = 90°) and a deployment depth 50 m. (a) The dimension of the tube is the same as Fig.2, (b) same as in (a) except L = 9 m.

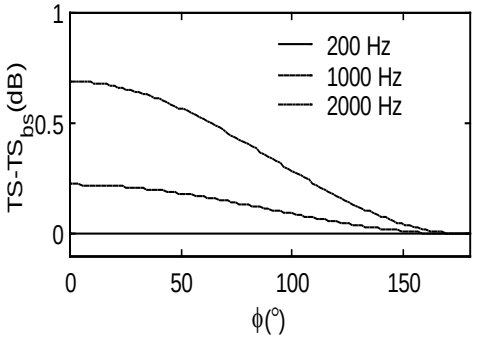

Fig.4. The difference between bistatic and backscatter (ϕ = 180°) TS versus azimuthal angle in the horizontal plane. Incidence is broadside (θ = π/2) and deployment depth is 50 m. The tube size is the same as that for Fig.2.

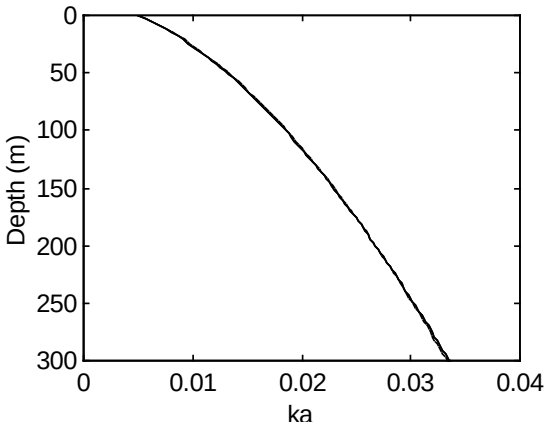

Fig.5. *ka* values at resonance versus deployment depth. Three curves, obtained from Eq.(14), Eq.(16), and by numerically finding the roots of $C_0 = 0$, overlap.

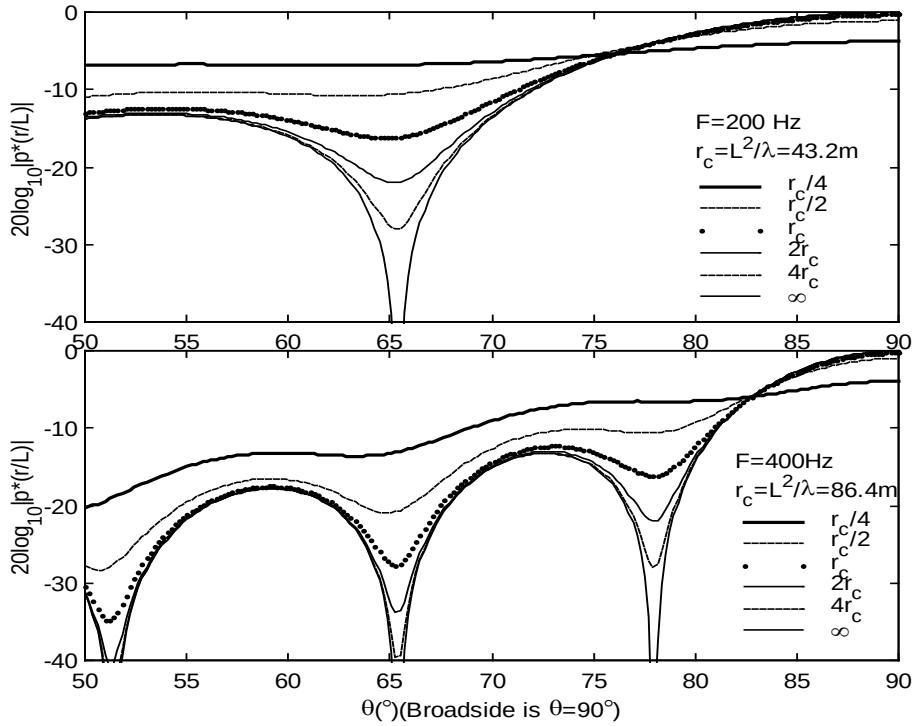

Fig.6. Beam pattern of exact and far field pressure amplitudes at multiple fractions of the characteristic range $r_c = L^2 / \lambda$, for frequencies 200 and 400 Hz.

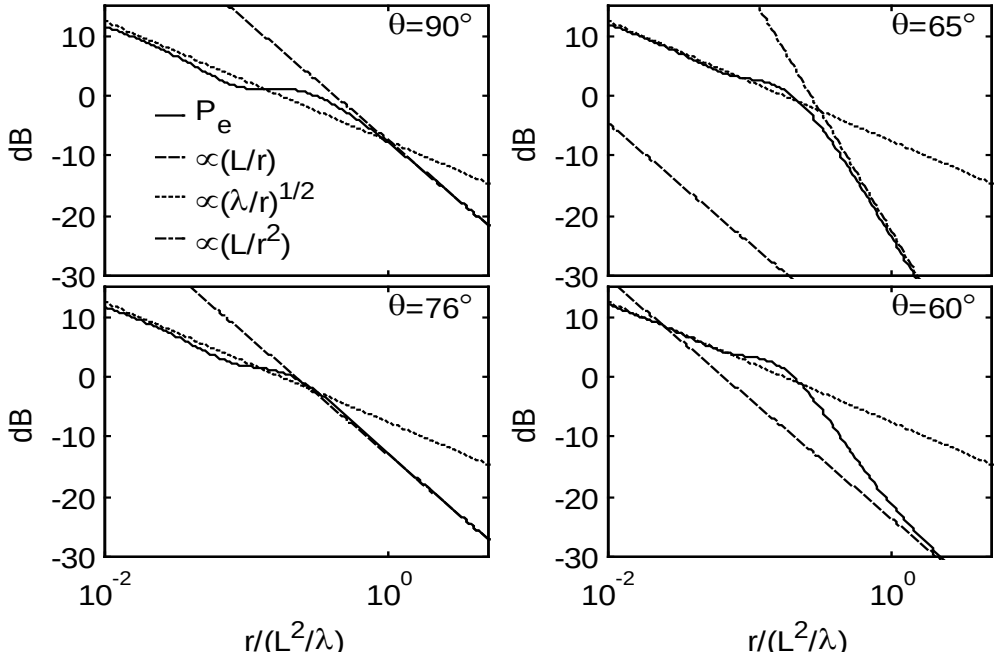

Fig.7. The exact, near, and far field pressure amplitudes versus range for different vertical scattering angles, illustrating the transition from near to far fields at 200 Hz. Broadside incidence is assumed. The far field solution near a pressure null ($\theta = 65°$) has large difference from the exact result. The extra dot-dashed line shows the results from Eq.(17) with a r^{-2} dependence.

ACOUSTICS - putting the science and technology to work

Conference of the Australian Acoustical Society
Joondalup Resort, Western Australia, 15-17 November 2000

Session AC-4 Acoustics And The Built Environment 1

Kwai Tsing Theatre - A Multi Purpose Venue With A Difference

Norm Broner and Michael J Smith

Vipac Engineers and ScientistsLtd, Victoria.

Abstract

The Kwai Tsing Theatre in Hong Kong opened in November 1999 and is expected to become a new focal point in the Hong Kong community. The new Theatre has a seating capacity of up to 940 seats and was especially designed to be a world class, multi-functional facility, catering for all different types of performances, including drama, dance, opera, music and meetings/conferences. This paper briefly discusses some of the associated acoustic issues.

Introduction

To increase access to the arts and provide local and overseas performing artists with the opportunity to showcase their rich and diverse talent, the Hong Kong Regional Services Department engaged the Architectural Services Department to design a theatre at Kwai Tsing. The HK$468 million Kwai Tsing Theatre in Hong Kong is expected to become a new focal point in the Hong Kong community. The new theatre has a seating capacity of up to 904 seats, with ancillary facilities encompassing a lecture room, an exhibition gallery, a rehearsal room, a dance studio as well as an open-air plaza.

Fig.1 View of Kwai Tsing Theatre

The Kwai Tsing Theatre auditorium was specially designed to be a world class, multi-functional facility, catering for all different types of performances, including drama, dance, opera, music and meetings/conferences.

Architectural Acoustics

The most important design aspect of any theatre is the architectural acoustics. The purpose of such design is to provide the optimum and equal sonic quality to every seat in the venue. This requires consideration of the acoustic properties of the whole venue, including the wall and ceiling surfaces, the seating and the patrons themselves. It is necessary to optimise various materials and their location to provide the desirable acoustic quality as the distribution of different materials can have a considerable impact on the perceived sound.

Today, software tools are available allowing the manipulation of the sound to provide the optimum result. These software programs include the consideration of the type of material eg. reflective, absorptive, or diffusive, and their respective locations as well as the need for an orchestral shell to “throw the sound” into the theatre and the impact of a fly-tower above the stage. To provide earlier reflections from the ceiling, reflective disks and panels have been specifically designed and strategically located. The modelling of the Auditorium Acoustics was completed by Sandy Brown Associates (UK) in cooperation with Vipac’s Hong Kong

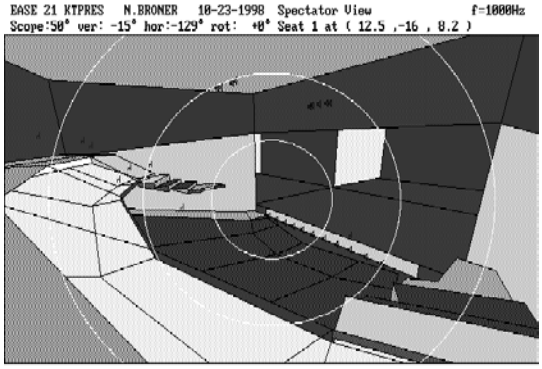

Fig. 2 Architectural Acoustics Model

office.

With the various models that can be built on the computer, it is possible to map the performance of all the important acoustics parameters and to provide a visual tool of the theatre. In addition, with the advent of fast DSP processing, auralisation of a theatre ,ie conducting a virtual sonic reality assessment of the theatre, is now possible. Such an approach helped with the final design of the Theatre. This Theatre was required to cater for many different types of use and it was necessary to consider the different Reverberation Time requirements as shown in Figure 3.

Presentation	**Ideal RT (sec@500Hz)**
Cinema	0.7 - 1.0
Pop Music	1.0 - 1.2
Speech	1.0 - 1.2
Drama	1.0 - 1.4
Op-era/Musical	1.4 - 1.6
Symphonic	1.8 - 2.5

Fig. 3 Comparison of ideal reverberation times for various types of usage for a given volume

Noise & Vibration Control

In order to achieve the optimum dynamic range for performances in the theatre, it was necessary to minimise the noise level due to extraneous and intrusive noise sources. Such sources include traffic and aircraft noise, noise due to rain on the roof, activities in the foyer of the theatre, air conditioning/heating systems and even bathroom/water noise.

To control any external noise sources, the building envelope was designed subject to consideration of wall and ceiling/roof thickness and material selection. With respect to mechanical services, it was necessary to control both duct borne and radiated noise. Duct borne noise was controlled by means of in-line silencers and in-duct absorption treatments whilst radiated noise was controlled by means of acoustic lagging and enclosure treatments. Furthermore, it was necessary to vibration isolate such plant as air handling units and fans to avoid “flanking of noise” intrusion. Kwai Tsing has an intricate network of duct work and the noise emission from the mechanical services was designed to achieve NR 20, a result that is even better than ambient noise levels in many other theatres.

Building Vibration Isolation

The Kwai Tsing Theatre is located in close proximity (18 metres away) to the KCRC WestRail underground railway line. Initial calculations resulted in a prediction that structure-borne noise was likely to exceed the noise and vibration criteria for audibility and perceptibility.

Given the initial assumptions re track location and freight train rail speed (5 metres and 100 kph), it was predicted that the use of a floating track isolation system on its own would not cater for all conditions that were possible. It was therefore decided to isolate the theatre structure from the remainder of the building in **addition** to the provison of a 8 Hz floating track slab isolation. The use of both isolation systems is a world first for this type of building. During construction, very careful attention was paid to detail as any bridging of the two structures would result in a significantly reduced acoustic performance.

Sound System Design

For venues such as the Kwai Tsing Theatre, speech intelligibility and musical clarity are of the highest importance. Vipac was involved with the design, specification and commissioning of a sound system for the Kwai Tsing Theatre. Prior to the design, client needs were reviewed with respect to the likely usage, leading to the preparation of a technical specification for the sound system, review of tenders, and on-site commissioning. Critical requirements included the achievement of the absolute sustained sound level with no clipping, uniformity of coverage, and an optimal frequency response covering the range from 20Hz to 12,000Hz. Other issues considered were channel separation, distortion, signal-to-noise ratio and the direct-to-reverberant ratio. With the help of various software tools interference/combing effects between speakers were investigated, allowing the setting of optimum delay times. Direct to reverberant ratios across the seating areas were also investigated in detail.

Electronic Reverberation Enhancement System (ERES)

To cater for all the different types of performances to be staged in the Kwai Tsing Theatre, the RT needs to

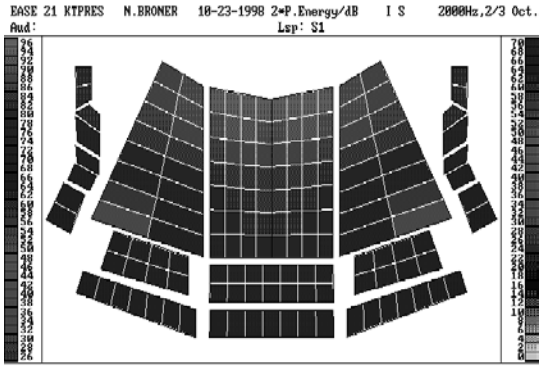

Fig. 4 Sound Pressure Level Distribution Map

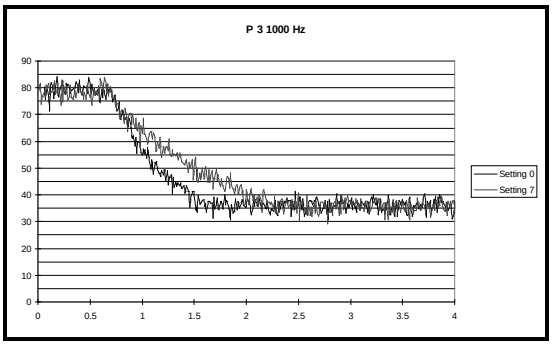

Fig 6. Sound Level Pressure Decay Curve for two ERES Settings

be altered to suit the different performance types thus improving the useability and revenue potential for the Theatre.

Two options were available for altering the RT. One is by means of varying the passive acoustics eg by changing panel orientations to alter the absorption characteristics or by means of hanging panels or retractable banner curtains which are lowered or exposed to the auditorium to introduce more absorption. The change in RT achievable using this approach is also only of the order of 0.3 to 0.5 sec, still limiting the range of venue uses.

The alternative is to install an Electronic Reverberation Enhancement System (ERES). An ERES is a recent innovation which allows the acoustics of the auditorium to be varied by electronically changing the reverberation using digital signal processing. There are two basic requirements:

- change the RT of the space in such a way that it is indistinguishable from the result that could have been achieved by architectural means;

- reproduce the sound/music without audible distortion or colouration. The objective is therefore to provide a natural sounding reflection pattern, by adjusting reflection sequences of the sound to suit various reverberation requirements.

In the case of the Kwai Tsing Theatre, the auditorium was therefore designed for a "dry" acoustics and the Electronic Reverberation Enhancement System was installed to Vipac's specifications to cater for all other performance types.

Eighteen microphones were located adjacent to the proscenium. The acoustic signal from these is fed into a digital signal processing unit (DSP) which digitally processes the inputs to provide a multi-channel digital frequency shift. This prevents feedback and provides the necessary time and magnitude shift which determines the variation of reverberation within the auditorium. This is done without any physical change to the location of or type of absorption already in the space. The result is the ideal RT to enhance the sound quality of any performance. Different RT requirements become achievable with the "flick of a switch".

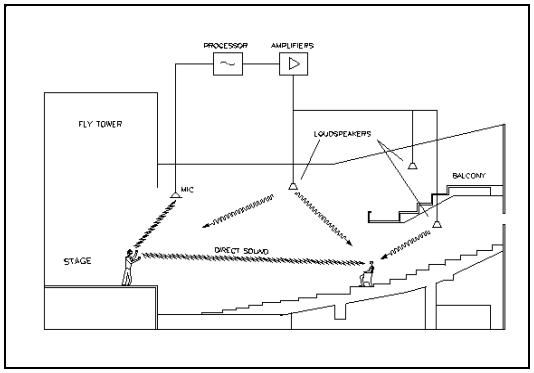

Fig 5. ERES Schematic

Enhancement Systems are capable of filling in reflection sequences in venues where "something is missing". The sound quality and naturalness of an ERES is mainly achieved by reflection density and the extent to which the reverberation sound reaches the listener's ears. Reverberation level and energy ratios of early to late and of lateral to total early reflections can easily be optimised to provide a more balanced acoustic experience. With an ERES, a performance hall can be used for many different events with the ideal reverberation time to suit each performance. For the Kwai Tsing Theatre, 7 presets were used to cater for the various performance categories from drama to musical to Chinese orchestra to Western classical.

Conclusion

The Kwai Tsing Theatre is an example of a high tech approach to theatre acoustic design and will ensure that patrons will enjoy the broad variety of performances - well into the Century.

Occupational Noise Exposure in the Building Industry

Marion Burgess and Joseph Lai

Acoustics & Vibration Unit, School of Aerospace & Mechanical Engineering
University College, The University of New South Wales,
Australian Defence Force Academy, Canberra, ACT 2600 AUSTRALIA

Abstract

There is great potential for excessive noise exposure in the general building industry as not only can the individual tools and equipment produce high noise levels but the worker is usually close to the source of the noise. This paper summarises the findings from studies of noise exposures and noise management in the building industry. The techniques for noise management are specified in Codes of Practice and should be applied in all workplaces. Investigations have shown that these techniques are not being applied in the building industry. Recommendations for strategies to encourage improved implementation are discussed. These strategies require action not just from government agencies but also from many organisations associated with the building industry. This paper summarises the findings and recommended actions necessary to put the noise management technology to work in the building industry.

Introduction

Exposure to high levels of noise is common in the construction industry as almost all the activities are noise producing. The statistics from around Australia for the building industry show that the high number of compensation claims for hearing loss, approximately 7%, is exceeded only by claims for sprains, strains, fractures, wounds etc. The types of noises that construction workers are exposed to include those which are almost constant in sound level, such as from grinding, pumping, sawing etc and those which comprise many short impact noises, such as from hammering, compacting etc. The worker is usually close to the machine or to the tool which is the source of the noise so the potential for excessive noise exposure is great. The nature of employment in the industry is quite different from most other industries. Only a small proportion of the workers are employed by a construction company and most of the workers on the sites are self employed contractors or subcontractors.

The general consensus is that there is an ongoing problem with the implementation of OHS in general on building sites. Even basic safety issues, such as hard hats and safety boots, are sometimes overlooked in order to get the job completed quickly. Protection of hearing is low on the priority list particularly as it does not become noticeable in the immediate short term. Australian National and State Codes of Practice for Noise Management [1,2] and Standards [3] have goals to minimise occupational noise-induced hearing loss and tinnitus and include sections on Noise Control Planning, Engineering Noise Control Measures, Administrative Noise Control Measures, Personal Hearing Protectors, Training and Education, Noise Assessments and Audiometric Testing. It is obvious from the high number of compensation claims that these codes are not being implemented on building sites. The aims of this project included identification of a baseline of current noise exposure levels on a representative range of building sites, assessment of the extent of the implementation of noise management codes on building sites and suggestions for strategies for improved implementation [4, 5].

Typical Noise Levels

Measurements of the noise levels for different activities on four categories of building sites were undertaken:

large city sites	large rural sites
small city sites	small rural sites

The findings were compared with data from the literature to gain an overall understanding of the noise exposure for the workers. The determination of daily noise exposure is based on both the noise level and time duration for each activity during the day. For a structured working environment where the activities are regular and predictable, the determination is reasonably straightforward. For a construction site where the activities can vary greatly throughout the day and from one day to another, the determination is far more complex. Hence there is little point in attempting to be too precise in the determinations. Based on advice from those in the industry, an estimation of usage time per day was made using only three categories:

Long	>2 hours
Medium	30 mins to 2 hours
Short	<30 minutes

This analysis led to a ranking of the tasks in terms of noise exposure as shown in Figure 1.

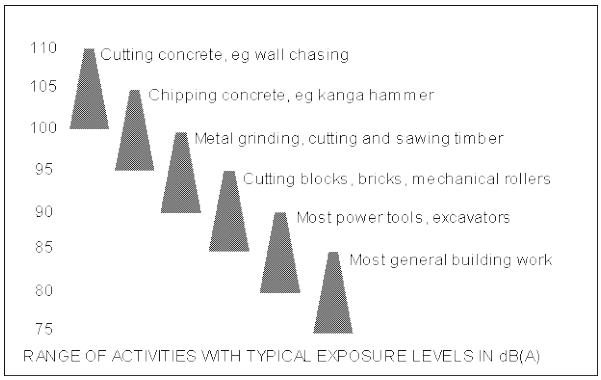

Figure 1 Ranking of tasks by noise exposure based on the types of tasks

To gain an indication of the noise exposure for various trades, they were categorised into four main groups commonly used in the industry:

Plant	includes excavation, bobcats, back hoes etc
Materials Handling	includes rigging, dogging, fork lifts, cranes, scaffolding etc
Construction	includes concreting, bricklaying, external carpentry etc
Fitout and Finish	includes plastering, tiling, painting, internal carpentry, etc

The estimated noise exposures were determined from the tasks undertaken by the various trades and are shown in Fig 2. This type of analysis shows that a large proportion of the workers on building sites are likely to have noise exposures greater than 85 dB(A) with a smaller proportion having much higher exposures. This shows that there is clearly a need for effective noise management programs for building sites.

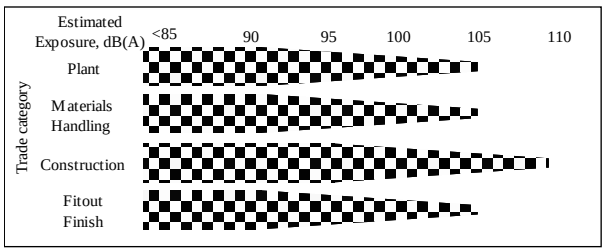

Figure 2 Estimation of noise exposure for different trades. About 50% of the workers in each trade would be within the rectangular area

Implementation of the Code of Practice

There is a similarity between the codes of practice for noise management for each of the States as they rely on the same basic principles. The examination of the extent of implementation of the Code of Practice in NSW is therefore likely to be applicable throughout Australia. Following is a summary of the assessment of the extent of implementation of each part of the code. This assessment was based on discussions with the various representatives from the industry and site inspections.

noise control planning – there was no evidence that planning for noise control was considered except where there were environmental noise constraints

engineering noise control measures – the only evidence was the use of low noise blades in brick saws and one case of placement of generator away from the workers on the site perimeter

administrative noise control measures, job rotation etc – there was no evidence that these measures were considered

personal hearing protectors – commonly these were available but usually not personally issued nor their use enforced

training and education – general OHS training usually includes some reference to use of hearing protectors but this had clearly not been adequate

noise assessment – there was no evidence that noise measurements had been undertaken

audiometric testing – there was no evidence of regular audiometric testing

Strategies for Improved Implementation

Government agencies faced with the task of improving noise management programs need to consider the actions which will be most effective for that particular industry while conforming to the government policies. For example, regular inspections and substantial fines for infringements may be effective but may not be in accordance with current policies. There are two main considerations which may be different depending on the policies and procedures for different agencies:

priority in taking action –
ie high, medium and low priority

time to implement strategy –
ie short , medium or long time

Based on the findings from this particular study, over twenty four strategies were recommended with almost

half being in the highest priority suggesting immediate action. Some strategies would only need a few months for implementation while others may take around two years. The issues addressed by the strategies for the main areas of the code of practice are summarised below.

noise control planning

A major limitation in adequate planning to minimise noise exposure is a lack of knowledge of the noise levels for plant and noise exposures for various activities. Legislation in some States includes requirements for the provision of noise level data for plant and equipment. Enforcement is needed to ensure that suppliers do in fact provide this noise level information as part of the technical data.

Many of the codes of practice for various trades, trade courses and OHS inductions include general advice about noise levels but this not sufficient for adequate noise control planning. Information is available to update and revise these documents to assist adequate noise control planning.

The implementation of work methods statements should encourage planning but they need to be checked for adequate inclusion of noise management.

engineering noise control measures

Australia imports most of the items of plant and equipment used on building sites. Thus the focus should be on encouraging the purchase or hire of those items with lower noise levels. The provision of noise data in specifications and promotional material is essential to encourage selections of items with low noise output.

Promotional material from the suppliers and the government agencies should include examples of the use of noise enclosures and simple screening as well as the importance of maintaining these noise control elements

administrative noise control measures, job rotation etc

The encouragement of multiskilling in the building industry effectively leads to job rotation which has great benefits in many aspects of OHS including opportunities for reducing noise exposure. There does need to be an effective plan and appropriate record keeping to achieve the reduction in noise exposure. Again promotional material and codes of practice can be used to encourage this aspect of noise management

personal hearing protectors

Undoubtedly these will continue to be the major form of noise management on building sites. Therefore high priority should be given to this part of the noise management program.

Unlike other protective equipment, such as hard hats and safety boots, hearing protectors are only required at specific locations on building sites so the placement of warning signs at the entry of the site is not appropriate. The warning signs should be placed at the location of the noisy activity as well as on the individual items of equipment for which typical use could lead to excessive noise exposure.

Protectors should be part of the personal safety issue to each worker and not just available from a common store area. They should be readily available so that the worker does not have to travel across the site for issue of disposable plugs.

All aspects of selection, use and care of the protectors should be an important part of the OHS induction training. Building sites can be particularly dirty environments so special attention to cleanliness and care is essential. Promotional material for the various trades should emphasise that other methods of noise control should be considered. When personal protectors are required they must be selected for personal issue in consultation with the employee to ensure comfort and suitability and to encourage consistent and correct use.

training and education

Training programs need to be targeted specifically at the building industry. A well presented training package which caters for the differing backgrounds of those working in the industry should include examples specific to the building sites. An effective mechanism would require visual presentation such as a video.

Regular items submitted to trade journals, newsletters and the general public media should increase the awareness and maintain the emphasis on noise management.

noise assessment

Government inspectors and union officers should be encouraged to undertake noise measurements as part of their visits to sites. These assessments should be primarily used for guidance to those on site for identifying potential excessive noise levels. Quantifying the noise levels would increase the general knowledge on typical noise levels and provide the opportunity to reinforce the education and training programs.

audiometric testing

While it is not a control measure itself, regular audiometric testing is an important tool for a noise management program. In particular it can be used to identify early loss of hearing and to reinforce the other aspects

of the noise management program. For many jurisdictions in Australia such testing cannot be enforced nor made a pre-requisite for continued employment or insurance cover. Under these circumstances encouragement may be provided with an incentive, such as a reduced insurance premium for regular testing.

Conclusion

This study has shown that the noise exposure for many on building sites can be excessive. Those trades involved with cutting and chipping concrete experience the higher noise exposures. The high number of claims for compensation for hearing loss indicates ineffective noise management on building sites. The study of current practices on a range of sites showed that the implementation of codes of practice for noise management is still far from satisfactory.

Strategies for encouraging improved implementation of the requirements of the codes of practice for noise management have been suggested. There is a high emphasis on education and training for all those in the building industry. Also promotion of the noise levels for different tools should encourage selection of low noise items. Personal protectors are likely to continue to be the main method of noise control and attention should be given to selection, care and maintenance.

Acknowledgment

This research is funded under the WorkCover New South Wales Injury Prevention, Education and Research Grants Scheme. The research conclusions and any views are not necessarily those of WorkCover. The authors are grateful for the financial support and technical advice from WorkCover NSW. The work would not have been completed without the enthusiastic support from the representatives of the bodies involved with OHS issues in the industry including the Construction Forestry, Mining and Energy Union, the Master Builders Association, COMET Training, Multiplex, Paynter Dixon, John Holland plus various contractors and consultants to the construction industry.

References

1 WorkCover NSW (1996a), *Code of Practice Noise management and protection of hearing at work,*

2 Worksafe Australia (1993) *Occupational Noise National Standard*, NOHSC:1007, and *National Code of Practice*, NOHSC:200

3 Australia/New Zealand Standard (1998) *Occupational noise management – Parts 0 – 4* AS/NZ 1269

4 Burgess M. and Lai J.C.S. (1999) *Noise Management For The Building Industry Current Practices and Strategies for Improvement Condensed Report*, WorkCover NSW (available at http://www.workcover.nsw.gov.au)

5 Burgess M. and Lai J.C.S. (1999) *Noise Management For The Building Industry Current Practices and Strategies for Improvement – Full Report*, WorkCover NSW (available at http://www.adfa.edu.au/amec/avu)

Further Development In Technical Textiles

Michael Coates, Marek Kierzkowski

I.N.C. Corporation Pty Ltd

Abstract

DECI-TEX® acoustic textiles are a practical alternative to foam and fiber based sound absorption materials. They help not only to eliminate the bulk normally associated with porous materials but also create new applications that are not feasible with traditional approaches. Application of acoustic textile in conjunction with traditional materials leads to weight reduction or thickness without compromising on sound absorption. Super light products, incorporating acoustic textiles have attracted the interest of the automotive manufactures where heavy felts are still widely used. Acoustic textiles laminated on to the back of the perforated panels, vastly simplifies installation in the field, which is very often the most expensive part of the project.

Note: All DECI-TEX® materials discussed in this paper are subject to pending Australian patents.

Introduction

The simplest classic sound absorber consists of a thin porous sheet located at some distance (an air gap) in front of the rigid wall. In order for this layer to be efficient as a sound absorber, the gap should not be smaller than about one tenth of the wavelength of the incident sound.

In a typical industrial environment, where a reasonable sound absorption is already required at 300-400Hz, this translates into 100mm thick gap. If the thickness of such a layer is vastly reduced such that the layer is practically in contact with a rigid backing there will be practically no absorption because the normal component of the sound wave velocity is almost zero.

This is also why the colloquial perception that the sound can be absorbed by lining a wall with a heavy fabric only is nonsense.

However, if the same thin sheet is moved away from the wall, leaving an air space or cavity between the sheet and the rigid reflective wall, such a system will display a substantial sound absorption.

There are four fundamental parameters, which control the acoustic behaviour of such a system:

- the distance between the sheet and the rigid wall
- the acoustic impedance of the enclosed media between the sheet and the rigid wall (air or selected porous materials)
- the flow resistance of the sheet
- the flexibility of the sheet

The limb sheets or flexible resistive screens are called later acoustic fabrics or DECI-TEX'es.

Low frequency response

Industrial noise control is dealing mostly with a low frequency range, where traditionally heavy and thick porous materials are used covered with perforated metal facing. Such a system will display a maximum sound absorption at one-quarter wavelength of the incident sound. For 100mm thick system the maximum is around 850Hz.

Varying the low frequency resonance

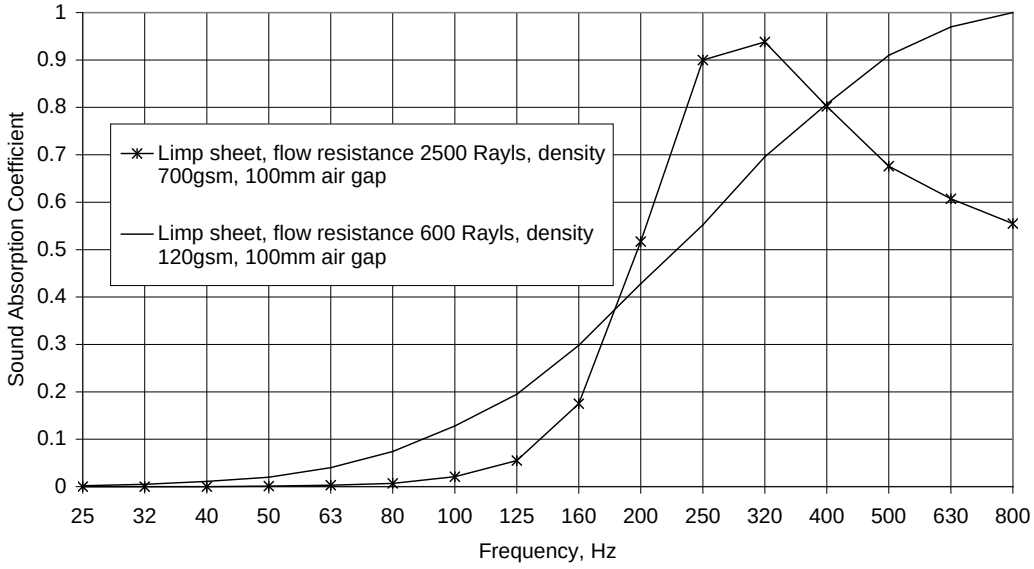

Figure 1

For a flexible flow resistive sheet, however, it is indeed possible to have the first resonance to occur at a much lower frequency. The most critical parameters in this case are the ratio between the mass of the limp sheet and the mass of the air trapped in the cavity between the limp sheet and the rigid wall and flow resistance.

At a given flow resistance of 600 Rayls (the most typical) and the mass ratio equal to 1, the resonance will occur at a predicted frequency equal to one quarter wavelength of the incident sound, ie around 850 Hz (see figure1). Increasing the flow resistance and at the same time increasing the density of the limp sheet will result in reducing the low resonant frequency down to 290 Hz. It is important that the required frequency shift was achieved without changing the air gap between the limp screen and the rigid wall.

Note: It is very important to note that for a limp screen the low frequency resonance decreases with increasing flow resistance. It will be shown later that it is not always the case in other applications.

Improved low frequency response

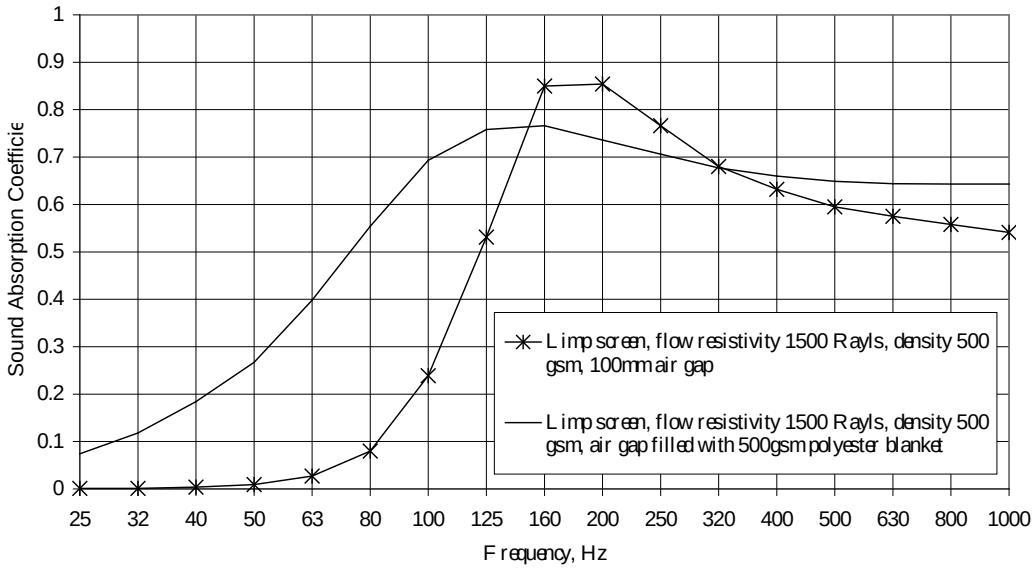

Figure 2

There is though an undesired side effect of increased flow resistance and limp screen mass – a high peak at the selected low frequency and the reduction of sound absorption coefficient in the higher frequency range.

In many situations this may be quite a satisfactory solution and a sound absorption coefficient in the range from 0.4 to 0.5 is sufficient. However for wide band noise spectrum some equalisation is required. The solution is illustrated in figure 2. The limp screen only response displays strong resonant character. Introducing light porous material infill changes this characteristic by smoothing out sharp decay in sound absorption at higher frequencies. Moreover, there is an added bonus of further improvement in the low frequency range.

Thin materials

As much as low frequency response is critical in many industrial applications, the overall product thickness is in some others. In a confined space arrangement it is important that the sound absorbing material would occupy the absolute minimum volume.

This is another excellent opportunity to implement the flexible limp screen approach:

The required frequency coverage can be achieved by tuning the flow resistance of the acoustic fabric, as explained above. Smooth and uniform frequency response can be supported by porous material infill. Indeed, in this instance, the porous material infill can also be utilised as a carrier of the acoustic fabric.

Results in sound absorption for such a construction are really amazing. Figure 3 illustrates a practical implementation of this concept. This thin and light product outperforms acoustically heavy felts, very popular in automotive and whitegoods industry.

The environmental aspect is also well addressed. One such product incorporates only polyester-based raw materials, including appropriate adhesives, and hence is recyclable.

Another good example of acoustic fabric application is a wall lining system. Traditional materials used as a wall lining provide good pin retention (notice boards) but being based on a closed cell structure, have no acoustic properties.

Acoustic fabric in this application plays a dual function. It ensures product acoustic properties as well as improves pin retention facility. The sound absorption properties are shown in figure 4.

Underbonnet insulator

The acoustic function of underbonnet insulator is rather controversial. It reduces the noise levels around the bonnet by 1.5-2dB although it has no impact on the noise exposure inside the vehicle. However it became a standard finish of the engine bonnet and all middle class and higher cars are equipped with such an insulator.

Vehicle bonnet construction is an ideal spot for the resistive screen application. Reinforcement ribs, present on every bonnet, form a natural construction support, ensuring a consistent air gap of about 20mm

Sound absorption tested in reverberation chamber to AS 1045 - 1988

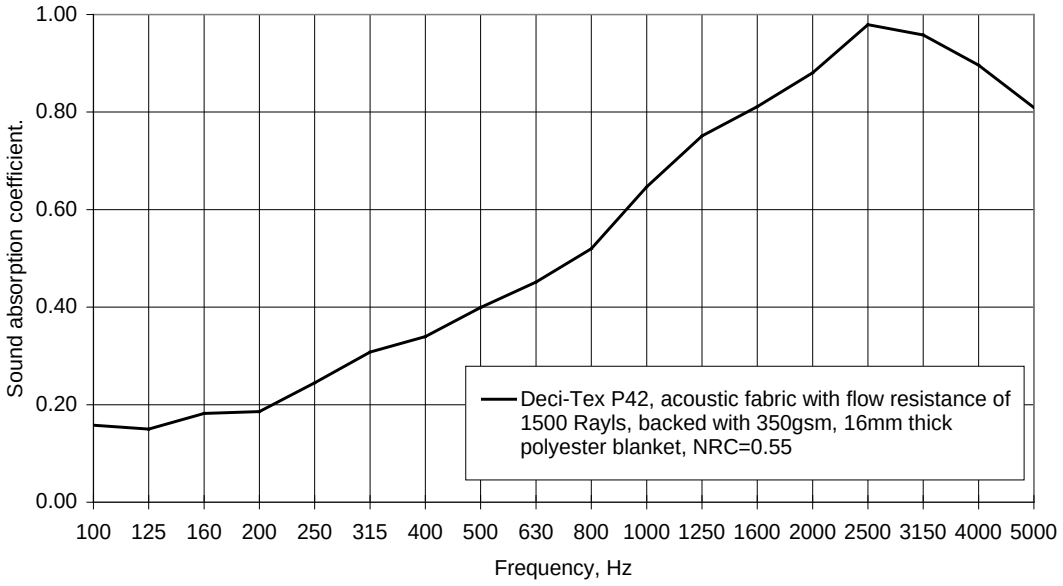

Figure 3

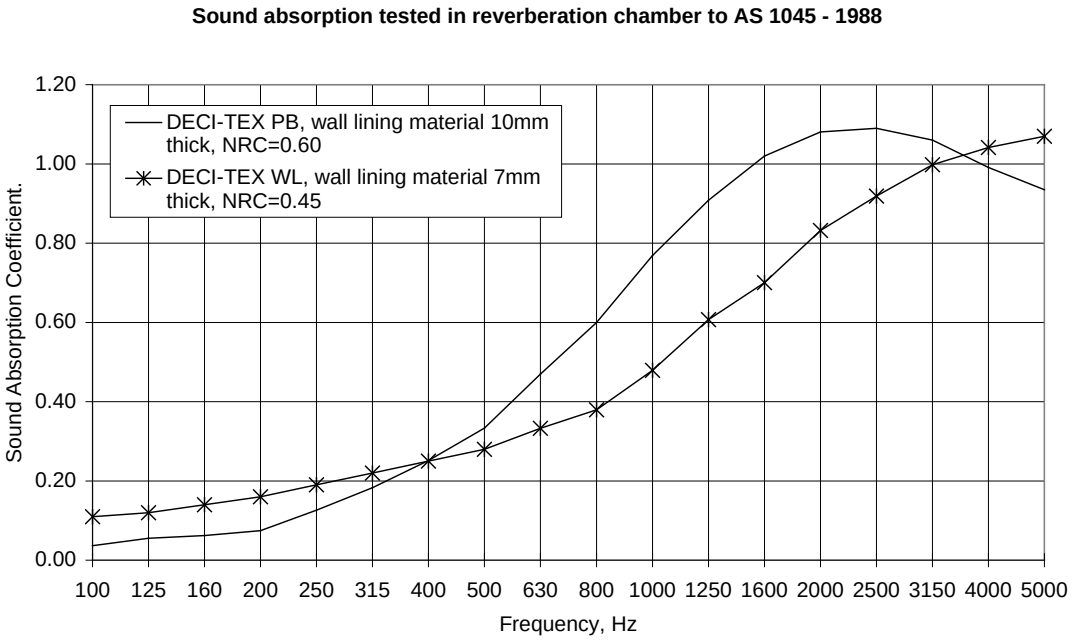

Figure 4

between the acoustic fabric and reflective surface.

Australian build cars are almost the last ones in the world still using a moulded fibreglass insulator. The most sophisticated are European cars, but also some Japanese companies have recently replaced moulded fibreglass insulators with resistive membranes.

We have developed our concept insulator about 5 years ago but there was no interest in the automotive industry at that time. Even now automotive industry in Australia still supports very old technology of moulding resin-impregnated fibreglass. During moulding process there is a substantial release of toxic gases polluting our environment.

DECI-TEX XT released recently complies with majority of the automotive requirements and is undergoing a thorough a very severe testing routine. The acoustic properties of this new resistive screen are shown in figure 5 as a comparison with actual fibreglass product.

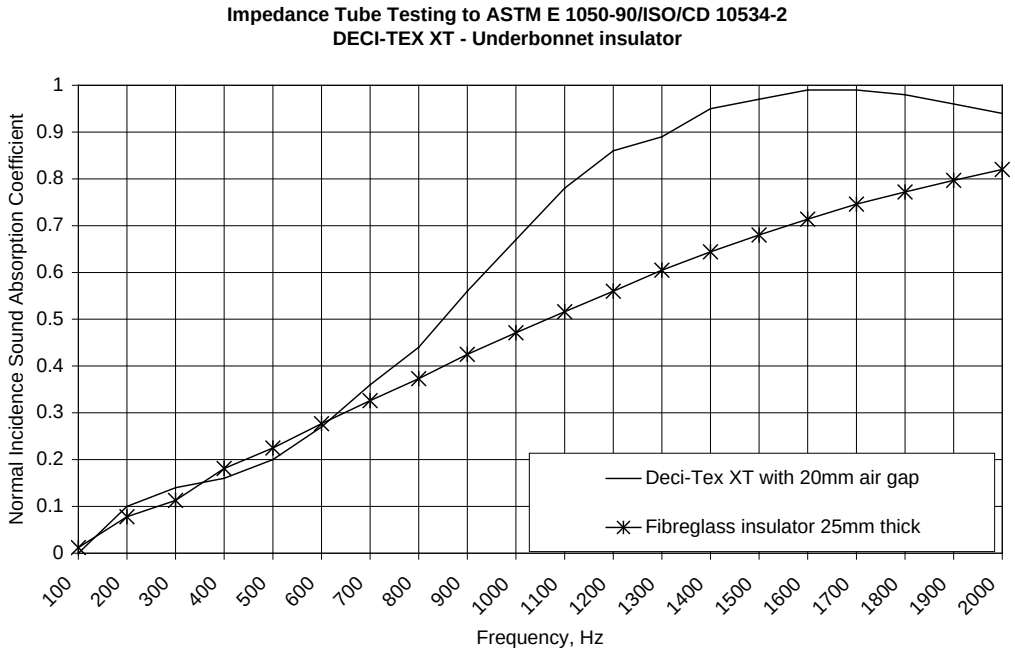

Figure 5

Conclusions

Acoustic fabrics are more recognised and are becoming more popular in all aspects of acoustics where sound absorption is required. Difficulties in understanding that something thin, light and inexpensive is acoustically efficient are the major constraint to accelerate acoustic fabric recognition.

In architectural acoustics they are price competitive, environmental friendly, easy to work with, inspiring new aesthetic designs.

In industrial application they are the only alternative to heavy and bulky products. They are durable, reliable, consistent and easy to install.

In automotive applications they are already recognised in United States as a great opportunity for weight reduction without compromising on acoustic properties. We believe that this perception will become more popular in Australia as well.

The Regulation of Sound Insulation in Australia

John L. Davy

CSIRO Building, Construction and Engineering

Abstract

On 5 April 1974, sound insulation requirements were introduced into the NSW building code. However, it was not until 1 November 1994 that sound insulation requirements applied in all states and territories. This was the date when Victoria adopted the sound insulation requirements of the Building Code of Australia (BCA). The current acoustical requirements of the BCA are less strict than those current in most other developed countries. Since 1995, there have been proposals to increase the current acoustical provisions in the BCA. These proposals appear to be nearing fruition. There are also less advanced proposals to extend the acoustical provisions of the BCA to external walls, in order to control the ingress of external noise. These increases and extensions are urgently needed because of the move back to city centres from the quarter acre block, to expensive units in multi-dwelling buildings. This need is increased by the trend to polished floorboards because of fashion and health reasons. It is further increased by the use of large woofer loudspeakers in home cinema and high fidelity sound systems.

Introduction

On 5 April 1974, sound insulation requirements were introduced into the NSW building code (NSW 1988). The current requirements for sound insulation in the Building Code of Australia (BCA) (ABCB 1996a) are based on the original NSW requirements. However, when the July 1990 version of the BCA (AUBRCC 1990) was published, its Victorian appendix deleted the application of the sound insulation requirements in Victoria. When CSIRO Building, Construction and Engineering (BCE) was trying to obtain funding for a round robin on the wall impact sound insulation measurement method in the BCA in February 1993, CSIRO BCE was told that there was a possibility that the sound insulation requirements would be deleted from the BCA because Victoria did not use them. CSIRO BCE did not obtain any funding for the proposed round robin research project because the state governments refused to match federal funding and because four research projects (mainly fire related) had already been approved in principle in advance of any money becoming available. Victoria finally adopted the sound insulation requirements of the BCA, more than twenty years after NSW, when amendment 7 was issued on 1 November 1994. This time difference is probably due to the much larger percentage of multi-dwelling buildings in NSW.

On 28 August 1995, the Association of Australian Acoustical Consultants (AAAC) proposed major increases to the sound insulation requirements. Although the proposed increases were probably justified acoustically, CSIRO BCE was concerned about the economic cost. In February 1999, the AAAC submitted their proposal again and included estimates of the cost increases of their proposed changes. However none of the proposed AAAC changes were included in the BCA amendments of the 1 January 2000.

The sound insulation requirements of the BCA only apply to floors between separate dwellings and walls between a separate dwelling and another separate dwelling or a common space. The BCA does not cover the sound insulation of building facades. The 1996 Guide to the BCA (ABCB 1996b) states that the reasons that the BCA "does not cover sound emanating from outside the building include:

- Builders, etc have little control over external sound, which are usually intermittent during daylight hours when the background ambience sound within buildings are greater; and

- Sound generated within a building is more likely to pass through walls and fittings, and cannot be controlled by simply closing a window. Such sounds can be more intrusive and disruptive to occupants."

The 1996 Guide to the BCA also states that "Because of its emphasis on building elements which separate sole-occupancy units and/or common spaces" the sound insulation requirement of the BCA" does not cover building elements which separate sole-occupancy units from outside of a building, and therefore does not cover:

- Sound generated outside a building; or

- Sound escaping from a building and re-entering via an external element."

It is probable that the main reason that the BCA does not cover the sound insulation of facades is that the external noise climate varies widely with location. Also windows and doors need to be shut in order to obtain the full sound insulation potential of the façade. Closed doors and windows mean that mechanical ventilation and probably mechanical cooling are also needed. Also the effects of acoustical shading are not well understood.

Airborne sound insulation of external facades

Australian Standard AS 2107 (1987) "Acoustics-Recommended design sound levels and reverberation times for building interiors" gives recommended satisfactory and maximum sound levels inside buildings. The requirements are expressed in A-weighted sound pressure level or noise rating number. If the external noise spectrum, the sound insulation spectra of the individual façade elements, the internal reverberation time and the effects of acoustical shading are known, the acoustical adequacy of different facades can be calculated by an acoustical expert. The first edition of AS 2107 was published in 1977.

Australian Standard AS 2021-1994 "Acoustics-Aircraft noise intrusion-Building siting and construction" gives a method for calculating the required Aircraft Noise Attenuation of each façade component (ANA_C). It also gives the average shape of spectrum for domestic or international jets landing or taking off. If the sound insulation spectrum of a façade element is known, AS 2021 gives a method for using the average spectrum shape to calculate the ANA_C. It also gives tables of the Sound Transmission Class (STC) and recommends subtracting 5 from the STC to obtain ANA_C. This value of 5 was the average difference calculated by CSIRO BCE (Dunn 1989). Unfortunately the individual differences have a large range and are systematically different between single leaf and double leaf facades. The tables should really contain ANA_C values calculated for the average spectrum shape. In the current version (AS 2021 (2000)) both the average spectrum shape and the STC tables have been deleted. Earlier editions of AS 2021 were published in 1977 and 1985.

Australian Standard AS 3671 (1989) "Acoustics-Road traffic noise intrusion-Building siting and construction" is similar to AS 2021. However it does not give an average spectrum shape for road traffic noise and the value to be subtracted from STC is 6. This value of 6 was the average difference calculated by CSIRO BCE (Dunn 1989). A draft Australian Standard on insulating buildings against railway noise is under preparation. It is similar to AS 2021 and AS 3671. The committee preparing it wishes to include tables of the railway noise attenuation of building façade elements.

Problems with AS 2107, AS 2021 and AS 3671 include that they are not mandatory under any legislation, they specify maximum internal sound levels rather than direct sound insulation requirements for the façade and that their tables of sound insulation specify the inappropriate STC.

Rating of airborne sound insulation of internal walls

In Australia, sound insulation is measured in eighteen or more different third octave frequency bands. For easy comparisons and simple calculations, an appropriate single number rating needs to be calculated from the eighteen or more individual sound insulation values. In many areas of acoustics, there is an "Atlantic divide" between the North American ASTM and ANSI standards and the European dominated ISO standards. In 1979 Australia adopted AS 1276 (1979), which specified the use of STC from ASTM E 413 (ASTM 1987) rather than the then current ISO Airborne Sound Insulation Index (I_a), which was defined in ISO R 717 (1968). I_a differed from STC only in that the bottom and top of the frequency range, that it used, were both one third octave frequency band lower than that used by STC. Both STC and I_a involved fitting the same reference curve to 16 third octave band sound insulation values such that the sum of the deficiencies below the reference curve was as close as possible to, but not greater than, 32 decibels (dB). No single deficiency was allowed to be greater than 8 dB. It should be noted that the NSW building regulations (NSW 1988) had already adopted the use of STC in 1974. The main reason for the reference curve approach was that it was much faster manually to fit a curve than to calculate a dB (A) reduction. The wide availability of personal computer spreadsheet programs has changed this situation completely. It is actually slightly harder to program the curve fitting than to calculate dB (A) reduction. The other argument advocated for the curve fitting approach is that it is less sensitive to experimental variation in individual third octave band results.

The preface to AS 1276 (1979) states that, "The classification system described in this standard applies to the derivation of a single number to denote the sound attenuation properties of walls, floors and ceilings used to divide spaces within commercial or domestic buildings. An order of rank is required for these partitions to correlate with subjective impressions of the reduction of many household and commercial sounds which have most of their energy in the mid-frequency range and relatively less in the higher and lower frequencies. The classification system described in this standard does not apply to conditions in which the sound spectra differ markedly from those of household and commercial sounds, especially in cases where low and/or high frequency components predominate. These include the sounds produced by motor vehicles, most forms of industrial machinery, and power transformers." Para-

graph A2 of AS 1276 (1979) states that "Sound transmission class…and airborne sound insulation index have application to sounds with spectra similar to that of 'standard' household sound….The 'standard' household sound is intended as an approximation of maximum sound levels that commonly occur in dwellings." Unfortunately, because there was no appropriate standardized single number rating available, STC has been widely used in Australia for rating the sound insulation of facades. As noted above AS 2021 and AS 3671 do give average corrections to STC. Unfortunately as noted above, there is large and systematic variation in the correction values for individual facades.

On 15 December 1982 ISO R 717 (1968) was replaced with ISO 717/1 (1982). In this new version, the deficiency calculations had to be carried out to an accuracy of 0.1 dB rather 1 dB, and the maximum 8 dB deficiency was deleted. Deficiencies greater than 8.0 dB were required to be reported. The resulting single number rating was given the name weighted sound reduction index and the symbol R_W. On 15 December 1996, the second addition of ISO 717/1 was published as ISO 717-1 (1996). This second edition introduced the spectrum adaptation terms C and C_{tr}. $R_W + C$ is the dB (A) reduction of a pink noise spectrum. $R_W + C_{tr}$ is the dB (A) reduction an average urban traffic noise spectrum. This strange way of expressing the dB (A) reductions is a compromise between the Germans who use R_W and the French who use dB (A) reduction of road traffic noise for rating facades. The requirement to report deficiencies greater than 8.0 dB was removed.

ISO 717-1 (1996) states that "The spectrum adaptation terms C and C_{tr} have been introduced in this second edition of ISO 717-1 … to take into account different spectra of noise sources (such as pink noise and road traffic noise) and to assess sound insulation curves with very low values in a single frequency band. (The validity of the rating obtained with the reference curve is limited in such cases.) The spectrum adaptation term in this sense replaces the 8 dB rule used in the first edition of ISO 717-1. C and C_{tr} have not been included as one single- number quantity but have been included as separate numbers. This is to ensure continuity with the reference curve system and to avoid danger of confusion of different single-number quantities of about the same magnitude. Furthermore, inter laboratory tests have shown that the reproducibility of the single-number quantity based on the reference curve is somewhat better."

"The spectra of most of the usual prevailing indoor and outdoor noise sources lie in the range of spectra" used to calculate C and C_{tr}."; the spectrum adaptation terms may therefore be used to characterize the sound with respect to many types of noise."

According to ISO 717-1 (1996), the spectrum used to calculate $R_W + C$ is appropriate for living activities (talking, music, radio, TV), children playing, railway traffic at medium and high speed, highway road traffic at greater than 80 km/h, jet aircraft at short distance, and factories emitting mainly medium and high frequencies. The spectrum used to calculate $R_W + C_{tr}$ is appropriate for urban road traffic, railway traffic at low speeds, propeller driven aircraft, jet aircraft at large distance, disco music, and factories emitting mainly low and medium frequency noise.

The second edition of AS 1276 was published on 15 November as AS/NZS 1276.1 (1999). It is a reprint of ISO 717-1 (1996) plus a preface and two appendices. As a result of this change, the BCA changed from STC to R_W on 1 January 2000. STC values measured before 1 January 2000 are allowed to be used instead of R_W.

The rating of airborne sound insulation of external walls

The Outdoor-Indoor Transmission Class (OITC) was introduced in ASTM E 1332-90 (ASTM 1990) to rate the sound insulation of facades. It is a dB (A) reduction method using the third octave band frequency range from 80 to 4000 Hz. In October 1995 CSIRO BCE was approached by the Australian Window Association (AWA) to help them develop a generic acoustical rating scheme for windows. The initial plan was for a $200,000 R&D Start project shared between National Acoustics Laboratories (NAL) and CSIRO BCE. Unfortunately this did not eventuate. At the end of January 1997, CSIRO BCE wrote a draft acoustical certification scheme for the AWA. Because CSIRO BCE was not aware that the second edition of ISO 717-1 had been published only a month earlier they recommended the use of OITC. Consideration was given to changing to $R_W + C_{tr}$ while writing the third draft in May 1997. This approach was rejected because OITC's spectrum shape agreed better with the average Australia road traffic noise spectrum shape used by CSIRO BCE to calculate the 6 dB correction to STC used in AS 3671 (1989).

More recently, under pressure from European colleagues, CSIRO BCE looked at the OITC spectrum shape again. The OITC spectrum is the average of aircraft take off, freeway and railway spectra. CSIRO BCE was surprised to discover that OITC's aircraft take off spectrum had more low frequency content than its freeway spectrum. It also has more low frequency content than the aircraft noise spectrum in AS 2021-1994. Members of Standards Australia's EV/11 committee, which was responsible for AS 2021-1994, told CSIRO BCE that the current wisdom is that the average aircraft noise spectrum in AS 2021-1994 is "about right". Prem Narang who has consulted for the Sydney Aircraft Noise Insulation Project (SANIP) has con-

firmed this. The reference for OITC's aircraft noise spectra is a 30 year old acoustical textbook The only spectral information in it that looks at all similar to the aircraft spectrum used by OITC is a graph which pertains to the time 10 seconds after the aircraft is overhead. This time was probably chosen because it is close to the middle of the over all sound pressure time history. This spectrum was measured "during take off for a commercial jet aircraft powered by four low-bypass-ratio turbofan engines, measured at a location 5500 m (18,000 ft) from brake release (the start of ground roll) with the aircraft at an altitude of approximately 350 m (1100 ft)." Given the change in aircraft noise spectra, this spectrum is probably no longer relevant. The OITC aircraft noise spectrum appears to be a smoothed version of this spectrum.

The reference for OITC's road traffic noise spectrum is a United Kingdom learned journal paper. Surprisingly the spectral information in this paper is octave band data. It is not clear how the octave band data has been extrapolated to third octave band data. The other surprise is that it is United Kingdom rather than North American data. The railway spectrum is from unpublished United States Gypsum Corporation test data. It is fairly irregular in shape. Thus there is probably not much averaging involved with this spectrum. All this new information casts some doubt on the current validity of the OITC spectrum.

More inquiries were made about the Australian road traffic noise spectra used by CSIRO BCE (Dunn 1989). Subjectively, the Canberra measurements were effected by low frequency rumble from distant traffic crossing a busy bridge across Lake Burley Griffin. The Australian Academy of Sciences, where the Canberra measurements were made, sits on relatively high ground overlooking Lake Burley Griffin. The new freeway, which was the reason for the measurements, passes through a tunnel in this high ground. The Rohans Road measurements in Melbourne were made on a secondary road, and may have been affected by low frequency noise from more distant major roads.

The Australian road traffic spectra were then compared to a number of international road traffic spectra. None of the international road traffic noise spectra had as much low frequency energy as the Australian road traffic spectra. This cast further doubt on the Australian road traffic spectra that had been used to support the OITC spectrum shape.

CSIRO BCE was also concerned about the greater uncertainty in sound insulation measurements at low frequencies. Much existing sound insulation data is only available down to 100 Hz. After considering all the above information, CSIRO BCE have recommended that the AWA draft acoustic certification scheme change from using OITC to $R_W + C_{tr}$.

The AWA had initially planned to run the acoustical certification scheme. However they have now decided that it should be an Australian Standard that is called up by the BCA. Thus the scheme still remains in its third draft form of May 1997.

In February 2000 CSIRO BCE published the final version of a report to the AWA on generic acoustical ratings for some common Australian windows and glass doors. In April 2000 CSIRO BCE wrote a two-page summary of this generic rating scheme for the AWA.

In NSW, local government authorities can specify requirements in excess of those in the BCA. Sydney City Council has exercised this right in relation to sound insulation requirements. However CSIRO BCE has been told that the councillor who pushed these extra acoustical requirements is longer in office.

Other CSIRO BCE research on sound insulation

The BCA contains four steel stud walls and a number of other types, which are deemed to meet the requirement of R_W (formerly STC) of 45. There are no deemed to comply timber stud walls. In 1988 CSIRO published a technical report, which gave the results of a literature search for timber stud walls with a STC of 45 or greater. This literature search was conducted for the Australian Timber Research Institute. This report identified a number of timber stud walls with STC's greater than 45, but none of these walls has found its way into the BCA. CSIRO has also conducted a sponsored technical study for the Brick Development Research Institute on the "Transmission of sound through single-leaf walls of clay-brick and the effect of rendering one side". Again the primary purpose of this research was to find walls with an STC or 45 or greater.

Between 1988 and 1995, CSIRO BCE conducted theoretical research on the sound insulation of double leaf partitions. A number of acoustical consultants have used this research. In November 1999, a Melbourne acoustical consultant, Douglas Growcott wrote to CSIRO BCE saying that the research had been very useful and that they would like to see further research in this area. He also suggested that research was needed in the directivity of sound radiation from large surfaces.

Impact Sound Insulation

In section FP5.1, the BCA requires that "Floors separating sole-occupancy units must provide insulation against the transmission of airborne and impact generated sound sufficient to prevent illness or loss of amenity to the occupants". Unfortunately the only requirement in the sound transmission and insulation deemed-to-satisfy provisions that applies to floors is that "A

floor separating sole-occupancy units must have an Rw not less than 45". There is no impact sound insulation requirement. An earlier commentary on the BCA (CSIRO BCE 1992) gives the following reason. "Although it is important that a floor separating sole-occupancy units adequately resists the transmission of impact sound, it has been unnecessary to raise the issue in this clause. The reason is that the deemed-to-satisfy floor constructions (for airborne sound) in Table 2 of Specification F5.2 can deal satisfactorily with impact sound as well. In reality, such floors might be covered with carpet or a resilient sheet material, either of which would improve their resistance to the transmission of impact sound.

It was thought unnecessary to impose impact sound insulation requirements for a floor with an R_W of at least 45 and which is going to be covered with thick carpet and underlay. Unfortunately this causes a problem if harder floor coverings are used in wet areas or because of allergies or decorating preferences. All the floors in the AAAC submission on the BCA are covered with carpet on underlay. This will not always be possible for the reasons given above. It is not clear what is the best way to regulate this situation. Maybe all floors have to be designed to adequately control impact sound when covered with hard floor coverings.

Although the BCA does not definitively regulate the impact sound insulation of floors, it does regulate the impact sound insulation of walls separating a bathroom, sanitary compartment, laundry or kitchen in one sole occupancy unit from a habitable room (other than a kitchen) in an adjoining unit. A wall satisfies the impact insulation requirement, if it is one of three deemed-to-satisfy walls, has two or more separate leaves without rigid mechanical connection except at their periphery, or is identical with a prototype that is no less resistant to the transmission of impact sound when tested in accordance with Specification F5.5 of the BCA than one of the three deemed-to satisfy walls. The impact isolation is measured in eighteen third octave bands. Specification F5.5 does not specify any single number rating to be used to determine if the prototype wall's impact sound insulation is better than one of the deemed-to-satisfy walls. This has caused endless argument in the acoustical community. Does the prototype wall have to be better at all eighteen third octave band frequencies? The impact sound insulation spectra of the three deemed-to-satisfy walls are known to be different. Which deemed-to-satisfy wall should one compare against? Most laboratories have only tested one of the deemed-to-satisfy walls. The most commonly tested deemed-to-satisfy wall has an airborne sound insulation of only R_W equals 47, rather than the required R_W equal to at least 50. The need to test at least one deemed-to-satisfy wall adds significantly to the cost of testing a prototype wall.

What is needed is a minimum (or maximum) single number rating for wall impact sound insulation that needs to be satisfied. The failed attempt to obtain funding for research in this area from the BCA committee means that no single number rating has been developed. Without funding, CSIRO BCE was eventually able to obtain normalized impact sound insulation spectra for one of the deemed-to-satisfy walls from four laboratories. The NAL and CSIRO Highett spectra were in rough agreement. The CSIRO North Ryde old chamber spectrum was significantly higher than the Highett and NAL spectra. The RMIT spectrum was in rough agreement with the Highett and NAL spectra at low frequencies, but crossed over to the old North Ryde spectrum at high frequencies. The test method uses a horizontal steel plate, which has to be held in contact with the test wall along its long edge. A tapping machine is operated on the steel plate. The steel plate is usually held in contact with the test wall by supporting it with two sloping legs and leaning it against the steel wall. The slope of the legs is obviously very important, but is not specified.

A little detective work revealed the following sequence of events. North Ryde developed the test and built the first plate rig. Amtek had a Sydney acoustical consultant perform some tests using a plate rig that they had built. Amtek then had Highett perform some tests using the same plate rig. Highett copied the Amtek plate rig. RMIT copied the Highett plate rig. NAL copied the RMIT plate rig. Unfortunately, Amtek had not copied the North Ryde plate rig, and the North Ryde plate rig has a different slope for its legs than all the other rigs. This explains the difference between North Ryde and NAL and Highett. RMIT have discovered and removed high frequency flanking between their two acoustical chambers. This flanking was due to concrete dags and reinforcing connecting the chambers through holes in the cork that was supposed to vibration isolate the chambers. This is believed to explain the high frequency difference between the RMIT spectra and the NAL and Highett spectra. Thus, until the plate rig and the test method are more closely specified, it is not possible to specify a single number rating limit for wall impact sound insulation.

The wall impact insulation test requires an expensive standard tapping machine of which there are relatively few available in Australia. NAL and CSR have been experimenting with single impacts from rods, balls and hammers swinging under gravity so that an impact sound insulation test could be conducted cheaply in the field. A firm of Sydney acoustical consultants has designed and constructed a horizontal tapping machine, which uses springs instead of gravity. A paper has been published in the Applied Acoustics learned journal by Taiwanese researchers (Huang *et al*. 1999) on using hard and soft ball pendulums for testing the impact sound insulation of walls. RMIT has also conducted

research on single impacts for testing the sound insulation of walls.

There is concern about the poor floor impact sound insulation provided by wood framed construction. The current impact sound insulation single number ratings appear to overrate the impact sound insulation of wooden framed floors. This is a problem when old inner city commercial buildings are converted to residential units. The Timber Development Association (NSW) has been conducting research on this problem. The standard tapping machine has five steel hammers, which it drops twice per second to create ten impacts per second. International researchers have experimented with heavier but softer impacts such as bouncing balls and tires. The standard single number impact sound ratings have very poor correlation with subjective annoyance. There is some evidence that giving more emphasis to the low frequencies improves the single number impact sound insulation ratings.

What is needed?

A suitable standard single number rating for the airborne sound insulation of external facades such as $R_W + C_{tr}$ needs to be established in the minds of all acoustical experts and the general public. Tables for this single number rating need to be produced for a wide range of generic façade elements. A range of required values of this single number rating and when they should be required needs to be made available to building inspectors, preferably through the BCA. Consideration needs to be given to increasing the existing internal wall airborne sound insulation requirements in the BCA along the lines suggested by the AAAC submission. Definitive values of impact sound insulation for floors need to be included in the BCA. The existing wall impact sound insulation measurement method in the BCA needs to be substantially improved and better specified or replaced with a better and cheaper method. Research into rating and improving the impact sound insulation of floors in timber framed buildings needs to be conducted. There should be further research into the prediction of sound insulation, the effects of acoustical shading, and the acoustical directivity of large surfaces, which radiate sound.

References

ABCB (1996a). Building Code of Australia, Volume One, Class 2 to Class 9 Buildings, Volume Two, Class 1 and Class 10 Buildings, Housing Provisions, Australian Building Codes Board, with current amendments.

ABCB (1996b.) Guide to the BCA, Class 2 to Class 9 Buildings, Australian Building Codes Board, with current amendments.

AUBRCC (1990). Building Code of Australia 1990, Australian Uniform Building Regulations Co-ordinating Council.

AS 1276 (1979). Australian Standard, Methods for determination of sound class and noise isolation class of building partitions.

AS 2021 (2000). Australia Standard, Acoustics – Aircraft noise intrusion – Building siting and construction.

AS 2107 (1987). Australia Standard, Acoustics – Recommended design sound levels and reveberation times for building interiors.

AS 3671 (1989). Australia Standard, Acoustics – Road traffic noise intrusion – Building siting and construction.

AS/NZS 1276.1 (1999). Australian/New Zealand Standard, Acoustics – Rating of sound insulation in buildings and of building elements Part 1: Airborne sound insulation.

ASTM (1987). ASTM E 413-87 (Reapproved 1999), Classification for rating sound insulation.

ASTM (1990) ASTM E 1332-90 (Reapproved 1998), Standard classification for determination of outdoor-indoor transmission class.

CSIRO DBCE (1992). Commentary on the Building Code of Australia 1990, CSIRO Division of Building Construction and Engineering, Second Edition 1992.

Dunn, I. P. (1989). Comparison of STC rating to dB(A) reduction for aircraft and traffic noise, Acoustics Australia, 17(1), 11-13.

Huang, S.-P., Chen, K.-T. and Lai, R.-P. (1999). Development of standardized impact sources for laboratory measurement of sound transmission through lightweight walls, Applied Acoustics, 58, 333-349.

ISO R717 (1968). ISO Recommendation, Rating of sound insulation for dwellings.

ISO 717/1 (1982). International Standard, Acoustics – Rating of sound insulation in buildings and of building elements – Part1: Airborne sound insulation in buildings and of interior building elements.

ISO 717-1 (1996). International Standard, Acoustics – Rating of sound insulation in buildings and of building elements – Part1: Airborne sound insulation.

NSW (1988). Ordinance No. 70 under the Local Government Act 1919, New South Wales, Reprinted as at July 1988.

Aircraft Noise Impact Assessment Validation and Single Event Descriptors

Dr Peter Teague

Vipac Engineers & Scientists Ltd

Abstract

We describe the prediction and assessment of the noise impact of aircraft movements associated with the Runway Extension project for the Adelaide International Airport. As a critical component of the Environmental Impact Statement, the work involved detailed modelling of aircraft movement and operational scenarios.

There has recently been a paradigm shift associated with using the standard ANEF system (equal energy contours) for the prediction of aircraft noise impact and community responses. As a result, in addition to the generation of time-averaged ANEF contours, simulation of individual aircraft events such as overflights, take-offs/breakaway thrust and ground movements (eg. taxiing) was undertaken. In particular, emphasis was placed upon single event noise descriptors (ie. peak indices such as LAmax as opposed to equivalent energy indices), which facilitated clear communication of the likely impact with community groups.

Two long term (over four months) noise monitoring programs were carried out at 15 sites in the vicinity of the airport. Over 20,000 recorded aircraft noise events were accurately (over 95% success rate) cross-correlated with flight time-stamp data and prevailing meteorological conditions. The statistically robust data-set provided accurate validation of the prediction of noise levels in nearby residential areas for different aircraft types and operational scenarios.

ACOUSTICS - putting the science and technology to work

Conference of the Australian Acoustical Society
Joondalup Resort, Western Australia, 15-17 November 2000

Session UW-4 Propagation And Geo-Acoustic Inversion 1

Long-Range Undersea Transmission of Aircraft Noise

Scott Foster

Maritime Operations Division, Defence Science and Technology Organisation

Abstract

When treating the transmission of spherical sound waves from air to water it is customary to take geometric acoustics as the first approximation, and add higher order correction terms to achieve successive approximations. This approach runs into serious difficulties when the geometric incidence angle is close to the critical angle of total reflection, at which point various correction terms approach infinity and the leading order geometric acoustics term bears little resemblance to the actual acoustic field. A uniform asymptotic expansion of the transmitted sound field that takes into account the behaviour at the critical angle, has recently been derived at DSTO. As with standard theory, the leading order term admits a geometric ray interpretation, however refraction angles for angle of incidence close to the critical angle deviate from Snell's law. In this paper we demonstrate how deviations from standard geometric acoustics close to the critical angle can have serious implications for the long-range transmission of aircraft noise in the undersea environment.

Introduction

The underwater sound field due to a source in air is of considerable interest in sonar applications, particularly the detection and tracking of aircraft from submarine and bottom mounted sonar arrays. Tracking and localisation algorithms rely on a clear understanding of the geometric relationship between the source location and the acoustic signal. This relationship is most simply and conveniently expressed via geometric ray theory which was first applied by Hudimac [1] and later by Urick [2] to characterise the underwater acoustic field due to a source in air.

The refractive index n of the air-water boundary is approximately equal to 0.2 which means that according to Snell's law of refraction ($\sin\theta_i = n\sin\theta_r$, where θ_i and θ_r denote the angles of incidence and refraction respectively), the critical angle of incidence at which the refraction angle becomes 90^o is less than 13^o. Thus, only that part of the incident acoustic field whose propagation direction is nearly normal to the surface is transmitted. It is therefore not surprising that most of the acoustic energy entering the water tends to be directed vertically downwards. In fact, ray theory predicts that the angular distribution of energy is proportional to $\cos^2\theta_r$. Thus, so far as an underwater observer is concerned a point source above the water is effectively equivalent to a vertically oriented dipole source at the ocean surface.

The use of the ray approximation in modelling air-water transmission has been justified by various authors based on application of the method of steepest descent [3,4] and normal mode approximation [5] to plane wave decompositions of the acoustic field. These methods give the ray theory solution (plus an evanescent surface wave which is negligible for depths greater than one wavelength) as the principle far-field component of the transmitted acoustic field; i.e. deviations from ray theory fall off rapidly with distance until, for observers sufficiently far from the source, the field is equivalent to that from an ideal dipole source at the air-water interface directly below the actual source.

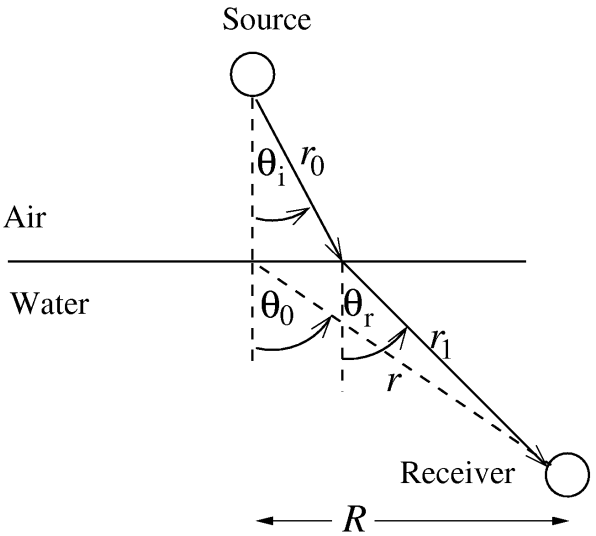

Figure 1. Geometry of air-water transmission

An immediate corrolory of these conclusions is that no "direct path" acoustic signal is transmitted to observers whose distance from the source is very large compared to their depth (i.e. as $\cos\theta_r \to 0$), and therefore that aircraft can not be detected at long range unless significant bottom interactions occur.

The approximations which lead to the above conclusions become invalid in the asymptotic region $\theta_r \cong \pi/2$ (i.e. as the incidence angle approaches the critical angle) where the field is predicted to approach zero. In this region the higher order corrections to geometric acoustics approach infinity and consequently the leading order "ray theory" term bears little relationship to the actual acoustic field. This is unfortunate since it means that these approximations have little useful to say on many of the questions that are important in underwater detection of aircraft. For example, determining maximum range of detection or predicting whether the measured signal is dominated by "direct-path" or "multi-path" propagation modes requires an understanding of transmission at refraction angles arbitrarily close to 90^o. On the other hand we are reluctant to abandon the ray model due to its geometrical simplicity and consequent practical usefulness.

An alternative quasi-geometric approximation, which remains regular at angles approaching the critical angle, has recently been proposed by the author [6]. The method taken differs from the standard one in that the acoustic field is represented as a sum over all possible propagation paths rather than a superposition of plane waves. The formulation of the problem is thus intrinsically geometric and the interpretation of solutions in terms of ray propagation paths is more immediate than is the case with plane wave decompositions where one relies on the identification of the wave-vector with the tangent to ray paths. This works well if the solution is dominated by a single plane wave component but becomes ambiguous otherwise.

When the underwater field is treated in terms of propagation paths one finds that as $\theta_r \to \pi/2$ the dominant path contributing to the far-field signal is one which does not satisfy Snell's law (although the deviation is small). Furthermore, unlike the cosine-squared distribution predicted by ray-theory, the angular distribution of refracted energy does not tend to zero as the refraction angle approaches 90 degrees but approaches a non-zero limit which is small but significant. Note that this angular distribution can not be derived using purely geometric arguments. Thus the non-zero energy at angles close to $\pi/2$ can be attributed to diffraction at the edges of the geometric "acceptance cone".

Although the deviations from geometric acoustics are small they have significant implications for the far field transmission of acoustic energy from airborne sources. In the current paper we illustrate this by considering a simple isospeed ocean environment.

We shall begin with a brief discussion of the plane wave decomposition of the acoustic field and how this leads to acoustic ray theory in the far field limit. It shall become clear that the ray approximation can not be applied close to the critical angle. We shall then introduce an alternative model of the underwater sound field based on the approach discussed above. Finally we shall present the results of simple underwater propagation modelling which suggest that the dipole source model leads to a serious underestimation of the significance of direct path propagation in the far field acoustic signal due to an airborne source.

Plane Wave Representation of the Sound Field and Ray Acoustics.

Consider a point source with frequency f located at some point $\mathbf{r}_0$ in air. Denote by c_a the speed of sound in air. This source gives rise to a spherical wave

$$p(r) = \frac{\exp[-i(\omega t - kr)]}{r} \qquad (1)$$

at distance r, where $\omega = 2\pi f$ and $k = \omega/c_a$. Henceforth we shall set $t=0$ and neglect the temporal variation of p. If we choose a coordinate system (x,y,z) with z being the vertical axis then, by taking the Fourier transform of the above equation with respect to x and y it can be shown [4] that

$$p = \frac{i}{2\pi} \int_{-\infty}^{\infty} \exp[i(\xi_1 x + \xi_2 y + \eta|z|)] \frac{d\xi_1 d\xi_2}{\eta} \qquad (2)$$

where

$$\eta = \sqrt{k^2 - \xi_1^2 - \xi_2^2} = \sqrt{k^2 - \xi^2}$$

and we have defined $\xi = (\xi_1^2 + \xi_2^2)^{1/2}$. Thus a spherical wave can be represented as a superposition of plane waves. Each plane wave component propagates at an angle θ to the vertical axis where $\xi = k \sin\theta$ and $\eta = k \cos\theta$. The refraction of plane waves at a planar interface is straitforward: the refracted plane wave is given by the product of the incident plane wave and the transmission coefficient

$$W(\theta) = \frac{2m\cos\theta}{m\cos\theta + \sqrt{n^2 - \sin^2\theta}}$$

where $n = c_a/c_w$ is the refractive index and $m = \rho_w/\rho_a$ is the ratio of the densities of water and air. For the air-water interface m=770. Thus $W \approx 2$ for almost all θ except near $\theta = \pi/2$ where it approaches $-2im\cos\theta$. If we choose coordinates such that the plane $\{z=0\}$ corresponds to the air water interface and the source has coordinates $(0,0,z_0)$, then the refracted wave at depth $-z$ becomes

$$p = \frac{i}{2\pi}\int_{-\infty}^{\infty} \exp\left[i\left(\xi_1 x + \xi_2 y + \eta z_0 - \eta_1 z\right)\right] W(\xi)\frac{d\xi_1 d\xi_2}{\eta}$$
$$= \frac{i}{2}\int_{-\infty}^{\infty} H_0^{(1)}(\xi R)\exp\left[i\left(\eta z_0 - \eta_1 z\right)\right] W(\xi)\frac{d\xi}{\eta} \qquad (3)$$

where $H_0^{(1)}$ is a Hankel function of the first kind, R is the horizontal distance from source to receiver (Fig. 1), and

$$\eta_1 = \sqrt{n^2 k^2 - \xi^2}$$

Equation (3) is an *exact* integral representation of the underwater acoustic field. We now seek an asymptotic approximation that may be identified with ray theory. The standard approach is to derive a series expansion in powers of R^{-1}. Note that the case when the receiver is directly below the source must be excluded. Consider the unique ray path joining the source and receiver which satisfies Snell's law of refraction at the air-water interface (Fig. 1). Let $R=r_0\sin\theta_i+r_1\sin\theta_r$ where r_0 and r_1 are the respective lengths of the in-air and in-water components of this path, as shown in Figure 1. Consider the case $r_1>r_0$ and define $\sigma=r_0/r_1<1$.

Introducing the new integration variable $q=\xi/k=\sin\theta$ it follows from the asymptotics of the Hankel function that for R large the integral may be written

$$p = \left(\frac{k}{2\pi R}\right)^{1/2} e^{i\pi/4}\int_{-\infty}^{\infty} dq F(q)\exp\left[ikr_1 f(q)\right] \qquad (4)$$

where

$$F(q) = \frac{2mq^{1/2}}{m(1-q^2)^{1/2} + (n^2-q^2)^{1/2}}$$
$$f(q) = q\sin\theta_i(\sigma + n^{-1}) + (1-q^2)^{1/2}\sigma\cos\theta_i + (n^2-q^2)^{1/2}\cos\theta_r \qquad (5)$$

When r_1 is large the integrand is a rapidly oscillating function of q except near points at which the derivative of $f(q)$ vanishes. In the vicinity of such points adjacent terms in the integral constructively interfere and reinforce one-another whereas otherwise they tend to destructively interfere. Thus it is reasonable to suppose that the integral will be dominated by those regions in the immediate viscinity of the stationary points. Suppose there exists a single stationary point q_s. The stationary phase approximation consists of Taylor expanding F and f in powers of $(q-q_s)$ and re-writing the integral as a series of standard integrals.

Neglecting the details, one finds that to leading order the integral term in (4) becomes

$$\exp[ikr_1 f(q_s)]\left(\frac{2\pi}{ikr_1 f''(q_s)}\right)^{1/2} \times \left(F(q_s) + O\left(r_1^{-1}\left(\left|F''(q_s)\right| + \left|F'(q_s)f'''(q_s)\right| + \left|f''''(q_s)\right|\right)\right)\right) \qquad (6)$$

where the $O(.)$ notation should be read "terms of order (.)" and the primes indicate differentiation with respect to q. It is easily verified that $q_s=\sin\theta_i$ is the unique stationary point of (4). Interpreted physically, this says that the dominant plane wave is precisely that one whose propagation direction is tangent to geometric ray path (satisfying Snell's law).

Evaluating f and F at q_s we find

$$F(q_s) = \frac{2(\sin\theta_i)^{1/2}}{\cos\theta_i}$$
$$f(q_s) = \sigma + n^{-1} \qquad (7)$$
$$f''(q_s) = -\frac{\sigma}{\cos^2\theta_i} - \frac{1}{n\cos^2\theta_r}$$

where a term of order m^{-1} has been ignored. To leading order in r_1^{-1} the expression for the pressure becomes

$$p = -\left[\frac{2n\cos\theta_r}{\cos\theta_i}\right]\frac{\exp[ik(r_0 + n^{-1}r_1)]}{r_1} \qquad (8)$$

which is in agreement with geometric acoustics. According to Snell's law $\theta_i^2<n^2<<1$. Thus, $\cos\theta_i\cong 1$ and the pressure field may be replaced by a dipole source at the surface with directivity $\cos^2\theta_r$ and intensity $4n^2$ times that of the true source.

We now turn our attention to the higher order terms in (6). The stationary phase approximation is rigorous when F and f are real analytic functions of q however inspection of (5) reveals singular points at $q=\pm 1$ and $q=\pm n$ where these functions become complex and their derivatives become infinite. In particular, as θ_i approaches the critical angle $\sin\theta_i=\pm n$, $q_s\to\pm n$; i.e. the point of stationary phase approaches a point where no Taylor expansion is possible. To see how this behaviour effects the approximation (6) we evaluate the higher derivatives of F and f at q_s. We find that the $r_1^{-3/2}$ term in (6) varies as $\cos\theta_r^{-3}$ which clearly diverges as $\theta_r\to\pi/2$. Moreover, inspection of (7) reveals that the $\cos\theta_r$ term in the ray approx (8) is actually a direct consequence of the fact that f'' diverges as $1/\cos^2\theta_r$ at the critical angle.

It is thus clear that the ray approximation resulting from the method of stationary phase is not valid in the limit $\cos\theta_r \to\pi/2$. It is important to note also that the error does not appear to be accounted for by an evanes-

cent surface wave as is often stated in the literature [2,4]. The evanescent wave decays as $1/z$ whereas the errors in the geometric approximation are of order $1/\cos\theta_r = r_1/z$. For r_1 sufficiently large the error can be arbitrarily large even when z is much larger than one wavelength.

Modelling the acoustic field in regions where the distance of the receiver from the source is much larger than its depth requires an alternative approximation than that provided by ray theory. It is not immediately obvious how to express the plane wave decomposition (4) in terms of a series of standard integrals since it is not possible to regularly transform the phase term $f(q)$ into a quadratic power; i.e. no smooth map $q \to s$ exists such that $f(q) \to a + bs^2$. In the next section we present an approximation based on an alternative decomposition of the acoustic field.

Kirchhoff Integral Representation of the Sound Field.

In the previous section the acoustic field was represented as an integral over plane waves. The advantage of the plane wave decomposition is that we know how to treat the refraction of a plane wave *exactly.* For this reason it represents a natural approach, however, it is by no means the only integral representation of the acoustic field. The breakdown of the stationary phase method can be interpreted physically as an indication that no single plane wave component dominates in the far field. We seek an alternative representation, which might admit a more simple asymptotic structure.

Let $\mathbf{r}=(x,y,0)$ be an arbitrary point on the ocean surface, $\mathbf{r}'=(x',y',z')$ be the location of the observer (underwater), and $r0=(0,0,z_0)$ be the source location. As before let r_0 and r_1 be the distances from source to $\mathbf{r}$ and $\mathbf{r}$ to receiver respectively. It is shown in [6] that the acoustic field at $\mathbf{r}'$ can be written

$$p = \frac{1}{2\pi}\int_{-\infty}^{\infty} \frac{\partial p}{dz}\frac{\exp[ikr_1/n]}{r_1}dxdy$$

where the integral is evaluated on the *lower* side of the ocean surface. The above is an example of the Kirchhoff integral representation of the acoustic field and is totally independent of the location or nature of the source in air. In physical terms it states that each point on the air-water interface may be viewed as a secondary point source with complex amplitude $\partial_z p/2\pi$. We shall argue below that the far field signal is dominated by contributions from a localised region directly below the source therefore providing a physical basis for modelling the underwater sound field in terms of a virtual source at the surface.

When the field is due to a point source at r0 it can be shown that there exists a transmission amplitude A such that the Kirchhoff integral becomes

$$p = \frac{-ik}{4\pi}\int_{-\infty}^{\infty} A(\theta)\frac{\exp[ik(r_0 + r_1/n)]}{r_0 r_1}dxdy \qquad (9)$$

where θ is the angle that $\mathbf{r}_0$-$\mathbf{r}$ makes with the vertical; i.e. $(x^2 + y^2)^{1/2} = r_0\sin\theta$. Inspection of (9) reveals that the pressure field has been represented as a weighted sum over all possible propagation paths between the source and receiver via an arbitrary intermediate point at the air water interface. Note that only one of these paths obeys Snell's law. This is precisely the path for which the phase term $r_0 + r_1/n$ is stationary with respect to variations of (x,y). This path is an extremal of the "optical path length" $r_0/c_a + r_1/c_w$ in accordance with Fermat's principle. This suggests that approximate "ray like" solutions might be found by expanding about this stationary path; i.e. by applying the method of stationary phase. The situation is complicated by the fact that A is a complex number whose own phase is dependent on θ. In applying the method of stationary phase it is important to identify the path (or paths) for which the overall phase of the integrand is stationary. This leads to a geometric acoustics for which the angle of refraction deviates from Snell's law. The detailed calculation is carried out in [6] while the main results are summarised here.

Although no exact expression for A is known, when $r_0 >> 1$ it may be approximated by the following

$$A(\theta) = 2^{5/2}(kr_0)^{-1/4}(\sin\theta\cos\theta)^{1/2}e^{u^2/4 - i\pi/8}D_{1/2}(u)$$

where

$$u = e^{-i\pi/4}(kr_0)^{1/2}\left(\frac{n^2 - \sin^2\theta}{2\cos\theta\sin\theta}\right)$$

$D_{1/2}$ is a parabolic cylinder function [7]. Note that the apparent singularity at $\theta=0$ is superficial. A is smooth and non-zero for all values of θ. Typical amplitude and phase behaviour is shown in Figure 2. Note that as $r_0 \to \infty$ A approaches the plane wave transmission amplitude (which is singular at $\sin\theta = n$). Taking the phase of A into account the path of stationary phase in (9) is found to be that which satisfies

$$n\sin\theta_r = \sin\theta_i + \phi'(\theta_i)/kr_0$$

where ϕ is the phase of A. Note that this reduces to Snell's law in the limit $r_0 \to \infty$. Since ϕ is a rather complicated function of θ it is difficult to explicitly invert this expression to obtain θ_i as a function of θ_r, however the following simplified refraction law provides an adequate approximation

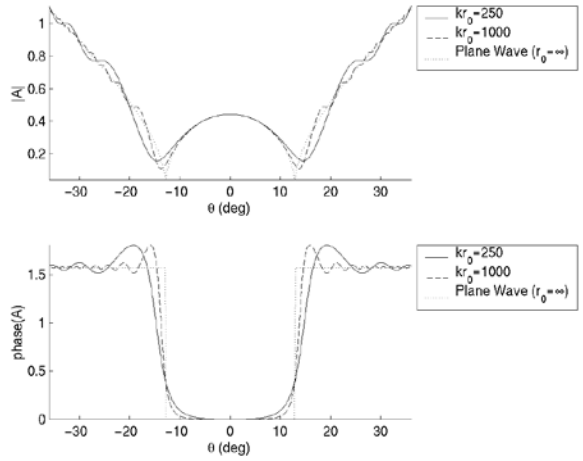

Figure 2. The transmission coefficient A.

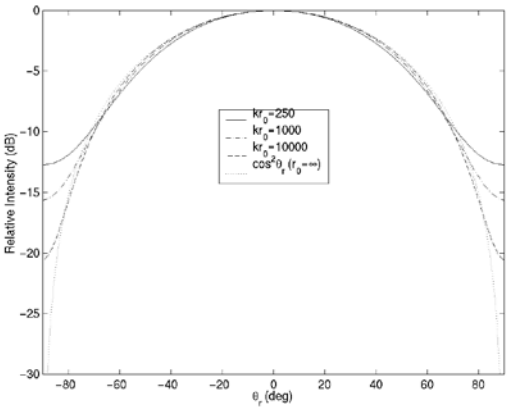

Figure 3. The transmitted directivity for various source heights.

$$\sin\theta_i = n\sin\theta_r - \beta(kr_0)^{-1/2}\left(\frac{2\theta_r}{\pi}\right)^3 \qquad (10)$$

where $\beta \cong 0.19$.

Having established a refraction law, the method of stationary phase may be applied to obtain an asymptotic expression for the underwater sound field as a function of range r_1 and refraction angle θ_r:

$$p = 2n\left(\frac{-A(\theta_i)}{4+4\gamma\left(\frac{2\theta_r}{\pi}\right)^{2\log kr_0-2}}\right)\frac{\exp[ik(r_0+n^{-1}r_1)]}{r_1} \qquad (11)$$

where $\gamma \cong 0.52$. Once again this expression has been simplified to avoid having to explicitly calculate derivatives of ϕ. θ_i and r_0 are evaluated for the particular path that satisfies the generalised refraction law (10). Equation (11) should be compared to the ray theory approximation (8). The two agree near $\theta_r=0$ but disagree in the limit $\theta_r \to \pi/2$ as shown in Figure 3.

Note that since θ_i is small r_0 can be identified with the height of the source above the water. In the limit $r_0 \to \infty$ (11) tends towards geometric acoustics.

Equation (11) may be interpreted as the principle spherically spreading component of the underwater acoustic field and, as with ray theory, it may be identified with a virtual point source at the ocean surface (once we identify r_1 with the range r in Figure 1, and θ_r with θ_0). Higher order components of the underwater field are significant only in the near field. Although the presence of the ocean bottom has not been taken into account in the above derivation we expect, on physical grounds, that the source characteristics as viewed from the far field should be largely independent of the environment. Thus, quite generally, it would seem reasonable to replace the airborne source with a source at the ocean surface characterised by a source strength $4n^2$ and a radiation pattern $I(\theta)$ equal to the magnitude squared of the bracketed term in (11). We shall call this the Kirchhoff source model. Alternatively, ray theory predicts a much simpler radiation pattern $I(\theta)=\cos^2\theta$, which we shall call the dipole source model.

In the next section it is demonstrated that the two models do not lead to qualitatively similar results.

Far Field Transmission in an Isospeed Ocean

It has been argued above that the ray theory model of air-water transmission is inadequate when the refraction angle is close to 90 degrees, and hence that it can not be applied when the distance of the receiver from the source is very large compared to its depth. In this section we show that the dipole source model can significantly underestimate the importance of direct path propagation at long ranges.

As discussed above, in order to model the underwater sound field we replace the source in air with a source at the surface directly below the aircraft. We shall use ray theory to model the *underwater* propagation. Each ray is assigned an intensity $4n^2 I(\theta) \times$ *true source strength* at 1 m from the virtual source according to its propagation direction θ. The intensity of each ray decreases as $1/r^2$, where r is the length of the ray.

We consider a simple iso-speed ocean of depth D. As usual we treat the water-air boundary as a perfect reflector so that the reflection coefficient for reflections

from the upper surface of the ocean equals 1. For a ray making an angle θ to the vertical the reflection coefficient at the lower surface of the ocean is given by the usual plane wave reflection coefficient [7]:

$$V(\theta) = \frac{m_b \cos\theta - \sqrt{n_b^{\,2} - \sin^2\theta}}{m_b \cos\theta + \sqrt{n_b^{\,2} - \sin^2\theta}}$$

where m_b is the ratio of bottom density to water density and n_b is the ratio of sound speed in water to sound speed in the bottom. The two parameters completely characterise the acoustic interaction with the sea floor. For simplicity we shall neglect absorption at the bottom; i.e we shall take n_b to be real.

To illustrate the qualitative differences between the field predicted by a dipole source model and the Kirchhoff model it is sufficient to consider the range dependence of the low order multi-path arrivals for a receiver located at some depth d below the surface. In particular we shall compare the intensity of direct path arrival with rays arriving via one bottom reflection and two bottom reflections (plus an intermediate surface reflection) respectively.

Figure 4 shows typical range intensity profiles for a 500Hz source where the bottom type is characterised as "clay" (m_b=1.31, n_b=1.03). Note that since the refractive index is greater than 1 some bottom loss occurs, even at shallow grazing angles. Observe that the dipole model predicts direct path energy to drop off rapidly with range until, by 5km, it is effectively negligible compared to the bottom reflected energy. On the other hand, the Kirchhoff model predicts that direct path actually dominates at long range and is about 10dB higher than the multi-path. Note that the dipole model also underestimates the *total* transmitted energy by a comparable amount, and is therefore likely to underestimate the detection range in this case.

In the example shown in Figure 4 the source height has been set at 100m to model a low flying surveillance aircraft however the results are similar for higher source altitudes, since the (Kirchhoff theory) directivity function varies only as $(kr_0)^{-1/4}$ and is therefore relatively insensitive to source height. For lower frequency sources (such as propeller blades) the relative intensity of the direct path is higher than for the case shown although, again, the variation with frequency is slow.

In not all cases is the direct path dominant over the multi-paths. Figure 5 shows the range intensity profiles for the identical scenario to that shown in Figure 4 except that the bottom is characterised as "quartz sand" (m_b=2.02, n_b=0.87). Since the refractive index is less than one, rays at shallow grazing angles are totally

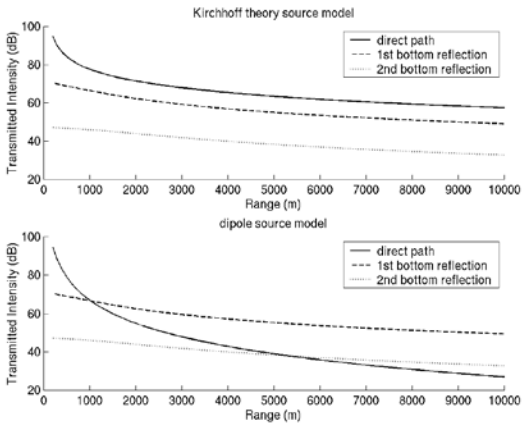

Figure 4. Comparison of ray theory intensity vs. range profiles based on Kirchhoff (upper plot) and dipole (lower plot) source models. In this example the source strength is 160dB, frequency 500Hz, source altitude 100m, ocean depth 500m, receiver depth 50m, bottom type "clay".

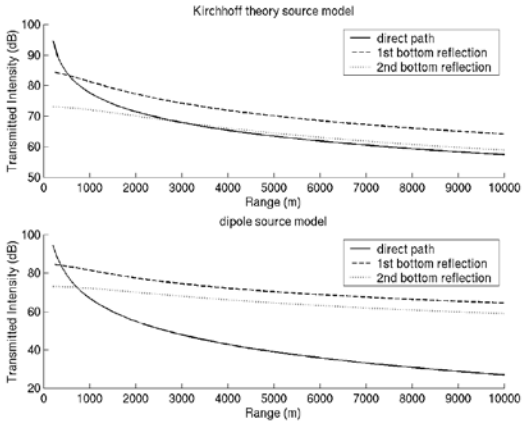

Figure 5. Ray intensity vs range. The details are as for Figure 4 except the bottom type is "quartz sand".

reflected at the bottom resulting in significantly enhanced multi-path. Note however that although the direct path is not dominant it is still far more significant than predicted by the dipole model. It should also be kept in mind that in the current model, bottom losses other than transmission into the seafloor are not being taken into account.

At long ranges the structure of the acoustic field is often more naturally described by modes rather than geometric ray components. If we had used normal mode theory to model the underwater propagation our conclusions would be similar to those above: the dipole theory would predict low order modes to approach zero since these modes are associated with refraction angles close to 90^o [5]. Kirchhoff theory, on the other hand, is

likely to predict these modes to be dominant at long ranges.

In conclusion, energy refracted at angles close to 90^o contributes significantly to the acoustic field (due to an aircraft) at long ranges. Models such as the dipole source model which do not take this component of the field into account are likely to provide misleading results when the distance of the receiver to the source is much greater than the receiver depth.

It is important to stress that the intention of the simple scenarios presented in this section was to highlight the deficiencies of the dipole source model rather than present realistic predictions of the far field acoustic intensity for an airborne source. The results of more detailed acoustic propagation modelling will be presented in future work.

References

[1] A.A. Hudimac, "Ray theory solution for the sound intensity in water due to a point source above it", J. Acoust. Soc. Am. **29**, 916-917 (1957).

[2] R.J. Urick, "Noise signature of aircraft in level flight over the sea", J. Acoust. Soc. Am. **52**, 993-999 (1972).

[3] D.I. Paul, "Acoustical radiation from a point source in the presence of two media", J. Acoust. Soc. Am. **29**, 1102-1109 (1957).

[4] L.M. Brekhovskikh, *Waves in Layered Media*, translated by R.T. Beyer (Academic Press, New York 1980), 2nd ed., Chap IV.

[5] D. M. F. Chapman and P. D. Ward, "The normal-mode theory of air-to-water sound transmission into the ocean", J. Acoust. Soc. Am. **87**, 601-618 (1990).

[6] S. Foster, in preparation.

[7] M. Abramovitz and I. A. Stegun (eds.), *Handbook of Mathematical Functions, with formulas, graphs and mathematical tables* (Dover Publications, New York, 1965).

[8] L. M. Brekhovskikh and Y. Lysanov, *Fundamentals of Ocean Acoustics*, Springer Series in Electrophysics 8 (Springer-Verlag, Berlin, 1982), Chap. 3.

Acoustic Propagation Prediction in Shallow Water

Justin P. Hoffman[1], John D. Penrose[1], and Darryl R. McMahon[2]

[1]Curtin University of Technology, [2]Defence Science and Technology Organisation, Australia.

Abstract

An acoustic propagation experiment was conducted on 17 May 2000 in a shallow water site off the Perth metropolitan coast with the view of obtaining reflection and refraction data to contribute to developing a geoacoustic model of the area. The site proposed has constant bathymetry, though the geological properties of the site are not well known. The experiment used two hydrophones, one situated mid-water and the other moored to the seabed to explore the possibility of receiving head waves. The acoustic sources used were a 20-cui air gun and imploding sources comprising 60W and 75W light globes and purpose built evacuated spheres.

From the air gun data head waves were observed and reduced arrival time vs. range data are discussed in this paper. The travel time data of the implosive sources were particularly useful, in conjunction with Differential Global Positioning System (DGPS) data recorded at 1 second intervals, for an accurate assessment of horizontal separation between the source and receiver due to their impulsive nature. This affords an accurate analysis of the head wave signals, given that the source and receiver depths are known accurately. The detection ranges of the implosive sources is investigated, where the comparatively weak light globe sources were detected to approximately 1.2 km. Head waves were not excited by the implosive sources.

Introduction

This paper describes acoustic propagation measurements using a 20-cui air gun and implosive sources in shallow water. The measurements were made on 17 May 2000 in shallow water off the Perth metropolitan coast. The positions of the tracks were specified so that the seabed depth would be relatively constant along their lengths. The seabed properties along these tracks were not well known. In addition to the acoustical data, oceanographic data was taken. Water-column temperature and salinity profiles were measured at two positions. Salinity measured by the CTD was however found to be unreliable. Figure 1 illustrates the experiment location.

Light bulbs in particular have been the topic of interest as an implosive underwater acoustic source by a number of authors recently (Heard *et al.* 1997, Chapman *et al.* 1997). Their advantages include ease of field use, a reduced primary pulse and bubble pulse duration that may be useful for shallow reflection work, and operation depth. However, their energy output is generally low and there is concern that these sources do not output sufficient energy for sub-bottom reflections to be distinguished from noise in the water column. Their potential usefulness in shallow reflection work may be reduced further by the fact that they can be very broadband sources, depending primarily upon internal gas pressure. This is particularly applicable to the evacuated spheres, where in a recent study by two of the authors (Hoffman & Penrose, 2000) it was found that there is significant energy even at frequencies as high as 5kHz. Consequently it is a concern that the energy at such high frequencies (1kHz and above) will be lost to an absorptive seabed. The results of the propagation measurements performed using light bulbs and purpose-built evacuated spheres are discussed in this paper.

From analysing the recordings on both mid-water and bottom mounted hydrophones it was found that head waves were generated by the air gun. Given that the geological properties of the experiment site are not known well, the head waves offer a useful insight and are discussed in this paper. In the simple method of interpreting a refraction profile, the following assumptions were made:

1) The sound speed in the water column is independent of both depth and range,
2) The seabed sound speed is independent of range,
3) The seabed sound speed profile is a monotonically increasing sequence of uniform layers that are sufficiently thick for the interfaces to yield resolvable head waves at low frequencies,
4) Each interface in the seabed is flat and smooth,
5) The waveguide itself does not yield waveform spreading (through dispersion) that is sufficient to overlap the head wave arrivals.

To varying degrees, these assumptions are likely to be less applicable in shallow water than in deep water i.e. it is more difficult to find regions of horizontally uniform stratification. In any water depth, the first seabed layer usually consists of unconsolidated sediment and will therefore exhibit a significant and continuous increase in sound speed with depth. If a head wave from an unconsolidated layer were detected, then the question of how the sound speed profile below the interface affects the sound speed would need to be addressed. By close examination of the results, it should be possible to conclude whether the assumptions apply to a particular case. If for example a positive sound speed gradient exists, then in the time-distance plane a curvature of the arrival lines should be observed.

The main emphases of this paper are on presenting results and examining the quality of those results. For each head wave, results are presented for the compressional sound speed c_p and depth of the contributing interface in the seabed. These are determined from measurements of the reduced travel time of the head waves i.e. arrival time before the direct path (water borne) arrival.

Field Measurements

The acoustic receivers were Brüel and Kjaer 8104 and GEC Marconi SH101-X hydrophones, positioned at approximately 100m (on the seabed) and at 47m depth respectively. The sound sources were a 20-cui airgun positioned at approximately 8m depth when drifting and approximately 5m when towed, and implosive sources (light globes and evacuated spheres) imploded at approximately 40m depth. The light globes were 6cm in diameter and the evacuated spheres were 8cm in diameter.

The experiment can be broken up into 4 tracks. The first three were "drift" tracks, whereby the vessel was allowed to drift away from the moored recording package. Each drift track followed (roughly) the 100m depth contour in a southwesterly direction. During each of these drifts the air gun was fired at 10-second intervals. The implosive sources were lowered to 40m depth and imploded when the air gun was switched off. As soon as the implosion was complete, the air gun was switched back on to fire at 10-second intervals. Each drift was performed in this manner between 100m and 1000m range. After the conclusion of the third drift (approximately 1.2km range), the vessel steamed away at approximately 2.7 kts with the air gun in tow at approximately 5m depth. The air gun was fired at 30-second intervals. The vessel maintained a constant bathymetry track (along the 100m contour) until DAT recording time expired.

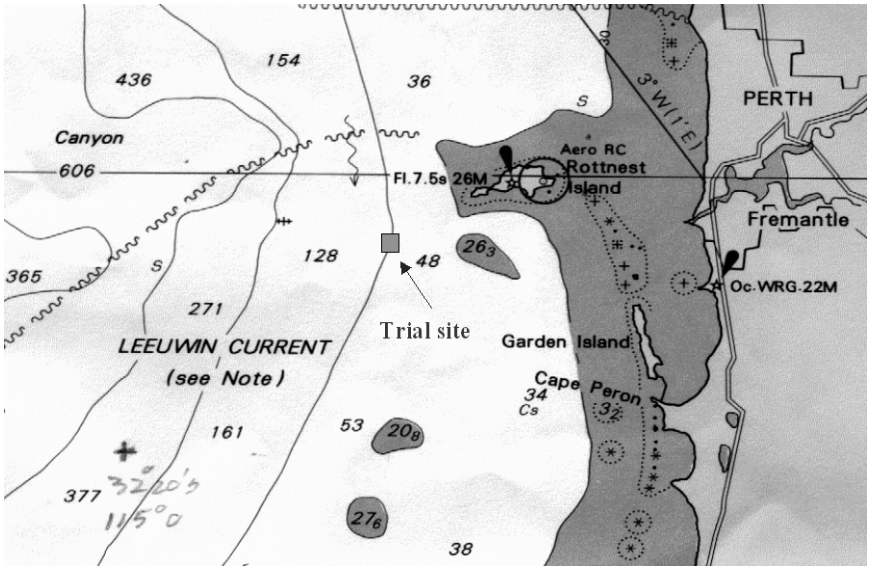

Figure 1: Experiment location where acoustic transmissions were measured. Depth contours are in metres.

The horizontal range between the moored recording package and the shots were determined from the difference in DGPS positions of the shot and the DGPS position of the recording package. This was compared to the horizontal separation calculated from the arrival times of the various propagation paths in the evacuated sphere time series. The evacuated sphere records were used due to their short pulse duration, meaning the arrivals from direct, surface reflected, and multiply reflected paths are easily time separated. The ranges calculated from these two methods are within 1% of each other.

The bathymetry along each track was obtained using the ship's Furuno FCV-581 echo sounder, operated at 200 kHz throughout.

Layer and thickness (m)	c_p (m/s)	c_s (m/s)	α_p (dB/λ)	α_s (dB/λ)	ρ (kg/m^3)
water column (102m)	1530	-	-	-	1025
medium sand (0.5m)	1600	-	0.5	-	1600
boundstone /soil (4m)	1700	-	0.5	-	1700
carbonate (~300m)	2500	1100	0.1	0.2	2100
unknown (basement)	3500	1500	0.1	0.2	2300

Table 1: Interpreted geoacoustic profile of the experiment site. Geoacoustic properties shown are based on data derived by Hamilton (1980).

Geoacoustic Profile

Table 1 describes a geoacoustic profile of the experiment site, derived from personal communication and a PhD thesis by Collins (1983). Literature concerning the geological properties of the area is sparse. It is expected that there are two thin layers of sediment at the surface of the seabed. The first layer is a thin veneer of medium-grained sand, typically less than 1m in thickness. Below this is a layer approximately 4m thick consisting of boundstone and soil. Below these layers is an unnamed carbonate formation, probably between 300 and 400m in thickness. At this stage it is not known what comprises the seabed below this layer. Compressional and shear sound velocities, attenuation coefficients, and associated densities have been interpreted from literature such as Hamilton (1980).

Data Analysis

Implosion Analysis

The purpose of the implosive sources was to investigate their properties and establish whether they are useful as underwater acoustic sources. The evacuated spheres, though extremely broadband due to their short pulse duration, are particularly useful in establishing multiple reflected paths.

The theoretical resonant frequency of an evacuated sphere or light globe implosion was approximated by Minnaert's resonant frequency equation,

$$f_0 = \frac{1}{2\pi R_0}\sqrt{\frac{3\gamma p_0}{\rho}}, \qquad (1)$$

which describes the resonant frequency of a spherical gas bubble of radius R_0 in a liquid, undergoing low-amplitude simple harmonic motion. f_0 is the theoretical resonant frequency, R_0 is the mean bubble radius, p_0 is the hydrostatic pressure, ρ is the density of the surrounding fluid, and γ is the ratio of specific heats for the gas within the bubble. This expression assumes that heat exchanges and surface tension effects are negligible.

The source level of the light globes and evacuated spheres at range is simply

$$SL = 20 \log (\text{Peak Pressure}) + 20 \log (r) \qquad (2)$$

where r is the direct distance between source and receiver.

Head Wave Analysis

Each of the air gun recordings at ranges between 400m and 5.5km contained precursors to the water borne arrival which have been interpreted as refraction arrivals that travelled along the seabed or sub-bottom interfaces. Only the signals received by the hydrophone positioned on the seabed are examined in this paper.

The stacked waveforms of shot arrivals on the final track were examined with the aim of identifying multiple series of pulses whose arrival times appeared to form a linear trend over range. The time of the onset of each signal was observed. From spectral analysis it was found that the head waves have a very narrow bandwidth, centred around 30 Hz, which is identical to the bubble pulse frequency of the air gun used.

The simplest method at hand to stack the waveforms was to align the direct water arrival of each signal and plot the result as reduced travel time with range. This means that to determine the velocity of the head wave (c_p), the actual arrival time, as determined by

$$t = r/c_p + t_0 \qquad (3)$$

where r is the range and t_0 is the time axis intercept of the distance-time plot, needs to be rearranged in terms of the reduced travel time. Since the reduced travel time, here assigned the variable x_r, is only a shift in actual travel time by the direct path time (r/c_w), it may be written that

$$x_r + r/c_w = r/c_p + t_0 \qquad (4)$$

which may be rewritten as

$$x_r = t_0 - r(1/c_w - 1/c_p) \qquad (5)$$

where c_w is the speed of sound in the water column. Thus it is a simple matter of rearrangement to determine the head wave velocity:

$$1/c_p = 1/c_w - 1/v \qquad (6)$$

where v is the gradient of the distance-reduced travel time graph.

The depth of the shallowest interface was obtained by first assuming that it coincided with the seabed. The depth was obtained from the time intercept t_0 in equation (5).

Results

The Water Column

Two CTD casts were taken during the acoustic transmission measurements. From the results obtained the water column was virtually isospeed to the seabed,

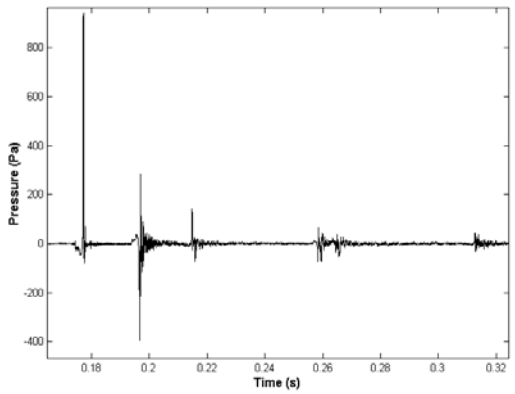

Figure 2: Time series of an evacuated sphere implosion at 137m range, illustrating the time separation of the various in-water arrivals. The sphere was imploded at 40m, where the receiver was positioned at 47m depth.

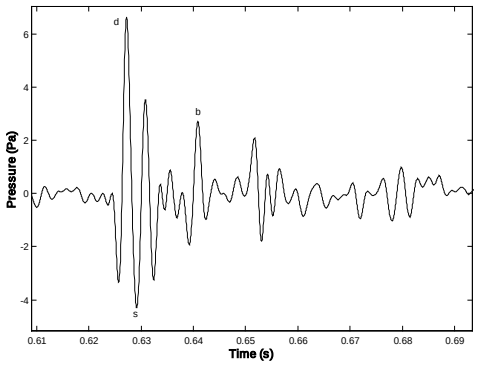

Figure 3: Light globe implosion, filtered through the band 10 to 500 Hz, at 1.2km range. Propagation path arrivals distinguished are **d** – direct path, **s** – surface reflection, and possibly **b** – bottom reflection.

with an average value of 1530 m/s.

In the head wave interpretation the depth-dependence of the water column sound speed was taken into account by using the average value.

Source	Depth (m)	Average Source Level (dB re 1μPa @ 1m)
Light globe	40	205.4
Evacuated Sphere	40	222.3
Air gun	8	218.7

Table 2: Comparison between average peak source level of 36 light globe, 7 evacuated sphere, and 444 air gun transmissions. Source levels are referred to a distance of 1m.

Implosive Sources

Figure 2 illustrates the time series for the shortest-range evacuated sphere implosion made (137m). Multiple reflection paths originating within the water column are easily observed. Given that the thin layers depicted in Table 1 may exist, a shallow sub-bottom reflection should appear very shortly after the bottom reflected arrival at t = 0.215s. The signal should be positive in magnitude since it would be a reflection from a positive reflection coefficient interface. However it does not look likely at this stage that such a reflection could be resolved. There exists a negative magnitude spike shortly after the arrival of the bottom reflection, though this is mostly likely to be an artefact of the original signal's small bubble pulse.

The fact that a sub-bottom reflection is not immediately obvious may not be completely due to the broadband nature of the source but rather due to a low impedance/velocity contrast between any shallow sub-bottom layers. Indeed, since the first "layer" of medium grained sand is only 0.5m in thickness, the bottom reflection received at t = 0.215s may in fact be from the boundstone/soil layer. It remains to be seen however if techniques such as *deconvolution* may be useful to extract the Earth's impulse response from the received signal to infer any sub-bottom reflection occurrences.

Figure 3 illustrates the received signal from a light globe implosion at 1.2km range, filtered through the band 10 to 500 Hz to remove the low frequency flow noise at the midwater receiver and other high frequency components. The reception range was suprising, considering the comparatively low output energy of these sources. However, the inter-water column reflections are not easily observed in this record. This, though attributable to the low output energy of the source, is also attributable to the fact that the pulse duration and the experimental geometry do not allow time separability of the arrivals.

Table 2 compares the average of the peak source levels of 36 light globe, 7 evacuated sphere, and 444 air gun transmissions, carried out between 100m and 1.2km range, referred to a distance of 1m. The difference in peak source level between the light globes and evacuated spheres is attributable primarily to the difference in internal gas pressure. To a lesser degree, the differ-

ence in size (radius) will be a contributing factor in this case. It is interesting to note that the peak source level of the evacuated spheres is higher than that of the air gun, albeit at 40m depth compared to the air gun's depth of 8m.

Refraction Profiling Data

The signal stacks for the final track of the experiment are shown in Figure 4 [(a) for range up to 2km, (b) for range to 5.5 km]. As mentioned previously, the easiest way to make the precursors readable on a stacked display was to stack the signals such that each were aligned by the water-borne arrival. In order to present a constant amplitude for each signal, the signals have been normalised to the same peak-to-peak amplitude. For each stack plot, diagonal lines were fitted visually to the onset of the head waves. There are two head waves marked in this fashion. One is from a shallow interface (close to the water/seabed interface) and is marked by a dashed line in Figure 4(a). The other is from a deeper interface and is marked by a solid diagonal line, also in Figure 4(a). Figure 4(b) illustrates shots between 2km and maximum range, approximately 5.5km. Unfortunately, after approximately 4km the distinction between head wave arrival and noise becomes increasingly difficult and no definite trend can be established.

Features of the Waveforms

The waveforms presented in Figure 4(a) and (b) exhibit the following properties:

- the precursors have significantly narrower bandwidth than the water waves,
- the phases of the initial peaks of the precursors are randomly positive or negative.

The finding that most precursors are narrow band (with a peak near 30 Hz) is consistent with their classification as head waves rather than modal ground waves.

A good example of the variation in phase of the initial peak of the head waves was obtained on the last track from shots at ranges of 2.28 and 3.06 km and is illustrated in Figure 5. It can be seen that the phase of the closest shot is negative and changes to positive between the third farthest and the farthest shot illustrated (the second farthest shot still contains a small negative precursor). To describe this phase change mathematically, the distance over which this phase change occurs can be related to the wavelength of the head wave. The head wave velocity illustrated in Figure 5 was found to be 2925 m/s, so it's wavelength at 30 Hz would be approximately 97m. If the change in phase was taken to occur between the second farthest and the farthest shot i.e. a shot separation of 145m, then the change in phase over 145m would be 1.5 cycles or approaching –90°. There will always be some error in reading the travel time of a head wave, so it was decided that less error

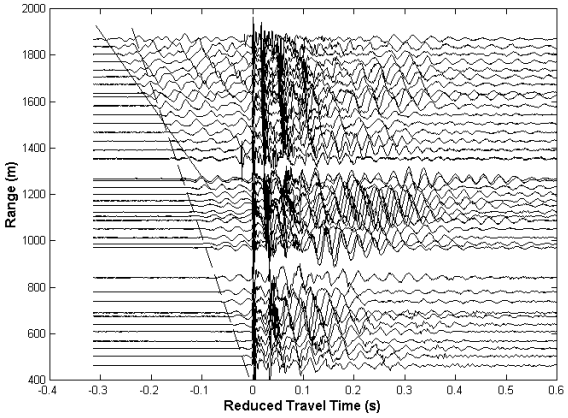

(a)

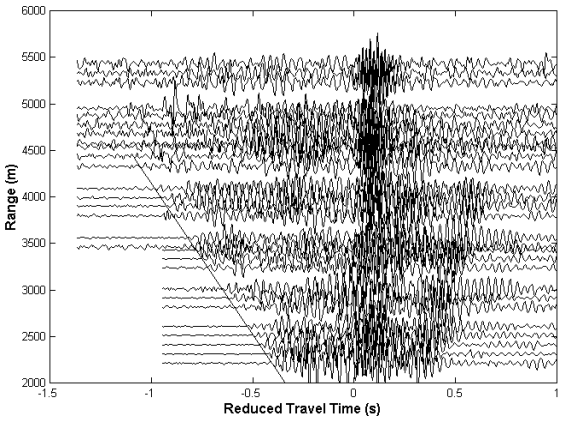

(b)

Figure 4: Signals from the final track stacked onto the range-reduced travel time plane. (a) Range to 2km, entire signal, (b) range to 5.5km, entire waveform (filtered through the band 14 to 70 Hz). Key to diagonal lines: ----- expected arrival of the shallow layer head wave, — expected arrival of the deep layer head wave. The solid line in (b) indicates the same head wave as the solid line in (a).

would be made by reading the first peak, regardless of phase, rather than reading the first peak of a particular phase.

Interpretation of the Data

Simple interpretation of the data has yielded two head wave structures, as illustrated by the diagonal lines drawn on Figures 4(a) and (b). The first head wave arrival (steepest gradient) has however originated from below the water/seabed interface. The sound speed derived for this layer is 1930 m/s. According to Hamilton (1980), sound speeds up to 2000 m/s indicate that

the sediment is of a calcareous nature (carbonate). From our knowledge of the region, this means the sediment is probably moderately cemented calcarenite. Since this was the first detected layer, an analysis concerning it's depth in relation to the water column depth

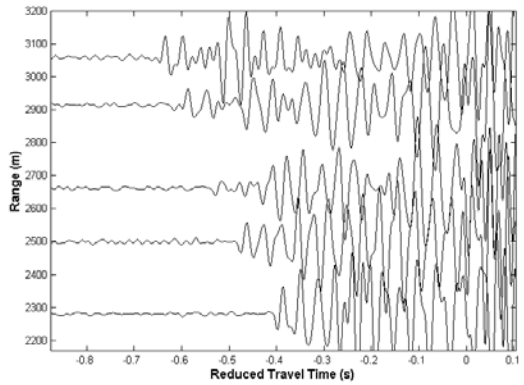

Figure 5: Detailed head wave precursors of five shots filtered through the band 14 to 70 Hz, illustrating the change in phase of the initial peak.

Layer and thickness (m)	c_p (m/s)	c_s (m/s)	α_p (dB/λ)	α_s (dB/λ)	ρ (kg/m^3)
medium sand (0.5m)	1600	-	0.5	-	1600
boundstone (4m)	1700	-	0.5	-	1700
calcarenite (327m)	1930	550	0.2	0.4	2000
chalk (basement)	2925	1300	0.1	0.2	2300

Table 3: Revised geoacoustic profile of the experiment site off Perth metropolitan coast.

was conducted and revealed that it exists approximately 3m below the water/seabed interface. Why a head wave was not excited from the surficial sediments is not known, though it is most probably due to the fact that these layers are too thin to yield head waves.

The depth of the next interface below the seabed was then computed using the geometry of refraction paths for a simple two (horizontal) sediment layer problem and found to be 330m. The compressional sound speed of this interface, as indicated by the solid diagonal line in Figures 4(a) and (b), was found to be 2925 m/s. From Hamilton (1980) it would appear that this layer is similar to chalk, a consolidated and cemented sediment.

A modified geoacoustic profile of the region is considered in Table 3 for comparison with the initial estimate depicted in Table 1. The shear velocities, compressional and shear attenuation coefficients, and densities for these layers have been interpreted from Hamilton (1980).

Conclusion

Imploding acoustic sources offer potential advantages in terms of operation depth, ease of field operation, bandwidth for shallow reflection purposes, and a significantly reduced bubble pulse presence. Whilst their *peak* energy output may be relatively high, as shown in Table 2, their overall energy output is generally low. However, the ability to detect a light globe implosion at 1.2km range is promising.

Using a sound source such as an air gun and a hydrophone on the seabed it is possible to measure head waves from interfaces that are close to (indistinguishable from) the seabed. Their velocities may be determined from their arrival times in the range-time plane. Of the only track studied here, one such head wave was found and its velocity was calculated to be 1930 m/s. Head waves from deeper interfaces can also be measured using this technique. From this experiment a layer was found at 330m beneath the water/seabed interface, where its velocity was calculated to be 2925 m/s.

The amount of data obtained for the seabed may be limited by incoherence of the signals, especially 4km onwards. Spacing between shots was not a problem since, on average, the shot spacing was approximately 140 m between 1.2 km and 5.5 km range. Curvature in the range-reduced travel time plots was not observed, so it may be concluded that there is no evidence of sub-bottom sound speed gradients.

Acknowledgment

The authors acknowledge the valuable assistance provided by Mr Robert McCauley and Mr Malcolm Perry from the Centre for Marine Science and Technology (Curtin University) in preparing for and carrying out the experimental work reported here. We also thank Mr Ahmad Zakaria (Curtin University), Mr Damien Killeen (Defence Science and Technology Organisation), and Mr Alessandro Ghiotto (Nautronix) for their valued assistance during the experimental work.

References

[1]. Heard, G. J., McDonald, M., Chapman, N. R., and Jaschke, L., (1997), "Underwater light bulb implosions: A useful acoustic source", *Oceans 97, M.T.S./I.E.E.E. Conference Proceedings*, vol. 2, (2), pp. 755—762.

[2]. Chapman, N. R., Jaschke, L., McDonald, M. A., Schmidt, H., and Johnson, M., (1997), "Matched field geoacoustic tomography experiments using light bulb sound sources in the Haro Strait Sea trial", *Oceans* 97, *M.T.S.*/I.*E.E.E. Conference Proceedings*, vol. 2, (2), pp. 763—768.

[3]. Hoffman, J. P., and Penrose, J. D., (2000), "Long range acoustic propagation prediction in shallow water", CMST Project 182, Report no. C00-10, Curtin University of Technology.

[4]. Hamilton, E. L., (1980), "Geoacoustic modeling of the sea floor", *J. Acoust. Soc. Am.*, 68, **5**, pp. 1313—1340.

An Issue for Sonar Prediction Tools – Ocean Depth Data

Janice S. Sendt[1], Adrian D. Jones[2] and Paul A. Clarke[2]

[1]Thomson Marconi Sonar, Australia, [2] Defence Science and Technology Organisation, Australia

Abstract

The Maritime Operations Division of DSTO is assisting the Royal Australian Navy in its assessment of a sonar performance prediction tool, TESS 2, which is being developed by Thomson Marconi Sonar Pty (TMS). Part of this assessment has involved comparisons between acoustic transmission loss data measured by MOD at shallow ocean sites with range-dependent transmission predictions obtained by TMS Pty. In carrying out these comparisons, as high resolution bathymetry (ocean depth) databases have become available, the significance of small scale bathymetric changes on acoustic propagation paths become apparent. Significant differences in the calculated transmission loss can occur when there are "aliasing" effects due to undersampling of the bathymetry. To give a correct representation of the bathymetry profile it is necessary in some locations to include both gridded and point data. Examples of this are included in this paper. In particular, it does seem that a variation of bathymetry values close to a sonar signal source is more significant than differences at greater range. This phenomenon is explained with reference to particular simulations.

Introduction

This paper addresses some aspects of a joint DSTO/TMS Pty task for benchmarking the range dependent acoustic transmission loss models used in the TESS 2 software. The TESS 2 software provides performance prediction for the RAN platform sonar sensor systems. The benchmarking task has been undertaken in two phases. The first phase was the comparison of a number of models, eg RAM (1), KRAKEN (2) with well documented benchmark scenarios (3). The second phase which is addressed in this paper has been the comparison of results from TESS 2 with measured results from a considerable number of shallow water sites around Australia which had been collected and analysed by DSTO. The TESS 2 software, in particular, the underwater component called SAGE (4), was developed by TMS Pty. SAGE allows the user to compute sonar performances in detection range for realistic ocean environments at a user defined latitude and longitude. It achieves its purpose by accessing appropriate internal global databases and supplying the necessary parameters to run range dependent sonar performance models. The databases include bathymetry, wave height, wind speed, temperature, sediment thickness and a global sediment province database. (TMS proprietary)

This paper addresses specifically the bathymetry issues, as the impact of different sediment descriptors on transmission loss has been well documented in the literature. (4,5)

The Data

The data available from the measured results included start of track and end of track core samples, a number of sound speed profiles along the track and echo soundings at approximately every 1 km for most tracks.

The data available from the SAGE databases included gridded 30" bathymetry and globally gridded 2' sediment province information. The latter provides sediment information along the whole length of the track whilst the core data only provides information at two points on the track. For the purpose of looking at the impact of bathymetry changes, the sediment province data were used. The measured SVPs were used in preference to the available historic data.

Track lengths varied depending on the site, but were generally between 15 and 40 km in length.

At this point in time this input data has been used only in the two SAGE transmission loss models, namely RAM which is a parabolic equation (PE) model and RAVE which is a ray model (TMS proprietary). The examples shown in this paper are from the RAM model.

Large Bathymetry Variations

At one site, a comparison of the bathymetry data showed an anomalous point where the echo sounder data recorded a point with a 30 m discrepancy (at 8 km along the track) to the gridded data. The DSTO data around this point was more sparse than the rest of the track, with the previous point at 6 km distance and next point at 2 km distance. Agreement along the rest of the

track was good. Thus one dataset was showing a gully 8 km wide. The question arose as to whether this point actually existed or was a misreading. It was also noted that the impact of this point on transmission loss was large (see Figure 1). A review of other data for this site showed that the track was crossing a relict river bed and that the point was indeed correct. However the agreement between the measured and calculated results showed that the gridded database bathymetry gave the best match. The transmission loss values calculated with the echo sounder data gave a discrepancy of up to 10 dB at the ranges of the bathymetry discrepancy. The discrepancy continued at further ranges by producing an "out of phase" transmission loss pattern.

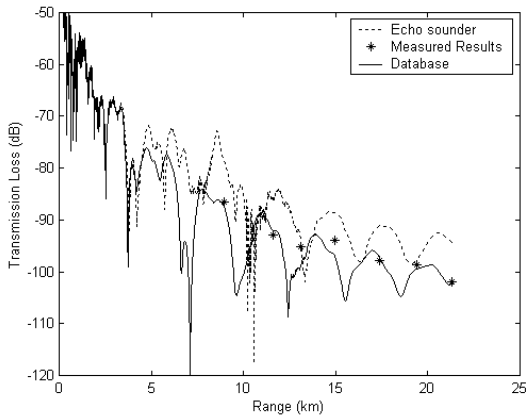

Figure 1 Comparison of calculated and measured transmission loss at 100 Hz for source and receiver at 18 m depth. 8 km wide, 30 metre gully centred 8 km from source in echo sounder bathymetry.

As the river channel does not appear in the gridded data set, its width may be presumed to be less than 1 km. Accordingly, the width of the gully was reduced to 1 km and the transmission loss results recalculated. Figure 2 shows that the transmission loss results for the revised echo sounder data now show better agreement with the measured results. Reducing the width further would allow the results to converge on the values obtained with the gridded data set. If the measured dataset was larger, it would then be possible to use the transmission loss model to infer the correct bathymetry profile, particularly as there is only a one point discrepancy.

The effect of moving the position of the gully in the range slice was also investigated. Here, the gully was moved to 2 km from the beginning of the track and the transmission loss discrepancy with the measured data increased up to 15 dB (see Figure 3). Clearly, short-range transmission data is affected significantly by this change in bathymetry.

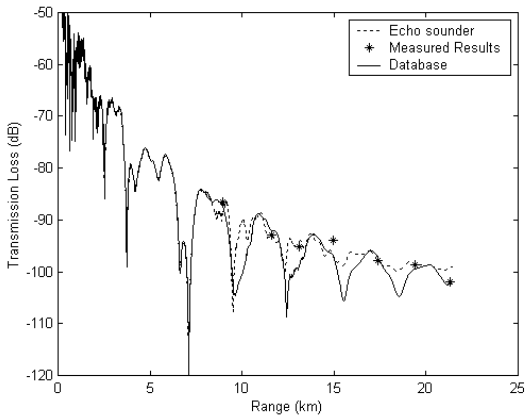

Figure 2 Comparison of calculated and measured transmission loss at 100 Hz for source and receiver at 18 m depth. Echo sounder bathymetry modified to reduce width of gully to 1 km.

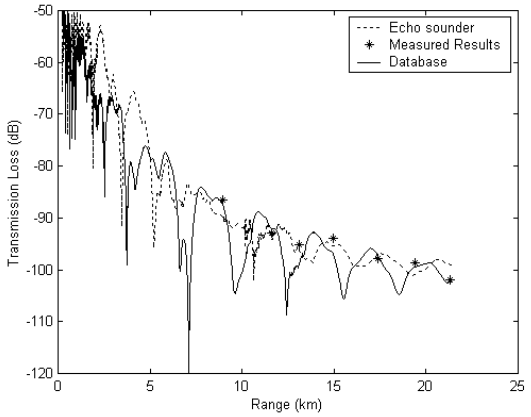

Figure 3 Comparison of calculated and measured tranmission loss at 100 Hz for source and receiver at 18 m depth. 1 km wide, 30 metre gully centred 2 km from source in echo sounder bathymetry.

Smaller Bathymetric Changes

Another point to be raised is that of the small discrepancies between the echo sounder and the gridded database. If one uses $\lambda/4$ as the criterion of the depth cell in RAM, then discrepancies of 5 m start showing as facet effects in the transmission loss calculations above 100 Hz. Whilst these effects are not so dramatic as the impact of gullies they may occur along the whole length of the track and their effect tends to be cumulative. Figure 4 compares the echo sounder and gridded database bathymetry at another site. Discrepancies along this 21 km track occur at five points, with less than a 4 m depth difference. Figure 5 compares the transmission loss for the two bathymetries given in Figure 4. The discrepancies in transmission loss are up to 3 dB.

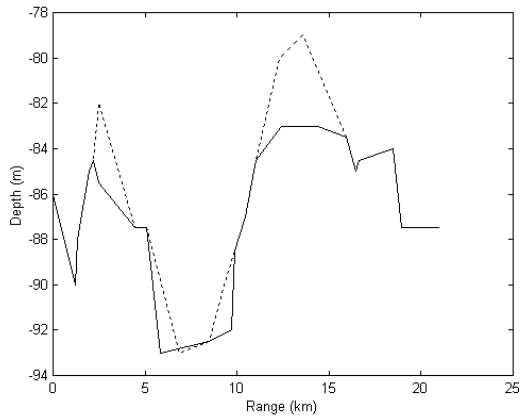

Figure 4 Comparison of the echo sounder and gridded bathymetry database for a track of length 22 km

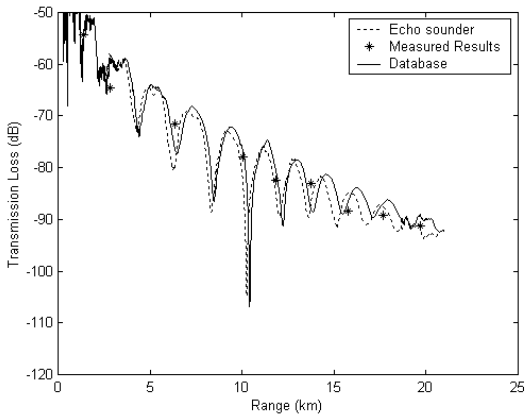

Figure 5 Comparison of calculated and measured transmission loss at 100 Hz for source and receiver at 18 m depth

As the frequency is increased, these facet effects become even more important (see Figure 6). The discrepancies in transmission loss are up to 5 dB. Thus the bathymetry is being undersampled in this instance and this facet effect may limit the upper frequency at which the model is run, rather than the processing time which has been the limitation to transmission modelling in the past.

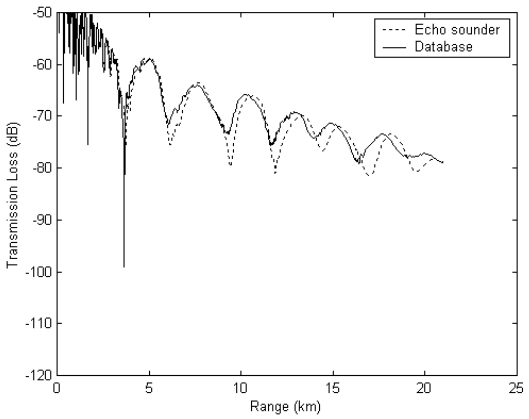

Figure 6 Comparison of calculated and measured tranmission loss at 300 Hz for a source and receiver at 18 m depth

Conclusions

The existence of relict river beds is not an uncommon occurrence on the continental shelf region. The results of this limited study emphasise the need for point bathymetry data to be used in acoustic transmission loss modelling as well as gridded data. This data is provided as a "bedform" database and includes the location, width and depth of relict river beds.

The range resolution of the bathymetry data set can be a source of error in transmission loss calculations even within high resolution data sets which contain small bathymetry variations. For accurate bathymetry profiles it maybe necessary to compare the bathymetry slice with the hydrographic charts, if avialable, so that alaising effects are minimized.

References

1. Collins. M.D. "User's Guide for RAM Versions 1.0 and 1.0p":anonymous ftp@ram.nrl.navy.mil

2. Porter, M. B. "The KRAKEN Normal Mode Pro1. gram"; 1995; SACLANT Undersea Research Centre

3. Chin-Bing, S. A.; King, D. B.; Davis, J. A. and Evans, R. B. "PE Workshop II Proceedings of the Second Parabolic Equation Workshop", NRL/BE/7181-93-001, May 1993

4. TESS 2 Operator's Manual, TMS, 2000

5. Jones, A. D.; Clarke, P. A.; Bartel, D. W. and Sendt, J. S. "Transmission Loss inferred from a seafloor database – comparison with measured data", 2000, Proceedings of UDT Pacific 2000, Darling Harbour, Australia, 7-9 February

6. Jones, A. D. and Bartel, D. W. “Spectral Variability in a Shallow Water Environment”, 1998, Proceedings of UDT Pacific 98, Darling Harbour, Australia, 24-26 February 2.

The Two Dimensional Numerical Modeling Of Acoustic Wave Propagation in Shallow Water

Ahmad Zakaria[1], John Penrose[1], Frank Thomas[1] and Xiuming Wang[2]

Centre for Marine Science and Technology, Curtin University of Technology, [2]CSIRO Petroleum.

Abstract

This paper describes progress on a two dimensional numerical simulation of acoustic wave propagation that has been developed to visualize the propagation of acoustic wave fronts and to provide time-domain signal representation in shallow water. It is intended that an extension of the work presented here, to account for three-dimensional effects, will later be compared with field results.

The numerical simulation of shallow water acoustic propagation has given rise to a wide variety of modeling techniques with various degrees of accuracy. One technique, involving finite difference methods, is more commonly used in the description of seismic propagation but also occurs in the shallow water propagation literature. This word reported here involves the application of finite difference techniques to model propagation in the time domain, together with associated code to allow wave front visualization.

Introduction

Many researchers have developed numerical interpretations of the wave equations suited to acoustic and seismic propagation (Alford, Kelly, and Boore, 1974; Kelly, Ward, Sven Treitel, and Alford, 1976; Cerjan, Kosloff, and Reshef, 1985; Williams, Rechtien, Anderson, 1996; Wu, Lines, and Lu, 1996, Keiswetter, Black, and Schmeissner, 1996; Aleksev, Mikhailenko, 1999). The numerical modeling of seismic data has been used to support interpretations of field data, to provide synthetic data for testing processing techniques and acquisition parameters, and to enhance seismologists' understanding of wave propagation (Keiswetter, Black, and Schmeissner, 1996). For these applications finite-difference methods have often been used.

This report terms the wave equations suited to waves in fluids, acoustic waves and wave in solids such that both shear and compressional, deformations are accounted for are termed elastic waves. Most seismic modeling necessarily uses the elastic wave equations. (Kelly, Ward, Sven Treitel, and Alford, 1976) but the acoustic wave equations have also been used for geophysical modeling techniques (Alford, Kelly, and Boore, 1974). The elastic wave equations are needed to fully account for wave propagation in the seabed but an acoustic wave approximation is often used for seabed sediments when shear velocities are low.

This paper reports on progress in developing a computer program, which deals with the two-dimensional numerical modeling of acoustic wave propagation in shallow water.

Key features of the model at present are:

(i) The use of acoustic wave equation

(ii) Time domain modelling

(iii) A comparison of the use of 2nd and 4th order accuracy

Theory

Acoustic wave equation

A two-dimensional acoustic wave equation can be found using Euler's equation and the equation of continuity (Brekhovskikh, 1960).

$$\frac{\partial p}{\partial t} + \rho c^2 \bar{\nabla} \bullet u = 0 \qquad \text{Continuity} \qquad (1)$$

$$\frac{\partial u}{\partial t} + \frac{1}{\rho} \bar{\nabla} p = 0 \qquad \text{Euler} \qquad (2)$$

Where u is the particle velocity, p is the acoustic pressure, $\rho = \rho(x,z)$ is the density, and $c = c(x,z)$ is the velocity of the acoustic wave in the acoustic media. Substitution of the divergence of the Euler equation and the time derivative of the equation of continuity yield,

$$\frac{\partial^2 p}{\partial t^2} + \rho c^2 \left\{ -\bar{\nabla} \left[\frac{1}{\rho} \bar{\nabla} p \right] \right\} = \delta(r) f(t) \qquad (3)$$

$$\frac{\partial^2 p}{\partial t^2} - \rho c^2 \left\{ \frac{\partial}{\partial x}\left(\frac{1}{\rho}\frac{\partial p}{\partial x} \right) + \frac{\partial}{\partial z}\left(\frac{1}{\rho}\frac{\partial p}{\partial z} \right) \right\} = \delta(r) f(t) \qquad (4)$$

Where $\delta(r)$ is the Dirac delta function associated with the position of the source in space and $f(t)$ is the source function.

For homogenous media, the acoustic wave equations can be simplified as follows,

$$\frac{\partial^2 p}{\partial t^2} - c^2 \left\{ \frac{\partial^2 p}{\partial x^2} + \frac{\partial^2 p}{\partial z^2} \right\} = \delta(r) f(t) \qquad (5)$$

Finite-difference solution

Acoustic wave equation

Finite-difference methods can be applied to the scalar acoustic wave equation. The second time derivative and first spatial derivative of the wave equation can be approximated using a second order central difference approximation as follows,

$$\frac{\partial^2 p}{\partial t^2} = \frac{p_{i,j}^{k+1} - 2.p_{i,j}^{k} + p_{i,j}^{k-1}}{(\Delta t)^2} \qquad (6)$$

$$\left\{ \frac{\partial}{\partial x}\frac{1}{\rho}\left(\frac{\partial p}{\partial x} \right) \right\}_{i,j}^{k} = \frac{1}{\rho_{i+1/2,j}^{k}} \frac{1}{\Delta x}\left(\frac{p_{i+1,j}^{k} - p_{i,j}^{k}}{\Delta x} \right) - \frac{1}{\rho_{i-1/2,j}^{k}} \frac{1}{\Delta x}\left(\frac{p_{i,j}^{k} - p_{i-1,j}^{k}}{\Delta x} \right) \qquad (7)$$

$$\left\{ \frac{\partial}{\partial z}\frac{1}{\rho}\left(\frac{\partial p}{\partial z} \right) \right\}_{i,j}^{k} = \frac{1}{\rho_{i,j+1/2}^{k}} \frac{1}{\Delta z}\left(\frac{p_{i,j+1}^{k} - p_{i,j}^{k}}{\Delta z} \right) - \frac{1}{\rho_{i,j-1/2}^{k}} \frac{1}{\Delta z}\left(\frac{p_{i,j}^{k} - p_{i,j-1}^{k}}{\Delta z} \right) \qquad (8)$$

Where,

$$\frac{1}{\rho_{i\pm 1/2,j}^{k}} = \frac{1}{2}\left(\frac{1}{\rho_{i\pm 1,j}} + \frac{1}{\rho_{i,j}} \right)$$

$$\frac{1}{\rho_{i,j\pm 1/2}^{k}} = \frac{1}{2}\left(\frac{1}{\rho_{i,j\pm 1}} + \frac{1}{\rho_{i,j}} \right)$$

An acoustic wave equation for homogenous media can be approximated in rectangular coordinates system by the second-order and fourth-order central difference (Alford, Kelly, Boore, 1974; Wang, Personal Communication, 2000) as follows,

$$p_{i,j}^{k+1} = 2\left(1 - 2\gamma^2\right) p_{i,j}^{k} - p_{i,j}^{k-1} + \gamma^2\left(p_{i+1,j}^{k} + p_{i-1,j}^{k} + p_{i,j+1}^{k} + p_{i,j-1}^{k} \right) \qquad (9)$$

Where $\Delta x = \Delta z = h$ is the grid size in the x and z directions, respectively and Δt is the time step.

Another alternate expression for higher accuracy uses the fourth-order central difference scheme of the acoustic wave equation. It is more accurate than second-order central difference scheme.

$$p_{i,j}^{k+1} = \left(2 - 5\gamma^2\right) p_{i,j}^{k} - p_{i,j}^{k-1} + \frac{4}{3}\gamma^2\left(p_{i+1,j}^{k} + p_{i-1,j}^{k} + p_{i,j+1}^{k} + p_{i,j-1}^{k} \right) - \frac{1}{12}\gamma^2\left(p_{i+2,j}^{k} + p_{i-2,j}^{k} + p_{i,j+2}^{k} + p_{i,j-2}^{k} \right) \qquad (10)$$

Where: $\gamma = \left(\frac{c\,\Delta t}{\Delta h} \right)$,

A finite-difference scheme will be stable if $\gamma = 1/\sqrt{2}$ for equation (9) and $\gamma = \sqrt{3/8}$ for equation (10) (Alford et. al., 1974)

Boundary conditions

Where transparent boundary conditions are involved, we use the method due to Reynolds (1978).

Transparent boundary condition

Left side boundary

$$p_{1,j}^{k+1} = p_{1,j}^{k} + p_{2,j}^{k} - p_{2,j}^{k-1} + c_{i,j}\frac{\Delta t}{\Delta x}\left(p_{2,j}^{k} - p_{1,j}^{k} - \left(p_{3,j}^{k-1} - p_{2,j}^{k-1} \right) \right) \qquad (11)$$

Right side boundary

$$p_{n+1,j}^{k+1} = p_{n+1,j}^{k} + p_{n,j}^{k} - p_{n,j}^{k-1} + c_{i,j}\frac{\Delta t}{\Delta x}\left(p_{n,j}^{k} - p_{n+1,j}^{k} - \left(p_{n-1,j}^{k-1} - p_{n,j}^{k-1} \right) \right) \qquad (12)$$

Surface side boundary

$$p_{i,1}^{k+1} = p_{i,1}^{k} + p_{i,2}^{k} - p_{i,2}^{k-1} + c_{i,j}\frac{\Delta t}{\Delta z}\left(p_{i,2}^{k} - p_{i,1}^{k} - \left(p_{i,3}^{k-1} - p_{i,2}^{k-1} \right) \right) \qquad (13)$$

Bottom side boundary

$$p_{i,m+1}^{k+1} = p_{i,m+1}^{k} + p_{i,m}^{k} - p_{i,m}^{k-1} + c_{i,j}\frac{\Delta t}{\Delta z}\left(p_{i,m}^{k} - p_{i,m+1}^{k} - \left(p_{i,m-1}^{k-1} - p_{i,m}^{k-1}\right)\right) \quad (14)$$

Nonreflecting boundary condition

We are at present investgating the approach due to Cerjan et al. (1985) which may be summarised as follows

The pressure amplitudes outside the boundary lines must be multiplied by G factor (Cerjan, et.al.1985).

$$G = EXP\left\{-\left[0.015(20-i)\right]^2\right\} \quad (15)$$

Where: $1 \le i \le 20$

This gives a value of 1 for $i = 20$ or at the nearest boundaries with boundary lines and a value of about 1/250 for $i = 1$ or at the outer boundaries.

Source function

As the source function f(t), a single cycle sinusoid was used.

Results

We present here some of the results of the numerical modeling comprising a comparison between the finite-difference results from second order (7) and fourth order approximations (10) using the transparent boundary condition. The wave front results are also compared with some original results from related acoustic wave simulation work that has been developed by Wang.

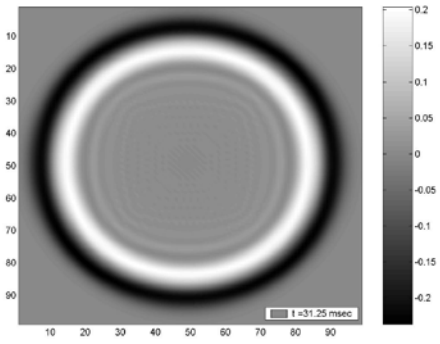

Figure 1.a: (2nd order)

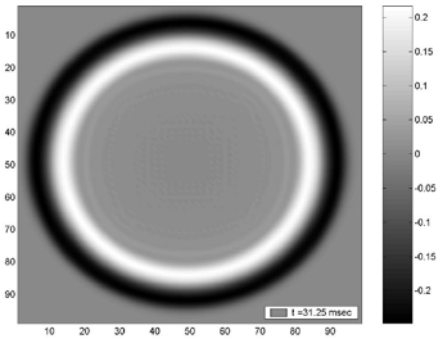

Figure 1.b: (4th order)

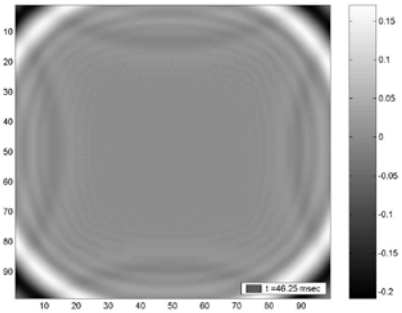

Figure 2.a: (2nd order)

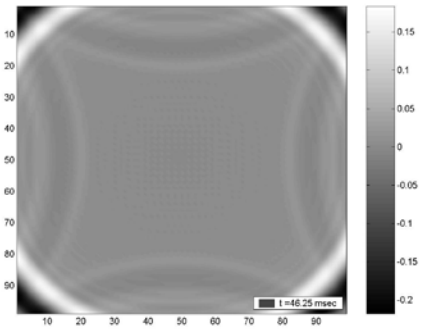

Figure 2.b: (4th order)

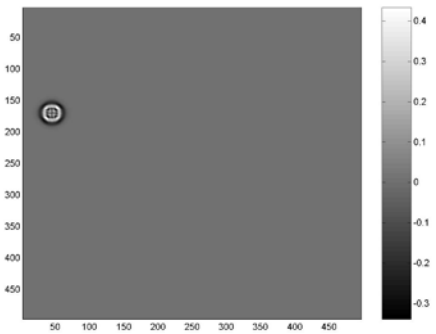

Figure 3: t = 5 msec (2nd order)

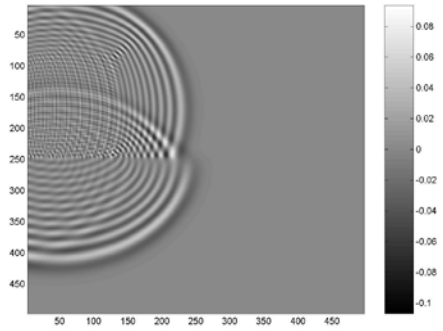

Figure 4.a: t = 50 msec (2nd order)

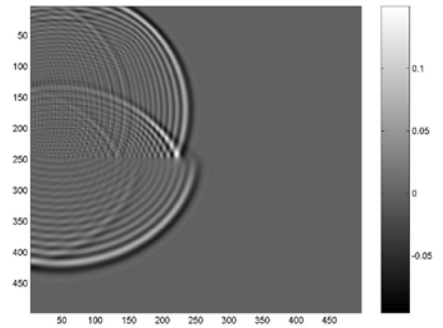

Figure 4.b: t = 50 msec (4th order)

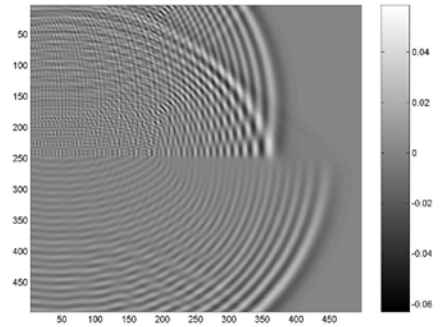

Figure 5.a: t = 85msec (2nd order)

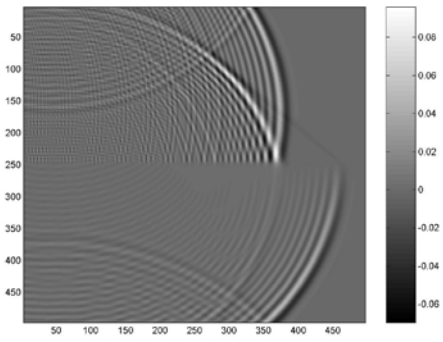

Figure 5.b: t = 85 msec (4th order)

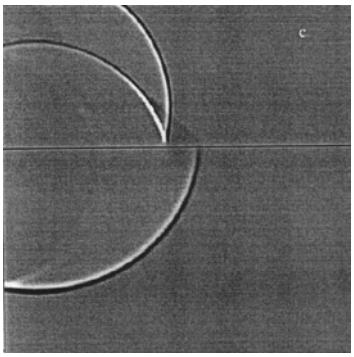

Figure 6.a: t = 50 msec (Wang)

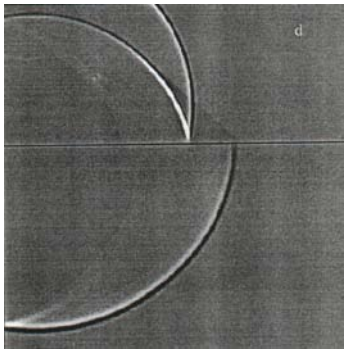

Figure 6.b: t = 60 msec (Wang)

Figure 1.a, 1b, 2a, and 2.b. show wave front simulation results in a homogeneous space represented using 101 x 101 grid points with c = 1500 m/s, ρ = 1025m^3/kg, Δx=Δz=1m, Δt= 0.025msec with a single sinusoid signal of source amplitude A = 2 and frequency (f) = 100Hz. Some reflections are observed. Figure 3 shows the source position used in the simulations represented in figues 4 and 5. Figures 4.a, 4.b, 5.a, and 5.b show the results using 201x201 grid points in a two-layer environment. Velocity c and density ρ in the upper and lower layers are 4000 m/s, 1300 m^3/kg and 6000 m/s, 1800 m/s respectively. Here Δx = Δz = 2.5 m, Δt = 0.025 msec with source amplitude A = 2 and frequency (f) = 400Hz. Figures 6.a and 6.b show acoustic wave front simulation results using 512 x 512 grid points, due to Wang. The acoustic velocities in upper and lower layers are 4000m/s and 6000m/s respectively but with constant density throughout. Figures 4.a – 5.b show evidence of dispersion, presently attributed to grid size effects. The effects of incomplete boundary transparency are still apparent. The 4th order results show somewhat less dispersion than those arising from the 2nd order computations. The results also can be compared with Wang's results in figures 6.a. and 6.b. .In all cases direct, reflected refracted and head waves are observed.

Amplitude signals from receivers for the homogeneous media case of figures 1 and 2 are shown as follows,

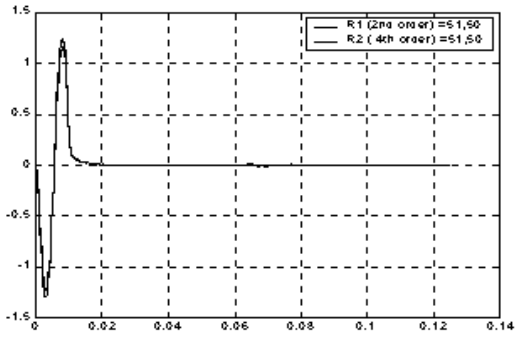

Figure C.1: At position S=51,51;R=5

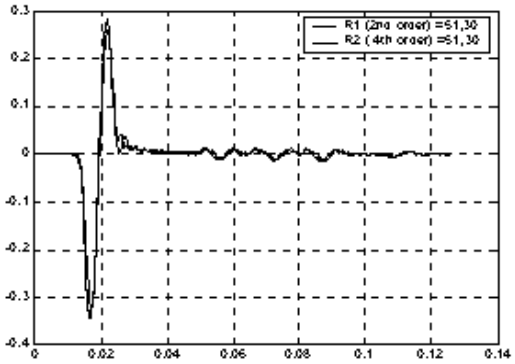

Figure D: At position S=51,51;R=51,30

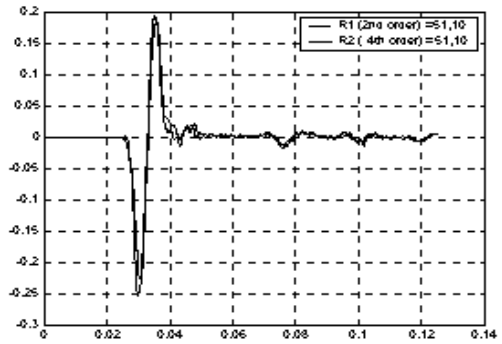

Figure E.1: At position S=51,51; R=51,10

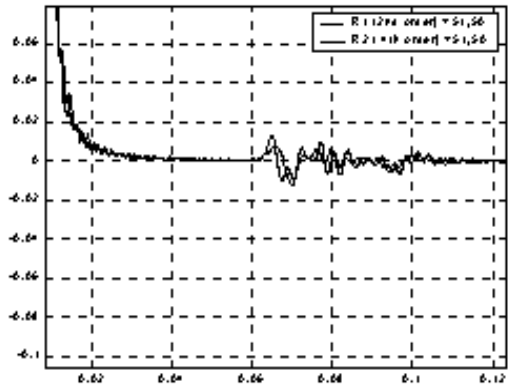

Figure C.2: zoom C.1

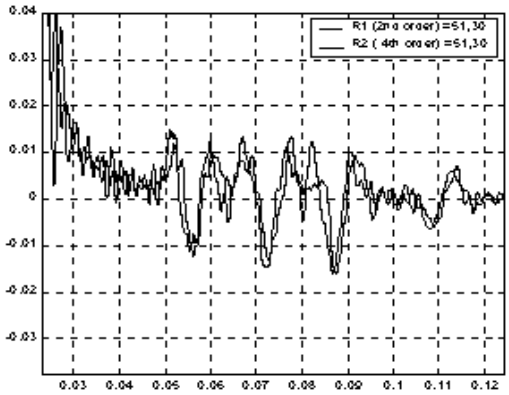

Figure D.2: Zoom D.1

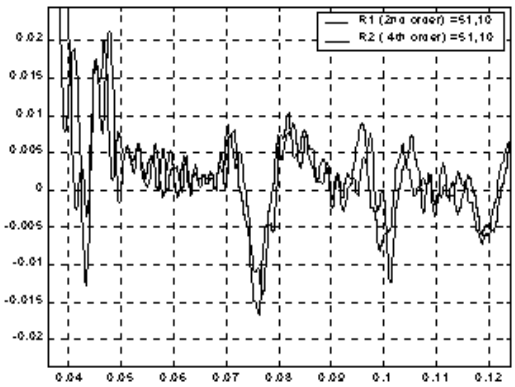

Figure E.2: Zoom E.1

Figures C.1, C.2, D.1, D.2, E.1, E.2 show in the time domain the influences of dispersed waves and transparent boundaries.

The range dependence of acoustic pressure is shown in figure F. This shows the average of the amplitudes of the initial positive and negative pressure excursions P as a function of range r. The relationship P(r) may be expressed by equation (16),

$$P = a.r^{b} \tag{16}$$

Curve fitting yields *a*, *b* and associated correlation coefficient as shown in the table 1,

Order	**A**	**b**	**R^2**
2^{nd}	1.2527	-0.4832	0.9982
4^{th}	2.6650	-0.4471	0.9993
Average	1,9589≈2	-0.4651≈-0.5	0.9993

Table.1: Coefficients *a* and *b*

Coefficient b is close to the – 0.5 value expected for cylindrical spreading.

Conclusions

We have developed 2-D acoustic finite-difference codes for second order in time and second or fourth order in space to model acoustic wave propagation in heterogenous media.

We have presented a comparison between wave fronts developed using 2^{nd} order and 4^{th} order approximations to the acoustic wave equations, shown dispersed wave problems and partial transparent boundary effects. The acoustic modeling shows the expected direct, reflected and refracted and head waves patterns in a two-layer space.

References

Alford, R. M., Kelly, K. R., and Boore, D. M., 1974, Accuracy of finite-difference modeling of acoustic wave propagation: Geophysics, v. 39, no. 6, p. 834-842.

Kelly, K. R., Ward, R. W., Sven Treitel, and Alford, R. M., 1976, Synthetic Seismograms: A finite-difference Approach: Geophysics, v. 41, no. 1, p.2-27.

Reynold, A. C., 1978, Boundary conditions for the numerical solution of wave propagation problems: Geophysics, v.43, p. 1099-1110.

Williams, R. S., Rechtien, Richard D., and Anderson, Neil L., 1996, The one-dimensional elastic wave equation: A finite-difference formulation for animated computer applications to full waveform propagation: Computers & Geosciences, v.22, no. 3, p.253-266.

Cerjan, C., Kosloff, D., Kosloff, R., and Reshef, M., 1985., A nonreflecting boundary condition for discrete acoustic and elastic wave equations: Geopgysics, v. 50, no. 4, p. 705-708.

Brekhovskikh, L. M., 1960, Waves in layered media: Academic Press, New York, p.171.

ACOUSTICS - putting the science and technology to work

Conference of the Australian Acoustical Society
Joondalup Resort, Western Australia, 15-17 November 2000

Session AC-5 Acoustics And The Built Environment 2

Sound Transmission Through Wall Panels: Effect of Fixing Method

J.R. Pearse

Department of Mechanical Engineering, University of Canterbury, Christchurch, New Zealand

Abstract

The effect of the fixing method on the sound transmission loss of a timber frame wall construction lined with gypsum plasterboard was investigated. The transmission loss varied significantly with the fixing system. However the STC ratings of the wall construction did not vary markedly with the method used to attach the plasterboard to the timber frame. When the plasterboard was nailed to the timber frame the transmission loss was up to 8dB higher at certain frequencies than when the plasterboard was attached by continuous gluing or by gluing and screwing at discrete points. The effect of the panel size between the timber studs was also examined.

Investigation of Mounting Conditions of Suspended Ceiling Tiles

Michael Vandenberg, Ross Leo, Peter Dale

[1]RMIT University Melbourne'

Abstract

Independent laboratories conducted tests to find sound absorption coefficient of ceiling tiles and returned dissimilar results over most of the frequency bands investigated. The differences in these results prompted our investigation into the mounting conditions of suspended ceilings tiles to determine the cause of differences between these results.

Whilst doing so International and Australian Standards were compared to determine the effect the permissible variations within the standards make on measurement of sound absorption coefficient of a ceiling system. For the sample to fit the size requirements of the standards and not collapse, a support system is needed in addition to the frame. Variations of this support system were explored as well as the presence of the frame and the support system in empty room measurements. Other variables investigated included the height and width of the frame.

It was found that large differences in absorption coefficient (up to 0.25 at certain frequencies) arose using discretionary variations *within* AS 1045 *and in comparison* to the International Standards. This investigation produced results, which suggest that products should only be compared if they are measured under the same conditions, especially in relation to empty room conditions.

It is important to note that one laboratory followed International Standards (ISO 354) whilst the other followed standards set in Australia (AS 1045). There are a few small discrepancies between the two but the clearest direct disparity involves the "empty room" conditions. The ISO recommendation is that "The measurement of the reverberation time of the empty room should be made in the absence of the frame or side walls of the test specimen." whilst AS 1045 states that "The measurements of the reverberation time of the empty room should be made with the frame or sidewalls present." (pg 8, AS1045).

Within the standards there is a wide range of scope for the distinct measurements of the frame. For instance AS 1045 state only that the frame is to be "constructed from sound reflective non-porous material of thickness not greater than 20mm and…surface density of the sidewalls shall be not less than 8 kg/m^2 ". It is important to note that there is no specification of the height of the frame apart from the fact that if the frame is to be less than 150mm in height, the density of the frame is to be no less than 4 kg/m^2. ISO345 does not mention the height of the frame at all. The tests performed in this investigation took the given recommendations into account and explored the limits in order to reveal the full extent of the range of scope within these recommendations.

In order to comply with both Australian and International Standards, the frame was constructed with MDF. This is a material is a non-porous material and has a face with a sheen. This is important so that it absorbs as little of the acoustic field as possible during testing. The frame dimensions were in accordance with both standards (2800 x3600mm) and care was taken to keep the relative humidity and temperature constant throughout a series of tests. The sound sources were positioned at least two metres from the frame and the microphone was positioned at least one metre from any other reflecting surface.

As the two laboratories conducted their tests in accordance with different standards, it was imperative that International and Australian Standards (ISO 345 and AS 1045) were compared to determine the effect the disparities make on measurement of sound absorption coefficient.

Discrepancies between the two standards in question and the techniques used by Nibotto and RMIT were found to be

- the height of the mount
- the width of the mount
- the mounting technique
- painting the mount

- sealing the edges of the frame
- the empty room conditions

Tests were conducted in order to investigate the effect each of these had on the calculation of sound absorption coefficient. Varying the parameter being considered whilst keeping all other variables constant is how this was done. Confidence intervals were measured by calculating the standard deviation in the reverberation time and taking this into consideration when considering the error in absorption coefficient.

It was found that none of the parameters had much effect on the measurement of the coefficient of absorption except for the empty room conditions. The measurements obtained in this part of the investigation follow.

The following graph shows a direct comparison of the difference between the empty room conditions specified in ISO 354 and AS 1045. As previously stated the international standards suggest that the frame should not be present whilst empty room measurements are taken. As this would mean that the reverberation time of the empty room measurements would be longer, a higher value of absorption coefficient might be expected.

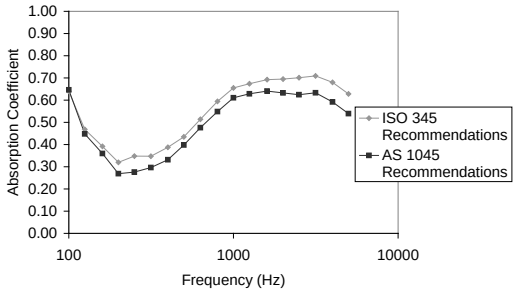

Fig 1. The difference that the empty room recommendations make on the measurement of absorption coefficient.

The tests done in accordance with international standards do show a higher value of absorption coefficient over all but one of the frequency bands investigated. This would suggest that measurements taken with differing empty room conditions should not be compared and that the term "should" in both the International and Australian Standards should be replaced by "shall". The term "should" leaves the decision up to the laboratory's discretion, which can lead to misleading results and favourable outcomes could be measured depending on the method chosen. If the term should is replaced measurements taken by different laboratories in accordance with the same standards could be directly compared.

The following graphs show the effect that different mounting conditions can have on measurements of sound absorption when both AS 1045 and ISO 345 are followed in respect to their respective empty room conditions. The two mounts are specified below.

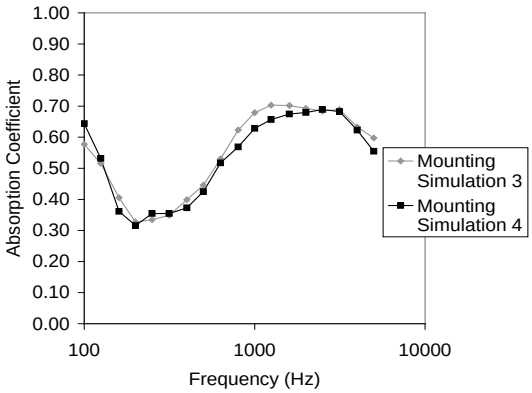

Fig 2. Graph of the effect that different mounting conditions can have on the measurement of absorption coefficient in accordance with AS 1045.

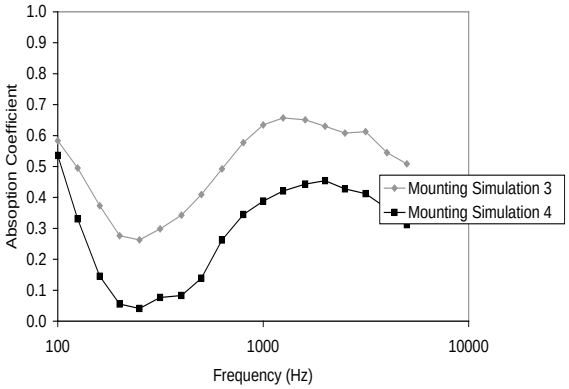

Fig 3. Graph of the effect that different mounting conditions can have on the measurement of absorption coefficient in accordance with ISO 345.

Fig 3 shows that when International Standards are followed the mounting simulation has little effect on the measurement of the sound absorption coefficient. When the same mounting simulations are compared in accordance with the Australian Standards in Fig 2 there is quite a different result.

The empty room measurement in this case was made with the frame and support system present, which is within the limitations that AS 1045 set since there is no mention of the supports within the standard.

The fact that there is no mention of the support system means that this can be interpreted that the support system

is part of the frame and can be present in the empty room measurement. As Fig 2 shows this can lead to quite large differences in results.

Support Systems

Suspended ceilings are mounted in reality on a rail, which is supported from above. Ideally this same practice would be used in testing these tiles but it is not always possible to mount the tiles suspended from a ceiling. This was the case for both laboratories so both did their best to simulate the situation using different mounting techniques. It is specified within relevant standards that in this case the tiles are to be suspended on a frame sitting on the floor of the reverberation chamber with an air gap behind the tiles. A t-shaped rail holds the tiles in place in reality so the tiles were tested with this t-shaped rail supporting them. These rails are usually supported from above but this too was difficult to simulate so different techniques were used to support the rail (see Support Systems). In attempting to simulate reality tiles were not sealed to the rail in any way except under their own weight due to gravity.

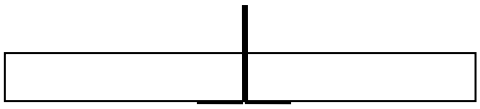

Fig 4. Tiles supported by a t-shaped rail, which in turn in reality is supported from above. Support System 3 has two large planks sitting upon the frame above the tiles with the rail tied to them. This allows the tiles to sit flush with the frame and not collapse under the force of gravity. Simulation 2, on the other hand involves five large planks screwed into the frame and supporting the tiles from below. This means that when the tiles are in place they are not subject to the sound field produced.

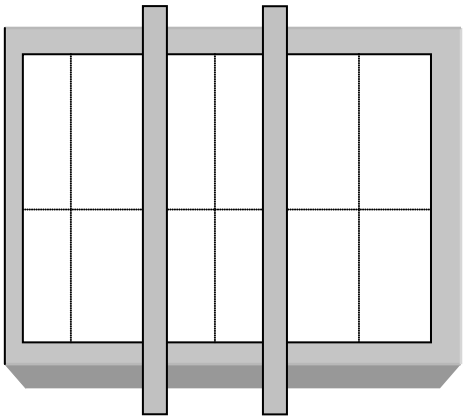

Fig 5. Support System 3

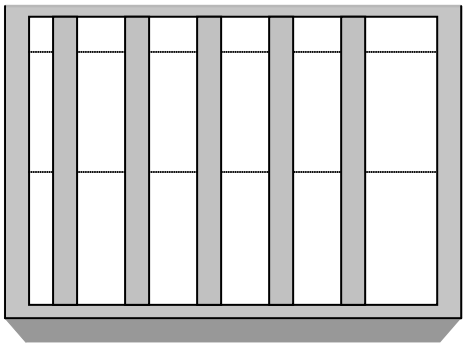

Fig 6. Support System 4

Conclusions

The fact that such large discrepancies can be measured within the limits of AS 1045 lead to the conclusion that if the frame is to be present during the empty room measurement, the support system (parts other than frame) must be specified or cannot be present whilst running an empty room test. If this were to happen, comparisons between tiles tested in accordance with AS 1045 would be more consistent.

Considerable differences could also be measured when empty room conditions were changed from having the frame present (without the support system) and not having the frame present for the empty room measurements. This suggests that the term “should” in AS 1045 should be changed to “shall” to inhibit laboratories from discretionary empty room measurements, which can lead to differences in results.

To solve the problem of controlling the effect of different mounting simulations and to be able to compare measurements made according to ISO 345 and AS 1045 empty room measurements must be made with a 'true' empty room measurement. Both standards must read “The measurement of the reverberation time of the empty room shall be made in the absence of the frame or side walls of the test specimen.” This would see that consistent results would be obtained and that measurements of absorption coefficient are comparable with measurements taken internationally.

Reverberation Measurement - The Original Process

Terrance Mc Minn

Curtin University of Technology

Abstract

This paper takes a look at the methods used by Wallace Sabine to determine reverberation time.

The Original Problem

The Fogg Art Museum lecture hall (Hunt Hall) at Harvard University exhibited, as described by Sabine (Sabine, 1964d pg. 9)*"the rate of absorption was so small that a word spoken in an ordinary tone of voice was audible for five and a half seconds afterwards"*.

Original Reverberation Chamber

The original chamber used by Sabine was the 'Constant Temperature' room in the Jefferson Physical Laboratory. This room was located in the centre of one wing of the building, and underground (see Figure 5). The room had separate footings and thick double walls of brick. There were no windows; the walls, floors and ceiling were smooth unbroken solid masonry (Sabine, 1964d pg. 6). The room had a single door set flush into the wall. The dimensions were 4.27 by 6.1 meters and 2.54 meters high. The ceiling was arched with an overall height of 3.17 meters at the centre.

First Equipment

In the article from the Proceedings of the American Institute 1898 (pg. 35) it is recorded that the first method for determining the rate of decay of sound was reported to involved the use of a sensitive manometric gas flame. (Sabine, 1964d pg 10) The size of the flame was measured using a micrometer telescope. Later photography of the gas flame was trailed.

Both methods were discarded. Why? Firstly they only confirmed what the unaided ear could perceive: that at any point in the room, the sound died away in a fluctuating manner; additionally the sound was often more intense immediately after the source had stopped. These methods provided much information on the decay process but could not give an accurate result.

The Final Apparatus

Finally it was determined that the ear in conjunction with a 'suitable chronograph' gave the required accuracy and sensitivity. The earlier measurement procedures attempted to measure the intensity of the sound. This did not allow a determination of the rate of decay of the sound.

Sabine determined, at this time, that the most effective method of determining the rate of decay was to measure the *'duration of audibility of the residual sound'*. The decisive element was his recognition that the *'the rate at which the reverberation would disappear was proportional to the rate at which the sound was absorbed'* (Sabine, 1964d pg. 10).

The sound source he used was an organ pipe - an octave above middle 'C' (512 Hz)[3]. The wind supply for the organ pipe came from a double tank, which was water-sealed and noiseless. It was switched on and off by an electro-pneumatic valve, similar to that used in large church organs. The same current, which controlled the valve, also controlled the chronograph. The chronograph was able to measure intervals from 0.5 to 10 seconds.

The role of the observer was to close the switch to record when the sound ceased to be audible. See figure 1 (Sabine, 1964d pg. 15).

The accuracy of the measurements came from the mean of about 20 observations; the average deviation from the mean was 0.11 seconds and the maximum being 0.31seconds. Over time, three different types of chronographs and three different valves were evaluated. The results for the same room were very nearly the same (Sabine, 1964d pg. 16).

Six years after the initial work based on the 'C' (512 Hz) organ pipe, Sabine expanded his investigations to *'extend this over nearly the whole range of the musical scale, from C_1 64 to C_7 4096'* (Sabine, 1964a pg. 78). Sabine makes an interesting comment, which most practitioners in the building acoustics field will relate to:

> *"…the previously published work with C_4 512 must be regarded as illusion, as a part of a lar-*

[3] This frequency was influenced by telephony. *'It was regarded at the time as the characteristic pitch determining the conditions of articulate speech'.* (Sabine, 1964b pg. 225)

Figure 1

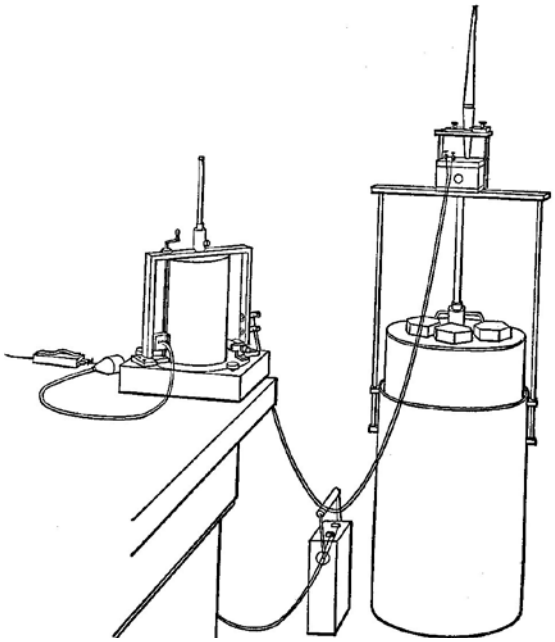

ger problem,… Thus a room may have great reverberation for sounds of low pitch and very little for sounds of high pitch, or exactly the reverse; or a room may have comparatively great reverberation for sounds of high and of low pitch and very little for sounds near the middle of the scale." (Sabine, 1964a pg. 78)

This increase in frequency range necessitated changes in equipment. An experiment was devised to *"determine the duration of audibility after cessation of two sounds, one having four or more, but a known multiple, times the intensity of the other. From these results it is possible to determine the rate of emission by the pipes, each in terms of the minimum audibility for that particular tome."* (Sabine, 1964a pg. 83)

As can be seen in Figure 2 (Sabine, 1964a pg. 84). The four small organ pipes were spread 5 meters apart as Sabine describes *'if placed near each other the four sounded together do not emit as four times the sound emitted by one.'* (Sabine, 1964a pg. 83) This work enabled the determination of the rate of emission of several pipes. From this point on, Sabine was able to use multiply pipes to expand the frequency range of his observations.

Figure 2

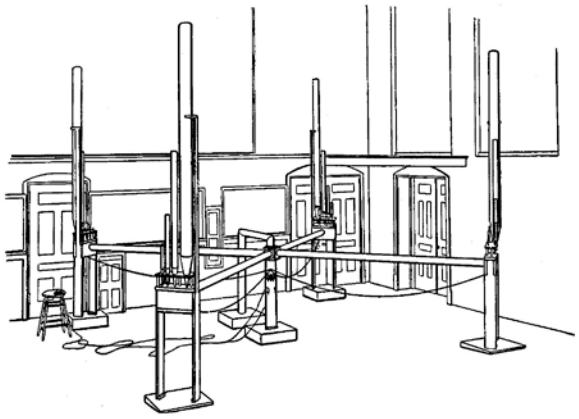

Figure 3 (Sabine, 1964a pg. 88) illustrates the apparatus used in determining the absorption coefficients of painted and unpainted bricks in the 'Constant Temperature Room'. Note the air reservoir in the room above.

Figure 4 (Sabine, 1964a pg. 91), illustrates a portable rig used to determine the in-situ characteristics of wood sheathing. This material was located in a building adjoining a 'night lunch room'.

Figure 3

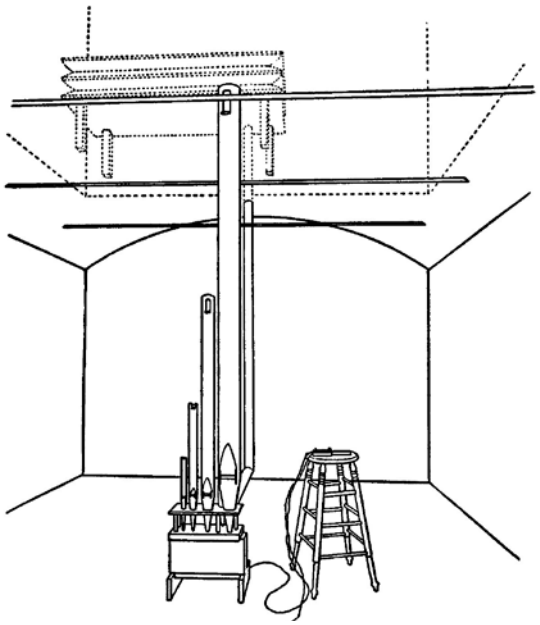

Most of Sabine's testing was done at night. Yet even in the first decade of the 20th century, there are many references to false readings due to extraneous noise. Often traffic, which in Boston at that time didn't stop until *'nearly two o'clock and began again about four'*. (Sabine, 1964a pg. 90) Other disturbances recorded include a 'street car' passing not far the building under observation. And, *'the interest of those passing by on foot throughout the night, and the necessity of repeated explanations to the police, greatly interfered with the work.'*

Adverse weather delayed for more than a year, observations on audience absorption. In the earlier experiment, factors cited for the unsuccessful test include: *'a threatening thunder storm… the sultriness of the atmosphere made open windows necessary, while the attempt to cover so many notes, thirteen in all, pro-*

Figure 4

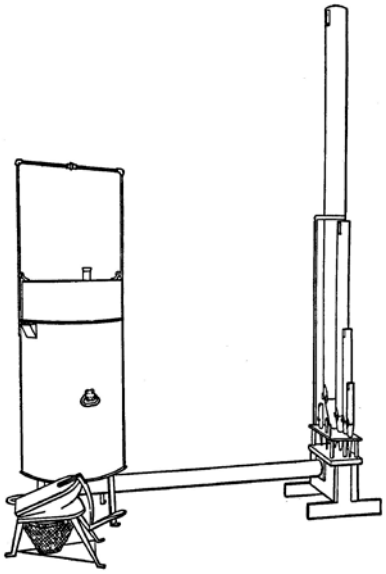

longed the experiment beyond the endurance of the audience.' (Sabine, 1964a pg. 85) It is interesting that in the follow-up experiment, only six frequencies C_1 64 Hz to C_7 4096 Hz were tested, three below and three above C_4 512 Hz. The C_4 value had been previously determined.

It is interesting to view the arrangements used in the 'Constant Temperature Room' for transmission investigation, see Figure 5 (Sabine, 1964c pg. 245). Notice the entrance door was used for the panel under test. This required the observer to be winched in and out using a block and tackle. The observer also sat in an enclosed boxed with only the neck and head exposed – to eliminate the effect of clothing from the results.

The method used to determine the transmission of the test panel required the reduction of the sound intensity in the main chamber until it was inaudible in the anteroom. The intensity of the sound in the main chamber was *'numerically equal to the reciprocal of the coefficient of transmission'* (Sabine, 1964c pg. 246). The revolving reflectors were used to average out the sound intensity in the chamber.

Conclusion

This paper has examined some of the published literature by Wallace Clement Sabine in relation to the types

Figure 5

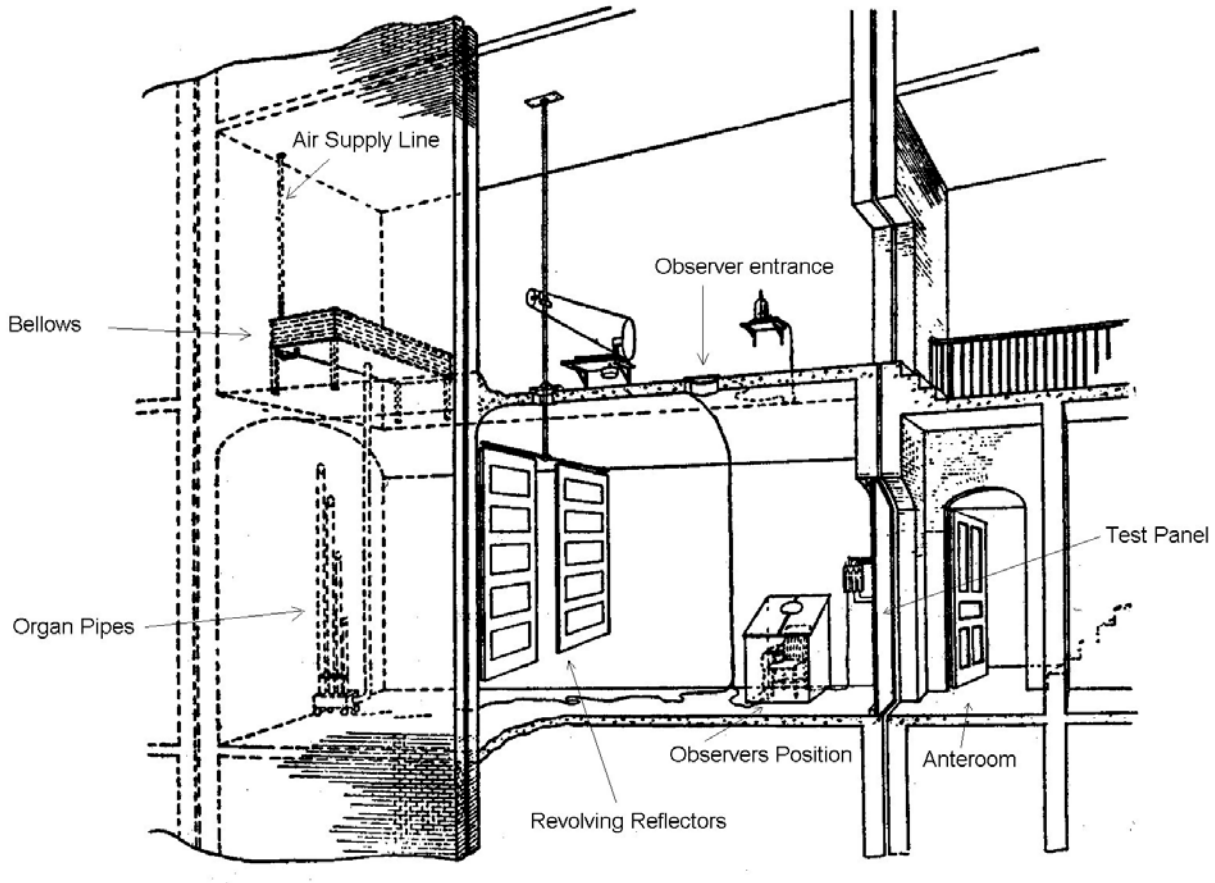

of equipment used in the historic development of the measurement of reverberation times. Considering the availability of equipment, it is extraordinary the extent that Sabine was able to formulate his theories and devise measurement procedures.

Those who have measured or followed the developments in the measurement of reverberation times in recent years can appreciate the inherent difficulties faced by Sabine. His work in this field is only over shadowed by his enormous discipline and scientific approach to the whole subject. What is more outstanding is when he embarked on the investigation of 'acoustical difficulties' in the lecture room of Harvard Fogg Art Museum (later renamed to Hunt Hall), he had been working in the area of optics and electricity and had *'revealed no special predilection for the problems of acoustics'*. (Hunt, 1964 pg. vi)

References

Hunt, F. V. (1964), 'Introduction', In *Collected papers on acoustics*, Dover Publications Inc, New York, pp. v-xiii.

Sabine, W. C. (1964a), 'The accuracy of musical taste in regard to architectural acoustics. The variation in reverberation with variation in pitch', In *Collected papers on acoustics*, Dover Publications Inc, New York, pp. 69-106.

Sabine, W. C. (1964b), 'Architectural acoustics', In *Collected papers on acoustics*, Dover Publications Inc, New York, pp. 219-236.

Sabine, W. C. (1964c), 'The insulation of sound', In *Collected papers on acoustics*, Dover Publications Inc, New York, pp. 237-254.

Sabine, W. C. (1964d), 'Reverberation', In *Collected papers on acoustics*, Dover Publications Inc, New York, pp. 3-68.

Human Response to Noise and Vibration due to Vehicle Movement

Nicole Kessissoglou and Tim Stonehouse

James Cook University, Townsville, Queensland 4811

Abstract

Vehicles (in air, land and water), as well as machinery (in industry and agriculture), expose man to mechanical vibration which can interfere with comfort, working efficiency and health and safety. In this paper, two studies of human exposure to noise and intermittent vibration due to vehicles and vibrating buildings are presented. In the first study, a sugar mill in the Burdekin, North Queensland, utilise locomotives for the transportation of harvested sugar cane. Noise and vibration problems arise with the existing locomotives due to their age (they were purchased in the 1970's). It is not a practical solution to replace the old locomotives with newer, ergonomically superior locomotives because the only access to the mill passes under a major traffic bridge which will not accommodate their height. Noise and vibration measurements were conducted in accordance with the relevant Australian Standard. In the second study, human response to building vibration generated by heavy truck movement on a major access road to the Townsville port is presented. Test results show that the amplitude of vibration levels greatly exceeds the base curves of the appropriate Australian Standard, indicating that the vibration levels are annoying to humans.

Introduction

Human response to vibration is the subject of much attention, and in particular, when the human body is subject to whole body vertical vibration. There has been extensive analytical modelling of the human body as a lumped spring-mass-damper system (Suggs *et al*. [1], Payne and Band [2]), as a distributed parameter system (Orne and Liu [3]), or even using the finite element method (Kitazaki and Griffin [4]). It is well established that man is very susceptible to vibration in the low frequency range (<10Hz). Such is the importance of this research field that regular meetings are held on the subject of Human Response to Vibration, and a collection of abstracts from these meetings published in the Journal of Sound and Vibration (Griffin [5]-[7]).

Vehicles (in air, land and water), as well as machinery (in industry and agriculture), expose man to mechanical vibration which can interfere with comfort, working efficiency and health and safety. Noise and vibration standards have been developed in order to evaluate human exposure to excessive noise and vibration levels. In this paper, two case studies are given: (i) noise and vibration assessment of out-dated locomotives employed in a north Queensland sugar mill, and (ii) human response to building vibration generated by heavy truck movement on a major access road to the Townsville port.

Background

Noise and Vibration Standards

Australian Standard AS2670-1990 entitled "Evaluation of human exposure to whole-body vibration" has been developed in order to assess the effect of human response to mechanical vibration. Part 1 of this standard is directly applicable to assess the effect of vehicle vibration on a human operator or passenger. Part 2 of this standard is applicable to assess the effect of structural vibration in buildings on the occupants due to intermittent vibration such as that generated by traffic passing by. In this second case, use of building (office or residential) and time of day (day or night) are taken into consideration.

Australian Standard 1269.1-1998 entitled "Occupational noise management" has been developed for noise assessment in the workplace. The exposure to noise of a worker is assessed in terms of an eight hour equivalent continuous A-weighted sound pressure level, where the maximum noise exposure level is 85 dB(A). Noise levels exceeding 85 dB(A) present a high risk to a person's health and safety in the workplace, and as a result, the person's hearing ability will become temporarily or permanently impaired.

For the vibration analysis, the appropriate frequency range in order to evaluate human response is from 1 Hz to 80 Hz in one-third octave bands. There are four factors that must be considered in order to assess the effect of mechanical vibration on man, corresponding to:

(i) level of vibration

(ii) frequency (1 to 80 Hz)

(iii) direction of vibration

(iv) duration of the vibration.

The preferred quantity to measure the level of vibration is acceleration in m/s^2. Vibrations transmitted to the human body are measured by a co-ordinate system in the x, y and z directions. AS2670-1990 considers vibration transmitted to the feet of a standing man, or the buttocks of a seated man. The z direction corresponds to the direction from the feet (or buttocks of a seated person) to the head, and is also commonly referred to as 'vertical vibration'. The x axis corresponds to the direction from the back to the chest of a person, and the y direction corresponds to the direction from the right side to the left side of a person. These axes are illustrated in Figure 1 [8]. To accurately assess the effect of mechanical vibration on man, the measurement of vibration are required to be taken on a structural surface supporting the human body at the point of entry to the human subject. For the locomotive study, the accelerometer was magnetically fastened to the chair of the operator, and vibration measurements were taken in all three directions (along the x, y and z axes). Measurements of the floor panels were also taken to determine the feet-to-head vibration transmission. In the second study, vibration measurements of a human subject seated in a chair in all three directions were taken. Measurements of the floor (in the z direction for a standing person and in the x direction for a person lying down) were also taken.

Limits of Human Exposure to Mechanical Vibration

Part 1 of AS2670-1990 specifies three limits of human exposure to mechanical vibration corresponding to (i) the 'Reduced Comfort Boundary', (ii) the 'Fatigue-Decreased Proficiency Boundary', and (iii) the 'Exposure Limit'. These limits give values of acceleration as functions of frequency and exposure time. The Exposure Limit corresponds to the occupational health and safety limit for humans. If the measured acceleration levels breach the boundaries specified in the Exposure Limit, the person's health is at risk. The Exposure Limit must not be breached regardless of the application. The Fatigue-Decreased Proficiency Boundary corresponds to the working efficiency of humans. If the boundaries in this limit are breached, exposure to vibration will result in a reduction in the working efficiency of the operator. A consequence of reduced efficiency is fatigue, which is known to worsen the performance of vehicle driving. The Fatigue-Decreased Proficiency Boundary is important in applications such as long distance heavy haulage where extended periods of concentration are required. The Reduced Comfort Boundary corresponds to the level of vibration for which humans' experience discomfort. This boundary is only relevant in applications such as family vehicles and passengers in human transport vehicles such as ferries, trains, etc.

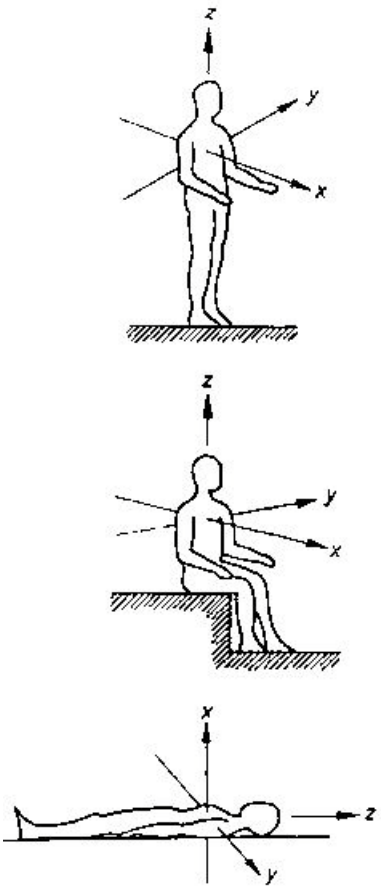

Figure 1. Directions of the x, y and z axes for a standing and seated man, and for a person lying down.

First Study – Noise and Vibration of Locomotives

Vibration Analysis

Due to an increasing concern expressed by locomotive drivers about the levels of vibration experienced during a working day, vibration measurements on three outdated locomotives employed in a north Queensland sugar mill were taken. In a given locomotive run, different acceleration levels caused by the different operating conditions of the locomotive were recorded in the x, y and z directions for a seated person, and in the z direction for a standing person. Care was taken to locate the sensor as close to the point of transmission as possible. Typical operating conditions corresponded to number of bins (empty and incremental increases), travelling along a straight track, turning a corner, etc. For each operating condition, vibration measurements

in all directions were taken with a corresponding duration time t_i. Since the measured vibration amplitude varied appreciably for the different operation conditions, it was necessary to calculate an equivalent exposure time. This was done as follows: first, a convenient acceleration level A' was chosen. This acceleration level has a corresponding permissible exposure time τ'. For this survey, A' was chosen such that τ' was eight hours. This was a convenient exposure time as it represents the eight hour working day of the operators. τ' was then used to calculate the equivalent exposure times t_i' using the following expression [8]:

$$t_i' = t_i \times \frac{\tau'}{\tau_i} \qquad (1)$$

where τ_i are the corresponding permissible exposure times for the measured acceleration levels. The total equivalent exposure time T' of the acceleration levels with respect to the reference level A' was calculated by the summation of all the individual equivalent exposure times t_i' in that locomotive run. If the total equivalent exposure time T' was found to be greater than the permissible exposure time of τ' (8 hours), then the limit has been breached.

Vibration measurements and equivalent exposure times were evaluated separately for each axis (corresponding to the x, y and z axes).

The procedure described above was repeated using equivalent exposure times corresponding to the human Exposure Limit for those one-third octave frequency bands which breached the Fatigue-Decreased Proficiency Boundary Limits.

Results and Discussion of Vibration Analysis

It was found that all three locomotives measured breached the Fatigue-Decreased Proficiency Boundary assuming that the operator was in the locomotive for seven hours out of an eight hour shift. The Exposure Limit was breached by one locomotive for a standing operator. None of the locomotives breached the Exposure Limit for a seated operator. Shown in Figures 2 and 3 are graphs of the equivalent exposure times, using the reference exposure time of 8 hours, for the z and y directions respectively of the locomotive 'A'. It can be seen that the Fatigue-Decreased Proficiency limit is breached in both cases, but the Exposure Limit is not breached. This means that there is no legal obligation for the company to attempt to reduce the vibration levels. However, it does mean that the performance of the operators will be affected, and they will feel some discomfort and fatigue by the end of their shift. From the results, it is also possible to determine at what frequencies the worst vibrations occur. This information is useful if an attempt is made to attenuate the vibration, as it gives an indication of the source of vibration. For example, if the vibration is predominantly in the low frequency range, then the suspension and structural rigidity of the cab should be examined, whereas high frequency vibration could be attributed to engine noise.

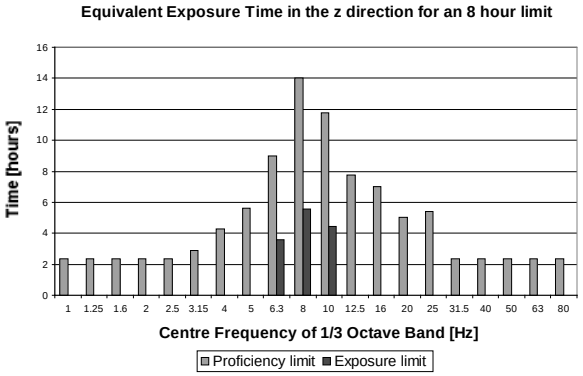

Figure 2. Equivalent exposure times for the locomotive 'A' measured in the z direction for a seated operator.

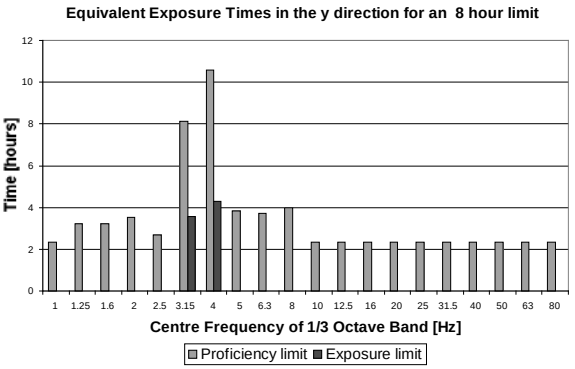

Figure 3. Equivalent exposure times for the locomotive 'A' measured in the y direction for a seated operator.

Noise Analysis

Noise levels were recorded at all variations of locomotive speed and load, and each noise level had a corresponding time interval. Sound pressure levels (L_{Aeq,T_i}) were obtained around the location of the worker's head, where L_{Aeq,T_i} represents the A-weighted sound pressure level for a time interval of T_i. Different measurement time intervals of T_i corresponding to the different locomotive speeds and loads were recorded so that all variations of noise levels inside the locomotive cab were taken into account. Hence, the total time T of a locomotive run was subdivided into part time intervals T_i for which L_{Aeq,T_i} values were recorded. An equivalent sound pressure level was obtained for the total duration of the locomo-

tive run. The equivalent sound pressure level was converted into an equivalent eight hour continuous sound pressure level ($L_{Aeq,8h}$) for comparison with the maximum eight hour continuous sound pressure level of 85 dB(A). $L_{Aeq,T}$ corresponds to the equivalent A-weighted continuous sound pressure level over the total time interval T, and was calculated by the following equation [9]:

$$L_{Aeq,T} = 10\log_{10}\left[\frac{1}{T}\sum_{i=1}^{n} T_i \times 10^{L_{Aeq,T_i}/10}\right] dB(A) \quad (2)$$

where $T = \sum_{i=1}^{n} T_i$ and n is the total number of part-time intervals. It is necessary to convert $L_{Aeq,T}$ to an equivalent eight hour exposure, $L_{Aeq,8h}$, in order to compare with the safety limit of 85dB(A). This is achieved by the following equation [9]:

$$L_{Aeq,8h} = L_{Aeq,T} + 10\log_{10}\left(\frac{T}{8}\right). \quad (3)$$

It is important to note that it is not necessary if the total exposure duration (T) is less than 8 hours. The noise exposure level of $L_{Aeq,T}$ for the time duration T is equivalent to a noise exposure level of $L_{Aeq,8h}$ for the time duration of 8 hours.

Results and Discussion of Noise Analysis

It was found that all three locomotives fell within the Occupational Health and Safety limits for human exposure to sound. The equivalent eight hour exposure levels were 83.3dB(A), 82.7dB(A) and 82.4dB(A). It was noted that high levels of noise were recorded during braking with heavy loads, the highest level being 86.4dB(A). However, as this noise level was only maintained for a brief period of time, and in general the noise levels were between 80dB(A) and 84dB(A), the noise levels were found to be acceptable.

Second Study - Human Response to Building Vibration due to Heavy Vehicle Movement

Boundary Street is the major access route to the Townsville port, and as a result there are high volumes of heavy traffic movement on a continuous basis. As Townsville continues to increase its surrounding industry, there is a corresponding increase in the volume of traffic to and from the port. This increase has prompted complaint from the Boundary Street residents. Due to these complaints, Main Roads Technical Services conducted a comprehensive residential survey and vibration study. In the survey, all respondents reported traffic vibration and the following occurrences: (i) windows or doors rattling; (ii) floor shaking or trembling; (iii) ornaments rattling; and (iv) traffic causing bed to shake. All respondents associated the vibration with heavy trucks passing by.

In the Main Roads study, peak vibration measurements were taken, and compared against AS 2187. This is The Explosives Code which discusses transmission of vibration from blasting. The Main Roads report concluded that the vibration levels observed would 'not normally be considered unpleasant to residents'. In reaching this conclusion, their report applies criteria used in the assessment of occasional short-term or transient vibration, such as those associated with blasting or construction activities (including road construction activities). However, such criteria are not suitable in the assessment of semi-continuous vibration, and also do not relate to situations for human comfort and perceptibility.

With regards to structural damage, the Main Roads Technical Services report correctly concluded that vibration levels 'generally <1mm/s' are substantially lower than those required to cause structural damage (generally >10mm/s is required). However, the report also concluded that peak vibration levels below 2mm/s would not 'normally be considered unpleasant to residents'. This conclusion is incorrect due to the fact that it was based on the <2mm/s vibration criteria which is provided by AS 2187. Hence, although the vibration levels appeared significant in engendering annoyance with the residents, the vibrations were not in the range to result in damage to buildings.

Due to the unsatisfactory outcomes of the Main Roads report, James Cook University was commissioned to carry out preliminary testing to determine if the vibration levels caused by the passing trucks were significant enough to be classified as annoying to the residents. In our vibration survey, AS 2670.2-1990 was used as outlined in the Background. Vibration measurements were taken in the late evening and very early morning at two different residential properties on Boundary Street. These vibration readings were compared to the curves representing magnitudes of approximately equal human response with respect to human annoyance. These curves were weighted in order to take into account the residential status of the premises and the time of day (night-time). The results of this preliminary work found that the levels specified in AS 2670.2-1990 were breached by as much as two times.

Following the JCU report, the Main Roads Technical Services department was again commissioned to carry out more vibration testing. In their second vibration study, a truck was repeatedly driven along Boundary Street at varying speeds and loads. Vibration measurements were taken and compared with BS 6472. BS 6472 is a British standard which defines the vibration

limit of annoyance to humans due to traffic passing by. This standard derives peak vibration limits (in mm/s) from the Root Mean Square vibration levels (in mm/s), and uses a crest factor of 1.4 (i.e. assumes the vibration is sinusoidal). The peak velocity criteria (sinusoidal) for residential spaces from BS 6472 are given as:

Time of Day	Vertical	Horizontal
Day	0.3 to 0.6	0.8 to 1.6
Night	0.2	0.6

The second report of the Main Roads Technical Services concluded that the vibration levels are exceeded on a very regular basis at the residential properties on Boundary Street. It was also concluded that the vibration amplitude was greatly dependent on the speed of the vehicle. The report stated that a 10km/h reduction in speed would reduce the level of vibration below the limits stated in BS 6472. The report also proposed resurfacing the road such that it was smoother, and thus would result in less vibration excitation.

Results and Discussion of the JCU Report

Measurements at two properties on Boundary Street were taken. It was observed that at one property, the amplitudes of vibration measured in all instances fell well below the levels considered annoying to humans. However, it was noted that on the day of testing, the volume of heavy vehicle traffic was very low. Also, this property was located quite far back from the road. Figure 4 shows the acceleration levels versus frequency at the first Boundary Street property in the z direction. As shown in the figure, the vibration levels specified in AS 2670.2-1990 are not breached. The second residential property is positioned close to the road, and also there was considerable traffic flow whilst measurements were being taken. In the results for the second property, the limits set out in AS2670.2-1990 were repeatedly breached in the z direction for a standing or seated person. Figures 5(a), (b) and (c) show the vibration measurements taken at the second residential property in the z direction. As shown in Figure 5, the standard levels were distinctly breached in both the low frequency range and the high frequency range. The source of the high frequency vibration is both tyre and engine noise. The source of the low frequency vibration can be attributed to the dynamic response of the truck (i.e. the vibration transmission from its suspension system) due to road irregularities such as bumps and potholes.

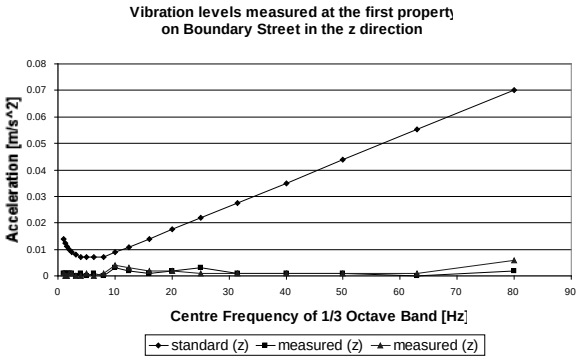

Figure 4. Vibration levels measured at the first property on Boundary Street in the z direction.

Both the JCU report and the second study conducted by the Main Roads Technical Services department concluded that the vibration levels experienced by the residents on Boundary Street are annoying. However, the difference between the two vibration studies is that Main Roads presented their vibration levels as a single peak value, whereas the JCU report presented the vibration levels as a function of the frequency range relevant to humans. Analysis of the acceleration levels in the various frequency bands allows determination of the source of vibration. Hence, accurate recommendations for vibration attenuation can be drawn from the results.

In conclusion, it is believed that the actions recommended by the Main Roads Technical Services department will successfully reduce the vibration levels. Resurfacing the road will eliminate vibration due to vehicle dynamics, and will also help reduce the tyre noise. Reducing the speed of the trucks will reduce both the engine noise and the tyre noise, as well as the vehicle dynamics.

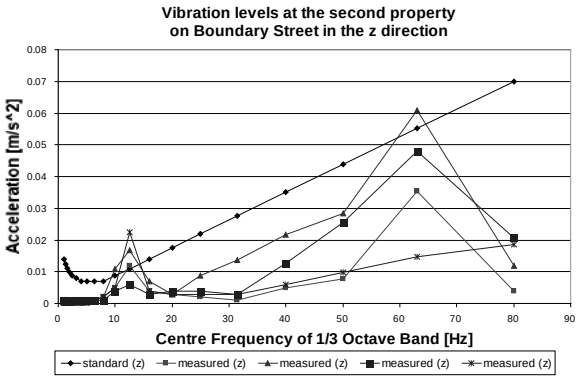

(a)

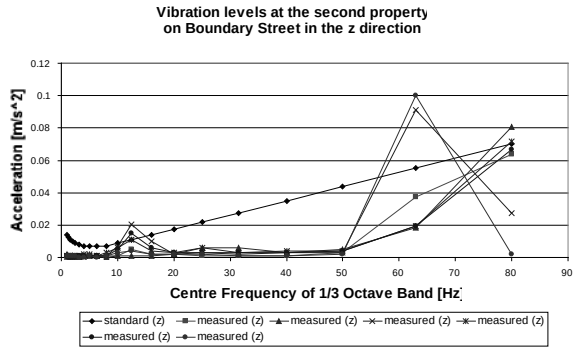

(b)

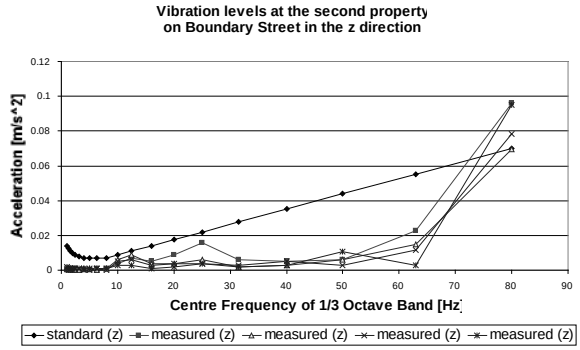

(c)

Figure 5. Vibration levels measured at the second property on Boundary Street in the z direction.

Conclusions

In this paper, human response to noise and vibration due to vehicle movement has been investigated. Two studies were conducted to assess human exposure to excessive vibration levels. The first study was conducted in a workplace environment to investigate the noise and vibration levels experienced by the operators of locomotives at a sugar mill. Results showed that although the health of the operators was not at risk, the performance of the operators was affected, which may result in fatigue and decreased concentration in the workplace. The second study was conducted at residential properties to measure the vibration levels experienced by residents due to trucks passing on a regular basis. The results from this study showed that the vibration levels experienced by the residents are annoying, and hence action is currently being taken to reduce the offending vibration levels. When evaluating human exposure to mechanical vibration, it is the engineer's responsibility to use the correct criteria (such as the proper measuring equipment and Australian Standards) in order to obtain relevant results.

References

[1] C. W. Suggs, C. F. Abrams and L. F. Stikeleather, "Application of a damped spring-mass human vibration simulator in vibration testing of vehicle seats", *Ergonomics* **12**, 79-90 (1969).

[2] P. R. Payne and E. G. U Band, "A four-degree-of-freedom lumped parameter model of the seated human body", *Aerospace Medal Research Laboratory, Wright-Patterson AirForce Base, Ohio, Report No. AMRL-TR*-70-35 (1971).

[3] D. Orne and Y. K. Liu, "A mathematical model of spinal response to impact", *Journal of Biomechanics* **4**, 49-71 (1971).

[4] S. Kitazaki and M. J. Griffin, "A modal analysis of whole-body vibration, using a finite element model of the human body", *Journal of Sound and Vibration* **200**, 83-103 (1997).

[5] M. J. Griffin, "Human Response to Vibration Abstracts", *Journal of Sound and Vibration* **190**, 875-879 (1996).

[6] M. J. Griffin and J. Griffin, "Human Response to Vibration", *Journal of Sound and Vibration* **228**, 1217-1221 (1999).

[7] M. J. Griffin and J. Griffin, "Human Response to Vibration", *Journal of Sound and Vibration* **232**, 1017-1020 (2000).

[8] AS 2670.1-1990 "Evaluation of human exposure to whole-body vibration. Part 1: General requirements."

[9] AS 1269.1-1998 "Occupational noise management. Part 1: Measurement and assessment of noise immission and exposure".

ACOUSTICS - putting the science and technology to work

Conference of the Australian Acoustical Society
Joondalup Resort, Western Australia, 15-17 November 2000

Session UW-5 Sources and Scattering

Measurement Of Radiated Noise Using A Vessel's Own Towed Array – A Progress Report

Alec J Duncan[1], John D Penrose[1], Darryl R McMahon[2]

[1]Centre for Marine Science and Technology, Curtin University,.[2]Maritime Operations Division, DSTO

Abstract

This paper describes progress to date on a project to investigate the feasibility of using a vessel's own towed array to measure the underwater noise radiated by the vessel.

Aspects of the problem discussed include the determination of array shape, the development of a forward simulation to provide data for algorithm development, the effects of ocean boundaries, the requirements for dynamic near-field beam forming / imaging, and the prediction of far-field signatures from the array data.

1. Introduction

All vessels radiate sound into the water to a greater or lesser extent as an inevitable by-product of the mechanical energy required to drive them through the fluid. To operators of most pleasure and commercial craft this is of little or no importance but to submariners and the crews of military surface vessels radiated underwater sound can be a critical factor in determining the vulnerability of their vessel to detection by a threat.

Fixed and portable acoustic ranges (see for example Mathews et al. 2000) have been developed to measure the acoustic radiation from vessels and, when coupled with acoustic propagation and ambient noise models, these measurements can provide reasonable estimates of the vulnerability of a particular vessel to detection in a given situation, *providing the acoustic signature of the vessel has not altered since it was measured*.

This last proviso can be of critical importance where a vessel is to be deployed into a theatre of operations at short notice, and it has been some considerable time since its acoustic signature was measured. Wear of machinery, minor propeller damage, and differences between the operational state of the vessel and its state when measured can all make significant differences to the acoustic signature of the vessel. Such differences in operational state could include a different fuel load, a requirement to operate at a different speed, or the use of some combination of auxiliary equipment that was not used when ranging took place.

It is thus extremely attractive for a vessel to have a means of measuring its own acoustic signature, or at least detecting changes in its signature, without recourse to a normal fixed or portable range and without relying on the presence of any other vessel or aircraft. Submarines are commonly fitted with hull mounted self-noise hydrophones for this purpose but it is highly problematic to accurately relate the far-field signature of the vessel to these near-field measurements.

Military surface vessels and submarines commonly carry towed arrays for the detection and tracking of other vessels. These arrays are streamed behind the vessel, may have a total length of more than 800 m and are typically populated with around 100 hydrophones. A diagram of a generic towed array is shown in Figure 1. The array shown has a total of 97 hydrophones arranged in three sub-arrays, each comprising 49 hydrophones. The total number of hydrophones and associated processing channels is minimized by designing the acoustic section so that some hydrophones are common

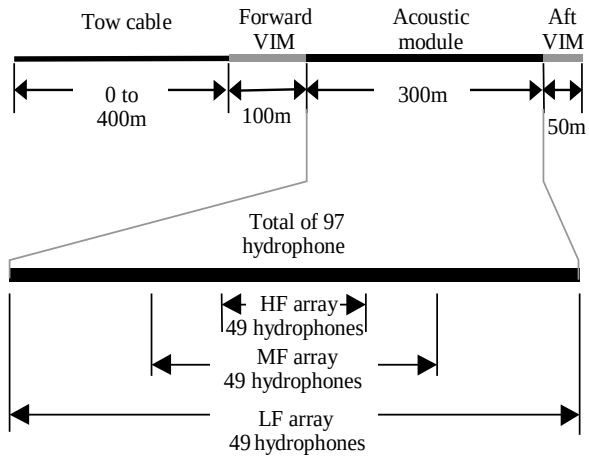

Figure 4 Schematic representation of a generic towed array. VIM = vibration isolation module. HF = high frequency, MF = medium frequency, LF = low frequency.

to two or three sub-arrays.

By carrying out an appropriate manoeuvre it is possible for a vessel towing such an array to bring the acoustic section of the array into a position that is favorable for imaging noise sources on the vessel. As will be seen below, while not necessarily in the true acoustic far-field of the vessel, the acoustic sub-arrays are at sufficient range that they are in the far-field of individual vessel noise sources and consequently the corrections required to estimate the far-field signature of the entire vessel are expected to be relatively minor (Anderson & McMahon 2000).

The research described in this paper forms the principal author's Ph.D. research topic which aims to explore the practical issues associated with using a vessel's own towed array for radiated acoustic noise measurement. There are many components to the task of predicting the performance of such a measurement method and the following sections detail the most significant of these and outline the progress that has been made on each so far.

2. Towed array hydrodynamic simulation

An initial requirement for this research was a method of determining realistic shapes for a towed array during a manoeuvre and the resultant hydrophone positions relative to the vessel. To this end a two-dimensional (horizontal plane) lumped-mass hydrodynamic simulation of a towed array was written in Matlab. The simulation uses reasonable estimates of the hydrodynamic and mechanical parameters of a typical towed array rather than measured values for a particular array and is intended to provide realistic results for simulation purposes and algorithm development rather than an accurate prediction for operational purposes.

The simulation output for one manoeuvre is shown in figures 2 and 3. Figure 2 shows the vessel and array positions in global coordinates whereas Figure 3 shows the position of the acoustic module of the array relative to the vessel during the manoeuvre. The latter figure is particularly revealing and leads to a number of important observations:

1. The acoustic module is in a reasonably good position and orientation to image the vessel from the 200 second mark to the 300 second mark. During this period the array is at a range of approximately 500 m from the vessel.

2. The motion of the hydrophones relative to the vessel is rapid (about 8 m/s) and the array shape and orientation also change quite rapidly. Note however that this simulation is for the relatively high tow speed of 5 m/s (10 knots) and that the relative speeds are proportionately slower at lower vessel speeds. To a first approximation the path the array takes is independent of tow speed so that array shapes at lower speeds can be estimated simply by changing the time labels on the plots appropriately.

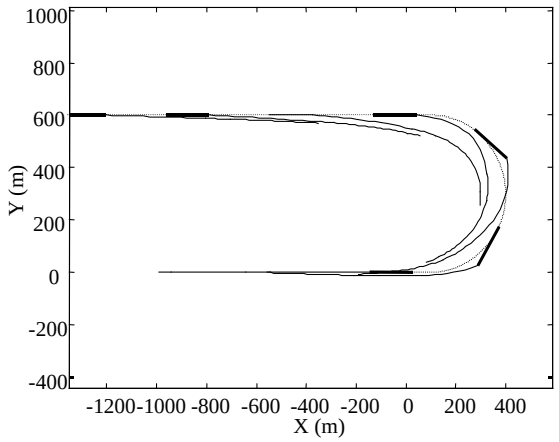

Figure 2 Six snap-shots of the simulated towed array shape during a U-turn manoeuvre. Thick line is vessel, dotted line is vessel track, thin line is towed array. Simulation starts with vessel at (0, 0) and moving to the right. Vessel speed = 5 m/s, turn radius = 300 m, tow cable length = 400 m.

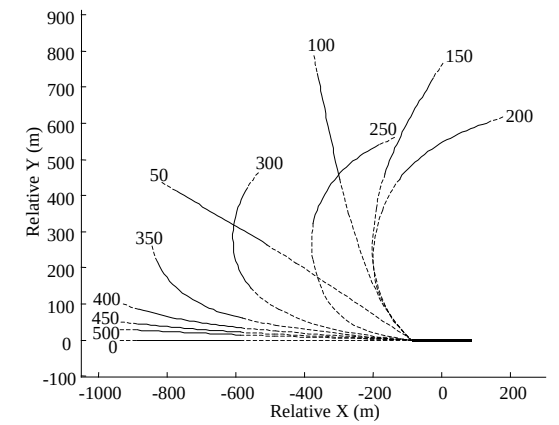

Figure 3 Simulated towed array shape relative to the tow vessel for the same manoeuvre as in Figure 2. Thick line is tow vessel, thin line is acoustic module, broken line is remainder of array. Numbers are time in seconds from start of simulation.

3. Acoustic sources on the vessel are in the near-field of the acoustic sub-arrays, with l^2/λ being 7200 m, 3600 m and 1800 m at the design frequencies of the LF, MF and HF sub-arrays respectively. (l is the length of the sub-array, and λ is the acoustic wavelength. The design frequency is the frequency at which the hydrophone spacing is half a wavelength.)

4. The hydrophones sample radiation emitted in a range of directions from slightly forward of the beam to directly aft of the vessel.

5. The time at which the array extends the most in a forward direction corresponds to the time at which the vessel straightens up after the turn.

6. During the first half of the manoeuvre there is a significant angle between the vessel and the tow cable where it leaves the aft end of the vessel. Avoiding violating the tow cable's minimum bend radius requirement at this point is likely to determine the minimum vessel turn radius that can be used.

3. Development of a forward simulation

A major component of the work on this project so far has been the development of a numerical simulation (in Matlab) of typical vessel noise sources and the propagation of these sounds to the moving hydrophones.

3.1 Simulation of typical vessel noise sources

The simulation has been configured to allow a variety of different noise sources to be specified and placed at arbitrary positions on the vessel. Far-field interfering sources and uncorrelated noise with a spectrum typical of noise in oceans and seas around Australia have also be included.

For reasons of computational efficiency each source has been approximated as a point source with a beam pattern that may be frequency dependent or frequency independent. This is a good approximation as can be seen by using the far-field criterion for a circular piston given in Medwin & Clay 1998, $R > \frac{\pi a^2}{\lambda}$ where R is the distance from the piston to the hydrophone and a is the radius of the piston, to solve for the piston radius for a hydrophone range of 500 m. The far-field criterion is met for all sources smaller than the calculated values shown in Table 1.

Table 1 Maximum radius of circular piston source that meets far-field criterion at a range of 500 m

Frequency (Hz)	Maximum source radius (m)
10	155
50	69
100	49
500	22

Surface vessel noise is usually dominated by propeller cavitation noise, although at low speed other noise sources may dominate. Cavitation noise has a broadband component due to the collapse of individual cavitation bubbles and a narrowband component due to fluctuations in the overall cavitation volume attached to each blade as the blade encounters different flow velocities and hydrostatic pressures through a revolution. Narrowband cavitation is at the blade passage frequency and its harmonics, whereas broadband cavitation has a wide frequency spectrum, usually peaking at around 100 Hz.

Broadband cavitation noise has been simulated by generating a sequence of gaussian random numbers of the required length, Fourier transforming this sequence to the frequency domain, applying a frequency domain filter of the required spectral shape, and then inverse Fourier transforming back to the time domain. The resultant time series can optionally be amplitude modulated at the shaft and blade rates.

Narrowband cavitation noise has been simulated by summing a deterministic and random component. The deterministic component was generated by summing sine waves with frequencies equal to the blade rate and its harmonics. The random component was generated in a manner similar to broadband cavitation noise but in this case band-pass filters were used centered on the blade-rate frequency and its harmonics. The filter bandwidths and relative amplitudes of the deterministic and random components were chosen to give time series with similar modulation characteristics to measurements reported in Gray 1981.

Due to a lack of consistency in the reported measurements cavitation noise has been simulated as having an omni-directional beam pattern even though there is some evidence in the literature for dips in the sound levels in the fore and aft directions (see for example Urick 1983).

Figure 4 shows the spectrum of the simulated propeller noise for a bulk carrier operating at 16 knots. The narrowband cavitation noise peaks can be clearly seen

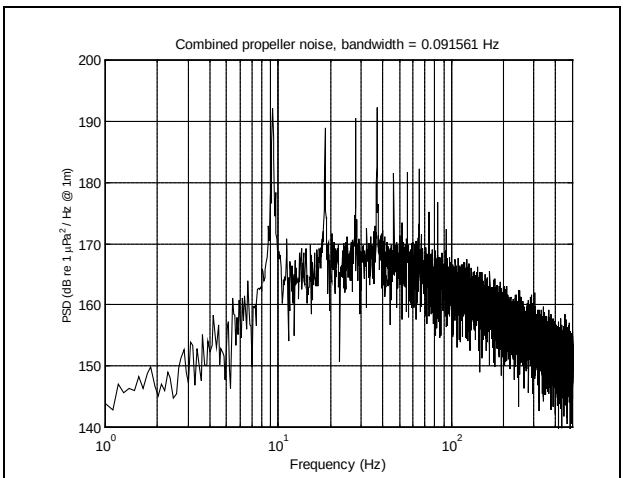

Figure 4. Simulated propeller cavitation noise for a bulk carrier

superimposed on the background of broadband cavitation noise.

Non-cavitating propellers also radiate sound, but generally at much lower levels than cavitating propellers and with a dipole (cosine) beam pattern which has a null at right angles to the propeller shaft. The primary mechanism is fluctuations in the force exerted on the fluid by the propeller as each propeller blade encounters different inflow velocities during a revolution. This mechanism directly radiates sound but can also excite resonances of the propeller blade and the hull which can greatly enhance the radiation (see Ross 1987).

Only direct radiation of non-cavitating propellers has been simulated so far. The characteristics of this mechanism are very similar to narrowband cavitation and it has been simulated by the same method apart from making due allowance for the lower source levels and different beam pattern.

The vibrations of rotating and reciprocating machinery can be coupled to the hull of the vessel by various structural elements and then radiate into the water as sound. All of these sources can be modeled as a well defined sequence of harmonics, possibly with some additional amplitude modulation, and this led to a simple implementation in the simulation as a sum of sinusoids. The beam pattern of the radiation depends on the detail of the excited hull vibrations and so a number of options have been provided for, including omnidirectional, circular pistons and rectangular pistons. More can be easily added as the need arises.

Several generic sources have also been included in the simulation for test purposes. These include a toneburst source and a general broad-band source. In both cases a variety of beam patterns can be specified.

3.2 Acoustic propagation modeling

The simulation will include three levels of complexity in modeling acoustic propagation from the sources to the hydrophones: boundless ocean, deep ocean, and shallow ocean. At the time of writing the boundless ocean case has been fully implemented, implementation of the deep ocean case is close to complete, and some preliminary work has been done on investigating algorithms appropriate to the shallow ocean case.

The boundless ocean case ignores the water surface and seabed reflections and deals only with the direct acoustic path between the source and hydrophone. This is quite straightforward in the case of a frequency independent beam pattern as the only requirement is the appropriate scaling and time shifting of the signal. For a frequency dependent beam pattern and a rapidly moving hydrophone, however, there is a significant complication because the beam pattern acts as a filter with a time varying frequency response. Although this situation can be dealt with exactly the computational cost is large and consequently an approximate method was devised which makes use of the relatively slow change in frequency response with time for realistic beam patterns and hydrophone motions.

The deep ocean case adds the complications of reflection and scattering at the water-air interface. Reflection is most conveniently dealt with by introducing a mirror image source corresponding to each real source on the vessel. Scattering has two effects - it reduces the amplitude of the coherently reflected signal and introduces an incoherently scattered signal with random phase. The reduction in amplitude of the coherent signal can be simply modeled in terms of the surface roughness, the acoustic wavelength and the angle of incidence (see, for example, Medwin & Clay 1998) whereas the calculation of the amplitude of the incoherent signal is significantly more complex and, for all but the simplest geometry, requires numerical integration over the region of sea surface contributing to the scattering. An efficient method of carrying out these calculations is currently being developed and will shortly be incorporated in the simulation.

Modeling propagation in the shallow ocean introduces another boundary - the sea floor - the acoustic properties of which are often not well known. A great deal of effort has been expended by many people on trying to accurately predict acoustic propagation in shallow water and a number of different techniques have emerged and been implemented in what have become standard numerical models. These include normal mode models (eg KRAKEN), parabolic equation models (eg RAM) and fast-field models (eg OASIS). Useful summaries of these methods are given in Etter 1991. Normal mode and parabolic equation models are intended for the prediction of propagation over ranges that are long compared to the water depth and are unlikely to give good results at the short ranges required for this simulation. Fast Field models are applicable to both short and long range propagation where the water depth and medium properties are independent of range (Kuperman et al. 1985). The Fast Field approach is being considered for this simulation although the rapid relative motions of the hydrophones and sources will require the development of special techniques. .

An alternative approach is outlined in Tolstoy & Clay 1987, and is an extension of the image method described above for the deep ocean case. In principle the presence of both an upper and lower boundary results in an infinite number of image sources. However, providing the lower (seabed) interface is lossy only a relatively small number of these image sources are important contributors to the received signal at short range, making the calculation manageable. Using this approach the seabed would be defined in terms of its complex plane wave reflection coefficient as a function

of incidence angle and frequency, and a correction given in Brekovskikh 1960 would be used to correct the reflection coefficient for the spherical divergence of the sound waves. (This correction is not required for reflection at the sea surface because at that interface the plane wave reflection coefficient is independent of the angle of incidence.) This approach is valid providing the angle of incidence is less than the critical angle and $kr >> 1$ where k is the acoustic wavenumber and r is the slant distance between the image source and receiver, which for r =500 m translates to $f >> 0.5$ Hz where f is frequency. Difficulties with this approach occur for incidence angles at and above the critical angle where beam displacement effects and the existence of interface waves make the simple image method less accurate and more complex to apply.

The image method has the advantage of being easily implemented with minor modifications to the code already developed for the deep ocean case. Sea surface scattering can also be handled in the same manner as for the deep ocean case.

4. Beamforming

Algorithms

From the discussion in Section 2 it is apparent that the algorithm used to perform the beamforming operation has to perform near-field beamforming in a situation in which both the array shape and the relative location of the source being tracked are changing rapidly with time.

There are many different beamforming algorithms of varying degrees of sophistication and efficiency described in the literature (see Krim & Veberg 1996, or Owsley 1985 for useful summaries), but none to the authors' knowledge that deal with the complexities of this particular requirement.

The saving grace is that the sources of interest are located on a relatively small, and known surface - the vessel hull. This should make it practical to apply a modification of delay and sum beamforming to dynamically focus the array at the required locations, with the delays being computed using the instantaneous locations of the hydrophones.

The dynamic nature of the beamforming problem may, in fact, turn out to be an advantage when it comes to suppressing interference from surface and seabed reflections and from far-field sources which will tend to be defocused as the array tracks the vessel.

Prediction of far-field signature

The results given in Table 1 show that in most cases the hydrophones will be in the far-field of the vessel noise sources, however it will be necessary to remove the effects of surface and seabed reflections in order to determine the source levels appropriate for computation of far-field signatures in different propagation conditions. There are a number of possible approaches to this:

- As mentioned above, dynamic near-field beamforming will tend to defocus the multipath arrivals relative to the direct path. The effectiveness of this mechanism is likely to be frequency dependent with it being least effective at low frequencies.

- Providing the depths of the sources and hydrophones and the sea state are known it should be possible to calculate and correct for the energy transmitted by the surface reflected path.

- If the seabed reflectivity is known then it would also be possible to compensate for the energy transmitted by bottom reflected paths. For this to be practical some in-situ method of determining the bottom reflectivity would have to be devised (see Kuperman et al. 1985 for one possible method).

- In the case of broadband sources it should be possible to detect significant multipath arrivals by autocorrelation techniques and then correct for them. This is complicated by the fact that in general the relative time delays of the multipaths will be changing quite rapidly, but given that the geometry is already reasonably well known it should be possible to compensate for this.

In the case of a high frequency source of large spatial extent or horizontally well separated sources that are coherent the far-field criterion may be violated and the computation of the vessel's far-field signature would become somewhat more complex. In this case, however, the shape of the source in the horizontal plane is likely to be resolvable by the beamformer which would allow the appropriate corrections to be calculated.

Hydrophone position errors

An important part of this project will be determining the required hydrophone position estimation accuracy for acceptable beamformer performance, and whether this degree of accuracy is likely to be achievable in practice.

A number of towed array shape estimation methods have been reported in the literature including those based on Kalman filters which use heading and depth sensors on the array as inputs (Gray, Anderson & Bitmead 1993, Riley & Gray 1993), and those that effectively use acoustic data from the array to find the shape that provides the sharpest focus (Quinn et al. 1993, Wahl 1993). If these methods are unable to provide the required accuracy then a third possibility would be to equip the vessel with one or two acoustic sources in known locations that emits short bursts of sound at the upper end of the array hydrophones' frequency range. Although obviously not covert, and therefore more limited in application, this would provide an accurate and straightforward way of determining the array shape.

Conclusions

This paper has summarised the work that has been carried out on an investigation of the practicalities of using a vessel's own towed array to measure its radiated acoustic noise signature, and has also scoped the issues that are still to be addressed and the approaches that are likely to be taken to tackling them.

Although there is still much work to be done, and there is no guarantee that the approaches outlined here will be the ones finally adopted, this technique appears to have the potential to be a very useful addition to existing signature measurement methods.

References

Anderson, D. & McMahon, D. 2000, 'Passive self-noise measurement for vulnerability estimation', in *Underwater Defence Technology Pacific 2000*, Sydney, Australia, pp. 31-34.

Brekovskikh, L. M. 1960, *Waves in layered media*, Academic Press, New York.

Etter, P. C. 1991, *Underwater acoustic modelling*, Elsevier Applied Science, London, New York.

Gray, D. A., Anderson, B. D. O. & Bitmead, R. R. 1993, 'Towed array shape estimation using Kalman filters-theoretical models', *IEEE Journal of Oceanic Engineering*, vol. 18, no. 4, pp. 543-56.

Gray, L. M. 1981, 'Investigation into modeling and measurement of propeller cavitation source strength at blade rate on merchant vessels', in *Propellers '81*, Society of Naval Architects and Marine Engineers, Virginia Beach, Virginia, USA, pp. 165-179.

Krim, H. & Veberg, M. 1996, 'Two decades of array signal processing research: the parametric approach', In *IEEE signal processing magazine*, pp. 67-94.

Kuperman, W. A., Werby, M. F., Gilbert, K. E. & Tango, G. J. 1985, 'Beam forming on bottom-interacting tow-ship noise', *IEEE Journal of Oceanic Engineering*, vol. OE-10, no. 3, pp. 290-8.

Mathews, D. N., Hall, M. V., Jessup, B. L., Mentjox, J. & Formby, P. 2000, 'Accurate measurement of ship acoustic signatures in shallow water', in *Underwater Defence Technology Pacific 2000*, Sydney, Australia, pp. 14-17.

Medwin, H. & Clay, C. S. 1998, *Fundamentals of acoustical oceanography*, Academic Press, San Diego, USA.

Owsley, N. L. 1985, 'Sonar array processing', in *Array signal processing*, ed. Haykin, S., Prentice-Hall, pp. 115-193.

Quinn, B. G., Barrett, R. F., Kootsookos, P. J. & Searle, S. J. 1993, 'The estimation of the shape of an array using a hidden Markov model', *IEEE Journal of Oceanic Engineering*, vol. 18, no. 4, pp. 557-64.

Riley, J. L. & Gray, D. A. 1993, 'Towed array shape estimation using Kalman filters-experimental investigations', *IEEE Journal of Oceanic Engineering*, vol. 18, no. 4, pp. 572-81.

Ross, D. 1987, *Mechanics of Underwater Noise*, Peninsula Publishing, Los Altos.

Tolstoy, I. & Clay, C. S. 1987, *Ocean Acoustics*, American Institute of Physics, New York.

Urick, R. J. 1983, *Principles of underwater sound*, 3rd edn, Peninsula Publishing, Los Altos, California.

Wahl, D. E. 1993, 'Towed array shape estimation using frequency-wavenumber data', *IEEE Journal of Oceanic Engineering*, vol. 18, no. 4, pp. 582-90.

Acoustic Source Analysis of Merchant Shipping in Dampier, WA.

D. Matthews, P. Formby, M. Hallett, J. Mentjox and M. Savage

Maritime Operations Division, DSTO, Pyrmont, Sydney, NSW 2009

Abstract

Acoustic measurements of several merchant ships were performed in Dampier, WA, earlier this year. This was a continuation of a previous trial completed back in 1998 where accurate positional information of the ships was not possible. This paper reports on the analysis of this new data with emphasis on investigating the nature of the acoustic source distribution along the length of the merchant ship and the acoustic source levels at various frequencies. In order to do this, 1/3 octave band levels of ship data as a function of range have been compared to similar data from a broad band point source that was towed over the same area. Since both sources were identically effected by the environment (same transmission loss) it was possible to make a direct comparison of the results. The close abeam distances and accurate positional information also allowed an analysis of the acoustic source distribution along the length of the ship at its transit speed. In addition to these measurements a calibrated J11 noise projector was towed over the same area while emitting single tones of 63, 125, 250, 500, 1000 and 2000 Hz. Since the source level at these frequencies is known it was possible to make some estimate of the source levels of the ships at these six frequencies. The results will be discussed.

Introduction.

To date there is very little information on the acoustic signatures of merchant ships in Australian waters. This paper attempts to address this problem by reporting on some merchant ship signatures measured in Mermaid Sound, Western Australia.

Mermaid Sound is the main shipping route into the port of Dampier. There are two main channels that service this port, the Hammersley and the Woodside channels. When fully laden the ships are constrained to travel up one of these two channels and consequently their position can be conveniently predicted allowing their acoustic signatures to be easily measured. The Hammersley channel caters mainly for the iron ore and salt industries while the Woodside services the oil and gas companies. Despite the latter having a predominantly higher percentage of larger ships, the Hammersley has a much higher shipping movement and consequently this channel was chosen to take acoustic signatures.

Experiment.

An acoustic, seismic, magnetic package was deployed in the Hammersley channel in Mermaid sound at the position 116^{o} 41.852' E, 20^{o} 33.998' S. The mean water depth in the areas surrounding the channel is ~15 m, whilst in the channel itself this increases to ~20 m. Measurements were made on five consecutive days. This paper will discuss only the acoustic results.

The hydrophone package used to collect the data was designed at the DSTO. It consists of a ITC 1032 hydrophone connected to a 25 dB preamplifier which is housed in a water tight container. The signal is then sent back for collection via a copper cable. The overall weight of the package (acoustic, seismic and magnetic) is less than 50 kg and consequently can easily be deployed from a zodiac by two people. This was placed just inside the channel and a cable run back to a ship anchored approximately 100 m to the East. Acoustic signatures of merchant ships were then collected on an opportunity basis. On board the stationary vessel the data was fed into an anti aliasing low pass filter with a cut off frequency of 20 kHz. It was then sampled at 50 kHz using a DT3005 A/D card housed inside a PC. Data was recorded simultaneously on a second channel to mark the position of the bow and the stern of the ships as they passed the package at the closest point of approach (CPA). This involved manually pressing a switch for the duration of the traverse, which recorded a DC voltage onto the second channel. Information about the ship length was then obtained at a later date which allowed the ship speed to be calculated. The ship data was collected for a total of 600 seconds which corresponded to a distance of approximately 3000 m depending on the ship speed. Additional positional information was obtained using a laser range finder. The distance between the recording vessel and the ranged ship was measured as a function of time and recorded onto the same computer used for the A/D conversion using the RS232 port. On the inbound run ranging was done by aiming at the front of the bridge while on the outbound run it was done off the back. The data was then corrected for the displacement on analysis to give the ship speed and range information.

In addition to the ship measurements acoustic data was also collected for two other sources towed over the same terrain. The first was an uncalibrated broad band point source towed 180 m behind a 25-foot banana boat travelling at 3.35 ms^{-1}. The source depth was 2 m. The second point source was a calibrated J11. This was towed 260 m behind the same tow vessel but at a depth of approximately 1.5 m. It was towed at an average speed of 2.5 ms^{-1} and for frequencies of 63, 125, 250, 500, 1000 and 2000 Hz. The source levels for the six frequencies were 154.0, 156.8, 155.7, 154.7, 156.0 and 155.9 dB re $1\mu Pa^2Hz^{-1}$@1m respectively. Since each frequency involved a separate run the abeam distances at CPA and the tow speeds were all slightly different. By towing these sources over the same track as the ship it was possible to make a direct comparison of the three sets of data. The advantage of the broad band source is that only one run is required for all frequencies and consequently the abeam distance and speed are the same for all analysis.

Results.

During the five day period of the trial several ships were collected on either their inbound or outbound journeys and some on both. This paper however will focus only on two of the ships, the Hyundai Olympia and the Sincere Gemini, both on their outbound journeys. Table 1 gives details about these ships together with the experimental information for the J11 and broad band source runs.

	Sincere Gemini	**Hyundai Olympia**	**BBS**	**J11**
Speed (ms^{-1})	5.35	3.84	3.35	<2.5>
Water Depth (m)	19.4	20.6	19.4	<21.0>
Ship Length (m)	160	292	-	-
Ship Draft (m)	10.3	18.0	-	-
Blade Rate (Hz)	10.6	10.8	-	-
Abeam Dist (m)	49	57	52	0-36
Source Depth (m)	4.4	9.5	2.0	1.5
Ship Breadth (m)	25	46	-	-

Table 1.

The source depths for the ships was derived from an equation reported by Gray and Greely [1] and is given by,

$$H = 0.25\left(0.12L^{0.75}\right)^{1.7}$$

where L is the length of the ship and H is the source depth.

Figure 1 shows a plot of the 1/3 octave bands as a function of horizontal range for Hyundai Olympia. The centre frequencies of the bands are indicated on the

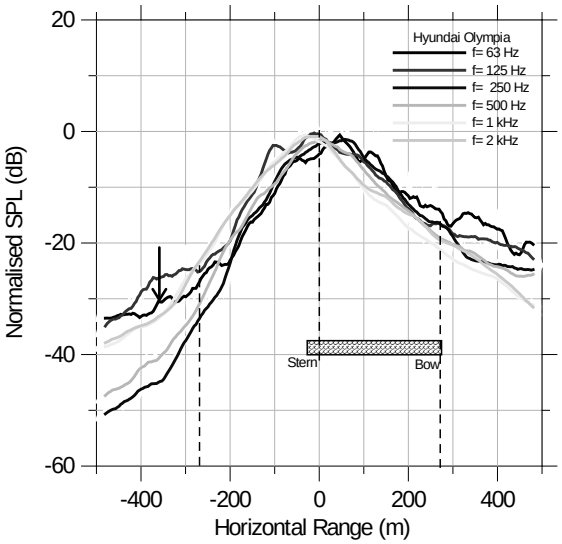

Figure 5

figure and go from 63 Hz to 2 kHz in octave steps. The sound pressure levels have been normalised to the maximum pressure, which occurs at CPA. The data was then smoothed in order to highlight the envelope shape of the acoustic signature. The horizontal range has been referenced to the bridge of the ship whose position has been indicated on the figure by the shaded rectangle.

As can be seen all the six frequencies peak around the stern of the ship. The 63 Hz and 250 Hz appear to peak close to the bridge position whereas the others are near the stern. For f ≥ 250 Hz there is a clear point of inflection at the horizontal range of –350 m after which the SPL increases rapidly with decreasing range. Once the ship has passed over the hydrophone the SPL decreases at a slower rate with increasing distance than that observed on the approach. This can be explained by considering the effect of the hull of the ship on the sound propagation. This is shown in figure 2. The side view shows the ship travelling down the channel towards the hydrophone that is positioned on the sea bed. In this case it is assumed that the ship will pass directly over the hydrophone. From the diagram it can be seen that the ship essentially reduces the effective

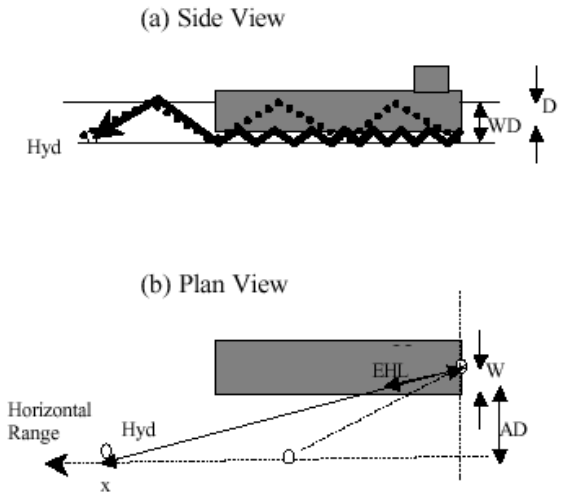

Figure 2

water depth to a value EWD = WD – D, where WD is the water depth and D is the draft of the ship. For the case of Hyundai Olympia and Sincere Gemini EWD= 2.6 and 9.1 m respectively. Consequently, in order for the sound to propagate from the stern of the ship to the hydrophone it will have to travel along the length of the hull before it enters the main water column where the EWD = WD ~ 20 m. This is shown by the solid black line in Figure 2(a). The dotted line path shows the equivalent ray path for a source located at the same position but ignoring the effect of the ship hull. As can be seen the solid ray path is subjected to many more bottom bounces than the dotted path. Since each bottom interaction will result in some attenuation of the sound the SPL measured at the hydrophone will be less if the hull is taken into account than without it. In reality the ships passed the hydrophone at an abeam distance similar to that shown in the plan view of figure 2(b). In this case the length of hull that the sound has to bounce along changes as a function of horizontal range. It is easy to show that this effective hull length (EHL) is given by,

$$EHL = \frac{W}{W + AD}\sqrt{x^2 + (W + AD)^2} \qquad (1)$$

where W is the ships beam/2, *x* is the horizontal range and AD is the abeam distance at CPA. Figure 3 shows the EHL as a function of horizontal range for Hyundai Olympia and Sincere Gemini. The abeam distances etc can all be found in Table 1. As can be seen, for ranges greater than 1050 m the EHL for Hyundai Olympia remains fixed at 300 m (the length of the ship) and its effect on the sound propagation will be constant for all ranges greater than this. However for ranges less than 1050 m the EHL decreases with decreasing range until at CPA it equals half the width of the ship. Consequently its effect on the transmission loss will vary with range. Once the ship passes the hydrophone the EHL becomes zero and it has no effect on the sound propagation. Similar results are shown in Figure 3 for Sincere Gemini. This ship is approximately half the length of Hyundai Olympia and has a draft of 10.3 m (~half the water column) compared to 18 m. For this ship the EHL is smaller for all ranges.

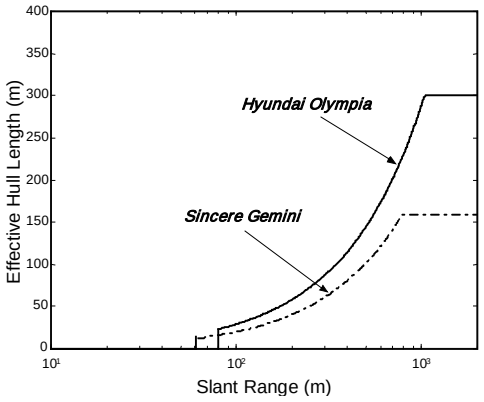

Figure 3

It should however be pointed out that it is the effective water depth (EWD) in conjunction with the effective hull length (EHL) that is the important parameter. In the case of Hyundai Olympia the EWD = 2.6 m and consequently the number of bottom reflections will be much greater than that for Sincere Gemini which has an EWD = 9.1 m. It would therefore be expected that the rate of increase of the SPL with decreasing range should be greater for Hyundai Olympia than that for Sincere Gemini. This indeed was the case as will be shown below.

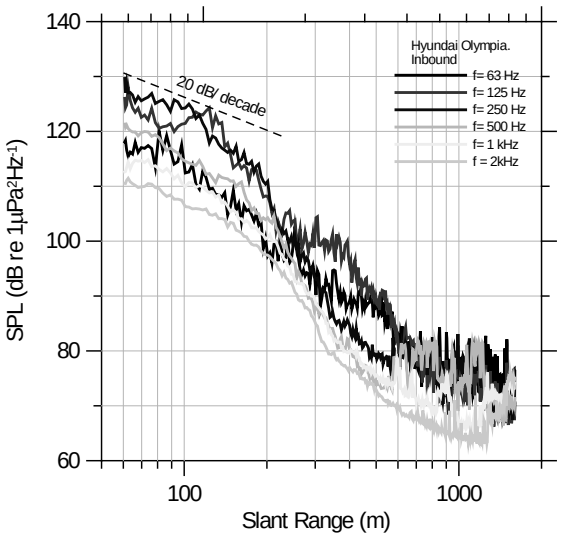

Figures 4 and 5 show the variation of the six 1/3 octave frequencies as a function of slant range for Hyundai Olympia. Figure 4 corresponds to the data for the ship as it is approaching the hydrophone (inbound) and Figure 5 is for the ship receding (outbound). The slant range has been plotted on a logarithmic scale in order to investigate the applicability of using an inverse

power law spreading model to predict the range variations of the SPL. As can be seen the inbound data (Figure 4) shows a different range variation than the outbound for all frequencies. For ranges less than 100 m the SPL drops off with range at 20 dB/decade. The rate of drop off then gradually increases until a maximum of 70 dB/decade is observed at approximately 300 m. The signal then merges into the background at the higher ranges. For the outbound run all six frequencies show a similar fall off of approximately 28 dB/decade with range as shown in Figure 5.

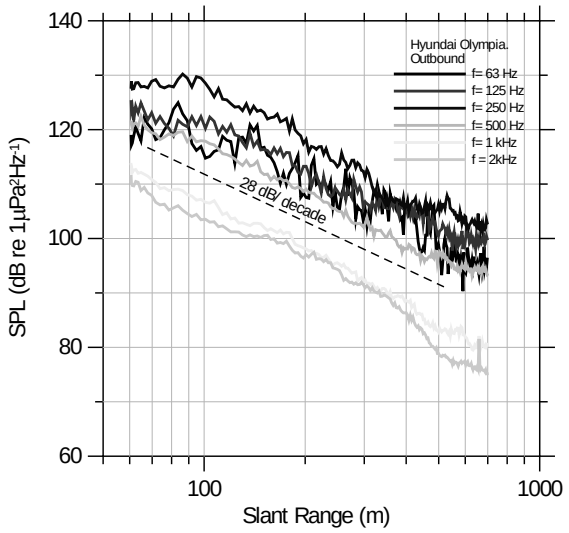

Figure 5

Figures 6 and 7 show the same analysis for Sincere Gemini. In this case the curvature present for the inbound run of Hyundai Olympia was not observed. As mentioned above, this can possibly be explained by the fact that the EWD below the ship was 9.1 m compared to 2.6 m for Hyundai Olympia. Consequently the number of bottom reflections will be reduced thus resulting in a shallower increase of SPL with range. Figure 6

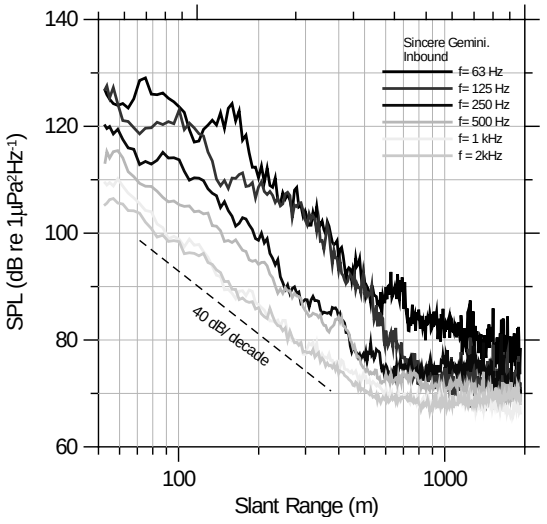

Figure 6

shows that for the inbound run an increase rate of approximately 40 dB/decade would account for all six frequencies. The irregularities observed in the 63 Hz and 125 Hz are due to the interference effects of the seabed and surface. As can be seen in Figure 7 the SPL falls off at approximately 28 dB/decade on the outbound run similar to that of the large ship.

As mentioned above a calibrated J11 point source was

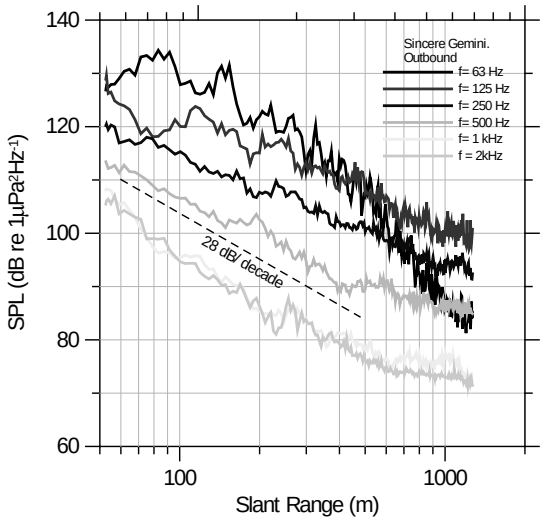

Figure 7

towed over the same location that the ships passed. This projected single tones at frequencies corresponding to the six used for analysing the ship data above. In order to make a comparison this data was converted into 1/3 octave data using a technique called range averaging used by Harrison et al [2]. Figures 8 and 9 show the J11 results for the equivalent inbound and outbound runs of the merchant ship runs respectively. For the North side runs (which correspond to the outbound ship data) the data will be contaminated by the tow vessel at certain frequencies. Despite this both sides show similar drop offs of the SPL with range at

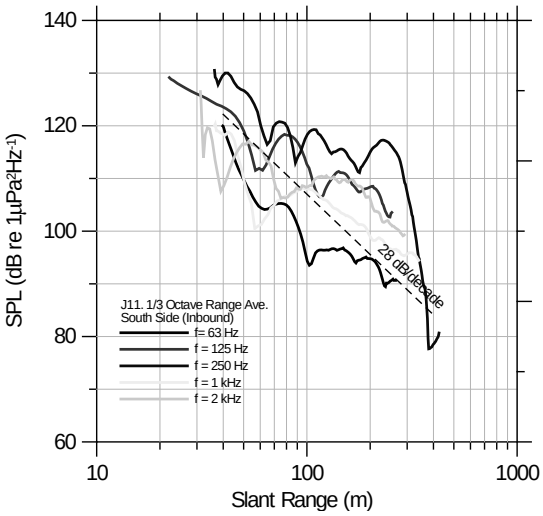

Figure 8

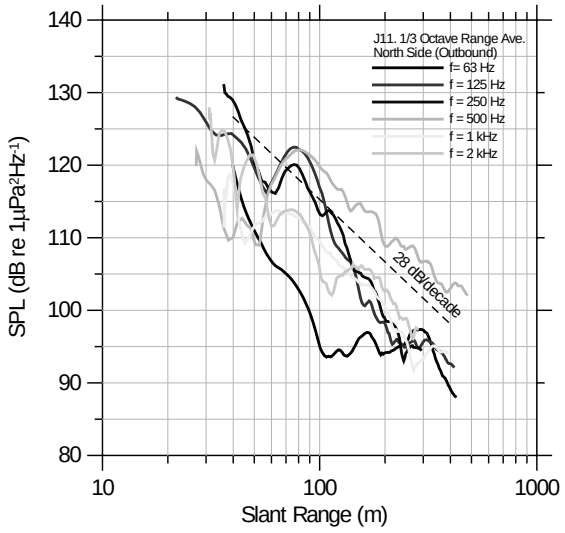

approximately 28 dB/decade which agrees with the two ships on the outbound runs.

One noticeable difference between the J11 results and the ships is that there is significantly more structure in the data. This could possibly be explained by the fact that there may be multiple sources of the same (within the limit of the 1/3 octave band) frequency distributed over a finite volume in the ship. If these sources have random phase relative to each other then their contribution to the overall SPL at some location away from the ship will be the incoherent addition of each source. Consequently the structure observed in the J11 data will not be present for the ship results. On a ranging scale these sources may appear to be all located around the stern of the ship whereas in reality they are all distributed through a volume of several cubic metres.

The similarity of both the North and South sides confirm that the asymmetry observed in the ship data is due to the ship itself and not the environment.

Conclusion

The acoustic signature of two ships collected in Dampier, WA have been carefully analysed. All results indicated that the ships can be considered as a quasi-point source with the source located very close to the stern of the ship. The position of the peak in the SPL showed very little variation with frequency but do show an asymmetry in the acoustic envelope as a function of range for 1/3 octave bands ranging from 63 Hz to 2 kHz. A model has been proposed to account for this asymmetry based on the effect of the hull reducing the effective water depth below its keel line. This results in an increase in the number of bottom interactions which gives rise to an increase in the transmission loss. These results have been supported by J11 data towed over the same location. This point source showed no asymmetry in the acoustic envelope and the SPL dropped off with range at a similar rate as that of the merchant ships on their outward journey away from the hydrophone.

References

[1] L.M. Gray and D. S. Greeley. Source Level model for propeller blade radiation for the worlds merchant fleet. JASA. **67** (2), Feb. 1980.

[2] C. H. Harrison and J. A. Harrison. A simple relationship between frequency and range averages for broadband sonar. JASA. **97** (2), Feb. 1995.

Acknowledgment

D. Matthews would like to thank the crew of Sail-A-Way in Dampier for being so helpful and flexible and M. V. Hall for his helpful discussions.

Investigating The Acoustic Properties Of The Underwater Implosions Of Light Globes And Evacuated Spheres

Alessandro Ghiotto[1], Supervised by Prof J.D. Penrose[2]

[1]Nautronix, Ltd., [2]Centre for Marine Sciences and Technology, Curtin University

Abstract

The dynamics of empty and gas filled cavities are reviewed from which estimations are made about source levels and spectra for cavities of particular size, depth and internal gas type and pressure. Household light globes and specially manufactured evacuated spheres were imploded at depths of 1m to 40 m and the pressure–time series and spectra of the implosions are presented.

The internal pressures of the unbroken vessels are estimated based on the bubble resonance frequency and implosion depth. Source levels and bubble resonance frequencies obtained from experimental results are compared with theoretical results derived from implosion depth and estimated initial internal gas pressure. The observed variability in source level, bubble resonance frequency and the presence of sub harmonics of the bubble resonance frequency are discussed.

Introduction

Household light globes have been used with increasing popularity as an acoustic source. Unlike an airgun source, the initial gas pressure in the bubble is much lower than the ambient pressure and the bubble reaches equilibrium after a small number of oscillations. (The bubble pulse is less than 100 ms at 40 m.) The peak pressure developed is typically around 150 dB re 1 μPa for implosions at 40 m depth. Higher peak levels may be obtained by using vessels with a lower internal gas pressure. A low gas pressure also results in a short bubble pulse which is desirable for easier deconvolution of received signals and their associated multipaths, but shortening the pulse causes the energy to be distributed over a wider frequency band. Glass spheres with very low internal gas pressure were used as an alternative to light globes to investigate the effect of a lower internal gas pressure on radiated spectra and pulse duration.

Bubble Dynamics

The Rayleigh Collapse

Assuming sphericity at all times, the collapse of a vacuous cavity in an *incompressible fluid* was determined by Rayleigh (1917). The work done by the hydrostatic pressure in contracting the radius of an empty cavity from a maximum (starting) radius R_m to an instantaneous radius R is equivalent to the kinetic energy of the liquid. The kinetic energy of the liquid can be predicted by integrating the spherically symmetrical energy distribution over shells of liquid of thickness Δr, mass $4\pi r^2\rho\Delta r$, and speed dr/dt. The work done by the hydrostatic pressure p_0 is $(4/3)\pi p_\infty(R_m^3 - R^3)$. Maintaining that the fluid is incompressible, at any time Δt, liquid of mass $4\pi r^2\rho\dot{r}\Delta t$ flows across the surface with radius r. Considering the flow at the cavity boundary,

$$\frac{\dot{r}}{\dot{R}} = \frac{R^2}{r^2} \tag{1}$$

The kinetic energy can now be evaluated as $2\pi\rho\dot{R}^2R^3$. The wall velocity, $\dot{R}$ can be found to be:

$$\dot{R} = \pm\sqrt{\frac{2p_\infty}{3\rho}\left(\frac{R_m^3}{R^3} - 1\right)} \tag{2}$$

The positive and negative roots correspond to the expanding and collapsing cavity respectively. Integrating the wall velocity with respect to time gives the collapse time.

$$t_{ray} = \int_{R_m}^{0} \frac{1}{\dot{R}}\,dR \quad \approx \quad 0.915\sqrt{\frac{\rho}{p_\infty}} \tag{3}$$

Withholding the assumption of an incompressible fluid, the derivation breaks down as dR/dt approaches the speed of sound in the liquid. This can be seen from equation (3), where as R becomes very small, the collapse speed becomes very large until finally when R=0, the result is undefined.

Collapse of a Cavity Containing Gas

The gas inside a cavity will be compressed as the cavity collapses, thus retarding the collapse. The cavity will reach a minimum volume at some maximum gas pressure and then expand again until the gas pressure is well below the ambient liquid pressure and then collapse again, oscillating about some equilibrium volume. Assuming no heat flow or dissipation, the gas pressure may be expressed as

$$p_g = p_{g,m}\left(\frac{R_m}{R}\right)^{3\gamma} \tag{4}$$

where γ is the ratio of specific heats of the gas in the cavity. The energy calculations now include the compression of the gas (which has pressure $p_{g,m}$), represented by the last term in the conservation of energy equation (5). Assuming surface tension and vapour content is minimal and the external pressure p_0 is constant, the energy equation for the bubble collapse is:

$$\frac{3\rho\dot{R}^2}{2} = p_0\left[\left(\frac{R_m}{R_{\min}}\right)^3 - 1\right] - p_{g,m}\frac{1}{1-\gamma}\left[\left(\frac{R_m}{R}\right)^3 - \left(\frac{R_m}{R}\right)^{3\gamma}\right] \tag{5}$$

The positions of maximum and minimum cavity radius are at R_m and at R_{min}, at which time dr/dt = 0. At the minimum radius, equation 5 can be simplified to

$$p_{g,m}\left(\frac{R_m}{R}\right)^{3(\gamma-1)} = p_0(\gamma-1) \tag{6}$$

The minimum radius is then:

$$R_{\min} = \frac{R_m}{\left(\frac{p_0(\gamma-1)}{p_{g,m}}\right)^{\frac{1}{3(\gamma-1)}}} \tag{7}$$

The Oscillating Bubble

Continuing with the assumption of a spherical bubble in an ideal fluid, a simple analogy can be made between the pulsating bubble and a bob of mass *m* attached to a spring. Using this analogy the stiffness, resonant frequency and the energy of the oscillator can be determined. The restoring force arises from the compressibility of the gas in the cavity and the inertia of the system is associated primarily with the moving liquid. The main flow of energy is between potential and kinetic energy, which is dependent on the acceleration of the bubble volume.

The bubble wall describes a motion $R_\varepsilon = -R_{\varepsilon 0}\, e^{i\omega t}$ about a mean radius R_0 and with resonance frequency ω_0 and displacement $R_{\varepsilon 0}$. The kinetic energy of the liquid is then:

$$\phi_K = \frac{1}{2}\int_R^\infty \left(4\pi r^2 \rho dr\right)\dot{r}^2 \tag{8}$$

which may be expressed as $\phi_K = 2\pi R^3 \rho \dot{R}^2$. ϕ_K is at a maximum at the equilibrium bubble radius $R\varepsilon_0$, At this position, dr/dt is also at a maximum, hence

$$\left|\dot{R}\right|^2 = (\omega_0 R_{\varepsilon 0})^2 \tag{9}$$

$$\text{i.e. } \omega_0 = \frac{\dot{R}}{R_{\varepsilon 0}} \tag{10}$$

Using the bubble energy equation (5) it can be shown that

$$\omega_0 = \frac{1}{R_0}\sqrt{\frac{3\gamma p_0}{\rho}} \quad \text{Minnaert (1933)} \tag{11}$$

This resonance frequency ω_0 requires that heat exchanges and surface tension effects are negligible. This has been shown to be an adequate approximation for bubbles as small as 1mm in diameter. (Leighton, 1997).

If the pulsating bubble is considered to behave as a harmonic oscillator, the 'spring stiffness' must be defined: Consider a bubble in a liquid of static pressure p_0 which collapses from an equilibrium volume of V_0 by ∂V to V, so the radius changes from R_0 to $R_0 - R_\varepsilon$. The gas pressure therefore increases from $p_{i,e} = p_0 + 2\sigma/R_0$ by ∂p_i to p_i.

If $p_i V^\kappa$ = a constant then

$$\Delta p_i = -\frac{\kappa}{V_0} p_{i,e} \Delta V \tag{12}$$

If $R_\varepsilon << R_0$ then $\partial V = 4\pi R_0^2 R_\varepsilon$

and $$\frac{\Delta V}{V_0} = -\frac{3R_\varepsilon}{R_0} \tag{13}$$

The force necessary to change the bubble volume is due to the excess pressure acting over the surface area of the bubble. Using equations 12 and 13;

$$F_A = 4\pi R_0^2 \Delta p_i = -12\pi\kappa R_0 p_i R_\varepsilon \tag{14}$$

The stiffness of the bubble can now be written as

$$k = 12\pi\kappa R_0 p_{i,e} \tag{15}$$

If the surface tension is omitted, then

$$k \approx \frac{3\kappa p_0}{R_0} \tag{16}$$

The inertia of the system is provided by the fluid mass flux in the vicinity of the pulsating cavity. This mass flux can be expressed as

$$Q = \rho \frac{\partial Vol}{\partial t}(t)$$

$$= \rho 4\pi R_0^2 \frac{\partial R}{\partial t} \tag{17}$$

Hence the equivalent mass of the system is 3 times the mass of the water displaced by the bubble at equilibrium.

i.e. $$m_e = \rho 4\pi R_0^3 \tag{18}$$

Damping

The formulas shown above describe a bubble which pulsates as a harmonic oscillator with no damping. The bubble is subject to damping, which is manifested in three ways:

- Energy radiated from the bubble in acoustic waves (radiation damping)
- Energy lost through thermal conduction between the gas and the surrounding liquid
- Work done against the viscous forces at the bubble wall (viscous damping)

The damping constant δ is defined for damping at the resonance frequency as δ = 1/Q, where Q, the Quality factor, is ω_0 / (½ power bandwidth).

The decay of bubble oscillations due to the radiation of sound energy is independent of bubble size, unlike thermal and viscous damping which increase with decreasing bubble size. The loss factor due to radiation is equal to the radiation efficiency of the vibrating sphere.

i.e. $$b_{rad} = \frac{R_r}{\sqrt{R_r^2 + X_r^2}} = \frac{kR_0}{\sqrt{1+(kR_0)^2}}$$

where k $= \dfrac{2\pi}{\lambda}$

$$\therefore kR_0 = \frac{\omega_0 R_0}{c} = \frac{R_0}{c}\frac{1}{R_0}\sqrt{\frac{3\gamma p_0}{\rho}} = \sqrt{\frac{3\gamma p_0}{\rho c^2}}$$

If $kR_0^2 << 1$

then $$\delta_{rad} = kR_0^2 = \sqrt{\frac{3\gamma p_0}{\rho c^2}} \tag{19}$$

As the bubble pulsates, more work is done by the liquid compressing the bubble than by the gas expanding the bubble. For energy to be conserved, energy must be released from the gas into the liquid upon expansion, and this is manifested in heat energy. This loss of heat energy to the liquid represents thermal damping. For an ideal gas where PV^κ = *constant* and TV^κ = *constant*

$$d_{th} = \frac{3(\gamma - 1)}{R_0 / l_D} \tag{20}$$

where l_D is the thermal boundary layer thickness and $R_0/l_D \geq 5$

At the resonant frequency ω_0,

$$\frac{R_0}{l_D} = R_0\sqrt{\frac{2\omega_0}{D_g}},$$

$$D_g = \frac{K_g}{\rho_1 C_p}$$

and K_g is the thermal conductivity of the gas, $\rho_1 C_p$ is the specific heat capacity of the gas for a constant pressure.

The Navier-Stokes Equation for a fluid of constant viscosity is

$$\rho\frac{D\vec{v}}{Dt} = \rho\left[\frac{\partial\vec{v}}{\partial t} + \left(\vec{v}.\vec{\nabla}\right)\vec{v}\right]$$
$$= \rho\Sigma\vec{F}_{ext} - \vec{\nabla}p + \frac{\eta}{3}\vec{\nabla}\left(\vec{\nabla}.\vec{v}\right) + \eta\nabla^2\vec{v} \tag{21}$$

If the fluid is incompressible then $\vec{v}.\vec{\nabla} = 0$ and if the fluid is irrotational then $\nabla^2\vec{v} = 0$, so equation (21) reduces to

$$\rho\frac{D\vec{v}}{Dt} = \rho\left[\frac{\partial\vec{v}}{\partial t} + \left(\vec{v}.\vec{\nabla}\right)\vec{v}\right] = \rho\Sigma\vec{F}_{ext} - \vec{\nabla}p \tag{22}$$

This suggests that there are no net viscous forces acting in an incompressible viscous liquid around the pulsating spherical bubble. Momentum transfer does occur through viscosity, but no *net* viscous force acts within the body of the liquid. Net viscous forces do occur at the bubble wall, where they result in an excess pressure. Volume elements at the bubble wall decrease in thickness and increase laterally as the bubble expands. In an incompressible fluid, these distortions must be the result of viscous stresses. As a result, there is an energy loss on compression. The viscous damping coefficient was derived by Devin (1959) as

$$\delta_{vis} = \frac{b_{vis}}{\omega_0 m_{rad}} = \frac{4\eta}{R_0^2 \rho \omega_0} \qquad (23)$$

where $b_{vis} = \dfrac{\eta}{\pi R_0^3}$

Total Damping Constant

The damping contributions due to radiation, heat and viscous losses are additive. The total damping constant at resonance is therefore:

$$\delta_{tot} = \frac{R_0 \omega_0}{c} + \frac{3(\gamma - 1)}{R_0 \sqrt{\dfrac{2\omega_0 (\rho_1 C_p)}{K_g}}} + \frac{4\eta}{R_0^2 \rho \omega_0} \qquad (24)$$

Pressure Radiated by a Spherical Pulsating Bubble

Firstly, consider the pressure radiated by a cavity with a non-varying internal pressure, so that the radiated acoustic pressure is governed by the interface movement only. The motion of the cavity wall may be described by

$$\begin{aligned} R &= R_0 - R_\varepsilon e^{i\omega t} \\ \dot{R} &= -i\omega t R_\varepsilon^{i\omega t} = U_0 e^{i\omega t} \\ \ddot{R} &= i\omega U_0 e^{i\omega t} \end{aligned} \qquad (25)$$

where the frequency of oscillation is ω and the amplitude is U_0.

The pressure at the bubble wall varies with time as

$$P(r,t) = \rho_0 c U_0 e^{-\beta(t - r/c)} \frac{R_0}{r} \cos(\chi_0) e^{i(\omega t - k(r - R_0) + \chi_0)} \qquad (26)$$

where β relates to the damping constant, such that

$$\beta = \frac{\delta_{tot}}{2m}$$

and χ_0 relates to the phase of the pressure wave, such that

$$\cos \chi_0 = \frac{kR_0}{\sqrt{1 + (kR_0)^2}}$$

Considering Bubble Acceleration

Rearranging equation (5)

$$\dot{R}^2 = \frac{2p_0}{3\rho}\left[\left(\frac{R_m}{R}\right)^3 - 1\right] - p_{g,m}\frac{1}{1-\gamma}\left[\left(\frac{R_m}{R}\right)^3 - \left(\frac{R_m}{R}\right)^{3\gamma}\right] \qquad (27)$$

hence the acceleration during bubble compression

$$\ddot{R} = \frac{p_\infty R_m^3}{\rho}\left\{\frac{p_{g,m}}{p_\infty}\frac{1}{(1-\gamma)}\left[R^{-4} - \gamma R_m^{3(\gamma-1)} R^{-(3\gamma+1)}\right]\right\} \qquad (28)$$

Substituting equation (5) into equation (25) yields

$$\ddot{R} = \frac{p_\infty}{R\rho}\left[\frac{p_{g,m}}{p_\infty}\left(\frac{R}{R_m}\right)^{-3\gamma} - 1 - \frac{3\rho}{2p_\infty}\dot{R}^2\right] \qquad (29)$$

During expansion, R_m is the minimum radius, and $p_{g,m}$ becomes $p_{g,max.}$

Vokurka (1985) relates equation (25) to the equilibrium radius:

$$\ddot{R} = \frac{p_\infty}{R\rho}\left[\left(\frac{R}{R_0}\right)^{-3\gamma} - 1 - \frac{3\rho}{2p_\infty}\dot{R}^2\right] \qquad (30)$$

with initial conditions for *R(t)* being *R(0)* = R_{max} and $\dot{R}(0) = 0$.

Vokurka (1985) showed that the pressure in the liquid at the bubble wall, when observed in the far field, is

$$p_{bl}(t) = p(t) - p_\infty \approx \rho \frac{R}{r}(\ddot{R}R + 2\dot{R}^2) \qquad (31)$$

Experiment

Two experiments were conducted: one in the sheltered waters of Jerviose Bay, W.A in a water depth of 10m and another just west of Rottnest Island, WA, near the

100m contour. The light globes and glass spheres were imploded using the device shown in figure 1 which is similar in design to that described by Heard *et al*, (1997) and by Chapman *et al* (1977).

Figure 6 - Imploder device used to break light globes and evacuated spheres

Data Acquisition

For both trials, the receiver used was a Brüel &Kjaer 8100 Hydrophone, with a sensitivity of –206 dB. The signal was recorded on a Sony portable DAT recorder at 22050 Hz. The analog signal from the DAT was resampled at 22050 Hz using a PC soundcard. Levels were calibrated using a white noise source at 96.2 dB re 1 μPa. Maximum pressure levels were retrieved before any filtering was done. Signals were then Butterworth high pass filtered at 15 Hz to eliminate surge noise and other unwanted low frequency components. The power spectrum densities were then calculated using 14 bit FFT's, using a boxcar window of the same width, overlapped by half the window width. The spectra were then normalised to energy spectrum densities, referenced to 1 μ Pa^2/Hz^2. These curves were smoothed with a 5 point running average filter as the output was still very spiky. The resonant frequency was then located.

Results

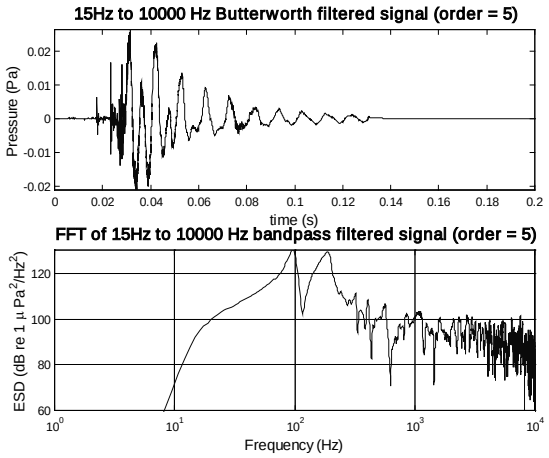

Figure 7 – Light globe at 5 m depth

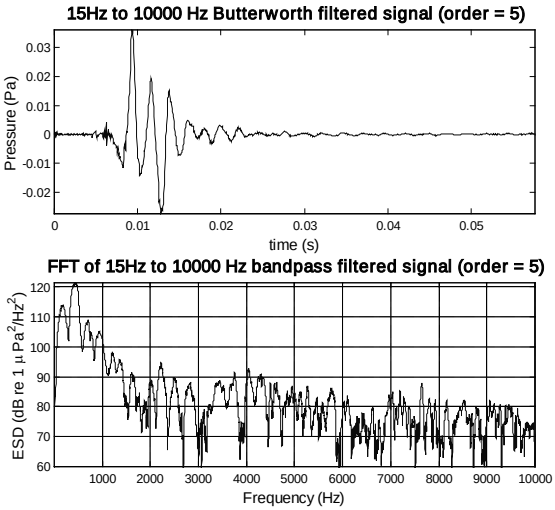

Figure 8 - Light globe at 40m depth

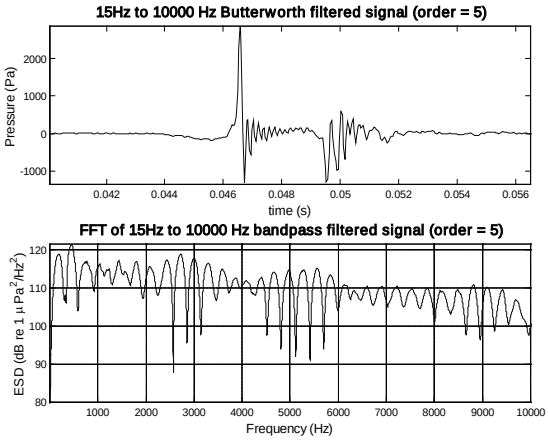

Figure 9 - Evacuated Sphere at 40m depth

If the resonant frequency is determined using Minnaert's (1933) equation, it is dependent on the equilibrium radius of the cavity, which may be found if the

initial internal pressure of the cavity is known. For the theoretical resonant frequencies shown in Figure 10, an average of p_i the internal pressures for the light globes (except those greater than 1 atm) was used. This average was 55% of atmospheric pressure. Calculated resonant frequencies fall close to the measured values, indicating that the adiabatic assumption needed to determine p_i is adequate for gas filled cavities in seawater.

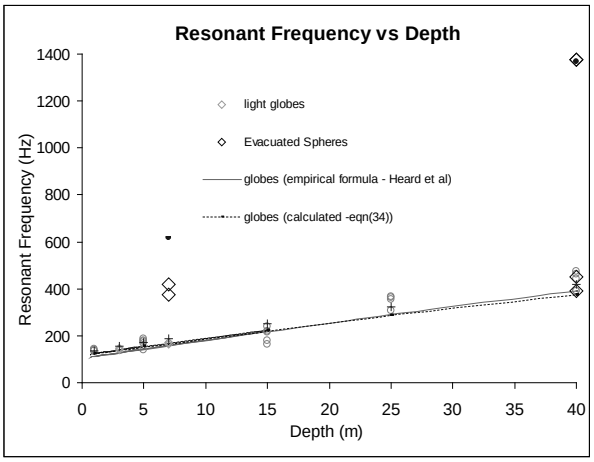

Figure 10 - Primary resonance of bubble oscillations as a function of depth.

This relationship can be found by applying the gas law $p_i V_i^{\gamma} = p_0 V_0^{\gamma}$ to find R_0 as a function of p_0 and p_i and substituting into Minnaert's resonance equation.

$$\text{i.e. } \omega_0 = \frac{p_0^{\frac{1}{3\gamma}}}{p_i^{\frac{1}{3\gamma}} R_i}\sqrt{\frac{3\gamma p_0}{\rho}} \qquad (32)$$

The value used for γ which gave resonant frequencies closest to those which were measured experimentally was γ = 1.40. This ratio of specific heats applies to diatomic gasses. If p_I, Ri and γ remain constant for all d, then f_0 is dependent on p_0 only. Hence:

$$\therefore \quad f_0 \propto p_0^{\frac{1}{3\gamma}} p_0^{\frac{1}{2}}$$

$$i.e. \quad f_0 \propto p_0^{\frac{2+3\gamma}{6\gamma}} \qquad (33)$$

$$i.e. \quad f_0 = k\left(\frac{d}{10}+1\right)^{\frac{3.1}{4.2}}$$

where d is the depth in meters. The value for k can then be determined from the measured data as

$$\log(k) = \log(f_0) - \frac{3.1}{4.2}\log(p_0)$$

Using an average value for k, the resonant frequency was found to have depth dependence:

$$f_0 = 114\left(\frac{d}{10}+1\right)^{\frac{3.1}{4.2}} \quad \text{(Hz)} \qquad (34)$$

This relationship is shown as a dashed curve in Figure 10. The measured resonant frequencies were consistent with Heard *et al's* (1997) empirical formula for the resonant frequency of light globe implosions at a given depth:

$$f_0 \propto g(d+10)^{\frac{5}{6}} \quad \text{(Hz)} \qquad (35)$$

Using g = 9.8 m/s^2 and d in meters, the constant of proportionality used in equation (32) was 2.5.

$$i.e \quad f_0 = 2.5\, g(d+10)^{\frac{5}{6}} \quad \text{(Hz)} \qquad (36)$$

This relationship is shown as a solid curve in Figure 10.

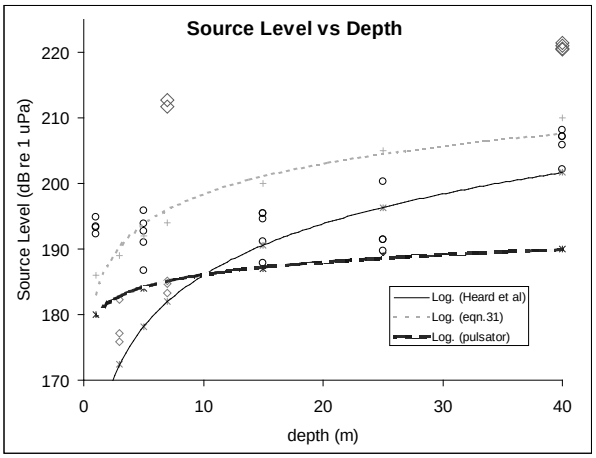

Figure 11 – Source Level vs. Depth

The equation used to calculate the peak pressures of the globes (equation (26)) is that of a rigid pulsator and does not account for the changing pressure within the bubble. Predicted source levels using equation (26), illustrated by the hashed curve in figure 6, are within the lower limit of experimental values for light globes at depths no greater than 25m.

$$i.e \quad SL_{pulsator} = 180 + 5.25\log(d) \quad \text{dB re 1 μPa @ 1m}$$

The source levels derived from the measured peak pressures received due to light globe implosions varied by up to 10 dB at each depth, whereas the evacuated sphere levels varied by only 1 dB at 7m and at 40m. Predicted source levels for the evacuated spheres are 14 dB lower than measured levels at 7m and 20 dB below the measured levels at 40m. If internal pressure

changes are taken into account and equation (31) is used to predict received levels, as illustrated by the dashed curve in figure 6 the predicted curve is much steeper than that which is indicated by Heard, *et al* (1997) or by the measured values. Using this model, the source level varies with depth as

$$SL_a = 183 + 15\log(d) \qquad \text{dB re 1 μPa @ 1m}$$

Predicted evacuated sphere source levels, using this method, were overestimated by ~ 40 dB at 7m and at 40m.

Predicting Bubble Motion

The source levels predicted by equation (31) are generally an overestimation of the measured levels, however an indication of the bubble radius as a function of time can be attained using equations (21), (25), (27), (29) and (30) from which the pressure equation is derived. Equations (25) describe the bubble's oscillation as simple harmonic. The damping factor of equation (24) is included in equation (26).

Bubble oscillations are not simple harmonic and bubble wall dynamics give rise to an asymmetry in the positive and negative pressure phases This asymmetry, which is described by Rayleigh's equation for bubble oscillations, may be understood by applying energy conservation constraints to the system. Equation (5) describes this and the equation for the squared velocity of the bubble wall and equation (28) is a rearrangement of the energy conservation equation (5). Two models were used to simulate the implosions, one of which incorporated the adiabatic change in pressure within the bubble, and one which treated the bubble as a rigid pulsator. Peak pressure levels calculated using the rigid pulsator model were generally lower than the measured levels and those calculated using the more sophisticated model were *much* higher than measured levels.

The spectra shown in figures 2, 3 and 4 show an interesting harmonic structure, particularly in the case of the evacuated spheres. Part of this structure is likely to be present at the source and due to harmonics of the bubble volume. Minnaert's (1933) resonance frequency is proportional to the equilibrium bubble radius and describes the principal resonance of a bubble of that size. It is unlikely that the bubble will collapse uniformly and remain always spherical. More probably, a cavity starting with a radius of 3 to 4 cm will collapse with multiple spherical harmonics (Leighton, 1997), as the surface tension effects (which act to retain sphericity) are not sufficient to dominate over external forces at these scale lengths. Each of these harmonics can be treated as a small bubble, with a resonant frequency and amplitude related to the order of the harmonic. Part of the harmonic structure is also due to interference from surface reflections of the signal, which arrive at the receiver out of phase with the direct signal.

For example, consider a source depth of 40m and a receiver depth of 3m, seperated by a horizontal distance of 10m, as was the case for the evacuated spheres. The direct signal path has a length of 37.9m and the signal path which involves one surface reflection has a length of 43.8m. This difference means that signals with $\lambda = n(43.8\text{-}37.9) = 4.9n$ will be attenuated due to destructive interference. This wavelength corresponds to multiples of 311 Hz at the measured sound speed of 1525 m/s. Figures 4 shows nulls occurring at multiples of 316 Hz, but other evacuated sphere spectra showed nulls occurring as low as 250 Hz. This variation may be attributed to the variation in receiver depth (and less significantly, source depth), induced by platform movement.

Experimental Uncertainties

The environment at Jervoise Bay was very quiet in comparison to the open water off Rottnest Island where the second trial was undertaken. A great deal of low frequency noise appeared on the original signals from the second trial, which was filtered out. During this trial, the hydrophone was hung off the side of the boat and as the boat rolled and pitched, the hydrophone depth would vary, introducing flow noise and depth uncertainty. The receiver depth uncertainty was determined to be no greater than ± 0.65m. A sea anchor was used to minimise drift. This contributed to flow noise as the drift rate was less than the current speed. The boat's hull is fiberglass, and the hydrophone cable was coupled directly to it. As waves interacted with the hull, noise was transmitted to the hydrophone via two channels: Transmission from the hull to the cable, and reflection from the hull to the hydrophone, only 3m away. Other noise sources which may have contributed were:

traffic: 1 large ship was observed to pass within approximately 2km of the experiment site

Biological noise – Snapping shrimp produce very loud impulsive clicks which may result in spikes in the observed signals. (A typical shrimp snap of 160 dB re 1 μPa @ 1m at 100m depth would result in a received level of approximately 120 dB re 1 μPa @ 1m.

These uncertainties in background noise levels can be minimised by measuring the average noise level over a period, calculating the spectrum density, and removing the components which are likely to interfere with results.

As seen in figure 1, the device used to implode the globes and spheres has a brass plate above the mount point for the globe. If the receiver is above the im-

ploder and the depression angle is large then there will probably be significant reflection of the signal. This was the case for implosions off Rottnest Island at depths of 25m and 40m, and at Jervoise Bay for implosions at depths of 7m. The extent to which this reflection has altered the source from the assumed monopole has not been investigated. One solution is to remove the brass plate from the imploder and replace it with a structure similar to that on which the globe is mounted.

There was also a large uncertainty in the depth of the water column for those globes imploded at 1m, 5m, 15m and 25m during the second trial. Several light globes were imploded at 1m depth as depth sounders throughout the experiment, as the boat drifted. These implosions had insufficient energy for a bottom-reflected signal to be detected, but the implosions at 40m depth were sufficiently energetic.. Distances calculated from the time delay between the direct signal and the first bottom reflection of the globes at 40m indicated depths of around 110m. i.e. Time difference between direct path and first bottom reflection of last light globe implosion at 40m (B.5.5) = 0.09s. The direct path length is approximately 38m, which at c = 1525 m/s, equates to 0.025 s. This makes a total travel time of 0.115 s for the reflected path. This time is equivalent to 178m. Add 43m for the receiver depth and source depth and the result is twice the water depth, plus a small amount due to the source – receiver separation. These depths were also referenced from local charts using GPS measurements.

The internal pressures of the light globes, calculated from using Minnaert's resonance equation and ideal gas laws, was seen to vary from ~0.3 atm to ~0.9atm. The (expired) globes imploded at Jervoise Bay had internal pressures of around 0.75 atm, whereas those which were imploded off Rottnest, which were new, varied widely in predicted internal pressure. The measured resonant frequency for globes imploded off Rottnest Island was also quite variable at any given depth, and this variation gave rise to the variation in the predicted internal globe pressures. It is feasible that internal gas pressure of light globes may vary, as the purpose of the gas is only to prevent the filament from being oxidised. An averaged internal pressure of 0.55 atm was used to model the depth dependence of source level and resonant frequency.

The spectra of globes imploded at 1m depth 1 globe which was imploded at 5m depth off Rottnest Island exhibited 2 strong peaks. The second of these was treated as the resonant frequency as it was consistent with predicted results. The first peak is possibly a subharmonic emission, which is possibly due to a prolonged expansion phase and a delayed collapse phase (Akulichev, 1967).

Other theories for subharmonics are described by Faraday (1831), Rayleigh (1883), Neppiras (1969), and others who describe surface waves which propagate at half the exciting frequency (due to the bubble oscillations).

Large bubble theory is summarised by Eller and Flynn (1969) wherein a threshold pressure exists for bubbles which may produce subharmonics at half the natural resonance

i.e. $$P_{A2} = \frac{6 p_0 \Delta_{\log}}{\pi}$$

where $\Delta_{\log}$ is the logarithmic decrement representing the damping of the oscillations.

Figure 2 shows a signal where it appears the bubble begins to collapse but then expands again before the collapse phase is completed. The process is repeated at least 4 times. This behaviour may be present at the source, in which case Akulichev's theory fits, or it may be due to surface reflections canceling out part of the signal at the correct phase. The difference in range between the direct path and the surface reflected path is 3.66m, which equates to 0.0024 s. The time difference between the observed double peaks occurs at intervals of ~ 0.025 s, ruling out surface reflections as the cause for this effect. The logarithmic decrement for this example is ~ 0.23, which corresponds to P_{A2} = 63845 Pa, given that the implosion occurred at 5m depth. The recorded peak pressure was –358 Pa, at a range of approximately 8.5m. Accounting for attenuation due to spherical spreading, the source level was approximately 3160 Pa, well below Eller and Flynn's subharmonic threshold.

Conclusions

The resonant frequency of light globe implosions was found to be in good agreement with Heard *et al* (1997)'s empirical equation, and fit well to theoretical models which employed Minnaert's resonance equation and assumed that the pulsation of the cavity volume was adiabatic.

Peak pressure levels varied by up to 9 dB over the sample tested and in order to find an empirical equation for the source level vs depth relationship samples are required over a greater range of depths. Heard *et al* (1997)'s empirical equation fit the data adequately well, although the data was spread sufficiently such that a linear fit would also have appeared to be good. A rigid pulsator model underestimated pressure levels as depth increased, where bubble wall acceleration is expected to be higher, and a model which incorporated bubble wall acceleration overestimated pressure levels.

Evacuated spheres were very consistent in peak pressure output at both depths at which they were tested and a pressure/depth relationship could be established given further tests at a range of depths.

Subharmonics were observed for implosion depths of 5m and Akulichev's (1967) large bubble theory may account for this.

References

Akulichev, V.A., *"The structure of solutions of equations describing pulsations of cavitation bubbles"*, Akusticheskii J. (Russian), 1967; 13: 533-537

Chapman, N.R., Jaschke, L, McDonald, M.A, Schmidt, H, Johnson, M, *"Mtched field geoacoustic tomography experiments using light bulb sound sources in the Haro Strait Sea trial"*, Oceans 1997 MTS/IEEE Conference Proceedings, Vol. 2, Pt. 2

Devin,C.Jr, *"Survey of thermal, radiation, and viscous damping of pulsating air bubbles in water"*, JASA 1959; 311654

Eller, A.I. & Flynn, H.G., *"Generation of subharmonics of order one half by bubbles in a sound field"*, JASA, 1969; 46: 722-727

Faraday, M., *"On the forms and states assumed by fluids in contact with vibrating elastic surfaces"*, Phil Trans Roy Soc., 1831; 121: 319-340

Heard, G.J, McDonald, M, Chapman, N.R, Jaschke, L, *"Underwater light bulb implosions: A useful acoustic source"*, Oceans 1997 MTS/IEEE Conference Proceedings, Vol. 2, Pt. 2

Leighton, T.,G., *"The Acoustic Bubble"*, Academic Press, 1997, USA.

Minnaert, M., "On musical air bubbles and sounds of running water", Phil Mag 1933; 16: 235:248

Neppiras, E.A., *"Subharmonic and other low frequency emmission from bubbles in sound-irradiated liquids"*, JASA,1969; 46: 587-601

Neppiras, E.A., *"Subharmonic and other low frequency emmission from sound-irradiated liquids"*, J Sound Vib,1969; 10: 176

Rayleigh Lord, *"On the pressure developed in a liquid during the collapse of a spherical cavity"*, Phil Mag 1917; 34: 94-98

Rayleigh Lord, *"On the crispations of fluid resting upon a vibrating support"*, Phil Mag Ser 5, 1883; 16:50-58

Vokurka, K., *"On Rayleigh's model of a freely oscillating bubble. I. Basic Relations"*, Czech J Phys 1985; B35: 28-40

Seabed Roughness Using Side-Scan Sonar

Wayne R. Arcus and John D. Penrose

Centre for Marine Science and Technology,
Curtin University of Technology, Kent St., Bentley 6102, Western Australia

Abstract

Work undertaken at the Centre for Marine Science and Technology has included the study of remotely sensing and describing seabed roughness using side-scan sonar. This has involved the review of a number of modelling strategies and subsequent model development to suit high frequency side-scan sonar interactions with seabeds typically found in harbours and seaways. Attention has been given to methods in which information on surface roughness may be inferred from backscattered signals such as leading and trailing edge analysis, parameterisations based on higher order echo statistics and spectral decomposition. Particular attention has been given to echo envelope modulation; a natural extension to earlier work conducted (Penrose et. al., Bull. Aust. Acoust. Soc. 12(2), 39 – 45 (1984)) that showed limitations of methods employing backscattered echo amplitude with incident angle to infer surface roughness. It should be noted that similar approaches have also been used, with some success, by other researchers (most notably Pace et. al.) in which seabeds have been characterised by geological composition.

A limited parameter set facet-ensemble type model has been developed to assist with both the understanding of the scattering process and for interpretation of results. Tank based experimentation has been conducted in order to validate the model generated results using a purpose built stylized (sinusoidal) surface. It is this work that this paper describes.

Differentiating The Acoustic Backscatter Signatures Of Lobster And Octopus

Peter Teague[1], Uwe Kopke[1], Danny Brock[2], Jin Lee Teh[3] and Shahrin Adzly Sainuddin[3]

[1] Vipac Engineers & Scientists Ltd, Adelaide, [2] South Australian Research Development Institute (SARDI) Aquatic Sciences, [3] Department of Mechanical Engineering, Adelaide University

Abstract

Currently, an estimated 7% of the total catch of the SA crayfish (lobster) industry is lost due to octopus predation, which amounts to about AUD$3.5million per annum. We investigate the acoustic backscattering properties of lobster and octopus using theoretical models and experimentally test an underwater acoustic sensor system to determine whether any difference in the backscattered sonar signatures is detectable.

We formulate appropriate mathematical models to predict the theoretical underwater acoustic target strengths of octopus and lobster. The primary model is based on a simplified distorted wave Born approximation (DWBA). Model results showed small differences in the predicted target strength for lobster and octopus for a range of parameters such as sonar wave frequency and angles of incidence.

We investigate a prototype acoustic sensor system that could detect the difference between the backscattered signatures of octopus and lobster. We describe the results from experimental tests using hydrophones in water-filled tanks with various targets. Source signals were 100μs pulses of sinusoidal waves in the frequency range 50 to 100 kHz and the backscattered received signal was determined for a range of target distances and angles. Preliminary results show measurable differences in the sonar transfer function and target strength for lobster and octopus.

ACOUSTICS - putting the science and technology to work

Conference of the Australian Acoustical Society
Joondalup Resort, Western Australia, 15-17 November 2000

Session AC-6 Workshop – Active Noise Control

ACOUSTICS - putting the science and technology to work

Conference of the Australian Acoustical Society
Joondalup Resort, Western Australia, 15-17 November 2000

Session UW-6 Marine Bio-Acoustics And Fisheries Acoustics

Ocean Noise And The Use Of Sound By Marine Mammals

Douglas H. Cato

Defence Science and Technology Organisation, PO Box 44, Pyrmont, NSW 2009, Australia

Abstract

Marine mammals make extensive use of sound for communication and for information about their environment because sound is the only effective means of transmitting information over distance through the ocean. There is some concern about the effect of anthropogenic noise on their use of sound and it has been suggested that the noise of shipping has significantly increased the prevailing background noise in the ocean, thus interfering with the use of sound by marine mammals. This paper discusses the noise generated by both shipping and natural sources, and what might be inferred about the impact on animal communication. It is based on measurements around Australia where noise from human activities varies from significant to negligible (measurements elsewhere have generally been contaminated by shipping noise). The results show that natural background noise in the ocean is often comparable to or greater than the background noise from shipping, and that anthropogenic noise has not increased ambient noise levels as much as has been supposed.

Introduction

Marine mammals rely on sound for communication and for information about their environment. It has been suggested that the noise of human activities has significantly increased the background noise levels in the ocean, thus interfering with the use of sound by marine mammals. The main prevailing source of anthropogenic noise is that from shipping, and because of the low absorption attenuation in the ocean, ships at great distances provide a general low frequency (> 200 Hz) background noise, known as "traffic noise" (Wenz, 1962). It has been suggested that traffic noise may impact on baleen whales which use sound at similar frequencies.

Most of our knowledge of ocean noise comes from measurements in waters around North America where shipping densities are high. In these waters, traffic noise tends to obscure the natural components of background noise at low frequencies, such as that generated by the sea surface. Estimates of these natural components by extrapolation of higher frequency measurements results in noise levels substantially lower than the observed traffic noise. This has lead to the idea that, prior to introduction of powered shipping, there was a "noise notch" at low frequencies which was exploited by whales, but is no longer available.

These ideas were based on the ambient noise prediction curves of Wenz (1962) which are still widely used. From a large amount of data, Wenz identified the main components of ambient noise. These included "traffic noise" which he defined as the background noise from many distant ships, none of which were detectable as such, and "wind-dependent noise" generated by sea surface motion. Wenz's wind-dependent noise spectra has a broad peak at around 500 Hz, and falls below traffic noise for frequencies below about 200 Hz. Wenz, however, noted that a few measurements showed evidence of the presence of a second component of wind-dependent noise, dominant at frequencies below about 200 Hz. This component has been difficult to measure in the Northern Hemisphere because of the masking by traffic noise, and was not included in the prediction curves. It is, however, clearly evident in measurements by Piggott (1964) on the Scotian Shelf and waters near Australia where traffic noise is lower (Cato, 1976; Burgess and Kewley, 1983). The earliest studies of ambient noise (Knudsen et al, 1948) had shown sea surface generated noise as having a simple spectral shape falling with frequency at the rate of about 5 dB per octave, consistent with the presence of the low frequency component.

It should be noted that there is no clear distinction in acoustical characteristics between traffic noise and wind-dependent noise. Both have the same spectral shape and because traffic noise results from the contributions from many ships, any characteristic modulation or line structure is averaged out. This makes it difficult to separate the two in data, and the only sure way to do this is to look for dependence on wind speed.

The Biological contribution to the sustained background ambient noise is often overlooked, even though it has been observed in many parts of the world. Biological noise is a major component of ambient noise in Australian waters, often being the dominant noise in tropical waters. Choruses that result when large num-

bers of fish are calling may exceed high levels of traffic noise at frequencies down to about 50 Hz.

Methods

Ambient sea noise has been measured at many locations in temperate and tropical waters around Australia using bottom moored systems and with buoyed hydrophones. The buoyed systems were designed to move with the water mass and with a system design to minimise the influence of surface motion. Wind speed was also measured.

Noise spectra were obtained by analysis in 1/3 octave bands and converted to spectrum levels. Spectral values were plotted as a function of wind speed after rejecting all data that was contaminated by sounds of ships, biological or mechanical sources. These plots still contained the contribution of traffic noise at low wind speeds, since it is not detectable as such in individual noise samples. The plots for low frequencies show no wind dependence at low wind speeds, presumably due to the presence of traffic and other non wind dependent noise. The plots do, however, show clear wind dependence at moderate and high wind speeds. Average wind dependent noise spectra were determined from lines of best fit to these plots, using the data above the wind speed for which the contribution of traffic noise was not evident.

Results

Figure 1 shows a summary of wind-dependent and traffic noise, and an example of a fish chorus spectrum in waters near Australia.

The more than 20 dB variation in traffic noise around Australia illustrates the wide variation that can occur as the result of variations in the concentration and distribution of shipping, and in propagation conditions. Traffic noise levels are presented as the average for each regions, the temporal variation in any region being about ± 5 dB about the averages shown. The highest levels are observed on the continental shelf of the Tasman Sea off the east coast, where the propagation is good along the shelf and from deep water, and there is considerable shipping. These levels are almost as high as those presented by Wenz (1962). Traffic noise is almost negligible in the shallow tropical waters to the north of Australia and in partially enclosed waters such as gulfs. The wide variation in traffic noise levels may be indicative of traffic noise over much of the worlds oceans, more representative in fact than those around North America and Europe where most data have been obtained.

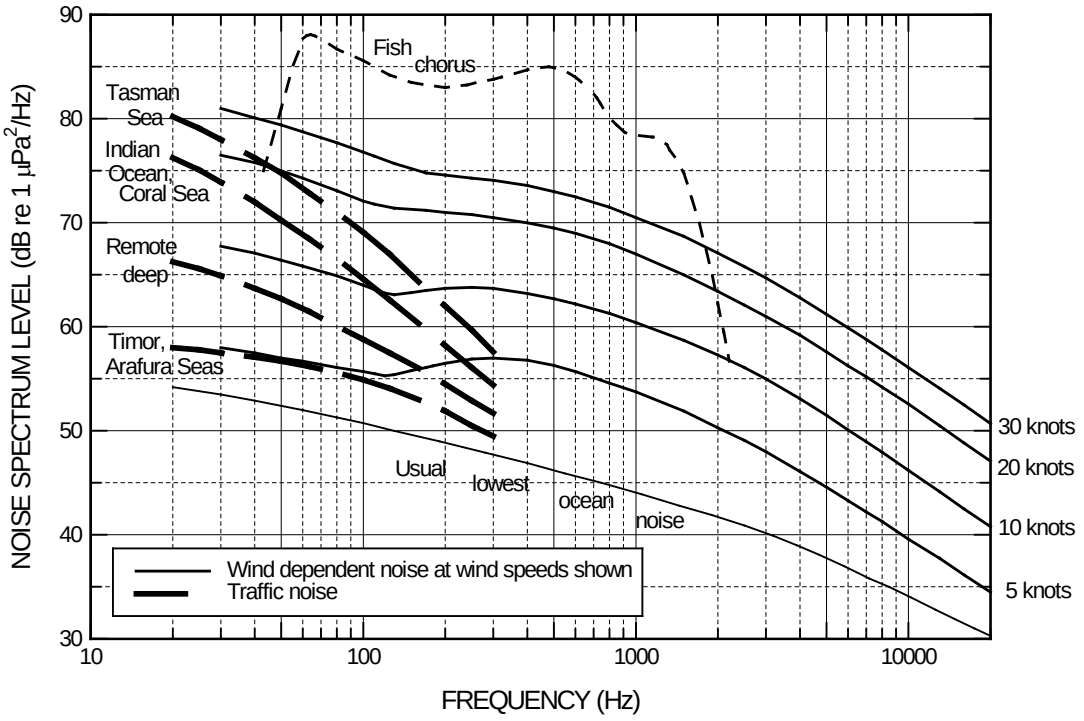

Figure 1. Summary of wind-dependent and traffic noise in waters around Australia with an example of a fish chorus.

The averaged wind dependent noise spectra obtained from the moored systems in open oceanic waters are shown in Fig. 1 for various wind speeds (Cato, 1997; Cato and Tavener, 1997). Results obtained using buoyed systems are consistent with these, but provided

a much smaller set of data points. The averaged wind dependent noise spectra show evidence of two components: the "Wenz" component with the broad peak at around 500 Hz, and a low frequency component. It should be noted that there is significant variation between different locations in the measured wind dependent noise spectra as a result of differing propagation conditions. The models of Kuperman and Ingenito (1980) and Harrison (1996) show that propagation conditions can significantly affect the noise field. The spread of data about the averaged spectra vary from ± 8 dB at the lowest frequencies to about ± 3 dB above 300 Hz.

Fig. 1 also shows an example of a fish chorus in which the swim bladder plays a significant role in sound production. Fish choruses are widespread around Australia (Cato, 1978; McCauley, 1992; McCauley and Cato 2000), and have been observed in other parts of the world (Knudsen et al, 1948; Fish, 1964; D'Spain et al, 1997). Chorus spectra usually show broad peaks in the 100 to 1000 Hz band, though some show substantial energy below 200 Hz in the region where traffic noise is significant.

Discussion

The averaged wind noise spectrum in Fig. 1 for 20 to 30 knot wind speeds lies within the range of Wenz's traffic noise below 250 Hz and exceeds it at higher frequencies. The spectrum for 10 knots lies within the range of traffic noise below 50 Hz. Thus, low frequency wind-dependent noise provides a significant contribution to the ambient noise, even in areas of high traffic noise where it may be difficult to separate the wind-dependent noise from traffic noise. These wind speeds are not unusual at sea, so for a significant proportion of the time, wind-dependent noise is at similar levels to traffic noise and just as limiting to the use of sound by whales as traffic noise, since there is no acoustical distinction between the two sources.

From Fig. 1 it is evident that the hypothetical "noise notch" at around 50 Hz has never existed and is an artefact of measurement in areas where it is difficult to separate traffic noise and wind-dependent noise. The combined wind-dependent noise spectra generally falls with frequency with only a slight peak at around 500 Hz due to the influence of the higher frequency component. This was evident in the broad spectra of the earliest studies of noise (Knudsen et al, 1948). This result is not inconsistent with Wenz's findings, but it is inconsistent with later interpretation of his work which ignored his evidence of the low frequency component of wind-dependent noise. Wenz shows examples of the low frequency wind-dependent noise measurements which are similar to the averaged spectra of Fig. 1.

The "remote deep" traffic noise is typical of areas around Australia in deep water with limited shipping lanes and well away from ports. It is probably indicative of traffic noise in many parts of the world. The "Timor, Arafura Seas" traffic noise is typical of areas in shallow water with relatively poor propagation and with limited port activity and traffic. Traffic noise levels in these kinds of environments are likely to be exceeded by wind-dependent noise for a significant part of the time.

Biological noise also adds significantly to the ambient at low frequencies and may at times be comparable to or exceed high levels of traffic noise.

The results presented here indicate that (a) wind-dependent noise is often comparable to traffic noise in areas of high shipping densities, (b) that the hypothetical low frequency "noise notch" in natural ambient noise never existed, and (c) that traffic noise levels in much of the worlds ocean are likely to be significantly lower than those given in prediction curves derived from northern hemisphere data (e.g. Urick, 1983) and are likely to be exceeded by wind dependent noise for much of the time. This suggests that marine animals have always been subject to sustained noise levels that are often comparable to moderate or high levels of traffic noise, and that anthropogenic noise has not increased ambient noise levels as much as has been supposed. The difference now is that noise levels are always high in high traffic areas, whereas prior to powered shipping there would have been times of quieter conditions when wind speeds were low. How useful it is for whales to be able to exploit those quiet conditions of low wind speeds is an open question, but it is clear that this is a far less useful than exploiting the hypothesised "noise notch."

The above comments refer to the effect of traffic noise which is the nondescript background noise from many distant ships that is evident over large areas. This must be distinguished from the effect of the noise of a nearby ship, which will be substantially higher in level than traffic noise, though localised in time and space. Noise from a close ship can be expected to have a much greater impact on the used of sound by whales, though the impact will be only for the short period that the ship is close by. Since the noise of a close ship significantly exceeds the highest levels of ambient noise, except in some exceptional circumstances, an estimation of the impact is not possible by the type of analysis used above.

References

Burgess, A.S, and Kewley, D.J. (1983). Wind-generated surface noise source levels in deep water east of Australia., *J. Acoust. Soc. Am.* **73**, 201-210.

Cato, D.H. (1976). Ambient sea noise in waters near Australia., *J. Acoust. Soc. Am.*, **60,** 320-3283.

Cato, D.H. (1978) "Marine biological choruses observed in tropical waters near Australia", *J. Acoust. Soc. Am.*, **64**, 736-743.

Cato, D.H. (1997) "Features of ambient noise in shallow water" in *Shallow Water Acoustics* edited by R. Zhang and J. Zhou, China Ocean Press, Beijing, 385-390.

Cato, D.H. and Tavener, S. (1997) "Spectral differences in sea surface noise in open and enclosed waters." In *Natural Physical Processes Associated with Sea Surface Sound*, ed. By T.G. Leighton, University of Southampton, Southampton, p 20-27.

D'Spain, G.L., Berger, L.P., Kuperman, W.A. & Hodgkiss, W.S. 1997 Summer night sounds by fish in shallow water. In *Shallow Water Acoustics* edited by R. Zhang & J. Zhou, pp 379-384. Beijing: China Ocean Press.

Fish, M.P. (1964) Biological sources of sustained ambient sea noise. In *Marine Bio-Acoustics*, edited by W.N. Tavolga, Pergamon, Oxford.

Harrison, C.H. (1996). Formulas for ambient noise level and coherence. *J. Acoust. Soc. Am.*, **99,** 2055-2066.

Knudsen, V. O., Alford, R. S. and Emling, J. W. (1948). Underwater ambient noise. *J. Mar.Res.*, **7,** 410-429.

Kuperman, W.A., and Ingenito, F. (1980). Spatial correlation of surface generated noise in a stratified ocean. *J. Acoust. Soc. Am.*, **67**, 1988-1996.

McCauley, R.D. (1992). Aspects of Marine Biological Sound in Northern Australia. Report to DSTO, James Cook University, Townsville.

McCauley, R.D. and Cato, D.H. (in press 2000) Patterns of fish calling in a nearshore environment in the Great Barrier Reef. *Phil. Trans. R. Soc. Lond. B.*

Piggott, C.L. (1964). Ambient sea noise at low frequencies in shallow water of the Scotian Shelf. *J. Acoust. Soc. Am.*, **36**, 2152-2163.

Urick, R.J. (1983) *Principles of Underwater Sound.* McGraw-Hill, New York.

Wenz, G. M. (1962). Acoustic ambient noise in the ocean: spectra and sources. *J. Acoust. Soc. Am.*, **34,** 1936-1956.

Blue whale calling in the Rottnest trench, Western Australia, and low frequency sea noise

Robert D. McCauley[1], Curt Jenner[2], John L. Bannister[3], Douglas H. Cato[4], Alec Duncan[5]

1,5 - Centre for Marine Science and Technology (CMST), Curtin University, GPO Box U 1987 Perth 6845, WA; 2 - Centre for Whale Research (CWR) PO Box 1622 Fremantle, WA 6160; 3 - Western Australian Museum, Francis St. Perth, WA; 4 - Defence Science and Technology Organisation, PO Box 44 Pyrmont NSW

Abstract

Through January-April 2000 research was carried out off the Rottnest trench to search for blue or pygmy blue whales. A consortium of researchers carried out aerial surveys, boat based studies and acoustical measures. Historical records led us to believe that a Western Australian population of pygmy blue whales (*Balaenopteridae musculus brevicauda*, sub species of the true blue whale, *B. m. musculus*) existed, while a preliminary boat survey in 1994 suggested that some of these animals aggregated in the Rottnest trench west of Perth. This was confirmed in the early 2000 observations, in 30 days boat based searching 17 pygmy blue whales were sighted. Five thousand acoustic records were made, almost all of which had blue/pygmy blue whale calling in, some having up to six animals calling at once. Although of a slightly different format, recorded call components were of a similar character to those described from other populations. Also common were impuslive 'clicking' calls which were shorter than the 12-23 s blue whale call components and of low to very low frequency (< 1 Hz to 20 Hz). The literature suggests these are produced by fin whales but none were sighted. The low frequency (< 100 Hz) sea noise spectra from a series of 90 s recordings made every 10 minutes for 33.5 days was dominated was dominated by blue whale calling.

Introduction

In the southern hemisphere two subspecies of blue whale are recognised, the 'true' blue whale (*Balaenoptera musculus intermedia*) and the 'pygmy' blue whale (*Balaenoptera musculus brevicauda).* The 'true' blue whale is the larger of the two and may be found south of the Antarctic convergence zone, particularly along the ice shelf edge feeding on euphausiid krill, whereas the slightly smaller pygmy blue whale is preferentially found further north (Bannister et al 1996). The two subspecies are extremely difficult to discern in the field. Based on recently released Russian whaling data Zemsky and Sazhinov (1994) presented the distribution of pygmy blue whales as being primarily in the Indian Ocean, along the African east coast, throughout the lower part of the Indian Ocean, along the Western Australian coast north to Indonesia, and along the Australian southern coast and east to encompass New Zealand. The migratory patterns and movements of the blue and pygmy blue whale are poorly understood although each are known to undertake extensive migrations between warm water (low latitude) breeding areas and cold water (high latitude) feeding areas (Bannister et al 1996).

These populations were heavily hunted during the whaling decades of the 1950 and 1960's. An international ban on blue whaling was established in 1966 due to alarmingly declining numbers, although it now known that illicit catches of blue whales continued up to the mid 1970's (Bannister et al 1996). The 'true' blue whales were almost driven to extinction during this period. From an estimated pre-whaling population of southern hemisphere 'true' blue whales of around 160,000-240,000 animals, whaling reduced numbers to < 1000 animals, which is still 34 years after the official cessation of whaling, near the estimated current population size of 1000-2000 animals (Bannister and Burton 2000). Pygmy blue whale stocks were less heavily exploited and dropped from an estimated total population size of 12,500-13,000 animals pre-whaling (Zemsky and Sazhinov 1994), with an estimate of the current population at 6000 animals (Bannister et al 1996).

Along the Western Australian coast both true and pygmy blue whales have been sighted and taken. A USSR factory whaling ship captured 269 animals along the coast from Albany to Exmouth in 1965, most of which were believed pygmy blue whales (Bannister and Burton 2000). True and pygmy blue whales were sighted to 45o S of WA in February-March 1993 (Bannister 1993). During a dedicated IWC blue whale cruise in 1994 up to five blue whales per day were sighted off Rottnest Island. Most of these were believed to be pygmy blue whales (Kato et al 1996). What are believed to be pygmy blue whales are regularly sighted off Dunsborough in the states south-west (Bannister and Burton 2000).

Given the historical records, the observations of blue whales off Perth in 1994, and the dearth of information on true and pygmy blue whales, a consortium of WA researchers carried out concurrent aerial surveys, boat based observations and acoustic surveys to study blue whales west of Rottnest Island. The aerial surveys began in January 1999 and were to be carried out on a monthly basis until mid 2000. Weather and aircraft availability restricted the number of successful flights. Over the period January-1999 to February-2000 eight flights were carried out during which 16 blue whales were sighted (Bannister and Burton 2000). Boat based observations in the region of the Rottnest trench were carried out through January-March 2000. In 30 days of searching 17 blue whales were sighted (Curt Jenner, pers. comm.). Concurrently with the boat based observations, acoustic records were made. Blue whales are known to produce intense low frequency signals (eg. Cummings and Thompson 1971). Several workers have used these signals to track animals using arrays and to gain insight into the animals underwater behaviour (eg. D'Spain et al 1995; McDonald et al 1995; Stafford et al 1998; Thode et al 2000). In this project the acoustic monitoring work was attempted primarily as a censusing technique, that is to determine if the animals were present, approximately how many calling animals were present at any given time within some range of the hydrophone, and how these characters varied with time. As it transpired the results offered all this information not only for blue whales but also for other baleen whale species. Additionally the recordings, particularly those from a bottom mounted receiver deployed over a 34 day period, provided a rich source of information on the behaviour of several baleen whale species in the area, as well as physical sea noise sources. There were many instances where calling blue and other baleen whale species passed within 500 m of the recording gear, providing some extremely high signal to noise ratio signals.

The following discussion presents a short summary of several of the call types recorded. At the date of writing this document only a small fraction of the data available had been analysed.

Methods

The study site was located in the region of the Rottnest trench, an indentation in the continental shelf which begins approximately 22 km WNW of the western end of Rottnest Island. The shelf slope in the trench region drops steeply to 1000 m depth. The general location of the study site is shown on Figure 1.

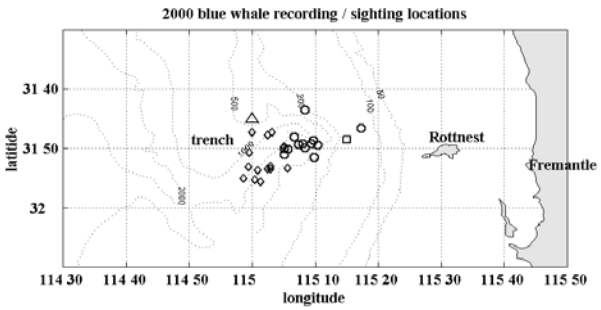

Figure 1: Location of the Rottnest trench region, west of Rottnest Island Western Australia. Recording locations are shown by the circles (drifting gear), square (inshore moored gear sampling over three days) and large triangle (moored gear sampling over 33.5 days). Whale sightings from the boat observations are shown by the diamond symbols. Depths in metres.

The deep and indented nature of the trench can be seen on Figure 2. Along the Western Australian continental shelf between the 100-500 m depth contours, flows the Leeuwin current, a southerly current of warm tropical water approximately 50-200 m deep. Over the study period of early January to April 2000, the Leeuwin current was particularly strong, with current speeds estimated at up to1.5 knot (0.75 ms-1) based on observations of moorings and drift rates. The sharp indentation of the trench lying across the path of the Leeuwin current may be expected to give rise to complex oceanographic conditions in the area.

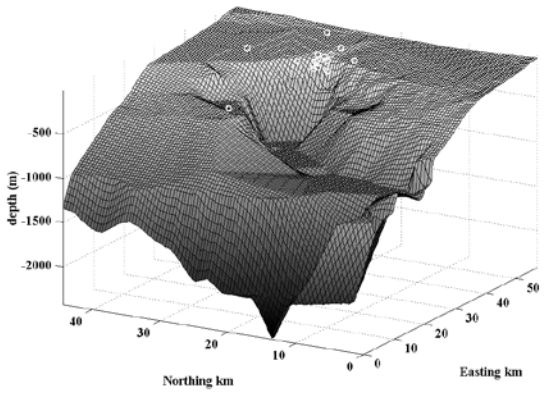

Figure 2: Surface representation of the trench bathymetry, showing the location of recording sites (white circles). The image is looking NE into the trench from the western side.

Acoustic recordings were made with a drifting package (13 sets, shown as circles on Figure 1) or using moored equipment (two sets, shown by square and triangle on Figure 1). The drifting package used a Massa TR1025C hydrophone suspended from a housing containing a purpose built pre-amplifier (40 dB gain) and Sony TCD D-8 digital tape deck operated at 32 kHz

sample rate to give 4 hour recordings per tape. System response was linear from 20 Hz to 14.5 kHz. To reduce surge from the surface gear and flow noise from cable strum, the hydrophone cable was spirally wrapped with twine and suspended on rubber strops from the housing while the housing was suspended from a rope weighted and buoyed to create a substantial catenary. A depth meter attached to the housing was used to log the housing, and hence hydrophone, depth. Under most conditions the hydrophone was at 40 m depth. Drifting sets were made during daytime, concurrent with the boat based observations.

A moored system was set at the head of the trench (eastern trench end, square symbol, Figure 1) in 160 m water. This comprised the same hydrophone and electronics as the drifting system, but with the tape deck operated by timer on a 3 minute sample time every 44 minutes. The gear was suspended from the mooring surface floats. Sixty samples were collected over a two day period (10-12 January).

A second moored system comprising a deepwater housing (the 'bluey' logger) was set on the bottom in 450 m of water on the northern trench edge (large triangle symbol, Figure 1) through 7-March to 10-April. This system comprised a General Instruments C-32 hydrophone connected to custom built electronics comprising an A-D converter and microprocessor controlled sampling and storage system (10 kHz sample rate, 90 s samples every 10 minutes, 9.1 GByte SCSII storage disk). The frequency response of this system was calibrated from < 1 Hz to 3.5 kHz. This system retrieved 4827 samples.

Continuous sections of sea noise from the DAT tape decks was digitised at 651 Hz using a calibrated Data-Physics DP430 spectral analyser card installed in a 166 MHz PC. The digital data from the 'bluey' logger was transferred to an IDE disk on a PC. All data analysis was then carried out in the Matlab environment.

Salinity, temperature and depth profiles were taken opportunistically with a Marimatech HMS 1820 CTD profiler. The Leeuwin current was a consistent feature throughout January to April. Most CTD profiles showed a warm body of water at 21-22.5o C from the surface down to 50-100 m where a sharp thermocline existed. Water temperatures dropped steadily below this depth with one record showing10o C water at 300 m depth but most settling between 13-19o C. On the last sample taken on the 10-April at the bluey logger site (square Figure 1) the Leeuwin current extended to 200 m depth below which the temperature steadily dropped. All sound speed profiles showed a sound speed maximum at the base of the Leeuwin current of 1530-1532 ms-1.

At the time of writing this document only a preliminary analysis of the data had been completed.

Results

Call types - 'blue' whale calls

The most common low frequency call observed with typical 'blue' whale characteristics (based on literature comparisons), was a sequence of three long tonal signals. The first signal type (referred to here as a type I) comprised an almost constant tone centred near 21-22 Hz and lasting for 22 s. This was followed 5-10 s later by a frequency sweep (type II), this beginning near 20 Hz, increasing to 21 Hz over 2-3 s then slowly increasing to approximately 26 Hz over a further 20 s period. The type III component then followed approximately 23 s later. This component was again an almost constant tone, centred near 18.5-19 Hz An example of a sequence of the three components (to make a single 'call'), taken with the drifting gear on the 29-January is shown on Figure 3. Each component has strong associated harmonics. This call type is similar, although not exactly the same, to spectrograms displayed by Cummings and Thompson (1971) from blue whale calls recorded off Chile in 1970.

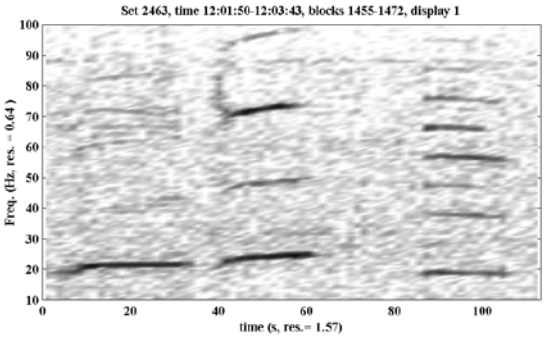

Figure 3: Spectrogram of the three components (I, II, III) believed attributable to pygmy blue whales.

The three call components were remarkably stereotyped in individual structure and in the timing between adjacent components. The distribution of the spectral peak frequency of 87 call components (recorded across a 24 hour sequence) determined from FFT averages at a resolution of 0.0763 Hz over the full duration of each component, is shown on Figure 4. The type III component was centred almost exclusively near 19 Hz, the type I component varied over approximately a 1 Hz band centred near 21.2 Hz, and the type II component varied in dominant frequency which reflected its frequency sweep nature.

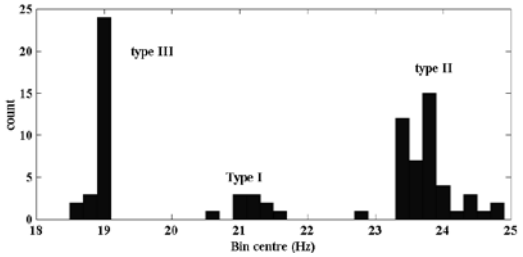

Figure 4: Distribution of the frequencies of the spectral peak for each call type, as determined by averaging the frequency content over each call duration (FFT's taken with a 0.0763 Hz resolution two averages per component, distribution shown with a 0.2 Hz bin width).

The precise tonal nature of the type I & II components was emphasised in several recordings in which amplitude modulation of the carrier tone can be discerned in spectrogram plots. An example of this can be seen on Figure 5 where a type III and type I components (separate calls) display strong sidebands which shift frequency with time.

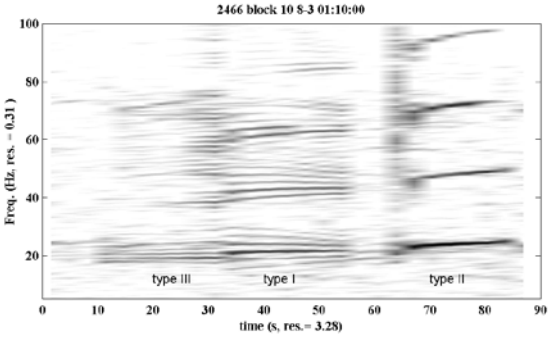

Figure 5: Spectrogram of three blue whale components (two separate calls) with the type I and III components displaying sidebands associated with amplitude modulation of the carrier tone.

For the same call, the three components consistently had different received levels. Based on matched components from the same call and using the mean squared pressure over the component duration, then the type II component was 3-10 dB higher in received level than the type I component and 0.4-3 dB higher than the type III component. This implies differences in source levels for each component. The nature of received calls emphasised this, for very long range calls, or those with low signal to noise ratios (SNR), it was always the type II component which showed up best. For the deep water moored hydrophone (bluey logger at 450 m depth) low SNR signals displayed the 20-26 Hz type II fundamental and the harmonics. For the drifted hydrophone (at 40 m depth) the 60-80 Hz harmonic of the type II component showed up best in spectrograms, with often the fundamental frequencies lost.

Given the precise tonal character of the calls then the possibility of using spectrogram cross correlation techniques to automate call identification seemed attractive (eg as described by Mellinger and Clark, 2000 for bowhead calls). Correlation techniques were thus developed using high SNR ratio components to set up kernels and correlating these against measured spectrograms after normalising the test signal to the total energy in the kernel. This was done at 1.22 Hz and 0.3 Hz spectrogram resolution. Although this method gave excellent discrimination for recordings with single calls, the presence of a large number of overlapping calls in some sequences greatly reduced the techniques sensitivity. In some of the 90 s sequences recorded from the bluey logger there were up to six different calling animals, with 3-4 of these at similar SNR. The ability of the spectrogram cross-correlation techniques to discriminate overlapping call components has so far been poor. Further techniques to enhance this discrimination are being pursued.

Call types - 'clicking'

A second call type commonly observed was 20 Hz 'clicks'. An example of several click waveforms is shown in Figure 6. These were common, occurred in bouts of several hours and were often recorded at very high levels (up to 146 dB re 1µPa peak-peak). They display several multipath reflections, from which it should be possible to estimate range and depth using an extension of the method described in Cato (1998). For example the middle call of Figure 6 was estimated to be at a depth of 286 m, and 1987 m from the hydrophone using a surface reflected time relative to the direct arrival of 82 ms and a bottom-surface reflected time of 169 ms relative to the direct arrival time.

During clicking bouts signals were received with a wide range of levels and separate clicks had different patterns of multipath arrivals. This indicated that several sources were active and responsible for the click bouts. Previous workers have attributed calls similar to these as being produced by fin whales (Watkins 1981). No fin whales were sighted in the area during the study period by the aerial surveys or from the boat searching, although fin and Brydes whales are known be found along the WA coast.

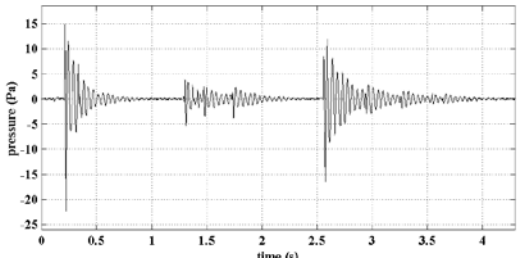

Figure 6: Example waveforms of 20 Hz clicks recorded.

Calling through time:

The 'blue' whale calls were evident all through the sample period of from 10-January to 10-April 2000. They were not sighted by the aerial or boat based surveys until early February. The maximum group size of blue whales sighted in the aerial surveys was two, and in the boat based surveys was four. To date only a 24 hour sequence of the bluey data has been analysed for the number of callers in each sample. From this analysis the number of calling animals in a 90 s sample ranged from zero to six, to give a mean number of two calling animals. The samples with no calling often correlated with nearby boat noise, as did a fourth call type (not described here).

It is not known what proportion of any group of blue whales call, but estimates could range from as low as 10% (as per humpback calling, Doug Cato pers. comm) to close to 100%. Drifting recordings were made in the vicinity of blue whales. Not all of these recordings had nearby animals calling, hence we would expect it unlikely that all animals present in an area would be calling at any given time. Thus simply assuming a 50% call rate, the bluey logger hydrophone results for the 24 hour period suggest that a mean of four, possibly ranging up to 12, animals may have been within some range from the hydrophone at any given time. Although the range brackets have not yet been calculated, a crude estimate of the outside detection range is approximately 10-15 km (based on an estimated mean squared pressure source level of blue whale calls at 180 dB re 1μPa, the minimum received signal level of close to 100 dB re 1μPa, and spherical spreading).

To give a display of the presence of blue whales through time, the power spectral density of each 90 s sample from the bluey logger (10 minute sample separation) was determined at a 1.22 Hz resolution using 219 averages (hanning window) per 90 s, and has been displayed with time on Figure 7 for the week 8-15 March. The presence of blue whales is indicated by the banding at 18-25 Hz, while the 'clicking' displayed above shows up as the intense narrow vertical stripes. It can be seen that the two call types dominate the sea noise spectra over this period. The bluey logger ran for almost five weeks. Although the degree of calling tapered slightly towards April, the sea noise spectra over the 18-80 Hz band was still dominated by blue whale calling and the clicking at the end of the sampling period.

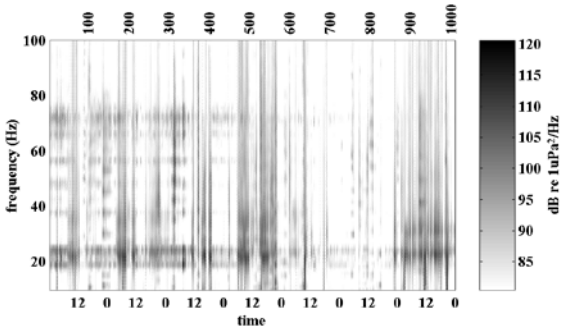

Figure 7: Power spectral density with time over the frequency band 10-100 Hz for the first week of deployment of the bluey logger. Blue whales were evident as the horizontal banding at 18-20 Hz and the narrow vertical stripes indicate the presence of the 'clicking' calls. See text for FFT parameters. Upper scale is sample number.

Discussion

Blue whale calling and a 20 Hz clicking call were found to predominate in sea noise records made over January to April 2000 in the Rottnest trench west of Perth. Up to six blue whales were evident at a given time in some records. The blue whale calls were made up of three, highly stereotyped components. The first and third components were very sharp tones, while the second was a slowly rising-frequency signal. Each component displayed strong harmonics. The three components had different source levels, with local sound propagation conditions determining the received signal character.

Time averaged sea noise spectra over the band 18-80 Hz was dominated by the two call types. From recordings in the deep sound channel off Cape Leeuwin made over three weeks in June-July 1998 Penrose et al (1998) determined that there was an increase in ambient sea noise across the band 20-80 Hz which could not be attributed to the local wind field. This suggested that a source other than wind was setting sea noise levels across this band. No easily discernible blue whale calls were found in the Penrose et al data set. The measurements described here show a similar increase in sea noise across the same frequency band which is definitively attributable to blue and other baleen whales. It may have been that the measurements over this frequency band made by Penrose et al were also dominated by baleen whales, which because of coupling into the deep sound channel meant that the calls emanated from great distances and so were not easily identifiable. Some workers in the northern hemisphere have attributed similar increases across a similar frequency band to shipping noise.

The fact that blue whales seem to aggregate in the Rottnest trench has now been confirmed. Just why the animals aggregate their is not yet clear. The complex

oceanographic conditions set up by the trench crossing the path of the southerly travelling Leeuwin current, and the strong offshore winds experienced in summers may result in localised upwellings around the trench. This would enhance plankton productivity and possibly result in the formation of dense macro-zooplankton aggregations, such as euphausiid krill swarms. Such swarms would maintain the attention of many species of large baleen whales. Further studies in 2000-2001 are proposed to elaborate this and other questions whilst the current data set is still under perusal.

References

Bannister, J.L. (1993). Whale Protection Act 1980: summary report on activities carried out under Scientific permit P1993/030. Unpublished report to Australian Nature Conservation Agency, Canberra, 13 pp.

Bannister, J.L., Kempe, C.M., Warneke, R.M. (1996). The action plan for Australian cetaceans. Australian Nature Conservation Agency, Canberra, 242 pp.

Bannister, J.L., Burton, C.L.K. (2000). Investigation of blue whales off Perth, Western Australia: aerial survey, 1999-2000. Report to Environment Australia, from Western Australian Museum, 10 pp.

Cato, D.H. (1998). Simple methods of estimating source levels and locations of marine animal sounds. **J. Acoust. Soc. Am.** 104(3):1667-1678

Cummings, W.C., Thompson, P.O. (1971). Underwater sounds from the blue whale. **J. Acoust. Soc. Am**. 4(2):1193-1198

D'Spain, G.L., Kuperman, W.A., Hodgkiss, W.S., Berger, L.P. (1995). 3-D localisation of a blue whale. MPL technical Memorandum 447, University of California, SCRIPPS

Kato, H., Bannister, J., Burton, C., Ljungblad, D., Matsuoka, K., Shimada, H. (1996). Report on the Japan/IWC blue whale cruise 1995-96 off the southern coast of Australia. Document SC/48/SSH9 presented to the IWC Scientific Committee, Aberdeen, 35 pp.

McDonald, M., Hildebrand, J.A., Webb, S.C. (1995). Blue and fin whales observed on a seafloor array in the Northeast Pacific. **J. Acoust. Soc. Am**. 98(2):712-721

Mellinger, D.K., Clark, C.W. (2000). Recognizing transient low-frequency whale sounds by spectrogram correlation. **J. Acoust. Soc. Am.** 107(6):3518-3529

Penrose, J.P., McCauley, R.D., Duncan, A.J., Woods, A., Hoffman, J., McLaughlan, D., Sherlock, M., Cato, D.H., Vosmer, T. (1998). Proposed Comprehensive Test Ban Treaty Cape Leeuwin Hydrophone site: Sea-noise measurements June-September 1998; Shipping movements and modelling of nearby ship noise into site. Report prepared for the Preparatory Commission, Comprehensive Test Ban Treaty Organisation, by CMST, Curtin University, WA. Report C98-25

Stafford, K.M., Fox, C.G., Clark, D.S. (1998). Long-range acoustic detection and localization of blue whale calls in the northeast Pacific Ocean. **J. Acoust. Soc. Am.** 104(6):3616-3625

Thode, A.M., D'Spain, G.L., Keperman, W.A. (2000). Matched-field processing, geoacoustic inversion, and source signature recovery of blue whale vocalisations. **J. Acoust. Soc. Am.** 107(3):1286-1300

Watkins, W.A. (1981). Activities and underwater sounds of fin whales. **Sci. Rep. Whales Res. Inst**. 33:83-117

Zemsky, V.A., Sahzinoz, E.G. (1994). Distribution and current abundance of pygmy blue whales. Translated by Gurevich, V.S. Edited by Donahue M.A and Brownell, R.L.Jr., National Marine Fisheries Service, Southwest Fisheries Science Centre, La Jolla California, LJ-94-02

Robust, Automated Remote Monitoring And Controlled Logging Of Multi-Frequency Hydroacoustic Data In The Southern Ocean And Coastal Waters Of Antarctica

Tim J. Pauly, David A. Wanless

Australian Antarctic Division.

Abstract

The Australian Antarctic Division's RV AURORA AUSTRALIS transits the Southern Ocean and large regions of Antarctic Coastal waters each Austral summer. Scientists at the Antarctic Division have developed an automated acoustic logging system to opportunistically collect acoustic backscatter data from the water column. The system uses one or two Simrad EK500 echosounders, and is remotely monitored and controlled via twice daily email links to the vessel. Data summaries can also be downloaded daily and viewed as echograms.

The system monitors echosounder status, vessel speed, DGPS data, acoustic data rates and free disc space. The logging is configured according to the location and vessel speed. Different geographic regions can be logged using different instrument settings. Once the vessel enters a logging region and meets all the logging requirements then logging is automatically re-configured and the data is logged under a pre-defined survey name.

A "Robust Daemon" monitors system processes, data rates and available disc space, shutting down processes and restarting them when an error state is detected. Once a disc is full then the logging directory is automatically changed to the next free disc in a disc array.

This system is currently in use to opportunistically collect acoustic backscatter data from the Southern Ocean in support of a monitoring program using a Continuous Plankton Recorder and for investigating the distribution of krill along the Antarctic coast.

Introduction

Recently several research projects using echosounder logging systems from unmanned automated vessels have been described, for example the use of the *Autosub* (Millard *et al.* 1998) for fish vessel avoidance studies (Fernandes *et al.* 2000), and the Portuguese Caravela project (Rodeia 2000) (autonomous oceanographic and bioacoustic vessel). The *Autosub* deployments are inherently of short duration (hours) whereas the Caravela project deployments are longer range – up to 2000 nautical miles (days). The system described here is deployed on a manned vessel but operates without direct intervention for periods of up to several months.

Motivation

We have four main objectives for the opportunistic logging of acoustic backscatter data from the surface waters (0 to 1000m) of the Southern Ocean and Antarctic coastal waters (0 to 200m). These are to:

- Improve our understanding of the relationship of backscatter signals to large scale oceanographic features;
- Better understand the large scale distribution of Antarctic krill around the coast of Antarctica;
- Investigate the correlation of acoustic backscatter data to continuous plankton recorder data; and
- Investigate the value of these data for long term environmental monitoring.

Reduction in the availability of resources (primarily ship time) to the Australian Antarctic Division's biological marine science programs over the last decade has meant a decrease in the frequency of regular transect surveys. The objectives listed above are, in part, a response to these trends in our levels of resourcing. We have set out a series of objectives that meet the Division's stated scientific priorities, and are achievable by opportunistic use of the vessel's typical cruise tracks. Given that appropriate logging systems provide data to meet these objectives we need to consider data

coverage and the facilities required of such a logging system.

Data Coverage

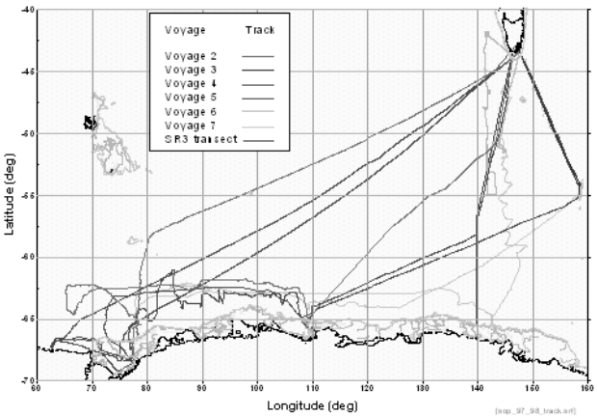

Fig 1: Vessel cruise tracks for summer season 1997/98.

RV AURORA AUSTRALIS provides both supply and marine research facilities to the Australian Antarctic Division. Figure 1 indicates the typical annual cruise tracks of these shipping activities and hence the possible data coverage within a shipping season.

Given this coverage a wide range of issues need to be considered in the automatic acquisition of acoustic backscatter data, for example:

- We need to minimize unwanted data (given the possible data rates from modern echosounder systems) but also the unnecessary fragmentation of data sequences.
- We need to optimize data resolution (and further minimize unwanted data) by collecting data only from appropriate components of the water column (e.g. when considering krill distribution we are only interested in the top 200m of the water column).
- The configuration of data acquisition needs to be tailored to meet the individual requirements of particular objectives (e.g. pulse lengths and data depth range); these requirements may vary between objectives.
- To facilitate data access we need to automate the logical partitioning of the acquired data to meet different objectives, and so on.

Facilities provided by the system

To effectively utilize this data coverage requires a flexible unmanned logging system which keeps us informed of its state, provides data summaries and is remotely configurable. However in the face of these complex requirements it is very important that the system is sufficiently robust to achieve worthwhile logging rates. On this basis our system has evolved to provide us with the following facilities:

- Obviously it provides us with a sequence of multi–frequency echogram data sets.
- Logging is robust. A simple process monitors all other processes, detects possible error conditions and attempts to correct them.
- The system is configured prior to each voyage to log a series of data sets based on the location of the vessel. Each data set can be independently configured.
- Nominated users are automatically provided with monitoring messages indicating system changes, status and summary data via email.
- The instrument can be remotely configured via email.
- All instrument changes are recorded whether they are implemented via email, control software or the instrument front panel.

System Description

Automated logging is achieved through the interaction of several different processes – the Data Acquisition Coordinator, the Logcontroller, the Previewer and the Robust Daemon.

Fig 2: Robust, remotely controlled logging of hydroacoustics data – system overview.

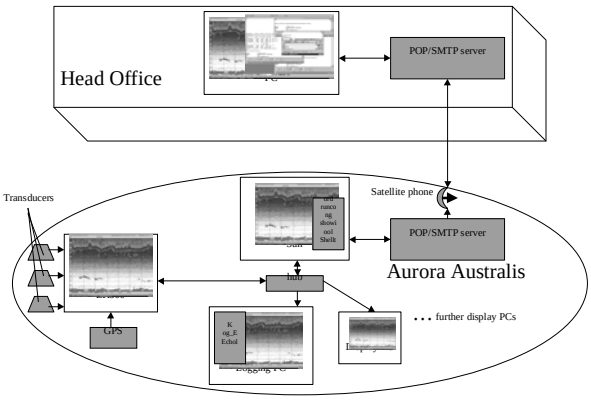

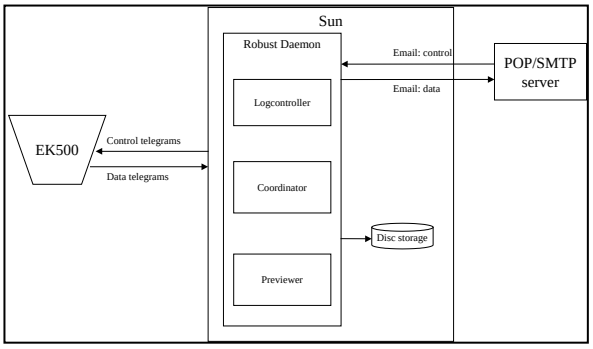

Fig 3: Processes and systems in main logging computer.

Data Acquisition Coordinator

The Data Acquisition Coordinator, or Coordinator for short, provides two-way communication between various other processes and the echosounder(s).

The Coordinator receives echogram, GPS, vessel log, echo integration, target detection and any other data broadcast by the echosounder(s) and sends them on to the Previewer, the Logcontroller and any other processes which have requested them. If so instructed, it also logs them to disc. Importantly this includes changes of echosounder parameters, whether initiated at the echosounder console or remotely. This provides vital information for interpreting other logged data.

The Coordinator also transmits commands to the echosounder(s) – e.g., commands to change the depth range or calibration of an instrument, or an instruction to turn on or off the transmission of a particular type of data.

Logcontroller

The Logcontroller process monitors echosounder status, vessel speed, DGPS data, acoustic data rates and free disc space. The logging is configured according to the location and vessel speed. Different geographic regions can be logged using different instrument settings. Once the vessel enters a logging region and meets all the logging requirements then logging is automatically re-configured and the data is logged under a pre-defined survey name.

The process controls logging by monitoring the GPS and vessel log data feeds from the echosounder(s), via the Coordinator. This information is compared against a set of parameters read from a configuration file and depending on the results of the comparison, and the current state of the logging process, a decision is made whether or not to start/stop logging.

Parameters available for defining when logging should start and stop are as follows:

- Minimum start logging speed - the minimum speed (in knots) required before logging is permitted.
- Minimum stop logging speed - the speed (in knots) below which logging will be stopped.
- Table of Latitude/Longitude delimiters - any number of separate navigational boxes that define where logging should occur. These are defined by the following parameters:
  - Minimum and maximum latitude
  - Minimum and maximum longitude
  - Survey name - the survey name associated with the box (used to create disc file names to allow easy separation of data from different logging areas).
- Hysteresis parameters for logging control. These margins are designed to avoid the situation where logging is frequently started and stopped as logging control data fluctuate around the preconditioned values; for example, GPS data fluctuations on the boundaries of navigational logging boxes:
  - Minimum time spent logging - the minimum amount of time that logging should occur, once started.
  - Number of GPS points over which to determine navigational criteria - the number of adjacent GPS points for which start logging criteria must be met before logging will start, and the number of adjacent GPS points for which stop logging criteria must be met before logging will stop.
  - Number of vessel log points over which to determine speed criteria - the number of vessel log points for which vessel speed of at least the minimum start speed must be maintained, before logging will be permitted to start. Also the number of vessel log points for which vessel speed of less than the minimum stop speed must be maintained, before logging will stop

The Logcontroller also monitors the arrival of vessel log, GPS and echogram packets from the Coordinator. If packets of a particular type have not been received for a specified period of time then this is noted on the log. If all three packet types fail to arrive within a

Fig 4: Sample Logcontrol configuration.

```
#### Voyage No. 1 2000-2001 - Sept-Nov 2000
lc_cruisename Voyage1_00-01("V1_Sep-Nov_00-01");
lc_minspeeds Voyage1_00-01(3.0, 0.5);
lc_minlogtime Voyage1_00-01(30);
lc_navpoints Voyage1_00-01(5,300);
lc_speedpoints Voyage1_00-01(10,300);
lc_navbox Voyage1_00-01(-30.00, -63.00, 60.0,
165.0, "sopem_00-01", "");
lc_navbox Voyage1_00-01(-63.00, -78.00, 60.0,
165.0, "AA_coast_V1_00-01", "");
```

specified time period then the entire Coordinator system (i.e., the Coordinator, the Previewer and the Logcontroller) is terminated. Prior to termination the Logcontroller investigates a history file maintained by the system to determine whether similar events have occurred within recent time intervals. Depending on the results the Logcontroller may then flag the controlling process (the Robust Daemon) to delay restart of the Coordinator system by varying time intervals.

Previewer

The Previewer process displays the current (and recent) echogram, GPS and vessel log data on a sliding window, and allows manual override of logging control, so that an operator on the ship can stop or start logging manually in response to interesting features seen in the echogram data, or take control in the event of completely changed circumstances, an email or other system failure.

Robust daemon - runcoord

The Robust Daemon, also known as Runcoord, monitors the status of the other processes - the Coordinator, the Logcontroller and the Previewer - and restarts any component if it stops for any reason. It also monitors the amount of disc space left in the logging directory and redirects the Coordinator to another directory if the current one is full. It sends email messages notifying the scientists of major changes of state, e.g., whenever it has to restart any process.

Email monitoring

Each of the major processes sends email messages to members of one of several predefined lists of email addresses whenever it undergoes a major change of state. There is a separate email list for each of the major processes. These email messages allow scientists either elsewhere on the ship or back at head office to be kept aware of the progress of logging, e.g., whenever a new logging survey 'box' is entered, any GPS failures, the filling up of logging discs or any process failures.

Fig 5: Examples of email messages notifying of change of state.

```
From:    echolog@AURORA.antdiv.gov.au
Date: Thu, 12 Feb 98 06:16:05 GMT
From: echolog@hydrophobia (Echo)
Starting Data Acquisition Coordinator for
ek2, logging to
/ihlea_e/echo/data/log
From:    echolog@AURORA.antdiv.gov.au
Subject: Log Control Status

Logging stopped.
  Leaving box no. 1.
    For survey 'SOPEM_V4'
      At 15/01/98 14:39:01
```

There is also the facility to email summary integration tables from the echosounder to the scientists, which give an overview of what the echosounders are actually seeing. This is designed to allow modification of logging parameters; and even remedial action in the case of equipment failure, rather than just waiting until the voyage returns to discover the bad news.

Email control

As well as being able to send email messages, the logging system can receive and act upon the following four types of email messages:

- Echosounder commands: a list of commands to be sent to the echosounder. The response to the commands is emailed back to the scientists (Figure 6).

- Echosounder command file: loads a pre-saved file of commands and sends them to the sounder. The response is emailed back to the scientists. This is useful for setting the instrument up for a new survey.

- Shell commands: a list of arbitrary Unix commands to be executed on the logging computer. The output from the commands is emailed back to the scientists. This is useful for carrying out maintenance, monitoring or troubleshooting on the logging computer – e.g., archiving and deleting logged data to free space, querying configuration files to help interpret returned data, or even querying file dates and sizes to check versions of logging software (Figure 6).

Fig 6: Examples of email commands and responses.

```
<EK_COMMAND_LINE>
/ethernet com. menu/telegram menu/echogram=1&2
/ethernet com. menu/echogram-1 menu/range=200 m
</EK_COMMAND_LINE>
To:        david_wan@antdiv.gov.au
From:      echolog
Subject:   EK Menu Status
Date sent: 05 Sep 00 12:01:46
SENDING --- 05/09/00 12:01:46 --- /ethernet
com. menu/echogram-1 menu/range=200 m
EK Status --- 05/09/00 12:01:44 --- Remote re-
quest executed
FINISHED --- 05/09/00 12:01:46 --- EK Settings
successfully sent
```

```
<SH_COMMAND_LINE>
ls -l /home/echolog/testfile.out
</SH_COMMAND_LINE>
To:        david_wan@antdiv.gov.au
From:      echolog
Subject:   Previewer Status - email report
Date sent: 06 Sep 00 16:57:16

Output of emailed shell command:
ls -l /home/echolog/testfile.out
-r--r--r--  1 echo  staff    41 Sep  6 16:49
/home/echolog/testfile.out
```

- Shell file creation: text and a filename to write the text into. Useful for creating new files of echosounder parameters to be loaded, modifying configuration files (which could be followed with a shell command to kill some of the logging processes, in order to reconfigure logging), or even conceivably patching logging software.

Results

In our first full season of operation, 1997/98, we logged only the Southern Ocean transit component of each voyage. To look at large scale krill distributions, logging has been extended to include the shelf break (1000m depth contour) coastal region. By comparing Figures 1 and 7 it can be seen that the majority of possible data was logged east of 110^0 (the western limit of the specified logging region). In earlier seasons considerable effort was required to capture event data to overcome a number of unexpected faults that occasionally stopped the system. These included operating system events that required user responses through modal windows which, if not acknowledged, eventually caused logging to fail, eliminating applications with memory leakage which would consume memory over the period of months, causing system crashes. We still suffer some memory leakage problems however they are not sufficient to cause trouble within 3 month periods. Large amounts of virtual memory provide an adequate safeguard against minor memory leakage.

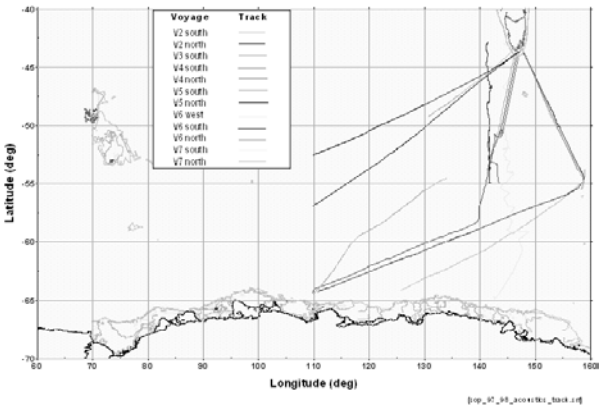

Fig 7: Component of cruise track where acoustic data were logged.

The system is now sufficiently stable that we have been able to determine that our last remaining known problem exists with the echosounder. Unpredictably once or twice every couple of months the instrument hangs, causing data loss. We have been able to detect this by using parallel logging systems. We are still investigating the cause of this however we have designed (but not yet implemented) a fix. Upon detecting a network interface failure on the EK500 we can trigger a power cycling for the instrument, hence resetting it.

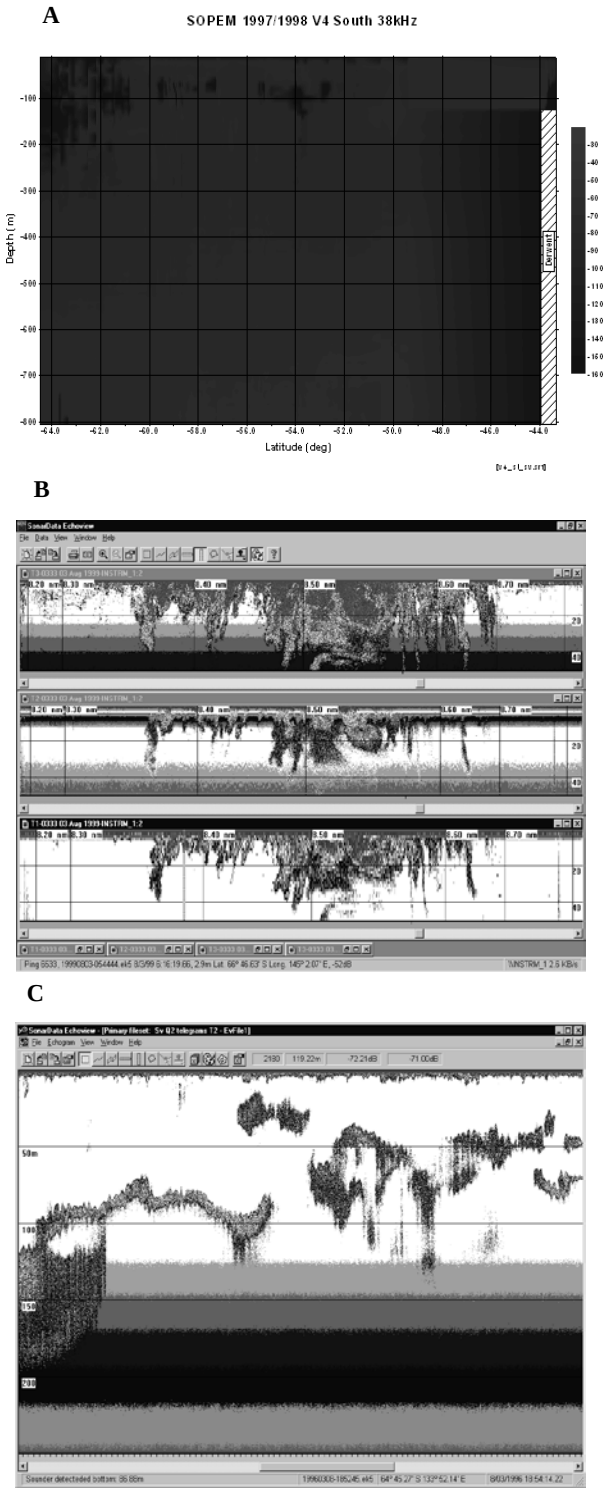

Fig 8: Example echogram data – A) Processed Southern ocean transit; B) Frazzle ice backscatter (at 200,120 and 38 kHz) from polynya off Mertz Glacier; C) Backscatter from krill aggregations.

Figures 8a, b and c provide examples of the type of data currently being acquired.

Figure 8a is a processed Southward transit through the Southern Ocean showing frontal features and scattering layers in the top 1000m of the water column. Figure 8b

shows data from within the winter polynya to the west of the Mertz Glacier. Similar echograms have been reported from the Amery Ice Shelf by Penrose *et al.* (1994). Backscatter data (120kHz) from krill aggregations in Antarctic coastal waters are shown in Figure 8c. These types of data are currently being acquired for a range of research programs being conducted by the Australian Antarctic Division.

Data Quality and Calibration

Although largely outside the scope of this document, the importance of maintaining data quality and calibration is such that it can not be left unmentioned. Once achieved, successful automated logging of multi-frequency acoustic data presents a number of issues. Given the large difference in value of calibrated and uncalibrated data to long term monitoring programs, considerable effort and resource is required to frequently calibrate and monitor transducer performance. Hence we have developed procedures of frequently monitoring a number of transducer parameters, including complex impedance, to detect failures and hence identify possible break points in data streams between calibrations.

Given the high data rates (10s of Mbytes/hour) and long logging periods (months) practical data quality assurance processes need to be established to deal with the data at least within an annual cycle. To achieve a level of basic data quality this requires an operator to inspect and tag all echogram data at each frequency for a range of bad data types, and we have also developed automated dynamic noise removal algorithms.

It is then necessary to produce a basic analysis product from all data. In our case this is an initial processing and plot of integrated data for 20m depth layers over 5nm intervals for the deep ocean transits, and 5m depth layers over 0.5nm for coastal segments.

Other considerations: Hardware robustness

There is little point providing this level of robustness and control for the software if simple hardware failures can render the whole system unusable. It is clearly vital to provide robust hardware with a high level of redundancy. This has been largely achieved on the Aurora by logging data on both the Sun and PC platforms, and providing the Sun with a RAID system for operating system and data storage. Over the development period of approximately four years , no large sections of data have been lost through computer hardware failure. However fires and broken propellers and transducers on the ship have certainly reduced data collection.

The robustness of the system would be further improved by email monitoring and control of the RAID storage system.

We are also investigating developing a robust logging system for the PC environment with a view to migrating completely over to PC's.

Security

The acceptance by the logging system of arbitrary operating system shell commands is clearly a security issue. This has been dealt with through three mechanisms – ensuring that output is returned to the predefined list of scientists rather than the sender of the commands, the existing file system and user restrictions of the operating system, and secrecy! Improved security could be achieved by verifying the sending address, refusing some sorts of messages, and potentially incorporating a password mechanism.

Conclusions

This flexible system successfully provides data to achieve a range of objectives that otherwise would not be feasible, particularly given the heavy resource constraints of most scientific institutions these days.

Provided that there is no requirement for ground truthing i.e., targeted trawls, it is possible to effectively operate unmanned and log valuable acoustic data. However dedicated acoustics people are still required for major programs particularly where other sampling, dependent on acoustics input, are required. The development of robust logging systems also complement manned voyages by further ensuring data acquisition.

Finally, ensuring or providing reliable data streams is only the humble beginning in a process which ultimately depends on quality data analysis and interpretation. However, valuable data products offering wide temporal and spatial coverage provide feedback to the development of interpretations.

References

Fernandes P. G., Brierley A. S., Simmonds E. J., Millard N. W., Mcphail S. D., Armstrong F., Stevenson P. and Squires M., (2000). *Fish do not avoid survey vessels*, Nature 404.

Rodeia J., (2000) University of Azores, personal comms. Sept. 2000.

Millard, N. W., Griffiths G., Finnegan G., Mcphail S. D., Meldrum D. T., Pebody M., Perrett J. R., Stevenson P. and Webb A. T., (1998). *Versatile autonomous submersibles - the realising and testing of a practical vehicle*, Underwater Technology, 23(1).

Penrose J. D., Conde M. and Pauly T.J. (1994). *Acoustic detection of ice crystals in Antarctic waters*. J. Geophys. Res., 99, 12573-12580.

Optimal Seabed Habitat Mapping Using Multibeam Acoustics With Associated Physical And Visual Sampling Devices – At Sea Trials

Rudy J. Kloser[1] and John D. Penrose[2]

[1]CSIRO Division of Marine Research, Castray Esp, Hobart, Tasmania, [2]Centre for Marine Science and Technology, Curtin University of Technology, Bentley, Perth, WA.

Abstract

Australia is custodian to a large marine jurisdiction with associated seabed habitats that need to be managed for multiple use purposes. Mapping seabed habitats or their surrogates is a fundamental first step in this process, with methods that can map large areas of seabed such as multibeam swath mapping sonars representing attractive tools. A methodology of optimally mapping the seabed is presented using a swath mapper in conjunction with biophysical, geophysical and video/photographic devices. A Simrad EM1002 swath mapper was used in April 2000 to map selected sites on the shelf and upper slope. The swath mapper produced three data products (being, bathymetry, backscatter and sun illuminated bathymetry imagery) that were visually inspected to target the variety of substrate types. Limitations in the imagery were observed due to instrument frequency, beamwidth, pulse length, depth and across track resolution as well as changing oceanographic and weather conditions. The biophysical, geophysical and video/photographic sampling was targeted on the contrasting features in the imagery. The video/photographic sampling proved the best tool for understanding the backscatter images and their relation to geological and biological attributes. The swath mapper proved (not surprisingly) to be an invaluable tool for undertaking investigations of the seabed, providing higher resolution bathymetry and backscatter than our existing single beam devices. A significant advantage for habitat mapping was the reduction in time consuming direct and visual sampling by mapping out seabed regions of like character. The ability of the swath mapped bathymetry and backscatter to provide a surrogate for specific geological and biological attributes that are independent of instrument parameters, depth/slope and applicable to broad regions is part of ongoing work. This program of research will work towards the combination of outputs from the swath mapper (depth, seabed hardness and roughness) and other variables such as current/wave stress and water temperature (as an example) to produce predictive maps of biological communities.

Introduction

Australia is custodian to a large marine jurisdiction with associated seabed habitats that need to be managed for multiple use purposes. As such it is proposed as part of Australia's Ocean Policy to manage our marine jurisdiction using regional ecosystem-based management principles. A first step in this process was established with the IMCRA3.3 report that provided a provincial-scale regionalisation over the continental shelf of Australia. To map seabed habitats of the whole Australian Marine Jurisdiction (AMJ) will require the development of surrogates due to the large region and difficulty/expense of sampling the marine environment. These seabed surrogates will need to describe the geological and biological features and be able to detect changes in them that are of management significance. Acoustic methods of sensing the water column and seabed habitats provide a potential method for developing these surrogates when used in conjunction with direct capture and visual sampling methods.

Seabed habitat is defined by a mix of recent biological, hydrological and chemical processes layered over a geological framework. The seabed habitats can be described in general terms by sediment types, depth, latitude, longitude and hydrological processes (eg Peterson 1913; Snelgrove and Butman 1994; Coleman et al 1997). However the links between seabed structure and animal communities are frequently not well described because of difficulty of sampling broad areas of seabed, especially over rough ground and at depth. Simple normal incident single frequency acoustic methods provide a useful sampling tool to map the seabed seascape in terms of broad scale bathymetry and seabed hardness and roughness on flat seabeds with associated ground truthing (Pace *et al* 1982; Orlowski 1984; Chivers *et al* 1990; Lurton and Pouliquen 1992; Collins 1996, Kloser in press). These narrow beam systems have major deficiencies when being used for seabed mapping as presently they can only be used on flat seabeds as a sloping seabed changes the reflection properties of the returned echo, (Kloser in press). Also these systems have single beams of 7-15 degrees full beam angle and sample a very small footprint of the seabed. This requires extrapolation between sampling lines,

(Siwabessy et al this volume). To improve the sampling resolution, depth resolution and account for seabed slope, multi-beam acoustic systems are being used.

In Australia, current national swath mapping efforts are underway within the Australian Geological Survey Organisation (AGSO) and the RAN Hydrographic Office (Hydro). AGSO have carried out swath mapping in deep water 500 – 6000 m over many years for geological surveying and UN Law of the Sea objectives, Exon and Hill, 1999. Recently AGSO have swath mapped the deep water 500 – 3000 m in the South East Australia region using the French IFREMER vessel *L'Atlanta* equiped with a Simrad EM12D. The RAN Hydro office have built two vessels *Leeuwin and Melville* equiped with shallow water Atlas Fansweep swath mappers. These are expected to be commisioned this year and will map the Hydrographic Services high priority areas on the continental shelf.

These multi-beam systems provide detailed bathymetry along the line of the vessels track with swath widths of 2-10 times water depth as well as producing detailed backscatter maps of the seabed. The backscatter maps have lower spatial resolution than those produced by side scan instruments but due to beam forming, multi-beams can correct for seabed slope. Investigations using multi-beam backscatter maps to date have concentrated on geological mapping, eg Todd *et al* (1999). What is less certain is the ability of the bathymetry and associated backscatter images to be used as a surrogate for habitat maps of a given region and to determine the level of ground truthing required. More investigation is required to establish the relationship of the backscatter maps to the sediment and biotic communities. This will require the correlation of biological and geological sampling at the various acoustically defined seabed types over a range of depths, seabed slopes and ensonification slant ranges.

Methodology

In April 2000, CSIRO in conjunction with the National Oceans Office fitted a 95 kHz swath mapper (Simrad EM1002, Seatex positioning system) to the 65m CSIRO research vessel *MRV Southern Surveyor*. The Simrad EM1002 is a phase interpolated beamforming swath mapper using a rounded head to reduce sound velocity beam forming errors. It forms 111 beams that are effectively 2 by 2 degrees per beam. The seabed depth per beam is calculated using an amplitude or phase algorithm depending on the angle of incidence. A mean backscatter per beam value is calculate and sidescan values are collected by digitisation along the beam with 1-40 samples collected for each beam. The beams are electronically controlled for roll stabilization.

The swath mapper and existing three frequency (12, 38 and 120kHz) normal incident echo sounders (Simrad EK500) were used to map various shelf regions in the south east and south west of Australia. The sites were chosen based on historic knowledge as having high importance for fisheries and physical characteristics of depth, seabed morphology (slope and roughness), sediment type, latitude and longitude. At the commencement of each survey site the seawater propagation parameters of absorption and sound velocity were calculated from the formulae of Francois and Garrison (1982) and MacKenzie (1981), respectively, based upon temperature and salinity profiles obtained with a Neil Brown conductivity-temperature-depth recorder (CTD). The swath mapping transect lines were in general carried out orthogonal to the seabed slope aided by the EM1002 data collection software.

The completed swath survey was processed using the Simrad Neptune software to provide three data products of bathymetry, backscatter and sun illuminated imagery. These three data products were visually inspected on board and the biophysical, geophysical and video/photographic sampling targeted at contrasting features in the imagery. The precise location of the direct sampling devices used the vessels dynamic positioning system and a Sonardyne USBL. In general the location of sampling gears could be directed to within 5-10m for depths less than 300 m.

The physical sampling of the geological and biological characteristics were carried out with a variety of instruments. Surficial sediments were obtained with a Smith-McIntyre grab and Box Corer. Box core samples were collected to obtain geoacoustic parameters such as porosity, sound velocity and density. Lithology samples were collected with a rock dredge. In-fauna and epi-fauna specimens were collected with a benthic dredge. Single and stereo video footage were obtained with a vertical drop and towed video platform. The video imagery was used to characterise the biological communities and geomorphology. The stereo footage was collected to measure seabed roughness and sizing of benthic biota. Details of the collection instruments sampling and analysis protocols will be reported elsewhere. The 'at sea' visual inspection of the derived samples has been used here to interpret the swath imagery.

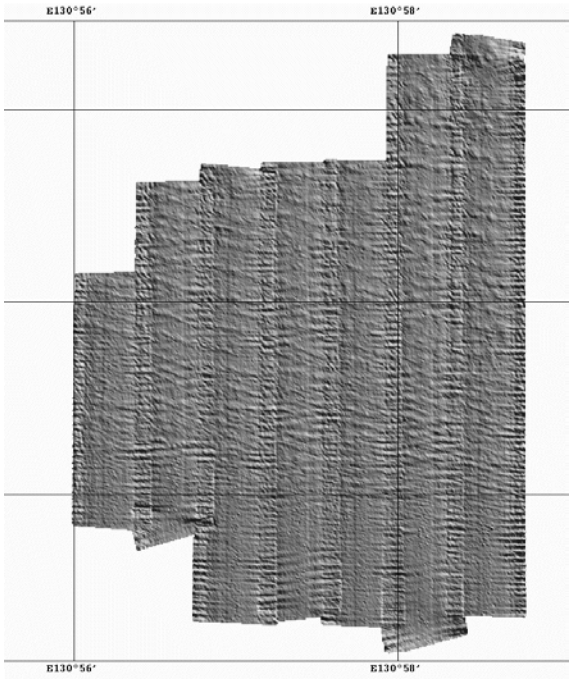

Figure 1. Example of 8 times vertical exaggeration sun illuminated bathymetry in the Great Australian Bight benthic protection zone, depth 135-145 m, showing the rippling on the outer beams due to a roll correction error.

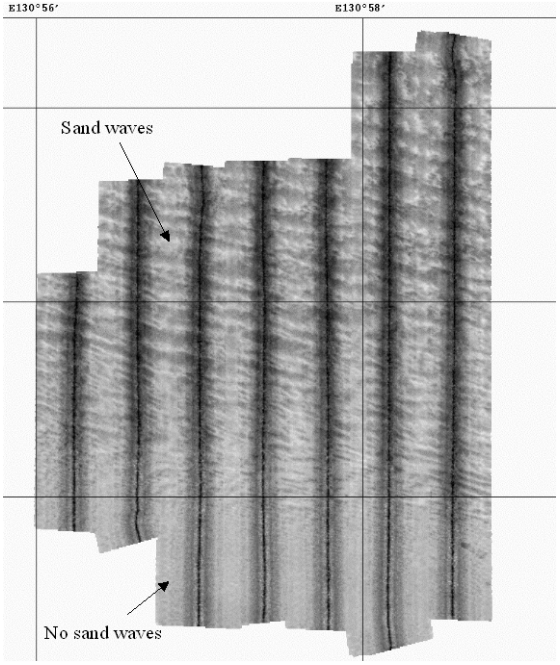

Figure 2. Example of mean acoustic backscatter per beam in regions with and without large sand-waves. High backscatter is black. The dark high backscatter nadir beam shows the vessels track. Note the uneven backscatter across the swath

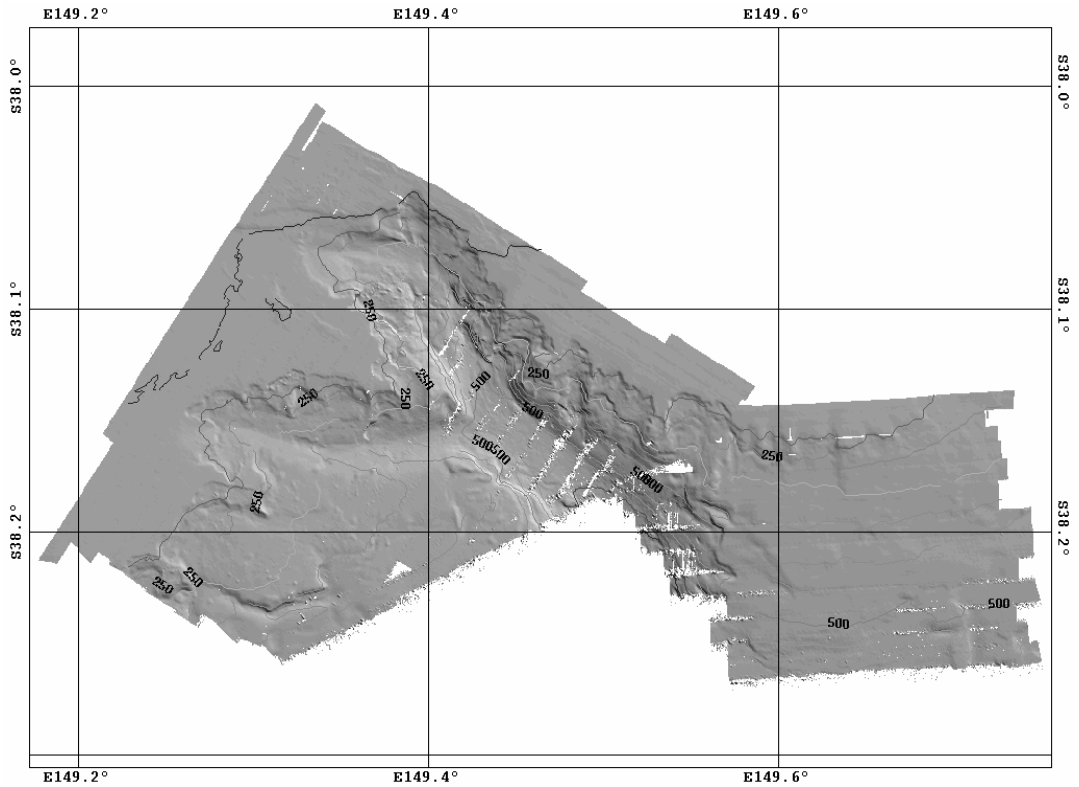

Figure 3. Sun illuminated bathymetry of the Big Horseshoe, a productive fishing ground showing the depth limitation of the swath mapper at approximately 600 m.

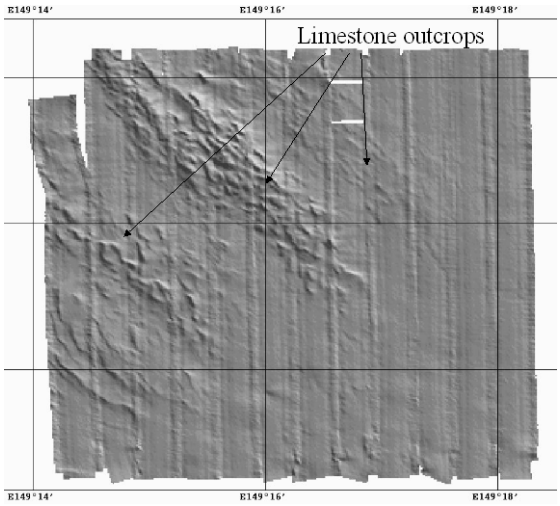

Figure 4. Sun illuminated bathymetry with 8 times height exageration showing limestone outcrops of 0.5 to 1 m height, north-south lines are swath mapper artifacts. Depth 110 – 120 m.

Results (preliminary)

Ten survey areas ranging in depth from 12m to 600m were mapped with the EM1002. In three areas, Maria Island, Big Horseshoe (SE) and Howe Reef (off shelf), swath mapping with the EM1002 was targeted to over-

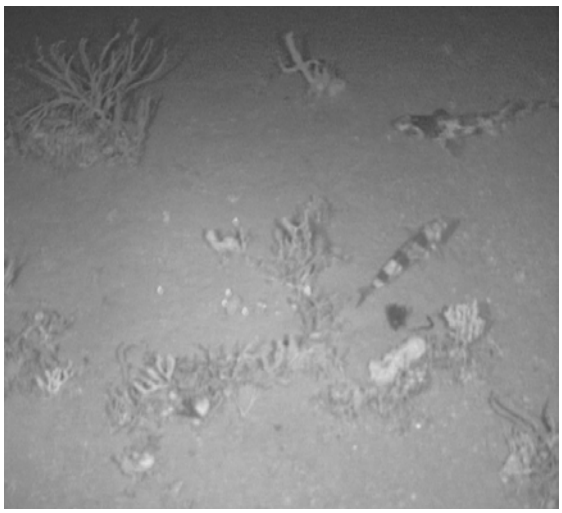

Figure 5. Limstone outcrop fauna image taken from a digital video. Lasers are used for sizing objects

lap areas previously mapped by AGSO with a 12 kHz EM12D. In total we collected 40 GBytes of swath mapped data and 9 GBytes of normal incident multi-frequency data. These sites provide 'reference' or 'training' areas for the calibration and cross-reference

distribution of backscatter of acoustic instruments from other vessels in future seabed mapping exercises.

Throughout the survey we operated the system at 140 degrees swath width, 5.5 times water depth. A problem in the outer beams between 60 to 70 degrees caused a vessel-roll related 'depth ripple'. This depth rippling effect of up to 1 m peak to peak amplitude was clearly seen in the sun illuminated maps, Fig 1. The backscatter imagery was also characterised by uneven strength across the swath profile, Fig. 2. An absorption coefficient of 35dB/km was used for most of the voyage that should have corrected the backscatter response based on the temperature and salinity profiles. The EM1002 was capable of recording data of useable quality to a depth of about 600 m in fine sea conditions. Generally, however, the depth limitation was closer to 400 m because data quality suffered where the seabed was steeply sloping and when sea conditions deteriorated, Fig. 3.

Of particular note was the ability of the system to highlight small-scale seabed features such as limestone outcrops of 0.5 - 1 m or less in height, Fig. 4. These are generally important for supporting communities of large sponges and other attached erect invertebrates that provide complex habitats for fishes, Fig. 5. The swath-mapper also revealed topographic patterns at scales of 100s of metres to kilometres that are not easily detected by single beam instruments. These include complex, rippled soft sediment substrata that dominate the seabed near Maria Island and in the Great Australian Bight Benthic Protection Zone, Fig. 2.

Discussion

In summary, although its performance was impressive, the Simrad EM1002 did not perform to all of its technical specifications. Some of the problems encountered were due to the temporary instalation of the equipment on our survey vessel. Whilst others associated to the limited swath width (3.5 times swath width) of the sonar and the uneven backscatter profile have not been resolved to date.

The bathymetric and backscatter images were of good enough quality to deliniate the major seabed characteristics and target our biophysical, geophysical and visual samplers. The detailed bathymetry of the instrument revealed a level of seabed classification that could not be ascertained with single beam acoustic devices.

The consistency and relationship of seabed type to instrument settings, depth, seabed slope and acoustic slant range for backscatter measurements will be investigated by repeat measurements over the ground truth sites selected and compared to model predictions of the backscatter returns (Jackson *et al* 1986). Further the ability for the acoustic devices to represent a surrogate for seabed type suitable for habitat description will also be explored.

Acknowledgements

This work is being supported by the National Oceans Office and CSIRO Marine Research. The co investigators in the project were Alan Williams and Alan Butler. In particular we thank Tim Ryan, Scott Gordon and Gordon Keith for collection and processing of the swath mapped data. Bruce Barker for extraction of video images. Matt Sherlock, Ian Helmond and their teams for installing the swath mapper on Southern Surveyor. Our fellow voyage scientists and technicians, master and crew on Southern Surveyor.

References

Bax, N.J. and Williams, A. [Eds.] (In Press). Habitat and fisheries productivity in the South East Fishery. *Final report to FRDC Project 94/040*, CSIRO Marine Research, Hobart, Tasmania, Australia.

Chivers, R.C., Emerson, N., and Burns, D.R. (1990). New acoustic processing for underway surveying. *Hydrological Journal* **56,** 9-17.

Coleman, N., Gason, A.S.H., and Poore, G.C.B (1997). High species richness in the shallow marine waters of south-east Australia. *Marine Ecology Progress Series*, 154: 17-26.

Collins, W., Gregory, R.,and Anderson, J. (1996). A digital approach to seabed classification. Sea Tech, August 83-87

Exon, N. and Hill, P., (1999). Seabed mapping using multibeam systems: and esential technology for mapping Australia's margins. *AGSO Journal of Australian Geology and Geophysics*, 17(5/6), 1-16.

IMCRA Technical Group (1998) Interim Marine and Coastal Regionalisation for Australia: an ecosystem based classification for marineand coastal environments. Version 3.3. *Environment Australia, Commonwealth Department of the Environment, Canberra.*

Jackson, D. R. and Briggs, K. B. (1992) High-frequency bottom backscattering: roughness versus sediment volume scattering. *The Journal of the Acoustical Society Of America*.; 92(2):962-977

Kloser, R.J., Bax, N.J, Ryan, T, Williams, A., and Barker, B.A. (in press). Remote sensing of seabed types-development and application of normal incident acoustic techniques and associated ground truthing. *Marine and Freshwater Research.*

Lurton, X. and Pouliquen, E. (1992). Automated seabed classification system for echo-sounders. *Oceans 92, Volume 1*. New York: IEEE. 936pp. [In 2 Vols] : 317-321.

Orlowski, A. (1984). Application of multiple echoes energy measurements for evaluation of sea-bed type. *Oceanologia* **19**, 61-78.

Petersen, C.G.J. (1913). Valuation of the Sea II. The animal communities of the sea bottom and their importance for marine zoogeography. *Report of the Danish Biological Station to the Board of Agriculture* 21: 1-44 (cited by Snelgrove and Butman 1994).

Siwabessy, P.J.W., Penrose, J.D., Fox, D.R. and Kloser, R.J., 2000. Bottom classification in the continental shelf: a case study for the North-west and South-east shelf of Australia. In Proceedings of the Australian Acoustical Society Nov. 2000, Perth.

Snelgrove, P.V.R., and Butman, C.A. (1994). Animal-sediment relationships revisited: cause versus effect. *Oceanography and Marine Biology: An annual review* 32: 111-177.

Todd, B.J., Faber, G.B.J., Courtney, R.C., and Pickrill, R.A.(1999). Quaternary geology and surficial sediment processes, Browns Bank, Scotian Shelf, based on multibeam bathymetry. *Marine Geology* 162, 165-214.

Bottom Classification In The Continental Shelf: A Case Study For The North-West And South-East Shelf Of Australia

P. Justy W. Siwabessy[1], John D. Penrose[1], David R. Fox[2] and Rudy J. Kloser[3]

[1]Centre for Marine Science and Technology, Curtin University of Technology, Bentley, Perth, WA6102, [2]CSIRO Division Mathematics Science, Floreat Park, Perth, WA6014 and [3]CSIRO Marine Research, Castray Esplanade, Hobart, TAS7001.

Abstract

Bottom classification has been conducted in the north-west and south-east continental shelf of Australia as a part of a CSIRO management program in those areas. Data used in this presentation were collected in the South East continental shelf of Australia from July to mid December 1996 and in the North West Shelf region of Western Australia between late July and mid August 1995, 1997. Acoustic data were collected by using a stand-alone EK 500 SIMRAD scientific echosounder operating three different frequencies; 12, 38 and 120kHz. Multiple echo energies were analysed using multivariate statistical tools to classify bottom features. The logarithm of the integration of the tail of the first bottom echo was used as a roughness index and the entire second bottom echo was used as a hardness index. A principal component analysis was used to identify echo components that provided the greatest contribution to seafloor classification. Class assignments were based on the iterative relocation technique. Results of bottom classifications on the two continental shelves and benthic assemblages overlaid to the acoustically derived bottom classification will be presented.

Introduction

The practice of resource mapping making extensive use of satellite remote sensing and airborne platforms is well established for terrestrial management. Marine biological resource mapping however is not readily available except in part from that derived for surface waters from satellite based ocean colour mapping. Perhaps the most fundamental reason is the sampling difficulty, which involves broad areas of seabed coverage, irregularities of seabed surface and depth.

Fishermen have traditionally used the first acoustic bottom echoes from a normal incidence echosounders for seabed characterisation. Only recently has attention been given to the potential use of acoustic bottom echoes from normal incidence echosounders for seabed classification in marine ecological applications. Commercial bottom classifiers available in the market that use normal incidence echosounders are the RoxAnn and QTC View systems. Both systems use shape and energy features contained in the range corrected acoustic bottom signals. Orlowski (1984) and Chivers *et al.* (1990) have used the energy features contained in the first and second acoustic bottom echoes as seabed descriptors, and Heald and Pace (1996) provide the theoretical background of relationships between energy features of the two echoes and seabed parameters. Lurton and Pouliquen (1992) and Collins *et al.* (1996) on the other hand use only a detailed analysis of the first acoustic bottom echoes. Only recently have studies on marine biological resource mapping of benthic communities used these acoustic techniques. Examples include Magorrian *et al.* (1995), Greenstreet *et al.* (1997), Kaiser *et al.* (1998), Sorensen *et al.* (1998) using the commercial RoxAnn system, Prager *et al.* (1995) using the commercial QTC-view system, and Bax *et al.* (1999), Siwabessy *et al.* (1999) and Kloser *et al.* (in press) using the RoxAnn-like technique of the energy features of the first and second acoustic bottom returns.

This paper describes methods used to classify the bottom type from echosounder records obtained during surveys of fisheries resources in the North-west continental shelf of Western Australia between late July and mid August 1995, 1997 and in the South-east continental shelf of Australia from July to mid December 1996. The approach used in this paper is similar to that used in the commercial RoxAnn system. In grouping bottom types however, multivariate analysis (PCA and CA) is adopted instead of the allocation system normally used in the RoxAnn system, called RoxAnn squares.

Reflection of acoustic wave from the bottom surface

Strictly speaking, acoustic waves incident on a boundary including seawater-seabed interface involve reflection and scattering at the boundary and transmission in the second medium. This process is determined primarily by the acoustic impedance ($Z = \rho c$) mismatch be-

tween media. In the simplest case of plane, normal incidence waves, the acoustic pressure reflection coefficient $\Re$ is defined as

$$\Re = \frac{p_i}{p_r} = \frac{Z_l - Z_u}{Z_l + Z_u} = \frac{\rho_l c_l - \rho_u c_u}{\rho_l c_l + \rho_u c_u} \quad (1)$$

where p_i and p_r are respectively the incident and reflected wave pressures, Z is the acoustic impedances, ρ is the density of the media, c is the sound speed, and u and l denote upper and lower media respectively. Although this formulation is based on and valid for a fluid-fluid interface, it is still applicable to the liquid-solid boundary and is the first, simplest approximation for the seawater-seabed interface. Kloser *et al* (in press) have listed a number of factors causing the reflected bottom signals to be different from the incident acoustic pulses; (1) Acoustic impedance mismatch of the seawater-seabed interface leading to surface scattering of the main pulse. (2) Acoustic parameters of the instrument. (3) Acoustic signal penetration into the seabed leading to volume scattering of the main pulse. (4) Directional reflections at the seawater-seabed interface because of seabed roughness. (5) Time delay of oblique returns because of spherical spreading with changing depth. (6) Scattering response from the sea surface, subsurface bubbles and vessel hull for the second acoustic bottom return. (7) Seabed slopes. (8) Seawater acoustic absorption. (9) Acoustic noise.

Neglecting acoustic absorption, the following relationship holds for normal incident echosounders (Brekhovskikh and Lysanov, 1982; Orlowski, 1984)

$$4\pi \int_0^{\theta_0} m_s(\theta,\omega)\sin 2\theta d\theta \le \frac{\langle p^2 \rangle}{p_0^2} \le \Re^2 \quad (2)$$

where $m_s(\theta,\omega)$ is the acoustic scattering coefficient, ω is the angular frequency, θ is the incident angle of the acoustic wave on the bottom, θ_0 is the half beamwidth, $\langle p^2 \rangle$ is the average square of the received pressure, p_0 is the received acoustic pressure from an ideal reflecting surface and $\Re$ is the acoustic pressure reflection coefficient of a smooth boundary.

For acoustic frequencies of interest in the present work, seabed surfaces are in general rough. It is therefore critical to consider the scale of the roughness with reference to the insonifying wavelength. $k\sigma$, where k is the acoustic wave number and σ is the rms deviation from the surface irregularities, is a common expression to scale the surface roughness. For $k\sigma << 1$, the normal incident backscattered return is coherent and the amplitude is determined by the reflection coefficient. For $k\sigma >> 1$, the magnitude of the coherent returns is much reduced. In addition, the distribution of the return signal from rough interfaces varies. Appropriate representations are Gaussian ($k\sigma << 1$) and Rayleigh ($k\sigma >> 1$). In general, signals of the acoustic bottom return comprise coherent and incoherent components (Brekhovskikh and Lysanov, 1982; Pace and Ceen, 1982; Orlowski, 1984) and the total average square of the returned acoustic pressure may be written as

$$\langle p^2 \rangle = p_c^2 + \sum_s p_{ic(s)}^2 \quad (3)$$

where p_c is the received acoustic pressure due to the coherent returns, i.e. the reflected components and p_{ic} is the received acoustic pressure due to incoherent returns, i.e. the "scattered" component of the return signals. A tail present in the received signals significantly longer than the transmitted ones may be attributed to the incoherent component (Pace and Ceen, 1982). Applying the concept depicted in equation (2) into equation (3), Orlowski (1984) defines the total acoustic pressure reflection coefficient as

$$\langle \Re^2 \rangle = \Re_c^2 + 4\pi \int_0^{\theta_0} m_s(\theta)\sin\theta d\theta \quad (4)$$

$$\langle \Re^2 \rangle = \Re_c^2 + \Re_{ic}^2 \quad (5)$$

Backscatter of the first and second acoustic bottom returns

Focusing on the second term of equations (4) and (5), Heald and Pace (1996) try to relate energy features from the first acoustic bottom returns and roughness parameters. Figure 1 shows the geometry of the first backscatter return from the seabed. For an incremental area dA_1 far from the axis, the first backscatter return becomes incoherent. Total backscatter return is subject to the sum of all backscatter return from all areas. Following Heald and Pace (1996), the received acoustic pressure may be expressed as

$$p_{bs1}^2 = p_0^2 \int_{\theta_a}^{\theta_b} \frac{m_s(\theta_1) G^2(\theta_1)}{(R_0')^4} dA_1 \quad (6)$$

where p_0 is the source pressure at a distance of 1 m from the source $dA_1 = 2\pi R_0'^2 \tan\theta_1 d\theta_1$, $R_0' = R_0\sqrt{(1+\tan^2\theta_1)}$, $G(\theta_1)$ is the transducer gain and $m_s(\theta_1)$ is the acoustic scattering coefficient; $m_s(\theta_1) \propto \Re^2$ and $m_s(\theta_1) \propto (\sigma/T)^2$ where σ is the rms height of the surface roughness and T is the correlation length of the surface roughness. Heald and Pace (1996) further suggest that the integration limit of the intensity envelope of the first backscatter return from the seabed is in the region where the insonified area is an annulus when $ct/2 > c\tau/2$, i.e. $\sqrt{c(t-\tau)/R_0} \le \theta_1 \le \sqrt{c\tau/R_0}$.

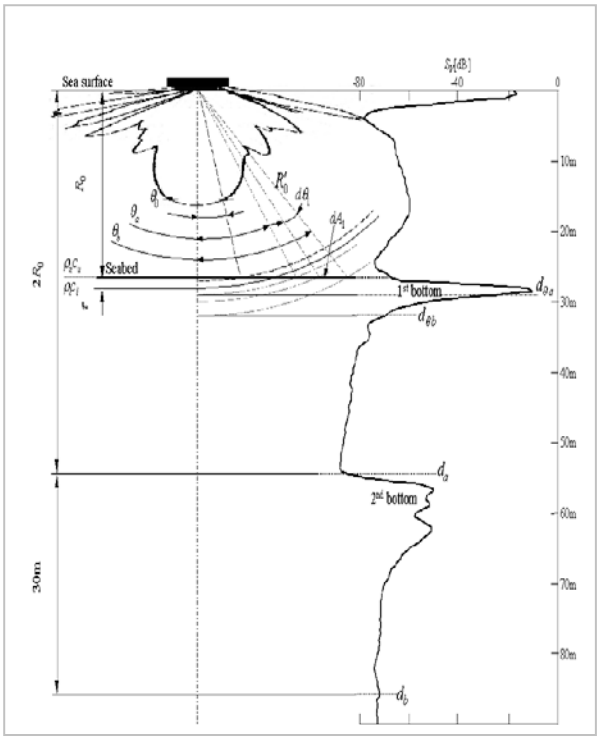

Orlowski (1984) used a monostatic geometry for treatments of the second backscatter return from the seabed whereas Heald and Pace (1996) used an on axis bistatic geometry. In the present work, the monostatic geometry is appropriate. Assuming the total acoustic pressure reflection coefficient is a best descriptor of the seabed hardness, the received acoustic pressure from the second backscatter return from the seabed must include coherent and incoherent components, i.e. the integration limit includes complete returned envelope. While the acoustic scattering coefficient $m_s(\theta_1)$ for the first acoustic bottom return is proportional to the square of the acoustic pressure reflection coefficient $\Re$, it is proportional to the 4th power of the acoustic pressure reflection coefficient $\Re$ for the second acoustic bottom return. For the second backscatter return from the seabed, the complete returned envelope is required and is obtained when $ct/2 \le c\tau/2$ and $ct/2 > c\tau/2$ (Heald and Pace, 1996).

Acoustic instrumentation and data analysis

A collection of acoustic bottom returns were conducted from the *RV Southern Surveyor* using a SIMRAD EK 500 echosounder operating three different frequencies, 12, 38 and 120 kHz. The 12 kHz transducer was a single beam unit whereas the 38 and 120 kHz transducers were split beam transducers. The echosounder was routinely calibrated with a 42 mm tungsten carbide calibration sphere. The volume reverberation signal S_v in logarithmic form implemented in the SIMRAD EK 500 echosounder is as follows

$$10\lg_{10}(s_v) = 10\lg_{10}(P_r) + 10\lg_{10}(r^2 10^{2\alpha r}) - 10\lg_{10}\left(\frac{P_t G_0^2 r_0^2 \lambda^2 c\tau\psi}{32\pi^2}\right) \quad (7)$$

Acoustic volume reverberation S_v data were continuously logged using *ECHO*, a software package developed by CSIRO Marine Research (Waring *et al.*, 1994; Kloser *et al.*, 1998).

Prior to analysis of the first and second acoustic bottom returns, recorded acoustic data were quality checked using the *ECHO* software. Faulty records mainly due to aeration usually caused by strong winds or sea-state or combination of the two were marked bad and excluded from further analysis. The RoxAnn E1 and E2 parameters were adopted. For analysis of acoustic bottom returns, the *ECHO* software provides several algorithms including a constant angular algorithm; see equation (6). This algorithm ensures that a constant angular sector of the incoherent field, irrespective of depth changes, is used for the integration of the first acoustic bottom backscatter. After several trials, the integration limit (θ_a and θ_b in equation (6) and Figure 1) after the falling edge of the acoustic pulse was between 27.4^o and 40^o for 12 kHz data and between 20^o and 31.6^o for 38 and 120 kHz data. Depths (after the bottom) corresponding to θ_a and θ_b varied with changing water depths and were estimated by

$$d_{\theta i} = R_0 / \cos\theta_i - R_0 + \tau \quad (8)$$

where R_0 is the bottom depth in meters and τ is the pulse length offset in meters. A constant depth algorithm was used for the integration of the complete envelope of the second acoustic bottom backscatter. The integration limit was defined as starting from twice the water depth (d_a) and ending at twice the water depth plus 30 m (d_b); see Figure 1. To reduce variability between pings in the backscatter returns and to standardise on a unit of length sampled, the integration was averaged over an along-track interval of 0.05 nmi. The integration of acoustic volume reverberation resulted in area backscatter coefficients that stem from fisheries acoustics for biomass assessments and are adopted as a relative measure of acoustic energy for scattering from the seabed

$$\bar{s}_A = 1852^2 4\pi \frac{\sum_{p=1}^{m} \delta d \sum_{d=d_a}^{d_b} s_{v(dp)}}{m} \quad (9)$$

where s_v is the linear volume backscattering coefficient. E1 and E2 parameters are obtained by taking the logarithm of the corresponding $\bar{s}_A$ values.

Seabed classification

To reduce the dimensionality of the acoustic data, Principal Component Analysis (PCA) was applied to the E1 and E2 data sets separately. PCA is in general a data transformation technique. It attempts to reduce the dimensionality of a data set formed by a large number of interrelated variables but retains sample variation (information) in the data as much as possible. The process includes an orthogonal transformation from the axes representing the original variables into a new set of axes called principal components (PCs). The new axes or the PCs are uncorrelated one to another and are ordered in such a way that the first few PCs hold as much of the total variation as possible from all the original variables. While PCs from the geometric point of view are orthogonal projections of all the original variables, PCs algebraically are linear combinations of the original variables. In addition, a linear combination of variables is an essential concept in multivariate analysis and is indeed fundamental to PCA.

Cluster Analysis (CA) was then performed to the first few PCs, hopefully only the first PC, of E1 and E2. This study used the iterative relocation technique (*k*-means method) for cluster analysis. This technique employs either the fixed, prespecified number of classes or seeds of initial centroids of known classes or combination of the two. The latter was adopted in this study. Firstly, a training set comprising distinct types of the seabed based on underwater photographs (for North-west shelf (NWS) region) and reference sites (for South-east shelf (SEF) region) was set up. Results from the training set then became the seeds of the initial centroids. Using these seeds of initial centroids, the iterative relocation technique was eventually performed on the rest of the data.

Results

E1 results were obtained by implementing a constant angular algorithm in an attempt to ensure that the proportion of the tail sector being integrated is independent of depth (Figure 2(a)). Figure 2(a) is a representative example of a scatter plot of E1 parameter versus depth for 12 kHz data from the SEF data sets. In Figure 2(b), a scatterplot of E2 parameter against depth at the same for the same data sets. Again, E2 is independent of depth.

Results from PCA applied to the E1 and E2 parameters showed that only the first PC of E1 and E2 separately held most of the variation of the original E1 and E2 separately. It turns out that the first PC of the E1 and E2 parameters are simply the average of the original E1 and E2 respectively. The first PC of E1 and E2 accounted for more than 70% of the total variation of the original E1 and E2 respectively. This indicates a quite high correlation between E1 from the three frequencies and between E2 from the three frequencies as well.

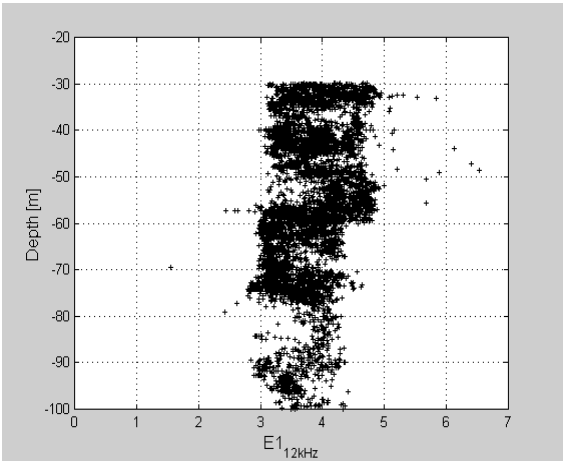

(a)

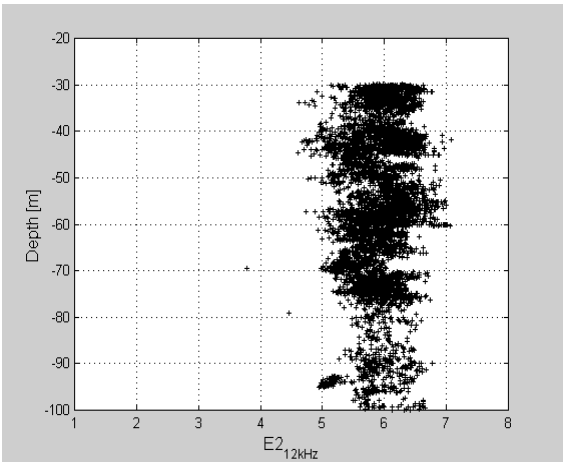

(b)

Figure 2. Scatterplot of (a) E1 versus Depth and (b) E2 versus Depth at 12 kHz from NWS data set.

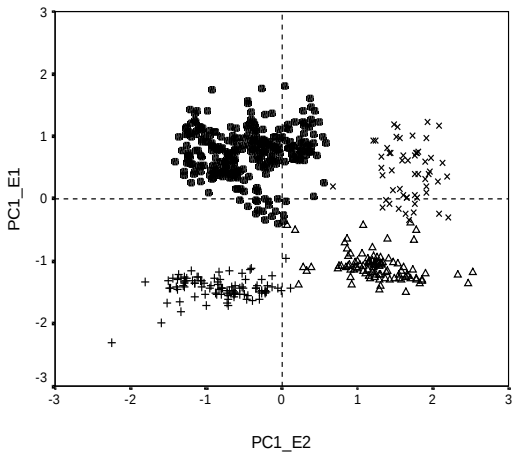

Figure 3. Scatterplot of PC1 of E1 vs PC1 of E2. × = Hard-Rough; • = Soft-Rough; + = Soft-Smooth; Δ=

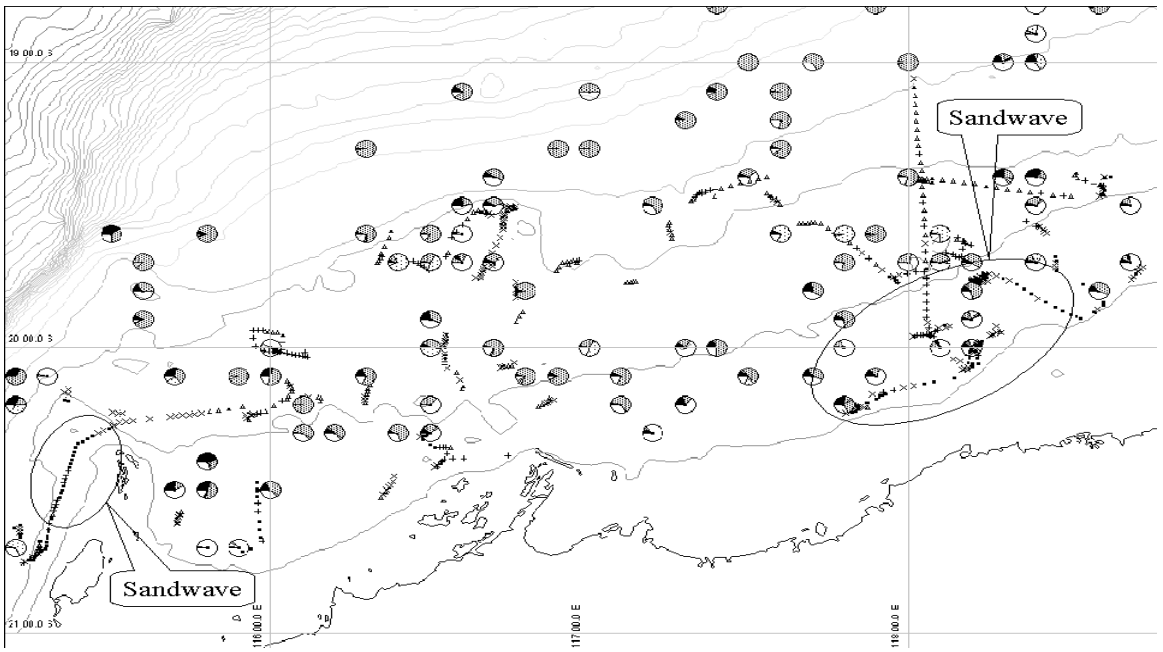

(a) NWS region

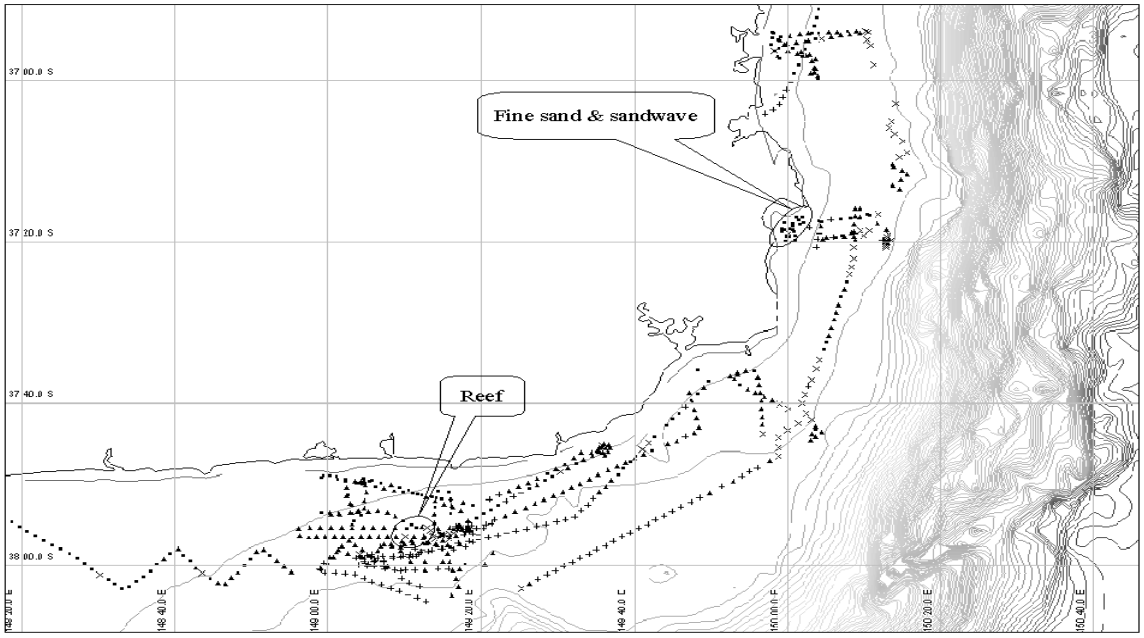

(b) SEF region

Figure 4. Along-track segmentation of seabed types. For the along-track segmentation, × = Hard-Rough; • = Soft-Rough; + = Soft-Smooth; Δ= Hard-Smooth. For pie charts, □ = Hard-Rough; ⊡ = Soft-Rough; ▨ = Soft-Smooth; ■ = Hard-Smooth.

In their study of the assemblage of benthic habitats in the NWS region based on the underwater photographs, Sainsbury *et al.* (in prep.) suggested a classification involving 5 different benthic habitats. In the present work, two of the benthic habitats were not distinguishable acoustically. The acoustics results presented here support 4 distinct seabed types, based on the underwater photographs taken in the NWS region and on reference sites in the SEF region. Figure 3 shows a representative example of the training set comprising four distinct seabed types in the SEF region. It is evident that the four classes in Figure 3 are well separated. Segmentation of bottom types along the vessel's track is shown in Figure 4(a) for the NWS region and Figure 4(b) for the SEF region. For the NWS region, benthic

habitats from Sainsbury *et al.* (in prep.) are included in Figure 4(a).

Conclusions

The method that combines the multiple bottom echo techniques from normal incident echosounder and multivariate analysis can be used for seabed classification. There is general agreement between derived seabed types and available supportive information. Distances over which variations of along-track bottom types occurred were shorter in the NWS study area than in the SEF study area. This indicates that the local variations are greater in the NWS study area than in the SEF study area. This might be related to the fact that the NWS study area is located in the tropics whereas the SEF study area is in the temperate and higher latitude region. A high diversity and a moderate abundance of resources are characteristic of the tropical region. The temperate and higher latitude region is on the other hand characterised by a lower diversity and a higher abundance of resources. A higher local variation of the bottom type in the NWS study area might be an indication of a higher diversity of resources which is expected to occur in the tropics.

References

Bax, N.J., Kloser, R.J., Williams, A., Gowlett-Holmes, K. and Ryan, T., 1999, "Seafloor habitat definition for spatial management in fisheries: a case study on the continental shelf of southeast Australia using acoustic and biotic assemblages." *Oceanologica Acta* 22(6): 705-719.

Brekhovskikh, L.M. and Lysanov, Yu.P., 1982, *Fundamentals of Ocean Acoustics* 2nd Ed. Springer Series on Wave Phenomena. Springer-Verlag, Berlin Heidelberg, Fed. Rep. of Germany: 270pp.

Chivers, R.C., Emerson, N. and Burns, D.R., 1990, "New acoustic processing for underway surveying." *Hydro. J.* 56: 9-17.

Greenstreet, S.P.R., Tuck, I.D., Grewar, G.N., Armstrong, E., Reid, D.G. and Wright, P.J., 1997. "An assessment of the acoustic survey technique, RoxAnn, as a means of mapping seabed habitat." *ICES J. Mar. Sci.* 54: 939-959.

Heald, G.J. and Pace, N.G., 1996, "An analysis of the 1st and 2nd backscatter for seabed classification." *Proc. 3rd European Conference on Underwater Acoustics*, 24-28 June 1996 vol. II: 649-654.

Kaiser, M.J., Armstrong, P.J., Dare, P.J. and Flatt, R.P., 1998, "Benthic communities associated with a heavily fished scallop ground in the English Channel." *J. Mar. Biol.* 78(4): 1045-1059.

Kloser, R.J., Sakov, P.V., Waring, J.R., Ryan, T.E. and Gordon, S.R., 1998, "Development of software for use in multi-frequency acoustic biomass assessments and ecological studies." CSIRO Report to FRDC project T93/237: 74pp.

Kloser, R.J., Bax, N.J., Ryan, T., Williams, A. and Baker, B.A., in press, "Remote sensing of seabed types in the Australian South East Fishery – development and application of normal incident acoustic techniques and associated "ground truthing"." *Mar. Freshwater Res.* special volume.

Magorrian, B.H., Service, M. and Clarke W., 1995, "An acoustic bottom classification survey of Strangford Lough, Northern Ireland." *J. Mar. Biol. Ass. UK.* 75: 987-992.

Orlowski, A., 1984. "Application of multiple echoes energy measurements for evaluation of sea bottom type." Oceanologia 19: 61-78.

Pace, N.G. and Ceen, R.V., 1982, "Seabed classification using the backscattering of normally incident broadband acoustic pulses." *Hydro. J.* 26: 9-16.

Prager, B.T., Caughey, D.A. and Poeckert, R.H., 1995. "Bottom classification: operational results from QTC view." *OCEANS '95 - Challenges of our changing global environment conference*, October 1995, San Diego, California, USA.

Sainsbury, K.J., He, X., Althaus, F., Stanley, C., Campbell, R. and Woolley, K., in prep., "Benthic habitat types and their associations on the Northwest Shelf of Australia." CSIRO Marine Research, Hobart, Australia.

Siwabessy, P.J.W., Penrose, J.D., Kloser, R.J. and Fox, D.R., 1999, "Seabed habitat classification." *Proc. International Conference on High Resolution Surveys in Shallow Waters* DSTO, 18-20 October 1999, Sydney, Australia.

Sorensen, P.S., Madsen, K.N., Nielsen, A.A., Schultz, N., Conradsen, K., and Oskarsson, O., 1998, "Mapping of the benthic communities common mussel and neptune grass by use of hydroacoustic measurements." *Proc. 3rd European Marine Science and Technology Conference*, 26 May 1998, Lisbon, Portugal.

Waring, J.R., Kloser, R.J. and Pauly, T., 1994, "ECHO -Managing fisheries acoustic data." *Proc. International Conference on Underwater Acoustics* University of New South Wales, 5-7 December. 1994, Sydney, Australia: 22-24.

ACOUSTICS - putting the science and technology to work

Conference of the Australian Acoustical Society
Joondalup Resort, Western Australia, 15-17 November 2000

Session AC-7 Noise Control

Virtual Sensors In Active Noise Control

Colin D Kestell, Colin H. Hansen and Ben S. Cazzolato

Department of Mechanical Engineering, University of Adelaide SA 5005, Australia

Abstract

Traditional active noise control systems achieve the greatest noise reduction at the locations of the error sensor(s). In many cases it is desirable to be able to achieve the maximum noise reduction remote from an error sensor. One way of doing this is to measure the transfer function between the desired location of maximum reduction and the error sensor and incorporate it in the control algorithm. The disadvantage of this method is that it is not robust to changes in the acoustic environment. Another method relies on using two or more microphones to estimate the sound level at a remote location using forward prediction. This method results in a lower performance but it can be adapted to changes in the acoustic environment as well as to changes in the location of the desired pressure minimum. This paper will report on a study that compares the relative merits of various forward prediction method in various situations. These commence with a free field environment (to introduce the concept) and then progress to a more practical application of an aircraft cabin. Single and multiple control sources will be considered as will sound pressure sensing and energy density sensing.

Introduction

Active noise control in modally dense and highly damped enclosures can result in small zones of attenuation that are centralised around the error sensors. In fact, an observer located close to a single acoustic pressure error sensor may not perceive any improvement in noise reduction as a result of active noise control, even though the error sensor may indicate that a significant reduction has been achieved. Consequently, research has recently been focused on finding alternative cost functions that results in a broader region of control that is sufficiently large to envelope the observer. Energy density is known to be more spatially uniform than squared acoustic pressure and can result in larger regions of attenuation when it is used as an active noise control cost function (Sommerfeldt and Parkins (1994)). However, for a multi-channel control system, the maximum attenuation in pressure is still likely to occur at the sensor location and the size of the zone of local control is inversely proportional to frequency (Cazzolato (1999)). The volume of the control region also tends to increase at the expense of reduced attenuation. An alternative to increasing the size of the control zone is to minimise the cost function at the observer rather than at the error sensor location by "virtual sensing", a concept first introduced by Garcia-Bonito et al. (1996). Their method was based on measuring the acoustic pressure transfer function between a permanently placed remote microphone and a microphone temporarily located at the observer location. With the temporary microphone subsequently removed, the signal from the permanent microphone was modified with the transfer function to create a *"virtual microphone"* at the observer location. However, any significant observer movement or environmental change within the vicinity of the sensors alter the transfer function and result in an error in the estimate of the acoustic pressure at the observer location. Kestell et al. (2000a,b) introduced *"forward difference prediction virtual sensors"* which use multiple sensors to estimate a trend in the acoustic field and predict (via extrapolation) the cost function at the observer location. They have demonstrated various strategies of error sensing that not only shift the zone of attenuated noise towards an observer but combine the benefits of "virtual sensing" and energy density minimisation. This paper shows a summary of the theory, introduces the concept with an idealised free field example and shows how the virtual sensors perform in an aircraft cabin.

Theory

With reference to figure 1, four *"forward difference prediction virtual sensors"* algorithms are summarised as follows:

1. Two microphone, first-order virtual micro-phone:

$$p_v = \frac{(p_2 - p_1)}{2h}x + p_2$$

2. Three microphone, second-order virtual microphone:

$$p_x = \frac{x(x+h)}{2h^2}p_1 + \frac{x(x+2h)}{h^2}p_2 + \frac{(x+2h)(x+h)}{2h^2}p_3$$

3. Two microphone, first-order virtual energy density sen-

sor:

$$\bar{E}_{D_x} = \frac{1}{4\rho c^2}\left[\left(1+\frac{x}{2h}\right)^2 p_2^2 - \frac{x}{h}\left(1+\frac{x}{2h}\right)p_1 p_2 + \left(\frac{x}{2h}\right)^2 p_1^2 - \frac{1}{(2hk)^2}\left(p_2^2 - 2p_1 p_2 + p_1^2\right)\right]$$

4. Three microphone second-order virtual energy density sensor

$$\bar{E}_{D_x} = \frac{1}{4\rho c^2}\left[\left(\frac{x(x+h)}{2h^2}p_1 + \frac{x(x+2h)}{h^2}p_2 + \frac{(x+2h)(x+h)}{2h^2}p_3\right)^2 - \frac{1}{k^2}\left(\frac{2x+h}{2h^2}p_1 - \frac{2x+2h}{h^2}p_2 + \frac{2x+3h}{2h^2}p_3\right)\right]$$

Where x is the distance between the observer and the nearest sensor, h (25mm) is the transducer separation distance, p_1, p_2 and p_3 are the measured pressures, p_x is the pressure at the observer location and E_{Dx} is the time averaged energy density at the observer location.

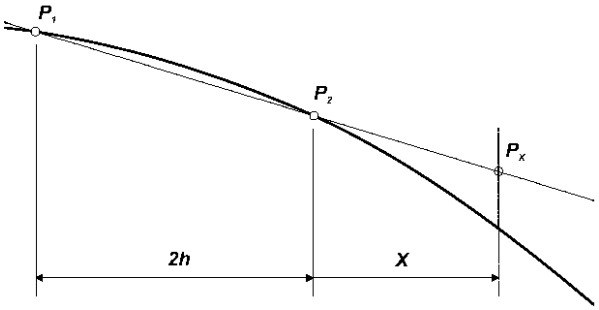

(a) First-order

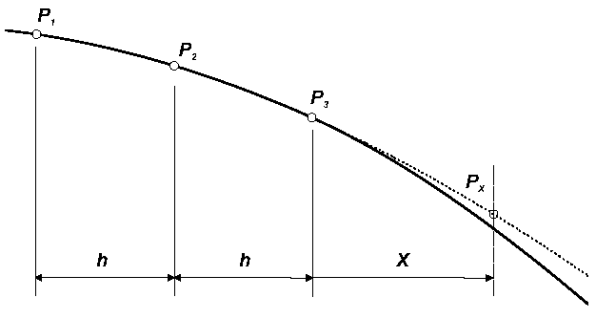

(b) Second order

Figure 1: Forward difference extrapolation

Method

The zone of local control around a "virtual energy density sensor" and a "virtual microphone" is compared with that achieved when using an actual energy density sensor and a single microphone. To introduce the concept, the analysis commences with a free field approximation in an anechoic chamber (figure 2) and then progresses to the more practical application of an aircraft cabin (figure 3).

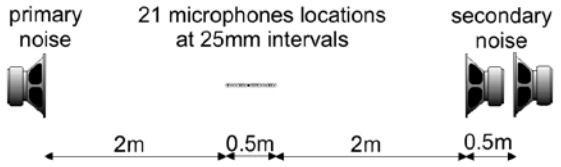

Figure 2: Schematic representation of the experimental configuration in an anechoic chamber.

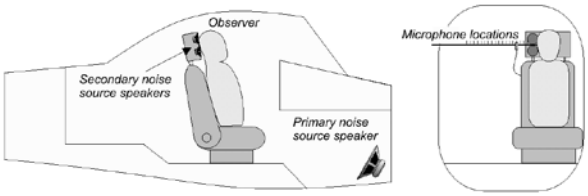

Figure 3: The speaker and microphone locations in the aircraft cabin.

In each example the primary noise was generated using a single acoustic source, the secondary (cancelling) noise was generated from either one or two control sources and the controlled sound field was analysed along a 0.5 m length at 25 mm increments. Minimising pressure at a single location only requires one control source, but Cazzolato (1999) showed that two control sources are required to effectively minimise energy density in one dimension. With two control sources, using a *first-order virtual energy density sensor* is identical to simply minimising energy density at the physical sensor location or acoustic pressure at two microphone locations (Kestell et al. (2000a,b)). This is because in a two sensor system the energy density estimate at the observer is a linear combination of the pressure and pressure gradient at the sensors. Therefore if these are zero at the sensors it follows that the estimated energy density will also be zero. Therefore, in the examples that follow, the use of a single control source is limited to observing the performance of a single microphone, a *first-order virtual microphone* and a *second-order virtual microphon*e. Two control sources are used to observe energy density minimisation directly at the sensors and at the observer location with a *second-order virtual energy density senso*r.

Results

Control in an anechoic chamber

Figure 4 shows the results that are obtained when controlling a 100 Hz monotone in an anechoic chamber. The results in figure 4(a) show the level of control achieved when using a conventional pressure squared

cost function, where the sensor is incre-mentally moved further from the observer location. The attenuation at the observer location is shown to reduces from 40 dB to 8 dB as the observer / sensor separation distance increases from *0h* to *4h* (100 mm).

In figure 4(b) the control results for a *first-order virtual microph*one are shown. Since the algorithm adapts to an increasing separation distance, the attenuation only reduces to 22 dB when observer / sensor separation distance increases to 100 mm, demonstrating a practical advantage over the conventional remotely placed single microphone (figure 1).

Figure 4(c) illustrates the performance of the theoretically more accurate *second-order virtual micro-phone* (refer to figure 1(b)), showing that it's accuracy is adversely affected by small spatial pressure variations that are primarily due to reflections from the walls of the chamber (figure 6). In this example the *second-order virtual microphone* offers no practical advantage when compared to a single remotely placed microphone.

Introducing a second control source allows the pressure to be independently controlled at two sensor locations and control of energy density either at the observer or the sensor location (Kestell et al. (2000a,b)). Energy density minimisation at the error sensor (or virtual first-order prediction at the observer location) is shown in figure 7(a).

Because of the second control source, this cost function produces a broader region of control (when compared to that obtained using a single error micro-phone and a single control source) and hence maintains an attenuation envelope around the observer location, until the sensors are moved to a separation distance of 100 mm (*4*h). At this observer/sensor separation distance the prediction inaccuracies result in a gain of 8 dB at the observer location.

In figure 7(b) the performance of the *second-order virtual energy density sensor* is shown. The second-order prediction of the energy density cost function at the observer location is more rugged in the presence of small spatial pressure variations and maintains the maximum attenuation at the observer location within a broad and practically sized zone of attenuation.

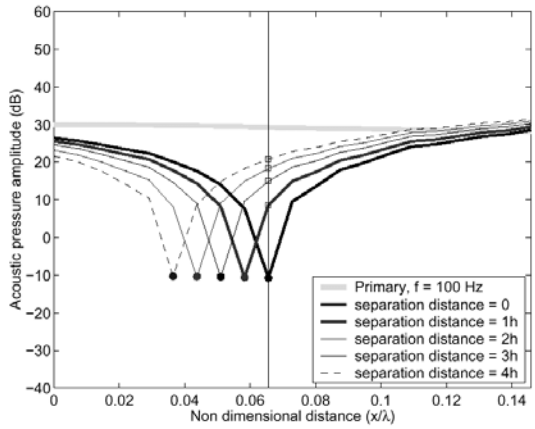

(a) Control via one microphone

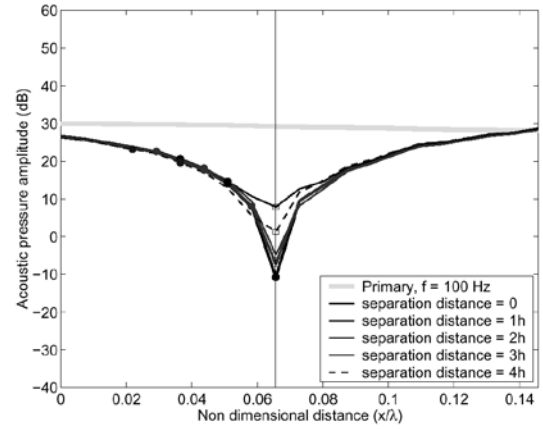

(b) A first-order virtual microphone

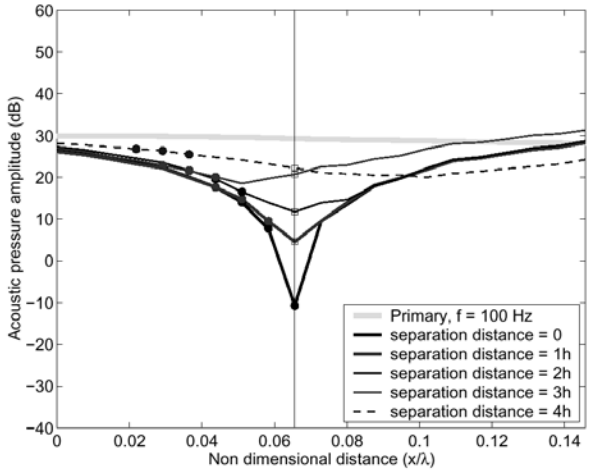

(c) A second-order virtual microphone

Figure 4: A 100 Hz primary sound source in an anechoic chamber controlled via one control source. The actual sensors are marked with a circle and the observer location by a vertical line.

Figure 5: Prediction errors in the absence of short wavelength spatial pressure variations.

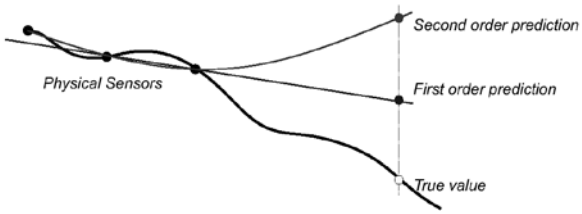

Figure 6: Prediction errors in the presence of short wavelength spatial pressure variations.

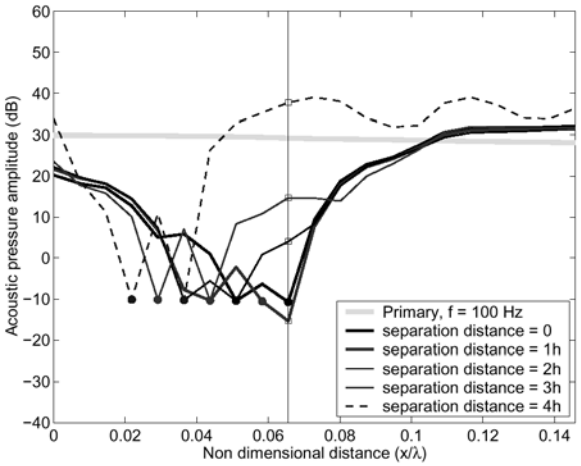

(a) Energy density control (and first-order virtual energy density control)

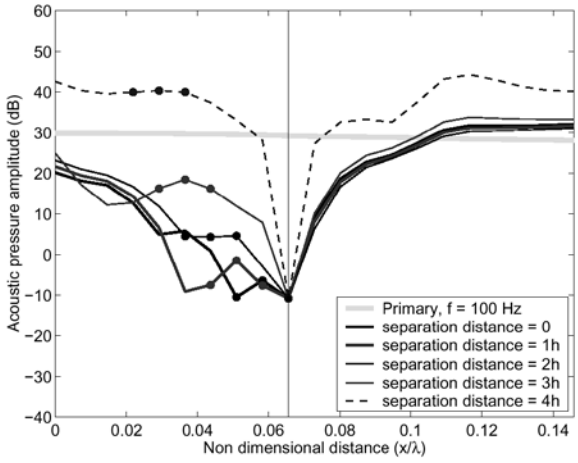

(b) Second-order virtual energy density control

Figure 7: A 100 Hz primary sound source in an anechoic chamber controlled via two control sources. The sensors are marked with a circle and the observer location by a vertical line.

An aircraft cabin

The results of actively controlling the primary noise between 50 Hz and 400 Hz with a single control source loudspeaker located in the head-rest of an aircraft cabin are shown in figure 8. Figure 8(a) shows how the uncontrolled noise levels at the observer location compare to the controlled noise levels using various error sensors, all located 100 mm from the observer.

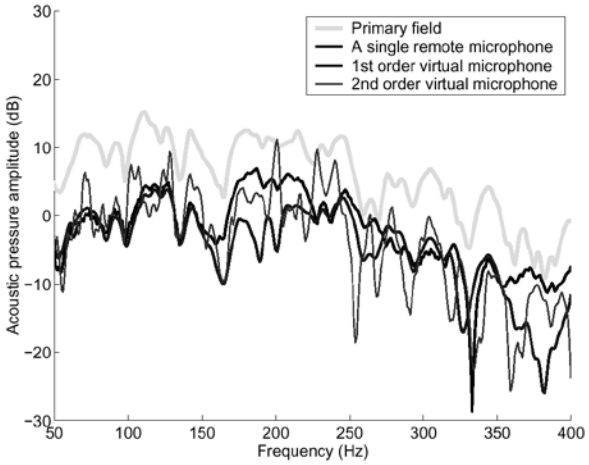

(a) The uncontrolled and controlled spectra for various error sensing strategies

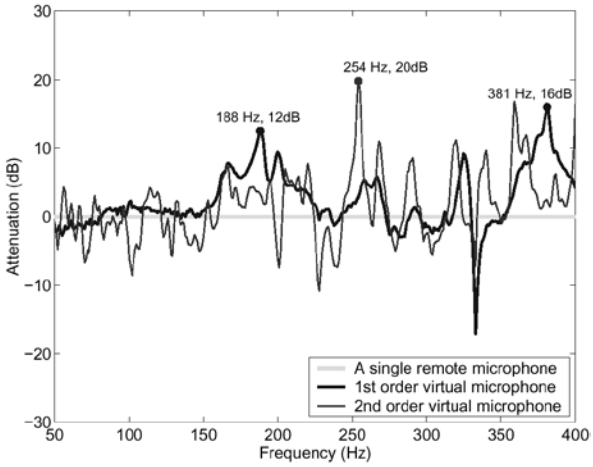

(b) The attenuation achieved with virtual microphones compared to a single microphone

Figure 8: ANC spectra at the observer location with one control source located in the observer's headrest. The sensors are located*4h* (100mm) from the observer's ear.

The *second-order virtual microphone* is shown to be extremely sensitive to short wavelength noise and produces an erratic control profile across the entire frequency range. For a clearer comparison, the noise attenuation at the observer location, when using the first and second-order virtual microphone error sensors, is compared directly to that obtained using a single microphone error sensor (the 0 dB reference) in figure 8(b). It is shown, that for this single control source ex-

ample, using a *first-order virtual microphone* results in an improved performance compared to that obtained using a remotely placed single microphone. Figure 9 shows the spatial variation of the uncontrolled primary noise and the controlled noise for each error sensor, at an example frequency selected from figure 8 (b), where using virtual microphones as error sensors improved the active noise control performance, compared to using a single micro-phone.

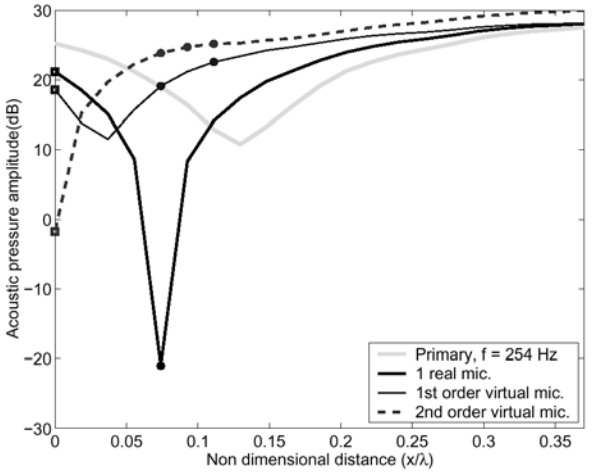

Figure 9: 254 Hz controlled using a single control source in the head-rest. The sensors are marked with a circle and the observer location is at the far left hand side of each graph.

In the 254 Hz example it can be seen that when the error sensor is a single microphone, the high level of noise attenuation achieved at the sensor does not extend to encompass the observer 100 mm away with only 5 dB of attenuation achieved at the observer location. At the same observer location, the *second-order virtual microphone* results in 8 dB of attenuation and the *first-order virtual microphone* results in 20 dB.

Figure 10 illustrates the results of actively controlling the primary noise between 50 Hz and 400 Hz with two control sources located in the observer's head-rest. The spectra corresponding to the active noise control when using a single microphone, a *first-order virtual microphone* and a *second-order virtual microphone* are compared to the uncontrolled noise spectrum at the observer location, with sensors separated from the observer by 100 mm. Figure 10(a) shows that all of the control strategies considered here reduced the noise at the observer location across the entire frequency range of interest. In figure 10(b) the error sensing performance of both types of virtual energy density sensor are directly compared to the use of a single microphone (with one control source) in which control via the single microphone is the 0 dB reference.

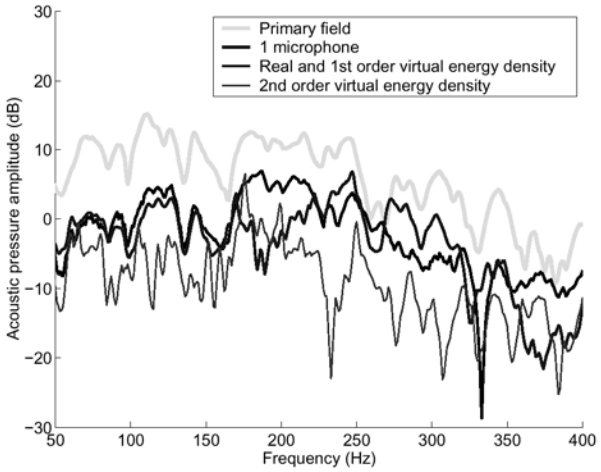

(a) The uncontrolled and controlled spectrum for various error sensing strategies

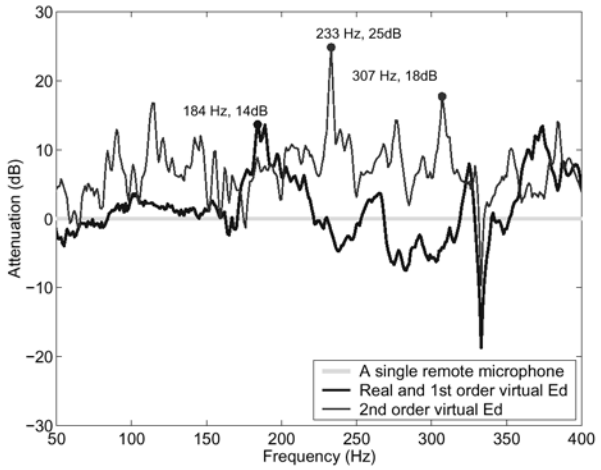

(b) The attenuation achieved with virtual microphones compared to a single microphone

Figure 10: ANC spectrums at the observer location with two control sources both located in the observer's headrest. The physical sensors are located *4h* (100mm) from the observer's ear.

Figure 11 shows that the zone of control increases with a *first-order virtual energy density sensor* (compared to using a *first-order virtual microphon*e), but as a result of the second control source (and the independent control of pressure at two locations) and not the cost function. Figure 10(b) and figure 8(b) show that the *second-order virtual energy density sensor* shows a superior error sensing performance when compared to using all of the other error sensing methods. Figure 11 shows how the control zones compare in the spatial domain around the observer location at an example frequency of 233 Hz chosen from figure 10 (b). It is shown that the *second-order virtual energy density error sensor* not only results in the highest noise attenuation at the observer location, but produces a broad zone (compared to a single microphone) of attenuated noise centered around the observer location.

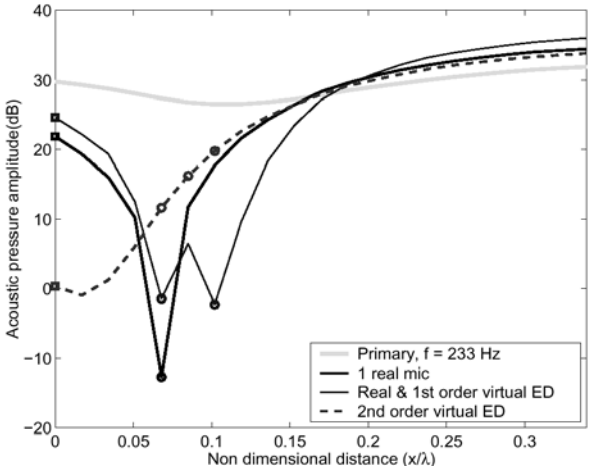

Figure 11: 233 Hz controlled using two control sources in the headrest. The sensors are marked with a circle and the observer location is at the far left hand side of each graph.

Conclusions

In the particular examples discussed in this paper, it has been demonstrated that the *first-order virtual microphone* (based on forward difference prediction) outperforms a conventional microphone (in terms of noise reduction at the observer location) for the same observer / sensor location separation distance. While the highest attenuation at the observer location should theoretically be achieved by using a *second-order virtual microphon*e, the attenuation actually achieved was found to be very sensitive to short wavelength spatial pressure variations and seldom offered an advantage in practice to the use of a conventional microphone. It has also been shown that first-order prediction methods for energy density estimation at a remote location (the observer) offer no advantage to controlling energy density directly at the remote sensor. In terms of offering both a high level of attenuation and a broad control zone around the location of the observer, the *second-order virtual energy density* sensor produced the best results.

References

1. B.S. Cazzolato. *Sensing systems for active control of sound transmission into cavitie*s. Ph.D. Thesis, The University of Adelaide, Adelaide, South Australia, April 1999.

2. J. Garcia-Bonito, S.J. Elliott, and C.C. Boucher. A virtual microphone arrangement in a practical active headrest. In *Proceedings of Inter-noise 9*6, pages 1115–1120, 1996.

3. C.D. Kestell, B.S. Cazzolato, and C.H. Hansen. Active noise control in a free field with virtual sensors. Accepted for publication june 2000, 2000a.

4. C.D. Kestell, B.S. Cazzolato, and C.H. Hansen. Active noise control with virtual sensors in a long narrow duct. *Journal of the Acoustical Society of Americ*a, 5(2):63–76, june 2000b.

5. S.D. Sommerfeldt and J. Parkins. Active control of energy density in three dimensional enclosures. *Journal of the Acoustical Society of Americ*a, 95 (5):2989, 1994.

Acoustic Performance Variations in Attenuators And Acoustic Louvres

Richard Devereux - B. Eng (Mech) M. AIRAH

Acran – Air Conditioning and Acoustics

Abstract

During the past two years, extensive testing has been undertaken in our Acoustic Testing Laboratory including comparative testing of attenuators and acoustic louvres typically used in the Heating, Ventilation and Air Conditioning (HVAC) industry. Comparative testing utilises the same basic attenuator or louvre while varying only the internal composition. The results have been enlightening and have created awareness among many HVAC practitioners of potential noise control problems when faithfully applying questionable and outdated acoustical test data.

Australian Standard 1277-1983

Testing was undertaken to AS 1277-1983 where the grade of acoustic infill was the only variable. Extensive testing was also completed using polyester film facings. Insertion Loss variations up to 25 dB have been produced with relatively insignificant changes to material combinations.

Australian Standard 1191-1985

Acoustic louvres have been tested in the laboratory to provide transmission loss data. Substantial test data variations have been demonstrated with only minor material combination changes. The paper will outline findings resulting from the testing program for both attenuators and acoustic louvres. This paper also draws some conclusions from our current product testing program.

To date the testing program has indicated that acoustic manufacturers test data may be outdated, quality control over raw materials selection is required and correct selection of the combination of construction materials is essential. Additionally, quality control is essential during all stages of manufacture of acoustic products for industry.

During the past two years, extensive testing has been undertaken in our Acoustic Testing Laboratory of attenuators and acoustic louvres typically used in the Heating, Ventilation and Air Conditioning (HVAC) industry. While this information has been used by the HVAC industry for some time, the findings are equally important for all members of the acoustics and noise control industry. The information contained in this paper is important for any company or individual involved in work pertaining to the reduction of noise levels in most environments.

During the past two years thousands of hours have been expended testing and modifying acoustic products in an endeavor to provide increased acoustic performance per unit size.

Today we would like to present some of the variations found during testing in our Acoustic Testing Laboratory.

All the results presented in this paper are comparative tests using the same basic attenuator or louvre and varying only the internal composition of the products.

The results have been enlightening and have created awareness among many noise control practitioners of potential noise control problems when faithfully applying questionable and outdated acoustical test data.

While we expected variations in the performance of certain products, it was a surprise to see the magnitude of variation between what we thought were extremely similar configurations.

While our raw material manufacturers e.g. rockwool /fibre glass suppliers continue to refine and streamline their processes they can make changes to their products that may not be publicised. These changes may not be visually apparent, however they may have some rather interesting effects on finished products.

Our testing has shown that although the physical construction of a product may not have changed, the performance may vary considerably.

Acoustic Testing Laboratory

The facility has been designed and constructed in accordance with the requirements detailed in the relevant Australian Standards.

The laboratory can be used to conduct tests in accordance with the following standards:

- Sound Power to AS1217-1985 Part 2
- Transmission Loss to AS1191-1985
- Sound Transmission Class (STC) to AS1276-1979
- Insertion Loss to AS1277-1983
- Absorption Co-efficients to AS1045-1988

The laboratory has been used to provide acoustic data for products including glazing, doors, masonry and other wall systems, road side traffic barriers and air conditioning and mechanical equipment.

The facility is complete with a fan forced air circulation system where we can measure not only noise levels but air pressure drop and noise levels with air flow. i.e. dynamic testing and regenerated noise level from air velocity.

Attenuators

The testing facility allows the testing of multiple configurations of attenuators with a minimal of time between tests. Some 400 individual tests have been undertaken in the last 12 months providing accurate insertion loss data for a large quantity of product.

Figure 1 is a diagram of the setup used to test the attenuators. The test involves using the speaker box to create a "white" noise. The noise level is measured in the receiving room with the test specimen in place. The test is then repeated, however the test specimen is removed and replaced with a section of un-lined ductwork. The difference between these levels is known as the Insertion Loss.

The particular sample we will discuss in this paper was a typical HVAC attenuator. The sample attenuator was 1200mm in length and a face size of 600mm x 600mm. The attenuator had an open area of 33%.

Figure 2 illustrates the results of some testing. These results are compiled from data measured in the 1/3 Octave bands.

It can be seen from the results that there is a wide variation in performance. Typically, differences in Insertion Loss of 5dB at 125 Hz, 13dB at 250 Hz and 20dB at 4000 Hz were observed.

The plotted variations represented various acoustic infills, variation of percentage open area of perforated metal and minor construction modifications.

Testing of a broad range of attenuators incorporating polyester film was also undertaken with even wider variations. The use of polyester film to provide a seal between the acoustic infill and the air has become more common throughout our industry.

While it has always been know that the polyester films reduce the performance of an attenuator at certain frequencies, it was not widely recognised and publicised that the method of wrapping the attenuator has a significant acoustic effect.

Figure 3 shows very clearly the variation when different methods are employed to wrap the absorber in only one type of polyester film.

Acoustic Louvres

The testing laboratory also allows for the determination of Transmission Loss data for acoustic louvres, along with many other types of building partitions.

Figure 4 shows the room laboratory layout for testing acoustic louvres. The speaker is positioned in the Source Room and a set of measurements are recorded in both the Source and Receiving Rooms. The difference between the two rooms is calculated and then adjusted for other variables including reverberation times. The final data is measured in dB and is known as the louvre's Transmission Loss.

Figure 5 represents the summary of extensive testing undertaken with a 600mm deep acoustic louvre.

The sample size was 900mm in width and 2100mm in height. This size was chosen to give fair representation of the true noise reduction of a louvre.

Again the Transmission Loss (dB) at various frequencies varies substantially on the composition of the build.

It is clear that if the need arises the louvre can be selected to more closely match the duty. The plot clearly illustrates the variation and combinations between the acoustic absorber and the selected perforated finish.

At this point in our testing programme we have concluded that at least:

- Acoustic manufacturers test data may be outdated
- Quality control over the absorbers need to be increased
- Quality control is essential during all stages of manufacture

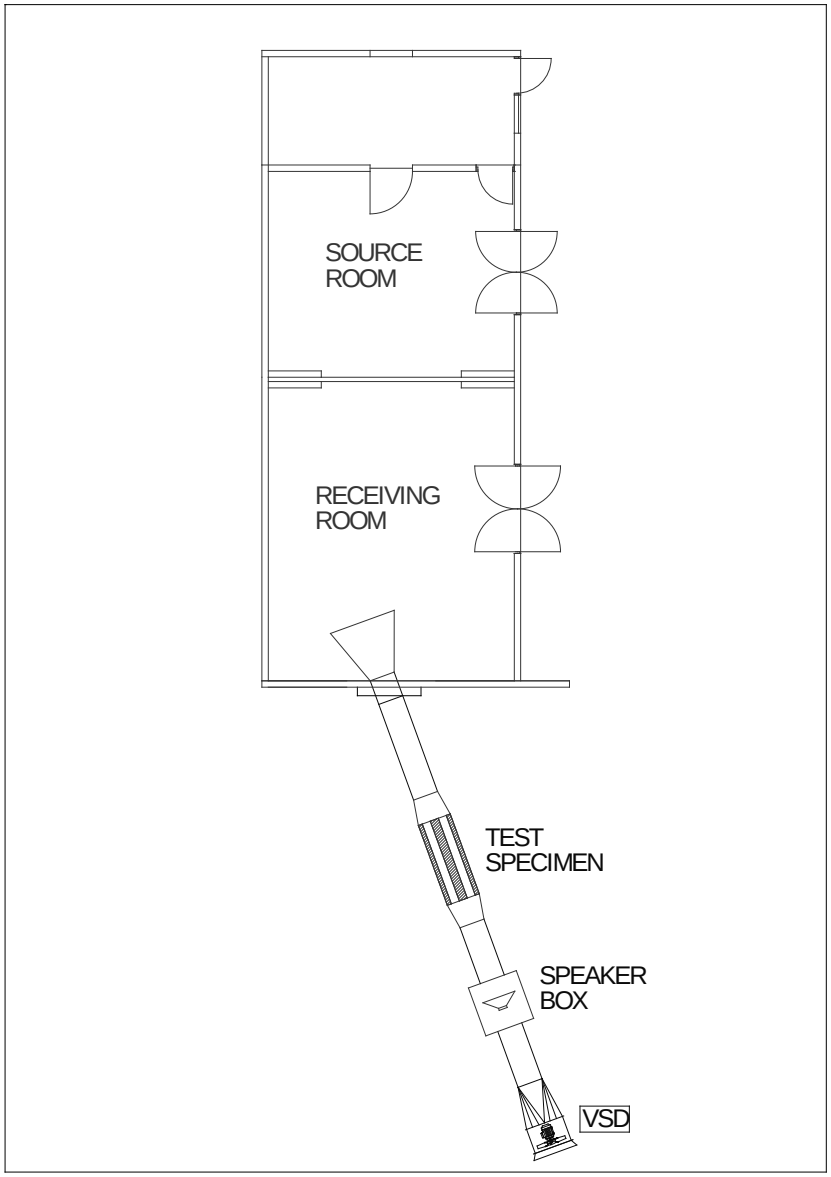

Figure 1

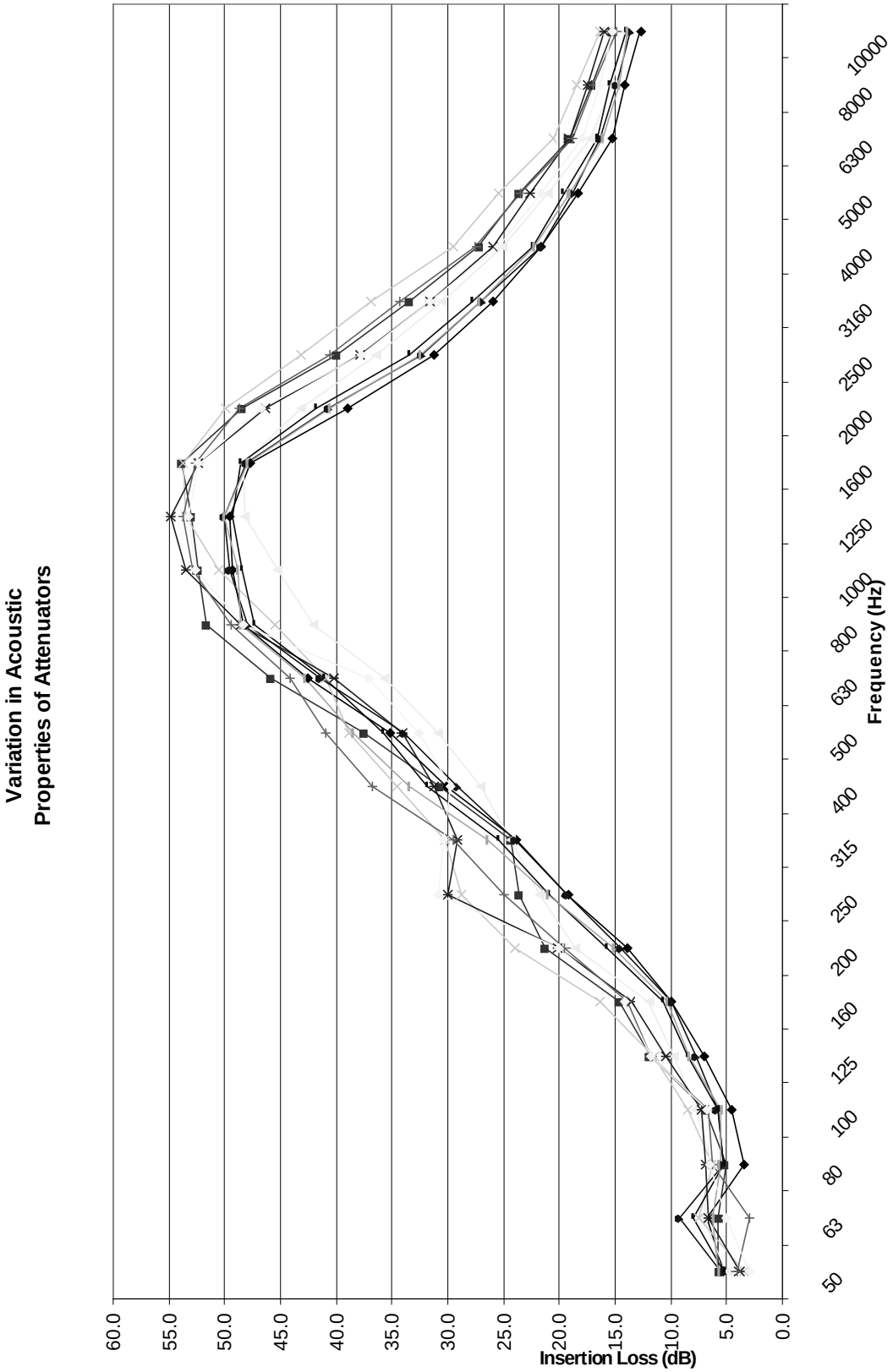
Variation in Acoustic Properties of Attenuators
Insertion Loss (dB)
60.0
55.0
50.0
45.0
40.0
35.0
30.0
25.0
20.0
15.0
10.0
5.0
0.0
Frequency (Hz)
50
63
80
100
125
160
200
250
315
400
500
630
800
1000
1250
1600
2000
2500
3160
4000
5000
6300
8000
10000

Figure 2

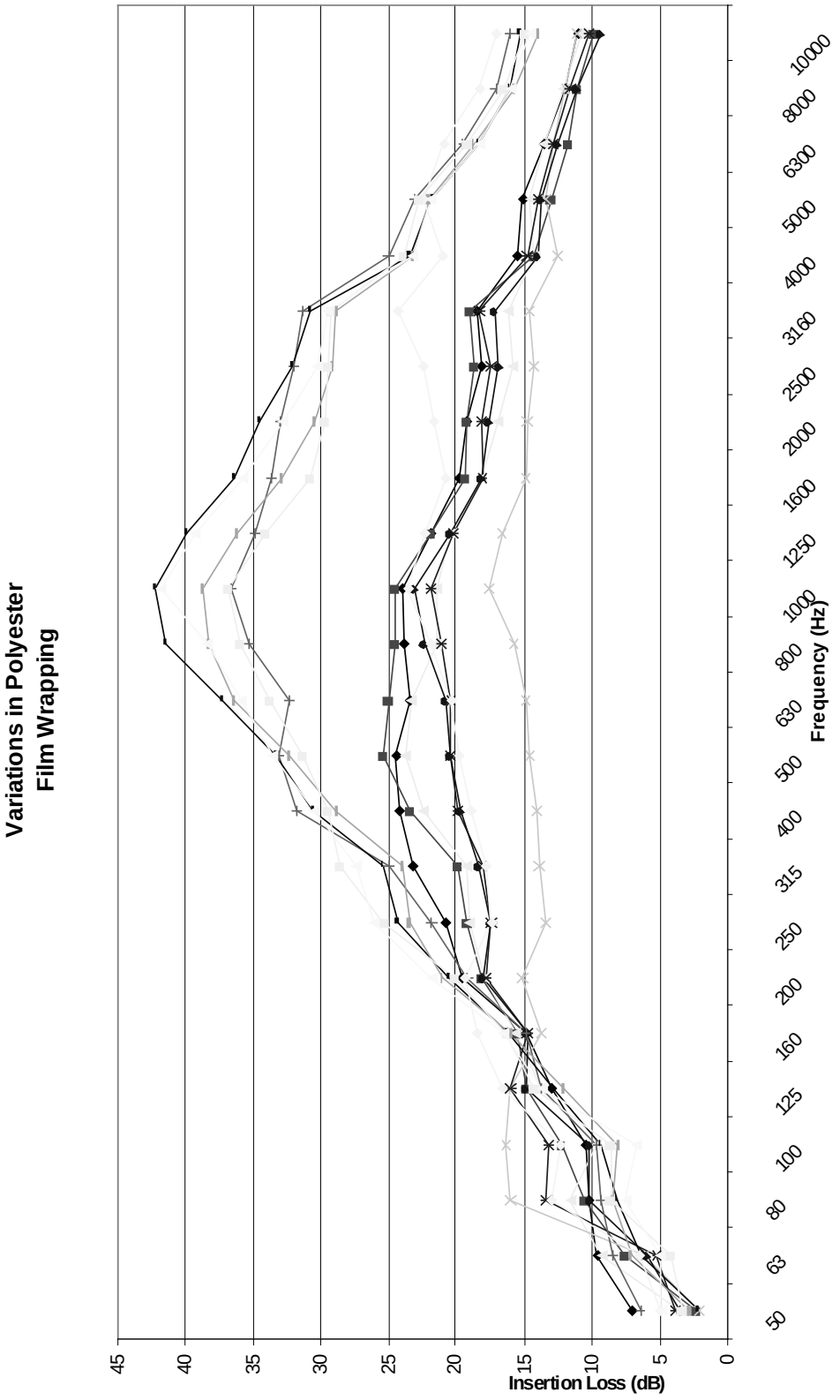
Variations in Polyester
Film Wrapping
Insertion Loss (dB)
45
40
35
30
25
20
15
10
5
0
Frequency (Hz)
50
63
80
100
125
160
200
250
315
400
500
630
800
1000
1250
1600
2000
2500
3160
4000
5000
6300
8000
10000

Figure 3

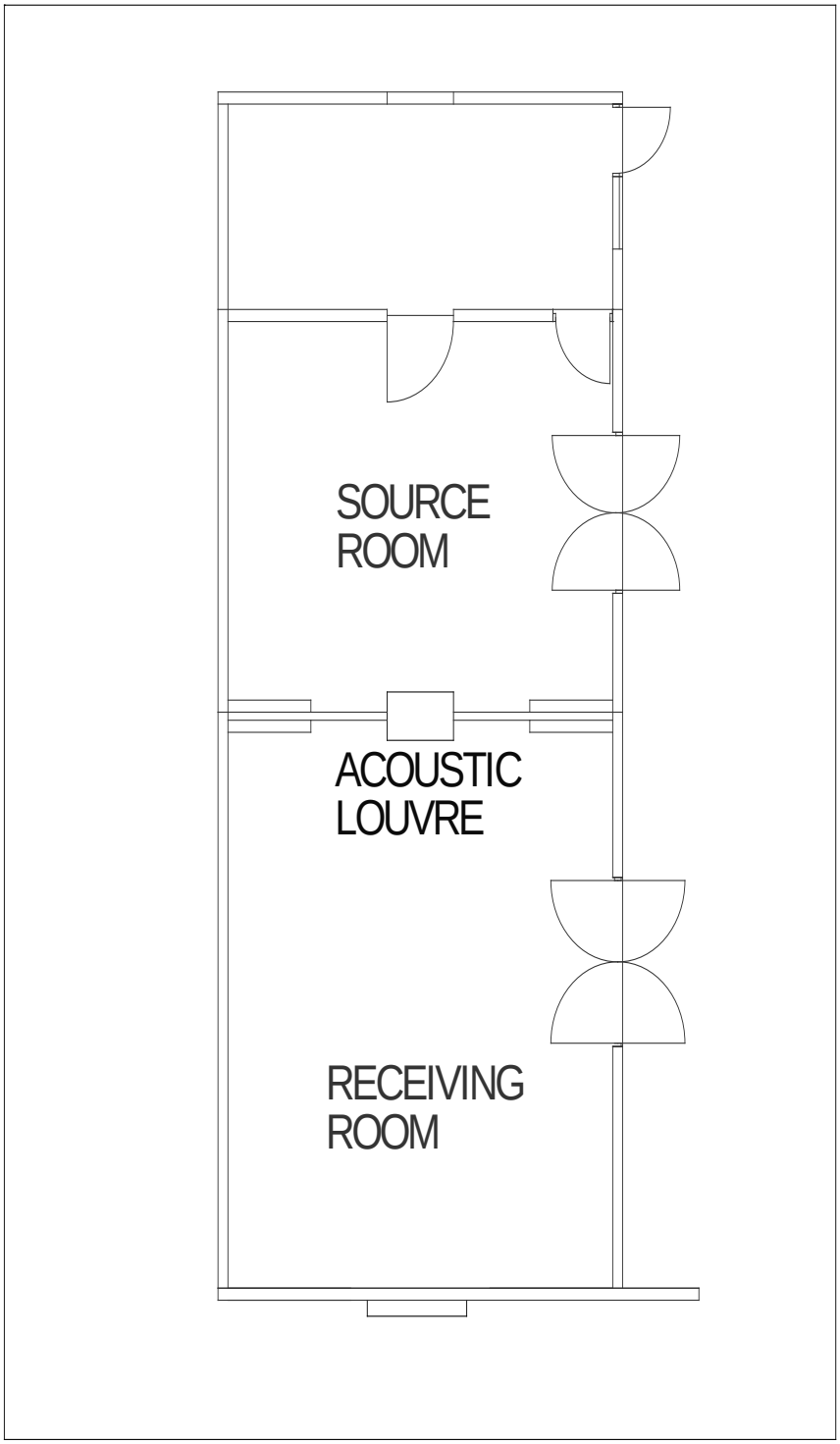

Figure 4

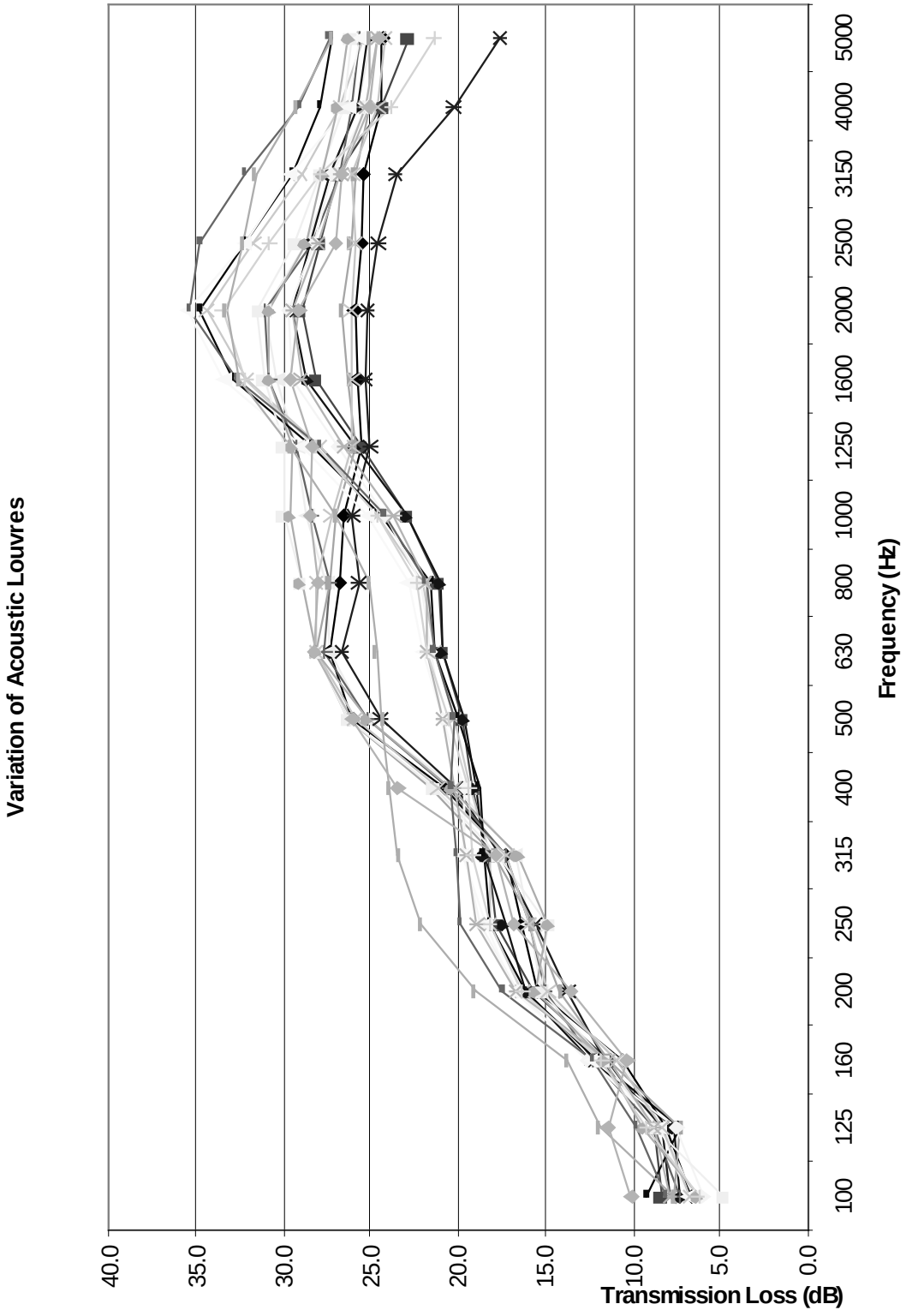
Variation of Acoustic Louvres
Transmission Loss (dB)
40.0
35.0
30.0
25.0
20.0
15.0
10.0
5.0
0.0
Frequency (Hz)
100
125
160
200
250
315
400
500
630
800
1000
1250
1600
2000
2500
3150
4000
5000

Figure 5

ACOUSTICS - putting the science and technology to work

Conference of the Australian Acoustical Society
Joondalup Resort, Western Australia, 15-17 November 2000

Session UW-7 Propagation And Geo-Acoustic Inversion 2

Applications of phase and group speed analysis

W.A. Kuperman[1], G.L. D'Spain[1] and Kevin D. Heaney[2]

[1]Marine Physical Laboratory/SIO and [2]Orincon

Abstract

The relationship between group and phase speed in an ocean waveguide is a robust descriptor of signal structure. Understanding this physics can be very useful. Some examples and applications are: 1) Different propagation paths have their own group-phase speed relation.; a pulse propagating long range has a single phone spectrogram from which range can be inferred. 2) The group speed dependence on phase speed is different in shallow water than in deep water; deep-water signals, which originated in shallow water, retain a shallow water "scar." These and related concepts are supported with experimental data.

Introduction

It is well known that quantitative and qualitative information about sound propagation in a waveguide can be obtained by studying the modal (or ray) group speed (or cycle distance) and phase speed (or launch angle). We can consider three manifestations of these quantities:

1) Total dispersion of a pulse;

2) focusing with respect to frequency of a fixed mode;

3) focusing of a group of modes at a fixed frequency.

The first case is simply the Ewing and Worzel suggestion [1] that one can obtain the range from the total dispersion of a pulse if the total span of group speeds is known from the environment. One can also perform source localization by considering a combination of cases 2 and 3. Furthermore, the application of these principles to range-dependent propagation paths is valid with appropriate modifications. Range-dependent environments can be thought of as a composite of range-independent environments. It then become obvious that it is the time of travel in each segment, or another words, the slowness, which must be summed over the total path.

In this paper we will discuss the basic principles underlying the importance of the relationship between phase and group speed. The principles are applicable to shallow and deep water propagation. We will also present analysis of experimental results for long-range deep-water propagation and long-range propagation between deep and shallow water. These results show that broadband sources can be localized at ranges of thousands of kilometers; Furthermore we show an example of explaining, what was thought to be, an extremely anomalous arrival structure by this simple analysis.

Airy phase

The physics of the second case is explained in the original work of Pekeris. As cited in Ref. [2], there is a detailed discussion of the Airy phase referring to waves associated with a stationary value of the group velocity. For an isospeed, lossless air-water, bottom-fluid waveguide, now commonly referred to as the Pekeris waveguide, Pekeris plotted dimensionless group speeds, versus a dimensionless waveguide as shown in Fig. 1. The Airy phase of each mode is a stationary

minimum; modal cutoff is to the left of the Airy phase and the group speed to the right of the cutoff ap-

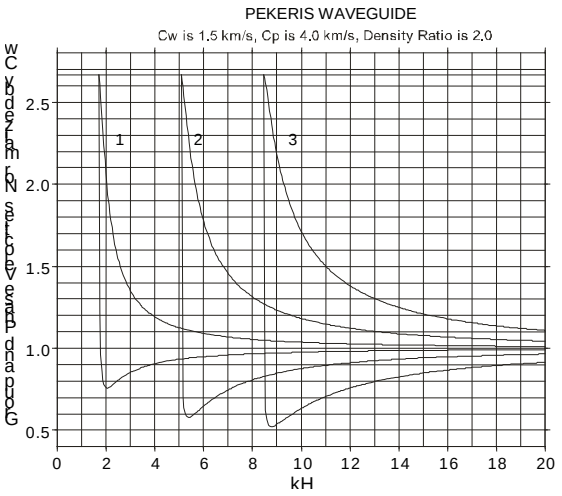

Figure 1. The lower and upper curves are normalized (to 1.5 km/s) phase and group speeds, respectively, for modes 1,2 and 3. The water depth of the waveguide is H and k= ω / c .

proaches the sound speed in the water column. A simple physical explanation of the higher amplitude of the Airy phase is that only in the region of the stationary points in the group velocity curves is there no intramo-

dal dispersion. Therefore, over a small frequency interval, all contributing frequency components for a specific mode arrive at the same time, a kind of frequency focusing. Each mode curve has a minimum group speed as a function of the waveguide parameter. For lower waveguide parameters, the group speed rises rapidly to the bottom sound speed indicating modal cutoff. In this region to the left of the Airy phase, modal cutoff combined with finite bottom attenuation results in the mode rapidly decaying with range. Therefore, a broadband mode arrival will have a duration determined by difference of the group speed at the Airy phase and the water column sound speed divided by the propagation range.

Nondispersive mode group

The physics of the third case is contained in the group speed dependence on phase speed. More recent efforts [3-6] characterize the dependence of group speed on phase speed through a waveguide "invariant" denoted β. Though completely related to what follows, the full invariant formalism discussed in these papers is not necessary to explain the phenomena under in this paper. Also, a partial motivation of this study is the concept of a weakly divergent bundle of rays (WDBR) [7] phase speeds intervals in which the modes have the same group speed. This is equivalent to the existence of launch angle intervals over which the cycle distances are constant. It is different than the Airy phase where a stationary region of group speed versus frequency exists for a single mode. For the WDBR case, there exists convergence zone ray bundles that do not diverge with range. Experimental confirmation was obtained by measuring the vertical distribution of the acoustic field at various ranges, i.e., the range-depth plane [7].

Spectrogram focal regions

We search for a combination of cases 2 and 3 where many modes have a nondispersive stationary region (analogous to the Airy phase) but at the same phase speed interval (analogous to WDBR). For this case, we expect a bunching of energy in the frequency-time plane (spectrogram) caused by the group speed being approximately constant in an interval of phase speeds and frequencies. This phenomenon occurs, among other places, in a deep water scenario in the transition region from purely refracted paths (RR) to refracted-surface-reflected (or bottom-reflected refracted) paths (RSR). This phenomenon should therefore occur for a more general class of sound speed profiles than that for the existence of WDBR. The surface-reflected-refracted transition was identified, for example, in the SLICE89 experiment [8] where a 3000 m vertical array was deployed. For one of the cases under study in this paper, we consider single phone arrival structure of a pulse, which shows a concentration of energy at a specific time across a frequency interval at a single point in space. The physical origin this "focal region" is discussed below.

Group speed vs phase speed for simple deep-water propagation

Consider two families of modes or ray paths, RR and RSR, in a simple deep ocean environment as shown in the ray schematic of Fig. 2. The sound speed profile

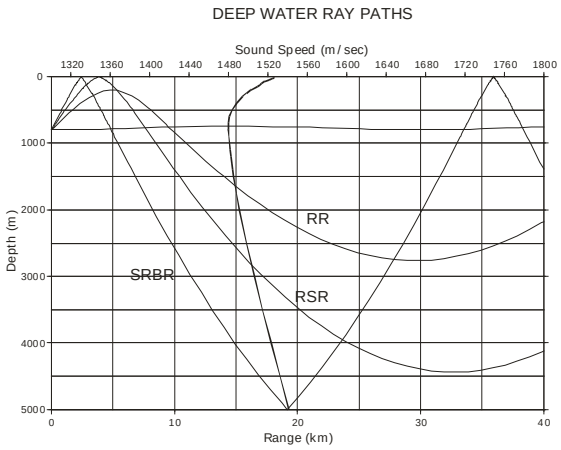

Figure 2. Deep water ray trace examples for the sound speed profile (ssp) shown. The ssp scale is on the upper horizontal axis whereas the ray trace range scale is on the lower axis. The discussion concerns the transition between the refracted-refracted (RR) and the refracted-surface-reflected (RSR) paths. Also shown is the surface-reflected-bottom-reflected (SRBR) path, Note that there is a positive critical depth meaning that there exists a RSR path; otherwise RR would transition to RBR and then to SRBR.

used in this example is a range-averaged profile for one of the environments we will compare data and theory with. For the purely refracted RR case the group speeds increase with increasing phase speed. (Recall that phase speed increases with increasing launch angle with respect to the horizontal.) That is, the up and down going rays are refracted in regions of higher medium speeds and this phenomenon dominates the group speed dependence on phase speed. For the refracted-surface-reflected (RSR) path, the upper surface reflects rays before they can be refracted at higher speed regions and hence this ray family has a different group speed dependence on phase speed. We transition from RR to RSR by increasing phase speed of the modes (or launch angles in the ray picture). Clearly, as we transition from RR to RSR or vice versa, the group speeds (or cycle distances) must approach each other in the transition region. This means that contributions of a point source from modes or rays in this transition region should arrive at a receiver more or less at the same time. If, over the finite bandwidth of a pulse, the modes

are only moderately dispersive, then it follows that the frequency-time arrival structure of a pulse should show a local maximum, or focus, in spectral level at an arrival time for all frequencies corresponding to the source-to-receiver range divided by the group velocity of the transition region. Lowering the frequency of a RR mode causes it to transition (actually an RR cut-off) into to an RSR mode. This is confirmed using data.

Spectrograms of range-dependent experiment

The data we examine in the paper comes from the Acoustic Thermometry of the Ocean Climate (ATOC) series of experiments [9-11]. The two paths are shown in Fig. 3 and the climatology derived sound speed

profiles [12] were used to calculate the effective range-dependent group speeds over these paths as described below. We obtain the curves in Fig. 4 from an adiabatic

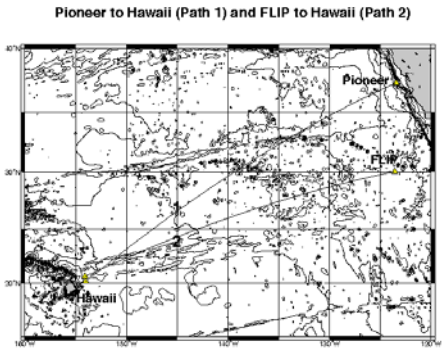

Figure 3. Two propagation paths. There was approximately one sound speed profile per 500 km.

normal mode computation [13] and approximate the phase speed to be a continuous variable. The local phase speed c_{pn} of the n-th mode at the source location (which corresponds to a launch angle) is related to the modal wavenumber k_n,

$$c_{pn}(\omega) = \frac{\omega}{k_n}.$$

The range-dependent effective group speed [12], $\langle u_n(r,\omega)\rangle$, is given by

$$\frac{1}{\langle \mathrm{u}_\mathrm{n}(r,\omega)\rangle} = \frac{1}{r}\sum_{\Delta r'_l} \frac{\Delta r'_l}{u_n(r',\omega)},$$

where the sum is taken over the approximately L range-independent subintervals of length $\Delta r'_l$. The harmonic average for group speeds is a result of time of propagation (or slowness) being the additive quantity of interest.

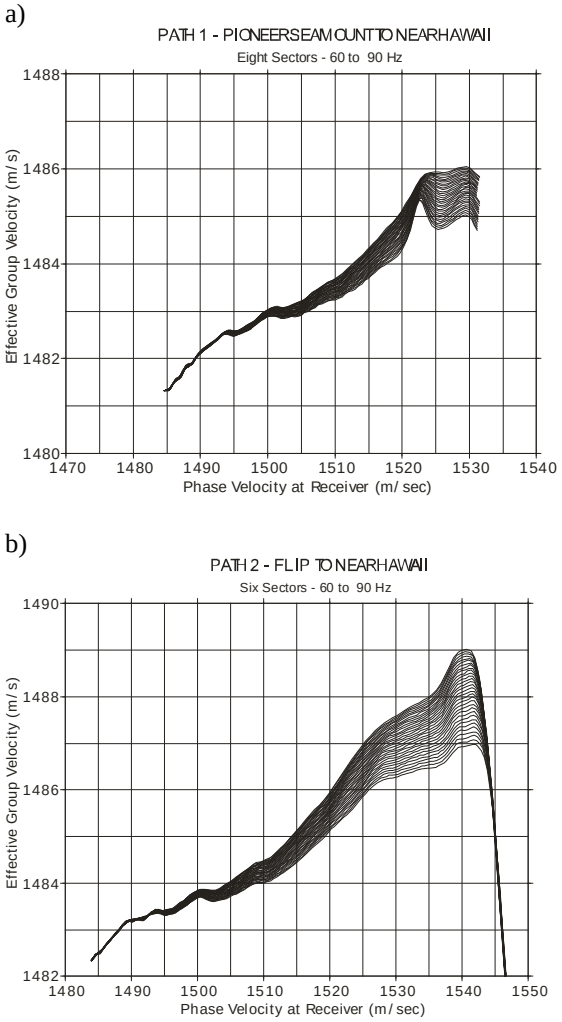

Figure 4. Group velocity as parameterized by frequency. for Path 1 1522 m/s corresponds to the surface sound speed. For Path 2, the last stationary region at about 1540 m/s corresponds to the onset of bottom-interaction. Hence, Path 1 will have a spectral focusing associated with the transition from refracted-refracted to surface refracted; corresponding to a group speed of about 1485.6 m/s. Path 2 does not have a well defined stationary region over a compact group speed/freqeuncy interval. This corresponds to the total dispersion case originally suggested in [1].

Figure 5 shows the data in the form of spectrograms for the two paths displayed in Fig 3. In both cases we see the well-known last arrival which travels with the slowest group velocity u_s representative of the axial

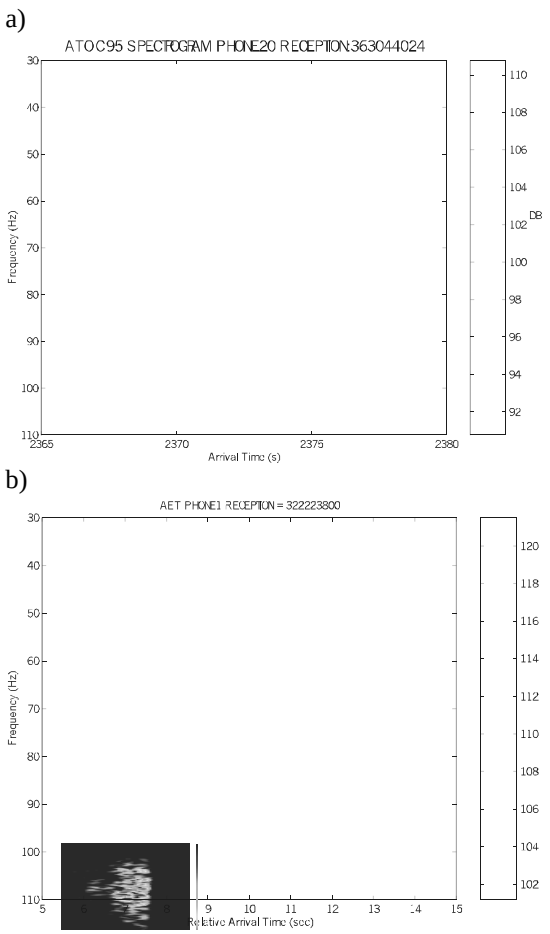

Figure 5. Spectrograms for paths 1 and 2. $\Delta t = 6.3$ and 5.2 s, respectively.

sound speed. Further, we see the earlier arrivals traveling with the faster group velocity u_f. For both cases, u_s and u_f can be taken from Fig. 5 but the latter group velocity has a different meaning for the two cases. For path 1, it is the group velocity at the RR to RSR transition (1520 is a surface sound speed) whereas for path 2, we have the transition from RR to RBR and the RBR (bottom interacting) path does not propagate long distances. Hence, the path 2 spectrogram represents the full pulse dispersion discussed by Ewing and Worzel [1]. In either case, we can obtain the range from the simple relation

$$r = \frac{u_s \Delta t}{1 - \frac{u_s}{u_f}},$$

where Δt is read off the spectrograms; for path 1, the time interval between the two focal regions; for path 2, the pulse length. The range estimate to $\pm 100 km$ is approximately 3430 and 3280 km for the two paths, respectively, vs GPS ranges of 3514 and 3252 km, respectively. Hence, it appears that our climatology group velocity analysis is representative of the propagation physics and that range localization can be achieved.

Propagation between deep and shallow water

Figure 6 shows the arrival structure from another ATOC example [14] for a bottom mounted receiver.

The ray trace is based on deep-water only propagation but the source was actually in shallower water dropping off very quickly to 3000 m after 10 km and then

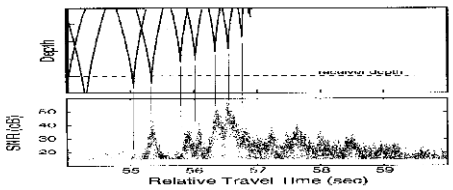

Figure 6. ATOC data on bottom mounted phone and ray based prediction of arrival structure [14]. Some data is below the ray predicted turning points

to 5000 m after 100 km. The original ray trace calculation is based on the assumption that downward launched paths are scattered off the bottom and do not propagate long distances (thousands of km). Note that the receiver depth is below the turning points of the later arrivals as predicted by the ray trace program. This discrepancy is explainable by noting that the group speed dependence on phase speed is opposite for shallow water (bottom reflecting paths) and deep water (refracted paths). For bottom reflected paths, group speed decreases with increasing phase speed (launch angle) whereas it decreases with increasing phase speed in deep water where paths are deeply refracted where the sound speed is high. Just as in the previous section, this analysis can be quantified. However, let us first present a full range dependent parabolic equation computation [15,16] to demonstrate that a full wave treatment will predict the arrival structure. That is, that some initial bottom interaction will not be attenuated over the long distance, but that, in effect, there will be shallow water "scar." Figure 7 shows the result of the parabolic equation result together with a baseline normal mode result which should be the wave equivalent of the original ray trace. The calculations are done for a fictitious vertical array spanning the water column; the last arrivals are on the right. Note that the later arrivals of the PE result extend down in depth as compared to the normal mode computation. Figure 8 is a calculation at 1500km range of the arrival structure averaged over a 250m-depth interval. The deep-water simulation shows the early arrivals corresponding to the high-angle energy and then fades quickly as the path (ray) turns above the receiver. The evidence of 25 dB

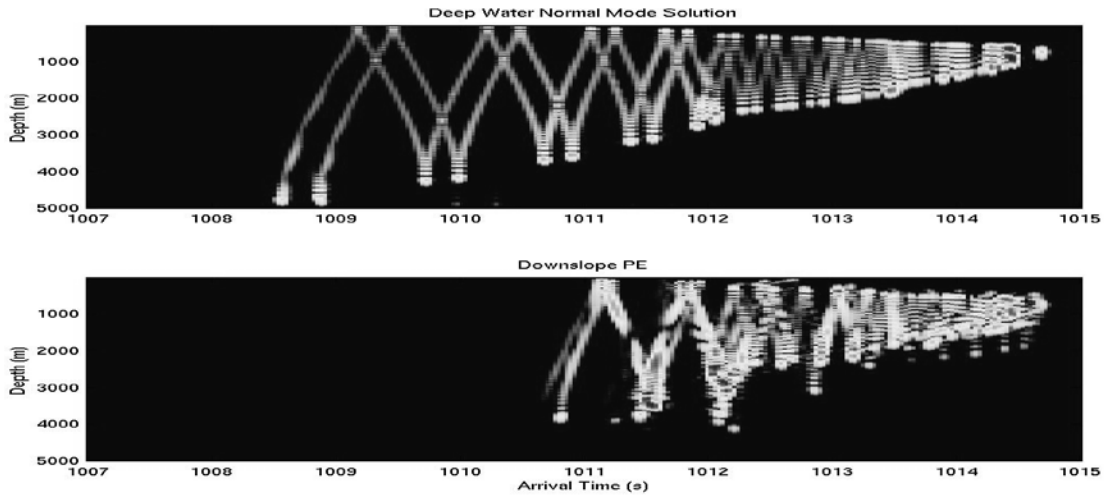

Figure 7. The upper panel is a deep-water normal mode simulation corresponding to the original ray trace computation. The lower panel is the downslope PE result.

stronger arrivals at times of 1011.5 and 1012 s we believe explains the basic features of the data.

By our above qualitative group speed discussion, we expect that the origin of this effect is that the faster higher modes were slowed down in the initial shallow water region. This should become apparent by plotting group speed vs phase speed for the deep water and downslope cases. Figure 9 shows is such a plot where we have replaced group speed with modal arrival times for a range of 1500 km. The higher phase speeds correspond to higher order modes. In the downslope case, we see the "scar"of the original bottom interaction in that higher modes have a later arrival time. Recall that the local travel time for each effective segment is the fundamental quantity. The initial slowing down of the high modes (over the first 10's of km's) is therefore apparent at 1500 km. The curves are most explanatory when one considers horizontal cuts.

For example, a horizontal cut at arrival time 1012 s indicates that for the deep water case, modes corresponding to phase speeds close to 1500 m/s are the

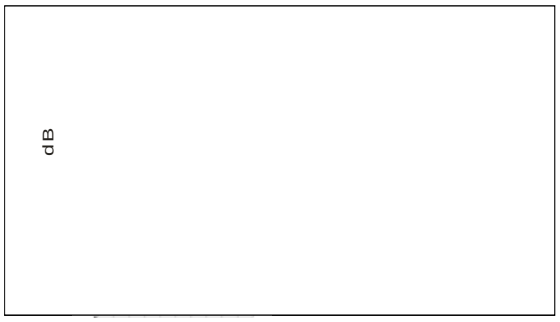

Fig 8. Simulated average reception (in relative dB) at depths=3500-3750m for deep-water (black) and downslope PE (gray).

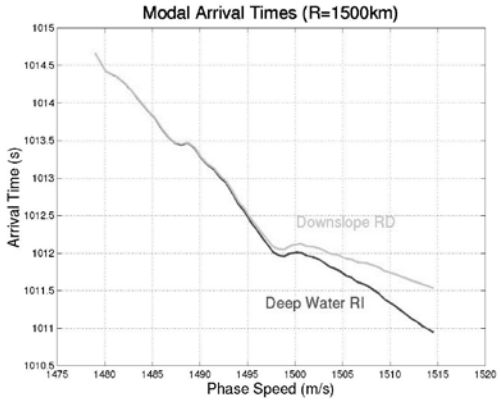

Figure 9. Modal arrival times computed from effective range-dependent group speeds.

main contributors whereas for the downslope case, the main modal contributors have phase speeds around 1504 m/s. Using a climatology derived Mid Pacific sound speed profile, we find that the ray turning depths for these two phase speeds differ by 400 m. We therefore have a consistent picture between data, simulation and phase-group speed analysis.

Conclusion

We have shown in this paper that studying the relation between group speed and phase speed for a particular propagation scenario yields both qualitative and quantitative information which can be used to localize the source or, predict the its arrival structure. We have also shown that even a short segment of bottom-interacting propagation in a long range, deep-water propagation scenario results in an identifiable scar in the arrival structure.

Acknowledgements

This work was supported by the Office of Naval Research. The data were kindly provided to us by the ATOC Group (A. B. Baggeroer, T. G. Birdsall, C. Clark, J. A. Colosi, B. D. Cornuelle, D. Costa, B. D. Dushaw, M. A. Dzieciuch, A. M. G. Forbes, B. M. Howe, D. Menemenlis, J. A. Mercer, K. Metzger, W. H. Munk, R. C. Spindel, P. F. Worcester, and C. Wunsch). The ATOC project was supported by the Strategic Environmental Research and Development Program through Defense Advanced Research Projects Agency (DARPA) Grant MDA972-93-1-0003.

References

9. M. Ewing and J. L. Worzel, "Long-Range Sound Transmission," *Geo. Soc. Am., Memoir 27*, (1948).

10. W. M. Ewing, W. S. Jardetzky, and F. Press, *Elastic Waves in Layered Media*, McGraw Hill Book Company, New York (1957).

11. S. D. Chuprov, "Interference structure of a sound field in a layered ocean," in *Ocean Acoustics, Current State*, ed. by L. M. Brekhovskikh, I. B. Andreevoi: Nauka, Moscow, 71-91, (1982).

12. L. M. Brekhovskikh and Y. P. Lysanov, *Fundamentals of Ocean Acoustics*, 2nd ed., Springer-Verlag, New York (1991).

13. G. A. Grachev, "Theory of acoustic wave invariants in layered waveguides," *Acoust. Phys*. 39(1), 33-35, Jan.- Feb. (1993).

14. G. L. D'Spain and W. A. Kuperman, "Application of waveguide invariants to analysis of spectrograms from shallow water environments that vary in range and azimuth," *J. Acoust. Soc. Am*., 106(5), 2454-2468, (1999).

15. L. M. Brekhovskikh, V. V. Goncharov and V. M. Kurtepov, "Weakly Divergent Bundles of Rays and Their Possible use in Inverse Methods ofOcean Acoustics," in *Full Field Inversion Methods in Ocean and Seismo-Acoustics*, ed. by O. Diaschok, Kluwer Academic Publishers, Dordrecht (1995).

16. P. F. Worcester, B. D. Cornuelle, J. A. Hildebrand, W. S. Hodgkiss, T, F. Duda, J. Boyd, B. M. Howe, J. A. Mercer, and R. C. Spindel, "A comparison of measured and predicted broadband acoustic arrival patterns in travel time-depth coordinates at 1000 km range," *J. Acoust. Soc. Am.*, 95(6), 3118-3129 (1991).

17. ATOC Consortium, "Acoustic Tomography, Satellite Altimetry, and Modeling," *Science* **281**,1327-1332, (1998).

18. P. F. Worcester, B.D. Cornuelle, M.A. Dzieciuch, W.H. Munk, B.M. Howe, J.A. Mercer, R.C. Spindel, J.A. Colosi, K. Metzger, T. G. Birdsall and A.B. Baggeroer, "A test of basin-scale acoustic thermometry using a large-scale vertical array at 3250-km range in the eastern North Pacific," *J. Acoust. Soc. Am.*, 105(6), 3185-3201 (1999).

19. J.A. Colosi, E.K. Sheer, S. Flatte, B.D. Cornuelle, M.A. Dzieciuch, W.H. Munk, P. F. Worcester, B.M. Howe, J.A. Mercer, R.C. Spindel, K. Metzger, T. G. Birdsall and A.B. Baggeroer, "Comparisons of measured and predicted acoustic fluctuations for a 3250-km propagation experiment in the eastern North Pacific," J. *Acoust. Soc. Am*., 105(6), 3202-3218 (1999).

20. W.A. Kuperman, G.L. D'Spain and K.D. Heaney, "Long range source localization from single hydrophone spectrograms," submitted, *J. Acoust. Soc. Am., (1999).*

21. F. B. Jensen, W. A. Kuperman, M. B. Porter and H. Schmidt, *Computational Ocean Acoustics*, AIP Press, Woodbury, N.Y. (1994).

22. B.D. Dushaw, B.M. Howe, J.A. Mercer, R.C. Spindel and the ATOC Group, "Multimegameter-Range Acoustic Data Obtained by Bottom-Mounted Hydrophone Arrays for Measurment of Ocean Temperature, IEEE J.. Ocean. Eng. Volume 24, pp 202-214 (1999).

23. M.D. Collins, "A split-step Pade solution for the parabolic equation method," *J. Acoust. Soc. Am*., 93, pp. 1736-1742 (1993).

24. K. D. Heaney and W. A. Kuperman, "Very long-range source localization with a small vertical array," J. Acoust. Soc. Am. 104(4), 2149-2159 (1998).

Determining A Geoacoustic Model From Shallow Water Refraction Profiling And Transmission Loss Data, Using A Simulated Annealing Inversion Algorithm

Marshall V Hall

DSTO Maritime Operations Division, PO Box 44, Pyrmont NSW 2009

Abstract

To characterise the propagation conditions in a shallow-water environment at low frequencies, measurements have been made of both CW transmission loss (TL) versus distance at 4 frequencies from 50 to 250 Hz, and travel times of airgun-generated head waves. The head wave data yield the sound-speed and time-intercept of a reflecting interface, and these results are used as known parameters when the CW data are inverted to obtain a complete geoacoustic model. The inversion algorithm was an adaptive implementation of the simulated annealing method [W L Goffe et al, Journal of Econometrics, 60, 65 - 99 (1994)]. For this particular environment it was found that the geoacoustic model should consist of 3 uniform solid layers overlying a solid uniform basement. The cost function is the RMS of the residuals between measured and OASES-modelled values for TL over the 4 frequencies; and the objective is to determine optimum values for the 5 elastic parameters and the thickness of each layer. To reduce the number of unknown parameters, regression equations were devised to relate the 2 less critical parameters (density and shear absorption) to the 3 that are usually found to be more important (sound and shear speeds, and sound absorption). With 11 unknown parameters (the head wave data yield one thickness), the inversion algorithm found a satisfactory geoacoustic model and, after nearly 34000 runs, gave indications that the result is likely to be the global optimum.

Introduction

The aim of the work described here is to determine an appropriate transmission correction to be applied to noise measurements at a particular site in shallow water.

The conventional term "Transmission Loss" (TL) denotes the distance correction factor (in dB) to add to acoustic pressure measured at a particular distance from a source, in order to obtain the corresponding Source Level at 1 m. In this paper, the term "Relative Pressure" (RP = – TL) will often be used.

The specific issue is the modelling of RP at horizontal distances of the order of 100 m in a particular shallow water area with a sandy seafloor at a depth in the region of 50 m. For this paper, the frequency band of interest is from 50 Hz to 250 Hz. The water is virtually isothermal, and prevailing windspeeds vary up to around 10 kt.

Shallow water propagation has been a subject of study for decades in many countries, mainly for its application to estimating sonar performance. Marsh and Schulkin (1962) fitted simple regression equations to a large amount of data that had been collected at frequencies from 100 Hz to 10 kHz. The term "long range" appears in the titles of the cited papers from which TL data were obtained, and results for spread in TL are given at distances from 3 to 80 km. It would therefore be surprising if a significant number of data at distances of the order of 100 m were included in their analysis. However, it could be inferred from a quick reading of this paper that, for short distances (r), the average RP exceeds –20 log r ("spherical spreading") by an amount that is independent of distance. Over a sand seafloor, the average difference is 7 dB at 100 Hz and 6 dB at 200 Hz, regardless of surface roughness (higher frequencies are affected by roughness). With regard to data spread, the "semi-inter quartile range" (half the difference between the first and third quartiles) at a distance of 3 km is reported to be 2 dB at around 100 Hz, and 4 dB at around 400 Hz and higher frequencies.

The Marsh and Schulkin paper does however contain the following important caveat:

> *"The principal problem in calculating the sound field in shallow water is the lack of detailed knowledge of the shallow water environment. However, highly variable sound speed is the rule, and this has an important bearing on high-frequency transmission. The properties of the bottom, important at any frequency, are controlling at the lower frequencies.*

Even given the detailed parameters of a particular environment, the variability to be expected is such that calculation will be very complex and tedious. There is thus the need for comparatively simple equations representing the average sound field, while retaining dependence upon the principal features of the environment."

When this paper was written in 1962, simple equations were needed because convenient and accurate computer algorithms for computing RP (such as OASES) were not available.

To compute RP, two items are required: first an algorithm that calculates RP at a given position (relative to a source) for a given environment; and second an accurate model of the elastic properties of the environment, including the seabed. An isotropic medium has the following five elastic properties: sound speed (Cp), shear speed (Cs), sound absorption (Ap), shear absorption (As), and density (D). For an inviscid fluid, Cs = 0 and As = 0 [4]. When a medium's elastic properties are described in this paper, they will be presented as a sequence of five numbers, in that order; that is (Cp, Cs, Ap, As, D). The speeds will be in m/s, the absorption coefficients in decibels per wavelength, and density in kg/m^3.

Prior to the work that is the subject of this paper, no measurements had been made of the elastic properties of the seabed at the site. Blanch and Ivansson (1998) published a study of RP in a "specific" shallow water waveguide, with a uniform sand seafloor 45 m deep. They gave the water the elastic properties of fresh water, and gave the seabed the following properties: 1800, 600, 0.7, 1.5, and 2000. They calculated RP at a fixed distance of 100 m for frequencies from 50 to 5000 Hz, and found that average values were around 4 to 5 dB higher than spherical spreading (SS). Although the accuracy of the RP algorithm used in that report ("RPRESS") is not in question, results produced by it for a specific area will only be accurate if it is provided with an accurate model of the environment. This issue will be revisited later in the paper when a comparison can be made with measured RP's.

Experimental method

Refraction profiling

The study of the elastic properties of the seabed commenced in May 1999 with a trial organised by the Sydney branch of DSTO Maritime Operations Division (MOD) to measure travel times of airgun-generated sub-bottom head waves. The airgun, owned and operated by the Centre for Marine Sciences & Technology at Curtin University (Perth, WA), was towed near the surface, and a hydrophone was deployed on the seafloor. The aim was to obtain the sound-speed and depth of reflecting interfaces. The results indicate that there is a sub-bottom high-speed (6100 m/s) reflecting interface in the seabed. Since the arrivals on the distance-time stacked diagram had a time-intercept of 0.07 s, the interface would be of the order of 100 m below the seafloor. For ease of discussion, this interface will be referred to as "granite".

CW measurements

The second phase was to take part in data acquisition during a calibration trial conducted in August 1999. The practical aim was to measure the distance variation of RP using CW tones at frequencies of 53, 63, 125 and 250 Hz. The receiver was a single sea floor hydrophone controlled by the Nautronix Company.

The source was the "Sonar Research Projector" (SRP) operated by staff from the Salisbury branch of MOD. SRP was mounted on a 197-tonne ship, and deployed at a depth of 20 m. Runs were conducted at a speed of 4 kt.

During the first 2 days the runs were eastward, and nearly over the top of the hydrophone. To obtain the sound-speed profile in the water, a CTD cast was made at 1720 local time on Day 2. No runs were completed on Day 3, due to roughness-induced pitching that was excessive for SRP. On Day 4 a CTD cast was made at 0740 local time. The SRP runs were southward, and passed the hydrophone at a nominal Closest Point of Approach (CPA) of 100 m. The signals from the hydrophone were recorded by Nautronix staff in a range control centre ashore.

For five Eastward runs (1, 2, 5, 6, and 7) and one Southward run (2S), the author was given system information and access to the local network so that Nautronix datafiles (32-bit data with a sampling rate of 12 kHz) could be copied to a separate PC.

Spectrograms of the 6 available SRP runs

During Run 1, SRP transmitted a 53-Hz tone [5]. The hydrophone signal was recorded for nearly 6 minutes and a spectrogram of this recording has been produced (after downsampling the Nautronix file to 1 kHz). Interesting features are the presence of harmonics (presumably due to the projector being driven near maximum power), and the diagonal streaks due to interference patterns in the wideband noise radiated by the

[4] a viscous fluid has an imaginary shear modulus $G = D\,Cs^2$.

[5] 50 Hz was planned, but electrical interference in the acquisition equipment occurred at that frequency.

ship (such a pattern should also be seen from any vessel). The ship's CPA to the hydrophone occurred just over 1 minute after the beginning of the record.

For Run 2, SRP transmitted a tone at 63 Hz. The hydrophone signal was recorded for around 5 minutes and the spectrogram again exhibited harmonics and diagonal streaking. CPA occurred at nearly 1 minute.

For Run 5, SRP transmitted a 125-Hz tone. The hydrophone signal was recorded for nearly 9 minutes and in the spectrogram harmonics and diagonal streaking are again present. CPA again occurred at nearly 1 minute.

For Run 6, SRP transmitted 6 tones, but only the 250-Hz tone will be considered here. The hydrophone signal was recorded for 4 minutes. In the spectrogram few harmonics are present (the source levels are lower), and the diagonal streaking is partially obscured by the number of lines. CPA occurred at around 30 s.

Results

Mean-square values of data from the first four runs have been used to produce RP at frequencies of 53, 63, 125 and 250 Hz. The averaging times (T) were usually around 1 or 2 s, which correspond to averaging distances of 2 to 4 m at the longer distances.

At 53 Hz, the RP data curve commences at a horizontal distance of around 25 m, where it is somewhat higher than SS. The data curve crosses the SS curve near 30 m, dips to a minimum (SS – 5 dB) near 70 m, rises to maximum (SS + 10 dB) near 110 m, and then falls to its next minimum (SS – 5 dB) near 310 m. The separation between the two minima is 240 m.

At 63 Hz, the RP data curve commences at a horizontal distance of around 15 m, where it is a few dB higher than SS. It crosses the SS curve near 50 m, dips to a minimum (SS – 12 dB) near 55 m, rises to maximum (SS + 5 dB) near 85 m, and then falls to its next minimum (SS – 2 dB) near 100 m. It then oscillates 4 times, remaining above SS even at its minima, until the distance reaches 310 m, where RP plunges to a deep and broad minimum (~ SS – 10 dB). The average separation between minima is 50 m.

At 125 Hz, the RP data curve commences at a horizontal distance of around 70 m, where it is a few dB lower than SS. It rises to a maximum (SS + 8 dB) at 85 m, dips to a minimum (SS – 6 dB) near 150 m, rises to maximum (SS + 6 dB) near 200 m, and then falls to its next minimum near 270 m (SS – 15 dB). It then has a maximum (SS + 12 dB) at 330 m. The average separation between minima is approximately 100 m.

At 250 Hz, the RP data curve commences at a horizontal distance of around 20 m, where it is a few dB higher than SS. It dips to a minimum (SS – 5 dB) near 30 m, rises to a maximum (SS + 4 dB) at 35 m, dips to a minimum (SS – 5 dB) near 42 m, rises to maximum (SS + 5 dB) near 60 m, and then falls to its next minimum (SS – 15 dB) near 65 m. It then fluctuates with distance, although generally remaining above SS. Noticeable features are two broad maxima (SS + 9 dB) near 240 and 380 m. Over a distance of 380 m, the curve drops below SS at 15 positions.

It can be seen from the above results that assuming RP = SS will frequently lead to errors of 10 to 12 dB, and setting RP = SS + 6 or 7 dB (per Marsh and Schulkin) will also lead to large errors. As frequency is increased from 50 Hz to 250 Hz, the "wavelength" of the fading due to multipath interference will decrease from 200 m to 20 m. It will be impossible therefore to simplify RP at such frequencies by setting it equal to SS plus a constant, or even a monotonically varying function of distance.

Inversion analysis

The only way to generalise the RP data to other frequencies and/or source depths is to have a model of the layer structure of the seabed, together with the elastic properties of each layer. This is called a "geoacoustic model" [GAM]. Thus a GAM consists of a sequence of layers and specifies the thickness and the five elastic properties of each. Roughness of a layer boundary can also be specified, although for these low frequencies that parameter has been neglected. An accurate RP algorithm that can take account of all the GAM parameters is required. In general, PE-type algorithms are not suited to short distance calculations. Ray theory may be suitable at higher frequencies, but the author is not aware of an algorithm that can cater for a seabed that contains multiple solid layers. There is no need to develop one however, since OASES (version 2.2) meets the requirements for computing RP in the environment, and is accurate over the entire frequency band [6].

The objective of the inversion analysis was to derive a GAM valid for these low frequencies. The inversion process developed has the following features:

- It uses the OASES algorithm for RP (which assumes the environment to not vary with horizontal distance)

[6] At frequencies below the cut-off frequency of the waveguide, the option in version 2.2 to use the Bessel function (rather than the default Hankel function) must be activated, although that was not required during the present computations.

- the sea surface roughness was assumed to be zero, and the seawater sound-speed set to the appropriate value for the measured temperature

- After trials with GAM's comprising 1, 2 and 3 uniform solid layers overlying a solid uniform basement, it was found necessary to construct a GAM of 3 layers in order to obtain satisfactory results. For each layer, thickness and five elastic properties need to be specified. The roughness of every layer was set to zero.

- After trials with approximate GAM's, the source depth for each run was varied so as to increase the match between model and data. It was found that depths that differed from the nominated 20 m by up to 1.5 m yielded closer matches with the data, and such amended depths were implemented.

- The number of models that the simulated annealing algorithm samples is proportional to the square of the number of unknown parameters. To reduce the number of unknown elastic parameters in the GAM, regression equations were devised to relate the less critical parameters (density and shear absorption) to sound speed, shear speed and sound absorption.

- The granite interface was regarded as the acoustic basement, and was given values for Cs and Ap obtained from the literature (Vasilev and Gurevich, 1962). This assumption is fairly safe, since (a) the basement was found to have only a small effect on RP at frequencies above 50 Hz, and (b) a rock with such a high Cp (indicating low porosity) will probably have similar values for its other elastic parameters, wherever it is found. In addition, knowledge of it gives an indication of what to expect for the average gradient in the sound-speed profile between itself and the seafloor.

- With 11 unknown parameters, the inversion algorithm sampled $11\times22\times20 = 4840$ GAM's at each of 7 reducing "temperatures", to give a total number of nearly 34000 GAMs

- The cost function was defined as RMS value of the residuals (in dB) between 80 data at various horizontal distances (20 at each of the 4 frequencies) and the corresponding RP algorithm predictions for each GAM. This type of cost function, which is used in other sciences, demands that the SL and sensitivity of the receiving system be accurately known. Most inversion schemes implemented in underwater acoustics assume on the other hand that the absolute levels are unknown, since they use a "Bartlett processor" cost function which is equivalent to the correlation between the measured and model datasets (Chapman and Lindsay, 1996, for example).

- It is found that the run time is 5 s for the four frequencies, for each GAM sample (on a 466-MHz Personal Computer). For 34000 samples, the total time is 46 hours.

The inversion process, together with the other assumptions made, yielded a GAM with the following features: The thicknesses of the 3 layers (top first) are 9, 23, and 50 m, and their values for Cp are around 1650, 2230, and 3550 m/s. For ease in discussing these results, the 3 layers may therefore be referred to as sand, chalk, and stone.

The RMS errors in the model predictions at the four frequencies are 2.6, 2.4, 2.4, and 4.0 dB respectively, and the overall RMS error is 2.9 dB. Ideally the errors would be smaller, but from an inspection of the data it is difficult to imagine that any alternative GAM would give a smaller overall error.

Conclusions

For a particular set of runs in shallow water with a calibrated sound projector and data acquisition system, it has been possible to produce a geoacoustic model that predicts low-frequency sound pressure levels in agreement with measured data. This result indicates that the source level and receiver sensitivity were both as nominated, and also that the environment was substantially stratified. The geoacoustic model replicates the significant acoustic properties of the seabed at these frequencies, and should therefore be useful for computing RP at any intermediate frequency, and for other source and receiver depths.

Acknowledgments

David Matthews of DSTO Sydney led the trial conducted in May 1999.

Paul Meakin of the Defence Acquisition Organisation invited and facilitated the author's participation in the August 1999 calibration trial.

Harry Protoolis and Gareth Cook of Nautronix Ltd provided datafiles of the runs, calibration data for the sensitivity of the data acquisition and signal processing system, and records of the prevailing winds.

Andrew Brennan of DSTO Salisbury operated SRP during the runs, and later provided records of GPS data.

References

Blanch J O, and Ivansson S (1998) "Comparison of spherical wave propagation and wave propagation in a specific waveguide" (Report 98-00747-409-SE). Defence Research Establishment, Stockholm, Sweden.

Chapman N R, and Lindsay C E (1996) "Matched-Field Inversion for Geoacoustic Model parameters in shallow water", IEEE Journal of Ocean Engineering, 21 (4), 347 – 354.

Goffe W L, Ferrier G D, and Rogers J (1994) "Global optimization of statistical functions with simulated annealing", Journal of Econometrics, 60, 65 – 99.

Marsh H W and Schulkin M (1962) "Shallow-water transmission", Journal of the Acoustical Society of America, 34, 863 – 864.

Vasilev Y I and Gurevich G I (1962) "On the ratio between attenuation decrements and propagation velocities of longitudinal and traverse waves", Bulletin of the Academy of Sciences USSR Ser. Geophys. No. 12, 1061 – 1074.

Seafloor Reflectivity – A Test of an Inversion Technique

Adrian D. Jones[1], Justin Hoffman[2] and Paul A. Clarke[1]

[1]Defence Science and Technology Organisation, Australia, [2]Student at Centre for Marine Science and Technology, Curtin University

Abstract

A technique has been developed at the Maritime Operations Division of DSTO to determine the reflective properties of the seafloor in a shallow ocean, by using a broadband signal received at ranges of several km. The theory behind this technique indicates that the determination of bottom loss versus grazing angle is robust to moderate changes in separation range between the sound source and receiver, and so affords a practical means of seafloor determination. This paper reviews the basis of the measurement technique and shows how it has been used to invert the bottom loss versus grazing angle function from at-sea data gathered by Curtin University using an air gun as a signal source. In this study, the sensitivity of the inversion technique to source and receiver separation is investigated and the robustness of the technique to the nature of the air gun spectrum signature is considered. Also, the derived reflectivity values are compared with those determined from existing geoacoustic datasets for the particular seafloor location.

Introduction

The optimised deployment of anti-submarine warfare (ASW) and anti-surface warfare (ASuW) sonar systems during naval operations in littoral waters, and continental shelf zones, requires knowledge of the local underwater environment. At low acoustic frequencies (less than 300 Hz approx.), or with a downwardly refracting sound speed versus depth function, the transmission of sound to long range (50 km or more) in such shallow ocean regions is affected significantly by the seafloor reflective properties (1). An accurate prediction of sonar system performance is thus dependent upon knowledge of the seafloor suitable for an accurate prediction of transmission loss (*TL*).

At low acoustic frequencies, *TL* models require that the seafloor boundary is described by physical parameters. Usually, the seafloor is described by geoacoustic parameters for the sediment and basement, with the model inputs for each distinct layer region as listed in Table 1.

Table 1: Seafloor Geoacoustic Parameters

Compressional sound speed	c_p m/s
Compressional attenuation	α_p dB/λ
Shear speed	c_s m/s
Shear attenuation	α_s dB/λ
Density	kg/m^3

As described by, for example, Jones et al (1), considerable efforts have been made to determine the parameters listed in Table 1 from geophysical data obtained by cores and grab samples. There is some risk applied to the process, and for many ocean regions the data coverage is sparse. In order to supplement these estimates, and to provide data for unsurveyed locations, MOD has developed a technique (2, 3) for the determination of the seafloor reflective properties based on *in-situ* acoustic measurements. An enticing aspect of the MOD technique is that the number of descriptive parameters is reduced (to one), whilst the ability to carry out phase coherent transmission predictions is retained. This paper describes recent work carried out as further validation of the MOD technique for seafloor property inversion.

Spectral Variability Inversion Technique

Many techniques exist by which acoustic signals may be used to determine the acoustic properties of the seafloor. Most of these techniques are, however, computationally intensive (e.g. matched field techniques - see, for example, Chapman and Lindsay (4)) or are otherwise not sufficiently practical for real-time seafloor properties determination within routine maritime defence operations.

At MOD, a new method has been devised. This technique is based on the statistics of multi-path transmission of broadband signals at medium source to receiver ranges (r = 2 to 5 km approx. in shallow water). As has been determined by Jones et al (3), the rate of variability of the received signal amplitude with frequency Δf_h is related to the geometry of the transmission situation, the speed of sound in the ocean medium, and the seafloor bottom loss as a function of grazing angle. By inverting the relationship, the frequency scale of transmission amplitude variability may be linked, directly, to a slope of bottom loss versus grazing angle,

F dB/radian . This data, in turn, together with an assumed function of reflection phase angle versus grazing angle, provides a description of the seafloor which may be prepared for input to *TL* models. In the work carried out by MOD, the reflection coefficient and phase angle data have been input, directly, to the KRAKEN modal model (5) for phase coherent *TL* calculations.

The MOD inversion technique has been developed to utilise broadband transient signals, as generated by impulsive signal sources. A processing tool, GRASP (6), has been developed to simplify the processing of received transient data. This determines the spectral variability parameter Δf_h and outputs the bottom loss function F dB/radian , via the MOD algorithm. The theory behind the MOD inversion algorithm shows that values of Δf_h are independent of source to receiver range, for ranges for which refraction is not significant. As explained in an earlier paper (2), Δf_h is defined as the frequency displacement at which the normalised autocorrelation of the amplitude of the sound channel frequency response, $\rho_{|p|}(\Delta f)$, falls to 0.5. This normalised autocorrelation is carried out as

$$\rho_{|p|}(\Delta f) = \frac{\langle |p(f)||p(f+\Delta f)|\rangle - \langle |p(f)|\rangle^2}{\langle |p(f)|^2\rangle - \langle |p(f)|\rangle^2}. \qquad (1)$$

where equation (1) implies that the autocorrelation is carried out on the zero-mean sound pressure modulus, that is, on $|p(f)| - \langle |p(f)|\rangle$.

Air Gun Data

The Centre for Marine Science and Technology (CMST) at Curtin University has considerable experience with the operation and use of air guns (7). Further, MOD and the CMST have carried out joint activities using air gun sound sources and a considerable data set has been generated for seafloor and underwater acoustic transmission research.

For the present study, transients received at source to receiver ranges out to 5 km were input to the GRASP processing tool. The transients were generated by an air gun of 20 cubic inch capacity. The transient data were obtained in the Rottnest Shelf area along a track for which the ocean depth was 100 m. Source depth was 10 m, receiver depth 40 m.

Based on available geophysical data, the geoacoustic properties for the relevant region of seafloor are assumed to be as shown in Figure 1.

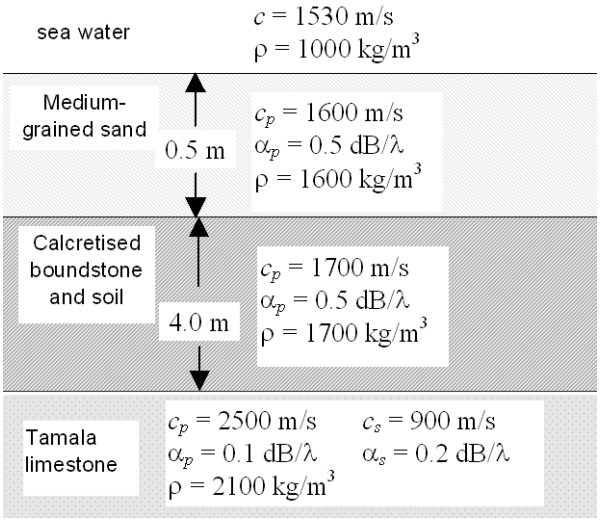

Figure 1 Geoacoustic Parameters – Rottnest Shelf

Inversion of Seafloor Reflectivity

Using the GRASP processing tool, the bottom loss function, F dB/radian , was determined for source to receiver ranges from 100 m to 4500 m at octave bands centred on 63 Hz, 125 Hz, and 250 Hz. These inverted data values are shown in Figure 2.

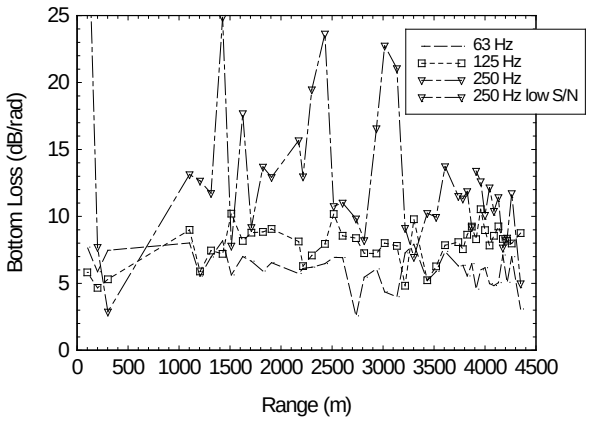

Figure 2 Bottom Loss Function F dB/radian derived from Rottnest Shelf air gun data

The data shown in Figure 2 for 63 Hz and 125 Hz show a remarkable consistency with range, as anticipated from the theoretical derivation of the MOD algorithm. The data for 250 Hz shows more scatter, but is also consistent with range. It must also be noted that the data shown in Figure 2 was obtained using raw spectra from the air gun signals – no spectral shaping was carried out.

Values of bottom loss versus grazing angle were determined by averaging the data in Figure 2 for each frequency band. The resultant bottom loss versus grazing angle variation is shown in Figures 3 and 4, to-

gether with bottom loss data obtained directly from the geoacoustic parameters of Figure 1. Here, the geoacoustic parameters were input to a plane wave reflection model.

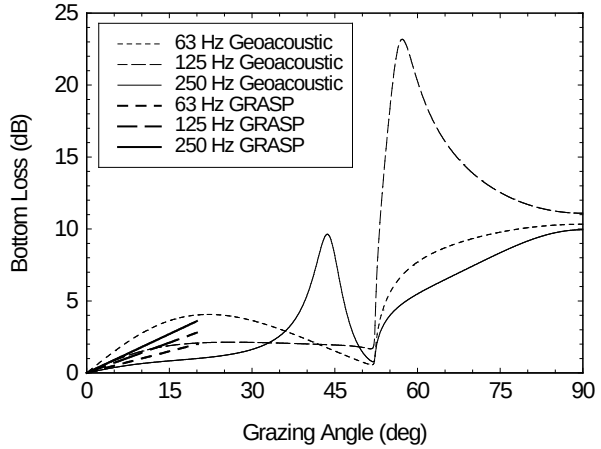

Figure 3 Bottom Loss for Rottnest Shelf 0º - 90º

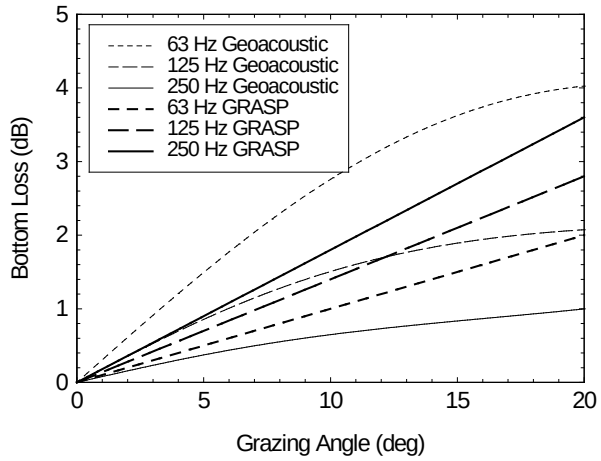

Figure 4 Bottom Loss for Rottnest Shelf 0º - 20º

In Figure 3, the inverted data is plotted to 20º grazing angle, only, as the MOD algorithm is valid for small grazing angles. The data in Figures 3 and 4 do show that the seafloor properties inverted by GRASP are similar to those implied by the geoacoustic parameters (labelled "geoacoustic") – the seafloor is moderately reflective at low frequencies. It must be noted that there is no absolute reference for the seafloor reflectivity, so the values implied by the data in Figure 1 are not necessarily correct.

Prediction of Long Range Transmission Loss

The inferred seafloor reflection data shown in Figures 3 and 4 were used as input to calculations of *TL* to long range (50 km). Here, it was assumed that the bottom loss rose linearly with grazing angle. The seafloor reflection phase angle was assumed to vary linearly from 180º at 0º grazing angle, to 0º at the grazing angle for which the bottom loss was 6 dB. These assumed bottom loss and phase angle data were supplied as input to the KRAKEN transmission model (5) which was run in the mode to use these data, directly. KRAKEN was run in phase coherent mode. For modelling, source depth was 10 m and receiver depth 20 m. *TL* predictions so obtained are shown in Figures 5, 6 and 7, for frequencies of 63 Hz, 125 Hz, and 250 Hz. Also shown in these figures are *TL* values obtained using the geoacoustic data in Figure 1. For these calculations, the ocean is assumed to be isovelocity.

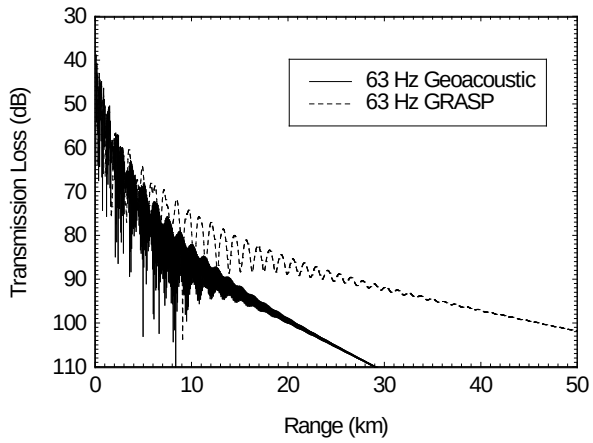

Figure 5 *TL* for Rottnest Shelf, 63 Hz

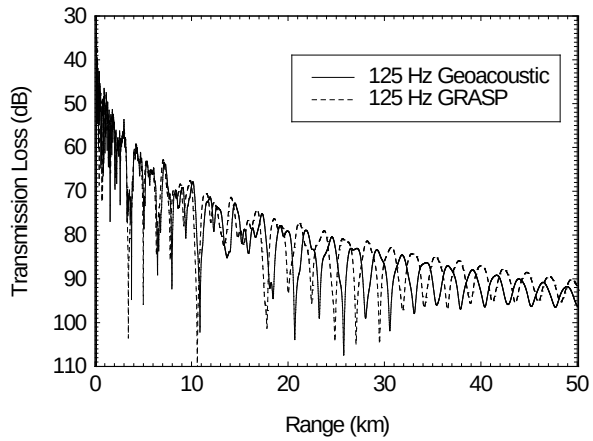

Figure 6 *TL* for Rottnest Shelf, 125 Hz

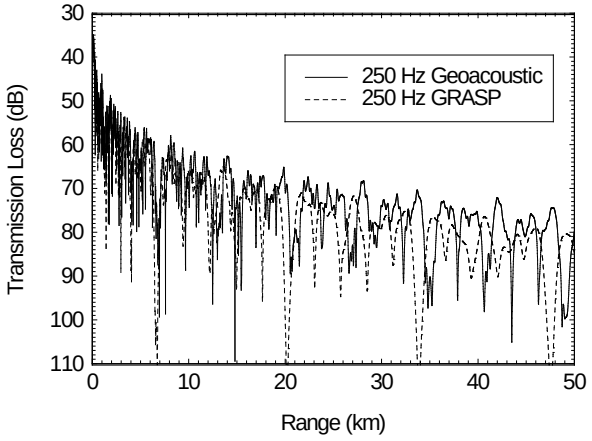

Figure 7 *TL* for Rottnest Shelf, 250 Hz

As expected from the good agreement between the inverted and geoacoustically-derived bottom loss data, the *TL* values shown in Figures 6 and 7 are in good agreement. The data for 63 Hz shown in Figure 5 show a poorer agreement as the bottom loss values shown in Figure 4 differ by more than a factor of 2.

Prediction of Short Range Transmission Loss

The inferred seafloor reflection data shown in Figures 3 and 4 were used as input to KRAKEN calculations of *TL* to short range (5 km). Again, it was assumed that the bottom loss rose linearly with grazing angle and that the seafloor reflection phase angle varied linearly from 180º at 0º grazing angle, to 0º at the grazing angle for which the bottom loss was 6 dB. These assumed bottom loss and phase angle data were supplied as input to the KRAKEN transmission model. *TL* predictions so obtained are shown in Figures 8, 9 and 10, for frequencies of 63 Hz, 125 Hz, and 250 Hz, together with *TL* values obtained using the geoacoustic data in Figure 1. Again, the ocean is assumed to be isovelocity.

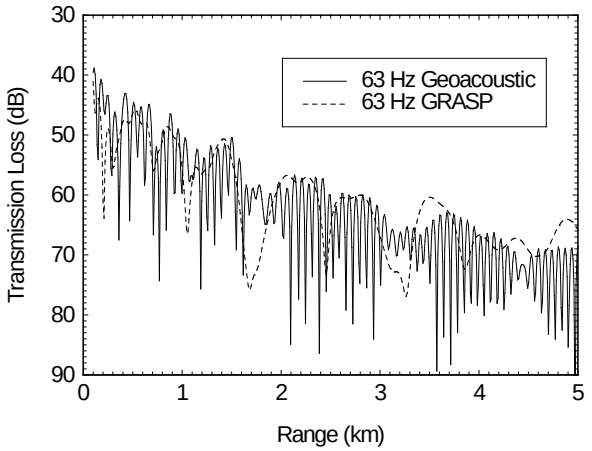

Figure 8 *TL* for Rottnest Shelf, 63 Hz

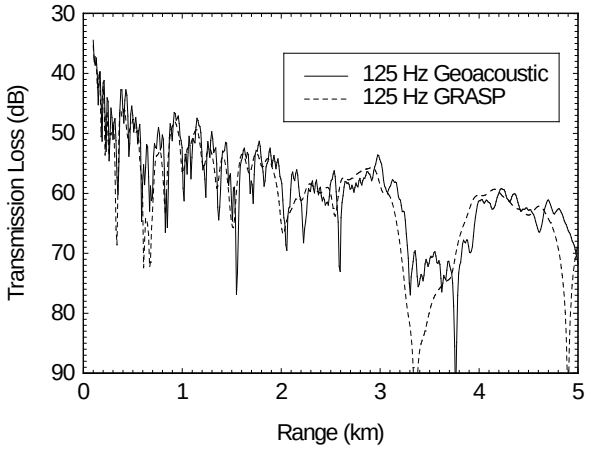

Figure 9 *TL* for Rottnest Shelf, 125 Hz

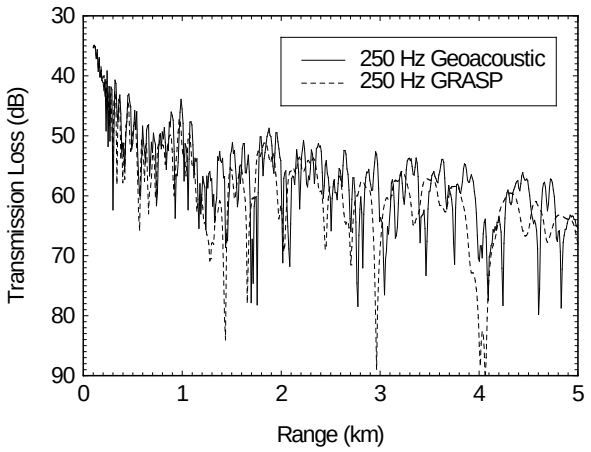

Figure 10 *TL* for Rottnest Shelf, 250 Hz

The data shown in Figures 8, 9 and 10 show an even better agreement in *TL* between the inverted seafloor and geoacoustic seafloor types. Here, both the amplitude of the *TL* and the gross features of the phase coherent *TL* are similar in each respective case. This is an interesting result, as the short range data requires knowledge of the bottom loss and phase angle at steep angles of incidence – the inverted seafloor description was expected to be overly simplistic for these cases.

Effect of Downward Refraction

The above transmission loss calculations were repeated for a downward refracting sound speed profile of gradient - 0.04 s^{-1}. This was expected to accentuate the effect of the seafloor on transmission loss, due to the increased bottom interaction.

Corresponding plots of *TL* for 250 Hz are shown in Figures 11 and 12.

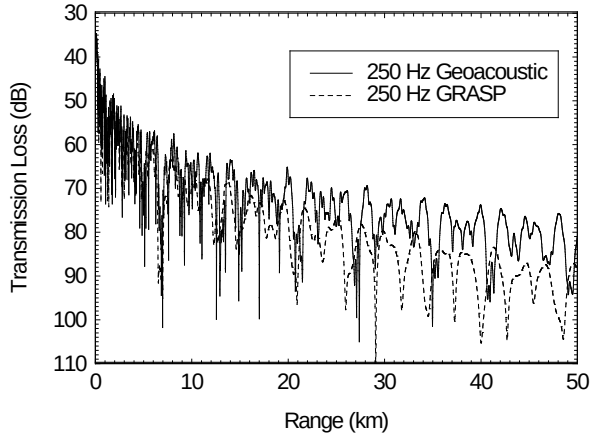

Figure 11 *TL* for Rottnest Shelf, 250 Hz, sound speed gradient – 0.04 s^{-1}

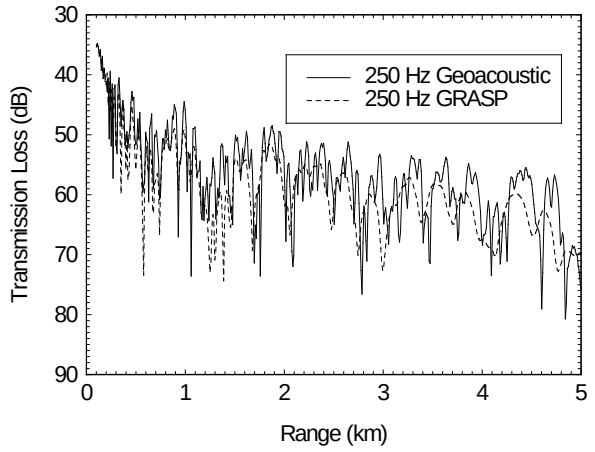

Figure 12 *TL* for Rottnest Shelf, 250 Hz, sound speed gradient –0.04

Figure 11 shows that the mean level of *TL* is sensitive to changes in bottom loss, but that the short range *TL* is less sensitive, as there is insufficient range over which the bottom can exert an influence. It is noteworthy that Figure 12 shows that the features of the phase coherent *TL* are still accurately predicted by the MOD inversion technique.

Conclusions

From the work presented above, it does appear that the MOD algorithm for the inversion of seafloor properties gives values of seafloor reflectivity for the Rottnest Shelf region which are in reasonable agreement with available geophysical data. Further, the MOD algorithm is shown to be robust to changes in source to receiver range, for small range values. Also, an air gun sound source, such as used by CMST, does appear suitable for use with the MOD technique.

If the reflectivity data inverted by the MOD technique are close to the actual values, it does appear that both long range and short range transmission data may be determined using that input data. With strong downward refraction, however, small errors in seafloor reflectivity do result in significant differences in long range transmission prediction.

References

1. Jones, A. D.; Clarke, P. A.; Bartel, D. W. and Sendt, J. S. “Transmission Loss inferred from a seafloor database – comparison with measured data”, 2000, Proceedings of UDT Pacific 2000, Darling Harbour, Australia, 7-9 February

2. Jones, A. D. and Bartel, D. W. “Spectral Variability in a Shallow Water Environment”, 1998, Proceedings of UDT Pacific 98, Darling Harbour, Australia, 24-26 February

3. Jones, A. D.; Bartel, D. W.; Clarke, P. A. and Day, G. J. “Acoustic Inversion for Seafloor Reflectivity in Shallow Water Environment”, 2000, Proceedings of UDT Pacific 2000, Darling Harbour, Australia, 7-9 February

4. Chapman, N. R. and Lindsay, C. E. “Matched-Field Inversion for Geoacoustic Model Parameters in Shallow Water”, October 1996, IEEE Journal of Oceanic Engineering, Vol. 21, No. 4, pp 347-354

5. Porter, M. B. “The KRAKEN Normal Mode Program”; 1995; SACLANT Undersea Research Centre

6. Mitchell, B. “GRaphical Acoustic Sediment Predictor (GRASP) using Spectral Variability”, AMRL Vacation Scholar Thesis, February 2000

7. Duncan, A. and McCauley, R. “Characterisation of an Air-Gun as a Sound Source for Acoustic Propagation Studies”, 2000, Proceedings of UDT Pacific 2000, Darling Harbour, Australia, 7-9 February

Low Frequency Bottom Reflectivity from Reflection

Alexander Kritski[1] and Chris Jenkins[2]

[1]School of Geosciences, University of Sydney, NSW, [2] Ocean Sciences Institute, University of Sydney, NSW.

Abstract

Ocean bottom reflectivity has been studied for a simple layered sedimentary model at shallow depth. Reflections from the bottom were determined from standard geophysical reflection data. The plane wave reflections have been obtained as bottom loss (-20log|R|) from the available reflection seismic data. Bottom loss estimated in the 10-250 Hz band are presented as functions of frequency and of angle of incidence (relative to horizontal) and are shown to depend on the properties of the layered ocean bottom. In the bottom loss results, a critical angle is observed which decreases from about 39° at 40-10 Hz to about 20° at 240 Hz. This critical angle is most likely associated with the reflection of compressional waves near the ocean-sediment interface. The frequency dependence indicates that the lower frequencies interact with a deeper sediment layer of greater sound speed than the near-surface sediments. At about 59° there is an indication of another critical angle, possibly due to reflection from the substrate beneath the sediments. The significance of these results is that reflection seismic data can be used to derive inputs for naval sonar prediction models, especially in the frequency range of passive sonars.

Indroduction

Plane-wave reflection and refraction coefficients play an important role in the interpretation of acoustic data in modern marine seismology. These coefficients are generally based on the partitioning of energy at the interface between water and an elastic solid , and the result is the classical Rayleigh reflection and transmission coefficients that relate to the amplitudes of homogeneous incident waves and homogeneous reflected and refracted waves. For the case of an elastic solid, only two kinds of body wave can propagate and the particle motion is either parallel or perpendicular to the wave normal depending on whether a dilatational or shear wave is being considered. The angles of incidence and emergence are related by Snell's law and when one of the angles corresponding to a reflected or refracted wave increases to 90^0, a "critical" angle of incidence is defined for the generating wave.

When the angle of incidence of the generating wave exceeds a critical angle, the body wave which has become parallel to the interface no longer propagates and an interface wave is necessary to satisfy the boundary conditions. This wave decays exponentially away from the interface and its phase velocity is determined by the phase velocity of the generating wave projected onto the interface.

A more realistic model of the sediments would include a viscous-elastic or porous viscous-elastic material rather then the elastic one. In this case there are fundamental differences in the response at the interface between water and sediment or/and between two different kinds of sediments. Reflected and refracted waves are rather inhomogeneous in the sense that the wave amplitudes vary in planes of constant phase and the trajectory of particle motion is elliptic in shape rather than parallel or perpendicular to the direction of the wave normal [8].

The reflectivity data used in the present work have been collected in experiments where receivers were located near the sea surface [1]. The geophysical information related to the all kinds of inhomogeneous waves including interface waves is not available at the receiving point as only compressional waves can propagate in the water column to reach the receivers.

In this work the simple layered model has been suggested. The ocean is described by a constant sound speed half space, the bottom is described by a near surface sediment layer (200-300m depth) of constant sound speed gradient overlying another solid half space (low sediments, and then crust) of constant sound speed.

The results of the reflectivity estimation, however, indicate that reflection coefficients become frequency dependent in a quite complex way. This effect might indicate viscous losses in the sediment layer or/and multilayering. Thus the bottom reflectivity measured from the interface for a simple model (homogeneous sediment layer with constant speed and attenuation) indicates that the properties of near-surface sediments fit a viscous-elastic model.

Seismic reflection experiment

Experimental setup

The reflection seismic data used in these studies was collected from North West shelf area in the North Bonaparte Basin which situates between NW margin and the Timor Trough (Australian Geological Survey Organisation, Timor Tie survey 118/8). The approximate depth in this area is about 150m. The range of frequencies: 10 Hz up to 240 Hz. The high frequencies are limited due to the experiment conditions. A total of 272.1 km of data were acquired along transect. The data contains 584 shot points and 116800 traces. Detailed information on the geometry and method of the experiment is presented in *Kritski & Jenkins* [7].

The bottom reflectivity data used in this work have been collected during the standard seismic reflection survey carried out with one ship (Figure 1).

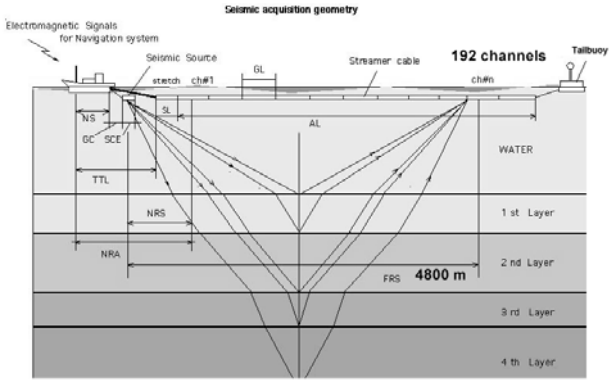

Figure 1. Seismic acquisition geometry.

The ship was towing an array of hydrophones which was suspended from a free floating tailbuoy at a depth of about 12 m. The total active section length of the array was 4800m with 192 active channels (Shot interval - 50m). Taking into account the geometry of the data collecting experiment covers the region of grazing (i.e., incidence) angles from 10^0-77^0. Calculations were carried out assuming that the bottom was a horizontally stratified medium.

Source data

The seismic reflection data we analysed in this work was obtained using a sleeve gun array (capacity 50 litres, 3000 cu in) [1]. Further details of which are given in *Kritski & Jenkins* [7]. Analysis of the far field signature of the gun and its spectrum are presented in *Kritski & Jenkins* [7]. The duration of the pressure pulse is about 96 ms. The source spectrum has useful components between 35 and 250 Hz.

Aside from using the far-field source signature in the calculations, no allowance was made for effects of seasurface reflection on the water-borne signal. A more detailed treatment would have required special inputs on sea state and deducted acoustic prediction modelling. Signal-to-noise ratio for the data was estimated from non-shot interval of each record. The average S/N ratio was 20–25 dB.

Geophysical data

Geopgysical data used in our studies are typical Common Shot Point (CSP) data. They are of variable quality, being subject to several types of noise of different origins [4,6]. Reflectors are recognised in these plots by their hyperbolic traveltimes. If the reflecting surface is horizontal then the apex of the reflection hyperbola is situated at zero offset. On the other hand if it is a dipping interface, then the reflection hyperbola is skewed in the undip direction (Details in [7]).

Figure 2 shows a variety of wave types at shallow depth (up to 2 sec two-way travel time) which corresponds to arrivals from the sedimentary structure.

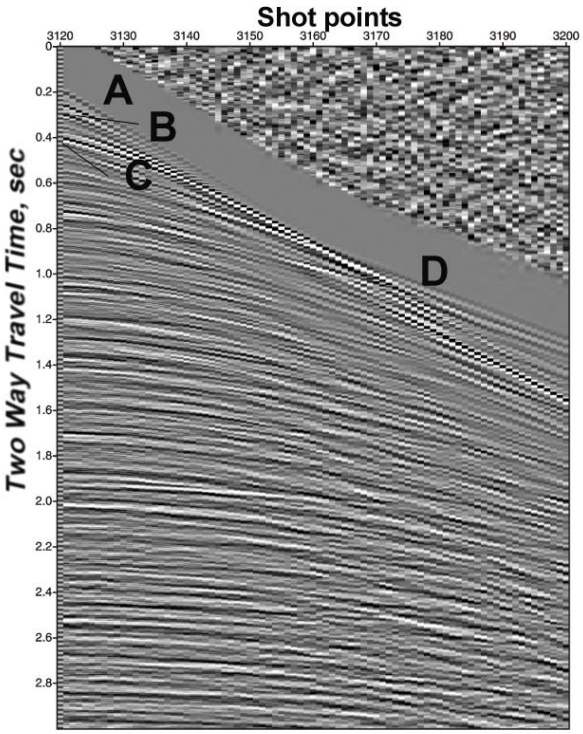

Figure 2 Example of Shot Point data

Direct arrivals *A* are significantly suppressed by receiver arrays in the field. *B* represents water bottom reflection on short-offset traces. Note the shallow reflector *C* and associated refraction arrival *D*. At about 0.7sec another reflector is seen. Much of the energy between 0.8 and 2 sec is most likely multiples associated with *B*, *C* and *E* arrivals. Linear noise (possibly cable noise) and low frequency noise (possibly propeller noise) appear in the deeper portions of the records.

Methods and programs for the reflection data reading and observations on the nature (sufficiency, quality) are presented in *Kritski, A. & Jenkins* [7].

Sesmic acoustic data

The data from three seismic shots were used for initial calculations. A 100000 traces were extracted form each individual shot, which allows to cover the region of grazing (i.e., incidence) angles from 10^0-77^0.

Signals recording amplitudes are normalized for source energy and spreading losses. For homogeneous medium without attenuation wave amplitudes decay as *(1/r)* where is the distance; energy decays as *1/(r^2)*. For a layered medium, amplitude decay can be described approximately by *1/[v^2*t]*, where *t* – two way travel time, *v* – average velocity of reflection. Thus, the gain function for geometric spreading is:

*g(t)=[v*v(t0)]^2[t/t(0)]*,

where v(0) is the velocity value at specified time t(0).

The bottom reflected signal was obtained by windowing the seismic traces from each shot so as to select the first arrival that interacted only with the ocean bottom. Time window (70ms for long offset)s gives ~70m for the depth of interaction. The multiple filter technique was applied also to analyze seismic traces in terms of frequencies and arrival times [3] - as illustrated in Figure 4.

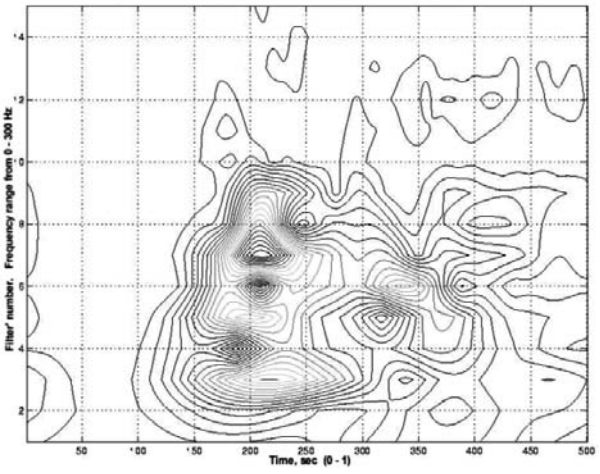

Figure 3. Example of multiple filter technique. Signals as a function of both time and frequency. The Y axis is in terms of Gaussian Frequency Window Number

The calculation uses a sequence of overlapping frequency windows, each window being a short frequency range compared to the whole spectrum range [3]. An amplitude spectrum was calculated from the windowed signals, using each window in turn. A Gaussian window function was used. The results are presented on a rectangular grid as a function of the time and of frequency (center of the each frequency window); the spectrum from each window contributes a column to the grid. The sonograms are obtained by contouring the resulting grid. The energy resulting from the sea floor reflection extends uniformly across the sonogram, at zero time, showing that the sea floor is almost equally reflective across the frequency range. The bottom reflections can be readily identified in the sonogram. The pattern of the sonogram after the first arrivals is complex. Each trace record is shifted in time so that the first arrivals in the sonograms are shifted as well. Each trace record has been filtered then using a frequency window calculated from the multiple window analysis for the first bottom arrivals.

Bottom loss calculations

The bottom loss

The organization of seismic reflection records allows separation of the water arrivals and reflections from the bottom at close offsets. At large offsets water arrivals were estimated assuming linear propagation through water column (initial water signals have been estimated from close offsets were water arrivals can be geometrically picked up from the reflection record section).

The bottom reflected signal was found by using time windowing of the first bottom arrival to select the first arrival which interacted only with the ocean bottom. The length of the window varied from 130ms at the closest ranges to about 70ms at large offsets.

The bottom reflection loss was determined from the measured propagation loss of the bottom bounce paths by subtracting an estimate of the water column loss along the paths. In this approach, the estimates of water column propagation loss were calculated by ray theory, assuming specular reflection with no loss from a single interface at the ocean bottom. The method is described by the expression [2]

$$BL = (H - Hcd + m)/n$$

Where *BL* is the bottom loss (in dB), *H* and *Hcd* are the measured bottom bounce propagation loss and calculated water column loss along the path; n is the order of the bottom loss bounce paths (*n*=1 in our case). The first bounce bottom only was used. The *m*(dB) correction is supposed to account for the number of first bottom interacting paths. These paths are associated with each order of bottom bounce. A random phase contribution from signals was assumed. No correction was made in this work as only the first arrival was taken into consideration.

The waveform used for the direct path arrivals was estimated from close range measurements of the acoustic source. This waveform was scaled using a sinx/x

interpolation to compensate for the effects of small variations in explosion depth observed between the generated direct path signal and the received signal from each shot deployed in the propagation run.

Transfer Function

First of all we present bottom reflectivity in terms of a bottom transfer function, for number of traces from each shot (Figure 4a and 4b).

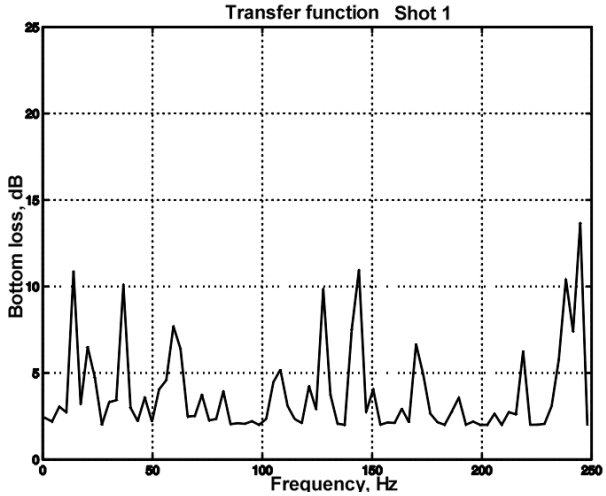

Figure 4a. Transfer function. Shot 1.

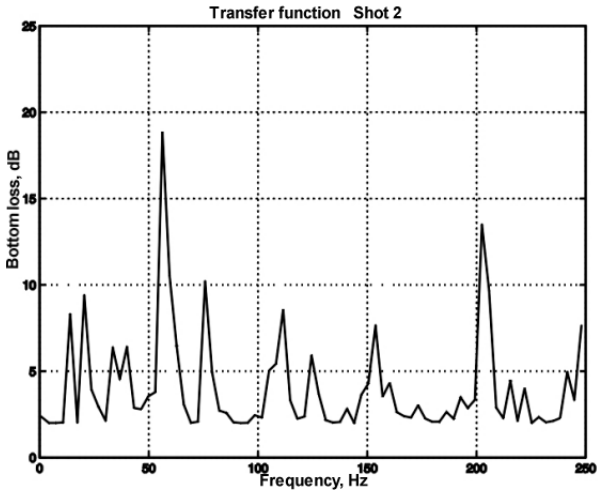

Figure4b. Transfer function. Shot 2.

The transfer function is formed from the ratio of the Fourier transform of the reflected signal to the Fourier transform of the incident signal [4]. By means of this formulation, the bottom loss can be expressed in the frequency domain as is shown in Figures 5a-5b for a 30^0 grazing angle. The rapid variations in bottom loss are characteristic of an interference phenomenon produced by reflections off multiple sub-bottom layers. The loss curve was obtained by reading the peak level output from the multiple filter.

Bottom loss

Bottom loss variations are presented as a function of grazing angle for different frequencies that cover the frequency range from 40 to 240Hz. The calculated reflection (bottom loss: $-20 \log |R|$) exhibits in general a complicated structure consisting of more or less regular sequence of peaks and dips.

The bottom reflection loss were calculated at frequencies 40, 80, 100, 140, 180 and 220Hz respectively for three different shots. Figure 5a, 5b and 5c show the bottom reflection loss versus grazing angle at frequencies 40, 80, and 220Hz respectively. Picks at these frequencies can be attributed to resonance phenomena of some sort. The distributions and widths of the resonance peaks contain the information about the interacting medium involved.

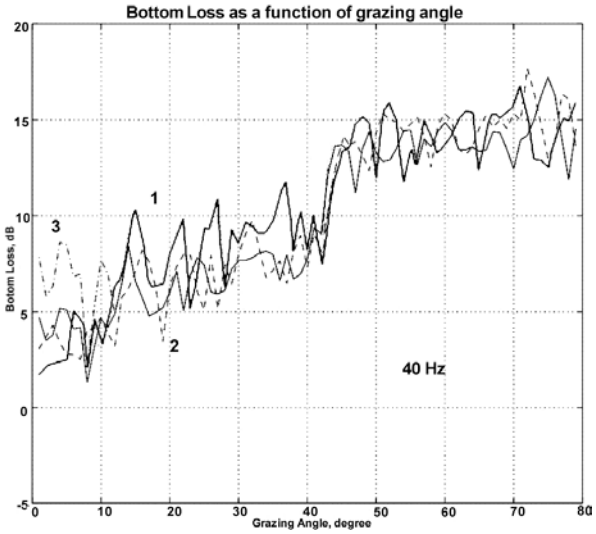

Figure 5a. Bottom loss a function of grasing angle calculated at 40 Hz

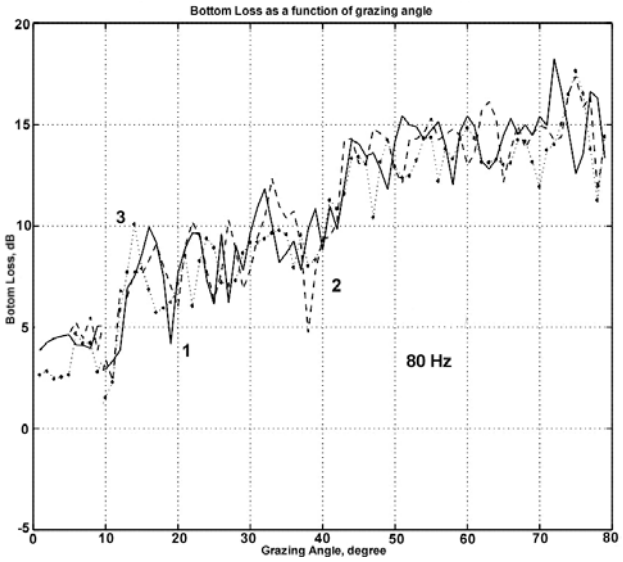

Figure 5b. Bottom loss as function of grazing angle, calculated at 80 Hz

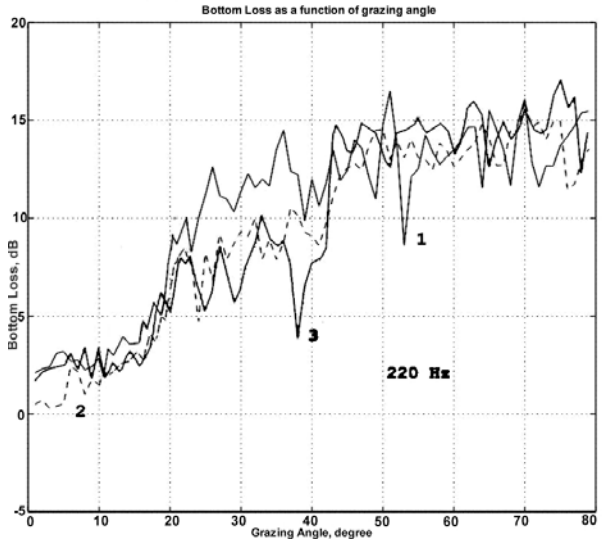

Figure 5c. Bottom loss as afunction of grazing angle calculated at 220 Hz

In the bottom loss results, a critical angle is observed which decreases from about 39^0at 40-10 Hz to about 20^0 at 220 Hz. This critical angle is probably associated with the reflection of compressional waves near the ocean-sediment interface. The frequency dependence indicates that the lower frequencies interact with a deeper sediment layer of greater sound speed than the near-surface sediments. At about 59^0 there is a small indication of another critical angle, possibly due to reflection from the substrate beneath the sediments.

Based on these observations, it appears that the bottom loss contains relevant information about the structure and properties of the interacting medium.

The cause of the unpredictable variations of bottom loss is probably fine-scale sub-bottom layering. Averaging of the bottom loss results along segments of the seismic trackline will probably smooth the variations.

Figure 6, 7 and 8 present a three dimensional surfaces that summarie *Bottom Loss* as a function of both grazing angle and frequencies for one shot.

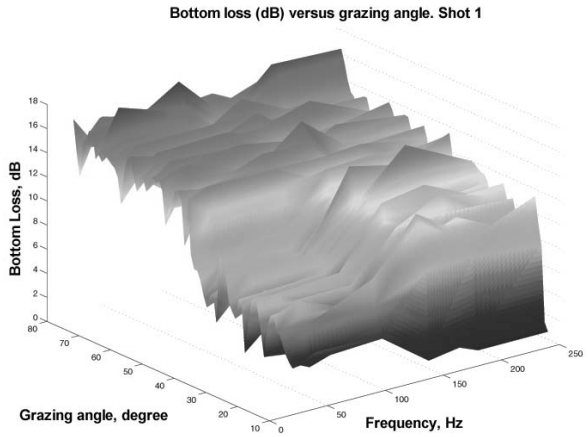

Figure 6. Three dimensional representation of bottom loss calculations as function of grazing angle and frequency for Shot 1.

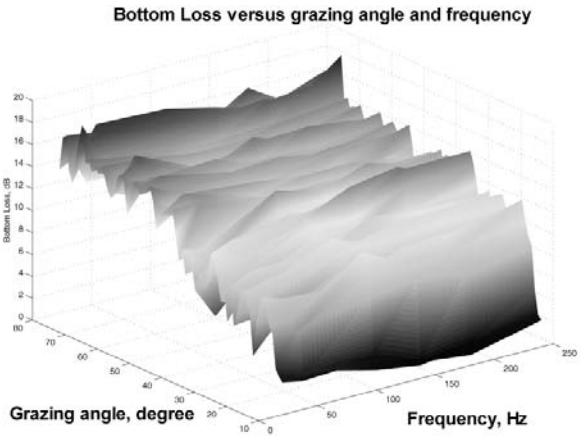

Figure 7. Three dimensional representation of bottom loss calculations as function of grazing angle and frequency for Shot 2.

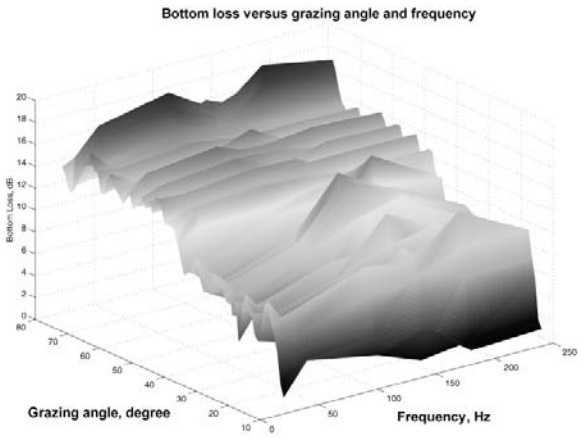

Figure 8. Three dimensional representation of bottom loss calculations as function of grazing angle and frequency for Shot 3.

Future steps

The next stage in development is to use the bottom loss structure to calculate some of the geoacoustic properties (velocities, porosities, attenuations) of the sediments, i.e. to solve the inverse reflection problem. Several smaller issues remain for additional work: the effect of the sea surface on far field source signature and the possibility of obtaining results for the very low grazing angles ($<10^0$) despite refraction effects.

Acknowledgements

The project was supported by the Defence Science and Technology Organization (DSTO) and the Australian Geological Survey Organization (AGSO). The authors thank Mike Sexton, Frank Brassil, Brandon Brown and Chris Pigram of AGSO for their cooperation and special efforts to help this project, and to AGSO for provision of the seismic reflection data.

References

1. AGSO, 1997. Reflection seismic data. Unpublished Technical Report.

2. Chapman, N.R., 1980. Low frequency bottom reflectivity measurements in the Tufts Abyssal Plain. In: Kuperman, W.A. & Jensen, B. (Eds) Bottom-interacting ocean Acoustics, New-York.

3. Dziewonsky, A., Bloch, S. and Lindsman, M., 1969. 'A Technique for the Analysis of Transient Seismic Signals'. Bull. Seism. Soc. Am., 59(1), p. 427-444.

4. Hanrahan, J.J. 1980. A perspective on bottom reflectivity and backscattering. In: Kuperman, W.A. & Jensen, B. (Eds) Bottom-interacting ocean Acoustics, New-York.

5. Spofford, C.W. Inference of Geo-Acoustic parameters from bottom-loss data. In: Kuperman, W.A. & Jensen, B. (Eds) Bottom-interacting ocean Acoustics, New-York.

6. Kritski, A. 1999. Extraction of Acoustical Properties of Sediments from Reflection Seismic Data: 1. Proposed Methods. Sydney University Ocean Sciences Institute Report, 85, 1-4.

7. Kritski, A. & Jenkins, C.J. 1999. Extraction of acoustical properties of sediments from reflection seismic data: 2. Data reading & display. Sydney University Ocean Sciences Institute Report, 86, 1-16.

8. Stoll, R.D. & Kan, T.K., 1981. Reflection of acoustic waves at the water-sediment interface. J.Acoust. Soc.Am., 70(1), 149-155.